UNIVERSITY OF NAPLES FEDERICO II

DEPARTMENT OF PHARMACY

PhD programme in Pharmaceutical Sciences

PEPTIDE BASED NANOFORMULATIONS FOR BIOMEDICAL APPLICATIONS

PhD student
ELISABETTA ROSA

Coordinator
Prof.
ROSARIA MELI

Tutor
Prof.
ANTONELLA ACCARDO

XXXV CYCLE (2020-2022)

ABSTRACT

Self-assembling short and ultra-short peptides and lipopeptides can act as building blocks for the construction of nano-architectures that find a potential application in different biomedical fields. These new materials arise from noncovalent bonds within and between molecules, including hydrogen bonding, metal coordination, hydrophobic, van der Waals, electrostatic and π-π interactions. Some of these peptide sequences are able to form hydrogels (HGs) that can be defined as networks of interacting hydrophilic molecules able to absorb high amounts of water and biological fluids. Through a submicronization procedure, HGs can be turned into nanogels (NGs), which are particles in the nano-range preserving the inner structuration of the HG they arise from, defined core, covered by a shell of surfactants. Thanks to their dimensions, making them able to exploit the Enhanced Permeability and Retention (EPR) effect, they can be considered useful tools for the delivery of Active Pharmaceutical Ingredients (APIs) in lesion sites. In this thesis, new peptide-based matrices have been proposed for three different biomedical scopes: i) tissue engineering, ii) delivery of drugs and iii) contrast agents for Magnetic Resonance Imaging (MRI) applications. Several peptide derivatives have been punctually designed and synthesized in order to satisfy the specific requests, and fully characterized through a series of spectroscopic techniques. Different strategies were used to prompt the self-assembling behavior, to improve the rheological response of the obtained matrices and to promote the encapsulation of drugs and contrast agents. Aromatic groups or alkyl chains were used to allow the hydrogel formation, and mechanical properties were increased by combining together different building blocks or by inserting cross-linkable entities. Electrostatic interactions between the carrier and the delivered molecules were exploited to help the loading. New formulation methods were tested and standardized for the obtainment of stable and

reproducible nanogel suspensions, which were used as reservoirs of drugs and contrast agents with the purpose of intravenous administration. The biocompatibility of the empty matrices was assessed *in vitro* and new insights were given on the internalization mechanism and cell specificity of peptide gelling nanoparticles. Tumor cell cytotoxicity assays were carried out to demonstrate the anticancer efficiency of Doxorubicin-loaded HGs and NGs and cell adhesion tests were used to detect the capability of the matrices to act as scaffolds for tissue engineering scopes. Also, *in vivo* studies were conducted to prove that peptide-based supramolecular contrast agents can be imaged by MRI technique.

A	ADNTs: *aromatic dipeptide nanotubes*
	ANS: *sulfonic acid ammonium salt*
	API: *Active Pharmaceutical Ingredient*
	APP: *amyloid precursor protein*
	Aβ: *amyloid β peptides*
C	CA: *contrast agent*
	CAC: *Critical Aggregation Concentration*
	CAV 1: *Caveolin 1*
	CD: *Circular Dichroism*
	CEST: *Chemical Exchange Saturation Transfer*
	CGC: *Critical Gelation Concentration*
	CR: *Congo Red*
	Cryo-TEM: *Cryo Transmission Electron Microscopy*
D	D: *diffusion coefficient*
	DCM: *dichloromethane*
	DIPEA: *diisopropylethylamine*
	DLC: *drug loading content*
	DLS: *Dynamic Light Scattering*
	DMEM: *Dulbecco's Modified Eagle Medium*
	DMF: *N, N-di-methyl formamide*
	DMSO: *Dimethyl sulfoxide*
	Dox: *Doxorubicin*
	DTNB: *5,5'-dithio-bis-(2-nitrobenzoic acid)*
E	ECM: *extracellular matrix*
	EDT: *ethanedithiol*
	EFS: *extracellular fluid space*
	EMA: *European Medicinal Agency*
	EPR: *Enhanced Permeability and Retention*
	ER%: *Encapsulation Ratio*
	E-TPGS: *d-α-tocopheryl polyethylene glycol 1000 succinate*
F	FBS: *fetal bovine serum*
	FCM: *Flow cytometry*
	FF: *diphenylalanine*
	FITC: *fluorescein isothiocyanate*
	Fmoc: *9-fluorenylmethoxycarbonyl*
	FRET: *Förster resonance energy transfer*
	FT-IR: *Fourier Transformed Infrared spectroscopy*
G	G': *storage modulus*
	G'': *loss modulus*
	Gd: *gadolinium*

Abbreviations

	Gd-AAZTA: *Gd(III) 6-amino-6-methylperhydro-1,4-diazepine-N,N',N'',N''-tetraacetic acid*
	Gd-BOPTA: *Gd(III) benzyl-oxy-methyl derivative of diethyltriamine pentaacetate dimethylglucamine salt*
	Gd-DOTA: *Gd(III) 1,4,7,10-tetrazacyclododecane NN'N''N'''-tetra-acetate*
	Gd-DTPA: *Gd(III) diethylenetriamine pentaacetate*
	Gd-DTPA-BMA: *Gd(III) diethylenetriamine pentaacetate-bis(methylamide)*
	Gd-EOB-DTPA: *Gd(III) ethoxybenzyl diethylentriamine pentaacetate*
	Gd-HP-DO3A: *Gd(III) 1,4,7-triscarboxymethyl-1,4,7,10-tetraazacyclododecane*
	GdL: *glucono-δ-lactone*
H	HAS: *human serum albumin*
	HEMA: *hydroxyethyl methacrylate*
	HFIP: *1,1,1,3,3,3-Hexafluoro-2-propanol*
	HG: *hydrogel*
	HLB: *hydrophilic-lipophilic balance*
	HOBt: *1-hydroxybenzotriazole*
I	ICP-MS: *inductively coupled plasma-mass spectrometry*
L	LMW: *low molecular weight*
	LVE: *linear viscoelastic*
M	MBHA: *4-methylbenzhydrylamine*
	MD: *molecular dynamics*
	Mn: *manganese*
	MRI: *Magnetic Resonance Imaging*
	MTS: *3-(4,5-dimethylthiazol-2-yl)-5-(3-carboxymethoxyphenyl)-2-(4-sulfophenyl)-2H-tetrazolium*
	MTT: *3-(4,5-dimethylthiazol-2-yl)-2,5-diphenyltetrazolium bromide*
	MW: *molecular weight*
N	NFS: *nephrogenic systemic fibrosis*
	NG: *nanogel*
	NMRD: *Nuclear Magnetic Relaxation Dispersion*
	NYS: *Naphthol yellow S*
O	O.D.: *optical density*
P	PAs: *peptide amphiphiles*
	PBS: *phosphate buffered saline*
	PCL: *polycaprolactone*
	PDI: *polydispersity index*
	PEG: *polyethylene glycol*
	PEGDA: *PEG diacrylates*
	PLA: *poly(lactic acid)*
	PLGA: *poly(lactic-co-glycolic acid)*
	PU: *polyurethane*

	PyBOP: *benzotriazol-1-yl-oxytris-pyrrolidino-phosphonium*
R	r_1: *longitudinal relaxivity*
	R_1: *relaxation rate*
	r_2: *transversal relaxivity*
	RES: *reticuloendothelial system*
	R_H: *hydrodynamic radius*
	RMSD: *root mean square deviation*
	ROS: *reactive oxygen species*
S	SAXS: *Small Angle X-ray Scattering*
	SEC: *size exclusion chromatography*
	SEM: *Scanning Electron Microscopy*
	SPAN® 60: *sorbitan stearate*
	SPAN® 85: *sorbitan trioleate*
	SPPS: *Solid Phase Peptide Synthesis*
T	TFA: *trifluoroacetic acid*
	ThT: *thioflavine T*
	TIS: *tri-isopropylsilane*
	TNB: *5-thio-2-nitrobenzoic acid*
	TWEEN® 60: *polyethylene glycol sorbitan monostearate*
	TWEEN® 85: *polyoxyethylenesorbitan trioleate*
W	W/O: *water in oil*
	WAXS: *Wide Angle X-ray Scattering*
	ζ: *zeta potential*
	τ_m: *exchange lifetime*
	τ_r: *molecular reorientation time*

1. GENERAL INTRODUCTION: SUPRAMOLECULAR CHEMISTRY AT THE SERVICE OF BIOMEDICINE.....1

1.1 NUTS AND BOLTS OF SUPRAMOLECULAR CHEMISTRY.....3

1.2 BOTTOM-UP APPROACHES TO BUILD NANOPARTICLES AND HYDROGELS.....4

1.3 AMYLOID PEPTIDES AS BUILDING BLOCKS.....8

1.4 FROM THE COMPREHENSION OF DIPHENYLALANINE STRUCTURAL ORGANIZATION TO NEW HYDROGELATOR.....10

1.5 Fmoc-FF HYDROGELS: STRUCTURAL MODEL AND PREPARATION METHODS.....13

1.6 PEPTIDE BASED NANOGELS.....16

1.7 OBJECTIVES OF THE PROJECT.....18

1.8 REFERENCES.....21

2. PEPTIDE-BASED HYDROGELS AND NANOGELS AS DRUG DELIVERY TOOLS.....25

2.1 **INTRODUCTION**.....27

2.1.1 The evolution of drug delivery technologies.....27

2.1.2 Enhanced Permeability and Retention (EPR) Effect as specific targeting strategy.....29

2.1.3 Supramolecular formulation for the delivery of doxorubicin anticancer drug.....30

2.1.4 Nanogels as innovative drug delivery systems.....32

2.2 **OBJECTIVES**.....33

2.3 **MATERIALS AND METHODS**.....37

2.3.1 Peptide synthesis.....37

2.3.2 Fmoc-FF nanogel formulation.....38

2.3.3 Formulation of empty hydrogels.....39

2.3.4 Formulation of hydrogels loaded with Dox or Doxil……40

2.3.5 Formulation of nanogels filled with Dox or FITC……..40

2.3.6 Dynamic Light Scattering (DLS) measurements……41

2.3.7 Nanoparticles Tracking Analysis (NTA) measurements……41

2.3.8 Circular Dichroism (CD) studies……42

2.3.9 Fluorescence measurements……..42

2.3.10 Confocal analysis……42

2.3.11 Dox release from hydrogels and nanogels……...43

2.3.12 Cell culture……...43

2.3.13 Cell viability evaluation by MTT assay……...44

2.3.14 Immunofluorescence Experiments……..44

2.3.15 RNA extraction and RT-PCR analysis……45

2.3.16 Cell cycle analysis……...……46

2.4 **RESULTS AND DISCUSSION**……47

2.4.1 Nanogel formulation methodologies……47

2.4.2 Fmoc-FF nanogel characterization……50

2.4.3 Cytotoxic effect of empty Fmoc-FF nanogel formulations on different cell lines……56

2.4.4 Fmoc-FF nanogels internalization mechanism……..59

2.4.5 HSA mediated caveolae saturation mechanism……62

2.4.6 Fmoc-FF nanogels selectivity toward MDA-MB-231 results from caveolin-1 overexpression……63

2.4.7 Formulation and characterization of Dox-filled hydrogels……..64

2.4.8 Formulation and characterization of Dox-filled nanogels……...67

2.4.9 Drug Release……69

2.4.10 Cytotoxicity assays for Dox and Doxil-loaded formulations……71

2.4.11 Determination of Dox loaded HGs and NGs cellular uptake by Immunofluorescence……..73

2.5 **REFERENCES**…….....75

3. PEPTIDE BASED SCAFFOLDS FOR TISSUE ENGINEERING APPLICATIONS……...……79

3.1 **INTRODUCTION**……....81

3.1.1 Tissue engineering: origin, principles and application……...……..81

3.1.2 Scaffolds for tissue engineering: characteristic and chemical composition……..82

3.1.3 Recently advances in cationic hexapeptides for tissue engineering applications……84

3.1.4 Co-assembly as new strategy to obtain hydrogels with enhanced rheological properties……...85

3.1.5 The intervention on the primary sequence can allow modulate the mechanical properties of the final hydrogel……....86

3.1.6 RGDS-containing lipopeptides for cultured meat applications……..87

3.2 **OBJECTIVES**……..87

3.3 **MATERIALS AND METHODS**……...92

3.3.1 Peptide Synthesis……93

3.3.2 Preparation of peptide solutions……...94

3.3.3 Preparation of pure and Fmoc-FF mixed cationic hydrogels……95

3.3.4 Preparation of mixed peptide/polymer hydrogels……..95

3.3.5 Preparation of FCFYFCF hydrogels……....96

3.3.6 Ellman's test……96

3.3.7 Molecular modeling and dynamics……96

3.3.8 Hydrogel swelling and stability studies……98

3.3.9 Circular Dichroism (CD) studies……99

3.3.10 Fluorescence measurements……..99

3.3.11 Fourier Transform Infrared (FTIR) spectroscopy….100

3.3.12 Dynamic Light Scattering (DLS)……...100

3.3.13 Congo Red (CR) assay……...101

3.3.14 Thioflavin T (ThT) assay……....101

3.3.15 Relaxometric studies……102

3.3.16 Scanning Electron Microscopy (SEM)……..103

3.3.17 Cryo Transmission Electron Microscopy (Cryo-TEM)……103

3.3.18 Wide Angle X-ray Scattering (WAXS)……..104

3.3.19 Small Angle X-ray Scattering (SAXS)……...104

3.3.20 Rheological studies……...……105

3.3.21 Naphthol yellow S encapsulation and release form peptide/polymer hydrogels……..105

3.3.22 Cell lines……106

3.3.23 Cell assays……106

3.4 **RESULTS AND DISCUSSION**……108

3.4.1 Fmoc-K and FmocFF-K peptides: synthesis and characterization……108

3.4.2 Gelation tests and HG structural and rheological characterization for cationic sequences alone…....112

3.4.3 Formulation of multicomponent cationic peptide/Fmoc-FF hydrogels…….....116

3.4.4 Structural, rheological and relaxometric characterization of multicomponent cationic hydrogels……...117

3.4.5 Cell viability assays for pure and mixed cationic hydrogels……...…128

3.4.6 Fmoc-FF/PEGDA mixed hydrogel formulation…...131

3.4.7 Water behavior in multicomponent peptide/polymer hydrogels……...132

3.4.8 Secondary structure, morphology and rheological analyses of Fmoc-FF/PEGDA mixed hydrogels…..135

3.4.9 Release of Naphthol Yellow S from peptide/polymer mixed hydrogels……143

3.4.10 Design, molecular modelling and dynamics of Cys-containing aromatic peptide sequences……..144

3.4.11 Aggregation studies for Cys-containing peptides……152

3.4.12 Formulation and characterization of FYFCFYF and PEG8-FYFCFYF based hydrogels……158

3.4.13 RGDS-containing lipopeptides: Investigation of secondary structure and CAC evaluation……164

3.4.14 Morphological and gelation evaluation of RGDS-containing lipopeptides……170

3.4.15 Cell viability studies for RGDS-containing lipopeptides……...…179

3.4.16 Structural and morphological characterization of cationic lipopeptides……183

3.4.17 Cell viability studies for cationic lipopeptides…...190

3.4.18 Hydrogelation test, structural and rheological characterization……192

3.5 **REFERENCES**…….....194

4. CATIONIC PEPTIDE FORMULATIONS FOR THE ENCAPSULATION OF MRI CONTRAST AGENTS……199

4.1 **INTRODUCTION**…….....201

4.1.1 Magnetic Resonance Imaging: principles and contrast agents……...……..201

4.1.2 Gadolinium-based T1 contrast agents……203

4.1.3 Strategies to improve the safety and the efficiency of gadolinium-based T1 contrast agents……208

4.1.4 Chemical Exchange Saturation Transfer MRI……..211

4.1.5 CEST-MRI contrast agents……212

4.2 **OBJECTIVES**……...…213

4.3 **MATERIALS AND METHODS**……214

4.3.1 Peptide Synthesis……..209

4.3.2 Formulation of peptide hydrogels loaded with Gd (III) complexes…...……...216

4.3.3 Formulation of peptide hydrogels loaded with iopamidol…...……217

4.3.4 Hydrogel stability studies……217

4.3.5 Scanning Electron Microscopy (SEM)……..217

4.3.6 Rheological studies……...…218

4.3.7 Formulation of peptide nanogel loaded with $[Gd(BOPTA)]^{2-}$……..…218

4.3.8 Dynamic Light Scattering (DLS)……..…..219

4.3.9 Circular Dichroism (CD) studies……...219

4.3.10 Relaxometric characterization……...…...219

4.3.11 Iopamidol release from hydrogels……...220

4.3.12 Cells culture……...220

4.3.13 Cells viability: MTT assay……..221

4.3.14 Animal models...……222

4.3.15 MRI and data analysis……...223

4.4 **RESULTS AND DISCUSSION**……224

4.4.1 Formulation and characterization of hydrogels loaded with Gd (III) complexes……224

4.4.2 Structural characterization of hydrogels loaded with Gd (III) complexes: SEM and Rheology……227

4.4.3 Hydrogel loaded with Gd (III) complexes relaxivity studies……229

4.4.4 Fmoc-K2+[Gd(BOPTA)]$^{2-}$) Nanogel: formulation and structural and relaxivity characterization……232

4.4.5 Formulation and characterization of hydrogels loaded with iopamidol……...234

4.4.6 In vitro release of iopamidol……236

4.4.7 Cell viability studies for hydrogels loaded with iopamidol……...…237

4.4.8 In vitro and in vivo imaging of Ac-K hydrogels by CEST-MRI……238

4.5 **REFERENCES**…….....241

5. **CONCLUSIONS**……...…245

5.1 PEPTIDE BASED NANOGELS: FORMULATION PROCEDURE, CELL INTERNALIZATION AND LOADING CAPABILITY……..247

5.2 PEPTIDE SYSTEMS FOR TISSUE ENGINEERING APPLICATIONS.....249

5.3 PEPTIDE BASED HYDROGELS AND NANOGELS AS SUPRAMOLECULAR CONTRAST AGENTS FOR MRI AND CEST-MRI APPLICATIONS.....254

5.4 REFERENCES.....256

6. APPENDIX.....257

7. PUBLISHED ARTICLES.....263

1. GENERAL INTRODUCTION

SUPRAMOLECULAR CHEMISTRY AT THE SERVICE OF BIOMEDICINE

Elisabetta Rosa | University of Naples Federico II | XXXV cycle

1.1 NUTS AND BOLTS OF SUPRAMOLECULAR CHEMISTRY

Supramolecular chemistry has developed as a versatile theme from a rational and systematic organization that knew its start in the 60s and represents even today a research area focusing the attention of many disciplines arising from the modern chemistry. The main reason of this big interest is firstly ascribed to the *"humans' attraction by the appearance of order from disorder"*, as sentenced by Whitesides and Grzybowski in 2002. [1] It has taken about a decade since the first reflections on the tendency of molecules to attract each other for Jean-Marie Lehn, in 1978, to propose the definition, which is widely accepted even today, of supramolecular chemistry as *"chemistry of the complex entities formed by the association of two or more species held together by non-covalent intermolecular forces"*. [2] The rise of an interdisciplinary field involving chemistry, physics and biology was so traced. The weak and reversible interactions between molecules, including water mediated hydrogen bonding, van der Waals interactions, metal coordination, π-π stacking, hydrophobic forces and electrostatic effects, have been so scrutinized under different perspectives. To clarify the mechanisms behind the self-assembly processes it is important to underline that they obey physical laws and can be either static *(S)* or dynamic *(D).* [1] Systems arising from *S* processes (like atomic, ionic or molecular crystals, lipid bilayers and globular proteins) present a global or a local equilibrium and, differently from the ones deriving from *D* self-assembly (bacterial colonies, actin filaments, histones to weather patterns and galaxies), they do not need dissipation of energy to maintain their organization. According to this, the building of ordered objects in static conditions may require energy, but, after their formation, stability is granted. Molecular self-assembly can be identified as a static and spontaneous process linked to the minimization of Helmholtz free energy ($\Delta F<0$), defined by *Equation 1.1*:

$$\Delta F = \Delta E - T\Delta S \qquad (1.1)$$

This may mean that an increase in the entropy (S) or a decrease in the internal energy (E) may occur during a spontaneous process. Therefore, even if, as already mentioned, self-assembly is perceived as a movement to "order" and even if the increase in entropy is generally attributed to an increased in "disorder", the paradox can be clarified taking into account these attributions are imprecise notions. Indeed, a high visible order can be associated with a high macroscopic disorder, and these two aspects grow proportionally. [3] By defining the total entropy as the contribution of three different components *(Equation 1.2),* which are the translational, the rotational (or orientational) and the vibrational ones, it is easy to infer that, when a self-assembly object is generated, the orientational entropy of the system decreases because the density is no longer uniform in orientation or position. However, this loss in entropy is escorted by a massive increase in translational entropy, since the available space for any aggregate raises.

$$S = S_{trans} + S_{rot} + S_{vib} \qquad (1.2)$$

1.2 BOTTOM-UP APPROACHES TO BUILD NANOPARTICLES AND HYDROGELS

Self-assembling materials with tailored properties can be opportunely designed and simply obtained through controlled processes starting from different and various building-blocks exhibiting the appropriate characteristics and chemical functional groups. In light of this, self-assembly phenomena are exploited to build bottom-up tools for many applications. Contrarily to top-down approaches, which consist into breaking down the bulk material into nanosized structures or particles, the bottom-up ones involve the building of the final nanomaterial from the bottom, molecule by

molecule and then cluster to cluster. These techniques allow to avoid the problem of the imperfection of the surface structure and refer to a clearer procedure in which less waste is produced. There are several examples of small building blocks simply offered by nature (like amino acids, [4] nucleic acids, [5] lipidic molecules [6]) giving rise to structures with increasing complexity degree, from a two-molecules interaction till the obtainment of the intricate cell membrane. Also, some natural modified molecules and metabolomic intermediates act as building blocks. [7] During the years, hundreds of synthetic compounds have been added to the list. Besides their composition, self-assembling materials can be characterized in relationship to their shape and size. Many nanostructures originate from organic matter and, thanks to their general nontoxic properties, are commonly proposed and used for the biomedical fields. [8] Among them, nanoparticles (NPs) with interesting features, (**Figure 1.1**) can be listed and described as follows:

1. Dendrimers are branched molecules with a tree-like nano-sized architecture, generally composed by a symmetric core, an inner shell, and an outer shell. Their surface presents many chains available to modification to perform specific functions. [9]
2. Micelles are composed by amphiphilic entities which polar region, once in a water solvent, faces the outside surface, whereas the nonpolar region forms the core. They are generally spherical, but other shapes can be accessed (such as ellipsoids or cylinders) through appropriate design and conditions. [10]
3. Liposomes are spherical vesicles with a lipid bilayer, most often composed by phospholipids. [11]
4. Nanocapsules are nanoscale shells made from biocompatible polymers. [12]
5. Nanofibers are fibers with a nano-sized diameter, controllable pore structures and high surface-to-volume ratio, which are mainly

obtained by natural polymers (collagen, cellulose, gelatin and polysaccharides such as chitosan and alginate) or synthetic polymers (like poly(lactic acid) (PLA), polycaprolactone (PCL), polyurethane (PU) or poly(lactic-co-glycolic acid) (PLGA)). [13]

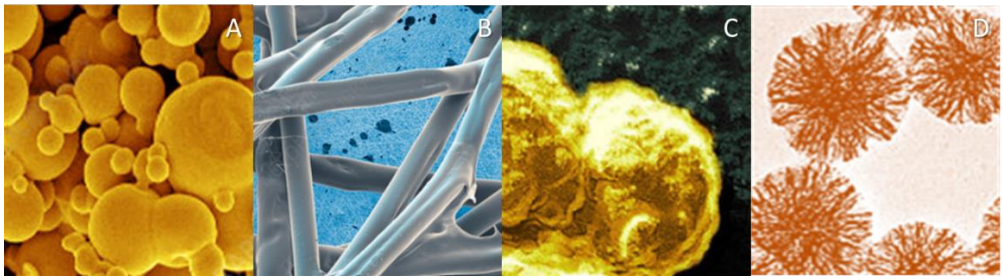

Figure 1.1: Colored SEM images of (A) liposomes, (B) nanofibers, (C) micelles and (D) dendrimers

A superior organization, derived from the mutual interaction between hydrophilic nanoparticles (generally nanofibers) is represented by hydrogels (HGs). Hydrogels are three-dimensional polymeric networks, which building blocks can establish interactions promoting high water retention without being solved. [14] The presence of hydrophilic groups allows to reserve large amount of water and confers swelling capability. The cross-linking process, occurring between the polymers to generate the final architecture, permits to avoid dissolution and can be either chemical or physical. (**Figure 1.2**) Chemical cross-linking derives from the instauration of covalent bonds, and it can so also be defined as "permanent". The physical cross-linking is a consequence of the self-assembling interactions previously described to be reversible (non-covalent). These last processes avoid the use of cross-linking agents, thus allowing a higher biocompatibility and low or non-toxic performances. The first example of a hydrogel has been provided by Wichterle and Lim, who produced crosslinked hydroxyethyl methacrylate (HEMA) HGs, more than 60 years ago. [15] From that moment, the

knowledge about this kind of structures has known a fast spread, till leading to invention that we now take for granted, like contact lenses, and HGs still focus the attention of many research groups, exploiting them for different purposes. Many advantages, like self-healing properties, biocompatibility, stimuli responsiveness and/or injectability, may be offered by these matrices to be used in biomedicine, [16] 3D-printing, [17] sensors, [18] and ion exchange. [19]

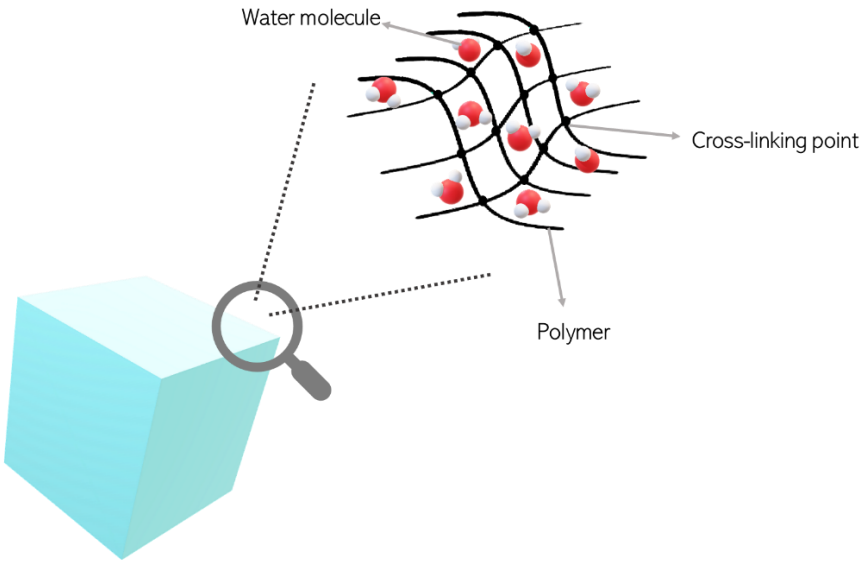

Figure 1.2: Schematic representation of the hydrogel inner organization

Hydrogels can be composed by different types of polymers, including gelatin, [20] hyaluronic acid, [21] chitosan, [22] collagen, [23] alginate [24] and dextran. [25] Polymers based on ethylene glycol, [26] ε-caprolactone, [27] vinyl alcohol [28] and hydroxyethyl acrylamide [29] have also been used to create hybrid matrices.

1.3 AMYLOID PEPTIDES AS BUILDING BLOCKS

Short peptides (number of amino acids ≤20) have also been proposed as building blocks for the development of materials. Peptide derivatives exhibit the great advantages to be biocompatible, biodegradable ad generally non-immunogenic. [30] Moreover, they can be really versatile since the modification of amino acids alternation and composition within the monomer can significantly affect the chemical features and, in turn, the interaction pathways. The morphology of the aggregated object strictly depends on the side chains' functional groups and sequence length. The first example of a peptide-based supramolecular nanostructure was given by Ghadiri and co-workers in 1993. [31] A cyclic peptide, containing residues in alternate configurations (D and L) was used as monomer undergoing stacking phenomena leading first to a flat β-sheet conformation, and then to hollow cylindrical nanotubes. Today, different types of peptides, including cyclic, [32] amphiphilic, [33] dendritic, [34] surfactant-like [35] and aromatic [36] ones, are exploited as building blocks to generate supramolecular assemblies. A big push for peptides use is the easy procedures required for their obtainment, mostly represented by Solid Phase Peptide Synthesis (SPPS) exploiting Fmoc/tBu strategies. According to this, the sequence is gradually built by consecutive couplings on a solid support, a resin, modified by appropriate handles, which enable anchoring the C-terminal of the first amino acid by ester or amide bonds, thus allowing the synthesis of peptide acids and peptide amides, respectively. Amino acids side chains are generally protected with groups which removal occurs in orthogonal conditions with respect to the ones required for the deblock of the Fmoc (9-Fluorenylmethoxycarbonyl) protecting the N-terminal of each residue (**Figure 1.3**). [37]

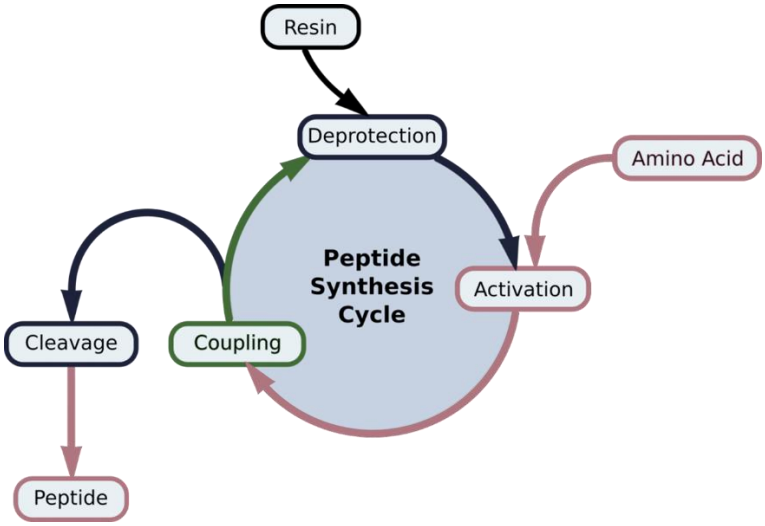

Figure 1.3: Schematic representation of SPPS steps

Some synthesized short peptides have the propensity to self-assemble *in vitro* into fibrils very similar to the ones found in amyloid diseases. [38] Amyloidosis is the name for a group of rare, serious diseases caused by protein misfolding generating, in various organs and tissues, abnormal protein, called amyloid from its propriety to react with iodine, similarly to starch (amylum in Latin). Protein misfolding can result from different processes such as mistranscription, [39] gene alteration and mutation [40] or mistranslation [41] and triggers the development of pathologies like Alzheimer, Parkinson, diabetes, β2m-amyloidosis, carpel tunnel syndrome, destructive arthropathy, transmissible spongiform encephalopathy and hemodialysis related amyloidosis. [42] Amyloidosis share a similar etiology characterized by extracellular deposition of insoluble fibrils of protein-based materials with low molecular weight. [43] Amyloid β peptides (Aβ), the main component of plaques in Alzheimer's disease, are peptides of 36-43 amino acids generated from amyloid precursor protein (APP) by sequential proteolysis. [44] During this process, many peptides with different C-termini are formed, among which Aβ (1-40) and Aβ (1-42) are

the most common. This last is the most hydrophobic and most amyloidogenic one and even its central sequence ^{16}KLVFFAE^{22} is known to form amyloid on its own, and probably generates the core of the fibril, being responsible for cross β formations. [45] Lately, Gazit group pointed out that the nanostructures originated by the single diphenylalanine (FF) dipeptide, occupying the 19-20 positions of Aβ (1-42), shares many functional properties with amyloid assemblies, [46] including the intrinsic luminescence features, the binding of amyloid-specific dyes, mechanical rigidity and the production of reactive oxygen species (ROS). The structures arising from FF self-assembly are ordered and discrete aromatic dipeptide nanotubes (ADNTs). The study suggested that the FF sequence represents a highly simplified model that reflects the structural, biophysical and biochemical properties of amyloid structures, [47] being the first ultra-short and all-aromatic dipeptide related to fibrils formation. From that moment, FF dipeptide has become the progenitor of a new class of simple building blocks with supramolecular aggregative behavior.

1.4 FROM THE COMPREHENSION OF DIPHENYLALANINE STRUCTURAL ORGANIZATION TO NEW HYDROGELATOR

By X ray crystallographic studies, two types of interactions were recognized as the driving forces at the basis of supramolecular phenomena leading to the generation of FF ADNTs: π-π interaction (between phenyl rings) and hydrogen bonding (that engage backbone terminals). [48] A hierarchical model for FF dipeptide, based on its peculiar arrangement of monomers in aqueous media, was proposed as a consequence of molecular dynamics algorithms, supported and confirmed by X-Ray diffraction. [49, 50] While, in vacuum, the simulated monomer configuration suggests the two phenyl rings located on different sides of the peptide backbone, in polar

environment, the two side chains are constricted in the same face of peptide backbone with an unusual torsion dihedral angle centered at 0°. This anomalous configuration is accessible thanks to repulsion effects occurring between the hydrophobic groups and the aqueous media, which increase the total entropy of the system. A hydrophilic interface, undergoing H-bonding, and a hydrophobic interface, undergoing π-π interactions, are formed. By assuming this conformation, six monomers can organize in a cyclic hexamer (**Figure 1.4**) with a Van der Waals diameter 9.2 Å. [51] Hexamer can then pack into a hexagonal peptide matrix in which hydrophobic groups are disposed inside the wall. The hydrophilic groups of the backbone face the central cavity. The whole structure, growing in one dimension, forms the nanotubes.

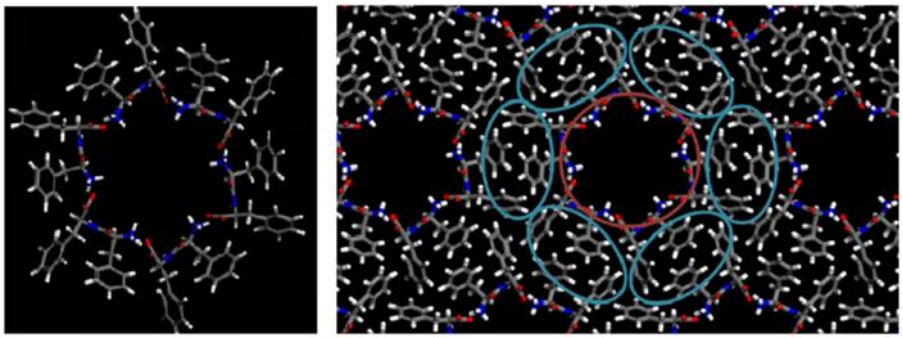

Figure 1.4: The cyclic hexamer, formed by six homopeptides, generate a peptide matrix in which a hydrophilic (red circle) and staking region (blue circles) can be recognized.

Following the aggregative process till larger scales, microsized hollow tubular structures forms from bundles of nanotubes. The modification of the FF motif has led, during the years, to the obtainment of many other ultra-short peptides able to generate nanomaterials with different chemical and structural properties. [52] In 2006, Ulijn and Gazit's groups [53,54] simultaneously discovered that, by leaving the N-terminus of the dipeptide capped with the Fmoc protecting group, ultrastructure and dimensions

extremely similar to the amyloid fibrils could be obtained. Fmoc-FF (**Figure 1.5**) became one of the most studied peptide monomers because of its ability to aggregate in stable self-supporting hydrogels at pH values compatible with physiological applications, including tissue engineering and drug delivery. Additional applicative areas are, as follows: chemical catalysis, nanoreactors development, optical engineering, wound treatments, ophthalmic preparations, energy harvesting, antifouling, and biocompatible coating applications, optoelectronics, potential immuno-responsive agents, and absorbents systems for oil/water separation. [55]

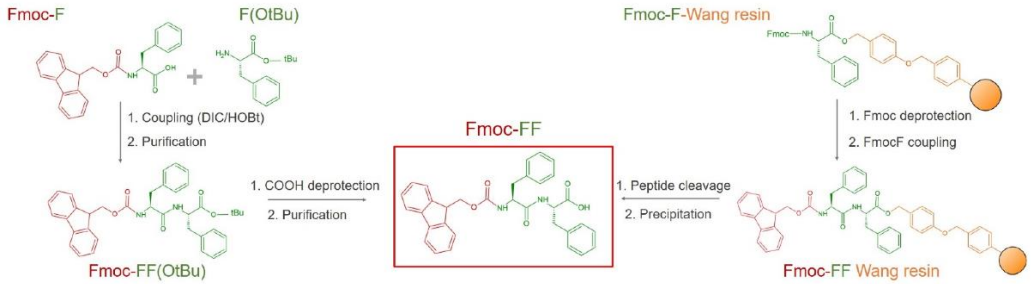

Figure 1.5: Scheme for the synthesis of Fmoc-FF (red rectangle) using liquid phase strategy (on the left) and solid phase peptide synthesis (SPPS) on the right. DIC: N,N′-Diisopropylcarbodiimide; HOBt: 1-Hydroxybenzotriazole.

The interest aroused by this simple building block over the years is ascribed to its chemical accessibility, biodegradability, biofunctionality and the possibility to adopt specific secondary, tertiary, or quaternary architectures. [56] Moreover, by simply modifying the gelation kinetic and other parameters (like pH, temperature, and solvent) structural and functional properties of the final matrix can be opportunely tuned.

1.5 Fmoc-FF HYDROGELS: STRUCTURAL MODEL AND PREPARATION METHODS

The first aggregation model for Fmoc-FF was proposed by Uljin and co-workers in 2008. [57] Structural characterization by Circular Dicrohism (CD) and Fourier Transformed Infrared spectroscopies (FT-IR) provided the evidence of an anti-parallel β-sheets arrangement of the peptide building blocks and anti-parallel π-stacking of the fluorenyl groups. (**Figure 1.6**)

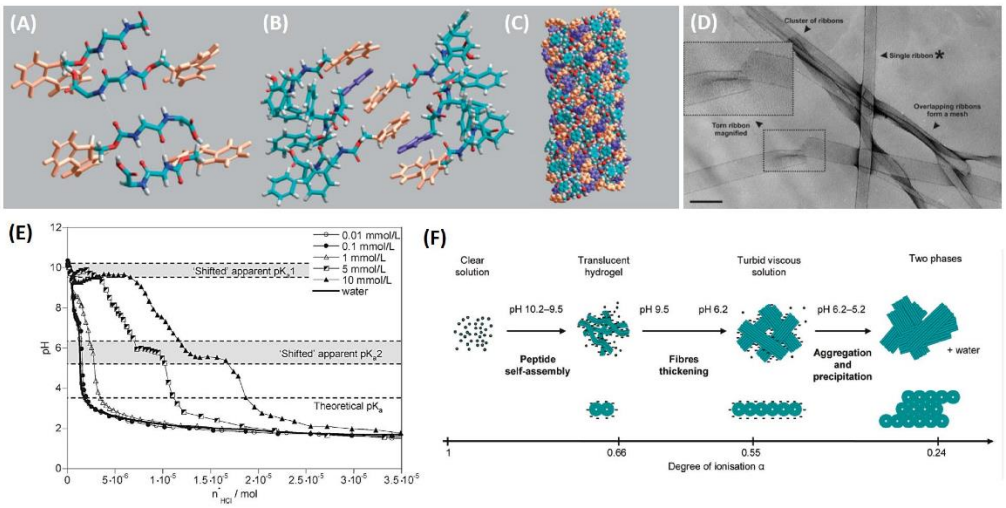

Figure 1.6: Structural model of Fmoc-FF peptides. (A) Dipeptide copies are arranged into β-sheet with an antiparallel orientation of β-strands. (B) π-stacked pairs due to the interlocking of fluorenyl groups from alternate β-sheets. (C) The final model obtained by energy minimization. In the model Fmoc and the phenyl groups are coloured in orange and in purple, respectively. (D) Transmission electron microscopy of Fmoc-FF xerogel (scale bar = 500 Å); the ribbon asterixed by authors was selected for other morphological analysis. (E) Titration curves of water and Fmoc-FF samples at different peptide concentrations (0.01, 0.1, 1, 5, and 10 mmol/L). (F) Mechanism proposed to explain the formation of Fmoc-FF aggregates as consequence of the pH decrease.

The dichroic signature of the fluorenyl group in disassembled systems such as Fmoc-Phe, is characterized by two bands at 307 nm and below 214 nm,

without contribution in the far-UV region. The CD characterization of Fmoc-FF gels, on the contrary, shows a negative peak centered at 218 nm, consistent with a β-sheet structure, and a signal in the range of 304–308 nm, attributed to the π→π* transition in the fluorenyl-moiety too. Moreover, two other CD prints (a local maximum at 192 nm and a minimum at 202 nm) are indicative for α-helix structure. FT-IR analysis supported the predominant β-arrangements of Fmoc-FF gels, which was shown to give rise to two peaks in the amide I region (1630 and 1685 cm^{-1}), compatible with an antiparallel organization of the peptides. By starting from this knowledge, the model of a nanocylindrical structure with an external diameter of ~3.0 nm (**Figure 1.6C**) was proposed by the authors. The nanostructure arose from the interlocking through lateral π-π interactions of four twisted anti-parallel β-sheets. These fibrils, forming J-aggregates, were then shown to be subjected to a further lateral self-assembly under specific pH conditions, resulting in large flat ribbons, as detected by TEM microscopy (**Figure 1.6D**). The diffraction shown by the scattering pattern of the Fmoc-FF-dried gel were found to be compatible with the structural organization of the proposed model. Saiani and coworkers studied the effect of pH on the Fmoc-FF self-assembly process. [58] By lowering the pH, the self-assembly of Fmoc-FF dipeptide is prompted as consequence of two apparent pK_a shifts (of ≈6.4 and 2.2 pH units, respectively) above the theoretical pK_a value (3.5) (**Figure 1.6E**). On the contrary, at more basic pH values, where the Fmoc-FF building blocks are in their ionized form, the self-assembly is mainly forbidden. Then, at pH 10.2–9.5, correspondent to the first pK_a, both protonated and non-protonated molecules begin to self-assemble into paired fibrils (**Figure 1.6F**). The further pH decrease up to a value of 6.2 causes a reduction in the fiber surface charge resulting in the formation of large rigid ribbons due to the lateral interactions of the fibers. Between pH 6.2 and 5.2 the second apparent pK_a shift is observed and a

further aggregation of the ribbons occurs. The properties of the final hydrogel material can be significantly affected by the formulation method. Three different approaches are generally exploited to produce Fmoc-FF HGs: (i) pH-switch method, (ii) solvent-switch method and (iii) catalytic method (**Figure 1.7**).

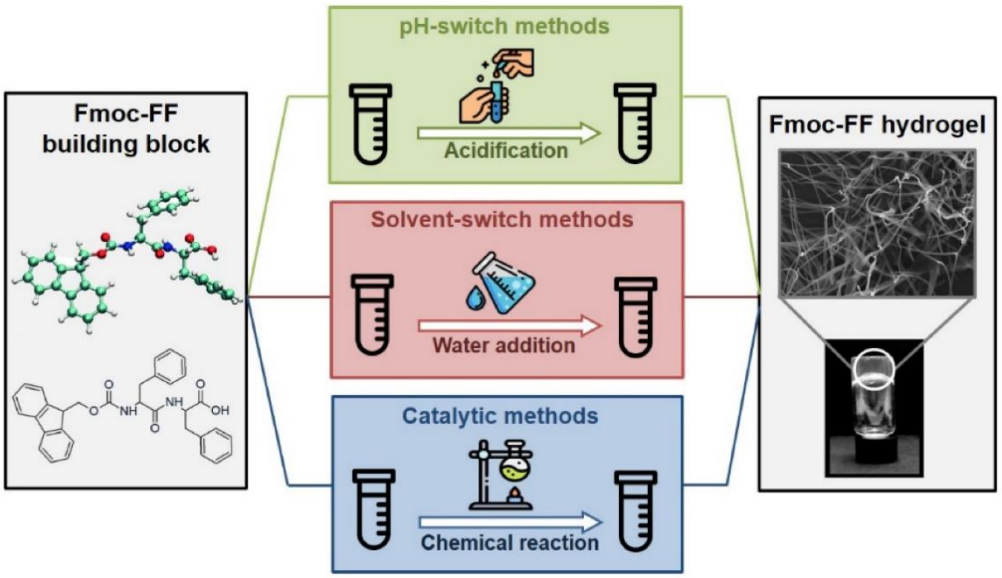

Figure 1.7: On the left, the molecular Fmoc-FF building block, reported both as 3D balls and sticks and as chemical formula. On the right, an inverted vial containing Fmoc-FF self-supporting gel and its TEM image. In the middle a schematic representation of three different methods (pH-switch, solvent switch, and catalytic one) commonly used for trigger gelation process.

The pH-switch method consists in the initial dissolution of the peptide in water at pH 10.5, ensuring the deprotonation of the C-terminal carboxylic acid, followed by addition of HCl to lower the pH and allow the progressive acidification leading to gelation. [57] It is worth nothing that basic conditions used by this methodology cause the cleavage of a part of the protecting group (<1%) and so a careful control of the pH is required.

Moreover, inhomogeneous gels are formed because of the kinetics of mixing being slower than the initial kinetics of fibrils formation and gelation. Consequently, it is difficult to reach a uniform pH in solution before the gelation process starts. Reproducible and more homogeneous hydrogels were obtained by the use of glucono-δ-lactone (GdL), allowing a decrease in the pH prompted by its slow hydrolysis to gluconic acid (≈18 h). [59] Beyond the pH-switch method, Fmoc-FF hydrogels can be also prepared with the solvent-switch method. This procedure consists in the peptide dissolution in an organic solvent at high concentration, followed by dilution in water which allows to trigger the gelation. Both dimethyl sulfoxide (DMSO) and 1,1,1,3,3,3-Hexafluoro-2-propanol (HFIP) are generally used as organic solvent. Both of them allow to obtain a storage modulus around 100 Pa. [54,60] A deeper investigation on the Fmoc-FF gelation process revealed that, after the addition of water to DMSO solution, the dipeptide initially self-assembles into a metastable non equilibrium state composed of spherical clusters of diameters of 2 μm, followed by a rapid rearrangement (below 5 min) into a fibrous network. After 4h of aging, the gel evolves towards a steady state comprising a highly uniform network of thin fibers with a mean diameter between 5 and 10 nm. Since these dimensions are smaller than the wavelength of the visible light, the gel appears transparent. [61] Finally, catalytic processes allow converting precursors unable to self-assemble into building blocks able to do. This conversion may occur thanks to enzymatic removal or hydrolysis of charged or steric groups that hinder the aggregation process. [62]

1.6 PEPTIDE-BASED NANOGELS

Fmoc-FF dipeptide has also represented the first sequence to be explored for the formulation of peptide based nanogels. [63] Nanogels (NGs) are

aggregates in the submicron range scale composed of an interior hydrogel-like network (core) stabilized by an external surfactant coating (shell). (**Figure 1.6**) They combine the advantages of traditional HGs, comprising high water accessibility a porous architecture able to confine molecules within, and nanosized particles. Indeed, their dimensions are compatible with intravenous administration. Moreover, the large surface area is accessible for multivalent bioconjugation. Thanks to their small size, nanogels are subjected to simple renal clearance, increased penetration through tissue barriers, and good stability for prolonged circulation in the blood stream. Analogously to HGs, nanogels can be prepared by the self-assembly of biocompatible and biodegradable polymers such as chitosan [64] hyaluronic acid, [65] and dextran [66] according to different methodologies including microfluidic, [67] micromolding [68] and photolithographic techniques. [69] However, most of these processes require extreme conditions of pH and temperature and some of them need crosslinking agents to promote the polymerization, thus not assuring a complete biocompatibility.

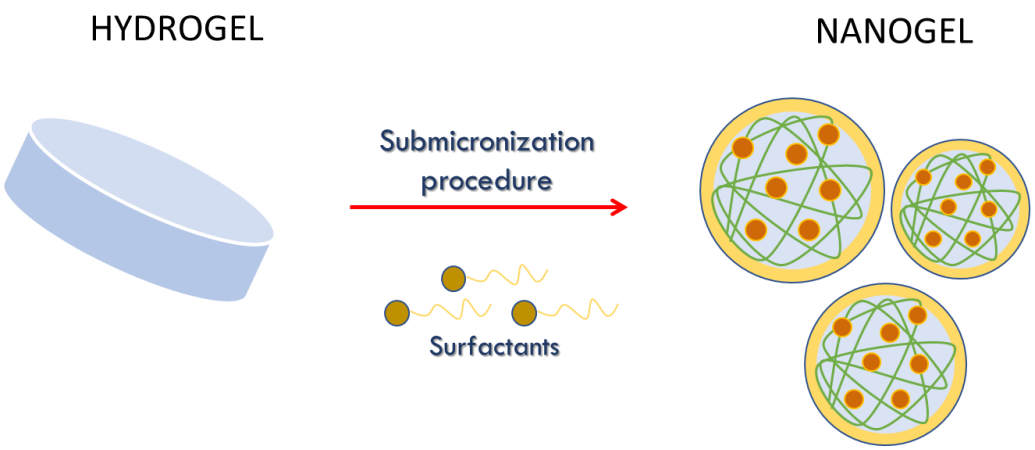

Figure 1.6: Schematic representation of nanogel obtainment through submicronization starting from a macroscopic hydrogel matrix.

In order to overcome these drawbacks, peptide-based nanogels could represent an innovative tool. Indeed, as previously mentioned, with respect to polymers, peptides exhibit several advantages such as high biocompatibility, biodegradability, non-immunogenic behavior and tunability.

1.7 OBJECTIVE OF THE PROJECT

In light of all these premises, the studies reported in this thesis have concerned the use of two types of systems based on self-assembling peptide sequences: hydrogels and nanogels. Short peptides, identified as building blocks for the hydrogel and nanogel formulation, have been initially designed, synthesized and characterized. Successively, the propensity of peptides to self-assemble and the aggregative behavior of the resulting supramolecular structures were investigated both in solution and at the solid state through a series of techniques, including Fluorescence, FT-IR, CD, UV-Vis spectroscopies. Their morphologies have been analyzed by the use of Scanning Electron Microscopy (SEM), Cryo Transmission Electron Microscopy (Cryo-TEM), Wide Angle X-ray Scattering (WAXS) and Small Angle X-ray Scattering (SAXS). Their ability to form hydrogels has been tested using different methods (including solvent and pH switch ones) and their mechanical behavior has been studied using rheological analyses.

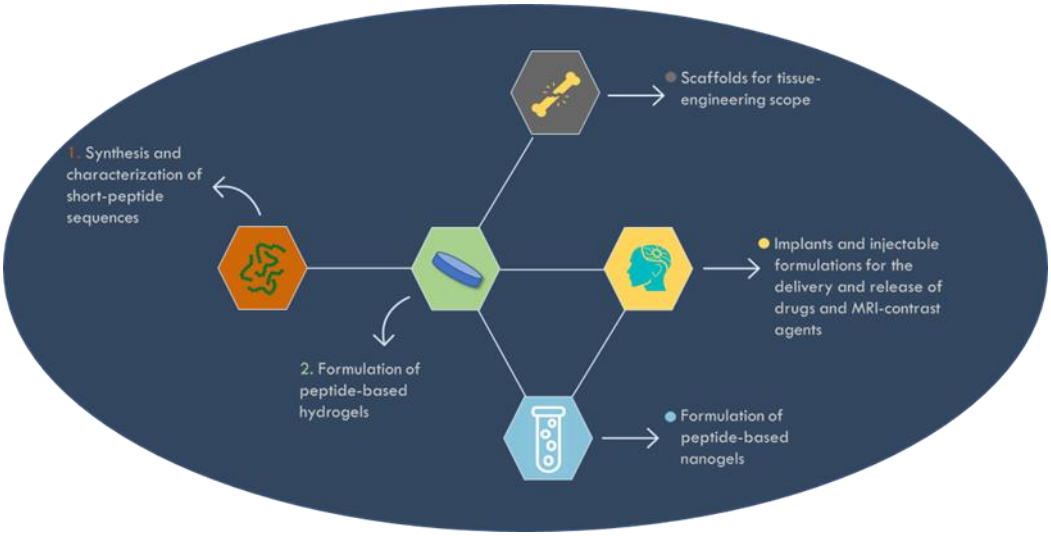

Figure 1.7: Schematic representation of the rationale followed for the obtainment of new gelling tools in the areas of tissue-engineering, drug delivery and MRI.

The obtained gel matrices have been used for three different scopes: i) tissue engineering, ii) delivery of drugs and iii) contrast agents for Magnetic Resonance Imaging (MRI) applications. Starting from some of these hydrogels, and by the use of new methods allowing the obtainment of reproducible and stable formulations, also peptide based nanogels have been tested and loaded with active pharmaceutical ingredients (APIs) to act both as drug reservoirs and supramolecular contrast agents (**Figure 1.7**). Details will be provided in the following chapters.

My contribution to the presented works has regarded the design, the synthesis and the secondary structure characterization of the peptides, the optimization of the formulation of supramolecular matrices and the evaluation of their stability and mechanical features, the encapsulation of drugs and contrast agents within the matrices and their release over time, and the *in vitro* cell studies and SAXS acquisitions on the peptide amphiphiles in the third chapter. All the other cell studies have been

performed in collaboration with IRCCS SDN SYNLAB, while all the other SAXS and WAXS data have been collected by Giannini's group of the Institute of Crystallography (IC), CNR. Relaxometric studies have been conducted in collaboration with Terreno and Gianoilio's groups of the University of Turin and Botta's and Tei's groups of the University of Piemonte Orientale "Amedeo Avogadro". Molecular modelling and dynamics studies have been performed in collaboration with Vitagliano's group of the Institute of Biostructures and Bioimaging (IBB), CNR.

[1] Whitesides, G. M.; Grzybowski, B. *Science* **2002**, 295, 2418–2421.

[2] Lehn, J. M. *Chem. Soc. Rev.* **2007**, 36, 151–160.

[3] Frenkel, D. *Physica A.* **1999**, 263, 26–38.

[4] Ren, H.; Wu, L.; Tan, L.; Bao, Y.; Ma, Y.; Jin, Y.; Zou, Q. *Beilstein J Nanotechnol.* **2021**, 12, 1140–1150.

[5] Krissanaprasit, A.; Key, C. M.; Pontula, S.; LaBean, T. H. *Chem. Rev.* **2021**, 121(22), 13797–13868.

[6] Israelachvili, J. N.; Mitchell, D. J.; Ninham, B. M. *Biochimica et Biophysica Acta (BBA)-Biomembranes* **1977**, 470(2),185-201.

[7] Zhang, S. *Mater. Today* **2003**, 6(5), 20-27.

[8] Nasrollahzadeh, M.; Issaabadi, Z.; Sajjadi, M.; Sajadi, S. M.; Atarod, M. *Interface Sci. Technol.* **2019**, 28, 29-80.

[9] Abbasi, E.; Aval, S. F.; Akbarzadeh, A.; Milani, M.; Nasrabadi, H. T.; Joo, S. W.; Hanifehpour, Y.; Nejati-Koshki, K.; Pashaei-Asl, R. *Nanoscale Res Lett* **2014**, 9, 247.

[10] Perumal, S.; Atchudan, R.; Lee, W. *Polymers* **2022**, 14(12), 2510.

[11] Liu, P.; Chen, G.; Zhang, J. *Molecules* **2022**, 27(4),1372.

[12] Lima, A. L.; Gratieri, T.; Cunha-Filho, M.; Gelfuso, G. M. *Methods* **2022**, 199, 54-66.

[13] Kenry; Lim, C. T. *Polymer Science* **2017**, 70, 1-17.

[14] Zhang, Z.; Jiang, W.; Xie, X.; Liang, H.; Chen, H.; Chen, K.; Zhang, Y.; Xu, W.; Chen, M. *ChemistrySelect* **2021**, 6, 12358–12382.

[15] Wichterle, O.; Lim, D. *Nature* **1960**, 185,117-118

[16] Zhang, P.; Yang, X.; Li, P.; Zhao, Y.; Niu, Q. *Soft Matter.* **2020**, 16, 162–169.

[17] Liao, H.; Guo, X.; Wan, P.; Yu, G. *Adv. Funct. Mater.* **2019**, 29, 1904507

[18] Gutierrez, E.; Burdiles, P.; Quero, F.; Palma, P.; Olate-Moya, F.; Palza, H. *ACS Biomater. Sci. Eng.* **2019**, 5, 6290–6299.

[19] Zhang, K.; Yuan, W.; Wei, K.; Yang, B.; Chen, X.; Li, Z.; Zhang, Z.; Bian, L. *Small.* **2019**, 15, 1900242.

[20] Jaipan, P.; Nguyen, A.; Narayan, R. *MRS Communications* **2017**, 7(3), 416-426.

[21] Bajaj, G.; Kim, M. R.; Mohammed, S. I.; Yeo, Y. *J. Control. Release* **2012**, 158, 386-392.

[22] Zhang, Y.; Tao, L.; Li, S.; Wei, Y. *Biomacromolecules* **2011**, 12(8), 2894-2901.

[23] Deng, C.; Li, F.; Hackett, J. M.; Chaudhry, S. H.; Toll, F. N.; Toye, B.; Hodge, W.; Griffith, M. *Acta Biomater.* **2010**, 6(1), 187-194.

[24] Narayanan, R. P.; Melman, G.; Letourneau, N. J.; Mendelson, N. L.; Artem Melman, A. *Biomacromolecules* **2012**, 13(8), 2465-2471.

[25] Schillemans, J. P.; Verheyen, E.; Barendregt, A.; Hennink, W. E.; Van Nostrum, C. F. *J. Control. Release* **2011**, 150(3), 266-271.

[26] Cha, C.; Jeong, J. H.; Shim, J.; Kong, H. *Acta Biomater.* **2011**, 7(10), 3719-3728.

[27] Ekaputra, A. K.; Prestwich, G. D.; Cool, S. M.; Hutmacher, D. W. *Biomaterials* **2011**, 32(32), 8108-8117.

[28] Bodugoz-Senturk, H.; Macias, C. E.; Kung, J. H.; Muratoglu, O. K. *Biomaterials* **2009**, 30(4), 589-596.

[29] Nitta, K.; Miyake, J.; Watanabe, J.; Ikeda, Y. *Biomacromolecules* **2012**, 13(4), 1002-1009.

[30] Yang Seow, W.; Hauser, C. A. E. *Mater. Today* **2014**, 17(8), 381-388.

[31] Ghadiri, M. R.; Granja, J. R.; Milligan, R. A.; Mcree, D. E.; Khazanovich, N. *Nature* **1993**, 366, 324-327.

[32] Valery, C.; Paternostre, M.; Robert, B.; Gulik-Krzywicki, T.; Narayanan, T.; Dedieu, J. C.; Keller, G.; Torres, M. L.; Cherif-Cheikh, R.; Calvo, P.; Artzner, F. *Proc. Natl. Acad. Sci. U.S.A.* **2003**, 100, 10258-10262.

[33] Koss, K. M.; Unsworth, L. D. *Acta Biomaterialia* **2016**, 44, 2-15.

[34] Navon, T.; Zhou, M.; Matson, J. B.; Bitton, R. *Biomacromolecules* **2016**, 17(1), 262-270.

[35] Tang, C.; Qiu, F.; Zhao, X. *J. Nanomaterials* **2013**, 9, 469261.

[36] Reches, M.; Gazit, E. *Phy. Biol.* **2006**, 3(1), S10-9.

[37] Coin, I.; Beyermann, M.; Bienert, M. *Nature Protocols* **2007**, 2, 3247–3256.

[38] Bucciantini, M.; Giannoni, E.; Chiti, F.; Baroni, F.; Formigli, L.; Zurdo, J.; Taddei, N.; Ramponi, G.; Dobson, C. M.; Stefani, M. *Nature* **2002**, 416, 507–511.

[39] Dukan, S.; Farewell, A.; Ballesteros, M.; Taddei, F.; Radman, M.; Nystrom, T. *Proc. Natl. Acad. Sci. U.S.A.* **2000**, 97(11), 5746-5749.

[40] Rajan, R. S.; Kopito, R. R. *Abstracts of papers of the Am. Chem. Soc.* **2004**, 227, U220.

[41] Drummond, D. A.; Wilke, C. O. *Cell* **2008**, 134(2), 341-352.

[42] Mannem, R.; Yousuf, M.; Sreerama, L. *Front. Chem.* **2020**, 8, 684.

[43] Blancas-Mejía, L. M.; Ramirez-Alvarado, M. *Annu. Rev. Biochem.* **2013**, 82, 745-774.

[44] Bensney-Cases, N.; Klementeiva, O.; Maly, T.; Cladera, J. "In vitro oligomerization and fibrillogenesis of amyloid-beta peptides," in Protein Aggregation and Fibrillogenesis in Cerebral and Systemic Amyloid Disease, ed J. R. Harris *Subcellular Biochemistry: Springer* **2012**, 53–74.

[45] Ge, X.; Sun, Y.; Ding, F. *Biochimica et Biophysica Acta (BBA) – Biomembranes* **2018**,1860(9),1687-1697.

[46] Reches, M.; Gazit, E. *Science* **2003**, 300, 625-627.

[47] Yan, X. H.; Zhu, P. L.; Li, J. B. *Chem Soc Rev.* **2010**, 39,1877–1890.

[48] Guo, C.; Luo, Y.; Zihou, R.; Wei, G. *ACS Nano* **2012**, 6, 3907-3918.

[49] Azuri, I.; Abramovich, L.; Gazit, E.; Hod, O.; Kronic, L. *J. Am. Chem. Soc* **2014**, 136, 963-969.

[50] Gör̈bitz, C. H. *Chem. Commun.* **2006**, 22, 2332–2334.

[51] Gör̈bitz, C. H. *Chem. Eur. J.* **2001**, 7, 5153-5159.

[52] Reches, M.; Gazit, E. *Nano Lett.* **2004**, 4, 581–585.

[53] Jayawarna, V.; Ali, M.; Jowitt, T.; Miller, A. F.; Saiani, A.; Gough, J. E.; Ulijn, R. V. *Adv. Mater.* **2006**, 18, 611–614.

[54] Mahler, A.; Reches, M.; Rechter, M.; Cohen, S.; Gazit, E. *Adv. Mater.* **2006**, 18, 1365–1370.

[55] Diaferia, C.; Morelli, G.; Accardo, A. *J. Mater. Chem. B* **2019**, 7, 5142–5155.

[56] Diaferia, C.; Rosa, E.; Morelli, G.; Accardo, A. *Pharmaceuticals* **2022**, 15(9), 1048.

[57] Smith, A. M.; Williams, R. J.; Tang, C.; Coppo, P.; Collins, R. F.; Turner, M. L.; Saiani, A.; Ulijn, R. V. *Adv. Mater.* **2008**, 20(1), 37–41.

[58] Tang, C.; Smith, A. M.; Collins, R. F.; Ulijn, R. V.; Saiani, A. *Langmuir* **2009**, 25, 9447–9453.

[59] Adams, D. J.; Butler, M. F.; Frith, W. J.; Kirkland, M.; Mullen, L.; Sanderson, P. *Soft Matter* **2009**, 5, 1856–1862.

[60] Orbach, R.; Adler-Abramovich, L.; Zigerson, S.; Mironi-Harpaz, I.; Seliktar, D.; Gazit, E. *Biomacromolecules* **2009**, 10, 2646–2651.

[61] Levine, M. S.; Ghosh, M.; Hesser, M.; Hennessy, N.; Di Guiseppi, D. M.; Adler-Abramovich, L.; Schweitzer-Stenner, R. *Soft Matter* **2020**, 16, 7860–7868.

[62] Williams, R. J.; Smith, A. M.; Collins, R.; Hodson, N.; Das, A. K.; Ulijn, R. V. *Nat. Nanotech.* **2009**, 4, 19–24.

[63] Ischakov, R.; Adler-Abramovich, L.; Buzhansky, L.; Shekhter, T.; Gazit, E. *Bioorg. Med. Chem.* **2013**, 21, 3517-3522.

[64] Pérez-Álvarez, L.; Laza, J. M.; Álvarez-Bautista, A. *Curr. Pharm. Des.* **2016**, 22, 3380–3398.

[65] Sagbas Suner, S.; Ari, B.; Onder, F. C.; Ozpolat, B.; Ay, M.; Sahiner, N. *Int. J. Biol. Macromol.* **2019**, 126, 1150–1157.

[66] Curcio, M.; Diaz-Gomez, L.; Cirillo, G.; Concheiro, A.; Iemma, F.; Alvarez-Lorenzo, C. *Eur. J. Pharm. Biopharm.* **2017**, 117, 324–332.

[67] Sugiura, S.; Oda, T.; Izumida, Y.; Aoyagi, Y.; Satake, M.; Ochiai, A.; Ohkohchi, N.; Nakajima, M. *Biomaterials* **2005**, 26, 3327–3331.

[68] Yeh, J.; Ling, Y.; Karp, J. M.; Gantz, J.; Chandawarkar, A.; Eng, G.; Blumling, J.; Langer, R.; Khademhosseini, A. *Biomaterials* **2006**, 27, 5391–5398.

[69] Rolland, J. P.; Maynor, B. W.; Euliss, L. E.; Exner, A. E.; Denison, G. M.; De Simone, J. M. *J. Am. Chem. Soc.* **2005**, 127, 10096–10100.

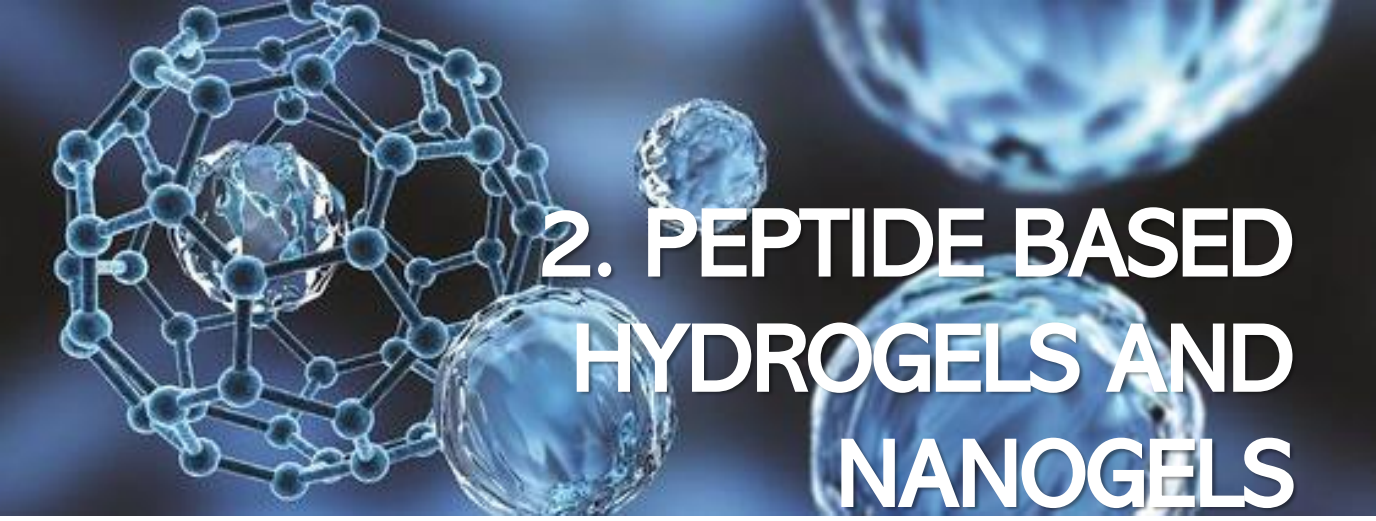

2. PEPTIDE BASED HYDROGELS AND NANOGELS AS DRUG DELIVERY TOOLS

Elisabetta Rosa | University of Naples Federico II | XXXV cycle

2.1 INTRODUCTION

2.1.1 The evolution of drug delivery technologies

Drug delivery strategies have significantly contributed, in the last 20 years, to let successful therapies develop starting from promising active principles. [70,71] The goal of delivery is to improve the efficacy of medicines, which can be realized through the selective transport and release in the target site, the increase in patients' compliance, the reduction of toxicity and of drug accumulation in non-target regions. [72] The challenging physicochemical properties of life-saving small molecules, proteins, peptides, nucleic acid and antibodies, like the low solubility, the chemical instability, the pharmacokinetic profile and the restricted bioactivity, paved the way to the necessity in promoting new approaches to these issues. [73] New technologies (**Figure 2.1**), many of them arising from the knowledge of supramolecular chemistry rules and principles, were so born.

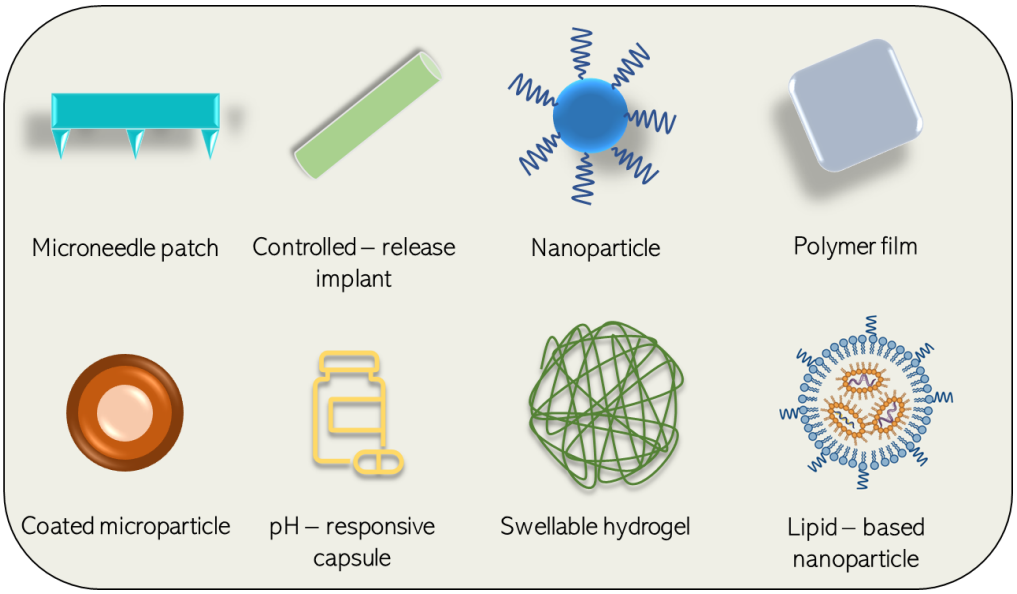

Figure 2.1: Schematic representation of some of the used drug-delivery systems.

Some of these systems have been commercialized and are successfully employed in clinics nowadays. Among them, leuprolide acetate (Lupron®; TAP Pharmaceuticals North Chicago, IL) was developed as depot microsphere suspension to provide continuous release of LA when administered as a monthly intramuscular injection. [74] Leuprolide is a gonadotropin-releasing hormone analogue (GnRH-a) for the treatment of endometriosis, which was previously administered once a day through nasal or subcutaneous route. The less frequent administration significantly increases the compliance in the patients and therefore their adherence to the therapy. During the COVID-19 pandemic, a central role has been occupied by mRNA-based vaccines (Comirnaty®, Pfizer/BioNTech; Spikevax®, Moderna), able to raise an immune response against the expressed spike protein and so to prevent the occurrence of the disease itself or its more severe symptoms. [75] The vulnerability of nucleic acid derivatives in the circulating blood was overcome by their entrapment in pegylated liposomal formulations, which guarantee the survival of the mRNA long enough on injection to produce virus proteins. A controlled release of drugs is also obtained thanks to the delivery through implants, which can be defined as both biodegradable and non-biodegradable flexible polymeric carrier generally inserted into the subcutaneous area. [76] Many of them have been exploited to obtain Long-Active Reversible Contraception (LARC) agents, by the gradual release of progestogen hormones into the surrounding tissues, which are then absorbed by the circulatory system and distributed systemically (*i.e.,* Nexplanon, Organon Italia S.r.l). [77] During the last years, also hydrogels have been studied as possible implants in many branches of medicine, including cardiology, oncology, immunology, wound healing and pain management. [78] Their high-water content makes them really similar to tissue extracellular matrix and provides the capability to easily encapsulate hydrophilic molecules.

2.1.2: Enhanced Permeability and Retention (EPR) Effect as specific targeting strategy

Despite the discovery and the synthesis of many small molecules displaying a marked efficacy against cancer cell proliferation and metabolism, chemotherapy for solid tumors is, nowadays, far to be completely fulfilling. Cancer remains one of the leading causes of mortality worldwide, affecting more than 10 million new patients every year. One of the main reasons of this widespread dissatisfaction is the lack of specific targeting, which is the basis of the unsafety of anticancer drugs. The Enhanced Permeability and Retention (EPR) effect is a pathophysiological phenomenon occurring in the vasculature of tumoral cells resulting from hypervascularization of these regions. [79] This characteristic allows macromolecular compounds to be trapped within the cancer tissue for a prolonged period. (**Figure 2.2)** The EPR effect, which has been studied in solid tumors of rabbits, rodents, canine and human patients, [80,81] results from the occurrence of different events characterizing the unique behavior of cancer tissues:

1. Diffused irregular neovascularization, where the tumor blood vessels are characterized by fenestrated endothelial cells with deficient basement membranes. Other abnormalities are also observed in the smooth muscle cells surrounding the vessels, where a lack of alpha actin, responsible of the response to blood pression, occurs.
2. Inefficient drainage of lymphatic system.
3. Overexpression of inflammatory factors sustaining the EPR effect, like prostaglandins, proteases, bradykinin, peroxynitrite, nitric oxide, interferon gamma, interleukin 1 beta, interleukin 2, Interleukin 6, VEGF and HIF−1 alpha.

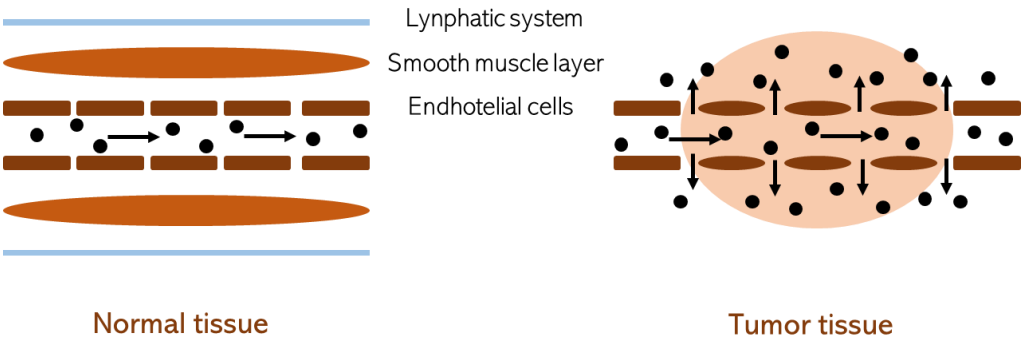

Figure 2.2: Schematic representation of the EPR effect in tumor tissues for macromolecules (10 to 200 nm or 40 to 800 kDa).

EPR effect has been exploited to design a selective delivery for anticancer drugs. A nanoparticle extravasation is observed in tumor regions because of the large fenestrations missing in normal tissues. These objects are then retained for a long time because of the deficiency of lymphatic system. A drug delivered by a nano-sized carrier can choosily accumulate in solid tumors and many adverse effects of these invasive molecules can be avoided. [82]

2.1.3 Supramolecular formulation for the delivery of doxorubicin anticancer drug

Breast cancer is the most common cancer disease for women in the United States, involving more than 200,000 newly diagnoses each year. [83] The currently proposed treatments include surgical resection, radiation, and chemotherapy. Many of the drugs involved in the chemotherapeutic option (doxorubicin, docetaxel, paclitaxel, and tamoxifen) can be used alone or in combination. [84] Among them, Doxorubicin (Dox, mostly sold under the brand name Adriamycin®) is a natural antitumor antibiotic of the anthracycline class, first extracted from *Streptomyces peucetius varcaesius*

in the 1970's and routinely used to treat bladder cancer, Kaposi's sarcoma, lymphoma, and acute lymphocytic leukemia, besides that breast cancer. This molecule was approved for medical use in the United States in 1974 and it is on the World Health Organization's List of Essential Medicines. Its toxic effect on cancer cells may be explained taking into account two different mechanisms of actions: (i) intercalation into DNA and inhibition of the progression of topoisomerase II, an enzyme which relaxes supercoils in DNA for transcription; (ii) generation of free radicals able to damage cellular membranes, DNA and proteins. [85] Briefly, after entering the nucleus, the planar aromatic chromophore portion of the molecule (**Figure 2.4**) can intercalate between two base pairs of the DNA, while the daunosamine sugar portion accommodates in the minor groove and interacts with base pairs adjacent to the intercalation site. Dox stabilizes the topoisomerase II complex after it has broken the DNA chain for replication, hindering the release of DNA double helix and therefore stopping the replication mechanism. Moreover, Dox is firstly oxidized to semiquinone, which, by converting back to Dox, releases reactive oxygen species (ROS) leading to lipid peroxidation and membrane damage, DNA damage, oxidative stress, and triggers apoptotic pathways of cell death. Despite its therapeutic importance, clinical use of Dox is largely hindered by its dose-limiting toxicity, represented by dilated cardiomyopathy, leading to congestive heart failure. [86] The rate of cardiomyopathy is dependent on its cumulative dose, with heart suffering occurring since the very first dose and then getting worse with each following anthracycline cycle. [87] Two main theories explain the exact mechanism od cardiotoxicity of doxorubicin: (i) iron-related free radicals release and formation of doxorubicinol metabolite and (ii) mitochondrial disruption. Dox encapsulating liposomal formulations (Caelyx®/Doxil®, Myocet® and their analogues), have been proposed and used in clinics as an alternative administration strategy able to reduce toxic side effects. [88] The confinement of Dox into a nanoformulation allows

altering the biodistribution of the drug, which, thanks to the EPR effect, is selectively delivered to the tumor site thus minimizing its toxicity. It also provides an increase of its half-life and therapeutic index and an improvement of the pharmaceutical profile, leading to increased patient compliance. [89]. In the last years, also polymer-based aggregates, [90] nanofibers, [91] nanodisks, [92] gold nanoparticles, [93] graphene, graphene oxide [94, 95] and hydrogels (HGs), [96] have been proposed as novel Dox-delivery tools. Among them, an example could be provided by polymeric micelles composed by Pluronic F127 and phenylboronic ester-grafted (PHE). When loaded with doxorubicin, these formulations were found to significantly reduce the IC_{50} in drug-resistant cell, thus underling how much the delivery strategy affects the therapeutic efficacy. [97] Thanks to its high hydrophilicity, low toxicity and low immunogenicity, polyethylene glycol (PEG) is another important polymer for the effective design of drug-delivery systems. Self-assembled polyphosphoester (PPE)-b-PEG were demonstrated to achieve pH-sensitive release of DOX through labile hydrazone bonds. [98] Poly(amidoamine) dendrimer has also been reported as Dox carrier against human alveolar carcinoma cells (in vitro). [99] This preparation was shown to possess enhanced aerosol characteristics, demonstrating to be a promising inhalation formulation to deliver DOX to the lungs. Functionalization of nanostructures is also a widely used strategy to increase the selectivity towards the cancer tissue. For example, liposomes decorated with Bombesin peptide were found to selectively target tumor site and provide anticancer efficacy in mice. [100]

2.1.4 Nanogels as innovative drug delivery systems

As previously mentioned, peptide-based nanogels could represent suitable platforms able to satisfy many of the requests of a system for the delivery of drugs. Before our studies, only two examples of peptide based nanogels were reported in literature. In the first one, the preparation of the nanogels

was achieved through the inverse emulsion technique, [63] which consists of the formation of a water-in-oil (W/O) emulsion composed by an aqueous phase, containing the Fmoc-FF dipeptide, and an oily phase containing a surfactant as stabilizer. The ratio behind the inspection of this methodology was its wide successful use in polymeric nanogels formulations. [101] In the second work, a top-down methodology was used to formulate hydrogel nanoparticles starting from the dipeptide H-Phe-ΔPhe-OH (phenylalanine-α,β-dehydrophenylalanine). [102] This technique consists in the sonication with a microprobe of preformed H-Phe-ΔPhe-OH, thus obtaining nanogels with an average hydrodynamic radius (R_H) of 150 nm. However, since no surfactant protected shell was present, the formulation was noticed to be subjected to a certain degree of particle instability, with an increase of the radius up to 350 nm, after 60 h. This is a problem since it is easy to infer that *in vitro* and *in vivo* stability represents an essential requirement for the success of a designed biomedical nanosystem. From this point of view, the presence of molecules able to reduce the surface tension it is a priority request for the development of this kind of delivery systems.

2.2 OBJECTIVES

Starting from these considerations, our interest was focused on the pursuing of four main goals. First of all, it was important, for us, to standardize a formulation methodology to be used to obtain stable and reproducible peptide-based nanogels. Second, their cytocompatibility, a fundamental request to propose them as vehicles to be injected, had to be demonstrated. Third, the mechanisms exploited from the nanostructure to enter the cell was investigated. Fourth, the possibility of a stable loading of a drug in our matrices (both peptide-based hydrogels and nanogels), together with its controlled release, had to be verified. To this last scope,

doxorubicin was selected as drug model and the applicability of the supramolecular peptide Dox reservoirs as anticancer agents was investigated. By starting from the literature, we explored three different methodologies to create stable and reproducible nanogel dispersions composed by a peptide core and a stabilizing shell. For all of them, the chosen peptide was the well-known and well characterized ultrashort gelator Fmoc-FF. The investigated methods for the formulation of the Fmoc-FF-based nanogels (**Figure 2.3**) were as follows: (A) the water-in-oil emulsion technique (or reverse emulsion technique, W/O); (B) the top-down methodology; and (C) a novel modified procedure designed by us and named "nanogelling in water".

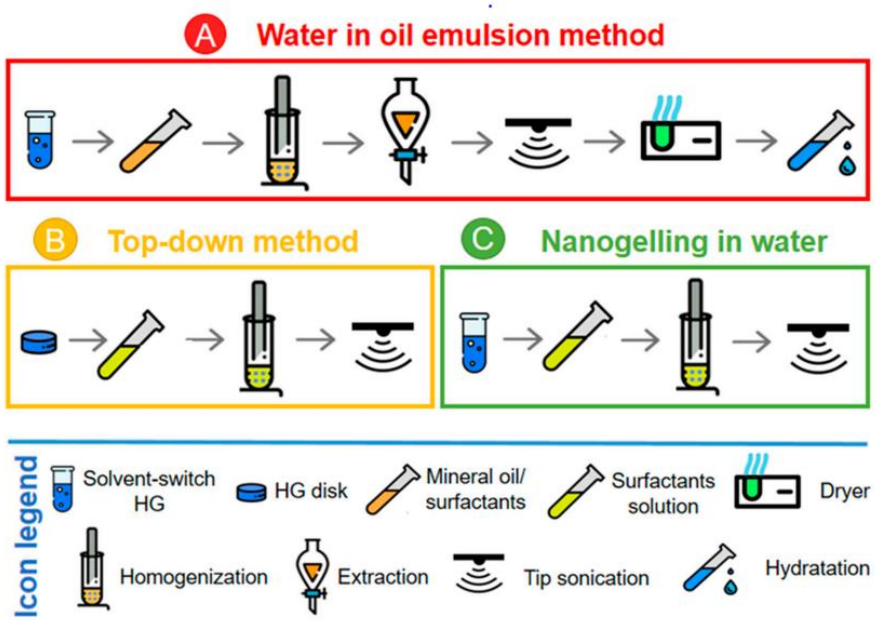

Figure 2.3: Icons graphical representation of the three different explored formulation methodologies: (A) Water in oil emulsion method; (B) Top-down method and (C) Nanogelling in water.

The hydrophilic-lipophilic balance (HLB) value was chosen as starting point to evaluate the best mixture of surfactants in terms of stabilizing capacity. This parameter was proposed by Griffin between the late 1940s and early 1950s [103, 104] and allows to predict how a surfactant can help the stability of an emulsion in which an aqueous phase is dispersed in the oily phase, or *vice versa*. The three different methods were compared in terms of size, stability, and feasibility of the formulation obtained from each of them.

After the formulation method was standardized, cytotoxicity of Fmoc-FF nanogels was tested on a panel of cells, including both tumoral and non-tumoral ones. No toxicity was detected on tumoral cells, whereas a specific cytotoxic effect was discovered against one triple negative breast cancer cell line, (MDA-MB-231) which can be considered the most aggressive subtype. [105] This data paved the way to understand the internalization mechanism exploited by our nanogel to enter the cell. To amplify their toxic effect against breast cancer cells, we decided to load doxorubicin in the supramolecular peptide matrix. Drug delivery platforms in both the macroscopic (hydrogel) and nanosized (nanogel) state were proposed and tested. Since it is well-known that hydrogels prepared by mixing two or more hydrogelators can exhibit novel functional and mechanical properties, besides the pure Fmoc-FF, also two-components building blocks were tested. The preparation of mixed Fmoc-FF/(FY)3 and Fmoc-FF/PEG_8-(FY)3 (at 2/ 1 or 1/1, v/v) hydrogels has recently been reported. [106] The (FY)3 hexapeptide contains, as peptide framework, the alternation of three tyrosine (Y) and three phenylalanine (F) residues and it is pegylated in its PEG_8-(FY)3 version. [107] The presence of PEG and its relative amount into the mixed formulation causes an increasing slowing down of the gelation kinetic and a decrease of the gel rigidity, which was attributed to the high flexibility and conformational freedom of these chains. Both pure and mixed

hydrogel and nanogel formulations were used to encapsulate Dox and their drug loading and drug release properties were tested and compared. (**Figure 2.4**)

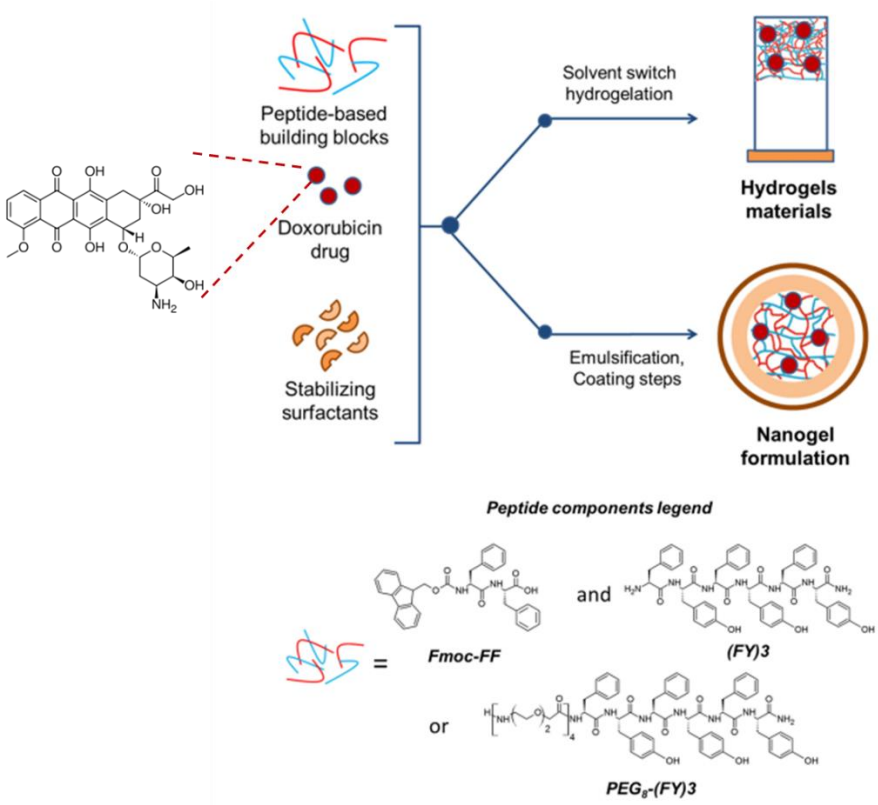

Figure 2.4: Schematic representation of components and methodologies for the formulation of HGs and NGs. Chemical formulas for peptide-based components are reported in the legend.

The *in vitro* cytotoxicity of both empty and Dox filled formulations was evaluated on MDA-MB-231 breast cancer cell line. The capability of peptide-based hydrogels to encapsulate the supramolecular nanodrug Doxil, together with their effective cytotoxicity, was also checked. This strategy could allow obtaining a composite drug delivery platform for a multi-stage delivery of Dox.

2.3 MATERIALS AND METHODS

Lyophilized Fmoc-FF powder was purchased from Bachem (Bubendorf, Switzerland), while TWEEN®60, SPAN®60, the mineral oil, and all the other chemicals were obtained from Sigma-Aldrich, Fluka (Bucks, Switzerland) or LabScan (Stillorgan, Dublin, Ireland). Protected N^{α}-Fmoc-amino acid derivatives, coupling reagents, and Rink amide MBHA (4-methylbenzhydrylamine) resin (Laufelfingen, Switzerland) were purchased from Calbiochem-Novabiochem. The monodisperse Fmoc8-amino-3,6-dioxaoctanoic acid (Fmoc-AdOO-OH, PEG2) was obtained from Neosystem (Strasbourg, France). Doxorubicin chlorohydrate (Dox·HCl) was purchased from Sigma Aldrich (Milan, Italy). Pegylated liposomal Dox, sold under the commercial name of Doxil, was kindly gifted by the Italian Cancer Institute in Naples (Italy) "Fondazione G. Pascale". All the compounds and the reagents were used as received unless otherwise stated. Solutions were obtained by weight using doubly distilled water as solvent. The effective peptide concentrations were then spectroscopically determined by UV-Vis measurements performed through a Nanodrop 2000c spectrophotometer (Thermo Fisher Scientific Inc., Wilmington, DE, USA). Solutions were placed in a 1.0 cm quartz cuvette (Hellma). For Fmoc-FF and Fluorescein-isothiocyanate (FITC-NCS, Merk) molar absorptivity (ε) values used were 7800 L/(cm×mol) at 301 nm and 75000 L/(cm×mol) at 480 nm, respectively.

2.3.1 Peptide Synthesis

(FY)3 hexapeptide and its PEGylated analogue, PEG_8-(FY)3, were synthesized by peptide solid phase synthesis. Briefly, peptides were elongated on Rink amide MBHA resin (substitution grade 0.73 mmol/g) by adding amino acids and monodisperse PEG spacers twice in N, N-di-methyl formamide (DMF) for 30 min in the presence of activating agents. After the

addiction of the last residue, peptides were cleaved from the support through treatment for 24h with TFA (trifluoroacetic acid)/TIS (tri-isopropylsilane)/H_2O (92.5/5.0/2.5v/v/v) at room temperature. The obtained crude products were precipitated with cold ether, dissolved in H_2O/CH_3CN mixture, and then freeze-dried. Purification was achieved through RP-HPLC chromatography and purity was assessed by ESI mass spectra, analytical RP-HPLC and ^{1}HNMR spectroscopy.

(FY)3: t_R=14.52min, MS (ESI$^+$): m/z calcd. for $C_{54}H_{57}N_7O_9$ = 949.1 [M+H$^+$]; found = 948.1 u.m.a.

PEG_8-(FY)3: t_R=12.21min, MS (ESI$^+$): m/z calcd. for $C_{78}H_{101}N_{11}O_{21}$ = 1526.7 [M+H$^+$]; found = 1528.7 u.m.a.

2.3.2 Fmoc-FF nanogel formulation

Fmoc-FF nanogel formulation was prepared according to three different methods:

a) Method 1: Water-in-Oil Emulsion Technique

1 mL of Fmoc-FF hydrogel at a concentration of 1 wt% was prepared according to the solvent switch method: 10 mg of Fmoc-FF were first dissolved in 100 µL of dimethyl sulfoxide (DMSO), and then rehydrated with 900 µL of double distilled water. The pre-formed hydrogel was added to a mineral oil solution of surfactants (9 mL). Surfactants were alternatively E-TPGS (3×10^{-5} mol) or a TWEEN®60/SPAN®60 mixture (3×10^{-5} mol), at different ratios (w/w) (**Table 2.1).** The sample was subjected to 5min homogenization at 35,000 min^{-1}. The emulsion was successively stirred at 4 °C, for 3 h, after which the oily phase was extracted by three consecutive washes with 6 mL of n-hexane each, departed by centrifugation. The product of the extraction was subjected to drying under vacuum for 3 h,

and then resuspended into 4 mL of sterilized water. The final sample was sonicated using a tip sonicator for 5 min at 9 W.

b) Method 2: Nanogelling in Water Technique

Fmoc-FF metastable DMSO/water mixture 1 wt % (1 mL), prepared in accordance with the solvent switch method, was added into 4 mL of an aqueous filtered suspension of TWEEN®60 and SPAN®60 surfactants (52/48 w/w and 3×10^{-5} mol) before the gelling process was completed. The sample was homogenized at 35,000 min^{-1} for 5 min, and then tip sonicated for 5 min at 9 W.

c) Method 3: Top-Down Methodology

1 mL of Fmoc-FF or Fmoc-FF/(FY)3 (2/1 v/v) hydrogel was prepared according to the solvent-switch method. The peptide containing DMSO/water mixture was transferred into a silicone mold before the hydrogel was formed. At the end of the gelling time, a gel disk was obtained. This disk was added to 4 mL of an aqueous filtered suspension of TWEEN®60/SPAN®60 at a w/w ratio of 52/48 (3×10^{-5} mol) and the sample underwent the same homogenization and tip-sonication procedure previously described.

2.3.3 Formulation of empty hydrogels

Pure Fmoc-FF and mixed Fmoc-FF/PEG8-(FY)3 and Fmoc-FF/(FY)3 hydrogels (1/1 or 2/1, v/v) were prepared using the solvent-switch method (final concentration of 0.5 wt%). Briefly, each peptide component (Fmoc-FF, (FY)3 and PEG8-(FY) 3) was dissolved in dimethyl sulfoxide (DMSO) to a final concentration of 100 mg/mL. 20 μL of the stock solution, composed by the only Fmoc-FF or the mixture with tyrosine-containing sequences in the above reported ratio, were then rehydrated with 380 μL of water.

2.3.4 Formulation of hydrogels loaded with Dox or Doxil

Hydrogels were loaded with Dox (a) or with Doxil (b).

(a) For Dox filled HGs, 20 μL of the peptide stock solution (100 mg/mL), prepared as above reported, were added to 380 μL of Dox water solution at a concentration of 4.0 mmol/L.

(b) For Doxil filled hydrogels, 20 μL of the peptide stock solution (100 mg/mL), prepared as above reported, were added to 380 μL of the commercial Doxil solution opportunely diluted in order to achieve a Dox concentration of 4.0 mmol/L.

2.3.5 Formulation of nanogels filled with Dox or FITC

Nanogels were loaded with Dox (a) or with FITC (b).

(a) Dox-loaded Fmoc-FF and Fmoc-FF/(FY)3 (1/1 v/v) hydrogels, prepared at 1 wt% concentration (Dox solution used for the rehydration step 0.018 mol/L), were subjected to a top-down procedure to obtain the nanogel formulation. Dox filled nanogels were purified from free Dox by gel filtration on a pre-packed column Sephadex G-50. The Dox concentration in the free fraction was determined by UV-Vis spectroscopy using calibration curves obtained by measuring the absorbance at λ = 480 nm The drug loading content (DLC) was calculated as $g_{Dox\ encapsulated}/g_{(surfactant+peptide)}$.

(b) 20 μL of Fmoc-FF DMSO solution (200 mg/mL) were mixed to 20 μL of FITC DMSO solution (12.8 mmol/L) and then diluted with 360 μL of water to obtain the macroscopic hydrogel, which was then subjected to the top-down procedure. The unloaded FITC was removed from the final formulation *via* size exclusion chromatography (SEC) on a prepacked gel filtration column (Sephadex G-50). The amount of FITC encapsulated was analytically

determined *via* UV-Vis spectroscopy using calibration curves obtained by measuring absorbance at λ = 492 nm.

2.3.6 Dynamic Light Scattering (DLS) measurements

Hydrodynamic radii (R_H) diffusion coefficients (D) and the zeta potential (ζ) of all the peptide nanogel formulations were measured by dynamic light scattering (DLS). After centrifugation of the sample at 13,000 rpm for 5min, measurements were carried out in triplicate. A Zetasizer Nano ZS (Malvern Instruments, Westborough, MA, USA) was used. Instrumental settings were, as follows: a backscatter detector at 173° in automatic modality, room temperature, disposable sizing cuvette as cell. Data of ζ were collected as the average of 20 measurements.

2.3.7 Nanoparticles Tracking Analysis (NTA) measurements

A Nanosight NS300 (Alfatest, Italy) was used to perform NTA measurements. Fmoc-FF nanogel formulation (0.1wt%) was subjected to 1000-fold dilution in double distilled water to a final volume of 1 mL. The sample was thus diluted in agreement with the ideal particle per frame value (20-100 particles/frame). The following conditions were chosen according to the manufacturer's software manual (NanoSight NS300 User Manual, MAN0541-01-EN-00, 2017): camera level was increased until all particles were distinctly visible, not exceeding a particle signal saturation over 20%; the detection threshold was determined to include as many particles as possible with the restrictions that 10-100 red crosses were counted while only <10% were not associated with distinct particles; blue cross count was limited to 5; autofocus was adjusted to avoid indistinct particles. For each measurement, five 1-min videos were recorded under the following settings: cell temperature: 25°C and syringe speed: 50 µl/s. After capture, the videos have been analysed by the in-build NanoSightSoftware NTA 3.4 Build 3.4.4 with a detection threshold of 4. Hardware: embedded laser: 45 mW at 488

nm; camera: sCMOS. The number of completed tracks in NTA measurements was always greater than the proposed minimum of 1000 in order to minimise data skewing based on single large particles.

2.3.8 Circular Dichroism (CD) studies

Far-UV CD spectra of hydrogels and nanogels were collected on a Jasco J-810 spectropolarimeter equipped with a NesLab RTE111 thermal controller unit, set at 25°C. Samples were placed on a 0.1 mm quartz cell. Hydrogel formulations were let to form in the cuvette before the analysis. The explored spectral region was between 300 and 200 nm. Other experimental settings were: scan speed = 50 nm min^{-1}, sensitivity = 10 mdeg, time constant = 16 s, bandwidth = 1 nm. Each spectrum was obtained by averaging three scans and then subtracted by the blank. All the spectra are reported in optical density (O.D.).

2.3.9 Fluorescence measurements

Fluorescence spectra of hydrogels and nanogels were recorded at room temperature with a spectrofluorophotometer Jasco (Model FP-750, Japan) with the tested sample placed in a quartz cell with 1.0 cm path length. The other settings were excitation and emission bandwidths = 5 nm, recording speed = 125 nm/min. The excitation wavelength was 280 nm (emission range 290-400 nm) for Fmoc-FF empty preparations and 480 nm (emission range 490-700 nm) for Dox.

2.3.10 Confocal analysis

Dox filled hydrogels were drop-casted and spread on a glass slide, air-dried at room temperature. Confocal images were obtained with a Leica TCS-SMDSP5 confocal microscope (λ_{exc} = 488 nm and λ_{em} = 505–600 nm). 0.8-µm thick optical slices were acquired with a 63× or 40×/1.4 NA objective.

2.3.11 Dox release from hydrogels and nanogels

To evaluate Dox and Doxil release from hydrogels, 400 µL of drug filled hydrogels were placed in a conic tube (1.5 mL) and 800 µL of 0.100 mol/L phosphate buffer were added on the top of them. At each time-point, 400 µL of this solution were removed and replaced with an equal fresh aliquot of PBS. Released Dox in each fraction was quantified by UV-Vis spectroscopy. All the release experiments were performed in triplicates. The extent of Dox release was reported as percentage of the ratio between the amount of released drug and the total quantity of initially loaded drug. Dox release experiment from nanogels was carried out using the dialysis method. Briefly, 1 mL of the nanogel was placed into a dialysis bag (MW cut-off = 3500 Da), which was immersed at 37°C into 20 mL of phosphate buffer and subjected to stirring for 72 h. At each well-defined time point, 2 mL of the dialyzed solution were moved away and replaced with an equal amount of fresh solution. Fluorescence measurements of each fraction of the dialyzed solution were recorded to quantify the amount of released drug using an analytical titration curve previously recorded for the free Dox in the same spectral range. Analogously to HGs, Dox release profile from NGs was reported as percentage of released drug/total drug initially loaded.

2.3.12 Cell culture

The human breast cancer cell lines (SKBR3, MDA-MB-231, MDA-MB-361, MDA-MB-453), the non-tumorigenic epithelial MCF10-a cell line, and the mouse pre-adipocyte cell line 3T3-L1 were obtained from the SYNLAB SDN Biobank. The SKBR3 cells were grown in McCoy's 5A Medium Modified supplemented with 10% fetal bovine serum (FBS). MDA-MB-231, MDA-MB-361, and 3T3-L1 cells were grown in DMEM medium supplemented with 10% FBS and 1 % GlutaMAX. MDA-MB-453 were grown in L-15 medium supplemented with 10% FBS. MCF10a cells were grown in the 10% FBS supplemented MEBM medium (CC-3151, Lonza, Belgium).

2.3.13 Cell viability evaluation by MTT assay

Cell viability was assessed by the MTT (3-(4,5-dimethylthiazol-2-yl)-2,5-diphenyltetrazolium bromide) assay (G4000, Promega, Italy). For Dox-loaded formulations, MDA-MB-231 cells were seeded in 24-well plates at a density of 50 × 10^4 per well. Free Dox at 1μmol/L, nanogels and hydrogels (these latter preformed into a hollow plastic chamber sealed at one end with a porous membrane) were added to the wells after 24h. Cells were treated with the hydrogels for 24 h and with nanogel solutions for 72 h and then the cell viability test was performed. For the determination of Dox IC_{50}, MDA-MB-231 cells were seeded in 24-well plates at a density of 50 × 10^4 per well and treated with different concentrations (0.25, 0.5, 1, 2 and 4 μmol/L) of Dox for 24 h. An MTT assay was conducted at the end of each treatment. In brief, MTT was dissolved in DMEM in the absence of phenol red (Sigma Aldrich) and added to treated cells at a final concentration of 0.5 mg/mL. After 4 h incubation at 37°C, the medium was removed, and the resulting formazan salts were dissolved by adding isopropanol containing 0.1 mol/L HCl and 10% Triton-X100. Absorbance values of blue formazan were determined at 490 nm using an automatic plate reader (EL 800, Biotek). Cell survival was expressed as percentage of viable cells in the presence of hydrogels or nanogels, compared to control cells grown in their absence. The assay was repeated twice with similar results. To determine the toxicity of Fmoc-FF NGs on different cell lines, cells were seeded in 96-well plates at a density of 5 × 10^3 per well. Cells were incubated with different concentration of nanogels for 24, 48 and 72h. The MTT assay was conducted as above described.

2.3.14 Immunofluorescence Experiments

MDA-MB-231cells (1 x 10^4) were seeded on polyethyleneimine coated coverslips in 24-well plates and cultured for 24 hours at 37° C. Cells were

then incubated for 1 hour at 37 °C with FITC loaded Fmoc-FF nanogels diluted in complete cell culture medium. When indicated, cellular nanogel uptake was first blocked at 4°C for 1 hour, and then permitted by re-shifting the temperature at 37 °C for 10 minutes. At the end of each treatment, cells were fixed in 3.7 % paraformaldehyde diluted in PBS pH 7.4 for 10 min at 25 °C. To promote the quenching of paraformaldehyde, cells were incubated with a solution 0.1 mol/L Glycine in PBS for 10 minutes and then permeabilized for 10 minutes with PBS containing 0.1% Triton X-100. To visualize caveolae, cells were incubated with a goat anti-human serum albumin (HAS) antibody (Invitrogen, code: AB_1954616, dilution 1:200 in PBS) and a secondary anti-goat antibody coupled to Alexa Fluor™ 3 (Invitrogen, Alexa Fluor™ 350, AB_2534100; dilution 1:400 in PBS) and placed in a humidified chamber for 1 hour at 25 °C in the dark. By the use of a solution of 50% glycerol in PBS, coverslips were lodged on glass slides and examined by confocal microscopy. Confocal images were obtained, as previously mentioned, with a Leica TCS-SMD-SP5 confocal microscope (for Alexa Fluor 350: λ_{exc} = 350 nm and λ_{em} = 440 nm; for FITC λ_{exc} = 488 nm and λ_{em} = 505-600 nm). Graphpad Prism 6 (Graphpad Software, Graphpad Holdings, LLC, CA, USA) was used to perform all the statistical analyses.

2.3.15 RNA extraction and RT-PCR analysis

Total RNA was extracted using the Trizol Reagent following manufacturer's instructions (Thermo Fischer Scientific, Waltham, MA, USA). After being extracted, RNA was quantified with Qubit 4 Fluorometer (Thermo Fischer Scientific). According to the manufacturer's protocol, 500 ng of total RNA from each sample were retro-transcribed in cDNA by using SuperScript III First-Strand Synthesis SuperMix kit (Thermo Fisher Scientific). The expression level of the indicated mRNA was measured by qRT-PCR on C1000 Touch Thermal Cycler (Bio-Rad, Hercules, CA, USA) using iQ SYBR Green Supermix (#1708882, Bio-Rad). Ribosomal Protein S18 (RPS18)

level was used as an endogenous control. The following forward (fw) and reverse (rev) primers were used:

• *RPS18*:

fw 5'-CGATGGGCGGCGGAAAATA-3'; rev 5-CTGCTTTCCTCAACACCACA-3'

• *CyclinA*:

fw 5'-AAATGGGCAGTACAGGAGGA-3'; rev 5'-CCACAGTCAGGGAGTGCTTT-3'

• *CyclinB*:

fw 5'-CATGGTGCACTTTCCTCCTT-3'; rev 5' AGGTAATGTTGTAGAGTTGGTGTCC-3'

• *CyclinE*:

fw 5'-GGCCAAAATCGACAGGAC-3'; rev 5'-GGGTCTGCACAGACTGCAT-3'

• *CyclinD*:

fw 5'-GCTGTGCATCTACACCGACA-3'; rev 5'-TTGAGCTTGTTCACCAGGAG-3'

Caveolin 1:

fw 5'-ACACGGCTGATGCACTGAACTC-3';rev 5'-GACACACAGGGAAGACCAAGACG-3'

2.3.16 Cell cycle analysis

Flow cytometry (FCM) was used to analyze cell cycle progression in MDA-MB-231. After being incubated with nanogels, cells were fixed and stained with propidium iodide (Beckman Coulter). The CXP software (Beckman Coulter) was used to record a minimum of 10.000 single-cell events. Number of cells in G0/G1, S, and G2-M phases were determined using Kaluza Analysis Software 2.1 (Beckman Coulter) with the Michael Fox algorithm.

2.4 RESULTS AND DISCUSSION

2.4.1 Nanogel formulation methodologies

Gazit et al. first described the formulation of peptide-based nanogels obtained through the inverse W/O emulsion technique, based on the well-known hydrogelator Fmoc-FF. [63] Stabilization was achieved by using, as surfactant, a pegylated derivative of vitamin E, named E-TPGS (d-α-tocopheryl polyethylene glycol 1000 succinate), (**Figure 2.5**), which choice was justified by its remarkable biocompatibility, biodegradability, and low immunogenicity profiles. After the preparation procedure, nanogels were described to be lyophilized and resuspended only at the time of use. According to this procedure, we were able to obtain nanoparticles with a mean diameter of ≈250, which stability in the suspension form was tested over time. Since DLS measurements highlighted a significant increase in the size of nanogels (mean diameter around 1000 nm) after the first 24 h from their preparation, we concluded that the lyophilization step was indispensable to preserve the formulation. With the scope of avoiding this step, we tried to develop novel and more stable peptide based nanogel formulations, moving our reflection from the careful evaluation of the surfactant stabilizing capacity. We chose to base this assessment on the HLB (Hydrophilic-lipophilic Balance) parameter, proposed by Griffin between the late 1940s and early 1950s, which is defined by the following *Equation 2.1* [103, 104]:

$$HLB = \frac{MW\ hydrophilic\ part}{MW\ lipophilic\ part} \times 20 \qquad (2.1)$$

According to this reference, to promote a good stabilization of the water-in-oil emulsion, the HLB value of the surfactant should be between three and six, but the E-TPGS has an HLB value of 13.2. It is important to underline that, in the reverse emulsion method, two steps, with different

stabilization needing, follow each other. In the first one, an oily phase needs to be stabilized in an aqueous one, but, after the extraction of the mineral oil and the rehydration, the system needs to be stabilized in water. For this reason, we first chose to use an HLB value of 10, which was in the middle of the proposed scale of values. Indeed, surfactants with HLB < 10 are good W/O emulsion stabilizer, while surfactants with HLB > 10 are good O/W emulsion stabilizer. The two surfactants we chose to combine were SPAN®60 and TWEEN®60 (**Figure 2.5**).

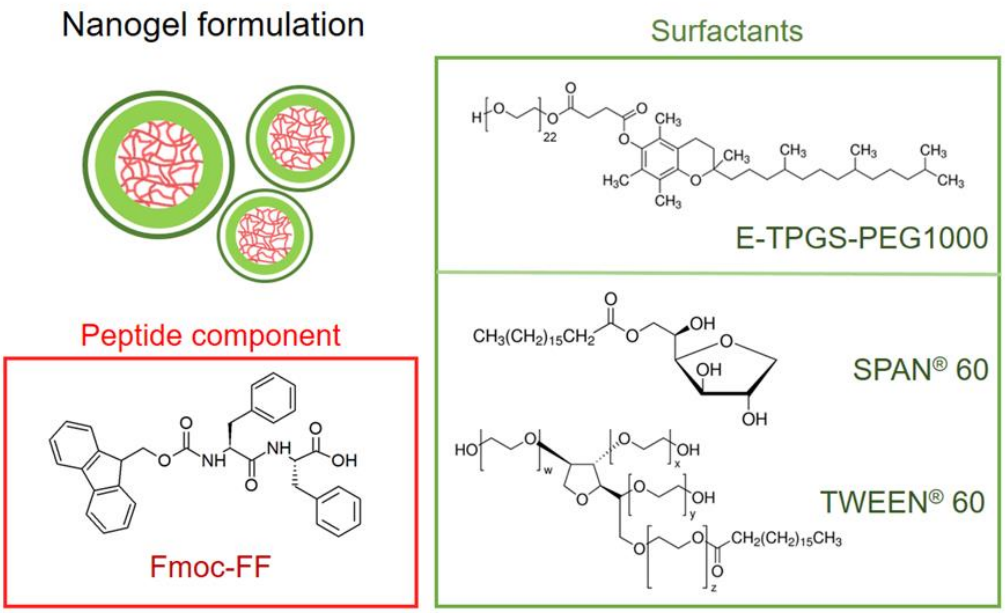

Figure 2.5: In the red box, chemical formulas of the peptide-component composing the inner nanogel core (Fmoc-FF); in the green boxes, chemical formulas of the molecules composing the external surfactant shell (E-TPGS and SPAN®60 and TWEEN®60).

SPAN®60 (sorbitan stearate) is a lipophilic neutral surfactant displaying an HLB value of 4.7 while TWEEN®60 (polyethylene glycol sorbitan monostearate) is a hydrophilic neutral surfactant with an HLB value of 14.9.

By mixing these surfactants in different ratios, it is possible to obtain all the HLB values ranged between 4.7 and 14.9, which are reported in **Table 2.1**.

Table 2.1: Hydrophilic-lipophilic balance (HLB) values obtained combining different percentages of SPAN®60 and TWEEN®60

Emulsifier Blend		HLB
SPAN® 60	TWEEN® 60	
100%	0%	4.7
87%	13%	6
68%	32%	8
48%	52%	10
28%	72%	12
6%	94%	14
0%	100%	14.9

Starting from the mixture allowing an HLB value of 10, we prepared Fmoc-FF nanogels through the reverse emulsion technique, which consists of the formation of a water-in-oil emulsion assisted by a mechanical homogenization step. The aqueous phase consists of the gelling DMSO/H_2O peptide solution, whereas the organic phase consists of a mineral oil, in which surfactants are solubilized. To ensure a complete coating of the peptide core, the total amount of TWEEN®60 and SPAN®60 was chosen to be 3×10^{-5} mol, with respect to 1.86×10^{-5} mol of the Fmoc-FF. In detail, 1 mL of the Fmoc-FF hydrogel was transferred into the mineral oil, containing the two surfactants, during its opaque-to-limpid transition step. The sample was then mechanically homogenized for 5 min (at 35,000 rpm), then the oily phase extracted with n-hexane, and the residue rehydrated with water. To study the relationship between the HLB value and the structural properties of each formulation in terms of size, stability, and feasibility, we explored also the other HLB values ($4.7 < HLB < 14.9$) that can be obtained using different surfactant ratios (**Table 2.1**).

We also tried to prepare Fmoc-FF nanogels according to the "top-down" methodology, previously described by Chauhan et al. [102] Phe-ΔPhe-based nanogels were obtained through the progressive size-reduction of a preformed hydrogel into an aqueous phase. By following this concept, we produced Fmoc-FF hydrogels in macroscopic disks using silicone molds. These disks were then unpacked, through first a homogenization and then a tip-sonication step, into an aqueous suspension of the two surfactants in the ratio 52/48 allowing an HLB = 10. Beyond these two methods previously reported in the literature, a third novel procedure, which we named "nanogelling in water", was tested. It consists in the addition of the DMSO/H_2O peptide metastable solution (before the gelling procedure is completed) to the aqueous solution of the surfactants. This methodology is very similar to the W/O emulsion one, but, since it avoids the use of mineral oil, no n-hexane is needed for its extraction. In both "top-down" and "nanogelling in water" approaches, the total amount of surfactants and of peptide were the same previously used for the reverse-emulsion method.

2.4.2 Fmoc-FF nanogel characterization

The size and stability of all peptide-based nanoformulations, obtained by the three different explored methods, were analyzed through DLS technique. Structural data (mean diameter, polydispersity index, PDI, and zeta potential) for all the samples are collected in **Table 2.2.** By using the W/O emulsion technique and an HLB value of 10, we were able to obtain nanogels with a mean diameter of 204 nm at t = 0, with a slight increase (around 10%, mean diameter = 224 nm) one month after the preparation. This result indicates good shelf stability and points out that the choice of the appropriate surfactant may allow avoiding the freeze-drying step. In **Figure 2.6** the intensity correlation functions and the DLS profiles for three selected HLB values (4.7, 10, and 14.9, representing the two extreme and the middle HLB conditions) are reported. According to the same formulation

procedure and by changing the HLB value, we were able to obtain stable peptide-based nanogels (final Fmoc-FF concentration 0.25 wt%) each time, even if some of them showed slightly more uneven profiles at DLS analysis. This result can be explained considering that the Z potential values measured for the nanogel formulations (see **Table 2.2**) is negative, with a high module ranged between −27 and −41 eV.

Table 2.2: Structural characterization (mean diameter, polydispersity index (PDI) and zeta potential) of Fmoc-FF nanogels prepared according to the different formulation strategies.

Method	HLB	Mean Diameter (nm) ± S.D.	PDI	Mean Diameter (nm) ± S.D. after 30 gg	ζ mV± S.D.
W/O emulsion	4.7	163 ± 87	0.180	189 ± 89	−40.2 ± 0.3
W/O emulsion	6	205 ± 85	0.174	241 ± 91	−40.9 ± 1.5
W/O emulsion	8	217 ± 93	0.201	249 ± 102	−30.4 ± 0.9
W/O emulsion	10	204 ± 115	0.192	224 ± 109	−27.4 ± 1.0
W/O emulsion	12[a]	d_1 = 161± 42 d_2 = 721 ± 230	0.168 0.264	d_1 = 243 ± 117 d_2 = 1844 ± 560	−29.5 ± 1.0
W/O emulsion	14.9	242 ± 100	0.208	332± 183	−27.2 ± 1.0
Top-down	10	174 ± 82	0.176	202 ± 97	−24.0 ± 0.1
Nanogelling in water	10	d_1 =61 ± 18 d_2 = 358 ± 186	0.132 0.210	D_1 = 98 ± 43 d_2 = 407 ± 235	−16.6 ±0.6
Top-down/Dox	10[a]	242 ± 102	0.190	----	−30.2 ± 0.3

[a] Two populations of aggregates (indicated as d_1 and d_2) were found for the W/O emulsion HLB 12 and for nanogelling in water HLB 10.

Surprisingly, we observed a good stability, also for formulations obtained by exploiting HLB surfactant values comparable or even higher than 13.2, corresponding to the HLB value of E-TPGS. Our assumption was that HLB is a parameter that, by expressing the ratio between the molecular weight

of the hydrophilic and the lipophilic parts, can provide a prediction of the intrinsic tendency of the surfactant to preferentially place itself in the aqueous or oily phase of the emulsion. However, it does not clarify or quantify the stabilizing capacity of a surfactant related to another one. It is evident since TWEEN®60 and E-TPGS, which have almost comparable HLB values, do not behave in the same way as shell components of the nanogel. This can be explained considering that, even if they own similar number of ethylene glycol moieties and a similar length of hydrophobic alkyl chains, in TWEEN®60 PEG chains are distributed on different OH groups. This structural feature probably confers more conformational freedom to the PEG chains, that can orientate themselves towards the aqueous phase, undergoing less folding.

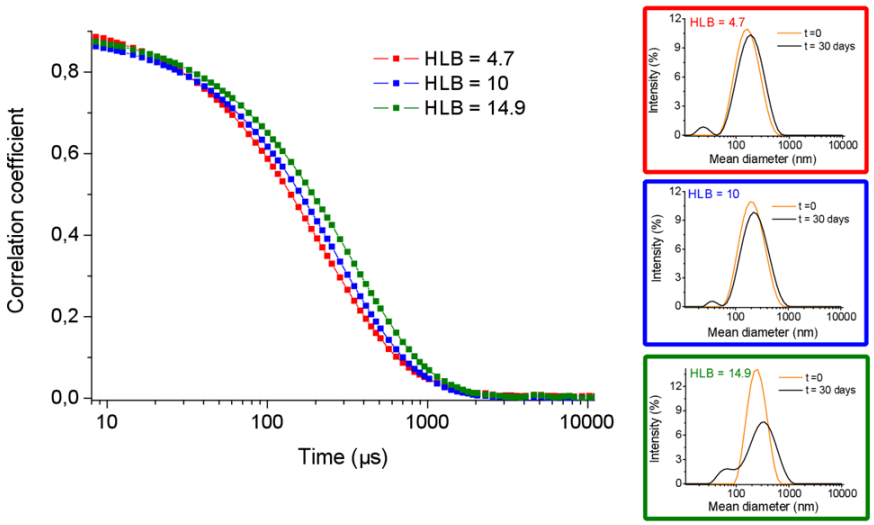

Figure 2.6: Intensity correlation functions for Fmoc-FF nanogels prepared according to the inverse emulsion at three different HLB values (4.7, 10, and 14.9). On the right, the dynamic light scattering (DLS) profiles for these formulations freshly prepared and after one month.

However, a moderate linear dependence between the nanogel size and the HLB value can be observed, as emerged from the comparison between the mean diameter values (ranged between ~160 and ~240 nm) in **Table 2.2** and between the intensity correlation functions in **Figure 2.6**. This consideration is supported by the DLS measurements carried out on pure SPAN®60 and TWEEN®60 aggregates obtained by treating the surfactants with the same procedure in the absence of Fmoc-FF. Indeed, pure SPAN®60 and TWEEN®60 aggregates present a hydrodynamic radius of 205 ± 111 and 310 ± 158 nm, respectively (see **Figure 2.7A**). These values are slightly higher (~20%) than the ones measured for the corresponding peptide nanogels, thus, indicating that attractive interactions occur between the hydrophobic portion of the surfactants and the Fmoc-FF dipeptide. As reported in **Figure 2.7B** and **Table 2.2,** nanogels obtained through the top-down methodology are slightly smaller (174 ± 82 nm) than those obtained with the W/O emulsion technique, in the same surfactant conditions (HLB = 10) whereas the nanogelling in water methodology provides larger objects (358 ± 186 nm). However, all the nanostructures were shown to be stable up to one month. We concluded that stability is not significantly affected by the formulation method, but it seems that the stabilizing agents play a determinant role. Aggregation properties of Fmoc-FF-based nanogels were studied by fluorescence spectroscopy. It is known that the fluorescence emission peak (λ_{em} = 313 nm) of the fluorenyl moiety of Fmoc-FF in its monomeric form undergoes a red shift in its aggregated form and can provide information on the mutual arrangement occurring in the aggregate. In **Figure 2.8A** the fluorescence spectrum of Fmoc-FF nanogel prepared according to the top-down technique is compared to the spectrum of the macroscopic Fmoc-FF hydrogel. As previously reported for other Fmoc-containing aggregates, [108] the maximum at 325 nm indicates an anti-parallel staking of two fluorenyl moieties.

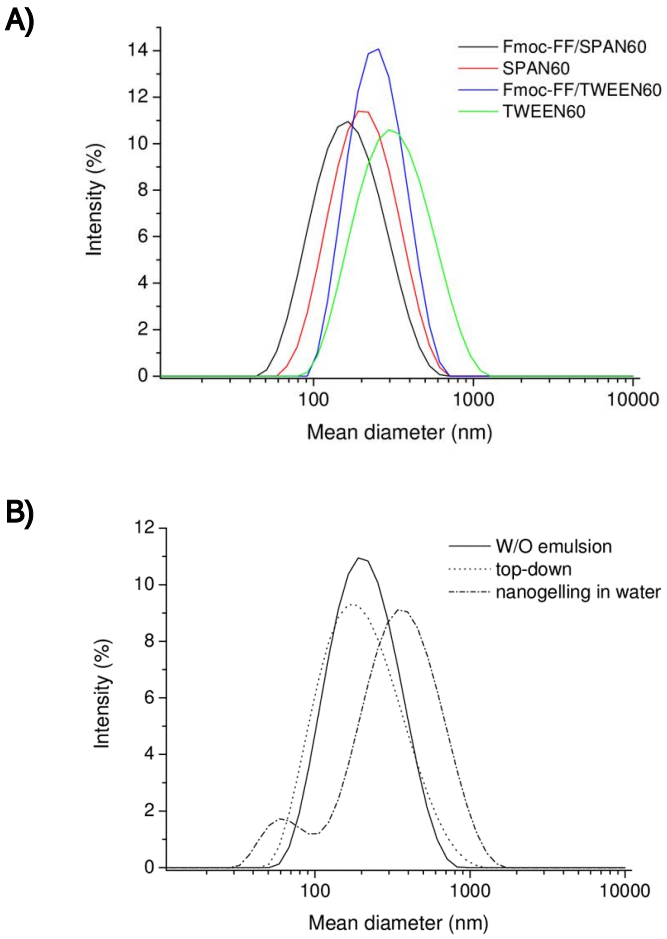

Figure 2.7: DLS profiles. (A) For Fmoc-FF/SPAN®60 (HLB = 4.7) and Fmoc-FF/TWEEN®60 (HLB = 14.9) as compared with the corresponding aggregates lacking the dipeptide; (B) For Fmoc-FF nanogels prepared according to W/O emulsion, top-down, and nanogelling in water methods (HLB = 10).

Since the fluorescence spectrum of the nanogel formulation is well superimposable with the one of the corresponding hydrogels, it can be concluded that the nanosized formulation does not alter the organization at the molecular level and it keeps the ability of Fmoc-FF to generate π–π interactions between the fluorenyl moieties.

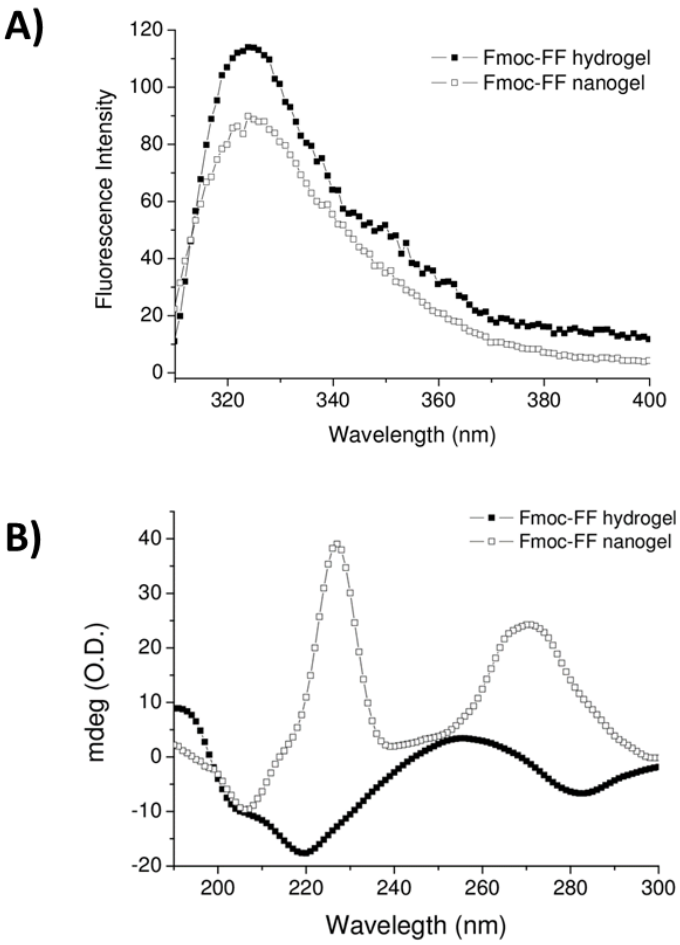

Figure 2.8: Structural characterization of nanogels prepared by top-down methodology. Fluorescence (A) and circular dichroism (CD) spectra (B) of Fmoc-FF nanogel formulation in comparison with Fmoc-FF hydrogel.

Information on the secondary structure of Fmoc-FF nanogels were obtained by CD characterization. In **Figure 2.8B** the CD spectrum for the nanogel (formulated by the top-down technique) is compared with the spectrum of macroscopic Fmoc-FF hydrogel. Both the profiles are characterized by two leading signals. The first one is located in the 220-230 nm region (221 and 228 nm for Fmoc-FF hydrogel and nanogel, respectively) and it is indicative

of β-sheet structuration of the peptide building block in the supramolecular system. [109] This signal, which is negative for Fmoc-FF hydrogel, undergoes a dichroic inversion for nanogel formulation, becoming positive and more intense. This effect can be ascribed to a difference in the global chiral environment which the two formulations are subjected to. However, the change in the three-dimensional surrounding does not alter the fundamental β-sheet organization, which can be recognized from the second signal, typical signature of the Fmoc moiety, centered at 259 nm for the hydrogel material and it is red shifted at 270 nm for nanogel. The bathochromic effect can occur as a consequence of a different dielectric constant in the nanogel core when covered by surfactants, or it can derive from scattering phenomena which may depend on the different physical state. [110]

2.4.3 Cytotoxic effect of empty Fmoc-FF nanogel formulations on different cell lines

The cytotoxicity of unloaded Fmoc-FF nanogels was evaluated on a panel of breast cancer cell lines, each of them used as prototype of a specific breast cancer subtype: MDA-MB-361 and MDA-MB-453 (representative of luminal breast cancer), SKBR3 (representative of Her2 positive) and MDA-MB-231 (representative of basal breast cancer) together with two non-tumoral cell lines, namely MCF10a (representative of mammary gland) and 3T3-L1 (representative of murine pre-adipocytes). **Figure 2.9** shows that, at the end of the tested incubation periods (from 24 to 72h) and for each of the tested concentrations, NGs were found to be toxic only for MDA-MB-231 cell line, in which a significant reduction in cell viability was registered after incubation for 24 h at peptide concentration of either $5 \cdot 10^{-3}$ or $2.5 \cdot 10^{-3}$ wt%.

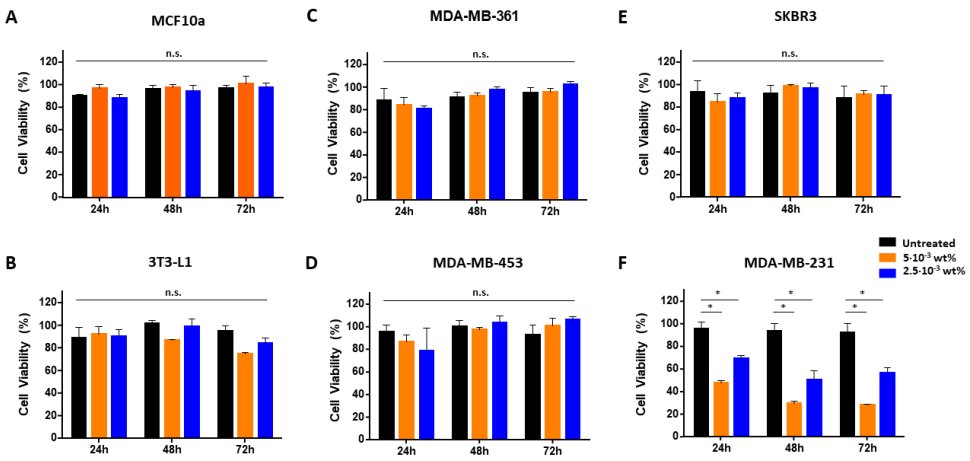

Figure 2.9: MTT assays conducted on MCF10a (A), 3T3-L1 (B), MDA-MB-361 (C), MDA-MB-453 (D), SKBR3 (E) and MDA-MB-231 (F) cells upon incubation for the indicated times with two different Fmoc-FF nanogels concentrations: $5 \cdot 10^{-3}$ wt% (red bars) or $2.5 \cdot 10^{-3}$ wt% (green bars). Cell survival is expressed as percentage of viable cells measured in the presence of nanogels, compared to control untreated cultures.

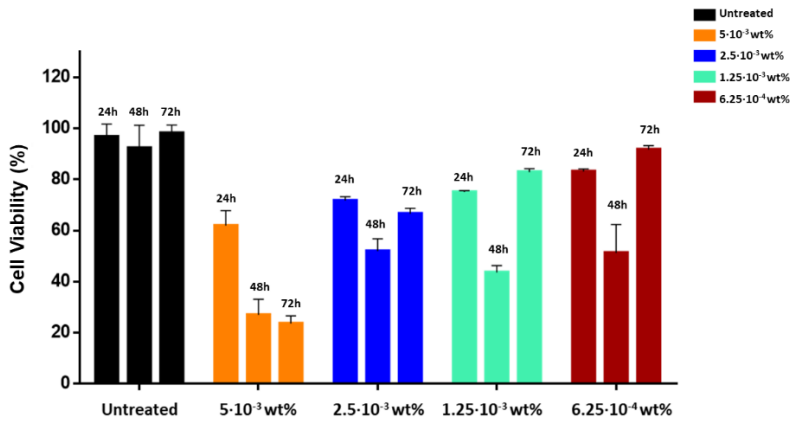

Figure 2.10: MTT assay conducted on MDA-MB-231 treated with Fmoc-FF nanogels for 24h, 48h and 72h and at the following concentrations: $5 \cdot 10^{-3}$ wt% (orange bars), $2.5 \cdot 10^{-3}$ wt% (blue bars), $1.25 \cdot 10^{-3}$ wt% (green bars) and $6.125 \cdot 10^{-4}$ wt% (bordeaux bars). Cell survival is expressed as percentage of viable cells measured in the presence of nanogels, compared to control untreated cultures.

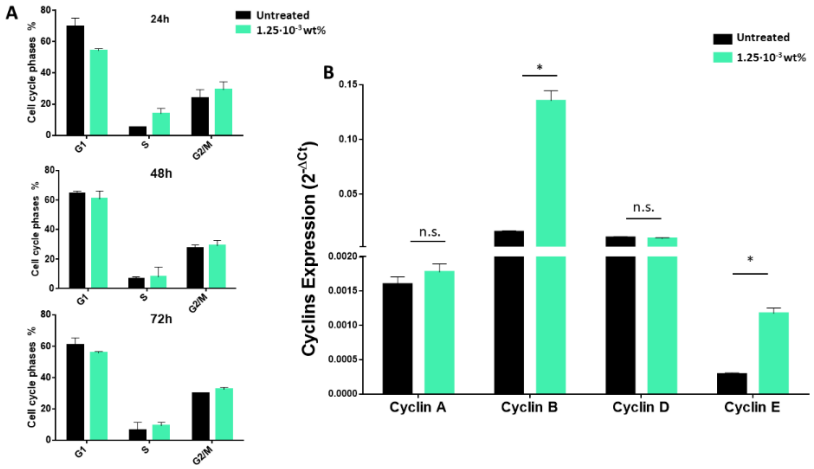

Figure 2.11: A) Percentage of MDA-MB-231 cells present in G0-G1, S, and G2-M phase upon treatment with Fmoc-FF nanogels at $1.25 \cdot 10^{-3}$ wt% dilution for 24 (top panel), 48 (middle panel) and 72h (lower panel). The percentages are reported as the mean of three independent experiments +/− SD. B). mRNA levels of the indicated cyclins in untreated (black bars) MDA-MB-231 cells and upon 24h of treatment with $1.25 \cdot 10^{-3}$ wt% Fmoc-FF nanogels (red bar). The relative expression was determined using the 2−ΔCt method. Cyclins relative expression is shown as mean +/− SD of three technical independent experiments. * = p-value < 0.05, Mann Whitney t-test. n.s.= not significative.

A maximum cytotoxic effect was observed upon 48 h of incubation. Moreover, the treatment with lower peptide concentrations ($6.25 \cdot 10^{-4}$ or $1.25 \cdot 10^{-3}$ wt%), caused a temporary growth arrest of MDA-MB-231, which started a cell recovery after 48 h of incubation and showed, at 72h, a viability similar to the untreated controls (**Figure 2.10**). This may suggest a reversible inhibitory effect on these cells. By analyzing their cell cycle, it was shown that MDA-MB-231 cells treated with Fmoc-FF nanogels resulted blocked in the S phase (**Figure 2.11A**). This result was further confirmed by checking the expression of four regulatory cyclins. Indeed, **Figure 2.11B**

shows a significant increase in the expression levels of cyclins E and B observed after 24h of incubation.

2.4.4 Fmoc-FF nanogels internalization mechanism

It is essential to deeply analyze the mechanism involved in NGs uptake to understand the biological properties of these delivery systems and, in turn, to tune their biological selectivity according to the desired goal. This mechanism may depend by a great extent on physical and interfacial characteristics of nanogels, like size, shape and surface properties (charge and hydrophobicity), which can regulate their interactions with the biological environment and the affinity with the cell membrane. For this reason, also the cell type, and thus membrane fluidity and availability of receptors, can affect nanogels uptake pathway.

To follow NGs entrance in MDA-MB-231, we loaded them with FITC, a fluorescent molecule commonly used for biological assays. FITC filled nanoformulations were prepared using the top-down approach and characterized by Dynamic Light Scattering (DLS) analysis (mean diameter184 ± 86 nm and ζ= -22.0±0.2 eV). MDA-MB-231 cells were incubated with FITC-loaded NGs at 37°C for 1 hour, and then they were analyzed by fluorescence microscopy. As shown in **Figure 2.12A**, an efficient internalization was confirmed by the presence of punctate FITC-fluorescent structures in the cytoplasm. Z stacks of confocal sections revealed the presence of structures with diameter ranging from 0.1 to 1 μm (**Figure 2.12B-C**). Polymer-based nanogels were shown to be mainly internalized through phagocytosis and/or pinocytosis mechanisms, with their intracellular fate varying depending on the cell type and growing conditions. [111] Pinocytosis exists in almost all the cell types, even if each of them presents a distinct profile of endocytic routes, such as macropinocytosis, clathrin-mediated endocytosis, caveolae-mediated endocytosis, or clathrin/caveolae independent endocytosis.

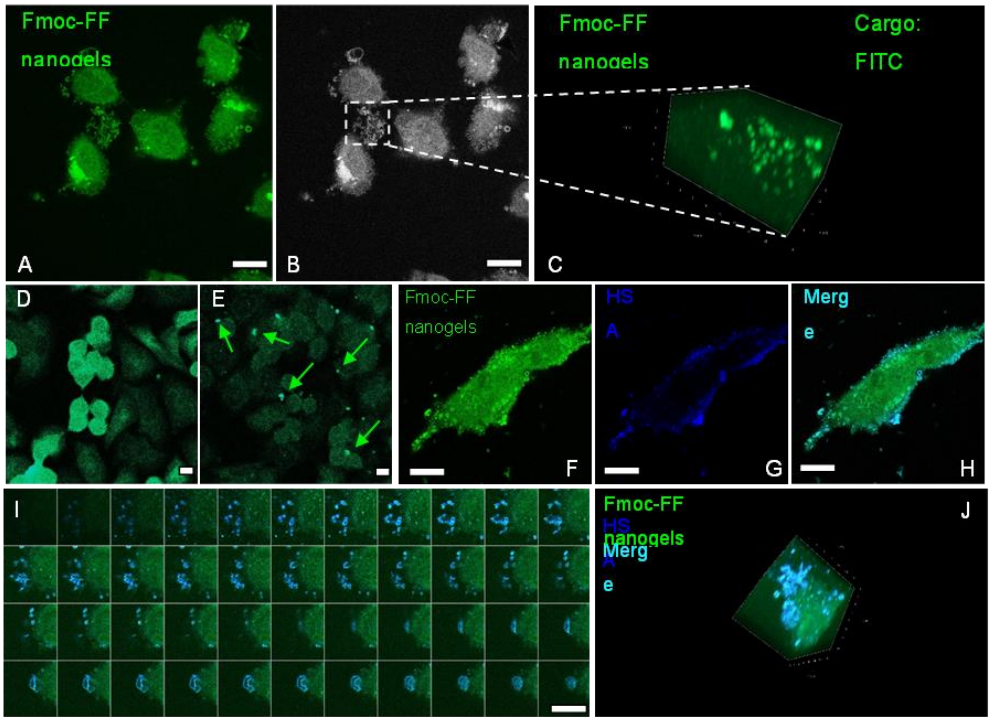

Figure 2.12: A) Confocal images showing the intracellular localization of FITC loaded Fmoc-FF nanogels (green signal) upon their incubation with MDA-MB-231 cell for 1 hour at 37 ° C. B-C) 3D rendering of a z-stack gallery of confocal sections showing FITC loaded Fmoc-FF nanogels in intracellular vesicles ~ 100 nm in diameter. D-E) Confocal images showing the fluorescence of FITC loaded Fmoc-FF nanogels incubated with MDA-MB-231 cell for 1 hour at 4°C (panel D, note the PM staining of the FITC signal) and then switched to 37° C for 10 min (panel E, note the vesicular staining of the FITC signal). F-H) Colocalization of Fmoc-FF nanogels (green, panel F) and HSA containing vesicles (blue, panel G) in MDA-MB-231 cells; the merge in panel H shows, in cyan, region of colocalization between green and blue signals. I-J) Gallery (panel I) and 3D rendering (panel J) of confocal z-sections showing FITC loaded Fmoc-FF nanogels (green) colocalizing with HSA (blue) containing vesicles. Cyan indicates region of colocalization between nanogels and HSA. (For all panels, magnification bar = 14 μm).

A temperature block was included in the uptake experiment with the aim to distinguish between nanogels permeation and endocytosis. In detail, cells were incubated with nanogels at 4°C for 1 h, and then a temperature of 37°C was reached to promote internalization (**Figure 2.12D-E**).

Differently from what occurs with perforation and permeation, endocytosis requires invagination and emi-fusion of the plasma membrane, a process that cannot occur at 4°C. Indeed, images collected for MDA-MB-231 cells when incubated with NGs at 4°C, do not show the presence of internalized fluorescent structures and the FITC appears to be localized and distributed on the plasma membrane. After re-shifting at 37°C, distinct puncta can be distinguished in the cytoplasm, thus confirming the involvement of an endocytic process. NGs dimension (up to 100 nm) should be not compatible with clathrin-dependent endocytic mechanism, and should require larger and more flexible membrane invagination, similar to those formed during caveolae-mediated endocytosis, which is the most diffused transendothelial pathway. Caveolae can be defined as plasma membrane microdomains enriched in caveolins, cavins, cholesterol, and sphingolipids.

To confirm the involvement of caveolae in the internalization by MDA-MB-231 cells, Fmoc-FF NGs were decorated with an anti-HSA (Human Serum Albumin) antibody. **Figure 2.12F-H** shows that Fmoc-FF nanogels colocalize well with HSA containing caveolae. Interestingly, HSA containing caveolae appear to be smaller and higher in number when the nanogel is absent, while, in its presence, their dimension increases, probably as a consequence of the massive cargo they are internalizing. A good colocalization between HSA and Fmoc-FF nanogels in caveolae was revealed by Z-stack reconstruction of confocal Z sections (**Figure 2.12 I-J**). We were so able to demonstrate that peptide based nanogels, with the Fmoc-FF dipeptide composing the inner core and SPAN®60 and TWEEN®60 composing the surfactant shell, enters MDA-MB-231 cells *via* caveolae-mediated endocytosis. A similar mechanism of uptake has been also described for other nanocarriers. [112]

2.4.5 HSA mediated caveolae saturation mechanism

A competition experiment between HSA and Fmoc-FF NGs was carried out. Briefly, the composition of the cell culture medium was altered by increasing the amount of either HSA and FBS or Glucose, which were used as control, in order to saturate their intracellular transport machinery.

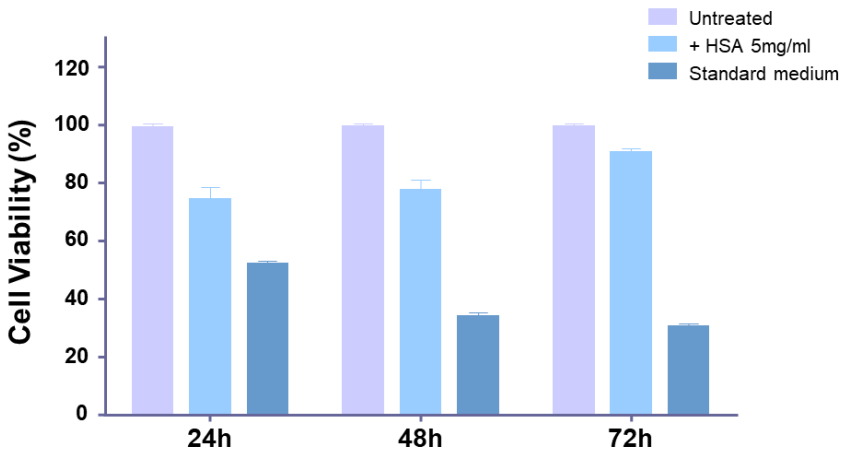

Figure 2.13: MTT assay was conducted on MDA-MB-231 to evaluate the effects of the higher concentration of NG ($5 \cdot 10^{-3}$ wt%) on cell viability in standard medium (dark blue bars) and in the presence of 5mg/ml of additional HSA (light blue bars), respect to untreated MDA-MB-231 (light violet bars). Cell viability, expressed as percentage of viable cells, is reported as function of the incubation time with Fmoc-FF nanogel.

The addiction of a double amount of FBS or Glucose did not alter $5 \cdot 10^{-3}$ wt% Fmoc-FF nanogels toxicity on MDA-MB-231, even if at lower peptide concentration ($2.5 \cdot 10^{-3}$ wt%) and in the presence of an increased Glucose concentration, a reduction of NGs cytotoxic effect at 24 and 48h of incubation was experimented (data not shown). On the contrary, a reduction of NGs toxicity was observed even for the highest peptide concentration, when the HSA quantity in the medium was doubled, with an increase in cell viability up to 80% (**Figure 2.13**). These data shows that caveolae-mediated

NG uptake is inhibited by elevated HSA concentrations, by suggesting the occurrence of a competitive mechanism, which is saturable and influenced by serum components.

2.4.6 Fmoc-FF nanogels selectivity toward MDA-MB-231 results from caveolin-1 overexpression

MDA-MB-231 cells have been shown to overexpress Caveolin 1 (CAV1) and thus to possess an efficient Caveolae-mediated endocytosis activity. [113] Caveolin 1 protein acts as cytosolic scaffold and, by promoting membrane invagination, helps caveolae formation.

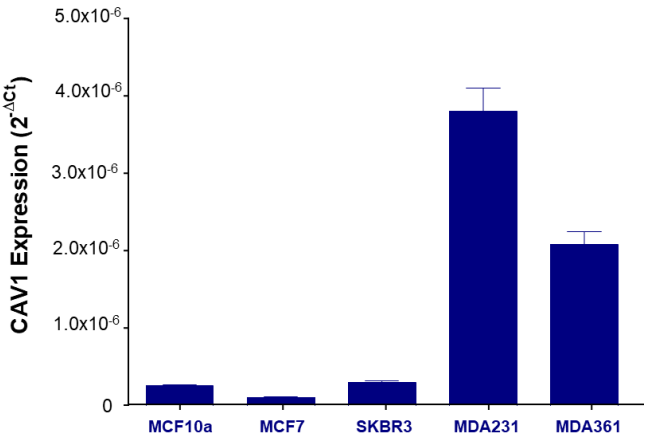

Figure 2.14: Caveolin-1 mRNA expression levels in the different breast cancer cell lines used in this manuscript. The relative expression was determined using the 2−ΔCt method. Caveolin-1 relative expression is shown as mean +/− SD of three technical independent experiments.

To compare expression levels of CAV1 in the panel of cell lines used for the previous experiments, for each of them we measured caveolin transcript by qPCR. As expected, the expression levels of Caveolin 1 in MDA-MB-231 was higher than the other cells (**Figure 2.14**). This outcome suggests that

the selective cytotoxicity towards MDA-MD 231 cells exerted by Fmoc-FF NGs derives from their specific internalization mechanism.

2.4.7 Formulation and characterization of Dox-filled hydrogels

The mechanical behavior is an important aspect to be considered for the therapeutic applicability of peptide-based drug-delivery formulations. As already mentioned, improved rheological and physical properties can be shown by mixed hydrogels in which more components are combined. Recently, mixed peptide formulations, composed by the dipeptide Fmoc-FF and sequences of aromatic amino acids, have been investigated. [106, 107]

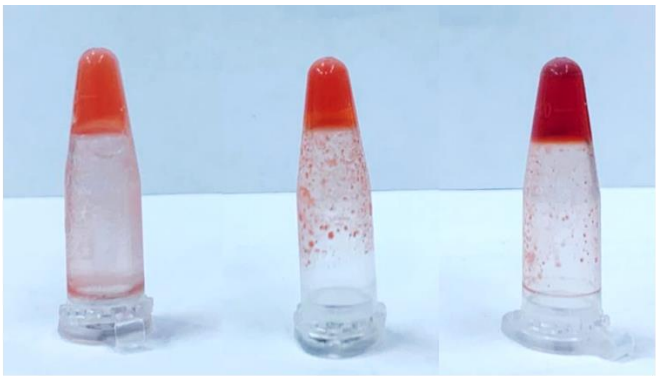

Figure 2.15: Inverted test tubes for Dox-loaded Fmoc-FF hydrogels at three different concentrations of doxorubicin.

To test their capability to be used as implants, pure and mixed HGs filled with the anticancer drug Dox were prepared according to the solvent-switch method. By dissolving the peptide or the mixture of peptides in DMSO (total peptide concentration 100 mg/mL) and by rehydrating this stock with a water solution of doxorubicin (4.0 mmol/L), Fmoc-FF, and Fmoc-FF/(FY)3 and Fmoc-FF/PEG_8-(FY)3 (each one at the two different ratios 1/1 and 2/1 v/v) macroscopic hydrogels were formulated. However, in the described

conditions, Dox-filled HG appears to be not completely homogeneous, even if, by progressively increasing the amount of Dox, an improvement of the hydrogel consistence and homogeneity can be obtained (**Figure 2.15**). This may occur because of a shield effect of the charges of the drug interfering with the ones of the peptide matrix. In any event, the drug concentration needed to formulate adequate hydrogels was too high to make it possible to compare Dox-loaded Fmoc-FF HG with the other two, so we preferred to not consider it in our discussion. The morphology of the other xerogels was analyzed through confocal microscopy. Confocal images of Fmoc-FF/(FY)3, 1/1 are reported in **Figure 2.16A,B** as example. Xerogels appear to be composed by the characteristic intricate network of entangled fibers with a red color suggesting the tight interaction of Dox with the network constituents. For mixed Fmoc-FF/(FY)3 and Fmoc-FF/PEG_8-(FY)3 matrices embedding Dox, no syneresis was detected after 10 days. The absence of water-loss allows to precisely modulate the quantity of water-soluble drug loaded in the system. Considering this experimental evidence, we can assume that all the drug was efficiently and quantitatively entrapped in the hydrogel matrix, and no release occur in static conditions. The amount of drug encapsulated in mixed HGs was so calculated to be 2.32 mg/mL, corresponding to a drug loading content (DLC) of 0.440 and to an encapsulation ratio (ER%, defined as the weight percentage of drug encapsulated in the HG on the total drug added during preparation) of 100%, respectively. This high encapsulation degree is probably a consequence of the attractive electrostatic forces occurring between the components, and in detail between the positive charge on the drug and the negative one located on the C-terminus of the Fmoc-FF peptide. By using a Doxil solution with a Dox concentration equal to the one used for free drug-loaded HGs, also Doxil-loaded HGs were obtained, despite the negative Z potential value we measured for the used Doxil solution ($\zeta \sim$ -11 mV). A macroscopic evaluation of the gelation kinetics for mixed drug-

filled hydrogels was conducted by simply following the opaque-to-transparent optic transition over time. A different time (between 20 and 40 minutes) for each mixed hydrogel is required to complete the gelling procedure.

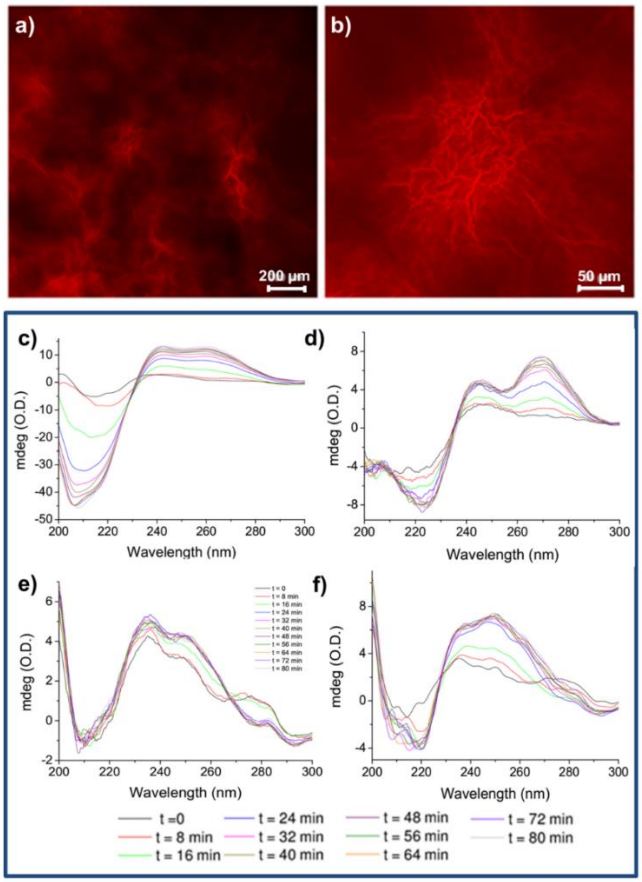

Figure 2.16: Confocal microscopy images of Dox-loaded Fmoc-FF/(FY)3 (1/1) xerogel. Scale bar 200 (A) and 50 µm (B), respectively. CD spectra, collected between 200 and 300 nm, of Fmoc-FF/(FY)3 2/1 v/v (C), Fmoc-FF/(FY)3 (1/1) (D), Fmoc-FF/PEG8-(FY)3 (2/1) (E) and Fmoc-FF/PEG8-(FY)3 (1/1) (F) as function of the time.

These times were found to be correlated with the ones calculated for the empty systems, [106] with faster gelation kinetics for increasing amount of

Fmoc-FF, which may be due to the capability of this dipeptide to gel in a very quick time (~2 min). [57] In detail, a more rapid gelation was observed for mixed HGs containing PEG_8-(FY)3 (24 and 30 minutes for 2/1 and 1/1, respectively) with respect to those containing (FY)3 (35 and 40 minutes for 2/1 and 1/1, respectively). The faster gelation observed for PEG containing HGs compared to lacking polymer ones, is probably due to additional interactions occurring between the hydrophilic PEG structure and the hydrophilic daunosamine sugar of Dox. To better determine the formation kinetics of the considered HGs, we decided to also follow the structural transitions over time through circular dichroism. CD spectra of Dox filled hydrogels were collected at several time points in the spectral region between 300 and 200 nm (see **Figure 2.16C-F**). From the inspection of the spectra, an evolution of the dichroic signal towards a stable state can be observed for all the analyzed matrices. The co-existence of several conformational states in the solution can be deduced by the presence of isosbestic points between 220 and 240 nm and around 267 nm for PEG_8-(FY)3 containing HGs. The gelation times obtained by plotting, for each sample, the optical density (O.D.) in the relative minima as function of the time, were found in good agreement with the ones macroscopically observed by following the transition from the opaque to limpid form (data not shown).

2.4.8 Formulation and characterization of Dox-filled nanogels

Pure Fmoc-FF and mixed Fmoc-FF/(FY)3 (1/1 v/v) nanogels loaded with Dox were prepared, as example formulations, according to the top-down methodology previously described, starting from a macroscopic hydrogel disk with a peptide concentration of 1 wt% and a Dox concentration of 0.018 mol/L. TWEEN®60 and/or SPAN®60 were used as stabilizing agents. As the corresponding empty formulations, Dox-filled Fmoc-FF nanogels were formulated using TWEEN®60 / SPAN®60 at 58/42 ratio (HLB= 10).

On the contrary, the mixed nanogel was found to be unstable when prepared with a value of HLB = 10, and an HLB = 14.9 (corresponding to 100% of TWEEN®60) was used to stabilize the sample. After size-exclusion chromatography purification, the red color showed by the nanogels macroscopically suggested the incorporation of the drug in the vehicle. The amount of Dox in the drug-loaded fraction was analytically quantified by UV-Vis spectroscopy, by checking the absorbance in the maximum at λ_{abs}= 480 nm. DLC and ER% values were found to be 0.137 and 0.093 and 63% and 35%, for the pure and mixed NGs, respectively. By considering these results, it can be concluded that, while DLC value for Fmoc-FF formulation is similar to that of the commercially available Dox-liposomal formulations Myocet (DLC=0.127) and Doxil (DLC=0.250), the insertion of (FY)3 peptide in causes a decrease of these parameters. This lower encapsulation may be ascribed to the presence, in the peptide (FY)3, of an amidated C-terminus, which is significantly less acidic compared to the carboxylic one, and a basic non protected N-terminal amino group that can support a positive charge after protonation.

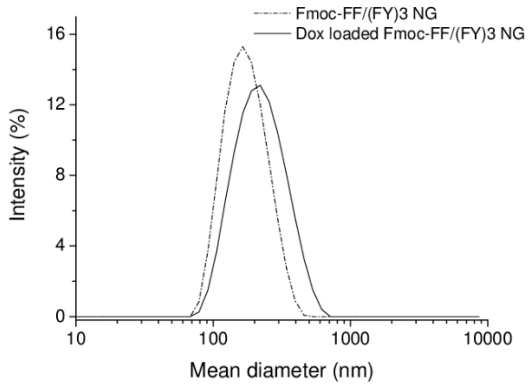

Figure 2.17: DLS profiles for empty and Dox filled Fmoc-FF/(FY)3 (1/1, v/v) nanogels prepared according to the top-down method.

These chemical features cause a reduction of the total negative charge in the inner sphere of NGs, by determining lower attractive forces between the drug and the peptide system. The size of empty and filled Fmoc-FF and Fmoc-FF/(FY)3 NGs, measured by Dynamic Light Scattering (DLS), were 174 / 241 nm and 168 / 214 nm, respectively for the pure and the mixed formulations (see **Figure 2.17**). For both the matrices, an increase in size (~25%) for Dox-filled formulations was thus observed.

2.4.9 Drug Release

Drug release profiles for HGs and NGs are reported in **Figure 2.17A**,**B**. Two different experiments were carried out. To evaluate Dox or Doxil release from hydrogels, these last, prepared into a conic tube, were directly put in contact with a double volume of physiological solution. At each time point, half of the above volume was collected and replaced with an equal aliquot of fresh one. On the contrary, the release of Dox from nanogels was studied using a dialysis method. Briefly, a dialysis membrane was loaded with the nanogel and immersed in phosphate buffer at 37° C. Since we assumed that the free Dox quickly crosses the dialysis membrane, the overall release of the free molecule from the nanostructures to the dialysis bag medium could be considered rate determining for the process. We also considered the API release from the system undergoing a diffusion process. The amount of released Dox in each fraction was estimated by UV-Vis and by fluorescence spectroscopies (at λ_{em}= 590 nm) for HGs and NGs, respectively. Release profiles report percentage ratio between the amount of released drug and the total drug initially loaded as a function of the time. A similar release profile for all the Dox filled hydrogels can be observed during the first 24 hours, but then it starts to be different for each of them, and, after 72h, the lowest release is found for Fmoc-FF/(FY)3 (2/1) (16%). A low drug release (21%) was also observed for the other mixed HGs Fmoc-FF/(FY) 3 (1/1).

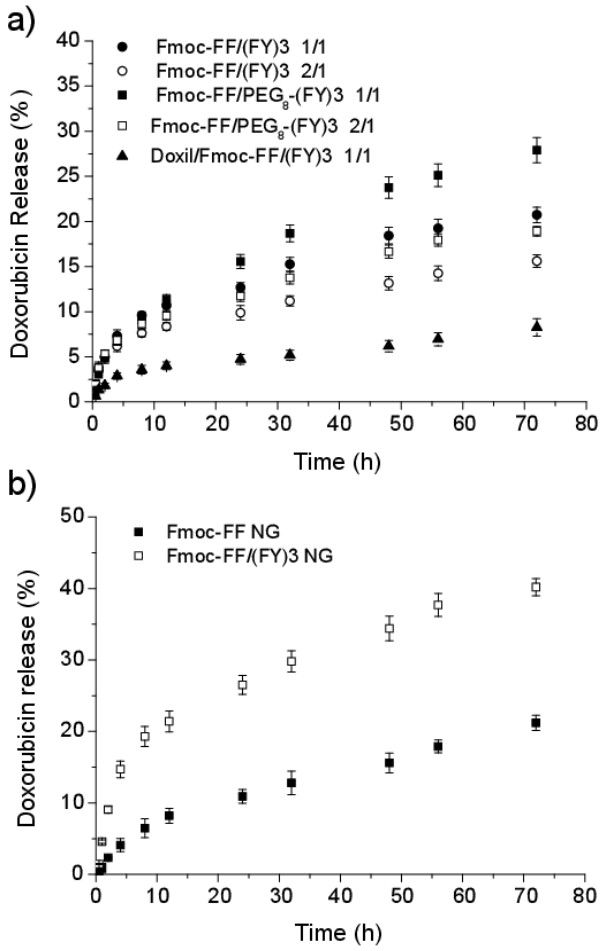

Figure 2.18: Drug release profiles for: (A) multicomponent Fmoc-FF/(FY)3 and Fmoc-FF/PEG_8-(FY)3 hydrogels up 72 hours; (B) pure Fmoc-FF and mixed Fmoc-FF/(FY)3 (1/1, v/v) nanogels.

PEG_8-(FY)3 containing hydrogels also displayed a low release of 19% and 28% for 2/1 and 1/1 ratios, respectively. These results are in agreement with the supposition that PEGylation of the peptide could affect the rigidity and the permeability of the hydrogels matrix and, in turn, the drug release. The amount of drug released from Doxil-loaded hydrogels (~8.5%) was lower than the drug released from the corresponding Dox-loaded one

(21%). Drug release profiles of nanogels show that, after 72h, a higher release occurs for the mixed than for the pure formulation (40% vs 20%, respectively). This can be interpreted as a direct consequence of the repulsive electrostatic interactions occurring between the components in Fmoc-FF/(FY)3 formulation.

2.4.10 Cytotoxicity assays for Dox and Doxil-loaded formulations

MTT assay was used to evaluate cytotoxicity of mixed Fmoc-FF/(FY)3 (1/1, v/v) hydrogel encapsulating Dox or its liposomal formulation Doxil, after 24 hours of incubation on MDA-MB-231 breast cancer cell line, previously found to be the selectively targeted one for Fmoc-FF NGs. For comparison, the cytotoxicity exerted by the free drug, as well and empty hydrogels, was studied in the same conditions. HGs were directly prepared into the hollow plastic chamber sealed at one end with a porous membrane. The experimental setting allowed to mimic the *in vivo* utilization imagined for hydrogels, that means implantation of the matrix at the level of the tumor lesion, where a controlled and constant drug release is achieved. In our experiments, hydrogels remained in contact with the cells for all the duration of the treatment. Cell viability of empty hydrogels was found to be more than 95%. (**Figure 2.19A**), similarly to what previously observed for Fmoc-FF and Fmoc-FF/(FY)3 hydrogels co-incubated with the Chinese Hamster Ovarian (CHO) cell line. [106, 107] This means that the support itself is not toxic on the considered tissue. On the contrary, Dox loaded hydrogels caused a significant reduction of MDA-MB-231 cells viability after only 24 h of incubation (49%) as well as free Dox at a concentration of 1µmol/L (55%), corresponding to its calculated IC50 on the considered cell line.

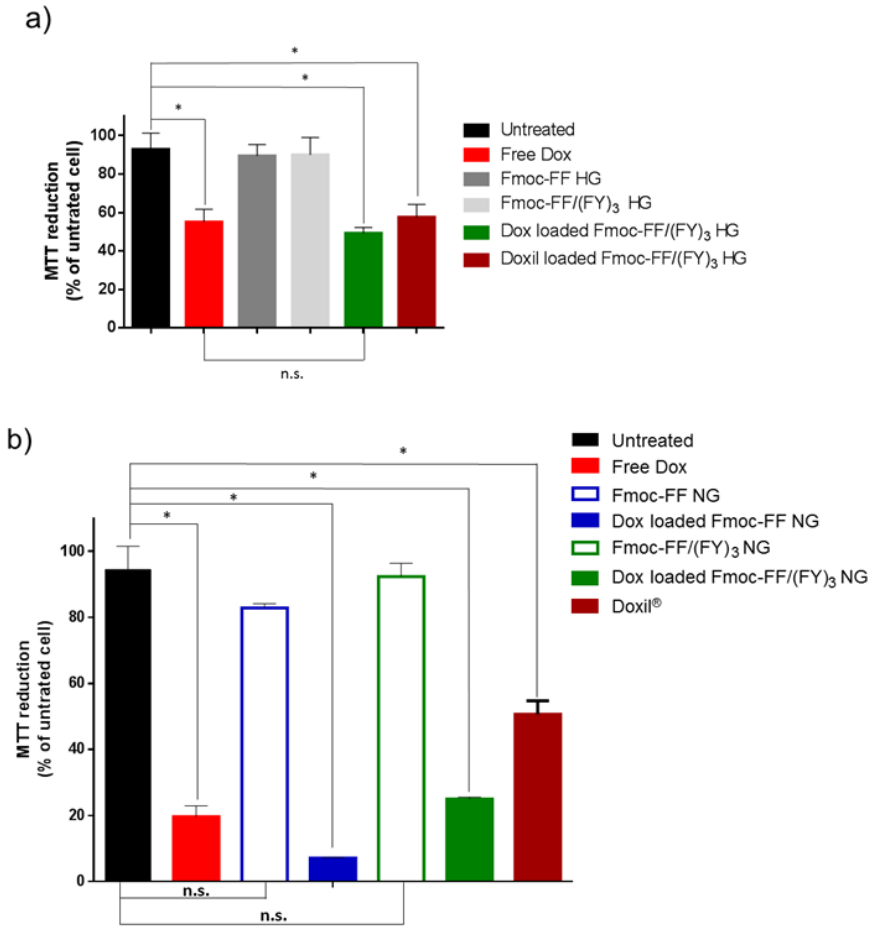

Figure 2.19: MDA-MB-231 cell survival after doxorubicin treatments. (A) MTT assay was conducted on MDA-MB-231 cells treated for 24 h with 1µmol/L of free Dox (red bar), empty Fmoc-FF HG (gray bar), empty Fmoc-FF/(FY)3 (1/1, v/v) HG (light gray bar), mixed Fmoc-FF/(FY)3 (1/1, v/v) HG loaded with Dox (green bar) and loaded with Doxil (burgundy bar) in comparison with untreated cells (black bar). Cell survival was expressed as percentage of viable cells in the presence of hydrogels, compared to control cells grown in their absence. (B) MTT assay was conducted on MDA-MB-231 cells treated for 72h with 1µmol/L of free Dox (red bar), empty Fmoc-FF NG (blue empty bar), empty Fmoc-FF/(FY)3 (1/1, v/v) NG (green empty bar), Dox loaded Fmoc-FF nanogels (blue fill bar), Dox loaded mixed Fmoc-FF/(FY)3 (1/1, v/v) NG (green fill bar) and Doxil (burgundy bar) in comparison with untreated cells (black bar). Cell survival was expressed as percentage of viable cells in the presence of hydrogels and nanogels compared to control cells grown in their absence (Error represents SD of four independent experiments. *p-value <0,05. Mann-Withey t-test). Abbreviation: n.s., not significant.

Hydrogels encapsulating Doxil showed a slightly lower cytotoxicity, with a cell viability of 57%, which was ascribed to the slower release offered by this system. **Figure 2.19B** reports the cell viability, expressed as percentage, after treatment of the same cell line with empty and loaded pure Fmoc-FF and mixed Fmoc-FF(FY)3 nanogels, in comparison to free Dox and Doxil. The cytotoxicity of empty nanogels was firstly evaluated at three different time points (24, 48 and 72 h) as function of the total peptide concentration. As previously underlined, a significant decrease in the cell viability during the first 48 h of incubation was observed, with a successive improvement at 72h. Cytotoxicity of NGs encapsulating Dox was checked after 72 h of incubation, when they were found able to significantly reduce breast cancer survival, with a cell viability of 7% and 25% for pure and mixed hydrogels, respectively. The higher cytotoxicity showed by pure HG when compared to the mixed one may be attributed to the higher intrinsic toxicity of the corresponding empty gel.

2.4.11 Determination of Dox loaded HGs and NGs cellular uptake by Immunofluorescence

Immunofluorescence analyses were conducted on 24h treated MDA-MB-231 cells to study the cellular internalization of Dox loaded HGs and NGs. Internalization of free Dox and Doxil are also reported for comparison. The overlapping of red fluorescence associated to Dox with blue signal associated to DAPI coloring the nucleus (**Figure 2.20A**) indicates that the free drug can internalize into the nucleus. On the contrary, for Dox loaded Fmoc-FF/(FY)3 mixed hydrogel Dox signal is not perfectly overlapped with DAPI, which means that internalization of Dox occurs at peri-nuclear level, even if it is also partially detectable in the cytoplasm together with the green Actin signal (**Figure 2.20B).** Liposomal Dox formulations were previously found to behave in the same way. [114] Finally, doxorubicin conveyed through the nanogels remained in the cytoplasm of treated cells

(**Figure 2.20C**), whereas the delivery by Doxil causes an equal distribution of the drug between the cytoplasm and the nucleus (**Figure 2.20D**). These results are in line with what previously experienced for Fmoc-FF NGs, which enter MDA-MB-231 cells *via* caveolae-mediated endocytosis.

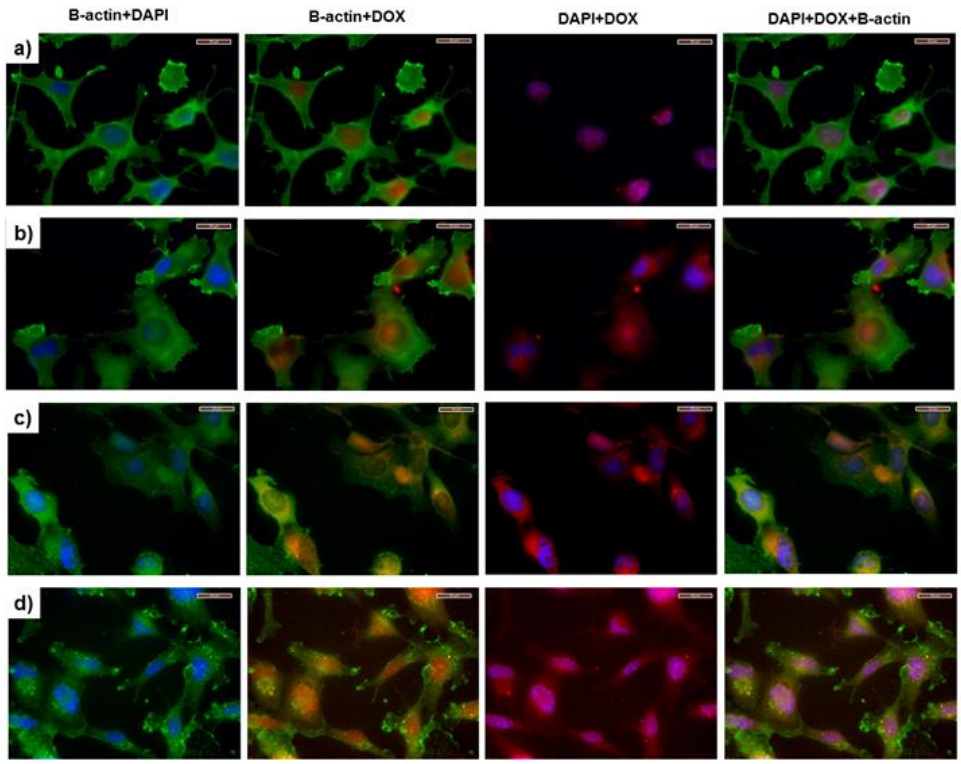

Figure 2.20: Immunofluorescence assay. MDA-MB-231 cells treated with: (A) free Dox; (B) Dox loaded mixed Fmoc-FF/(FY)3 (1/1, v/v) HG; (C) Dox loaded Fmoc-FF/(FY)3 (1/1, v/v) NGs and (D) Doxil. Column I corresponds to Nuclei (DAPI, blue) and B-actin (FITC, green) staining. Column II corresponds to II β-actin (FITC, green) and doxorubicin (red) staining. Column III corresponds to Nuclei (DAPI, blue) and doxorubicin (red) staining. Column IV corresponds to Overlapping of FITC, PE and DAPI channels. Magnification 63×. Scale bars 20 μm.

[70] Langer, R. *Nature* **1998**, 392, 5-10.

[71] Cullis, P. R. *Science* **2004**, 303, 1818-1822.

[72] Vargason, A. M.; Anselmo, A. C.; Mitragotri, S. *Nat Biomed Eng.* **2021**, 5, 951-967.

[73] Serajuddin, A. T. *J. Pharm. Sci.* **1999**, 88, 1058–1066.

[74] Dlugi, A. M.; Miller, J. D.; Knittle, J.; Group, L. S. *Fertil. Steril.* **1990**, 54, 419-427.

[75] Gregoriadis, G. *Med Drug Discov.* **2021**, 12, 100104.

[76] Stewart, S. A.; Domínguez-Robles, J.; Donnelly, R. F.; Larrañeta, E. *Polymers (Basel).* **2018**, 10(12), 1379.

[77] Guida, M.; Farris, M.; Aquino, C. I.; Rosato, E.; Cipullo, L. M. A.; Bastianelli, C. *Biomed Res Int.* **2019**, 3726957.

[78] Li, J.; Mooney, D. *Nat Rev Mater* **2016**, 1, 16071.

[79] Wu, J. *J. Pers. Med.* **2021**, *11*, 771.

[80] Duncan, R. *Pharm. Sci. Technol. Today* **1999**, 2, 441-449.

[81] Maeda, H.; Wu, J.; Sawa, T.; Matsumura, Y.; Hori, K. *J. Control. Release* **2000**, 65, 271-284.

[82] Stylianopoulos, T. *Ther. Deliv.* **2013**, 4, 421-423.

[83] Siegel, R. L.; Miller, K. D.; Jemal, A. *Cancer J Clin.* **2020**, 70(1), 7-30.

[84] Poustchi, F.; Amani, H.; Ahmadian, Z.; Vahid Niknezhad, S.; Mehrabi, S.; Santos, H. S.; Shahbazi, M. A. *Adv Healthc Mater.* **2021**, 10(3), e2001571.

[85] Gewirtz, D. A. *Biochem Pharmacol.* **1999**, 57, 727-741.

[86] Carvalho, C.; Santos, R.; Cardoso, S.; Correia, S.; Oliveira, P. J.; Santos, M. S.; Moreira, P. I. *Curr Med Chem.* **2009**, 16(25), 3267-3285.

[87] Unverferth, D. V.; Fertel, R. H.; Talley, R. L.; Magorien, R. D.; Balcerzak, S. P. *Toxicol Appl Pharmacol.* **1981**, 60(1), 151-154.

[88] Falciani, C.; Accardo, A.; Brunetti, J.; Tesauro, D.; Lelli, B.; Pini, A.; Bracci, L.; Morelli, G. *ChemMedChem.* **2011**, 6(4), 678–685.

[89] Joniec, A.; Sek, S.; Krysinski, P. *Chem Eur J.* **2016**, 22(49), 17715-17724.

[90] Lipowska-Kur, S. R.; Trzebicka, B.; Dworak, A. *Eur Pol J.* **2018**, 109, 391–401.

[91] Diaferia, C.; Gianolio, E.; Sibillano, T.; Mercurio, F. A.; Leone, M.; Giannini, C.; Balasco, N.; Vitagliano, L.; Morelli, G.; Accardo, A. *Sci Rep.* **2017**, 7(1),307.

[92] Jiang, T.; Zhang, C.; Sun, W.; Cao, X.; Choi, G.; Choy, J. H.; Shi, X.; Guo, R. *Chem Eur J.* **2020**, 26(11), 2470-2477

[93] Saini, M.; Ghosh, S.; Kumar, V.; Roy, P.; Sadhu, K. K. *Chem Eur J.* **2020**, 26(66),15150-15158.

[94] Hashemzadeh, H.; Raissi, H. *Appl Surf Sci.* **2020**, 500, 144220.

[95] Alinejad, A.; Raissi, H.; Hashemzadeh, H. *RSC Adv.* **2020**, 10(52), 31106.

[96] Diaferia, C.; Rosa, E.; Accardo, A.; Morelli, G. *J Pept Sci.* **2022**, 28(1), e3301.

[97] Cheng, X.; Lv, X.; Xu, J.; Zheng, Y.; Wang, X.; Tang, R. *Eur. J. Pharm. Sci.* **2020**, 146, 105275.

[98] Sun, C. Y.; Dou, S.; Du, J. Z.; Yang, X. Z.; Li, Y. P.; Wang, J. *Adv. Healthc. Mater.* **2014**, 3, 261-272.

[99] Zhong, Q.; da Rocha, S. R. P. *Mol. Pharm.* **2016**, 13, 1058-1072.

[100] Accardo, A.; Mansi, R.; Salzano, G.; Morisco, A.; Aurilio, M.; Parisi, A.; Maione, F.; Cicala, C.; Ziaco, B.; Tesauro, D.; Aloj, L.; De Rosa, G.; Morelli, G. *J Drug Target.* **2013**, 21(3), 240-249.

[101] Raghupathi, K.; Eron, S. J.; Anson, F.; Hardy, J. A.; Thayumanavan, S. *Mol. Pharm.* **2017**, 14, 4515-4524.

[102] Panda, J. J.; Kaul, A.; Kumar, S.; Alam, S.; Mishra, A. K.; Kundu, G. C.; Chauhan, V. S. *Nanomedicine* **2013**, 8, 1927–1942.

[103] Griffin, W. C. *J. Soc. Cosmet. Chem.* **1949**, 1, 311-326.

[104] Griffin, W. C. *J. Soc. Cosmet. Chem.* **1954**, 5, 249-256.

[105] Foulkes, W. D.; Smith, I. E. *N Engl J Med.* **2010**, 363(20), 1938-1948.

[106] Diaferia, C.; Ghosh, M.; Sibillano, T.; Gallo, E.; Stornaiuolo, M.; Giannini, C.; Morelli, G.; Adler-Abramovich, L.; Accardo, A.; *Soft Matter.* **2019**, 15(3), 487–496.

[107] Diaferia, C.; Balasco, N.; Sibillano, T.; Ghosh, M.; Adler-Abramovich, L.; Giannini, C.; Vitagliano, L.; Morelli, G.; Accardo, A. *Chem Eur J.* **2018**, 24(26), 6804-6817.

[108] Yang, Z.; Wang, L.; Wang, J.; Gao, P.; Xu, B. *J. Mater. Chem.* **2010**, 20, 2128–2132.

[109] Castelletto, V.; Hamley, I.W. *Biophys. Chem.* **2009**, 141, 169-174.

[110] Miles, A. J.; Wallace, B. A. *Chem. Soc. Rev.* **2016**, 45, 4859-487.

[111] Ding, J.; Xu, W.; Zhang, Y.; Sun, D.; Xiao, C.; Liu, D.; Zhu, X.; Chen, X. *J Control Release.* **2013**, 172(2), 444-455.

[112] Sahay, G.; Oh Kim, J.; Kabanov, A. V.; Bronich, T. K. *Biomaterials.* **2010**, 31, 923-933.

[113] Dong, X.; Li, Y.; Li, W.; Kang, W.; Tang, R.; Wu, W.; Xing, Z.; Zhou, L. *Med. Oncol*. **2021**, 38, 73.

[114] Accardo, A.; Arena, F.; Gianolio, E.; Marasco, D.; Ringhieri, P.; Boffa, C.; Bardini, P.; Aime, S.; Morelli, G. *J Biomed Nanotechnol.* **2016**, 12(5), 1076-1088.

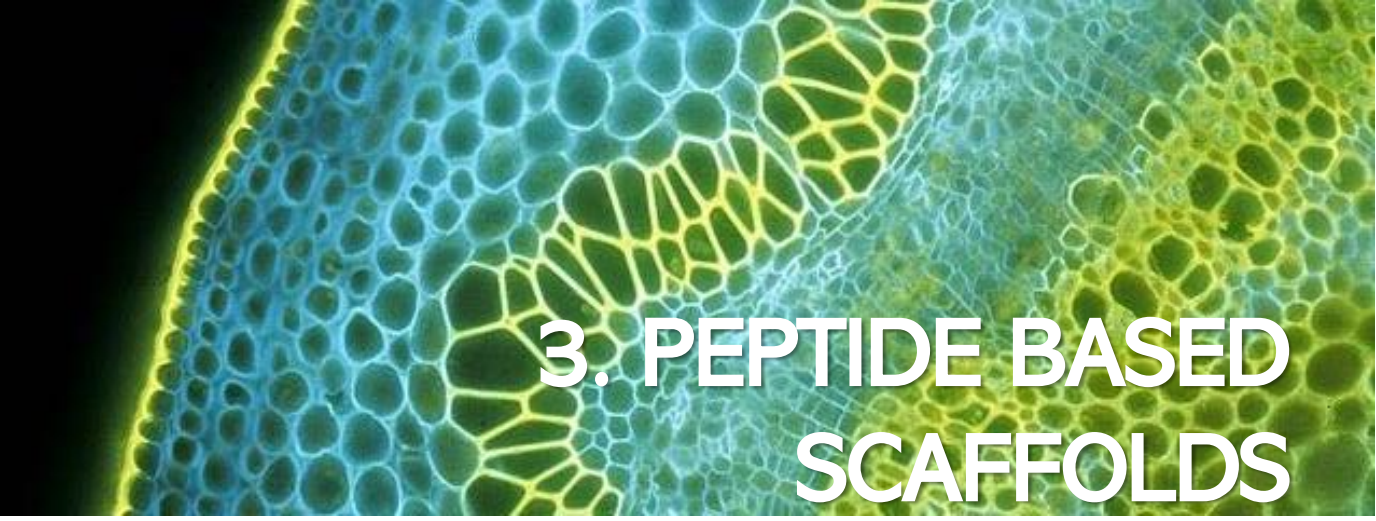

3. PEPTIDE BASED SCAFFOLDS FOR TISSUE ENGINNERING APPLICATIONS

Elisabetta Rosa | University of Naples Federico II | XXXV cycle

3.1 INTRODUCTION

3.1.1 Tissue engineering: origin, principles and application

The loss or failure of an organ or a tissue, which can result from accidents or diseases, has been generally treated with surgical procedures consisting in the transplantation from a donor to the patient. However, this approach is extremely limited by donors' shortage. During the last three decades, starting from the fascinating evidence that the human body is able to heal itself, tissue engineering has emerged as a new therapeutic solution. [115] This innovative field was first proposed, at the end of the 80s, by bioengineer Dr. YC Fung at the National Science Foundation's Director for Engineering, Bioengineering and Research to Aid the Handicapped Program meeting [116] and started to attract the attention of many scientists for its ambition to treat many clinical challenges. The goal of tissue engineering is to restore, improve or replace biological tissues by the combination of different disciplinary approaches, including stem cell biology, functional scaffold materials, nanotechnology and three-dimensional (3D) printing. [117] The scaffold, in which the cells are incorporated, has the role to mimic the extracellular matrix and, once implanted into the desired site in the human body, permits the growth of a new tissue (**Figure 3.1**). This concept has been successfully translated to many clinical areas, especially the skin reconstruction and the cartilage repair. [118,119] Many progresses have also been done to make the engineered tissues able to substitute nerve conduits, [120] blood vessels, [121] liver, [122] bones [123] and heart. [124] Moreover, tissue engineering has been also occupying a main role in the effort towards a "greener" food industry, specifically in the field of cultured meat. [125] This novel meat production approach involves *in vitro* culture of animal muscle tissues, allowing animal-free harvest and controlled conditions. The laboratory cultivation of muscle cells leads to healthier and

safer food to be consumed and has the power to reduce the adverse environmental effects caused by traditional meat production.

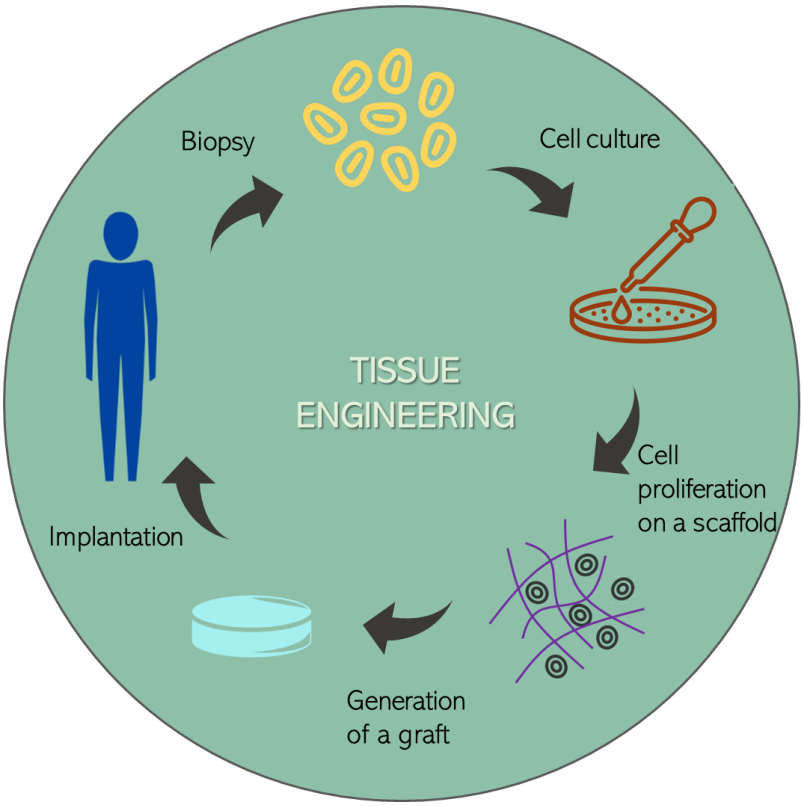

Figure 3.1: Schematic representation of a tissue engineering process

3.1.2 Scaffolds for tissue engineering: characteristic and chemical composition

Cells, scaffolds and growth stimulating signals can be considered as the three main components that are necessary for the development of an engineered tissue. With the exception of blood ones, all the other cells are supported, surrounded and structured by the Extracellular Matrix (ECM), which allows them to be fed, to attach and to communicate with other nearby cells, thus explaining a crucial role in the tissue growth. [126] It is mainly composed by macromolecules and minerals, such as collagen,

enzymes, glycoproteins and hydroxyapatite, but its composition may vary according to the supported tissue. To mimic the ECM, a tissue engineering scaffold must:

1. Provide structural support for exogenous cells to attach, grow and differentiate both in vitro and in vivo; this function can be exploited by the presence of binding cell sites and a porous architecture to allow the migration and the diffusion of nutrients, together with a temporary resistance to biodegradation once implanted.
2. Possess shape and mechanical properties similar to the tissue they are substituting, like opportune rigidity and stiffness.
3. Serve as reservoir of growth-stimulating factors
4. Possess a physical environment, like the presence of empty regions, allowing the response to endogenous tissue and dynamic stimuli, which may be represented by vascularization and wound healing.
5. Be biocompatible and non-immunogenic.

Natural or synthetic biomaterials can be used as starting points to obtain an adequate scaffold. Polymers comprising aliphatic polyesters, like poly(glycolic acid) (PGA), poly(lactic acid) (PLA), and copolymers (PLGA) of these materials, have been largely studied for this scope. [127-129] However, their use in this field requires incisions large enough to enable their placement in the lesion site. Cells may be alternative delivered by the use of injectable scaffolds, like hydrogels, which can reduce the invasiveness of the surgical approach. Hydrogel composition and structure show high resemblance with ECM ones, enabling survival and proliferation of cells entrapped within. [130] During the years, many biomaterials have been proposed as suitable building blocks for hydrogel scaffold preparation. Among them, macromolecules deriving from natural sources, such as collagen and Matrigel, have been tested for their high biocompatibility. [131,132] However, their clinical translation underwent some limitations,

mostly related to batch-to-batch differences and residual undesired biological entities. These drawbacks have been overcome by the use of polymeric hydrogels, generally comprising poly-ethylene glycol (PEG) moieties, presenting better physicochemical properties and tunability. [133] Some issues were found, in any case, to be related with cytotoxicity derived from chemical crosslinking and lack of biological functions. The use of synthetic peptides, as alternative, allows to combine the advantages presented by both natural macromolecules (good biocompatibility and bioactivity) and synthetic polymers (reproducibility, tunability). [134] The porous network, forming as a consequence of the capability of amyloid peptides to self-assemble into nanofibers, nanotubes or nanospheres, is able to encapsulate cells and bioactive molecules. Moreover, the intermolecular interactions occurring between the units acting as building blocks, are noncovalent ones, thus supplying important functions, such as self-healing, shear thinning and shape memory, to the final material. [135,136]

3.1.3 Recently advances in cationic hexapeptides for tissue engineering applications

According to the peptide sequence, the preparation method and the experimental conditions used for their formulation (concentration of polymers, ionic strength, pH and temperature), hard or soft hydrogels with different elasticity, dimension and porosity, can be generated. Peptide hydrogelators may be classified on the basis of the amino acids alternation. Where polar/charged residues are alternated coexist with apolar ones, gelification is triggered by the formation of two interfaces (an hydrophilic and lipophilic one). [137,138] Recently, some amphiphilic cationic tri-, tetra- or hexapeptides, were found able to self-assemble and were proposed for bioprinting applications. [139] Their primary sequence was composed by an aliphatic portion, comprising Gly, Ala, Val, Leu and/or Ile

residues, followed by a Lys at the amidated C-terminus, whereas an acetyl group was used to protect the terminal ammine. Self-assembling hydrogels resulted, for these peptides, from the interconnection between unbranched and elongated fibers, in which hydrogen bonds and van der Waals hydrophobic interactions occurred between the amphiphilic monomers. Among the investigated sequences, three hexapeptides were found to possess the best gelling properties. The HG formulation in the presence of phosphate buffer allowed to decrease the critical gelation concentration (CGC) and to increase the storage modulus (G') up to 40 kPa.

3.1.4 Co-assembly as new strategy to obtain hydrogels with enhanced rheological properties

Co-assembly is a widely used strategy to modulate the morphological features of the final macroscopic material and to improve its physical properties. For example, Fmoc-FF/pentafluorinate Fmoc-F, [140] and Fmoc-FF/Phe-Tyr containing peptides [106] systems have been recently formulated and proposed as multicomponent scaffolds for tissue regeneration and drug delivery applications. Beyond its combination with other peptide entities, Fmoc-FF has also been added to synthetic polymers, [55,141] polysaccharides [142] or dyes [143]. Hybrid Fmoc-FF based-matrices have been obtained by combining the dipeptide with chitosan, polyethylene-glycol (PEG) [144] or polyaniline (PAni) [145] In particular, thanks to the high biocompatibility offered by PEG and its α- and/or ω-substituted derivatives, PEGylation is widely used to the increase in solubility and the *in vivo* protection of bioactive macromolecules, [146] becoming, after FDA approval, the method of choice for the delivery of biopharmaceuticals.

3.1.5 The intervention on the primary sequence can allow modulate the mechanical properties of the final hydrogel

The wide study of peptide building blocks as tissue engineering scaffolds is also related to the easy modulation of the mechanical properties of the final matrix by intervening on the primary sequence. Indeed, the substitution of an amino acid with another, can significantly affect the final physicochemical features of the material, like its hydrophobicity and the total charge, and, in turn, the mechanical behaviour, while maintaining its self-assembling capabilities. The presence of a cysteine residue, for example, due to the thiol group, leads up to the possibility to obtain cross-linked and stimuli-responsive hydrogels with interesting storage modulus (G') values. [147] Recently, a class of peptides lacking positive or negative charges, were shown to be able to form hydrogels at a concentration of 1 wt%. [107,134]. These peptides presented a whole aromatic amino acid alternation, comprising Phe, Tyr, Dopa and/or Nal as residues. (Nal-Dopa)3, (Nal-Y)3, (F-Dopa)3 sequences and the PEGylated PEG_8-(FY)3 and PEG_8-(NalY)3 ones, were structural characterized through analyses which highlighted the presence of an antiparallel β-sheet organization. The study of solid (FY)3 fibers through Wide angle X-ray scattering (WAXS), combined with molecular dynamics (MD) simulation studies, allowed to propose an assembly model in which the presence of two different interfaces was supposed: the first one, being hydrophobic and highly rigid, deriving from Phe rings interactions, and the second one, more hydrophilic, generated by interacting Tyr side chains. The introduction of PEG moieties on the Nal and/or Dopa derivatives was found to alternatively increase or decrease the gelation properties, according to the positive or negative influence exerted on the hydrophilic-lipophilic balance, respectively.

3.1.6 RGDS-containing lipopeptides for cultured meat applications

Lipopeptides represents peptide analogues in which the primary sequence is linked to one or more alkyl chains, which insertion confers amphiphilic properties and a general aggregative behavior, often resulting in extended fibril structures, even if a proper molecular design can be exploited to obtain architectures with different morphologies (like micelles or vesicles). [148] Lipidation is also a widely used strategy to improve the stability of peptide therapy in vivo, since lipopeptide derivatives confer more stability to peptidase activity. [149] All these interesting features make lipopeptides the starting point for the development of many bio-inspired/bio-derived materials for applications in nanotechnology, nanobiotechnology and nanomedicine, with involvement also of the tissue engineering field.

3.2 OBJECTIVES

Starting from all the cited preliminary information, many paths have been trodden by us to obtain new interesting tissue engineering scaffolds. First, the effect of the substitution of the acetyl group with the fluorenylmethyloxycarbonyl (Fmoc) or the Fmoc-diphenylalanine ones on the aggregation capability of three previously reported cationic peptide sequences, has been evaluated. The rationale behind the choice of these protecting groups is that aromatic moieties can promote the aggregation process through the instauration of π–π stacking interactions, due to the long-range aromaticity of these molecules. Moreover, as already mentioned, the Fmoc-FF dipeptide is a well-known hydrogelator sequence. A library of 6 hexapeptides, presenting 5 aliphatic amino-acids, the Lys as cationic source, and the differently modified N-terminus, were synthesized and studied in terms of their self-assembling and gelation capability, alone or in combination with Fmoc-FF at different weight/weight ratios (1/1, 2/1 or

1/2 w/w). (**Figure 3.2**) The biocompatibility of pure and mixed matrices, together with their applicability as tissue engineering scaffolds, were evaluated by cytotoxicity and cell adhesion tests carried out on 3T3 fibroblasts and on HaCat cell lines.

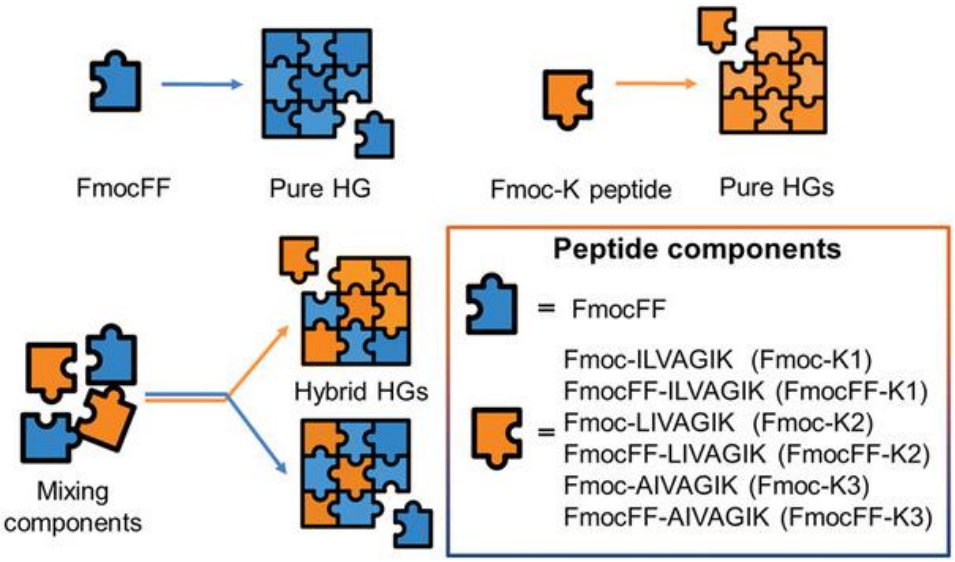

Figure 3.2: Graphical representation of the strategy used to formulate pure and mixed hydrogels derived from Lys-containing peptides; peptide sequences are also reported on the right.

Moreover, the formulation of multicomponent hydrogels, resulting from the incorporation of PEG diacrylates (PEGDA, **Figure 3.3**) into the Fmoc-FF matrix, was also tested. Two polymers with different mean molecular weight (PEGDA 575 and PEGDA 250 named as PEGDA1 and PEGDA2, respectively), were thus selected and combined with Fmoc-FF in different molar ratios (1:1, 1:2, 1:5 and 1:10 mol/mol). According to these choices, the effect of both molecular weight and relative polymer amount on the architecture and on the properties of the final material, were so analysed. Taking into account that, as previously mentioned, water entrapped within the network plays a key role in the final biomedical transability of hydrogels,

the water behaviour in each of the obtained matrices was studied according to the following parameters: the swelling ratio, the Langmuir frequency, the dehydration curves and the relaxometric properties. Secondary structure organization was analysed using various spectroscopic techniques and the rigidity of the matrices were studied, compared and discussed.

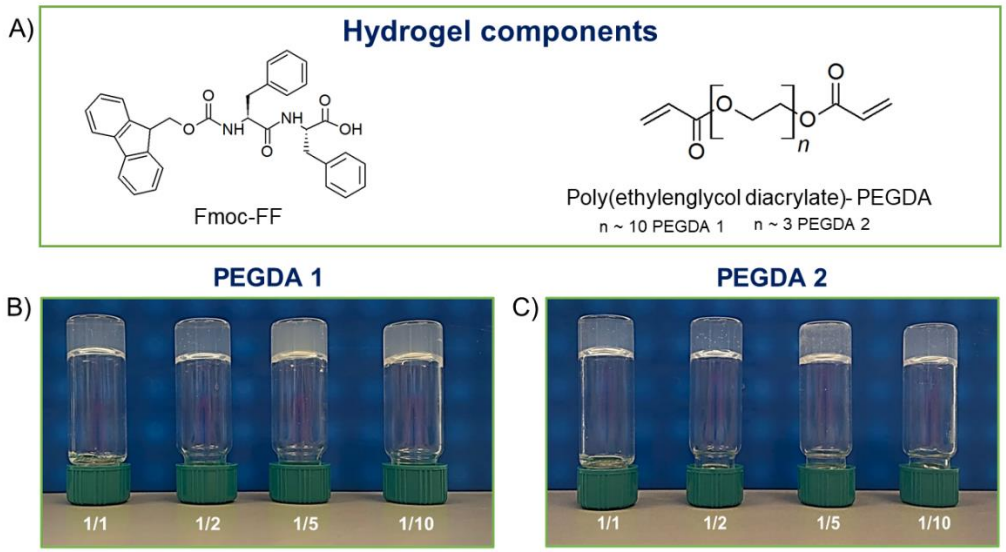

Figure 3.3: Chemical structure of hydrogel components (A). Inverted test tube for mixed hydrogel formulations (0.5 wt% in Fmoc-FF) with PEGDA1 (B) and PEGDA2 (C)

Starting from the previously cited studies [106,107] and from the knowledge that an appropriate modulation of the primary sequence is an important key for the scaffold design, a Cys residue was inserted in the middle of the (FY)3 primary sequence to study its effect, both in the reduced and oxidized form, on the final material. (**Figure 3.4**) The resulting FYFCFYF peptide was further studied in its PEGylated variant, to better investigate the role of the hydrophilic component on the final properties. The synthesized peptides were studied in terms of gelation capability,

secondary structuration and mechanical response, both in their cross-linked and non-cross-linked forms.

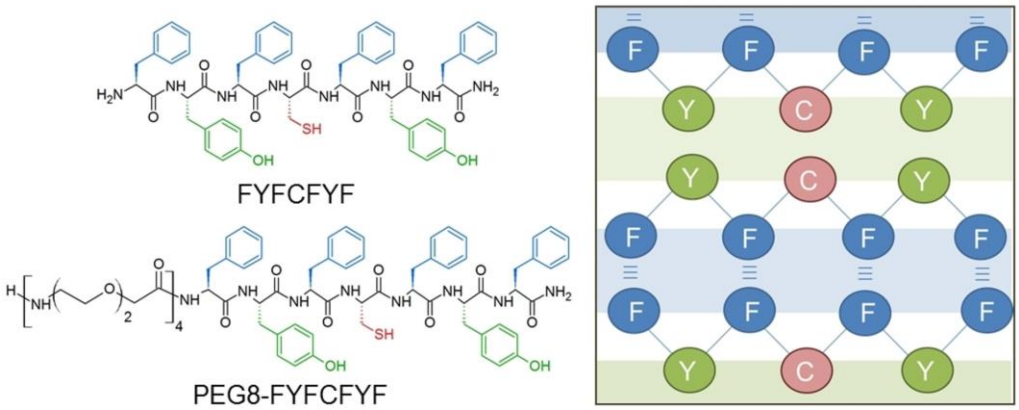

Figure 3.4: Chemical structure of FYFCFYF and PEG_8-FYFCFYF cysteine containing peptides. Schematic representation of the double interfaces supposed organization: hydrophilic (green region) and lipophilic (blue region) ones.

Regarding lipopeptides, it's easy to infer that their aggregative modes depend on a series of molecular characteristics affecting both the peptide sequence (amount and position of charged or hydrophobic residues) and chain length. The influence of these characteristics on the final obtained material, was explored starting from 4 lipopeptides, consisting of two different peptide sequences and two different lipid chains, myristyl (tetradecyl, C_{14}) and palmitoyl (hexadecyl, C_{16}), both of sufficient length (above C_{12}) to make them amphiphile and, therefore, to lead to the self-assembling. The cell adhesion tetrapeptide RGDS was inserted into the peptide sequence and separated from the alkyl component by two spacers, WGG and GGG. The polyglycine moiety has been chosen for its amyloid-like aggregates induction properties [150], whereas Tryptophan has been inserted, for comparison, to have a chromophore as marker. The cell adhesion sequences RGD and RGDS represent the basic units of a domain present in proteins such as fibrinogen, fibronectin and vitronectin,

conferring the capability to bind integrins. [151] These sequences have represented, for many researchers, the starting point for development of synthetic biomaterials for applications in cell growth and differentiation, as tissue scaffolds, [152] or for the delivery of Active Pharmaceutical Ingredients (APIs). [153] Moreover, the RGDS sequence, due to the inhibition of platelet aggregation, confers antithrombotic activity. [154] In some works, tetrapeptide RGDS has been shown to possess an increased bioactivity due to the presence of the additional serine residue. [155]

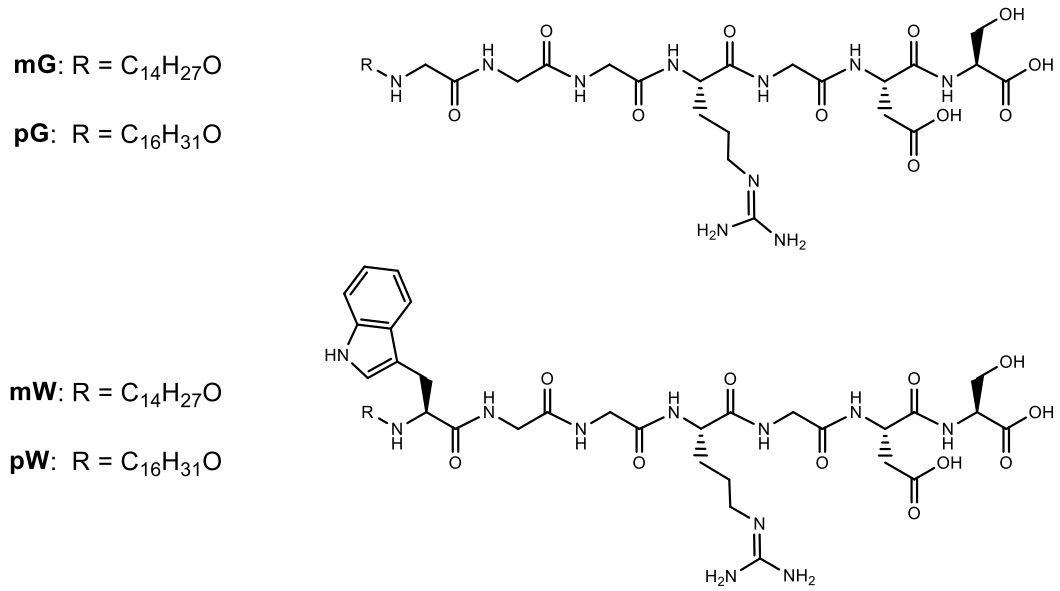

Figure 3.5: Structures of the four lipopeptides.

The molecular structures of the four lipopeptides are reported in **Figure 3.5**. They were characterized from the point of view of their self-assembly performances (including gelation properties) and cytotoxicity effects on L929 fibroblasts and C2C12 myoblasts, to examine their potentiality to be used as tissue engineering scaffolds, with a specific focus on the cultured meat field.

In order to evaluate the impact of the insertion of an alkyl chain on the afore mentioned K peptides, we synthetized three peptide amphiphiles (PAs), C_{19}-K1, C_{19}-K2 and C_{19}-K3 and their truncate version, C_{19}-VAGK, by end-capping the N-terminus with the nonadecanoic acid. (**Figure 3.65**) Our choice was inspired from the knowledge that not covalent van der Waals interactions in peptide amphiphiles can allow spontaneous self-assembling phenomena in water. The aggregation properties of these PAs were initially assessed by fluorescence titration assays. Successively, the structural characterization was carried out using a set of biophysical techniques like CD and FTIR, while the morphology of the aggregates was studied by Cryo-TEM.

3.3 MATERIALS AND METHODS

Protected N^{α}-Fmoc-amino acid derivatives, coupling reagents, and Rink amide MBHA (4-methylbenzhydrylamine) resin are commercially available from Calbiochem-Novabiochem (Laufelfingen, Switzerland). The lyophilized powder of Fmoc-FF was purchased from Bachem (Bubendorf, Switzerland), while Poly(ethylene glycol) diacrylates (PEDGA) with average MW of 250 and 575 u.m.a. are commercially available from Merck (Bari, Italy). The monodisperse Fmoc-8-amino-3,6-dioxaoctanoic acid, [Fmoc-AdOO-OH, PEG2] was purchased from Neosystem (Strasbourg, France). Lipopeptides were obtained from Peptide Synthetics (Peptide Protein Research), Farnham, UK as TFA salts with >95% purity as confirmed by RP-HPLC. Molar masses by ESI-MS are 814.94 g/mol (C_{14}-GGGRGDS, mG), 842.98 g/mol (C_{16}-GGGRGDS, pG), 943.68 g/mol (C_{14}-WGGRGDS, mW), 971.72 g/mol (C_{16}-WGGRGDS, pW). 1,1,1,3,3,3-hexafluoropropan-2-ol (HFIP), 8-anilino-1-naphthalene sulfonic acid ammonium salt (ANS), thioflavin T (ThT) and 5,5'-dithio-bis-(2-nitrobenzoic acid) (DTNB) and all the other chemical products were obtained from Merck (Milan, Italy), Fluka (Bucks, Switzerland),

or Labscan (Stillorgan, Dublin, Ireland) and they were used as received, unless stated otherwise.

3.3.1 Peptide Synthesis

Cationic and Cys-containing peptide derivatives were synthesized according to standard SPPS (solid-phase peptide synthesis) procedures using the Fmoc/tBu strategy, using the Rink amide MBHA resin (substitution 0.71 mmol/g) as solid-phase support to provide amidated peptides at the C-terminus. Each peptide was synthetized using a scale of 0.20 mmol in DMF. The resin was left to swell for 30 min in the reactor, and then the Fmoc group was deprotected by treating the resin with 30% (v/v) piperidine in DMF (two cycles of 10 min). The coupling of each Fmoc-amino acid and Fmoc-monodisperse oxothylene was performed by adding a 2-fold molar excess of the protected Fmoc-amino acid, with equimolar amounts of 1-hydroxybenzotriazole (HOBt), benzotriazol-1-yl-oxytris-pyrrolidino-phosphonium (PyBOP), and a 4-fold molar excess of diisopropylethylamine (DIPEA) in DMF/NMP. All couplings were performed twice for 40 min. The coupling of the nonadecanoic acid for C_{19}-K peptides was performed by solving the powder in DCM in a 4-fold molar excess. This solution was then mixed to a DMF solution of 4-fold molar excess HOBt and PyBOP and 8-fold molar excess DIPEA. The heterogeneous phase was then left to react with the resin for 3h. At the end of the synthesis procedure, crude cationic peptides were fully cleaved from the resin by treating it for 3h with a mixture of TFA (trifluoroacetic acid)/TIS (triisopropylsilane)/H_2O (92.5/5/2.5 v/v/v). Cys-containing peptides were treated with a TFA/TIS/EDT (1,2-Ethanedithiol)/ water solution at 92.5 %, 2.5 %, 2.5 % and 2.5 % v/v/v/v. All the peptides were precipitated with cold ether and freeze-dried for three times. After lyophilization, crude products were purified by RP-HPLC, carried out on a LC8 Shimadzu HPLC system (Shimadzu Corporation, Kyoto, Japan) equipped with a UV lambda-Max Model 481detector using

Phenomenex (Torrance, CA) C18 column. Using a flow rate of 20 mL/min, elution solvents were H2O/0.1% TFA (A) and CH3CN/0.1% TFA (B) from 30 to 80% over 30 min for cationic peptides, and from 20 to 70% over 30 min. The purity of the products was assessed by analytical RP-HPLC analysis with a C18-Phenomenex column eluting at a flow rate of 200 μL/min with (A) and (B) from 20 to 80% over 20 for both cationic and Cys-containing peptides. Identity of peptides was assessed by MS spectrometry using a LTQ XL Linear Ion Trap Mass Spectrometer, ESI source (see **Figures 6.1-6.6**, **6.9-6.12** and **Table 3.1** for analytical data of peptides).

Table 3.1: Formula, theoretical and experimentally found molecular weight (MW) and retention time (t_R) of investigated peptides.

Peptide	Formula	MWcalc. (a.m.u)	MWdeter. (a.m.u,)	t_R (min)
Fmoc-K1	$C_{43}H_{64}N_8O_8$	821.0	821.6	18.37
Fmoc-K2	$C_{43}H_{64}N_8O_8$	821.0	821.6	18.43
Fmoc-K3	$C_{40}H_{58}N_8O_8$	778.9	779.6	16.28
FmocFF-K1	$C_{61}H_{82}N_{10}O_{10}$	1115.4	1115.7	21.93
FmocFF-K2	$C_{61}H_{82}N_{10}O_{10}$	1115.4	1115.6	21.89
FmocFF-K3	$C_{58}H_{76}N_{10}O_{10}$	1073.3	1073.3	20.32
FYFCFYF	$C_{57}H_{62}N_8O_9S$	1035.2	1058.1 ($M+Na^+$)	13.65
PEG_8-FYFCFYF	$C_{81}H_{106}N_{12}O_{21}S$	1615.8	1638.8 ($M+Na^+$)	12.90
C_{19}-VAGK	$C_{35}H_{68}N_6O_5$	652.9	653.7	-
C_{19}-K1	$C_{47}H_{90}N_8O_7$	879.3	879.9	-
C_{19}-K2	$C_{47}H_{90}N_8O_7$	879.3	879.9	-
C_{19}-K3	$C_{44}H_{84}N_8O_7$	837.2	837.9	-

3.3.2 Preparation of peptide solutions

Cationic peptide solutions were prepared by weight using double distilled water as solvent, while lipopeptides were dissolved at different concentrations in phosphate buffered saline (PBS) solution 10 mmol/L at pH = 7.4. Solutions of FYFCFYF were prepared using a HFIP as solvent, and then diluting it in water. N_2 flow was used to remove the organic solvent. Peptide solutions of PEG_8-FYFCFYF were prepared by simply adding water to the lyophilized powder, allowing the solubilization by sonication for 30minutes. The concentration of each aqueous solution was

spectroscopically determined by absorbance on UV-Vis Thermo Fisher Scientific Inc (Wilmington, Delaware USA) Nanodrop 2000c spectrophotometer equipped with a 1.0 cm quartz cuvette (Hellma).

3.3.3 Preparation of pure and Fmoc-FF mixed cationic hydrogels

The gelation capability of Lys-containing peptide sequences was tested by initially dissolving peptides in 300 μL of water at 2 wt% concentration (6 mg) and then by adding 50 μL of 100 mmol/L phosphate buffer. The hydrogel formation was macroscopically verified by the inverted test tube. Fmoc-FF/Fmoc-K or Fmoc-FF/FmocFF-K mixed hydrogels at total peptide concentration of 1.0 wt% (10 mg/mL) were formulated by DMSO/H_2O solvent-switch method. The explored ratios for mixed hydrogels were 2/1, 1/1, and 1/2 w/w. In details, stock solutions of each peptide mixture were prepared in DMSO at a total peptide concentration of 100 mg/mL. After a 10 times dilution with water, sample was vortexed for 2 s in order to promote the homogeneity of the sample. The hydrogel formation was macroscopically verified by the inverted test tube.

3.3.4 Preparation of mixed peptide/polymer hydrogels

Mixed peptide/polymer hydrogels were prepared by the DMSO/H_2O solvent switch methodology. Briefly, 400 μL of hydrogel at a peptide concentration of 0.5 wt%, were obtained by solving Fmoc-FF in DMSO at 100 mg/mL. 20 μL of this stock were then hydrated 380 μL PEDGA solutions at different polymer concentrations. The metastable and opaque mixtures were vortexed for 2 seconds and left at room temperature until the macroscopical visualization of a clear self-supporting HG, evaluated using the inverted test tube. The different Fmoc-FF/PEGDA molar ratios were obtained using PEGDA solutions, prepared by solving in double distilled water (5 mL) different amounts of pure polymers. ρ=1.11 g/mL ρ =1.12 g/mL for PEGDA 250 (PEGDA2) and PEGDA 575 (PEGDA1), respectively.

3.3.5 Preparation of FCFYFCF hydrogels

400μL of HG were prepared via dilution in water of peptide HFIP stock solutions at different concentrations (200, 100 or 50 mg/mL). The solvent-switch method allowed HG immediately formation after the addition of water to the organic solvent. The oxidized HG forms were prepared by hydrating the organic solvent with variously concentrated NH_4HCO_3 (ammonium bicarbonate, AmBic) solutions (10.0, 6.0, 5.0, 2.0 and 1.0 mmol/L). HFIP was then gently removed using N_2 flow, avoiding any physical stress.

3.3.6 Ellman's test

The chromogenic reagent 5,5'-dithiobis-(2-nitrobenzoic) acid (DTNB) was used to determine the free sulfhydryl groups in gels, in normal or oxidizing conditions. The DTNB was dissolved at 2.0 mmol/L in sodium acetate 50 mmol/L (stock A). Tris · HCl solution at a concentration of 1.0 mol/L was adjusted to pH=8.0 (stock B). The final stock C solution was obtained by mixing 50 μL of stock A, 100 μL of stock B and 840 μL of H_2O. 20 μL of gels were added to 980 μL of stock C, being then vortexed, properly diluted and incubated at room temperature for 10 minutes. Free thiols amount was then calculated by indirectly quantification of the formed 5-thio-2-nitrobenzoic ion (TNB) yellow solutions via UV-Vis measurements at 412 nm (ε=13600 L/ (cm× mol)).

3.3.7 Molecular modeling and dynamics

A single sheet model of FYFCFYF was generated using the structure of the hexapeptide fragment KLVFFA of the amyloid-beta peptide II (Protein Data Bank entry 3OW9) as template. Starting from this structure, we generated a model composed of a single fifty-stranded β-sheet. A steric zipper model was then produced through the association of a pair of these sheets using

the organization of the KLVFFA peptide in the crystalline state (FYFCFYF_ST50_SH2). Starting from the evaluation of the hydrophobicity/hydrophilicity of Tyr and Phe residues, the two-sheet model was built by locating the Phe side chains at the dry interface, whereas Tyr and Cys were considered to be exposed to the solvent. A more complex system was generated by considering four ten-stranded β-sheets (FYFCFYF_ST10_SH4). This assembly is endowed with two different steric zipper interfaces: a hydrophilic one made of Tyr/Cys residues and two hydrophobic ones composed of Phe side chains. Moreover, in this model two surfaces made by Tyr/Cys residues are solvent exposed. Finally, a variant of FYFCFYF_ST10_SH4 in which the Cys residues placed in the hydrophilic interface form disulfide bonds was also characterized (FYFCFYF_ST10_SH4 SS).

Molecular dynamics protocol: The GROMACS software36 was used to perform MD simulations on the three generated models previously described. The force field and water model were Amber03 and TIP3P, respectively. The systems were solvated with water molecules in triclinic boxes. Cl^- counterions were added to balance charges. Electrostatic interactions were computed by means of the particle-mesh Ewald (PME) method with a grid spacing of 1.2 Å and a relative tolerance of 10^{-6}. For the Lennard-Jones (LJ) interactions, a 10 Å cut-off was applied. The LINCS algorithm was used to constrain bond lengths. The systems were initially energy minimized using steepest descent (50,000 steps) and then equilibrated in two phases. During the first step, systems were heated to 300 K temperature for 500 ps (NVT). Then, the pressure was equilibrated at the value of 1atm for 500 ps (NpT). To control temperature and pressure, the Velocity Rescaling and Parrinello-Rahman algorithms were used, respectively. The MD production runs were performed at constant temperature (300 K) and pressure (1 atm) with a time step of 2 fs. The

analysis of trajectory structures was performed by using the VMD program37 and GROMACS tools. The achievement of an adequate convergence in the production runs was checked by calculating the root mean square inner product (RMSIP) values between the two halves of the equilibrated trajectories.

3.3.8 Hydrogel swelling and stability studies

The swelling behavior of hydrogels was tested by adding 800 µL of doubly distilled water to each hydrogel sample (V = 400 µL), which was then incubated overnight at 30 °C. After this time, the excess of water was removed, and fully swollen hydrogels were weighed (Ws) and then freeze-dried and weighed again (Wd). The swelling ratio was expressed, according to *Equation 3.1,* as q:

$$q = \frac{(Ws - Wd)}{Wd} \qquad (3.1)$$

In vitro hydrogel degradation assay was examined by adding 1.5 mL of Ringer's solution (12.9 mg of NaCl, 0.45 mg of KCl and 0.48 mg of $CaCl_2$) to 400 µL of the preformed hydrogels. Each sample was then incubated at 37 °C for 20 or 40 days. Hydrogels were weighed before the addition of the Ringer's solution (Wo) and after its removal (Wt). The weight loss ratio (ΔW) was calculated as percentage according to *Equation 3.2:*

$$\Delta W = \left(1 - \frac{Wt}{Wo}\right) * 100 \qquad (3.2)$$

Dehydration profiles for peptide/polymer mixed hydrogels were acquired by locating 100 µL of each gel in a silicon mask on a glass slide. Samples were weighed at: 0 min, 5 min, 10 min, 20 min, 30 min, 1h, 2h, 3h, 4h, 5h, 6h, 7h and 24h. Dehydration behavior was evaluated in terms of changes in weight variation. The curve was reported as residual weight percentage as function of the time.

3.3.9 Circular Dichroism (CD) studies

Far-UV CD profiles were collected, for cationic, Cys-containig and polymer mixed peptide formulations, on a Jasco J-810 spectropolarimeter (equipped with a NesLab RTE111 thermal controller unit) and performed at 25 °C in a 0.1 or 1 mm quartz cell, alternatively. Other experimental settings used for the measurements are the following: sensitivity=5 mdeg, scan speed = 20 nm/min, time constant=16 s, bandwidth =1 nm. Each spectrum was obtained by averaging three different scans and correcting for the blank. All the spectra are reported in optical density (mdeg/O.D.). Far-UV CD spectra for the 4 lipopeptides mG, mW, pG and pW, were obtained using a Chirascan spectropolarimeter (Applied Photophysics, Leatherhead, UK). PBS Peptides solution and hydrogels were placed in 0.1 or 10 mm quartz cells depending on their concentration. Other experimental settings were: 0.5 nm step, 1 nm bandwidth, 1 s collection time per step. Each spectrum was obtained by averaging three scans and subtracting for the blank. The Critical Aggregation Concentrations (CACs) of the peptides were obtained by plotting the molar ellipticity at the wavelength of maximum ellipticity, λ_{max}, as a function of the concentration.

3.3.10 Fluorescence measurements

Fluorescence spectra of all the samples were collected on a spectrofluorometer Jasco (Model FP-750) using a 10.0 mm ×5.00 mm quartz cell. The other settings were excitation and emission bandwidths = 5 nm; recording speed = 125 nm/min, and automatic selection of the time constant. Excitation wavelengths were 257 and 301 nm, and 257 and 276 nm or cationic and Cys-containing peptide-based samples, respectively. Emission spectra for mW and pW at different concentrations were collected upon exitation at 280 nm. The self-fluorescence properties of lipopeptides were studied exciting them at a range of wavelengths between 350 and

580 nm. The determination of the critical aggregate concentration (CAC) for all the peptide derivatives was assessed by titration fluorescence spectroscopy methods, in which ANS (8-anilino-1-naphthalene sulfonic acid ammonium salt) and/or Thioflavin T were used as dyes. In detail, experiments were carried out by adding small volumes of peptide solutions in 200 μL of 20 μmol/L ANS water solution or in 200 μL of 50 μmol/L ThT water solution (λ_{ex}=350 nm for and 450 nm for ThT). Differently, lipopeptide solutions at different concentrations were prepared by directly dissolving the peptide powder in a PBS solution of ThT, concentration 50 μmol/L.

3.3.11 Fourier Transform Infrared (FTIR) spectroscopy

Fourier Transform Infrared spectra of cationic, Cys-containing and polymer mixed peptide solutions and/or hydrogels were collected on a Jasco FT/IR 4100 spectrometer (Easton, MD, USA) in an attenuated total reflection (ATR) mode and using a Ge single-crystal at a resolution of 4 cm^{-1}. For each sample, a total of 100 scans were recorded with a rate of 2 mm/s against a KBr background. After collection in transmission mode, spectra were converted to emission. FTIR spectra of lipopeptides at the concentration of 0.1, 0.5 and 1 wt% for mG and pG and 0.1 and 0.5 wt% for mW and pW, were collected by using a Thermo-Scientific Nicolet iS5 instrument equipped with a DTGS detector, with a Specac Pearl liquid cell with CaF_2 plates to fix the samples. A total of 128 scans for each sample were recorded over the range of 900 – 4000 cm^{-1}.

3.3.12 Dynamic Light Scattering (DLS)

A Zetasizer Nano ZS instrument (Malvern Instruments, Westborough, MA) employing a 173 backscatter detector, was used to measure the hydrodynamic radius of Cys-containing peptides through DLS analysis. Room temperature was set, and disposable sizing cuvettes were used. DLS

measurements were carried out in triplicate on aqueous samples at 2.0 mg/mL, subjected to prior centrifugation at 13000 rpm for 4 minutes.

3.3.13 Congo red (CR) assay

Congo Red spectroscopic assay was carried out by UV/Vis measurements on Fmoc-K hydrogels and C_{19}-K solutions. 10 μL of a 0.3 mg/mL water solution of CR were added to 200 μL of the preformed gel or the solution. The resulting sample was vortexed for 30 s and then sonicated for 15 min at room temperature. Before the UV-Vis measure, samples were diluted by adding 200 μL of water. The spectrum was recorded between 400 and 700 nm at room temperature. The spectrum of CR alone at the same final concentration, was also recorded, in the same conditions, for comparison. CR analyses were also carried out on Fmoc-FF/cationic peptide-based xerogels. The preformed hydrogel (≈40μL) was drop casted on a micro-scope glass slide and dried overnight. Then, samples were stained for 15 s with 5μL of a CR solution, which excess was gently removed using filter paper. Films were thus observed under bright-field illumination and between crossed polars by using a Nikon AZ100 microscope. For lipopeptide-based samples, CR assay was directly carried out on the hydrated gel or solution. A drop of peptide preparation was placed on a microscope slide and stained with a 1 wt% CR solution. After covering the sample with a microscope coverslip, it was observed through the crossed polarizers of an Olympus BX41 polarized microscope. Images were captured using a Canon G2 digital camera fitted to the microscope.

3.3.14 Thioflavin T (ThT) assay

ThT assay was conducted on Fmoc-FF/PEGDA xerogels. After their formulation, macroscopic HGs were spread on a clean coverslip glass and dried overnight. The obtained samples were stained for 30 sec with 50 μL of a water solution of ThT (50 μmol/L). The excess of dye was removed with

filter paper, and samples were then dried overnight. Stained xerogels were imaged using a fluorescence Leica DFC320 video-camera (Leica, Milan, Italy) connected to a Leica DMRB microscope equipped with a 20 X objective and Green Fluorescent Protein (GPF) filter. The software Image J (National Institutes of Health, Bethesda, MD) was used for analysis.

3.3.15 Relaxometric studies

NMRD (Nuclear Magnetic Relaxation Dispersion) profiles at 25°C for Fmoc-FF/Lys-containing peptide HGs and for peptide/polymer ones were obtained using a Stelar SMARtracer fast-field-cycling relaxometer (Stelar S.n.c., Mede (PV), Italy) from 0.01 to 10 MHz equipped with a Stelar VTC-91 for temperature control. 500 μL of 1.0 wt % HGs were prepared in 10 mm NMR tubes. The relaxation rate (R_1) was measured, for each profile, at 16-32 different values of applied magnetic field. Relevant acquisition parameters were: polarization field 8.5 MHz; acquisition field 7.2 MHz (proton Larmor frequency); polarization time and relaxation delay 4 times T_1; switching time 3 ms; 16 sampled delay times. A sum of two Lorentzians was used to fit each NMRD profile according to the model-free approach, as generally performed on biomolecules in the presence of two distinct levels of motions (slow and fast). [156] The same functional form can be used to analyze water relaxation in hydrogel systems where two different water populations can be distinguished: one relative to water constrained in the peptide scaffold (slow motion), and a second one composed by more free molecules (fast motion). Relaxation rates (R_1) as a function of the proton Larmor frequency ($\upsilon=\gamma B_0/2\pi$) were fitted by using the *Equation 3.3*:

$$R_1 = A_0 + \beta\left[\frac{A_1\tau_1}{1+(2\pi\nu\tau_1)} + \frac{A_2\tau_2}{1+(2\pi\nu\tau_2)}\right] \qquad (3.3)$$

Where A_0 is the part of R_1 that remains in the extreme-motional narrowing regime up to the highest sampled frequency, β is the integral of the

dispersion profile, τ_1 and τ_2 are the correlation times associated to fast and slow motions, respectively, and A_1 and A_2 are their relative weight coefficients. From parameters determined by fitting of experimental R_1 data to *Equation 3.3*, the average correlation time, and the percentage of slowly moving water (% slow) can be calculated according to *Equations 3.4* and *3.5*, respectively:

$$\tau_C^{av} = \frac{A_1\tau_1 + A_2\tau_2}{A_1 + A_2} \qquad (3.4)$$

$$\%\ \text{slow} = \frac{A_2}{A_1 + A_2} \qquad (3.5)$$

3.3.16 Scanning Electron Microscopy (SEM)

Morphological analysis of cationic, Cys-containig and polymer mixed peptide xerogels was carried out by field emission scanning electron microscope (PhenomXL, Alfatest); 10 µL of peptide hydrogel were drop-casted on an aluminum stub and air-dried. A thin coat of gold and palladium was sputtered at a current of 25 mA for 75 s. The sputter-coated samples were then introduced into the specimen chamber and the images were acquired at an accelerating voltage of 10 kV, spot 3, through the Secondary Electron Detector (SED).

3.3.17 Cryo Transmission Electron Microscopy (Cryo-TEM)

Images of lipopeptides were collected using a field emission cryo-electron microscope (JEOL JEM-3200FSC), operating at 200 kV, in bright field mode and using zero loss energy filtering (omega type) with a slit width of 20 eV. A Gatan Ultrascan 4000 CCD camera was used to record micrographs. During the imaging, the specimen temperature was maintained at -187 °C. Vitrified specimens were prepared using an automated FEI Vitrobot device using Quantifoil 3.5/1 holey carbon copper grids with a hole size of 3.5 µm. Before their use, grids were plasma cleaned with a Gatan Solarus 9500

plasma cleaner and then transferred into the environmental chamber of a FEI Vitrobot at 100 % humidity and room temperature. Then, 3 µL of sample solution were placed on the grid and blotted twice for 5 seconds and then vitrified in a 1/1 mixture of liquid ethane and propane at temperature of -180 °C. The grids with vitrified sample solution were maintained at liquid nitrogen temperature and then cryo-transferred to the microscope.

3.3.18 Wide Angle X-ray Scattering (WAXS)

WAXS patterns were recorded on solid fibers prepared by the stretch frame method. Briefly, an aliquot of ~20 µL of a metastable gel forming sample was placed between the ends of a wax-coated capillary (spaced 1.5 mm apart). Fibers were obtained after the droplet was air-dried overnight. 2D WAXS data were collected from the fibers at the X-ray MicroImaging Laboratory (XMI-L@b), equipped with an Fr-E+ SuperBright rotating anode table-top microsource (Cu Kα, λ = 0.15405 nm, 2475 W), a multilayer focusing optics (Confocal Max-Flux; CMF 15-105), and a three-pinholes camera (Rigaku SMAX-3000). An image plate (IP) Raxia detector with 100 µm pixel size and off-line reader was placed at around 10 cm from the sample to acquire the WAXS data. After being acquired, the 2D WAXS data were centered, calibrated by means of the Si NIST standard reference material (SRM 640b) and folded into 1D WAXS radial profile.

3.3.19 Small Angle X-ray Scattering (SAXS)

Small-angle X-ray scattering experiments were performed on beamline SWING at SOLEIL synchrotron (Gif-sur-Yvette, France). Solution samples were delivered to a quartz capillary under vacuum in the X-ray beam using a BioSAXS setup. Gels Samples were loaded into a plastic support sandwiched between two polyimide foils held in place by a metal frame. Data were collected using an in-vacuum EigerX-4M detector, with an X-ray

wavelength 1.033 Å at two sample-to-detector distances, 6.217 m and 0.517 m. Data were reduced to one-dimensional form (except the raw two-dimensional patterns where anisotropy was observed) and averaged and background subtracted using the software Foxtrot.

3.3.20 Rheological studies

Rheological properties of cationic, polymer mixed and Cys-based peptide HGs were evaluated using a rotational controlled stress rheometer (Malvern Kinexus) using a 15 mm flat-plate geometry (PU20:PL61). 400 µL of freshly prepared hydrogel sample were tested each time. All the experiments were performed at 25 °C using a humidity chamber and a gap distance of 1 mm. Preliminary parameters optimization was performed via oscillatory frequency (0.1–100 Hz) and strain sweep (0.1–100%). Time-sweep oscillatory tests (in 0.1 % strain and 1.0 Hz frequency regime) were performed for 20 minutes. Final analyses are reported as G'(Storage elastic modulus)/G" (Shear loss or viscous modulus) ratio in Pascal [Pa].

3.3.21 Naphthol yellow S encapsulation and release form peptide/polymer hydrogels

Naphthol yellow S (NYS) was encapsulated in 400 µL of hybrid peptide/polymer HGs at final concentration of 6.02 mmol/L. A solution of NYS, prepared in water, was analytically quantified via UV-Vis, using as molar extinction coefficient ε_{430} = 9922 L/(cm×mol). ([NYS] = 0.012 mol/L). 200 µL of this solution were added to properly more concentrated solution of PEDGA used for the rehydration step. To study the dye release kinetics, 800 µL of water were located on top of the HGs. At each selected time-point, 400 µL of this solution were removed and replaced with an equal freshwater aliquot. Released NYS, in each fraction, was quantified by UV-Vis. All the release experiments were performed in triplicates. The extent of

released dye was plotted as percentage of the ratio between the amount of molecule release at each time and the initially total loaded quantity.

3.3.22 Cell lines

For cell experiments with mono and multicomponent cationic peptide and lipopeptide formulations, aneuploid immortal keratinocyte cell line HaCat and mouse pre-adipocyte cell line 3T3-L1 were used. They were obtained from IRCCS-SDN Biobank (10.5334/ojb.26) and grown in Dulbecco's Modified Eagle Medium (DMEM) supplemented with 10% fetal bovine serum (FBS) and 1% GlutaMAX. Cells were incubated at 37 °C and 5% CO_2 and seeded in 100 mm culture dishes. Cell studies on RGDS-containing lipopeptides were conducted on L929 murine fibroblast and C2C12 immortalized mouse myoblast cell lines (both from ECACC General Cell Collection). These cell lines were grown in DMEM supplemented with 10% FBS, 20 mM HEPES and 1% GlutaMAX and incubated at pH 7.4, at 37 °C and 5% CO_2 in 25 cm^2 cell culture flasks.

3.3.23 Cell assays

For cationic peptide-based formulation the adhesion test was performed on 3T3-L1 cells seeded in 96-well plates at a density of 0.5 $\times 10^4$ cells per well. Each well was filled with the indicated hydrogels, before cell seeding. 16 h after seeding, cells were stained with Acridine Orange/Propidium Iodide stain. Cell adhesion was reported as % of adherent viable cell (fluorescing green) on total plated cells. Dead cells were visualized as fluorescent red. Viability upon adhesion was reported as % viable cells and total adherent cells. Duplication rate was reported as the ratio between viable cells upon 48 h from seeding and the number of viable adherent cells upon 16 h from seeding. The MTS (3-(4,5-dimethylthiazol-2-yl)-5-(3-carboxymethoxyphenyl)-2-(4-sulfophenyl)-2H-tetrazolium) test was used to test the toxicity of hydrogels conditioned media. (CellTiter 96® AQueous

One Solution Cell Proliferation Assay, Promega, Italy). Briefly, HaCat and 3T3-L1 cells were seeded in 96-well plates at a density of 0.7 × 10^4 cells per well. The conditioned media resulted from the 16h incubation at room temperature of hydrogels, formed in a hollow plastic chamber sealed at one end with a porous membrane, with 2 mL of completed DMEM medium. No color change of the media was detected and the tested pH value (7.5-7.8) was suitable for culturing. The conditioned media were used to grow the cells for 24, 48, and 72 h. At the end of the treatment, MTS was added to the cells at a final concentration of 0.5 mg/mL. After 30 min of incubation at 37 °C, samples were analyzed using the VICTOR Nivo (Perkin Elmer, Buckinghamshire, UK) at 490 nm absorbance. Cell survival was expressed as percentage of viable cells in the presence of hydrogels, compared to control cells grown in their absence. MTS assay was repeated twice with similar results. To assess cell viability in the presence of lipopeptides, MTT [3-(4, 5-dimethylthiazolyl-2)-2, 5-diphenyltetrazolium bromide] assay was performed. Cells were seeded in 96-well plates at a density of 0.6 × 10^4 cells per well. Cells were then treated with peptides solved in the medium at the concentrations of 0.1 and 1 x 10^{-4} wt% or 5 x 10^{-5} wt%. To test cytocompatibility in the presence of the hydrogels, wells were filled with 1 wt% mG and pG hydrogels before seeding. At the end of the treatment (after 24 or 72 hours), after the removal of the culture medium, MTT, dissolved in DMEM at a concentration of 0.5 mg/mL, was added to the cells and incubated for 4 h at 37 °C. The resulting formazan crystals were dissolved by adding dimethyl sulfoxide (DMSO). Absorbance values of blue formazan were determined at 560 nm using an automatic plate reader. Cell survival was expressed as percentage of viable cells in the presence of peptides, compared to control cells grown in their absence. The assay was repeated three times and the results were averaged. Statistical significance was tested using multiple Welch's t-tests. All analyses were conducted using Prism 7.

3.4 RESULTS AND DISCUSSION

3.4.1 Fmoc-K and FmocFF-K peptides: synthesis and characterization

Figure 3.6 schematically shows the structure of the six Fmoc-protected cationic peptide sequences, composed by a common part comprising five aliphatic residues followed by a lysine at the amidated C-terminus. For FmocFF-K octapeptides, two additional Phe residues were introduced with the aim to study their influence on the aggregative behavior. All the peptides were obtained through the standard solid phase peptide synthesis procedures, purified by RP-HPLC and analyzed trough LC-MS to assess their purity (**Table 3.1**).

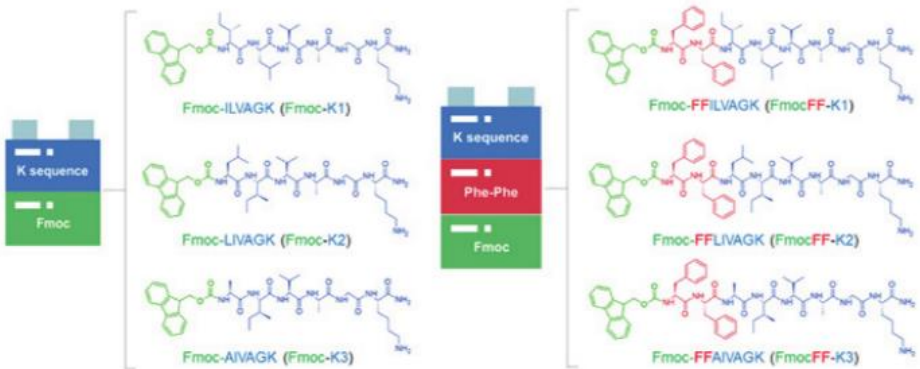

Figure 3.6: Schematic representation of Fmoc-K1, Fmoc-K2, Fmoc-K3, FmocFF-K1, FmocFF-K2 and FmocFF-K3 peptides, also reported according to the one letter code. The three K sequences are composed of five aliphatic amino acids (Ile, Leu, Val, Gly and/or Ala) followed by a Lys at the amidated C-terminus. K sequences differ one from another for the first two amino acids.

As it can be easily forecasted by looking at the peptide sequences, each peptide is characterized by a different water solubility, summarized in **Table 3.2.** Reasonably, the three peptides containing the aromatic amino acids exhibit a ~3-fold lower solubility than their Phe-lacking analogues. Fluorescence analyses were conducted by exciting the octapeptide at both 257 and 301 nm (corresponding to the λ_{exc} of the phenyl and the fluorenyl

groups, respectively), whereas hexapeptides were only excited at 301 nm. The aggregative behavior of all the peptides is confirmed by the red shift of the emission peak, upon excitation at 301 nm, from 313 nm (emission associated with the monomeric state) to 328 nm. This bathochromic effect is, indeed, generally associated to an antiparallel stacking of the fluorenyl groups. [108] For FF dipeptide containing sequences, the same emission peak was observed by exciting peptide solutions at 257 nm. This behavior underlines the occurrence of a Förster resonance energy transfer (FRET) phenomenon between the phenyl and fluorenyl groups. [157] Together with the peak at 328 nm, also a broad emission around 460 nm was observed for the three octapeptides, thus indicating the formation of excimer derived from further stacking phenomena. [158]

Table 3.2: Water solubility, logP, storage modulus (G') and loss modulus (G") values calculated for the six peptides.

Peptide	Water Solubility (mg/mL)	logP	G′ (Pa)	G″(Pa)
Fmoc-K1	1.24	4.30 ± 0.84	557	40
Fmoc-K2	2.56	4.30 ± 0.84	925	89
Fmoc-K3	3.21	2.89 ± 0.84	2526	273
FmocFF-K1	0.508	7.47 ± 0.90	—	—
FmocFF-K2	0.253	7.47 ± 0.90	—	—
FmocFF-K3	0.345	6.06 ± 0.90	—	—

The critical aggregation concentration (CAC) for all the peptides was determined by ANS titration with increasing amounts of the peptide solution. The fluorophore ANS is able to emit fluorescence between 460 and 480 nm when in presence of a hydrophobic environment, which is formed in peptide aggregated state from the interactions between the aliphatic/aromatic amino acid side chains. [146] The ANS emission was reported as function of the peptide concentration (**Figure 3.7**) and CAC values, extrapolated at the break point, were found to be in the range between $1.16 \cdot 10^{-6}$ and $3.39 \cdot 10^{-5}$ mol/L for all the studied peptides.

FmocFF-K peptide sequences aggregate at lower concentration, as it was expected by the inspection of the higher logP values theoretically estimated by ACD/3D Viewer (**Table 3.2**). CD analyses were carried out to study the secondary structure of peptides. Spectra were collected between 320 and 190 nm (**Figure 3.8**) for Fmoc-K solutions at 1.0 mg/mL and FmocFF-K solutions at the maximum of their solubility. CD profiles of Fmoc-K1, Fmoc-K2, and Fmoc-K3 show a similar dichroic signature, confirming the presence of a β-sheet structure and characterized by two well distinct regions: the first one is ranged between 212 and 220 nm and can be attributable to n→π* transitions; the second one is associated with the π–π* transition of fluorenyl absorption and it is extended from 250 and 310 nm. The signal around 305 nm, indicative of the coupling of fluorenyl chromophores in the hydrogels, is more pronounced for Fmoc-K3 peptide. A better overlapping of Fmoc moieties can be so deduced for this sequence.

Peptide	*CAC (mol/L)*	*CAC (μg/mL)*
Fmoc-K1	$3.39 \cdot 10^{-5}$	27.8
FmocFF-K1	$1.16 \cdot 10^{-5}$	12.9
Fmoc-K2	$1.23 \cdot 10^{-5}$	10.0
FmocFF-K2	$5.98 \cdot 10^{-6}$	6.53
Fmoc-K3	$2.34 \cdot 10^{-5}$	18.2
FmocFF-K3	$1.83 \cdot 10^{-5}$	11.5

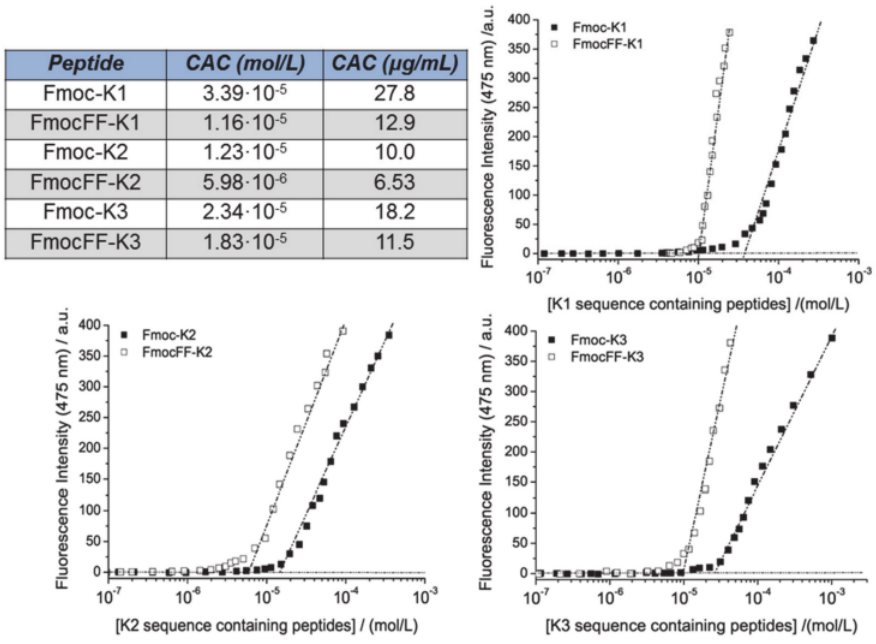

Figure 3.7: Plotted fluorescence intensity of the ANS fluorophore at 475 nm versus the peptide concentration of each. CAC values, calculated from the break points, are reported in the Table on the left.

For aromatic residues containing octapeptides, an inversion of the CD signature around 220 nm is observed respect to the hexapeptide analogues: a minimum in place of a maximum is present. This effect can be ascribed to an apparent inversion of the amino acid configuration, which may be caused by a different orientation of the amino acids in the final three-dimensional network. This signal undergoes a red shift for FmocFF-K3, which was explained by considering that, because of the presence of an Ala residue, in place of a Leu or Ile one, a better packing and thus a major aggregation is probably allowed.

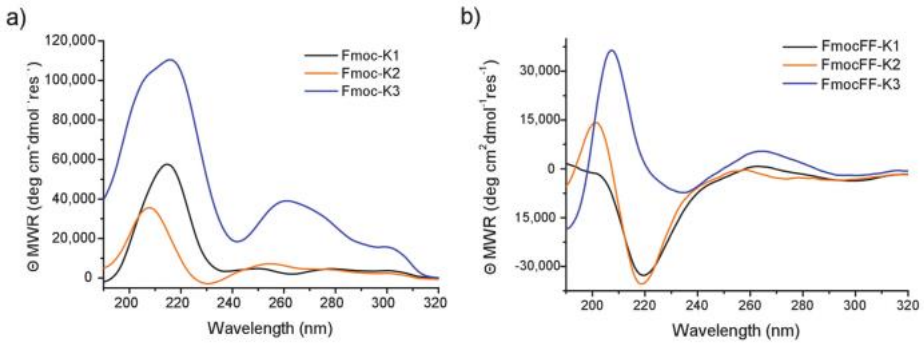

Figure 3.8: CD profiles for (A) Fmoc-K1, Fmoc-K2 and Fmoc-K3 peptides and (B) FmocFF-K1, FmocFF-K2 and FmocFF-K3 ones.

FTIR analyses provided further information on the secondary structure of self-assembled peptides (maximum solubility). In **Figure 3.9A**, the IR spectra for Fmoc-K3 and FmocFF-K3 peptides are reported as examples, since very similar results were obtained by the study of the other analogues (data not shown). Two main signals can be distinguished: in the amide A region (~3500–3300 cm^{-1}), the band at 3405 cm^{-1} is attributable to NH stretching vibrations polarized along the N-H bond and to the O-H stretching (both symmetric and asymmetric) indicative of strong H-bonds between bulk water and nanostructure; the band at 1640 cm^{-1}, in the amide

I region (ranged from 1700 to 1600 cm^{-1}), is attributable to C=O stretching vibration and is generally indicative of β-sheet elements. Deconvolutions of this signal are reported in **Figure 3.9B,C** and confirm the presence of a β-sheet arrangement for all the peptides.

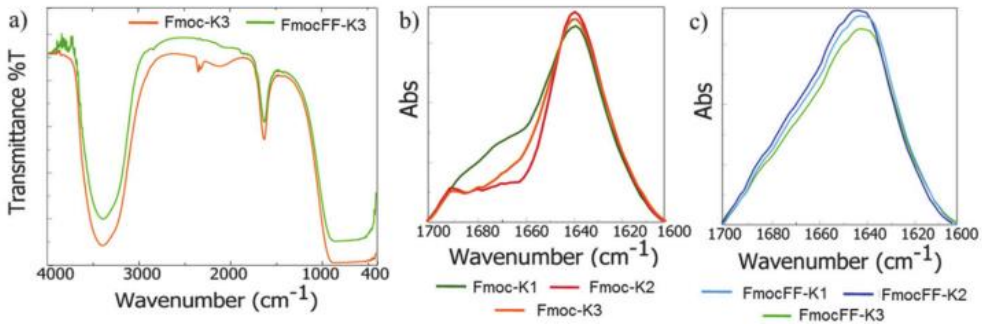

Figure 3.9: (A) FTIR spectra of Fmoc-K3 and Fmoc-FFK3. Absorbance deconvolution in the amide I region for (B) Fmoc-K1, Fmoc-K2, and Fmoc-K3, and for (C) FmocFF-K1, FmocFF-K2, and FmocFF-K3

For Fmoc-K1, Fmoc-K2, and Fmoc-K3 an additional band at 1675 cm^{-1} is detected, thus indicating an antiparallel orientation of the β-strands. The insertion of the two Phe residues probably interferes with this kind of arrangement.

3.4.2 Gelation tests and HG structural and rheological characterization for cationic sequences alone.

Gelation tests were carried out by dissolving the peptide in water at a concentration of 2 wt%, and then by adding a small aliquot of 100 mmol/L PBS as trigger. Phosphate buffer has the role to reduce the electrostatic repulsive forces occurring between the positive charges of the monomers. In these conditions, only the three peptides lacking FF motif were found able to form self-supporting hydrogels, as demonstrated by the inverted test tube (**Figure 3.11A**). By comparing these peptides behavior to the one

of their acetylated analogues, [139] it can be deduced that the substitution of the N-terminus protecting group does not compromise the gelation properties. However, the elongation of the sequence with two aromatic residues hinders the HG formation, even when a solvent switch procedure (peptide concentration 0.5 wt%), using HFIP or DMSO as organic solvents, was tested. For this reason, the aromatic/aliphatic balance was considered to play a key role in the gelation capability of these cationic sequences. For the obtained hydrogels, the swelling degrees (q) were found to be quite independent from the primary sequence (55.2%, 56.6%, and 54.3%) for Fmoc-K1, Fmoc-K2, and Fmoc-K3, respectively.

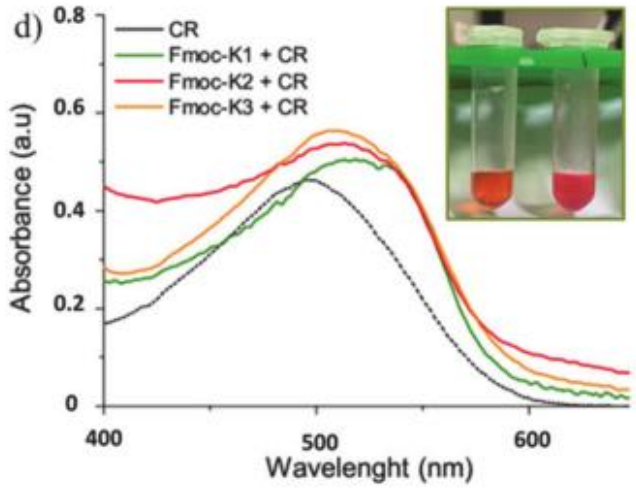

Figure 3.10: UV–Vis spectra of CR alone and co-incubated with Fmoc-K HGs. Macroscopical appearance of CR solution and Fmoc-K3+CR HG is reported in the insert.

These values are higher than those found for Fmoc-FF and other aromatic peptide HGs, which swelling properties in the same conditions lead to an increase of around 40% weight. [106] This behavior may be due to a weaker physical crosslinking, resulting in a more porous architecture, occurring in Fmoc-K HGs respect to the other considered matrices. CR

assay, carried out on Fmoc-K hydrogels, confirmed the presence of β-sheet structures. CR is a dye able to selectively stain β-sheet nanofibers with a consequent increase and red shift (from 490 to ~530 nm) of its absorption. This shift, together with an immediate color variation, was observed for HGs prepared in the presence of CR, respect to the CR alone (**Figure 3.10**).

Scanning electron microscopy (SEM) and rheology analyses were conducted to obtain morphological and viscoelastic information about the three hydrogels, respectively. The presence of a dense and wavy fibrillar tight network in the hydrogels was shown by SEM micrographs (**Figure 3.11C-E**). G' (storage modulus) and G'' (loss modulus) for the three hydrogels, resulting from the time sweeps oscillatory profiles (1.0 Hz and 0.1% strain, 20 min), are reported in **Figure 3.11B**

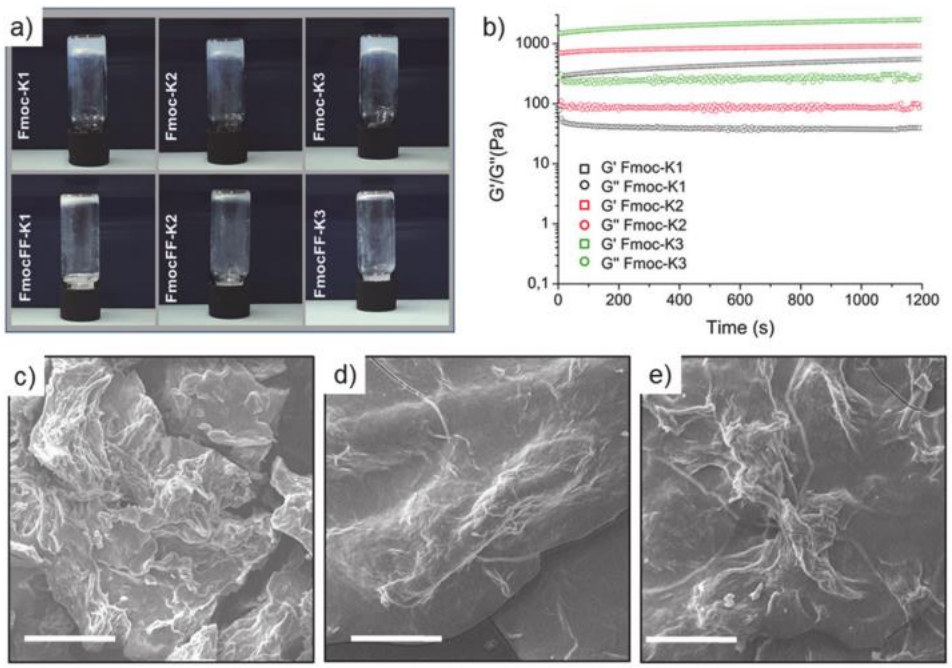

Figure 3.11: (A) Inverted test tubes for the six peptides at a concentration of 1.7 wt% in PBS 14 mmol/L; (B) hydrogel rheological analysis: time sweep rheological analysis of Fmoc-K hydrogels reported as storage modulus (G') and loss modulus (G''). SEM micro-photos of Fmoc-K1 (C), Fmoc-K2 (D), and Fmoc-K3 (E). Scale bars are 30 μm, 2700×.

The preliminary dynamic oscillation strain sweep (at a frequency of 1 Hz), and dynamic frequency sweep (at 0.1% strain) analyses showed that the linear viscoelastic region (LVE region) was, for all the samples, in the range of 0.01–4.2% strain. The viscoelastic behavior of samples was confirmed by the higher G' values respect to the G'' ones, resulting in tan δ ratios (G'/G'') of 13.9, 10.4, and 9.25 for Fmoc-K1, Fmoc-K2, and Fmoc-K3, respectively. The higher tan δ ratios for Fmoc-K1 is indicative of a more dissipative feature for this HG when compared with the others, even if it is less rigid (G' of 557, 925 and 2526 Pa for Fmoc-K1, Fmoc-K2 and Fmoc-K3, respectively). The higher rigidity of Fmoc-K3 HG may be ascribed, once again, to an improved monomer packaging promoted by the substitution of Leu or Ile residues with the smaller Ala one. Fmoc-K HGs were found to be less rigid than the corresponding acetylated ones (G' moduli around 40 KPa in similar conditions). [139] This lost in stiffness may be due to the fact that the insertion of the Fmoc group perturbs the forces (van der Waals interactions and the hydrogen bonding) governing the aggregation in K1, K2, and K3 peptides. The resistance of these matrices to biological fluids, which is a fundamental request for tissue engineering scaffolds, was evaluated through the degradation test in the presence of Ringer's solution (incubation at 37 °C for 20 days). The stability of the HGs, reported as ΔW, was 43.2, 39.7, and 41.8% for Fmoc-K1, Fmoc-K2, and Fmoc-K3, respectively. The degradation degree was found to be faster in comparison to other Fmoc-FF peptide-based hydrogels, [106] maybe because of the less rigid nature of Fmoc-K HGs. A higher solubility of Fmoc-K peptides in the presence of the high salt concentration in the Ringer's solution could also be recognized as the cause of this fast degradation. However, from a clinic point of view, the degradation of the implant after a certain time is desirable since the decomposition of the macroscopic matrix in its monomeric component could allow an easy excretion.

3.4.3 Formulation of multicomponent cationic peptide/Fmoc-FF hydrogels.

The cationic peptides capability to gel also in combination with Fmoc-FF was checked according to the "solvent-switch" method, using DMSO as organic solvent. (**Figure 3.2**) Final 1 wt% formulations were obtained by mixing the two components according to three different volumetric ratios (2/1, 1/1, and 1/2 v/v), resulting in a total of 18 possible combinations. As it can be observed in **Figure 3.12** from the inverted test tubes analyses, only seven of all the explored combinations (identified from A to G) resulted in the generation of self-supporting HGs.

a)

Hydrogel composition	1/1	1/2	2/1
FmocFF/Fmoc-K1	A		
FmocFF/FmocFF-K1			B
FmocFF/Fmoc-K2	C		
FmocFF/FmocFF-K2	D		
FmocFF/Fmoc-K3			E
FmocFF/FmocFF-K3	F	G	

b)

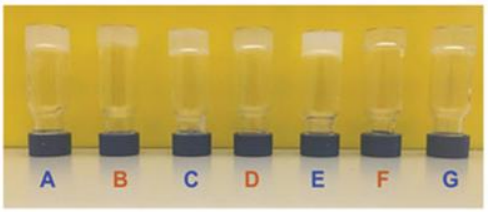

Figure 3.12: (A) In green, combinations, named with letters from A to G, resulting in the formation of HGs, which inverted test tubes are reported in (B) section.

Analogously to the pure Fmoc-FF hydrogel, all the explored multicomponent ones form with a kinetic <3 min after vortexing the DMSO/H_2O peptide suspension, thus indicating that the insertion of the cationic peptide does not slow down the time required for the HG complete organization. The stability of the obtained matrices was tested, as previously described, according to the Ringer's solution test. Differently from the single-component Fmoc-K HGs, ΔW(%) values for the mixed formulations, ranged between 2.5 and 8.2%, indicate very low weight loss (**Table 3.3**). They can be thus considered very stable matrices, even more than the pure Fmoc-FF HG, which undergoes a degradation degree of 10% in the same tested conditions. However, a higher stability was found to

correspond to multicomponent HGs in which the cationic peptide lacks the FF motif.

Table 3.3: chemical composition and ΔW (%) values for the seven multicomponent hydrogels.

Sample	Mixed Hydrogels	w/w ratio	mol/mol ratio	ΔW (%)
A	Fmoc-FF/Fmoc-K1	1/1	1.5/1	4.7
B	Fmoc-FF/FmocFF-K1	2/1	4.2/1	8.2
C	Fmoc-FF/Fmoc-K2	1/1	1.5/1	2.9
D	Fmoc-FF/FmocFF-K2	1/1	2.1/1	5.7
E	Fmoc-FF/Fmoc-K3	2/1	2.9/1	5.5
F	Fmoc-FF/FmocFF-K3	1/1	2.0/1	7.8
G	Fmoc-FF/FmocFF-K3	1/2	1.0/1	3.1

3.4.4 Structural, rheological and relaxometric characterization of multicomponent cationic hydrogels.

Fluorescence spectra of mixed HGs were collected, analogously to what previously done for single-component samples, by exciting them both at λ = 257 and λ = 301 nm. In **Figure 3.13** the fluorescence spectra of Fmoc-FF/Fmoc-K mixed matrices are reported. Similar profiles were also obtained for Fmoc-FF/FmocFF-K HGs (data not shown). All the spectra are characterized by a main emission peak centered between 325 and 328 nm. Moreover, two shoulders at 350 and 361 nm are visible, together with a red-shifted peak around 420 nm. After excitation at 301 nm, the signal centered around 325 nm, which was previously observed also for these peptides in their self-assembled form, indicates an antiparallel overlapping of the Fmoc group. However, the simultaneous occurrence of both the parallel and antiparallel orientations is suggested by the presence of the

peak at 361 nm, even if the higher intensity of the first peak seems to imply that the antiparallel overlap is preferred.

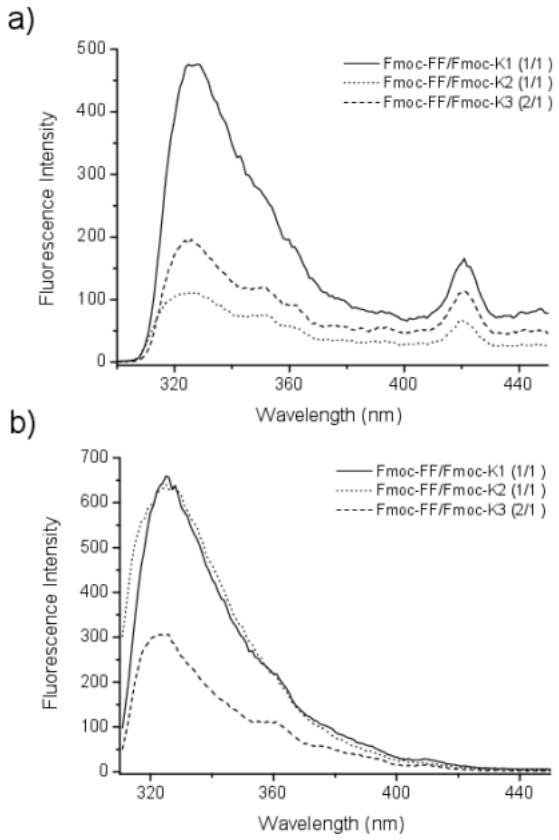

Figure 3.13: Fluorescence spectra of mixed Fmoc-FF/Fmoc-K1, Fmoc-FF/Fmoc-K2 and Fmoc-FF/Fmoc-K3 excited at 257 nm (A) and at 301 nm (B)

Moreover, the band at 420 nm could indicate the formation of excimeric species. The fact that the emissive profile observed for samples excited at 257 nm is similar to the one obtained upon excitation at 301 nm, indicated the occurrence of a FRET phenomenon. The structural organization of the components in the mixed HGs was investigated through CD and FT-IR spectroscopies (**Figure 3.14**). A dichroic signature similar to the one of single-component samples, was observed also for the multicomponent

ones, thus confirming also for these last the occurrence of a β-sheet organization. By comparing CD spectra of mixed hydrogels with the sum of the ones of the single components it can be deduced that a possible self-sorted arrangement of the two peptides occurs. Indeed, contrarily to what would be observed for a co-assembly HG, in which the two components interact each other to originate mixed aggregates at a dimeric level, CD profiles of the considered HGs are enough superimposable with the sum of CD spectra of the individual peptides.

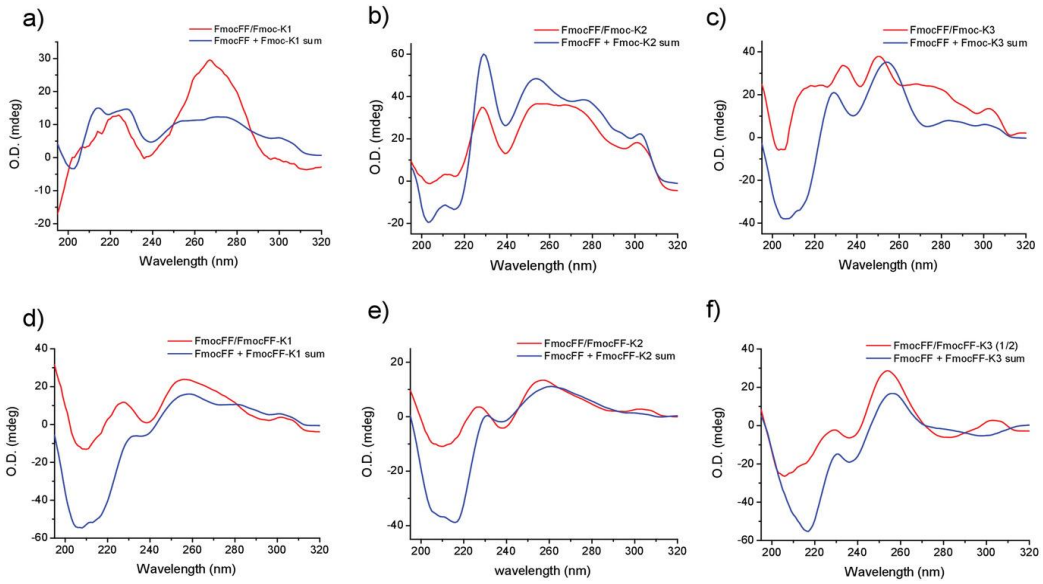

Figure 3.14: Comparison between CD spectra of hybrid P-HGs recorded between 320 and 195 nm and calculated spectra obtained by summing CD spectrum of each component in the same experimental conditions.

To obtain further information on the secondary structure, FT-IR spectra of the samples were recorded between 4000 and 400 cm^{-1}. Absorbance deconvolution profiles in the amide I region, together with the secondary structure percentage, are reported in **Figure 3.15**. For samples A, C, and E, the dominant peak at 1640 cm^{-1}, associated with a shoulder centered at

1675 cm^{-1}, indicates a β-sheet structure with an antiparallel orientation of the strands, even if the signal at 1675 cm^{-1} could also be referred to residual trifluoroacetic acid. Samples deriving from FmocFF-K peptides mixing with Fmoc-FF present a principal band red-shifted to 1650–1653 cm^{-1} and seem to be characterized by a mixture of secondary structures in which, however, β-arrangements are still prevalent.

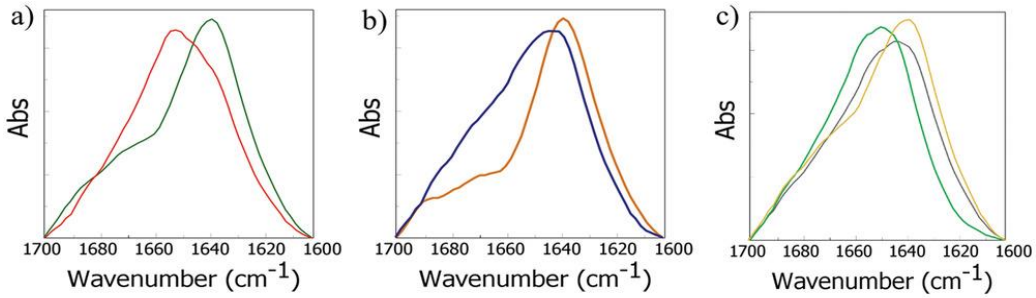

Sample	*α-helix*	*β-sheet*	*β-turn*	*other*
A	0	62	18	20
B	34	26	20	20
C	1	86	11	2
D	9	42	25	24
E	5	49	21	25
F	20	40	19	21
G	23	39	18	20

Figure 3.15: FT-IR amide I deconvolution profiles for (A) Fmoc-FF/Fmoc-K1 1/1(green line) and Fmoc-FF/FmocFF-K1 2/1 (red line); (B) Fmoc-FF/Fmoc-K2 1/1 (orange line) and Fmoc-FF/FmocFF-K2 1/1 (blue line); (C) Fmoc-FF/Fmoc-K3 2/1 (dark yellow line), Fmoc-FF/FmocFF-K3 1/1 (gray line), and Fmoc-FF/FmocFF-K3 (light green line). The table reports the deconvolution percentage analysis.

SEM micrographs and images collected after CR assay of the seven mixed hydrogels are reported in **Figure 3.16.** Multicomponent xerogels appear to be composed by long fibrils, involved in a mutual physical entanglement. Even if no substantial differences in morphology are detectable for the seven matrices, Fmoc-K1, Fmoc-K2, and Fmoc-K3 fibers are more visible and defined in mixed hydrogels with respect to the corresponding pure

ones. In the second and third rows of the figure, images of CR-stained xerogels in bright field and under polarized light are shown.

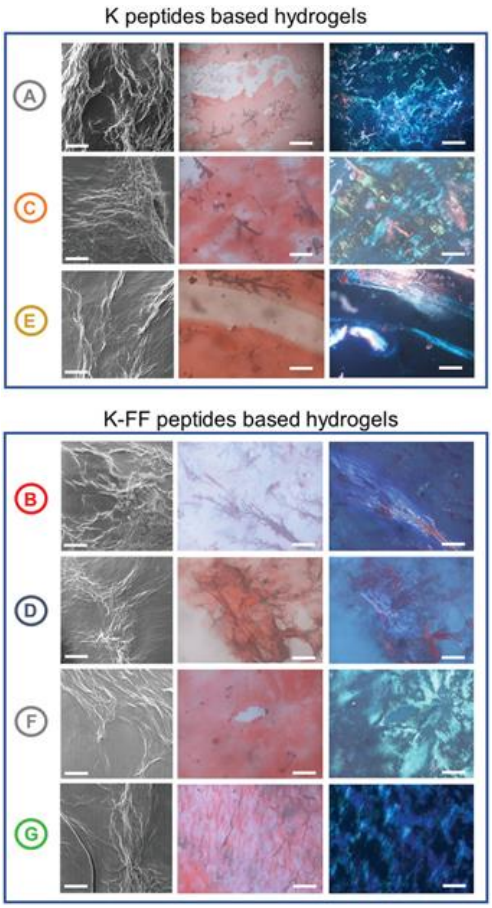

Figure 3.14: on the left, selected SEM micrographs of hybrid hydrogels (scale bar 10 μm); at the center staining of Congo Red xerogels in bright field; on the right Congo red stained xerogels under cross-polarized light (scale bar 100 μm). List of samples: (A) Fmoc-FF/Fmoc-K1 1/1; (B) Fmoc-FF/FmocFF-K1 2/1; (C) Fmoc-FF/Fmoc-K2 1/1; (D) Fmoc-FF/FmocFF-K2 1/1; (E) Fmoc-FF/Fmoc-K3 2/1; (F) Fmoc-FF/FmocFF-K3 1/1; (G) Fmoc-FF/FmocFF-K3 1/2.

The typical CR birefringence is observed for all the samples, thus confirming the presence of amyloid like fibers. Two different colors are detectable: the transmission of blue derives from negative birefringence, while the

transmission of yellow demonstrates a positive one. Their mixture is visualized as green. WAXS analyses were also performed on dried fibers of mixed hydrogels prepared according to the stretch-frame method. [159] **Figures 3.15** and **3.16** report the 2D WAXS data for Fmoc-K and FmocFF-K series and their corresponding 1D profiles, respectively. Several continuous diffraction rings can be seen in the 2D data of the Fmoc-FF/Fmoc-K1 fiber (**Figure 3.15A**), thus indicating the absence of a clear preferred orientation into the illuminated volume of the fiber. On the contrary, for Fmoc-K2 (**Figure 3.15B**), Fmoc-K3 (**Figure 3.15C**) and FmocFF-K fibers (**Figure 3.16**) show a growing partial orientation of the fiber, with the typical diffraction pattern of the cross-β amyloid structure. The collected 2D WAXS patterns were centered and calibrated, and radially folded into 1D profiles. The 1D data were integrated along the meridional and equatorial axes to obtain the corresponding 1D profiles along the axis of the fiber and perpendicular to it, respectively.

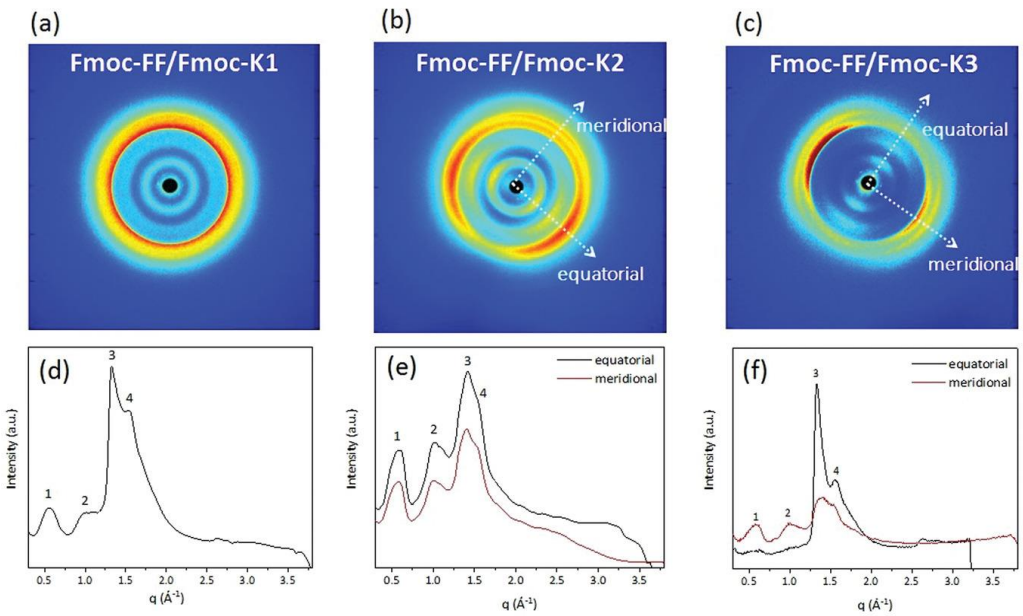

Figure 3.15: WAXS characterization of the mixed hydrogels Fmoc-FF/Fmoc-K: 2D WAXS data (on the top row right), and 1D WAXS meridional/equatorial profiles (on the bottom row).

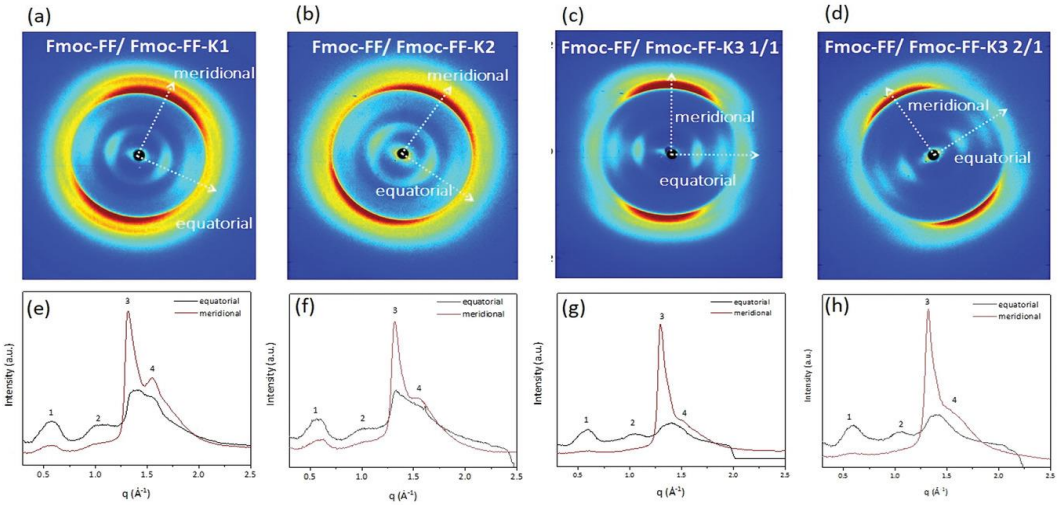

Figure 3.16: WAXS characterization of the mixed hydrogels Fmoc-FF/FmocFF-K: 2D WAXS data (on the top row right), and 1D WAXS meridional/equatorial profiles (on the bottom row).

The main meridional and equatorial peaks are reported in **Table 3.4**. The diffraction patterns are characterized by several common main peaks occurring at q_1 = 0.58 Å^{-1} (d_1 = 10.8 Å), q_2 = 1.05 Å^{-1} (d_2 = 5.9 Å), q_3 = 1.32 Å^{-1} (d_3 = 4.8 Å), and q_4 = 1.53 Å^{-1} (d_4 = 4.1 Å). q1 (equatorial peak) and q_3 (meridional peak), corresponding to the main distance between two distinct β-sheets perpendicular to the fiber axis and to the distance between adjacent peptide backbones organized into β-strands along the fiber axis, respectively, are both typical features of amyloid-like fibers. [134] These data are in good agreement with those previously measured for pure Fmoc-FF, [106] thus suggesting that the structural organization of the Fmoc-FF hydrogelator is not significantly modified by the addition of K peptides in the formulation.

Table 3.4: Meridional and equatorial peak positions in q ($Å^{-1}$) and corresponding distance d = 2π/q (Å) of the mixed hydrogels

Systems	Equatorial reflections		Meridional reflections	
	q [$Å^{-1}$] ± 0.02	d [Å] ± 0.5	q [$Å^{-1}$] ± 0.02	d [Å] ± 0.5
FmocFF/Fmoc-K1	$q_1 = 0.58$	$d_1 = 10.8$	$q_3 = 1.32$	$d_3 = 4.8$
	$q_2 = 1.05$	$d_2 = 5.9$	$q_4 = 1.53$	$d_4 = 4.1$
FmocFF/Fmoc-K2	$q_1 = 0.58$	$d_1 = 10.8$	$q_3 = 1.32$	$d_3 = 4.8$
	$q_2 = 1.05$	$d_2 = 5.9$	$q_4 = 1.53$	$d_4 = 4.1$
FmocFF/Fmoc-K3	$q_1 = 0.58$	$d_1 = 10.8$	$q_3 = 1.32$	$d_3 = 4.8$
	$q_2 = 1.05$	$d_2 = 5.9$	$q_4 = 1.53$	$d_4 = 4.1$
FmocFF/FmocFF-K1	$q_1 = 0.58$	$d_1 = 10.8$	$q_3 = 1.32$	$d_3 = 4.8$
	$q_2 = 1.05$	$d_2 = 5.9$	$q_4 = 1.53$	$d_4 = 4.1$
FmocFF/FmocFF-K2	$q_1 = 0.58$	$d_1 = 10.8$	$q_3 = 1.32$	$d_3 = 4.8$
	$q_2 = 1.05$	$d_2 = 5.9$	$q_4 = 1.53$	$d_4 = 4.1$
FmocFF/FmocFF-K3 (1/1)	$q_1 = 0.58$	$d_1 = 10.8$	$q_3 = 1.32$	$d_3 = 4.8$
	$q_2 = 1.05$	$d_2 = 5.9$	$q_4 = 1.53$	$d_4 = 4.1$
FmocFF/FmocFF-K3 (2/1)	$q_1 = 0.58$	$d_1 = 10.8$	$q_3 = 1.32$	$d_3 = 4.8$
	$q_2 = 1.05$	$d_2 = 5.9$	$q_4 = 1.53$	$d_4 = 4.1$

Table 3.5: Storage modulus (G'), loss modulus (G''), and Tan δ for the studied multicomponent hydrogels.

Sample	G' [Pa]	G'' [Pa]	Tan δ
A	3226	340	9.5
B	801	76	10.5
C	2000	229	8.7
D	232	38	6.1
E	35161	2169	16.2
F	5092	354	14.3
G	227	25	9.1

Rheological analyses were conducted to study the mechanical responsivity of the mixed 1 wt% hydrogels, in the same experimental conditions previously explored for the single component matrices. The storage modulus G' storage and the loss modulus G'' are collected in **Table 3.5** and reported as histograms in **Figure 3.17A**. Since for all the explored sample

G' was found to be higher that G'' and tan δ >1, the hydrogel state was confirmed. Even if HG formation was achieved in different conditions, matrices obtained by the mixture of Fmoc-K1, Fmoc-K2, and Fmoc-K3 peptides with Fmoc-FF (samples A, C, and E) possess higher G' values and thus a higher mechanical rigidity with respect to the corresponding self-assembled ones. In particularly, for sample E, the G' value increases from 2526 to 35161 Pa. The comparison between the G' values for hydrogel couples containing the same aliphatic sequence K (A/B, C/D, and E/F-G) underlines a trend in the mechanical response of the multicomponent HGs. Specifically, the insertion of the diphenylalanine moiety seems to result in a decrease of the stiffness, particularly evident for the C/D couple, in which the same ratio between the cationic peptide and Fmoc-FF is preserved. This effect could be imputable to the variation in the aromatic/aliphatic balance following the addiction of two aromatic residues. This balance was previously described as a key factor for the gelation behavior of K peptides.

The water dynamics within the hydrogel network were studied using a relaxometric approach. The same approach has been previously applied for the analysis of the frequency dependence of spin-lattice relaxation rates in hydrogels [160] and polymers. [161] The variation of the relaxation rate (*R1*) has been measured as a function of the applied magnetic field in the range of proton Larmor frequencies between 0.01 and 10 MHz (**Figure 3.17B**). Dynamic parameters associated with the occurrence of two levels of water motion were identified. The slower motion belongs to water molecules constrained in the peptide scaffold, whereas the faster one is related to water molecules undergoing less restricted motions. Fitting parameters shown in **Table 3.6** were obtained from the analysis of nuclear magnetic relaxation dispersion (NMRD) profiles reported in **Figure 3.17C** (samples A, C, E) and **Figure 3.17D** (samples B, D, F, G) according to

Equation 3.3. % slow motion and average correlation time were also calculated.

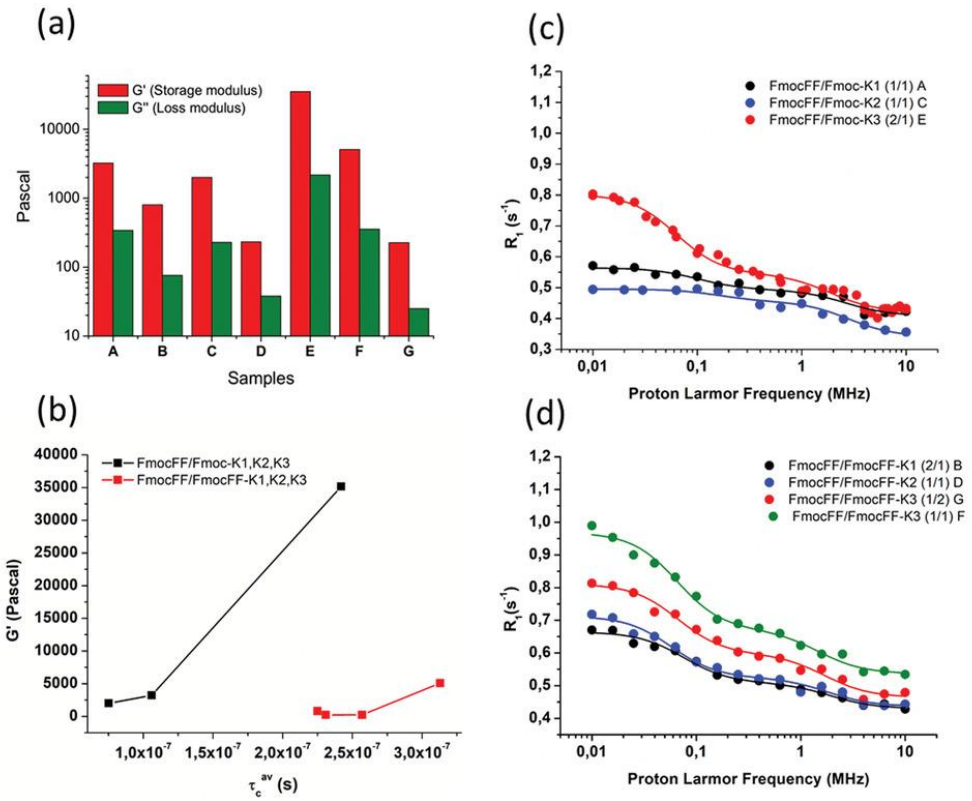

Figure 3.17: (A) Rheological histogram analysis performed on 1.0 wt% hybrid P-HGs. Graph reports both G' (red bar) and G" (green bar) moduli of each time sweep experiment (20 min, strain of 0.1%, frequency 1 Hz). Values are expressed in Pascal (Pa) logarithmic scale. (B) Correlation between average water correlation time (calculated from fitting of data reported in (C) and (D) and G' C, D 1H NMRD profiles (longitudinal relaxation rate (R_1) as a function of the Proton Larmor frequency) measured on (C) samples A, C, E and (D) B, D, F, G at 298 K. Continuous lines represent the best fits obtained with a sum of Lorentzian functions.

As it can be observed from NMRD profiles in **Figure 3.17C,D**, the relaxation rates values over all the frequency range for our HGs are significantly lower (<1 s^{-1}) in comparison to those previously reported for other peptide

nucleic acid-based HGs. These lower values can be explained by a comparing A_0, β, τ_1, and τ_2 parameters extrapolated from the data fitting for our HGs with respect to the other ones. A_0 and β values are essentially constant for all the investigated matrices. τ_1 values of the faster motion are in the same range (5.65×10^{-8} to 1.07×10^{-7} s), of those observed for other peptide-based hydrogels. However, a significant difference is observed for the slower τ_2, which, being in the range 9.9×10^{-7} to 2.74×10^{-6} s for our hydrogels, is three to six times shorter than those reported for previously reported ones ($6–7 \times 10^{-6}$ s), thus indicating an acceleration in the motion of slower water molecules. This effect causes the occurrence of lower observed relaxation rates (R_1). A different trend may be observed for the two types of mixed HGs. Indeed, in FF-K series, the correlation times associated with both the slower and the faster motions are comparable for all the matrices and no dependance on the composition of the system is observed.

Table 3.5: Best-fit parameters of the ^{1}H NMRD profiles of the hybrid hydrogels

Sample	A	C	E	B	D	F	G
System	FmocFF/Fmoc-K1	FmocFF/Fmoc-K2	FmocFF/Fmoc-K3	FmocFF/FmocFF-K1	FmocFF/FmocFF-K2	FmocFF/FmocFF-K3 (1/1)	FmocFF/FmocFF-K3 (2/1)
A_0 (s^{-1})	0.41	0.34	0.42	0.42	0.43	0.54	0.46
β (s^{-1})	0.40	0.40	0.39	0.40	0.41	0.45	0.44
A_1	3.5×10^6	5.0×10^6	3.7×10^6	2.4×10^6	2.4×10^6	2.8×10^6	3.2×10^6
τ_1 (s)	6.1×10^{-8}	5.6×10^{-8}	8.4×10^{-8}	8.2×10^{-8}	8.7×10^{-8}	1.1×10^{-7}	9.3×10^{-8}
A_2	1.1×10^5	1.0×10^5	2.6×10^5	1.8×10^5	1.7×10^5	2.7×10^5	2.0×10^5
τ_2 (s)	1.6×10^{-6}	9.9×10^{-7}	2.5×10^{-6}	2.1×10^{-6}	2.7×10^{-6}	2.4×10^{-6}	2.4×10^{-6}
% slow[a)]	3.0	2.0	6.5	7.1	6.4	8.9	6.0
τ_C^{av} (s)	1.1×10^{-7}	7.5×10^{-8}	2.4×10^{-7}	2.2×10^{-7}	2.6×10^{-7}	3.1×10^{-7}	2.3×10^{-7}

[a)] The percentage of water experiencing slow motion (% slow) was obtained by comparing the weight of the Lorentzian functions (% slow = A_2/A_1+A_2) in each sample.

On the other hand, HGs containing FF-lacking cationic sequences, show an increasing trend of τ_1, τ_2, , and % slow in the order C < A < E, which corresponds to the same trend of increasing stiffness, as extrapolated from rheological measurements. However, it is worth noting that the values found

for the sample E are similar to those of hydrogels containing the FF moiety (B, D, F, G), despite its higher G' value. For this reason, a direct correlation between stiffness or rigidity of the hydrogel scaffold and the motional dynamics of entrapped water cannot be extrapolated all the times, and in this context, it appears that the correlation between rigidity and water dynamics can be predictable only for hydrogels prepared using structurally similar building blocks in terms of primary amino acid sequence, hydrophobicity/hydrophilicity, and aromaticity.

3.4.5 Cell viability assays for pure and mixed cationic hydrogels

The toxicity of both pure and mixed cationic peptide based HGs, together with their ability to support cell adhesion, was tested *in vitro*. 3T3-L1 (mouse fibroblast) cells were used to study the cell adhesion of Fmoc-K1, K2, and K3. As shown in **Figure 3.18A,** when compared to cells plated in the absence of hydrogels, Fmoc-K1 and Fmoc-K2 disfavored cell adhesion (cell attachment to 20 ± 3% and 36 ± 8% of the total seeded cells, respectively), whereas a higher adhesion efficiency was observed for Fmoc-K3 HGs (85 ± 12%). This may be explained on the basis that more rigid gels are able to support more efficiently the cell adhesion respect to the softer ones. [162] However, independently from their ability to favor adhesion, the cytotoxicity caused by the three supports was minimal (cell death of 9 ± 3, 11 ± 2, and 3 ± 1% for, respectively, Fmoc-K1, K2, and K3 after 24 h from plating). Cells adhered remained thus viable up to 72 h (92 ± 3, 95 ± 3, 94 ± 3% cell viability for Fmoc-K1, K2, and K3, respectively). Fmoc-K3 was shown to favor cell duplication, with a duplication rate of 1.7 ± 0.2 similar to cell plated in the absence of HGs (duplication rate 1.9 ± 0.1). Instead, a cell growth impairment was measured for cell growing on Fmoc-K1 and -K2 hydrogels (duplication rate 0.4 ± 0.1 and 1.2 ± 0.2, respectively).

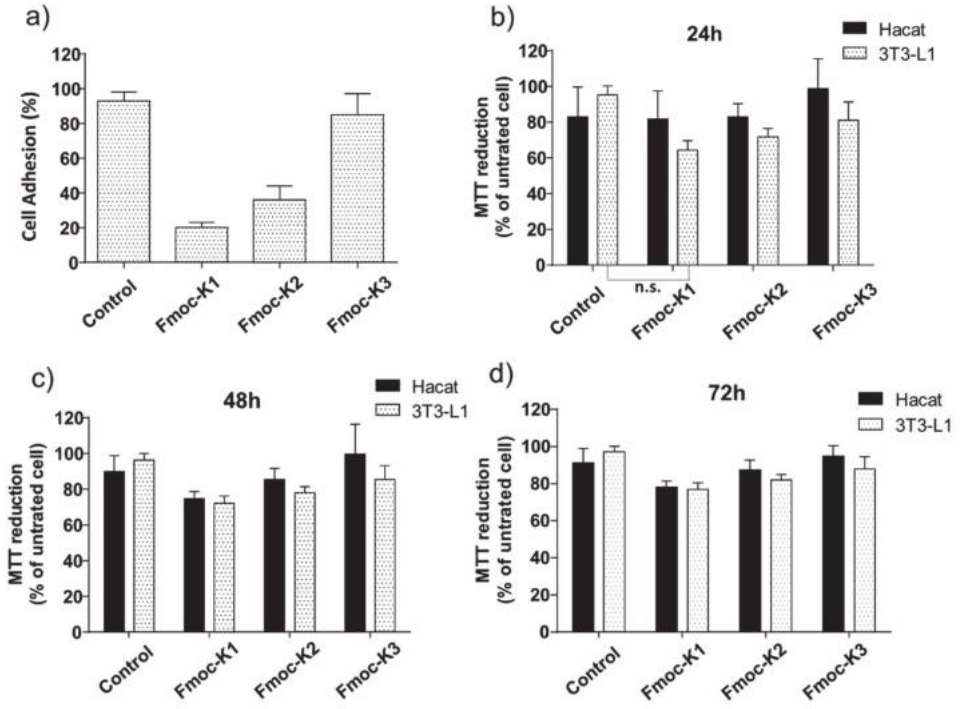

Figure 3.18: In vitro biological assays. (A) Cell adhesion on pre-casted hydrogels. (B-D) Compatibility of hydrogels with eukaryotic cell culture. The 3T3-L1 cells were seeded on the indicated hydrogel pre-casted in 96-well plates. Cell adhesion (% of adherent viable cell), viability upon adhesion (% viable cells upon plating) and duplication rate for the indicated hydrogels are reported as mean ± SD of at least three replicates. MTT assay conducted on HaCat (black bars) and 3T3-L1 (dotted white bars) cell lines treated for 24 h (B), 48 h (C), and 72 h (D) with Fmoc-K1, Fmoc-K2, and Fmoc-K3 hydrogels conditioned media. Cell survival was expressed as percentage of viable cells in the presence of conditioned media, compared to control cells grown in their absence. Error represents SD of three independent experiments. n.s. = not significant, Mann–Whitney t-test.

Conditioned medium cytotoxicity assays were performed to verify if growth arrest was due to chemicals released by Fmoc-K1 and -K2 hydrogels in the cell culture. As shown in **Figure 3.18B-D**, no significant cytotoxicity on 3T3-L1 cells or on HaCat (human fibroblast) cells was observed for all the tested samples up to 72 h. The same cytotoxicity test was carried out for mixed

hydrogels to study their biocompatibility. As shown in **Figure 3.19**, only for the samples C, F, and G, a reduction of cell viability of about 20% was observed on HaCat cells. For 3T3-L1 cell line, an increased cytotoxic effect is detected, but cell viability remains higher than 65% after 72h of treatment for all the explored samples, thus indicating a general high biocompatibility. Cell adhesion tests were conducted on 3T3-L1 cells also for multicomponent matrices, and viability was estimated by acridine orange/propidium iodide staining. Among all the tested hydrogels, C was found to be the one able to favor the higher cell adhesion, spreading, and duplication (**Figure 3.19B,C**).

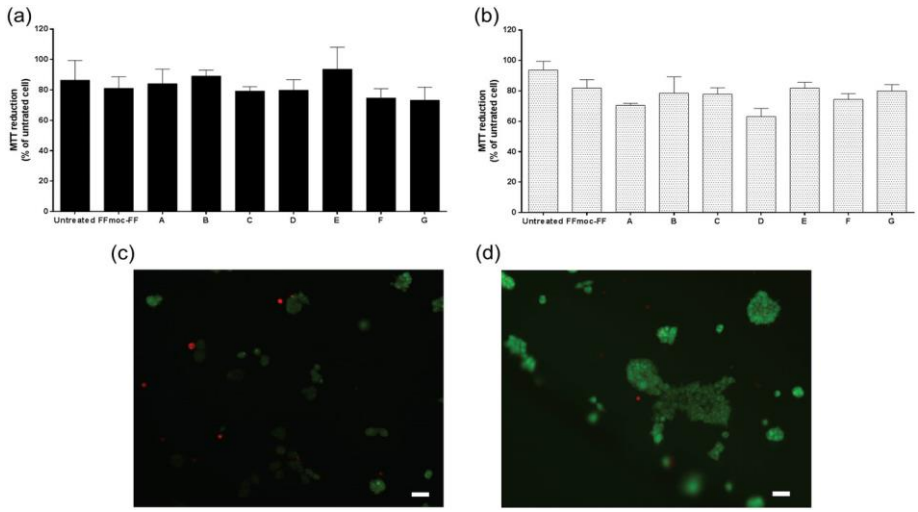

Figure 3.19: MTS assay for mixed HGs conducted on: (A) HaCat and (B) 3T3-L1 cell lines. Cells were treated for 72 h with Fmoc-FF and A-G mixed hydrogels (see table for details). Cell survival was expressed as percentage of viable cells in the presence of hydrogels, compared to control cells grown in their absence. Error represents SD of three independent experiments. All P-HGs do not perturb cell viability in a significant manner (Mann–Whitney *t*-test). For the adhesion test, 3T3-L1 cells were seeded on (C) uncoated or (D) on hydrogel C precasted 96-well plates. 16 h after seeding, cell adhesion and viability were estimated by acridine orange/propidium iodide stain to identify viable cell (fluorescing green) and dead cells (fluorescing red) (scale bar = 50 μm).

3.4.6 Fmoc-FF/PEGDA mixed hydrogel formulation

To formulate the peptide/polymer hydrogels, in which the polymeric part is represented by PEG dyacrilates (PEGDA), a modified solvent-switch procedure was used. After the preparation of a DMSO Fmoc-FF stock solution, a water solution of PEGDA was used for the rehydration step. By leaving the amount of the peptide component unchanged ($9.53 \cdot 10^{-6}$ mol), different concentrations of the two PEGDA species (at different length) were tested. The selected peptide/polymers ratios were 1/1, 1/2, 1/5 and 1/10 mol/mol. All the tested ratios allowed the formation of a self-supporting material, as confirmed by the inverted test tube in the **Figure 3.3B,C**. No hydrogel was formed above the 1/50 ratio for Fmoc-FF/PEGDA1 matrices and 1/10 for Fmoc-FF/PEGDA2 ones. The formation of the self-supporting matrix was associated with an opaque-to-limpid macroscopic transition. By following the variation in transparency, the gelation kinetics were evaluated. This kinetics was found to be very similar to the one of pure Fmoc-FF HG (~3 min) for the 1/1, 1/2 and 1/5 ratios. A slight increase of the gelation time (~1 min plus) was only detected for 1/10 Fmoc-FF/PEGDA ratio. **Figure 3.3** shows that samples differ in turbidity. More translucent matrices are formed for 1/1 and 1/2 ratios, whereas 1/5 and 1/10 ones result in opaque hydrogels. By looking at the absorbance value at 600 nm, the macroscopic evidence in turbidity was quantified. At the considered wavelength, the light absorption from peptide chromophores is absent and absorbance values can be ascribed to scattering phenomena. [163] An increase in the absorbance values from 0.183 to 0.270 a. u. for Fmoc-FF/PEGDA1, and from 0.166 to 0.224 a. u. for Fmoc-FF/PEGDA2, was observed by passing from the ratio of 1/1 to 1/10 one. By keeping the hydrogels inverted up to 6 months, no macroscopic changes in terms of homogeneity, visual appearance, and self-supporting behavior were

observed, thus confirming the stability of all the explored matrices. Only for 1/10 ratios, a modest syneresis event (weight loss ~ 5%) was detected.

3.4.7 Water behavior in multicomponent peptide/polymer hydrogels

The analysis of the water behavior in HGs can provide interesting information about the supramolecular organization, permeation properties, pores architecture and solutes diffusion. Several techniques were used to analyze the water behavior in the proposed matrices: swelling ratio, stability test in Ringer's solution and dehydration test were carried out. Moreover, the water longitudinal relaxation rate ($R1$=1/T1) as a function of applied magnetic field was measured. Values of the swelling ratio q, reported in the **Table 3.6**, increase with the amount of PEGDA in the hybrid materials and respect to pure Fmoc-FF (q= 29.7 %). Moreover, q values for PEGDA1 were found higher than the corresponding PEGDA2 containing matrices. This difference can be probably attributed to the higher number of ethoxylic repetitions in PEGDA1 (around 3-fold higher) respect to PEGDA2, which make it more hydrophilic and, acting like H-bonding acceptor groups, are able to reinforce the interactions with the water. Even the stability ratios (ΔW), extrapolated with Ringer's test, were found to depend on the amount of incorporated PEGDA (see **Table 3.6**). Indeed, a higher stability can be detected for higher PEGDA ratios, by evidencing that the polymer is able to preserve the matrix from degradation. All the peptide/polymer mixed hydrogels are more stable than the pure Fmoc-FF matrix (ΔW= 27.4 % in the same experimental conditions).

Table 3.6: Results of swelling and stability studies.

	Swelling ratio (q)				Stability ratio (ΔW)			
Sample	**1/1**	**1/2**	**1/5**	**1/10**	**1/1**	**1/2**	**1/5**	**1/10**
PEGDA1	31.5	32.9	35.4	39.7	5.53	1.23	1.31	1.15
PEGDA2	30.1	31.2	33.1	36.1	4.47	3.01	2.85	2.09

Moreover, dehydration studies showed that PEGDA containing HGs can hold back elevated percentage (< 92 %) of entrapped water, much higher than the pure Fmoc-FF matrices (< 9%) (data not shown), independently from both PEGDA molecular weight and its amount. This may be explained considering the hydrophilic nature of PEGDA, able to avoid evaporation of water, by keeping it strongly anchored *via* noncovalent interactions.

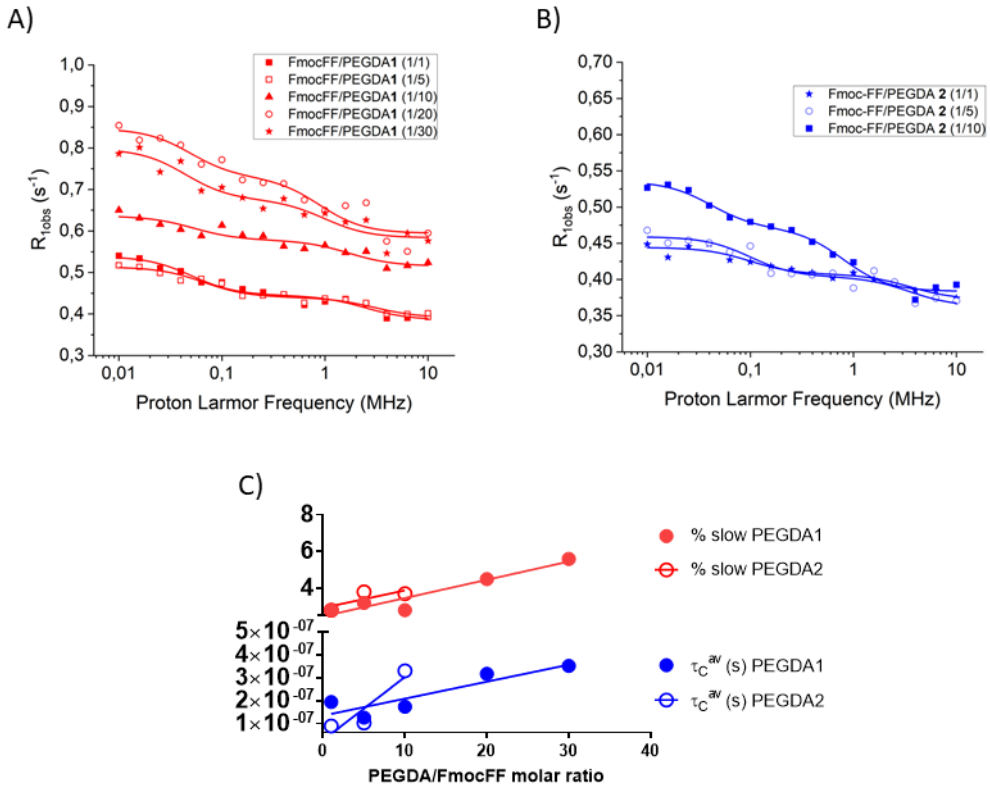

Figure 3.20: ^{1}H NMRD profiles measured on HGs with PEGDA1 (A) and PEGDA2 (B) at 298 K. Continuous lines represent the best fits obtained with a sum of Lorentzian functions. (C) Variation of the average water correlation time (and the percentage of slowing moving water (% slow) as a function of PEGDA molar content.

Finally, a relaxometric approach was used to investigate water dynamics in the hydrogel matrix, similarly to what previously done for Fmoc-FF/cationic peptides mixed formulations. NMRD profiles acquired for Fmoc-FF/PEGDA HGs are reported in **Figure 3.20**. In the case of PEGDA1 containing HGs two additional samples with higher PEG polymer content (1/20 and 1/30) were investigated. The relative fitting parameters collected in **Table 3.7**. τ_1, τ_2, , and % slow are rather like those previously observed for analogous Fmoc-FF containing hybrid HGs. For both PEGDA1 and PEGDA2, the values of % slow and , increase with the amount of PEGDA in the hybrid materials, but, quite surprisingly, are considerably lower respect to pure Fmoc-FF. Moreover, the parameters associated with water mobility were found independent from PEGDA molecular weight.

Table 3.7: Best-fit parameters of the 1H-NMRD profiles of the hybrid hydrogels.

Sample	A_0 (s^{-1})	β (s^{-1})	A_1	τ_1 (s)	A_2	τ_2 (s)	% slow*	(s)
Fmoc-FF	0.41	0.30	3.2×10^{6}	1.3×10^{-7}	2.6×10^{5}	$3.1\times10\text{-}^{6}$	7.6	3.5×10^{-7}
Fmoc-FF/PEGDA1 (1/1)	0.38	0.35	2.3×10^{6}	7.8×10^{-8}	6.5×10^{4}	4.3×10^{-6}	2.8	1.9×10^{-7}
Fmoc-FF/PEGDA1 (1/5)	0.39	0.41	2.3×10^{6}	5.2×10^{-8}	7.5×10^{4}	2.4×10^{-6}	3.2	1.3×10^{-7}
Fmoc-FF/PEGDA1 (1/10)	0.51	0.35	1.9×10^{6}	9.3×10^{-8}	5.5×10^{6}	3.0×10^{-6}	2.8	1.7×10^{-7}
Fmoc-FF/PEGDA1 (1/20)	0.59	0.22	3.4×10^{6}	1.8×10^{-7}	1.6×10^{5}	3.2×10^{-6}	4.5	3.2×10^{-7}
Fmoc-FF/PEGDA1 (1/30)	0.58	0.33	1.7×10^{6}	1.6×10^{-7}	1.0×10^{5}	3.6×10^{-6}	5.6	3.5×10^{-7}
Fmoc-FF/PEGDA2 (1/1)	0.37	0.49	1.6×10^{6}	4.5×10^{-8}	4.7×10^{4}	1.6×10^{-6}	2.8	9.0×10^{-8}
Fmoc-FF/PEGDA2 (1/5)	0.36	0.80	1.1×10^{6}	4.5×10^{-8}	4.3×10^{4}	1.6×10^{-6}	3.8	1.0×10^{-7}
Fmoc-FF/PEGDA2 (1/10)	0.38	0.40	1.1×10^{6}	2.0×10^{-7}	4.2×10^{4}	3.9×10^{-6}	3.7	3.3×10^{-7}

*The percentage of water experiencing slow motion (% slow) was obtained by comparing the weight of the Lorentzian functions (% slow $=A_2/A_1+A_2$) in each sample

3.4.8 Secondary structure, morphology and rheological analyses of Fmoc-FF/PEGDA mixed hydrogels

The effect of PEGDA incorporation in the structural arrangement of Fmoc-FF network was evaluated through a series of techniques like CD, FTIR spectroscopies and ThT and CR colorimetric assays. First of all, CD spectra (**Figure 3.21A**) were acquired for both 1/1 an 1/10 ratios between 350 and 190 nm range and reported as optical density (mdeg/O.D.). The CD signature was found to be similar, independently from PEGDA molecular weight or their relative amounts, thus suggesting no significant differences into the gel organization and topography. Three main dichroic signals can be detected for all the samples: a negative peak around 209 nm, a positive one at 231 nm and a broad signal centered at 267 nm. It is well known that the signal at 231 nm is generally indicative of β-sheet structuration. This signal undergoes a blue- shift (228 nm) in 1/10 matrices, which could be due to a reduction of the material's ability to absorb light as a consequence of the increased turbidity. On the contrary, the positive and broad band at 267 nm, commonly attributed to the fluorenyl group on the peptide, undergoes a bathochromic effect respect to Fmoc-FF (259 nm). This red-shift can be explained taking into account the difference in dielectric constant induced from the incorporation of PEGDA into the hybrid peptide-polymer matrices. However, by comparing these spectra with the typical Fmoc-FF one, a substantial maintenance of gel matrix topology without alteration of the antiparallel β-sheet organization, can be deduced. Additional analyses of the secondary structuration were carried out by FTIR spectroscopy. Two different bands can be observed for all the samples (**Figures 3.21B,C**): an intense signal in the amide A region (~ 3300 cm^{-1}) and a band in amide I region (centered at 1636 cm^{-1}). Spectral deconvolution is dominated by a main peak around 1650 cm^{-1}, conducible to C=O stretching and suggesting the presence of β-sheet secondary

structures. (**Figures 3.21D,E**). Moreover, the additional band at ~1690 cm^{-1} indicates an antiparallel orientation of the β-strands in assemblies.

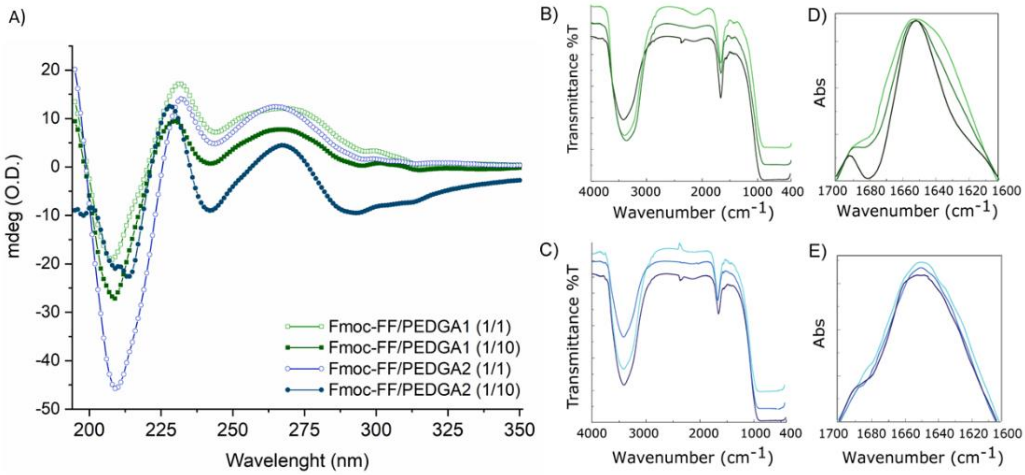

Figure 3.21: (A) CD spectra (in the 190 and 350 nm range) of Fmoc-FF/PEGDA1 (1/1 and 1/10) and Fmoc-FF/PEGDA2 (1/1 and 1/10). FTIR characterization. (B) FTIR spectra of Fmoc-FF/PEGDA1 matrices (1/1, light green; 1/5 green grass; 1/10 dark green). (C) FTIR spectra of Fmoc-FF/PEGDA2 matrices (1/1, light blue; 1/5 blue; 1/10 dark blue). Amide I deconvolution profiles of PEGDA1 (D) and PEGDA2 matrices (E).

The presence of β-sheets on xerogels was further confirmed by the thioflavin T (ThT) assay. The cationic benzothiazole structure of this dye adopts a stabilized conformation when bound to aggregates thus inducing an enhancement and a shift of the fluorescence emission peak from 445 to 482 nm, after excitation at 450 nm. [164] From the inspection of **Figure 3.22**, it can be observed that ThT dye can stain the PEGDA containing HGs giving rise to a fluorescent emission in the GFP spectral window, thus highlighting the presence of amyloid-like structures. This result was also confirmed by CR assays (**Figure 3.23**). Mixed hydrogels, prepared in the presence of 10 μmol/L CR, were investigated by UV-Vis spectroscopy.

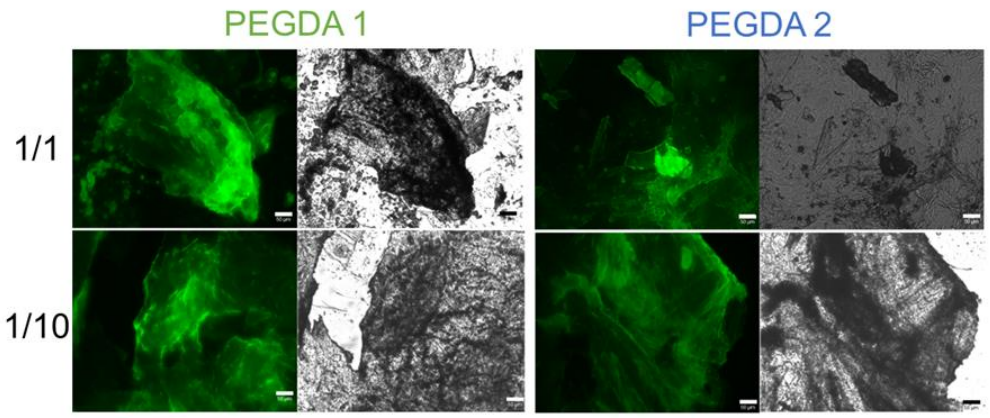

Figure 3.22: Immunofluorescence images of mixed xerogels of Fmoc-FF/PEGDA1 and Fmoc-FF/PEGDA2 at 1/1 and 1/10 molar ratio stained with 50 μmol/L ThT solution. Samples are imaged in the spectral regions of the GFP (Green Fluorescent Protein λ_{exc} = 488 nm, λ_{em} = 507 nm) (A, C) and in the bright field. The scale bar = 50 μm.

As expected, a red shift of the absorbance peak from 480 to 540 nm, attributable to the presence of β-sheets, was detected for CR/hydrogel compared to the spectrum of the CR alone. Analogously, optical microscopy images, under bright field and cross-polarized light, of mixed xerogels stained with CR showed the typical birefringence of amyloid-like structures.

SEM images were collected to explore the morphology of the hydrogels. Micrographs, reported in **Figure 3.24**, show that substantial differences in the surface topography of systems can be detected with respect to the sponge-like structure generally reported for PEGDA-based matrices [165] and the typical fibrillar network of Fmoc-FF HGs. [166] For PEGDA1 xerogels, a quasi-fractal drapery surface is detected. The geometric distribution, the fineness, and the grade of detail increase with the amount of PEGDA polymer, letting us postulate that the change in surface morphology is attributed to its intermolecular interactions. On the contrary,

PEGDA2 hydrogels show fiber-like architectures, which manifest more in matrices with higher polymer ratios.

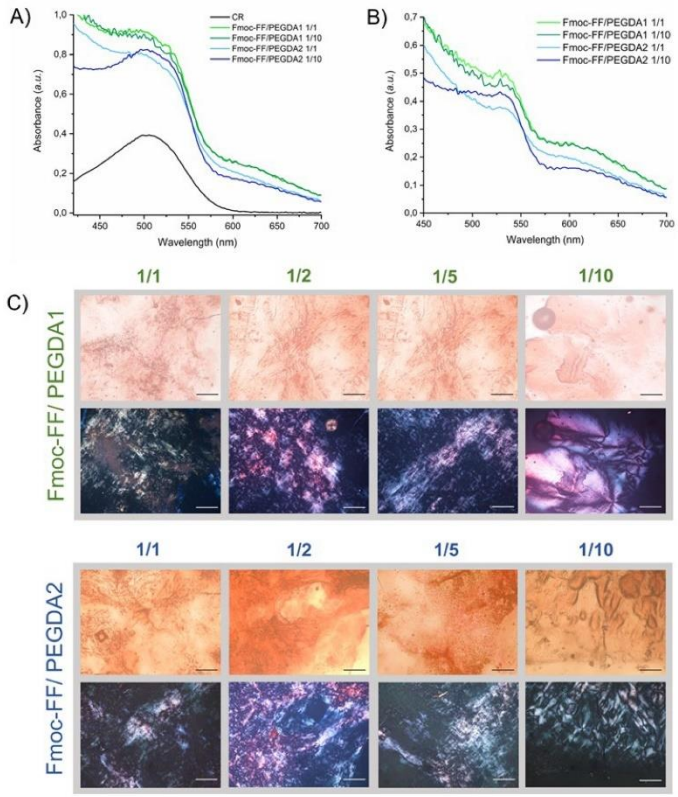

Figure 3.23: CR assay in solution and in the solid state. UV-Vis spectra of CR alone and co-incubated with Fmoc-FF/PEGDA1 (A) or with Fmoc-FF/PEGDA2 (B) at the different molar ratios. (C) Staining of Congo Red xerogels in both bright field (first row) and under cross-polarized light (second row). Scale bar =100 μm.

The evident discrepancies between PEGDA1 and the two samples indicate a rule of polymer molecular weight in the topological arrangements of the matrices, probably imputable to a different network of H-bonds. This specific physicochemical parameter also changed the peptide-polymer

interaction networking, in turn producing very different superficial morphologies in hybrid matrices. WAXS data collected on HGs fibers present the typical fiber diffraction pattern with two crossed main axes: the meridional along the fiber direction and the equatorial perpendicular to it (depicted by white arrows in 2D WAXS patterns).

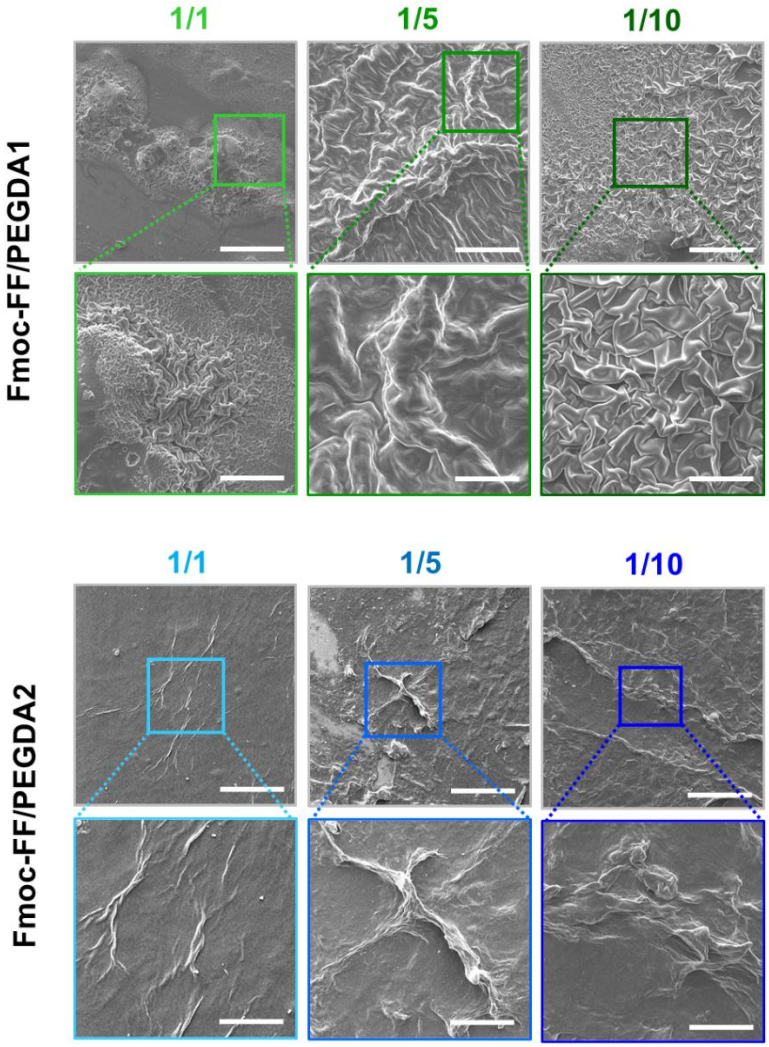

Figure 3.24: Selected microphotos of mixed xerogels of PEGDA1 (A) and PEGDA2 (B) series. Scale bar = 100 μm and 30 μm.

The 2D data were integrated along the meridional and equatorial axes to obtain the corresponding 1D profiles and are reported in **Figure 3.25 and X.26 (E-H)**.

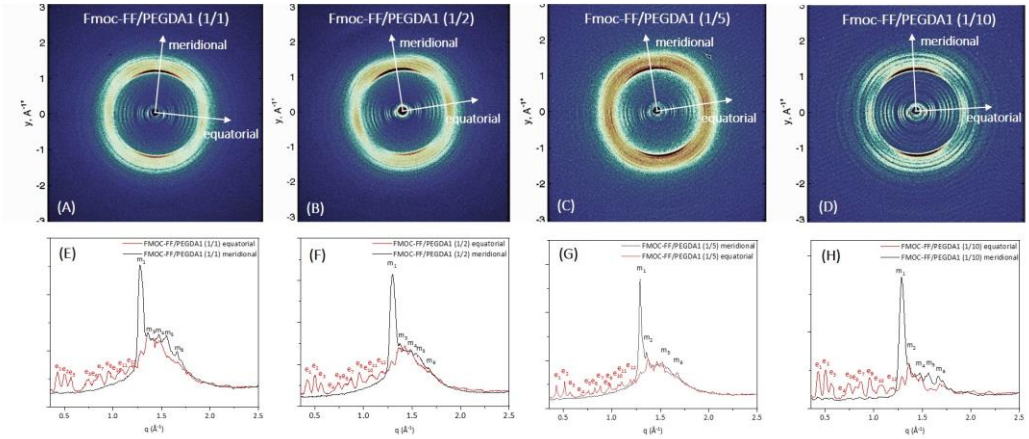

Figure 3.25: WAXS characterization of the mixed hydrogels Fmoc-FF/PEGDA1 at different concentrations: 2D WAXS data (on the top row right), and 1D WAXS meridional/equatorial profiles (on the bottom row).

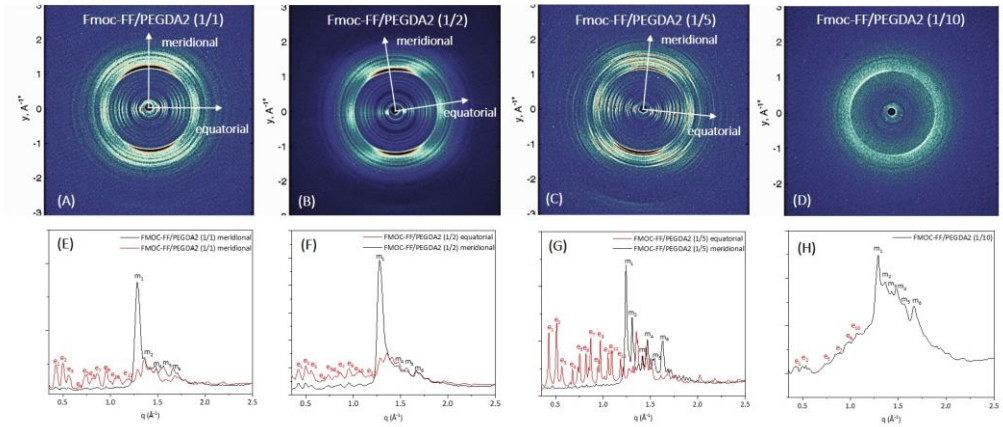

Figure 3.26: WAXS characterization of the mixed hydrogels Fmoc-FF/PEGDA2 at different concentrations: 2D WAXS data (on the top row right), and 1D WAXS meridional/equatorial profiles (on the bottom row).

The most intense diffraction peak at q = 1.29 $Å^{-1}$ (d = 4.9 Å) corresponds to the distance between adjacent peptide backbones organized into β-strands along the fiber axis, while the one at q ~ 0.5 $Å^{-1}$ (d = 12.5 Å) corresponds to the distance between two distinct β-sheets. Only Fmoc-FF/PEGDA2 does not show cross-β amyloid-like structures for the sample, because of the difficulty to realize the solid fiber with the stretch-frame method. Mixed Fmoc-FF/PEGDA hydrogels present several additional equatorial and meridional reflections respect to pure Fmoc-FF, which can be related to an increase in the hierarchical order along the fiber induced by the polymer, especially at higher PEGDA concentrations. Rheological analyses were conducted on the mixed hydrogels to explore their mechanical properties. The linear viscoelastic region (LVE region) was found in the 0.02-3.0% stain range. G' and G'' time sweep values (**Figure 3.27; Table 3.8)** analytically confirmed the gel state of all the tested matrices, due to the values of G' higher than G'' and tan δ >1. All these values are higher than pure Fmoc-FF ones at the same concentration (G'~ 950 Pa), indicating that the multicomponent systems are characterized by enhanced mechanical properties. This evidence confirms that co-assembly and co-aggregation strategies are suitable methodologies to improve the mechanical performance of matrices. PEGDA1 matrices exhibit higher G' values than PEGDA2 ones at the same polymer ratio. This evidence is also pointed out observing comparable strain break points (5 and 6 % for PEGDA1 and PEGDA2, respectively) for systems at 1/10 ratios. In contrast, significant differences were found for strain break points of PEGDA1 and PEGDA2 at 1/1 ratios (61 and 12%, respectively). This may be explained on the basis of the higher number of no-covalent interactions (H-bound) in PEGDA1. According to thermodynamic principles, for pure PEG hydrogels it is also suggested a linear correlation between the storage modulus and both molecular weight and concentration of the polymer. In the analysis of Fmoc-FF/PEGDA series a different trend can be detected for the two polymers. In

PEGDA1 series, G' value is four-time higher passing from 1/1 to 1/2 ratios (2123 Pa to 8099 Pa).

Table 3.8: Rheological parameters collected for all the mixed matrices

Samples	G' value (Pa)	G'' value (Pa)	Tan δ
Fmoc-FF/PEGDA1 (1/1)	2123	210	10.1
Fmoc-FF/PEGDA1 (1/2)	8099	577	14.0
Fmoc-FF/PEGDA1 (1/5)	7695	672	11.5
Fmoc-FF/PEGDA1 (1/10)	4323	497	8.70
Fmoc-FF/PEGDA2 (1/1)	6569	646	10.2
Fmoc-FF/PEGDA2 (1/2)	6233	625	9.97
Fmoc-FF/PEGDA2 (1/5)	5411	586	9.23
Fmoc-FF/PEGDA2 (1/10)	4220	462	9.13

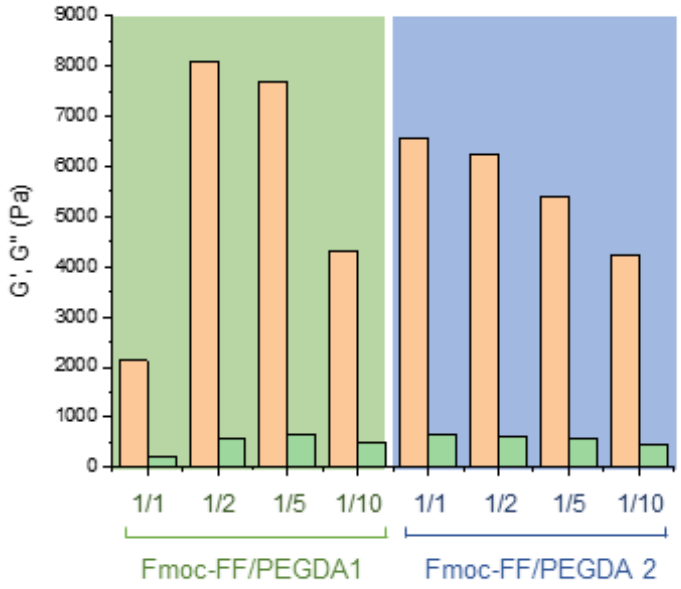

Figure 3.27: Rheological histogram analysis performed on 0.5 wt% mixed HGs. Graph report both G' (orange bar) and G" (green bar) moduli of each time sweep experiment (20 min, strain of 0.1%, frequency 1 Hz). Values are expressed in Pascal (Pa) logarithmic scale.

However, a further increase of the polymer does not cause an additional increase of the gel rigidity (7695 Pa for 1/5 ratio). Finally, it can be observed a decrease of G' for the gel at 1/10 ratio (4323 Pa). On the contrary, a gradual and constant reduction of G' value is associated with the PEGDA2 series. Analogously, this decrease is also detectable in tan δ ratios. The general rheological behavior of Fmoc-FF/PEGDA hydrogels is not the expected one. Indeed, it was previously observed that an increase of the PEG concentration can allow an improvement of the mechanical matrix rigidity. This evidence is indicative of a multifactorial correlation between the final G' and the total intermolecular network interactions and physical parameters (including water mobility, total hydrophilicity of the system, progressive increase of the hydrophilicity for higher PEGDA ratio, and predictable modification of supramolecular entangling).

3.4.9 Release of Naphthol Yellow S from peptide/polymer mixed hydrogels

The capability of the scaffolds to encapsulate molecules was tested by loading HGs with naphthol yellow S (NYS), a water-soluble disodium salt of 5,7-dinitro-8-hydroxynaphthalene-2-sulfonic acid used as histological dye. (**Figure 3.28**). NYS-loaded HGs were formulated by the solvent-switch method. The loading does not affect the gelation process at the tested dye concentration (6.02 mmol/L). Release profiles of NYS from PEGDA based HGs over time (up to 144 hours) show that all the mixed HGs exhibit a slower release respect to pure Fmoc-FF HG. Moreover, the released percentage decreases from 88 to 73% and from 90 to 80% for PEGDA1 and PEGDA2, respectively within the series by moving from 1/1 to 1/10 molar ratio. This trend suggests that the increase of PEGDA into the mixture allows a higher retention of the NYS into the aqueous hydrogel matrix. This result is not surprising considering the ability of PEGDA to establish hydrogen bonds with hydrophilic molecules.

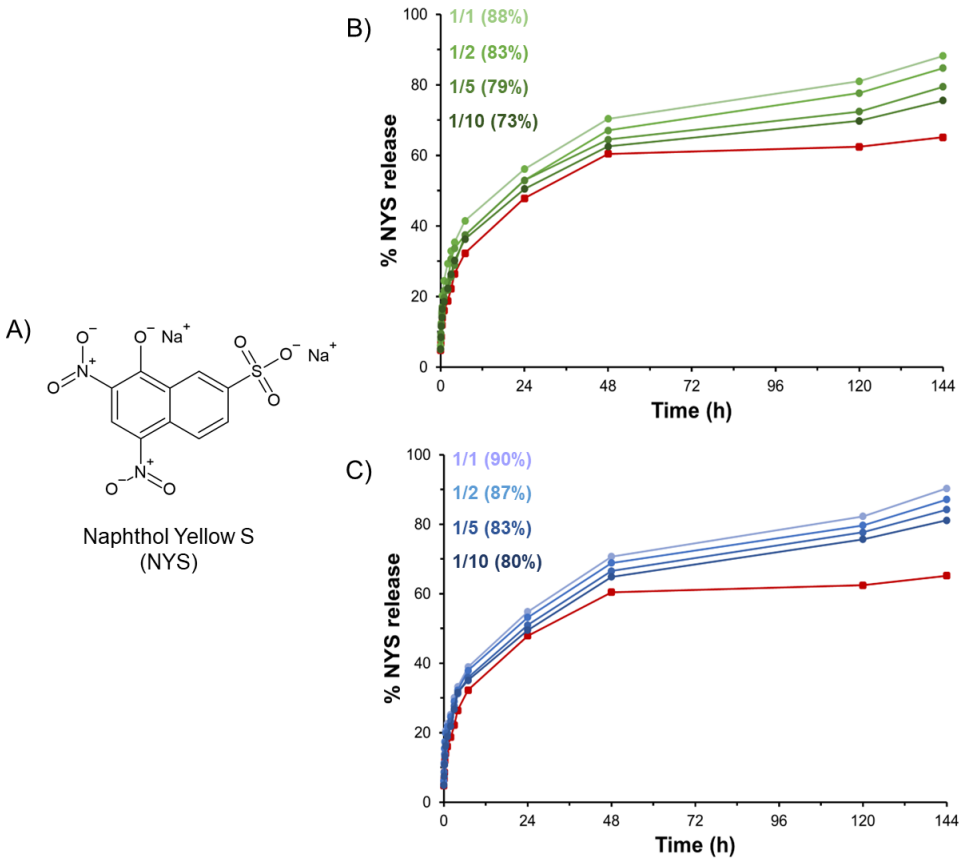

Figure 3.28: (A) Chemical structure of Naphthol Yellow S (NYS); (B) Release profiles for PEGDA1 matrices; (C) Release profiles for PEGDA2 matrices. The release from Fmoc-FF matrix is reported as red line. The release is reported in terms of % of released NYS.

3.4.10 Design, molecular modelling and dynamics of Cys-containing aromatic peptide sequences

By starting from the previously studied (FY)3 peptide and its PEGylated analogue PEG8-(FY)3, here we designed two novel derivatives, FYFCFYF and PEG_8-FYFCFYF (chemical formulas in **Figure 3.4**) in which a Cys residue is inserted in the middle of the aromatic peptide sequence. These two peptides contain a thiol group at the center of a symmetric sequence. The choice to employ a Cys residue is related to the polar neutral nature of this

amino acid, which allows to modify the hydrophilic/lipophilic balance of (FY)3 peptide without introducing additional charges. Moreover, it worth noting that, respect to other similar amino acids (Ser or Gln), Cys containing thiol group, can allow chemical cross-linking within the nanostructure as a consequence of the formation of disulfide bonds. In particular, the aim was to formulate hydrogels undergoing a different mechanical response depending on their reduced or oxidized state. Peptides were synthesized using the SPPS protocols. After their purification, identity was confirmed by mass spectrometry (**Table 3.1**). A preliminary computational study was carried out to forecast the aggregation capability of the two peptides. By performing this, it was chosen to generate a molecular model of FYFCFYF, which also constitutes the structural spine of its PEGylated derivative. The information derived from the characterization of the (FY)3 peptide [107] was used as starting point. Indeed, by assuming, also for this sequence, an antiparallel association of the β-strands, a first individual β-sheet was generated, in which an apolar surface composed by Phe residues and a polar one made by Tyr and Cys residues are present. A potential basic element for FYFCFYF system was obtained through the juxtaposition of two β-sheets by associating their apolar surfaces. This starting model (FYFCFYF_ST50_SH2), containing two fifty-stranded β-sheets, is three-dimensionally represented in **Figure 3.29A**, and its stability and dynamics was evaluated by MD simulations. A significant structural rearrangement was evidenced for this model undergoing a 500 ns simulation. From the inspection of the gyration radius and by the root mean square deviation (RMSD) values of the trajectory structures *versus* the initial model, reported in **Figure 3.30**, it can be deduced that an equilibrated region is reached only after 250 ns of the simulation. By looking at RMSD values, it can be noted that, even if the secondary β-structure of the assembly is well preserved over the entire simulation timescale, a clear twisting of the two-sheet model occurs.

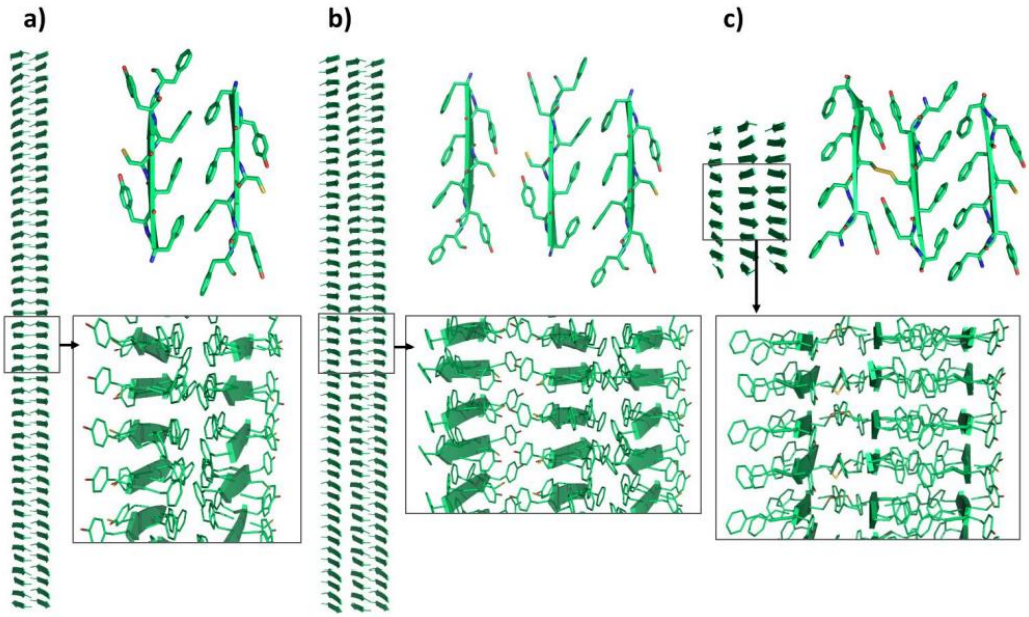

Figure 3.29: Three-dimensional representations of the starting models used in the molecular dynamics studies: FYFCFYF_ST50_SH2 (A), FYFCFYF_ST50_SH3 (B), and FYFCFYF_ST10_SH3_SS (C).

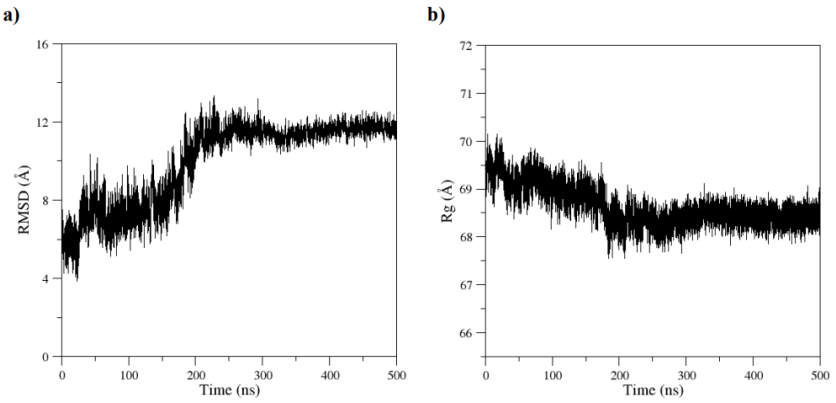

Figure 3.30: Time evolution of several structural parameters in the MD simulation performed starting from the flat model of FYFCFYF_ST50_SH2: (A) RMSD values computed on the Cα atoms of trajectory structures against the starting model and (B) gyration radius.

Also, the inter-sheet distance (~11 Å) is well preserved during the simulation: this data confirms the stability and relative rigidity of the model.

The analyses of the flexibility (**Figure 3.31A**) and the rotameric states (**Figure 3.31B**) of the side chains provides information about stability and rigidity of the aggregate. Indeed, the presence of recurrent and preserved rotameric states can be seen for the inter-strand interacting side chains with the alternation of strands with residues either in the trans or gauche χ1 dihedral angle state. Even the hydrophobic interface is stabilized by the interactions derived from the alternation of the side chains.

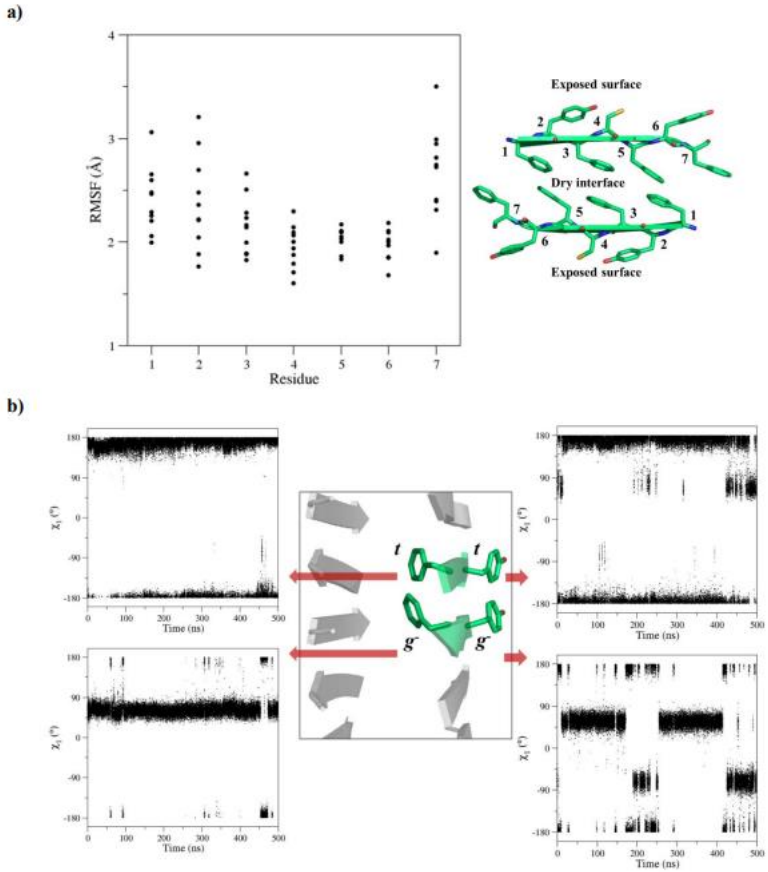

Figure 3.31: (A) RMSF values computed on the side chains of the FYFCFYF_ST50_SH2 model in the equilibrated region of the trajectory (250–500 ns). For clarity, only the values of the central ten β-strands (five strands per sheet) are reported. (B) Representative examples of the time evolution of the χ1 dihedral angle of Phe/Tyr side chains.

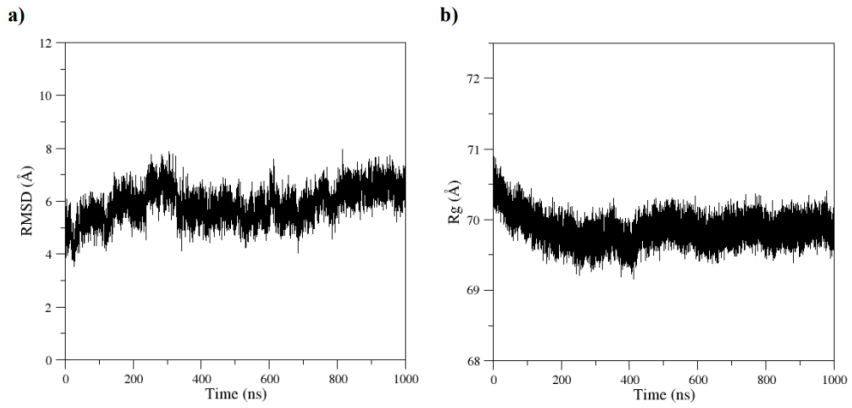

Figure 3.32: Time evolution of several structural parameters in the MD simulation performed starting from the flat model of FYFCFYF_ST50_SH3: (A) RMSD values computed on the Cα atoms of trajectory structures against the starting model and (B) gyration radius.

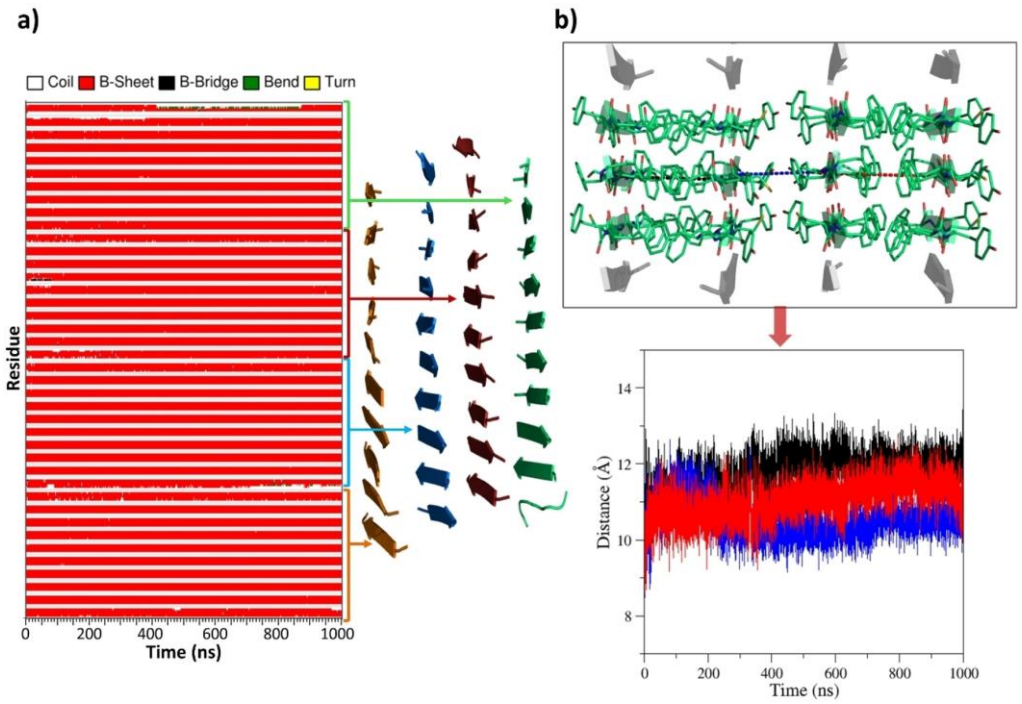

Figure 3.33: (A) Time evolution of secondary structure in the MD simulation carried out starting from the flat model of FYFCFYF_ST10_SH4. The average structure computed in the trajectory region 500–1000 ns is also shown. (B) Time evolution of the distances between two representative Cα atoms of the facing sheets along the MD trajectory.

A four ten-stranded β-sheets (FYFCFYF_ST10_SH4, **Figure 3.29B**), containing both hydrophobic and hydrophilic interfaces, were considered to expand the analyses. The MD characterization of this model clearly indicates that there is no significant variation in the stability previously detected for FYFCFYF_ST50_SH2. (**Figure 3.32**).

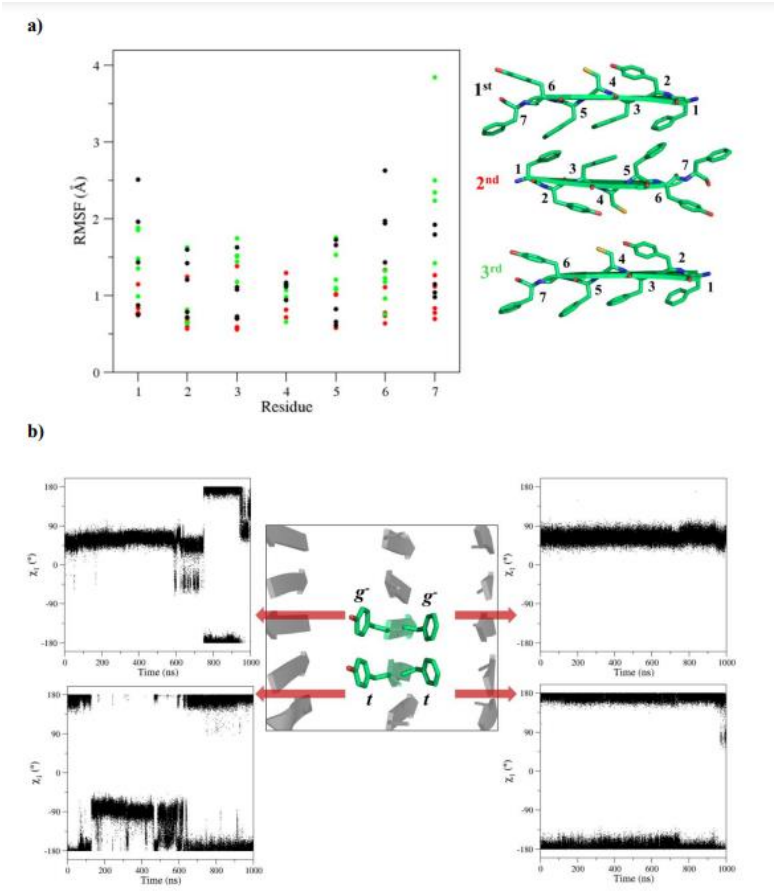

Figure 3.34: (A) RMSF values computed on the side chains of the FYFCFYF_ST50_SH3 model in the equilibrated region of the trajectory (500–1000 ns). For clarity, only the values of the central fifteen βstrands (five strands per sheet) are reported. (B) Representative examples of the time evolution of the χ1 dihedral angle of Phe/Tyr side chains of the central β-sheet.

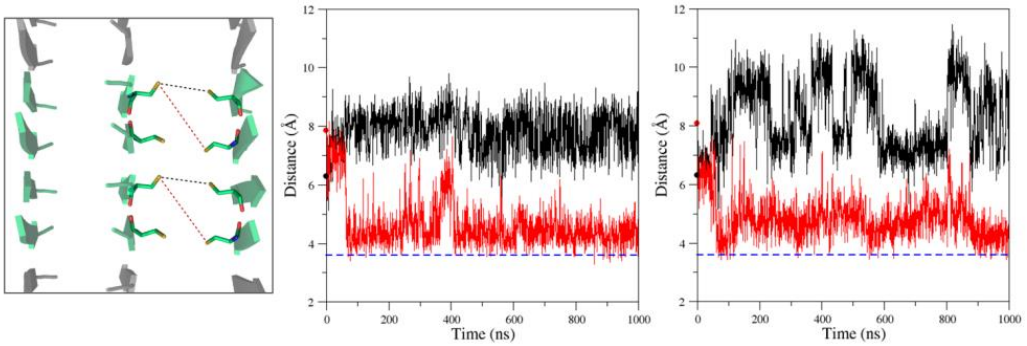

Figure 3.35: Representative examples of the time evolution of the S-S distance between the side chains of the Cys residues located in facing sheets in the MD simulation of FYFCFYF_ST50_SH3. The dashed blue line represents the theoretical interatomic distance (3.6 Å) between sulfur atoms based on their van der Waals radius (~ 1.8 Å). The color of the line (black or red) corresponds to the color that designates the corresponding distance as a dashed line in the left panel. The black/red dot reported on the vertical axis represent the value of the distance at t=0 ns.

The inter-sheet distance found for the hydrophilic interface is ~11 Å, like the one detected for the hydrophobic interface (**Figure 3.33**). Moreover, also the side chains of FYFCFYF_ST10_SH4 are empowered with a remarkable rigidity (**Figure 3.34**). This is particularly evident for the internal β-sheets within this four-sheet model. By analyzing the distances between the side chains of the Cys residues in the hydrophilic interface, it can be deduced that sulfur atoms may come as close as 3.5 Å, the minimal distance expected on the basis of their van der Waals radius (~1.8 Å) (**Figure 3.35**). The possibility of having Cys residues in their oxidized state in this kind of assembly was verified by considering the model FYFCFYF_ST10_SH4_SS (**Figure 3.29A**), in which a disulfide bridge was formed. The compatibility of the Cys-Cys bond with the formation of β-rich assemblies was confirmed through a 1 μs MD simulation. (**Figure 3.36**) Moreover, the inter-sheet distances detected in FYFCFYF_ST10_SH4_SS are very similar to those detected in FYFCFYF_ST10_SH4 (**Figure 3.37**).

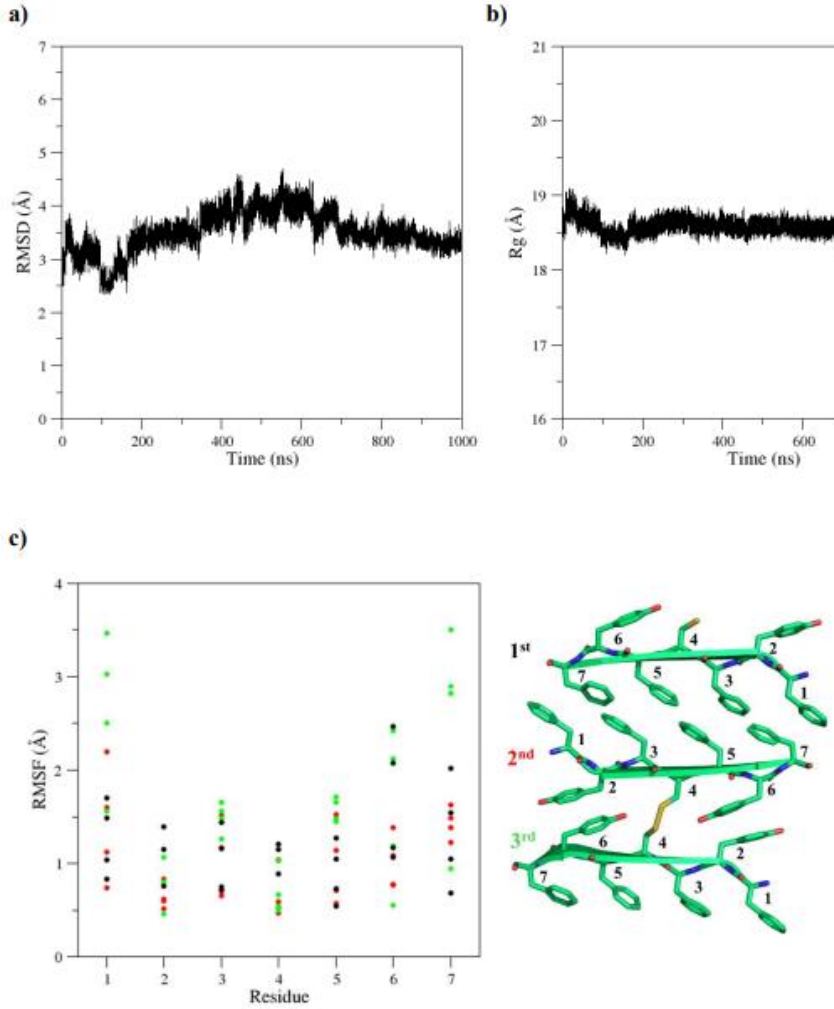

Figure 3.36: Time evolution of several structural parameters in the MD simulation performed starting from the flat model of FYFCFYF_ST10_SH3: (A) RMSD values computed on the Cα atoms of trajectory structures against the starting model and (B) gyration radius. (C) RMSF values computed on the side chains of the FYFCFYF_ST10_SH3_SS model in the equilibrated region of the trajectory (700–1000 ns). For clarity, only the values of the central twelve β-strands (four strands per sheet) are reported.

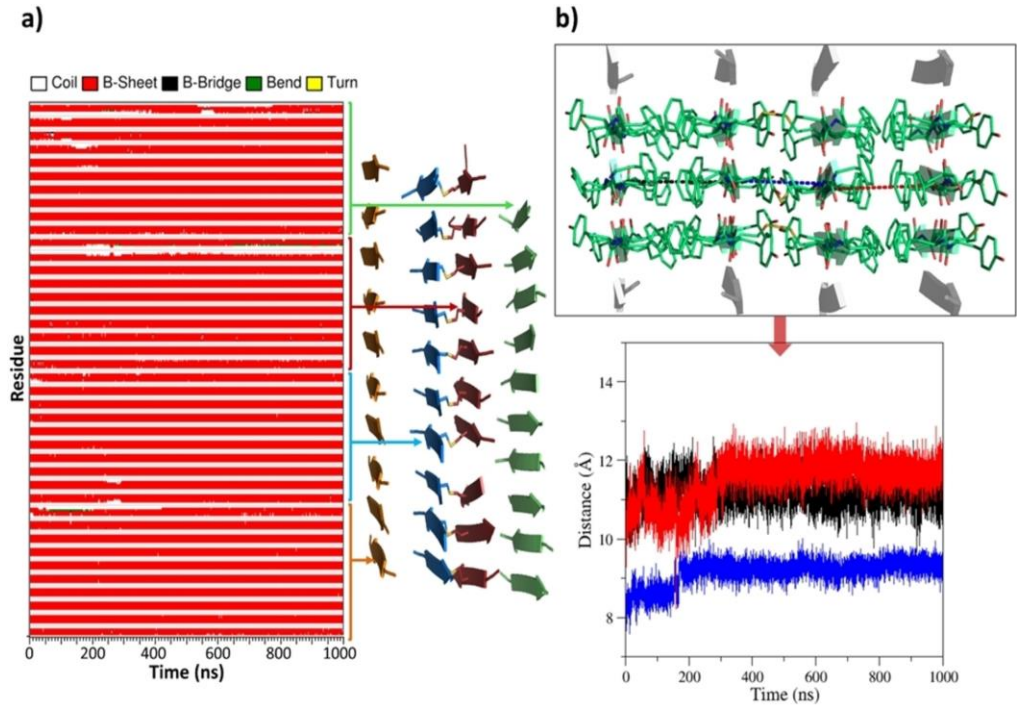

Figure 3.37: (A) Time evolution of secondary structure in the MD simulation carried out starting from the flat model of FYFCFYF_ST10_SH4 SS. The average structure computed in the trajectory region 500–1000 ns is also shown. (B) Time evolution of the distances between two representative Cα atoms of the facing sheets along the MD trajectory.

3.4.11: Aggregation studies for Cys-containing peptides

The logP values of the two sequences were estimated using the ACD Lab ChemSketch software and, as expected, were found to correlate with the experimental estimated solubility. PEG chains obviously confer to PEG_8-FYFCFYF (logP=3.57±1.05) a water solubility being 40-fold higher (~10.0 mg/mL) than FYFCFYF (logP=7.57±0.92; water solubility of 0.240 mg/mL). An opposite behavior was observed for peptides dissolved into 1,1,1,3,3,3-hexafluoro-isopropan-2-ol (HFIP) (solubility up to 200 mg/mL for FYFCFYF and 5 mg/mL for its PEGylated analogue). For this reason, peptide solutions were prepared using two approaches: PEG_8-FYFCFYF solutions were

prepared by directly solving the lyophilized powder in water, while, for, FYFCFYF a 100 mg/mL stock solution in HFIP was diluted in water, and the final sample was obtained by removing the organic solvent using N_2 flow. Analytical quantification of the peptide concentration in each sample was carried out by UV-Vis spectroscopy. The capability of both the peptides to aggregate in solution at a concentration of 2.0 mg/mL was initially evaluated by Dynamic Light Scattering (DLS) studies.

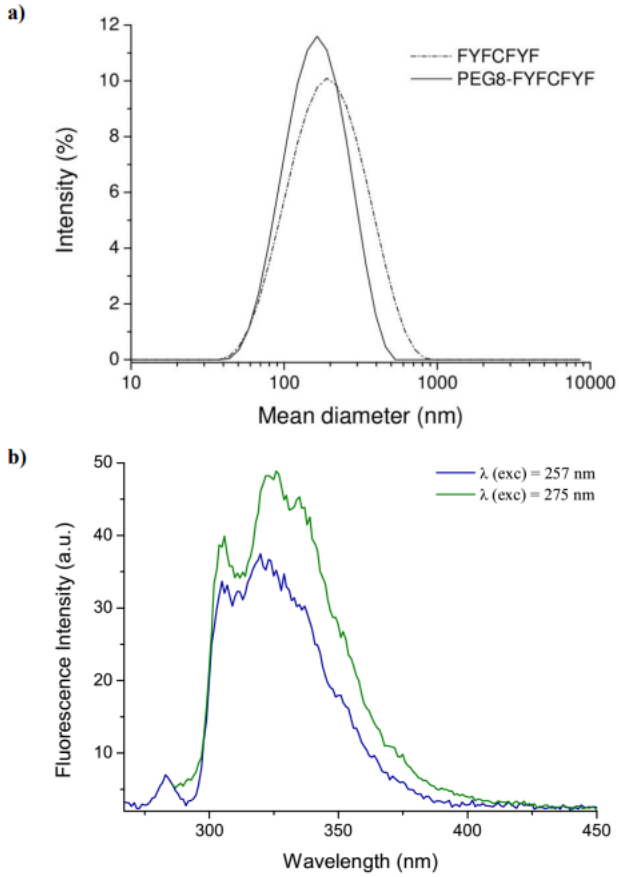

Figure 3.38: (A) DLS intensity profiles of peptide aggregates recorded at 2.0 mg/mL. (B) Emission spectra for PEG_8-FYFCFYF peptide solution at 0.005 mg/mL. Excitation wavelength corresponding to λ=257 nm and λ=275.

A monomodal distribution was observed for both the sequences, forming aggregates with a mean diameter of 164 and 197nm for PEGylated and unPEGylated derivatives, respectively. (**Figure 3.38A**) Fluorescence studies carried out on 0.005 mg/mL solutions (**Figure 3.38B**) show that emission profiles obtained after excitation at 257 and 275 nm (λ_{ex} of Phe and Tyr, respectively) can be superimposed. This result underlines the occurrence of a FRET phenomenon between the aromatic groups of Phe and Tyr amino acids, working respectively as the donor and the acceptor dye.

By exciting peptide solution at different concentrations at the wavelength of Tyr, an emission peak at 305 nm can be detected. (**Figure 3.39**) The decrease in its intensity with the increase in peptide concentration underlines that quenching phenomena occur. By further diluting the peptide solution below 0.05mg/mL, another more intense peak centered at 340 nm appears (**Figure 3.39B**). The presence of this additional band suggests that different equilibria can exist in solution. The CAC values, extrapolated by ANS titration, (**Figure 3.40A**) were found to be $9.09 \cdot 10^{-5}$ mol/L (94.1 μg/mL) and $1.50 \cdot 10^{-5}$ mol/L (24.2 μg/mL) for FYFCFYF and PEG8-FYFCFYF, respectively. As previously observed also for (FY)3 and PEG_8-(FY)3 analogues, [107] the PEG moiety promotes further interactions, improving the aggregation behavior. Moreover, since no differences can be evidenced between the CAC values of both PEGylated (FY)3 and FYFCFYF sequences, it can be deduced that the insertion of the Cys residue in the more hydrophilic variants, does not affect the aggregation propensity. On the other hand, a slight increase of the CAC value can be pointed out for FYFCFYF respect to (FY)3 (CAC = $5.98 \cdot 10^{-5}$mol/L). This may be due to an interference of the Cys residue with the mechanism of hydrophobic collapse driving the self-assembling phenomenon.

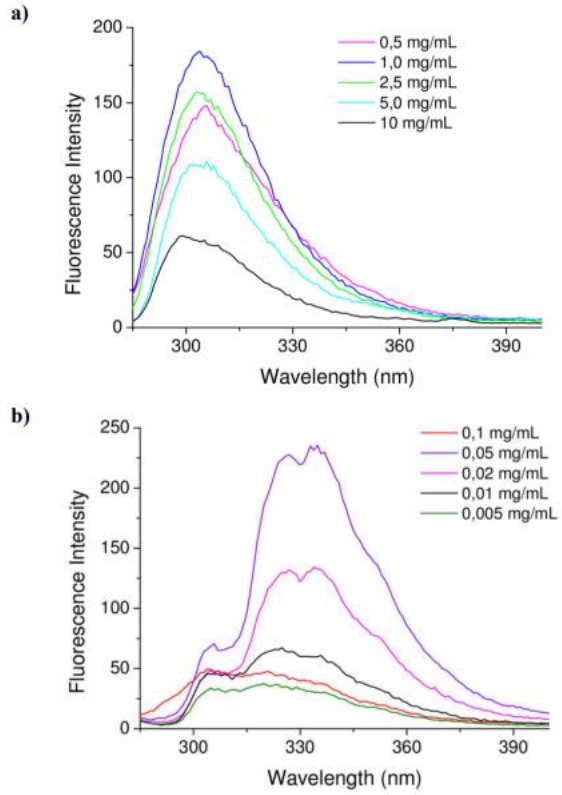

Figure 3.39: Fluorescence spectra of the peptide PEG8-FYFCFYF as function of the concentration between 0.5 and 10 mg/mL (B) and between 0.005 and 0.1 mg/mL (C). Excitation wavelength 275 nm.

Secondary structure into peptide aggregates were studied through CD and FTIR analyses. CD spectra of samples at 1.0 mg/mL concentration were recorded between 190 and 300 nm (see **Figure 3.40B**). A common profile is observed for both the samples, showing a maximum at 195 nm (indicative of $\pi \rightarrow \pi^*$ transitions), a relative maximum at 210 nm and two minima located at ~204 nm and at 221 or 217 nm for FYFCFYF and PEG_8-FYFCFYF, respectively (these last attributed to the $n \rightarrow \pi^*$ transition). This signature is typical of a β-sheet organization, preferentially observed for the unPEGylated analogue.

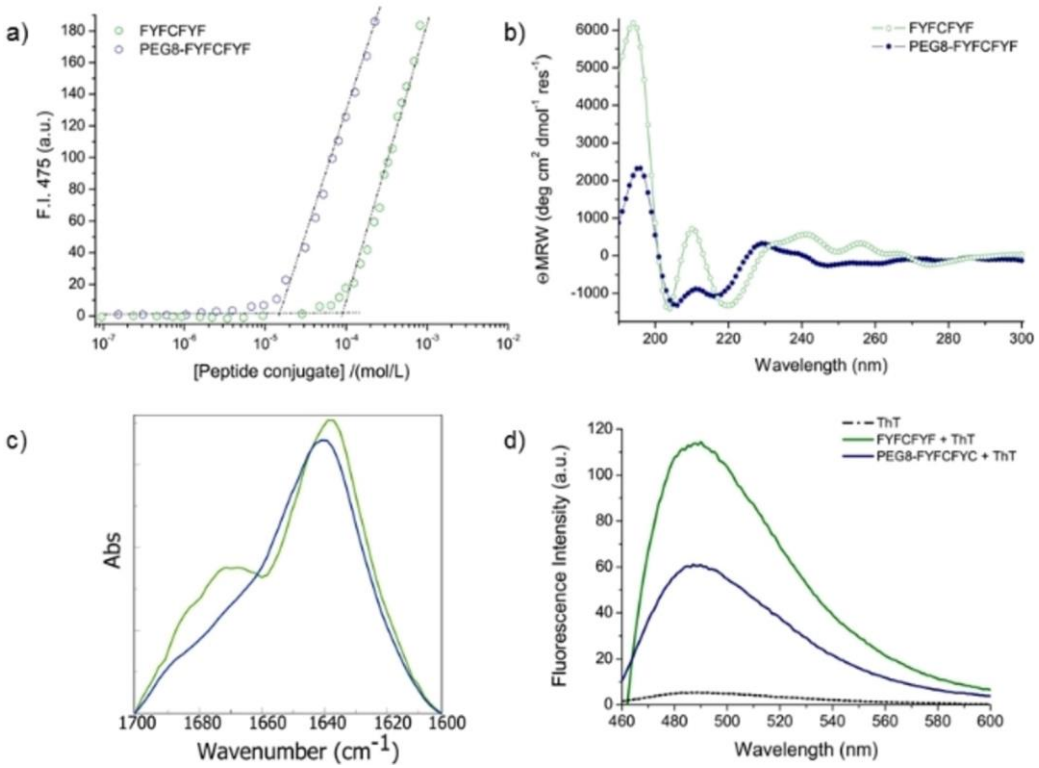

Figure 3.40: Characterization of peptide aggregates in solution. (A) Fluorescence intensity of the ANS fluorophore at 475 nm *versus* the concentration of each peptide. CAC values are calculated from the visual break points. (B) CD spectra of peptide solutions at a concentration of 1.0 mg/mL. All the spectra are recorded between 300 and 190 nm. (C) Absorbance deconvolution of FTIR spectra in the amide I region for FYFCFYF and PEG_8-FYFCFYF. (D) Fluorescence spectra of ThT coincubated with each peptide derivative after the subtraction of the peptide self-fluorescence. The spectrum of ThT alone is also reported for comparison.

Multiple signals, attributed to contribution of aromatic and thiol side chains, can be detected in the region between 240–300 nm. [167] The secondary structure characterization was furthermore studied using FTIR spectroscopy (**Figure 3.40C**). Deconvolution profiles of the amide I region are dominated by a band located at 1637 and 1640 cm^{-1} for FYFCFYF and PEG_8-FYFCFYF, respectively, accompanied, for the unPEGylated peptide, to an additional

signal at 1675 cm^{-1}. These profiles indicate the presence of β-sheet secondary structure with an antiparallel orientation of strands. The predominant tendency of FYCFYF to adopt a β-sheet conformation with respect to the PEGylated analogue, previously observed from CD studies, was also confirmed by the inspection of FTIR results. The structuration in β-sheet rich aggregates was analytically quantified by a spectroscopic assay with ThT. Cys-containing peptides were solubilized at 10 mg/mL concentration in a 50 μmol/L solution of ThT. After excitation at 450 nm, an emission peak is detectable at 482 nm for both the samples. (**Figure 3.40D**) The higher intensity of this peak for FYFCFYF can be explained by considering the different molar concentration of the two peptides (9.7 and 6.2 mmol/L for unPEGylated and PEGylated peptides, respectively). CAC values for Cys-containing peptides, obtained by ANS experiments, are in line with those extrapolated from ThT titration ($1.22 \cdot 10^{-4}$ mol/L (126 μg/mL) for FYFCFYF ans$1.81 \cdot 10^{-5}$ mol/L (19.1 μg/mL) for PEG_8-FYFCFYF, data not shown). WAXS analyses were carried out on the FYFCFYF fibril obtained with the stretch frame method and reported **Figure 3.41**. Several continuous diffraction data are shown by the 2D WAXS data. This indicates the absence of a clear preferred orientation within the illuminated volume of the fiber. The main peaks at q_1=0.58 $Å^{-1}$ (d_1=10.8 Å) and q_3=1.32 $Å^{-1}$ (d_3= 4.75 Å) evidenced in **Figure 3.41C** and explained as the inter-sheet distance detected in the trajectory structures and the inter-strand distance within each sheet, respectively, are in agreement with the structural models previously described. Two additional peaks were found at q_2=1.05 $Å^{-1}$ (d_2=6.0 Å), and q_4=1.53 $Å^{-1}$ (d_4=4.0 $Å^{-1}$) too. The 1D WAXS azimuthal profile (**Figure 3.41C)** indicates a slight preferred orientation mainly for the peak at q_1=0.58 $Å^{-1}$ that typically identifies the equatorial direction (the direction perpendicular to the fiber axis).

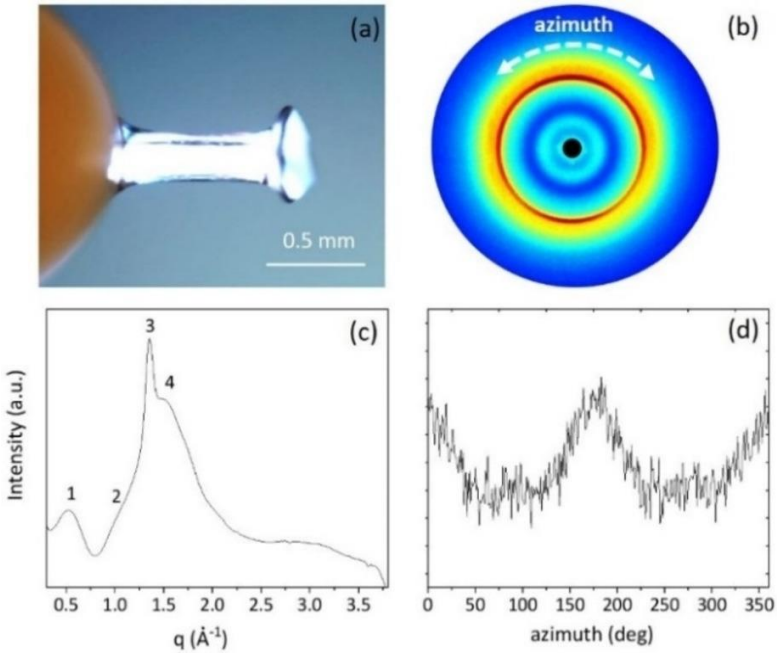

Figure 3.41: (A) Image of the investigated FYFCFYF dried fiber (scale bar=0.5 mm); B) 2D WAXS data of the FYFCFYF fiber; (C) radial integrated 1D WAXS profile; (D) intensity distribution along the azimuth of the equatorial peak at q_1=0.58 $Å^{-1}$ peak.

3.4.12 Formulation and characterization of FYFCFYF and PEG8-FYFCFYF based hydrogels

The capability of the two peptides to form hydrogels was investigated in the range of concentrations between 0.25 and 2.0 wt% using the inverted test tube. The critical gelation concentration (CGC) for FYFCFYF can be identified in the range 0.5wt%<CGC<1.0wt%, (**Figure 3.42**) while the PEGylated analogue was not able to form hydrogels in any of the explored concentrations. This was not expected on the basis of Cys-lacking analogues, in which only the PEGylated derivative was able to gel [107] Once again, the hydrophilic/lipophilic balance was recognized as the key to gelation processes for these peptides. The swelling capability of FYFCFYF hydrogel was found to be q=15 % for 1 wt% formulations, meanwhile a

swelling value of 29 % and 33 % was measured for 1.5 and 2.0 wt% samples, respectively.

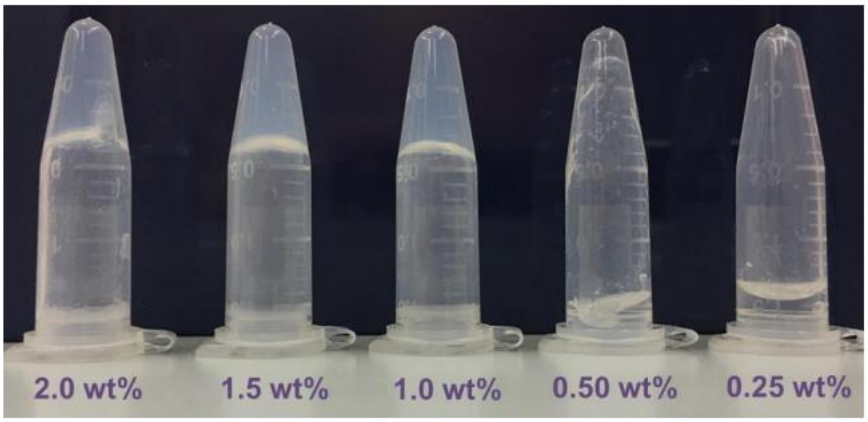

Figure 3.42: Inverted test tubes for FYFCFYF at different concentrations.

An inverted test tube conducted on the HGs for a long period evidenced that the 1.0 wt% samples resulted less stable (20 days) respect to the samples at 1.5 wt% (up to 40 days) and to the samples at 2.0 wt% (up to 65 days). This last formulation did not report visible modification after more than 2 months of inversion, thus suggesting that the increase in concentration can improve the hydrogel stability. In addition, no syneresis was noted for 1.5 wt% and 2.0 wt% HGs, whereas ~15 % of water is expulsed from 1 wt% matrix 5 days after its preparation. To further improve HG stability, the possibility of generating additional chemical linking in the supramolecular network was considered. To this scope, HGs were prepared in the presence of ammonium bicarbonate (NH_4HCO_3, AmBic) at different concentrations (10.0, 6.0, 5.0, 2.0 and 1.0mmol/L). The AmBic promotes air oxidation of Cysteine residues with consequential formation of disulfide bonds. [168] In our experiments, by using AmBic solution at a concentration of 10 mmol/L, an inhomogeneous HG is formed, while self-supporting and translucent HGs ara obtained in the presence of AmBic solutions at the

concentrations of 1.0, 2.0 or 6.0 mmol/L. By increasing the concentration of AmBic, faster gelation kinetics were observed (35 and 45 minutes for a concentration of 2.0 and 1.0 mmol/L, respectively, and instantaneous gelation for a concentration of 6.0 mmol/L). The disulfide bond formation was experimentally confirmed by ESI-MS analysis (**Figure 3.43A**), which shows the prevalent presence of dimeric species.

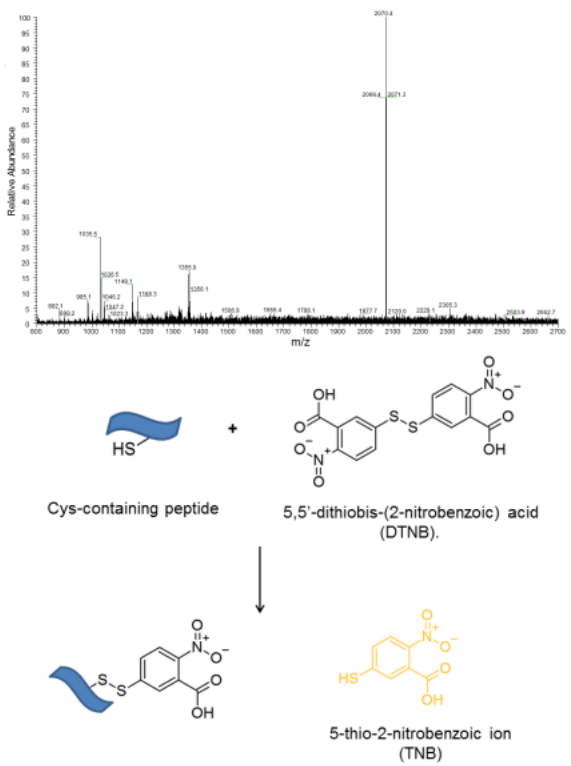

Figure 3.43: (A) ESI mass spectrum of the oxidized peptide; (B) the mechanism of reaction between DTNB and the Cys-containing peptide.

A moderate decrease of the CGC value, together with an increase of the swelling ratio, were observed for samples prepared in the presence of 6.0 mol/L AmBic solution (0.25 wt%<CGC<0.50 wt%; q up to 34 % and 40 % for 1.5 and 2.0 wt% samples, respectively). In these conditions, also the

shelf stability was shown to increase up to three months. Ellman's test was conducted to confirm the efficiency of oxidation procedure. [169] Ellman's reagent (5,5'-dithio-bis-(2-nitrobenzoic acid)), also known as DTNB, is a chromogenic compound with an oxidizing disulfide bond that, in the presence of free thiols, undergoes reduction, releasing one molecule of 5-thio-2-nitrobenzoic acid (TNB, yellow) and a mixed disulfide as products. (**Figure 3.43B**)

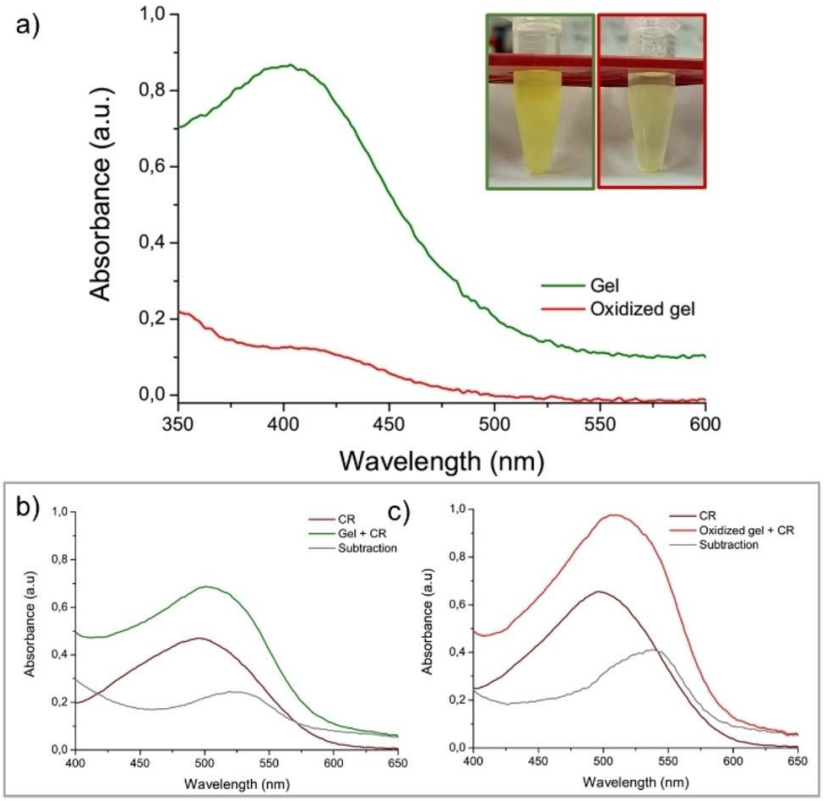

Figure 3.44: UV-Vis spectra of oxidized and not oxidized peptide hydrogels co-incubated with the Hellman's reagent (DTNB). Macroscopical appearance of hydrogels analyzed by UV-Vis are reported in the insert. Absorbance spectra of CR alone or co-incubated with hydrogels before (B) and after the oxidation (C). The subtraction of spectra is also reported.

The free thiol concentration can be then indirectly determined by measurement of TNB UV-Vis absorption at 412 nm (**Figure 3.44A**).

Moreover, a macroscopic evaluation of the positivity of the test can be derived from the observation that the DTNB solution added in FYFCFYF gel aliquot immediately becomes more colored with respect to oxidized gel (insert in **Figure 3.44A**). No alteration in the β-sheet structuration was observed for HGs prepared via AmBic, as evidenced by the positive response to Congo Red UV-Vis assay. Both the samples, prepared in the presence or in the absence of AmBic, exhibit a bathochromic shift of the CR maximum from 480 to ~540 nm (**Figure 3.44B,C**). Scanning Electron Microscopy (SEM) analyses allowed to analyze the HGs morphology. Microphotos of the xerogels are reported in **Figure 3.45**. Differently from what observed for the parental (FY)3 hexapeptide [107] and for the other analogues containing DOPA and Nal residues in place of Tyr and Phe ones, [134] no dense network of interconnected fibers was observed for FYFCFYF. On the contrary, mesoscopic fibrillary clusters that interact themselves by intermolecular forces were shown. This kind of organization is typically observed in solid-like colloidal gels. [170] After the disulfide bridge formation an increase in clusters can be detected, even if it can be not excluded that this effect is due to the increase of the ionic strength caused by AmBic. Rheological analyses were carried out on reduced and oxidized FYFCFYF gels at a concentration of 1.5 wt%; the oxidized version was prepared at the same concentration using 6.0 mmol/L AmBic.

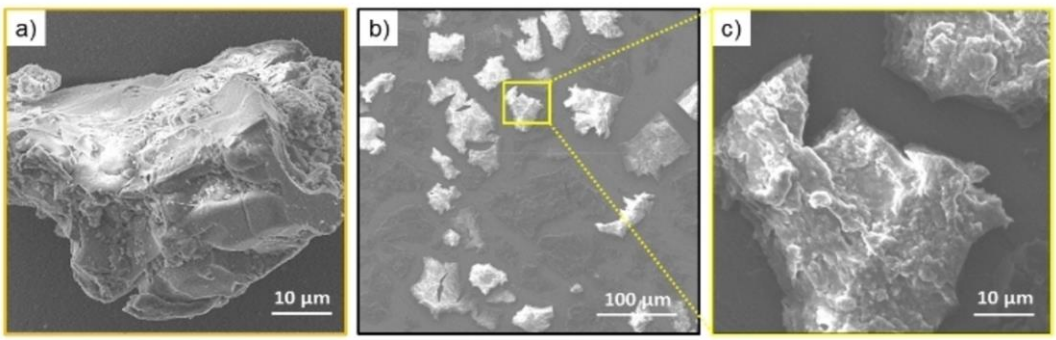

Figure 3.45: SEM microphotos of FYFCFYF xerogels before (A) and after oxidation (B, C).

Results were collected after preliminary evaluation of the optimal measurement parameters, these identified according to dynamic oscillation strain sweep (at a frequency of 1 Hz) and dynamic frequency sweep (at 0.1 % strain) for both the tested gels. The linear viscoelastic region (LVE region), in which the rheological tests can be carried out without destroying the structure of the sample, was identified in the 0.03-3.0 %. G' and G'' time sweep profiles (**Figure 3.46**), analytically confirmed the gel state (G' > G'' and tanδ > 1). The storage and loss moduli for FYFCFYF gel were found to be 979 and 71 Pa, respectively. (tanδ=13.6). It means that the Cys-containing peptide is able to produce a matrix ten time more rigid if compared to the PEG_8-(FY)3 precursor (G'~100 Pa). These values, after AmBic oxidation, increase to G' = 3360 Pa and G'' = 273 Pa (tan δ=12.3). A significant improvement of the mechanical rigidity is thus observed after the chemical cross-linking. The capability of disulfide bonds to enlarge the network of interactions, resulting in an accentuated viscoelastic response of the material, was thus demonstrated.

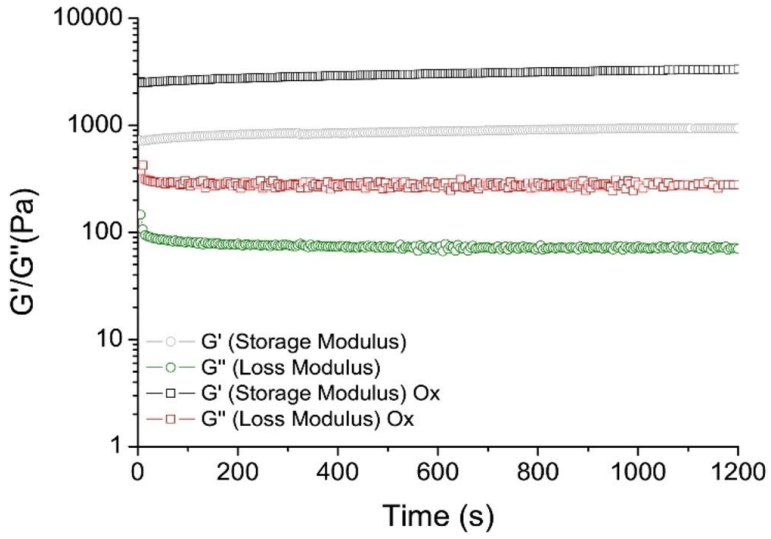

Figure 3.46: Time sweep (20 minutes) for FYFCFYF gel and for FYFCFYF oxidized one. Rheological analysis is reported in terms of G' (Storage modulus) and G'' (Loss modulus).

3.4.13 RGDS-containing lipopeptides: Investigation of secondary structure and CAC evaluation

The four lipopeptides containing the adhesion sequence RGDS (myristyl-GGGRGDS, mG; palmitoyl-GGGRGDS, pG; myristyl-WGGRGDS, mW; palmitoyl-WGGRGDS, pW, **Figure 3.5**) were analyzed from their aggregation capability point of view. Their secondary structure was probed in PBS using CD and FTIR spectroscopic techniques. From the inspection of their CD profiles, it can be deduced that, at lower concentrations, all the peptides present a random coil organization, confirmed by the presence of a minimum at 205 nm. (**Figure 3.47**).

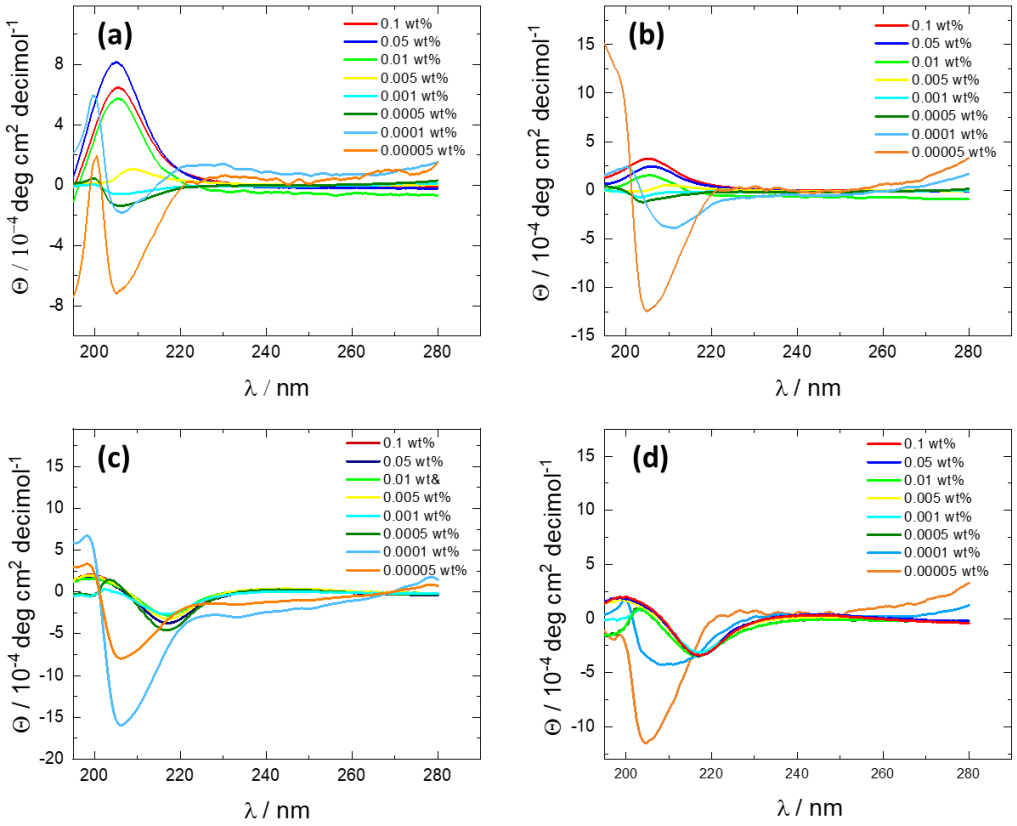

Figure 3.47: CD spectra at the concentrations indicated for (A) mG, (B) pG, (C) mW, (D) pW.

For higher lipopeptide concentrations, mG and pG CD spectra are dominated by a positive band with a maximum centered at 205 nm, while for mW and pW the characteristic signature of β-sheet structures is observed. [171] In details, for Trp-containing sequences a negative band centered at 216 nm and a positive one centered at 203 nm can be detected. PAs nanostructures with a β-sheet organization are typically characterized by CD positive bands at ~200-205 nm and negative ones around 220 nm, associated with $\pi \rightarrow \pi^*$ and $n \rightarrow \pi^*$ transitions, respectively. [172] However, in some cases, the signal centered around 220 nm is only weakly or completely not detectable in non-aromatic PA negative. The lack of this CD band can be ascribed to overlap with the absorption region of other groups such as arginine, as previously observed for RGD containing PAs. [173] Even if mG and pG do not show typical β-sheet CD signature, the presence of β-sheet structures was revealed by FTIR, SAXS and Cryo-TEM analyses. The CAC values were determined from the comparison of different techniques, starting from CD analyses performed ad different PA concentrations by plotting the molar ellipticity of the signal near 205 nm, as a function of the concentration. (**Figure 3.48**) The CACs determined at the break points were found to be ($6.02\times10^{-3} \pm 0.03\times10^{-3}$) wt%, ($6.49\times10^{-3} \pm 0.08 \times10^{-3}$) wt%, ($2.16\times10^{-4} \pm 0.05\times10^{-4}$) wt% and ($1.26\times10^{-4} \pm 0.03\times10^{-4}$) wt%, for mG, pG, mW and pW, respectively. These CAC values were compared, for tryptophan-containing lipopeptides, with the ones obtained from W self-fluorescence measurements. Emission spectra of the two tryptophan-containing peptides were collected at different concentrations after excitation at 280 nm. At higher concentrations, an emission peak at 320 nm is visible, thus indicating that tryptophan is in a hydrophobic environment. [157] By plotting the fluorescence intensity at 320 nm as a function of the concentration (**Figure 3.49**), the CAC values were calculated to be $2.16\times10^{-4} \pm 0.05\times10^{-4}$ wt%

for mW and $3.75\times10^{-4} \pm 0.04\times10^{-4}$ wt% for pW. These data are consistent with those obtained with the CD studies.

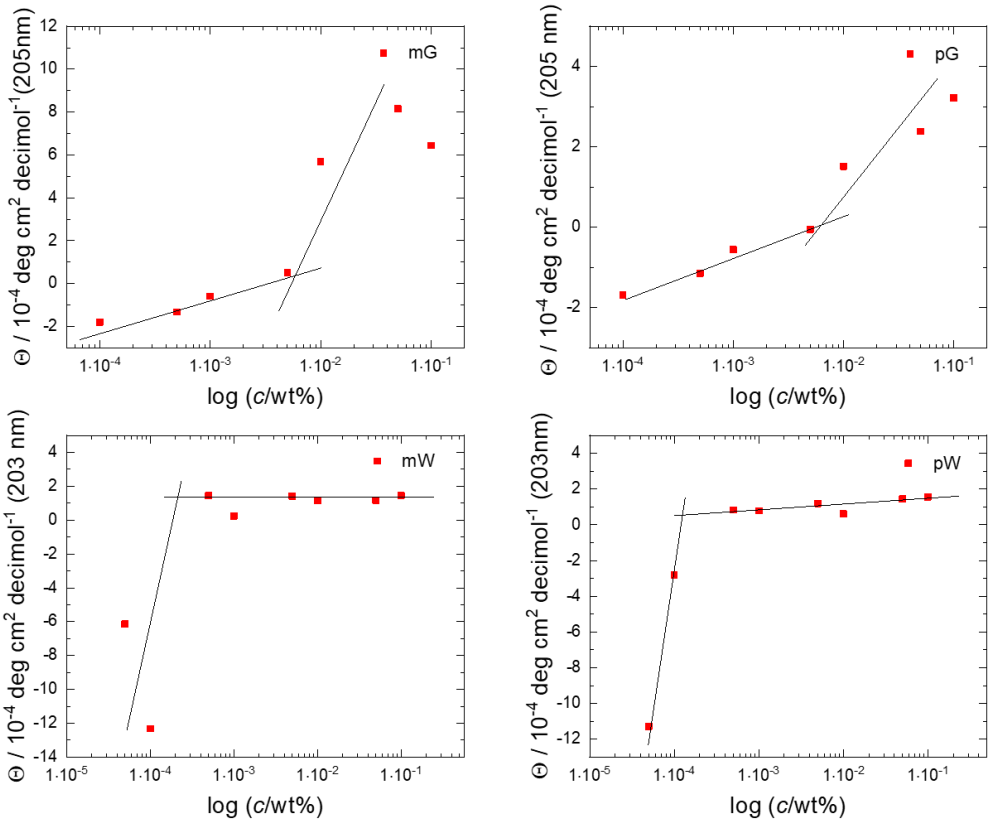

Figure 3.48: Determination of CAC values from concentration-dependent discontinuities in molar ellipticity values (at 205 nm for mG and pG and 203 nm for mW and pW)

For all the peptides, the CAC was also determined by collecting emission spectra of the amyloid-sensitive dye ThT in the presence of increasing amounts of lipopeptide. By plotting the fluorescence intensity at 482 nm as a function of the concentration (**Figure 3.50**), the following CAC values were obtained: $4.59\times10^{-3} \pm 0.05\times10^{-3}$ wt%, $2.87\times10^{-3} \pm 0.04\times10^{-3}$ wt%, $3.10\times10^{-3} \pm 0.07\times10^{-3}$ wt% and $3.55\times10^{-3} \pm 0.08\times10^{-3}$ wt% for mG, pG, mW and pW, respectively.

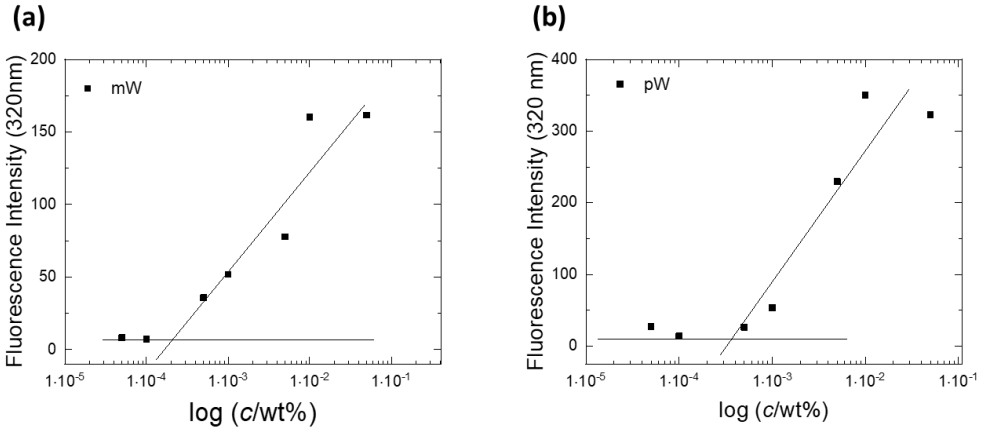

Figure 3.49: Concentration-dependent W fluorescence measurements to determine CAC values (from intersection of straight lines shown). (A) mW, (B) pW.

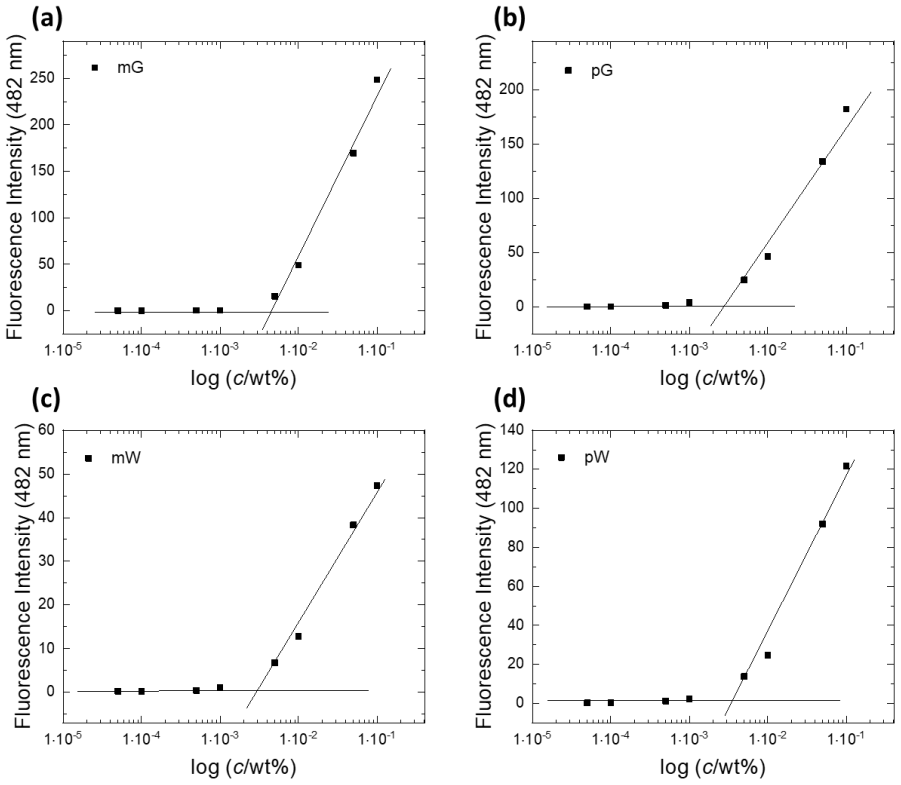

Figure 3.50: Concentration-dependent ThT fluorescence measurements to determine CAC values (from intersection of straight lines shown). (A) mG, (B) pG, (C) mW, (D) pW.

The data obtained by ThT analyses are in good agreement with those found from the CD spectra extrapolation only for mG and pG. On the contrary, for mW and pW, these values were found to be significantly higher (by about an order of magnitude) than those obtained from CD or tryptophan fluorescence studies. This difference may be ascribed to a possible interference occurring between ThT and W fluorescence (e.g., resonance energy transfer). Moreover, tryptophan in its aggregated form can exhibit a weak emission that can partially overlap with the spectral region of ThT-aggregates (450-480 nm). These findings suggest that measurements using ThT fluorescence in the presence of peptides containing tryptophan should be used with caution. CAC values obtained with different methods are summarized and compared in **Table 3.9.**

Table 3.9: CAC values obtained from different techniques.

	CAC / CD (wt%)	CAC / ThT (wt%)	CAC / self-fluorescence (wt%)
mG	$6.02\times10^{-3} \pm 0.03\times10^{-3}$	$4.59\times10^{-3} \pm 0.05\times10^{-3}$	
pG	$6.49\times10^{-3} \pm 0.08\times10^{-3}$	$2.87\times10^{-3} \pm 0.04\times10^{-3}$	
mW	$2.16\times10^{-4} \pm 0.05\times10^{-4}$	$3.10\times10^{-3} \pm 0.07\times10^{-3}$	$2.16\times10^{-4} \pm 0.05\times10^{-4}$
pW	$1.26\times10^{-4} \pm 0.03\times10^{-4}$	$3.55\times10^{-3} \pm 0.08\times10^{-3}$	$3.75\times10^{-4} \pm 0.04\times10^{-4}$

In other to obtain further information on the secondary structure of these lipopeptides, FTIR spectra were measured for 1 wt% mG and pG and 0.5 wt% mW and pW samples. Spectra, reported in **Figure 3.51**, are plotted, as absorbance, in the amide I region. Results suggest that a significant β-sheet structure is present in all the examined samples, as confirmed by the presence of bands at 1631 and 1612 cm^{-1} for mG and pG and 1633 and 1626 cm^{-1} for mW and pW. The peak at 1672 cm^{-1} can be attributed to the TFA counterions bound to cationic arginine residues in the peptide.

[174] Moreover, the band centered at 1651 cm^{-1} suggests that a minor α-helix component is observed for all the peptides, while mG and pG also contain a minor random coil component, which gives rise to the peak at 1644 cm^{-1}.

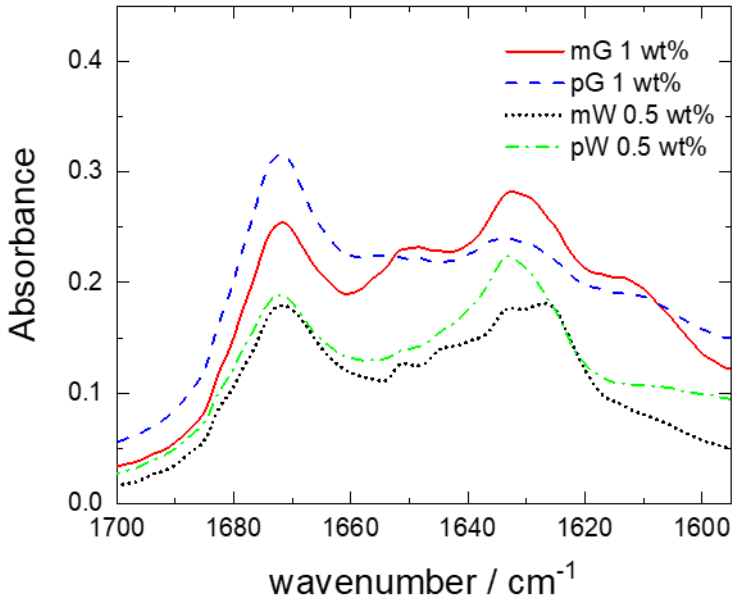

Figure 3.51: FTIR spectra for the four PA at the indicated concentrations.

The self-fluorescence properties of many amyloid-like peptide aggregates rich β-sheets have been widely evidenced. [175] Self-fluorescence of the two myristyl-modified peptides (mW and mG) at a concentration of 0.05 wt% was tested by exciting the sample in a range of wavelengths between 350 and 580 nm. A self-fluorescence phenomenon is visible after excitation between 380 and 400 nm (**Figure 3.52**).

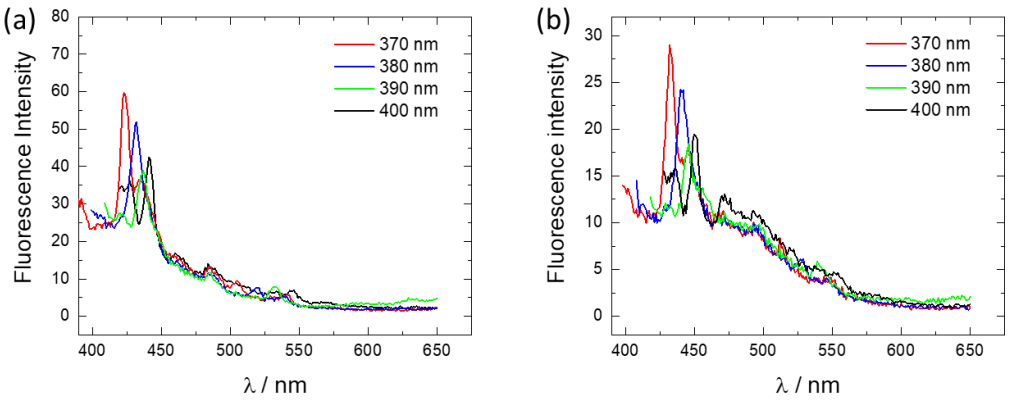

Figure 3.52: Self-fluorescence for (A) mG and (B) mW lipopeptides.

3.4.14 Morphological and gelation evaluation of RGDS-containing lipopeptides

Cryo-TEM images were collected for lipopeptides at a concentration of 0.1 wt% (**Figure 3.53**). From the inspection of images, it is evident that mG forms twisted nanotape structures comprising arrays of individual filaments. A similar organization is also observed for pG, although with a less pronounced filament structure within the nanotapes. However, images collected for the two tryptophan-containing PA point out a different organization. Remarkably, mW forms right-handed twisted helical ribbons coexisting with closed nanotubes (in which the wrapped helical ribbon structure can still be seen within the walls). The mean diameter of the nanotubes is (178 ± 25) nm with a wall thickness less than 10 nm. The fact that helical ribbons coexist with nanotubes allows to understand that the mechanism of nanotube formation occurs *via* closure of helical ribbon structures. This process has been previously reported for several lipopeptide systems, [176,177] and shows that nanotube walls comprise layers of lipopeptide molecules arranged perpendicular to the tube walls.

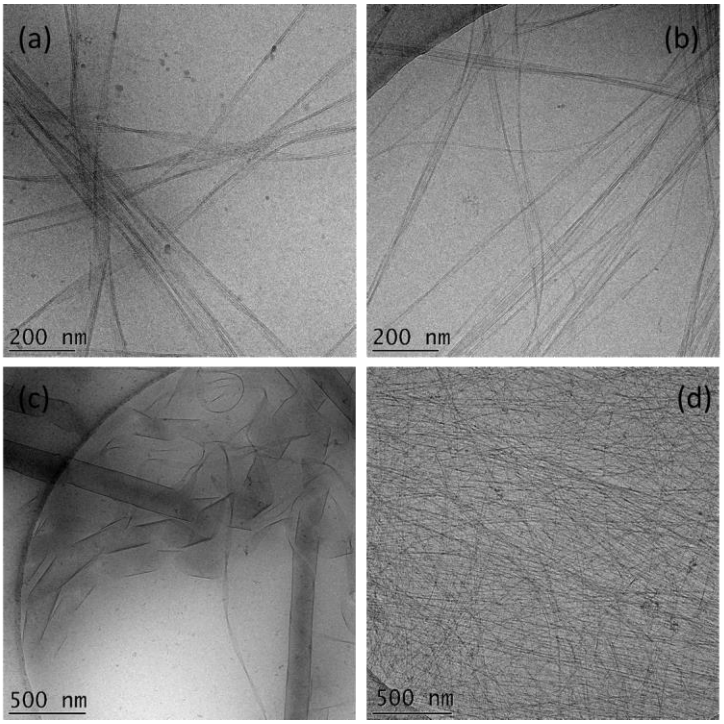

Figure 3.53: Cryo-TEM images from 0.1 wt% solutions (A) mG, (B) pG, (C) mW, (D) pW.

Instead, pW seems to form a dense network of long intertwined thin fibers with a mean diameter of 4.0 nm. Results provide evidence that the presence of the tryptophan in the lipopeptide structure significantly alters the molecular packing.

SAXS measurements were used to provide quantitative information on the shape and dimensions of self-assembled nanostructures *via* analysis of the form factor. [178] Data collected for the four PA are reported in **Figure 3.54**. As suggested from cryo-TEM results, the form factors for mG, pG and pW can be fitted using form factors of nanotapes with an internal bilayer structure (hydrophobic lipid and peptide sub-layers). The fit parameters are listed in **Table 3.10**. The bilayer thickness is in the range 35-46 Å. Since the estimated molecular lengths for myristyl or palmitoyl conjugated heptapeptides are 42 and 44 Å, respectively, highly interdigitated bilayers

and/or regions where residues are not in extended β-sheet conformation are indicated. As revealed by cryo-TEM, mW exhibits unique self-assembly behavior into helical ribbons coexisting with nanotubes. The SAXS form factor data could be fitted using a simple model of nanotubes (*i.e.* a cylindrical shell). The fit parameters in **Table 3.10** indicate a nanotube radius 750 Å, consistent with the cryo-TEM information. The nanotube wall thickness is 64 Å, which means that it comprises a bilayer (of partly interdigitated molecules), this also being consistent with cryo-TEM results.

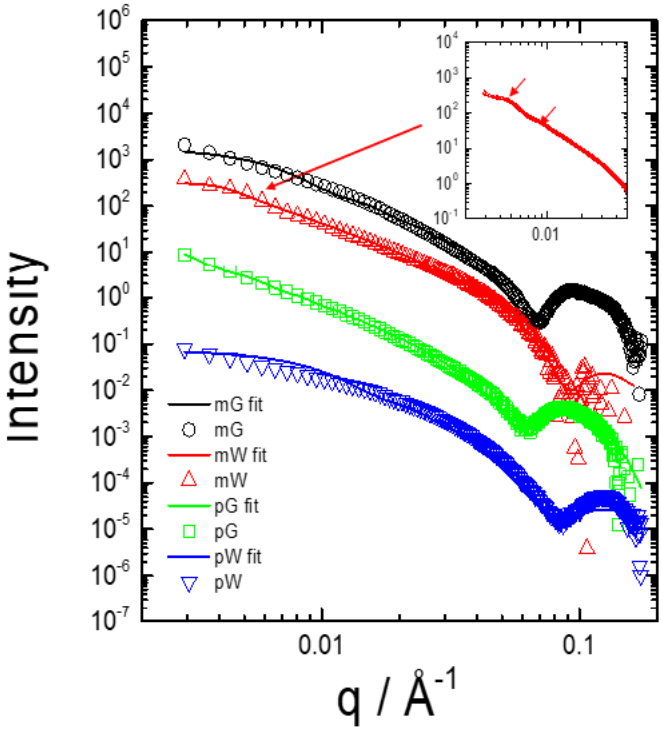

Figure 3.54: SAXS data from solutions (every 5th data point shown, and curves shifted for ease of visualization, along with model form factor fits described in the text. Inset: data for mW at low *q* on expanded intensity scale (and with all data points shown along with form factor fit) to show form factor oscillations resulting from nanotube structure.

Table 3.10: Parameters extracted from the fitting of the SAXS data[a]. All samples were 0.5 wt% aqueous solutions. **Key: Gaussian bilayer:** layer thickness t (Gaussian polydispersity Δt), scattering contrast of outer layers η_{out}, and inner layer η_{in}, Gaussian widths σ_{in} and σ_{out} of inner and outer layers respectively, D diameter (width) of layer system (when $D >> t$ as here, it acts as a scaling parameter for the form factor). Nanotubes: R core radius, ΔR shell thickness, scattering contrasts of core η_{core}, shell η_{shell} and solvent η_{solv}, L length. **Background:** constant background, C.

	mG **0.5 wt%**	**pG** **0.1 wt%**	**mW** **0.1 wt%**	**pW** **0.5 wt%**
$t \pm \Delta t$ [Å]	46.2 ± 5.0	39.0 ± 7.6		35.0 ± 3.0
η_{out}	3.3×10^{-6}	6.0×10^{-7}		3.0×10^{-6}
σ_{out} [Å]	10.6	12.3		10.0 [b]
η_{in}	-1.1×10^{-6}	-4.2×10^{-7}		-5.0×10^{-7}
σ_{in} [Å]	29.4	18.0		10.0[b]
D [Å]	745	2103		500[b]
R [Å]			751 ± 200	
ΔR [Å]			64	
η_{core}			1×10^{-7} [b]	
η_{shell}			2.3×10^{-7}	
η_{solv}			1×10^{-7} [b]	
L			2000[b]	
C	0.001[b]	0[b]	0.01[b]	0.1[b]

[a] Data fitted using Gaussian bilayer for nanotapes (mG, pG and pW) and for nanotubes (mW) using the software SASfit.[2]

[b] Fixed parameter

Two-dimensional SAXS patterns (**Figure 3.55A,B**) show that mW and pW solutions (0.5 wt%) present, at low wavenumber q, strong anisotropy thus

indicating that the samples comprise nematic phases which align under flow (some anisotropy was also observed for the corresponding solution of mG). This feature was also confirmed by the macroscopic birefringence examined for samples placed in glass vials between crossed polarizers (**Figure 3.55C,D**).

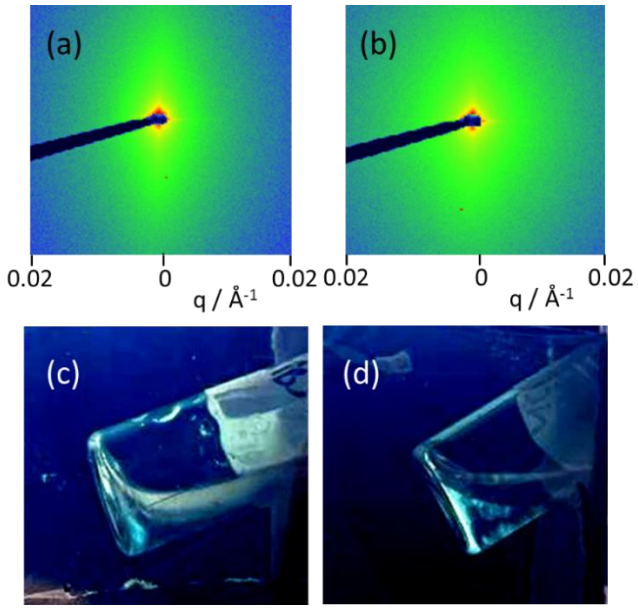

Figure 3.55: Data showing nematic phase formation by mW and pW (0.5 wt% solutions). Spontaneous alignment in SAXS patterns due to flow in capillaries: (A) mW, (B) pW. Images of solutions in vials between crossed polarizers: (C) mW, (D) pW.

The gelation capability of the lipopeptides was tested in PBS at a concentration of 1 wt%. As shown by inverted test tube study, (**Figure 3.56**) after 10 minutes of sonication, only mG and pG were able to form self-supporting hydrogels. This behavior could be explained considering the less hydrophobic nature of the Gly residue compared to Trp. This feature could enable the formation of a more hydrophilic interface within the peptide network, with the capability to retain larger amounts of water. Moreover,

Gly residue has a lower steric hindrance compared to Trp one, thus allowing a better packing of peptide side chains.

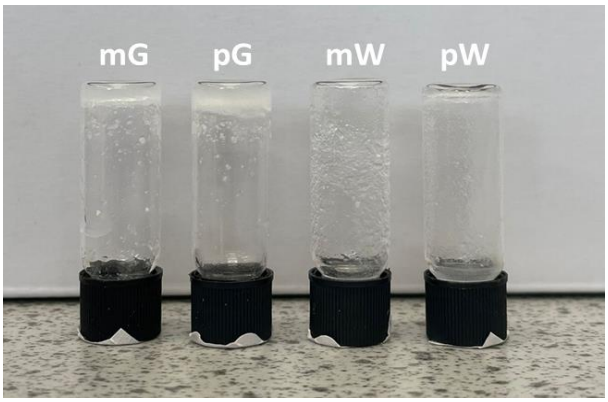

Figure 3.56: Tube inversion test showing hydrogel formation in 1 wt% PBS solutions of mG and pG.

The morphology of the resulting HGs was investigated by Cryo-TEM analyses. Image of mG-based HG, reported in **Figure 3.57**, reveal aligned straight nanotapes that apparently comprise parallel filaments, as previously shown in solution, with a mean thickness of 13.6 nm. Similarly to 0.1 wt% preparations, pG-based HG contains twisted nanotapes.

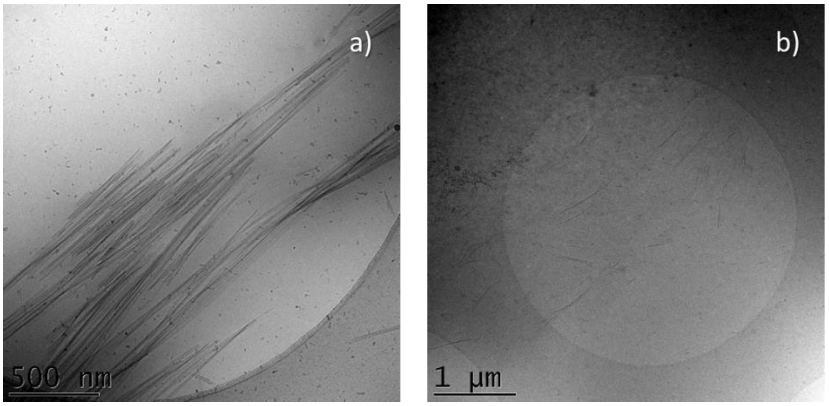

Figure 3.57: Cryo-TEM images for (A) mG and (B) pG hydrogels

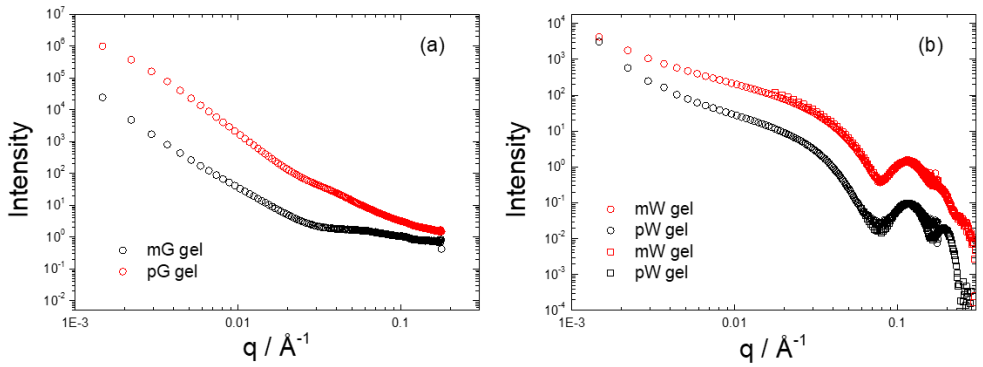

Figure 3.58: SAXS intensity profiles from gelled 1 wt% samples of (A) mG and pG (single *q* range, no background subtraction). (B) mW and pW. Data were measured over two *q* ranges shown with two symbols, profiles were manually overlapped. The data for pW has been scaled down by a factor of 10.

These data are also supported by the SAXS data for hydrogels shown in **Figure 3.58A**, presenting similar form factor profiles to those shown for the solutions.Spontaneously formed 1 wt% hydrogels of mG and pG and 0.5 wt% suspensions of mW and pW were stained with a Congo Red solution and then visualized by optical microscopy (**Figure 3.59**). The characteristic green birefringence was detected for all the samples when placed under cross-polarized light, thus suggesting an amyloid-like organization. CD spectra collected for these HGs were found to show the same signature previously observed for the more concentrated mG and pG suspensions (**Figure 3.60**). By rotating the samples to four different positions, the CD profile was not found to differ (data not shown). This result excludes the presence of artefacts such as contributions from linear dichroism and confirms the homogeneity of the hydrogels.

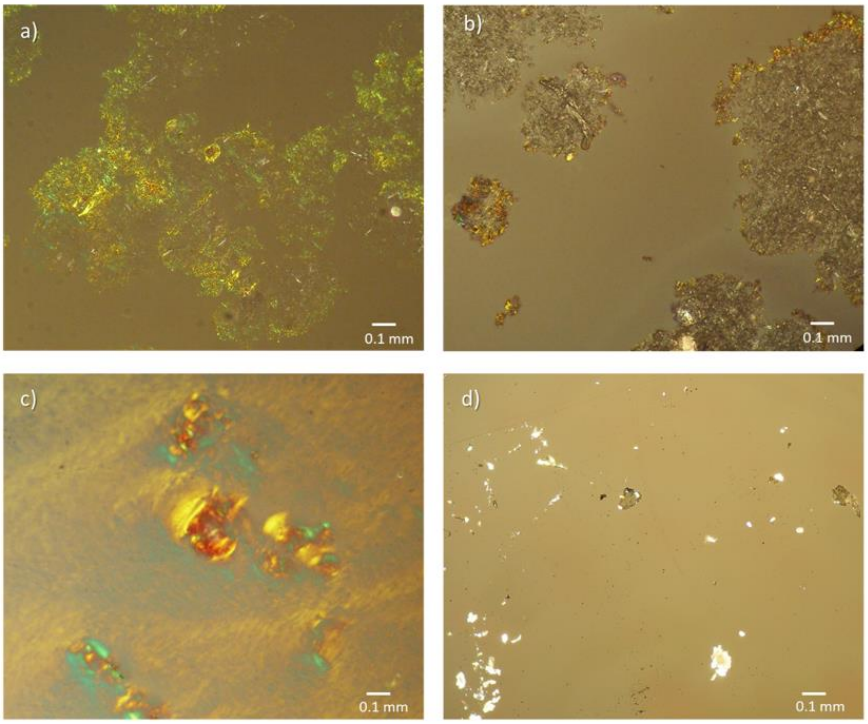

Figure 3.59: Polarized optical microscopy images of 1 wt% samples stained with Congo red, (A) mG, (B) pG, (C) mW, (D) pW.

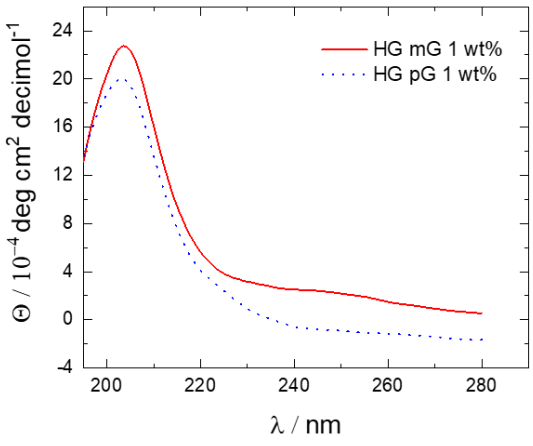

Figure 3.60: CD spectra for mG and pG HGs at 1 wt% concentration.

Moreover, HG formation for all the lipopeptides was observed for 0.5 wt% samples after heat treatment. In details, after heating the PA suspensions at 60 °C and the letting them cool at room temperature overnight, a hydrogelation process occurs, as shown by inverted test tubes in **Figure 3.61**. Only pW formed a really soft and not completely self-supporting matrix. SAXS data for mW and pW HGs at 0.5 wt%, prepared as above described, are shown in **Figure 3.58** and form factors were found to be similar to those previously observed in solutions, thus underling that a network of entangled fibers is present.

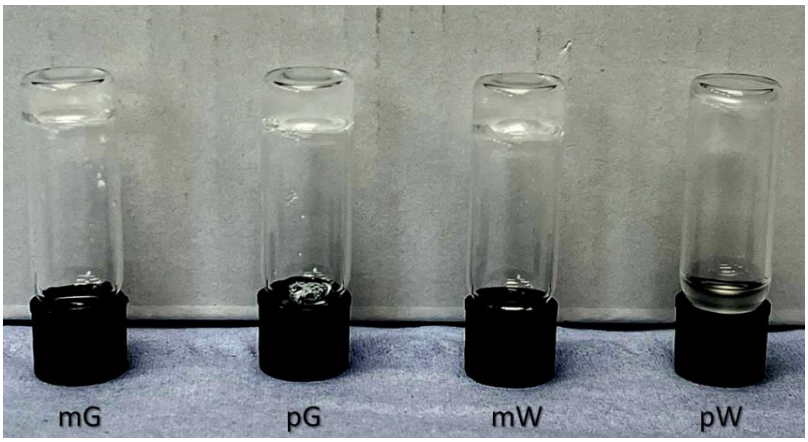

Figure 3.61: Inverted test tubes for hydrogels prepared according to a heating procedure.

FTIR spectra measured for hydrogels formed after heating 0.5 wt% peptide solutions (**Figure 3.62**), reveal that a β-sheet organization is preserved for all the samples, as attested by the peaks at 1632 cm^{-1} for mG, 1629 cm^{-1} for pG, 1632 and 1624 cm^{-1} for mW, 1636 and 1623 cm^{-1} for pW. Peaks at 1651, 1649 and 1652 cm^{-1} reveal a minor α-helix component for mG, mW and pW, respectively. Peaks at 1647, 1643 and 1646 cm^{-1}, observed for pG, mW and pW, show that a minor component of unordered peptide is present. The CD spectra for the heat-treated hydrogels also point out similar features to the higher concentrated suspensions one.

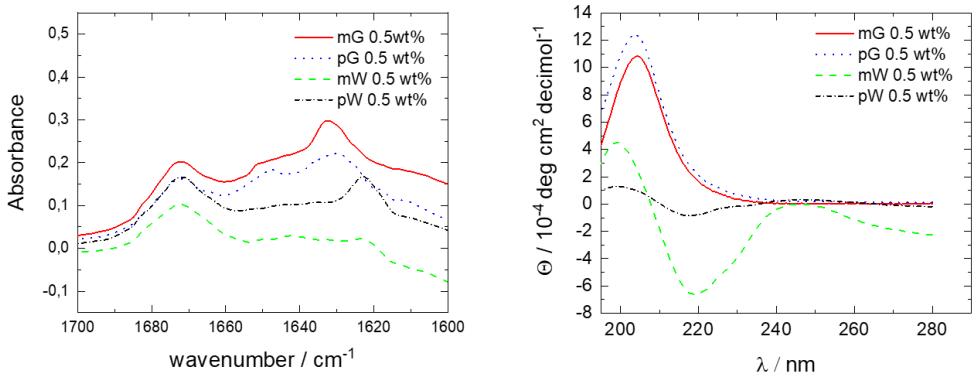

Figure 3.62: FTIR (on the left) and CD (on the right) spectra for 0.5 wt% HGs obtained through the heat protocol.

3.4.15 Cell viability studies for RGDS-containing lipopeptides

The cytotoxicity of PA was evaluated using MTT assays on L929 murine fibroblast and C2C12 immortalized mouse myoblast cell lines. The results obtained after 24 and 72 h cell culture are shown in **Figure 3.63** and **3.64**, respectively. The t-test probability values are presented in **Table 3.11** and **3.12**. After 72h, high cell viability is observed in all plates containing the lipopeptide concentration below the CAC (1×10^{-4} wt%) solutions, with no significant differences depending on the sequences. However, at 0.1 wt% (i.e. above the CAC for all samples) the cell viability is significantly reduced to 30.7± 4.7%, 31.8±5.1%, 28.1±3.1%, 36.3±5.1 % for mG, pG, mW and pW respectively. These results suggest that self-assembled aggregates are not well tolerated, while monomers are. The cytotoxicity after 3 days follows the trend observed after 24 h, even if, reasonably, the relative observed cytotoxicity was lower after 24 h incubation when compared with 72 h incubation. For L929 cells in contact with hydrogels (1 wt%), remarkably no significant cytotoxicity was observed for mG (cell survival of 92.6±8.8

% at 24h and of 94.6±12.6 % at 72 h), but a notable reduction in cell viability for pG was observed. Surprisingly, the cytotoxicity at this concentration is lower for both the peptides than for 0.1 wt% solutions, indicating that hydrogels are more cytocompatible than solutions, even if the lipopeptide content is higher.

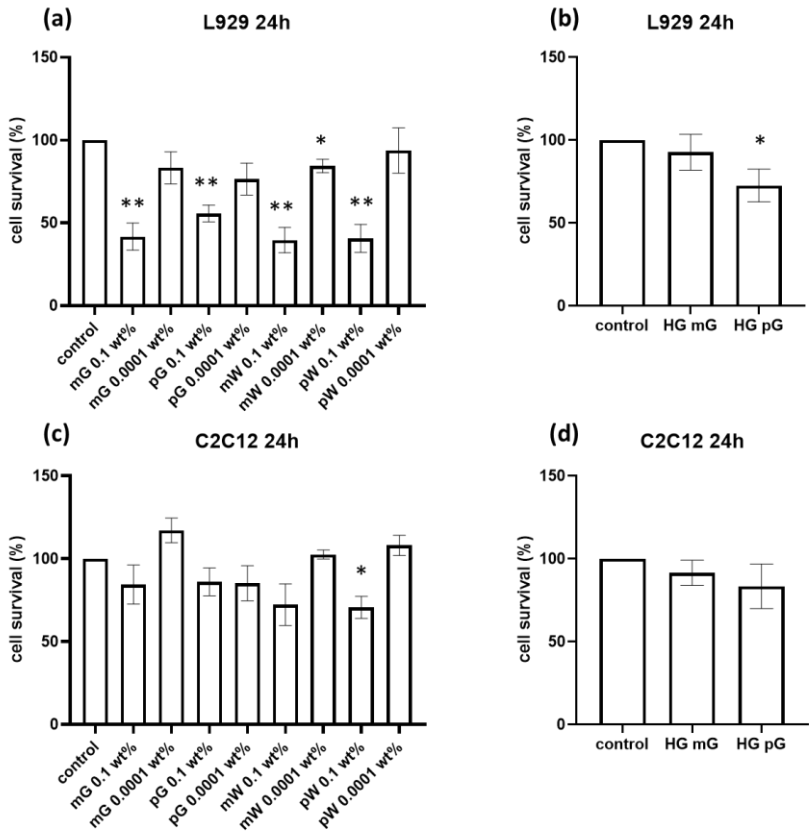

Figure 3.63: Cytotoxicity data from MTT assays obtained after 24 h. (A) L929 cells on solution coated plates, (B) L929 cells on hydrogels, (C) C2C12 cells on solution coated plates, (D) C2C12 cells on hydrogels.

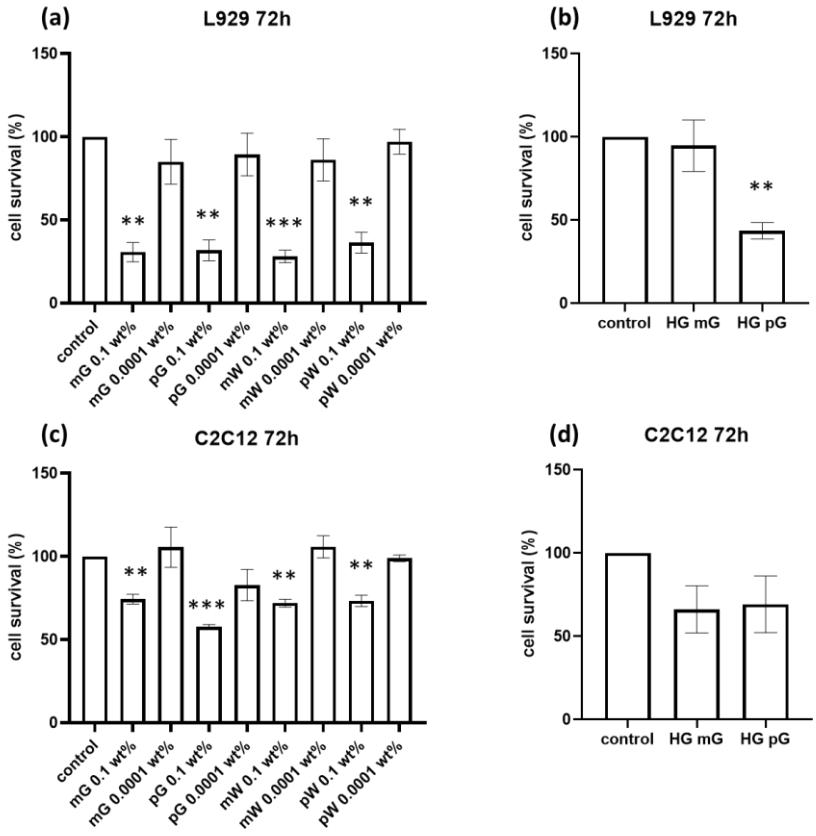

Figure 3.64: Cytotoxicity data from MTT assays obtained after 72 h. (A) L929 cells on solution coated plates, (B) L929 cells on hydrogels, (C) C2C12 cells on solution coated plates, (D) C2C12 cells on hydrogels.

Cell viability measurements with C2C12 myoblasts revealed notable improvements in cytocompatibility at higher peptide concentrations. After 72h, the cell viability was 84.4± 9.6%, 86.0±6.8%, 72.3±10.2 % and 73.3 ±2.8 % for mG, pG, mW and pW, respectively. After 24 h, there is no significant cytotoxicity even for the higher concentration of lipopeptide, with the exception of pW. The solutions prepared with 1×10^{-4} wt% lipopeptide showed minimal cytotoxicity, as for the L929 fibroblasts. Hydrogels were well tolerated by C2C12 cells with no substantial difference between mG

and pG gels, in contrast to the superior cytocompatibility of mG gels with L929 fibroblasts.

Table 3.11: Statistical significance *t*-test p values for L929 and C2C12 cells after 24h and 72h.

T-test	P value / L929 24h	P Value / L929 72h	P Value / C2C12 24h	P Value / C2C12 72h
control vs. mG 0.1 wt%	0.0065	0.0023	0.1490	0.0045
control vs. mG 0.0001 wt%	0.0957	0.1932	0.0588	0.4702
control vs. pG 0.1 wt%	0.0042	0.0027	0.1023	0.0004
control vs. pG 0.0001 wt%	0.0522	0.2845	0.0716	0.0874
control vs. mW 0.1 wt%	0.0054	0.0009	0.0617	0.0024
control vs. mW 0.0001 wt%	0.0216	0.1973	0.2534	0.2741
control vs. pW 0.1 wt%	0.0068	0.0032	0.0167	0.0053
control vs. pW 0.0001 wt%	0.5100	0.5647	0.1497	0.4295

Table 3.12: Statistical significance *t*-test p values for L929 and C2C12 cells on hydrogels after 24 h and 72h

T-test	P Value / L929 24h	P Value / L929 72h	P Value / C2C12 24h	P Value / C2C12 72h
control vs. HG mG	0.3593	0.6118	0.1915	0.0533
control vs. HG pG	0.0406	0.0026	0.1658	0.0881

3.4.16 Structural and morphological characterization of cationic lipopeptides

The self-assembling capability of the C_{19}-K1, C_{19}-K2, C_{19}-K3 and C_{19}-VAGK amphiphilic peptides (**Figure 3.65**), synthesized through classical SPPS methods, was probed in water. The critical aggregation concentration (CAC) was calculated by titration of an ANS solution with increasing amounts of the peptide. Plotting the fluorescence intensity as a function of the peptide concentration (see **Figure 3.66**), the CAC, calculated at the break point, was found to be (5.90 ± 0.07) × 10^{-4} wt%, (1.35 ± 0.01) × 10^{-3} wt%, (9.83 ± 0.08) × 10^{-4} wt% and (2.47 ± 0.04) × 10^{-3} wt%, for C_{19}-VAGK, C_{19}-K1, C_{19}-K2 and C_{19}-K3, respectively.

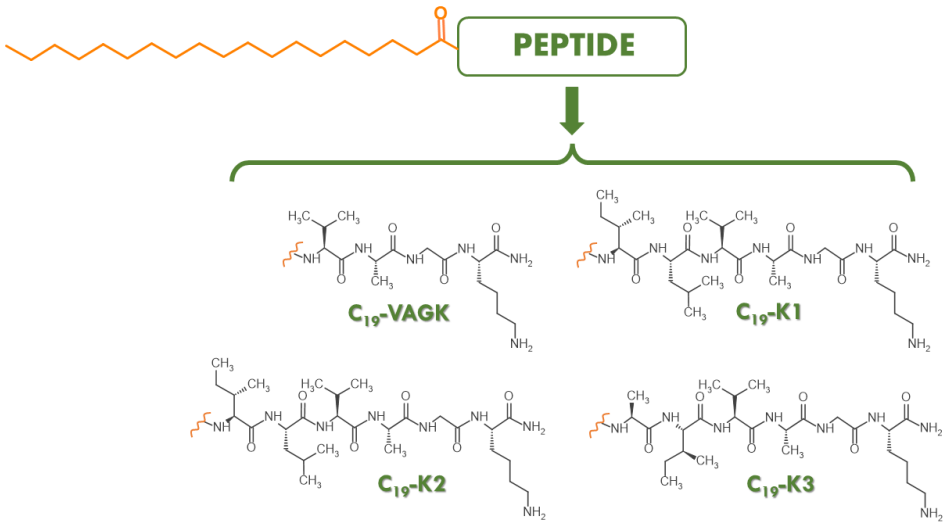

Figure 3.65: Chemical structures of the four cationic lipopeptides

These values are in good agreement with the values expected for peptide amphiphiles containing an alkyl chain at nineteen carbon atoms. These CAC values are low enough to be compatible with their intravenous administration.

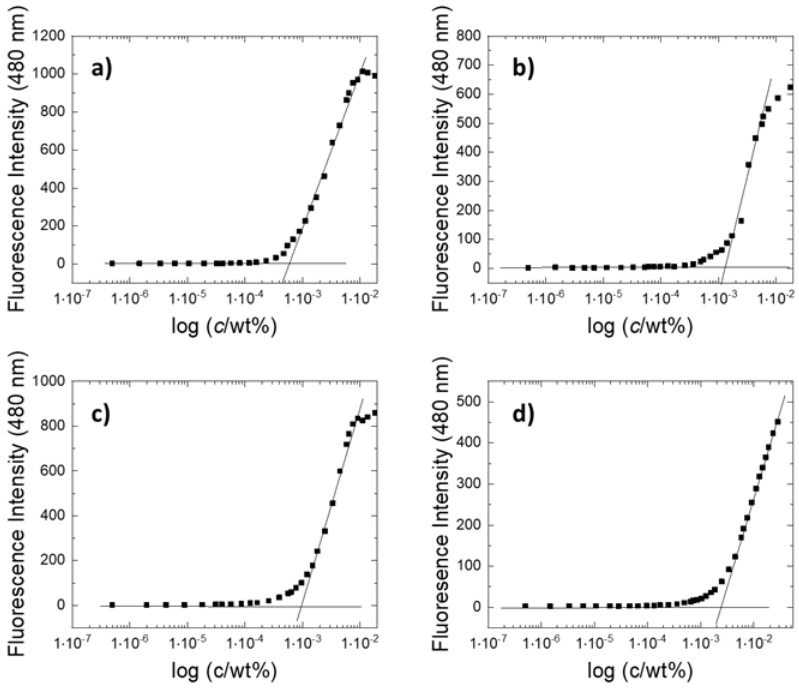

Figure 3.66: ANS titration curves for (A) C_{19}-VAGK, (B) C_{19}-K1, (C) C_{19}-K2 and (D) C_{19}-K3 lipopeptides.

CD measurements were conducted on two different concentrations, one above (0.1 wt%) and one below (5×10^{-5} wt%) the CAC for all the peptide sequences (**Figure 3.67** and **3.68 A-D**). At the concentration of 5×10^{-5} wt%, the CD profile of C_{19}-VAGK, showing positive bands with a maximum at 193 and 205 nm and a negative band with a maximum at 221 nm, indicates a mixture of α-helix like aggregates and a disordered conformation. The same mixture can be supposed to exist for C_{19}-K1 and C_{19}-K3, because of the negative band centered at 205 and 203 nm, respectively. C_{19}-K2, analyzed at the concentration below the CAC, shows a random coil organization, suggested by the presence of a positive band around 222 nm. At the concentration of 0.1 wt%, while C_{19}-K1 and C_{19}-K2 show a β-sheet secondary structuration, the organization seems to be a mixture between β-sheet and α-helix like for C_{19}-VAGK and C_{19}-K3.

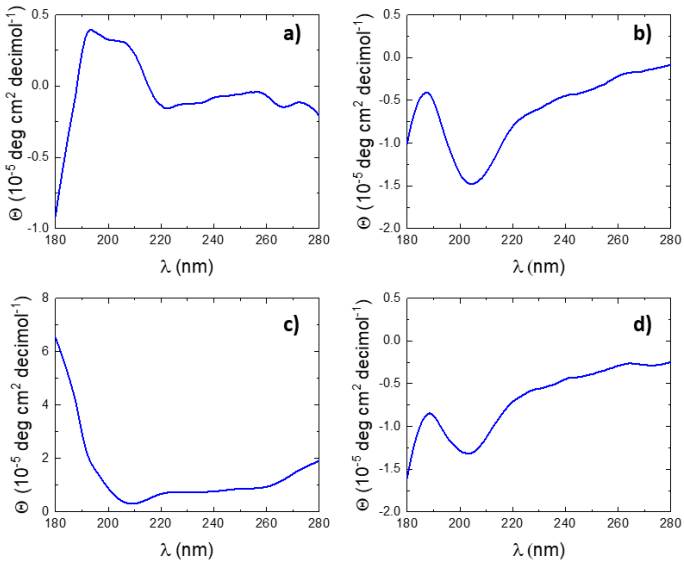

Figure 3.67: CD profiles of (A) C_{19}-VAGK, (B) C_{19}-K1, (C) C_{19}-K2 and (D) C_{19}-K3 at the concentration of 5×10^{-5} wt%.

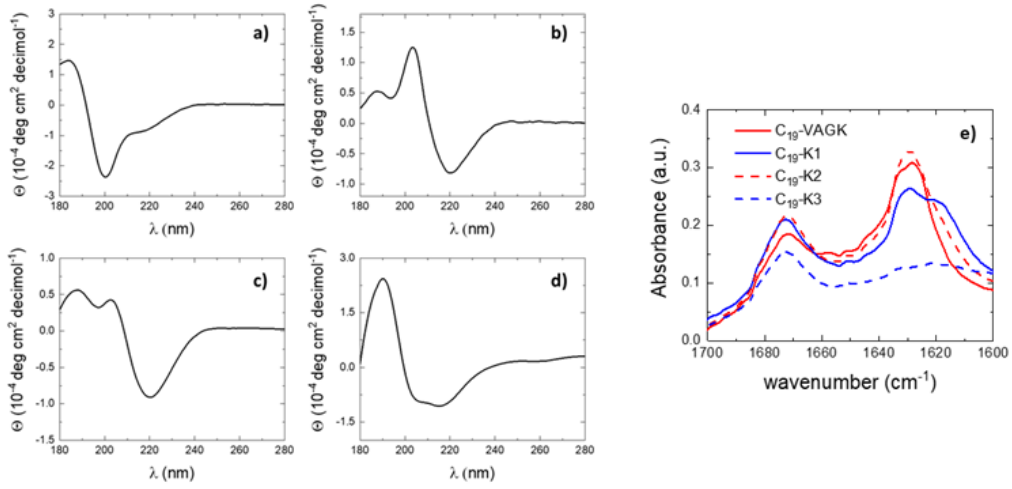

Figure 3.68: Secondary structure characterization. On the left: CD profiles of (A) C_{19}-VAGK, (B) C_{19}-K1, (C) C_{19}-K2 and (D) C_{19}-K3 at the concentration of 0.1 wt%. CD spectra are recorder in the range between 280 and 180 nm. On the right: (E) IR spectra of the four peptide sequences at the concentration of 0.5 wt%.

These assumptions found their basis in the presence, in C_{19}-K1 and C_{19}-K2 CD spectra, of a positive signal centered at 203 nm and a negative one with a maximum at 220 nm. Conversely, the shape of the CD profiles belonging to C_{19}-VAGK and C_{19}-K3, with the positive band around 190 nm (185 nm for C_{19}-VAGK and 190 nm for C_{19}-K3) and the two negative bands around 205 and 215 nm (201 and 218 nm for C_{19}-VAGK; 205 and 216 nm for C_{19}-K3) encouraged the hypothesis of a α-helix like organization, with signals slightly blue-shifted compared to the classical signature of this type of arrangements. However, the two negative bands at 218 and 216 nm are characteristic of a β-sheet secondary structure. An α-helix like structure was also observed for acetylated analogues at a concentration similar to the one explored for the C_{19}-derivatieves (0.07 wt%), while at higher concentrations (0.13 wt%) a β-turn arrangement was allowed. [139] Similarly, Fmoc- and Fmoc-FF hexapeptides were shown to have a β-sheet secondary structuration at the concentration of 0.1 wt%. These behaviors may suggest that the peptide component partially prompt towards an α-helix arrangement, which is still visible in part for some of the amphiphilic sequences, but is mainly avoided by the higher concentration and the substitution of the small acetyl group with more voluminous ones like Fmoc, Fmoc-FF and the nonadecanoic acid. FTIR analyses were performed to confirm data obtained through CD measurements on all the peptides solved in deionized water at the concentration of 0.5 wt%, allowing a good signal intensity. In all the spectra, reported in **Figure 3.68E** as absorbance conversion, the signal at 1672 cm^{-1} indicates the presence of the TFA counterion. For C_{19}-K1 and C_{19}-K2, the intense signal at 1629 cm-1, together with the one at 1620 cm^{-1}, only visible for C_{19}-K1, suggests the preponderance of a β-sheet structuration, even if minor α-helix like and random-coil components are evidenced by the peaks at 1651 and 1643 cm^{-1}, respectively. Supporting what pointed out by CD measurements, FTIR

spectra seem to hint that C_{19}-VAGK and C_{19}-K3 sequences present a α-helix like arrangement evidenced by the peaks at 1651 and 1650 cm^{-1}, respectively, but the main organization is still β-sheet, as proved by the more intense signals at 1632 and 1628 cm^{-1} for C_{19}-VAGK, and at 1633 and 1620 cm^{-1} for C_{19}-K3. Moreover, a minor random-coil component is pointed out for C_{19}-VAGK, since a signal at 1643 cm^{-1} is present. To further investigate the secondary structure of PAs in water solution we carried out the Congo Red (CR) assay. The colorimetric change from light to dark red after incubation with peptides rich in β-sheet structures is also detectable by UV-Vis spectroscopy with a red-shift of the CR absorbance peak from 490 to 540 nm. From the inspection of **Figure 3.69**, it can be concluded that all the PAs, except for C_{19}-K3, assume a β-sheet conformation at the concentration of 0.1%wt. This result agrees with the FTIR study at the same concentration.

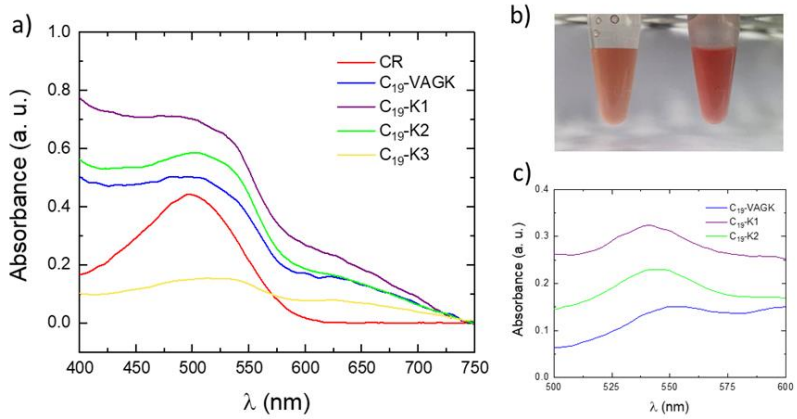

Figure 3.69: CR assay: (A) Absorbance spectra of CR alone or coincubated with peptide solutions. (B) Macroscopical appearance of the analysed peptide solution alone or incubated with CR. (C) UV-Vis spectra reported after the subtraction of the spectrum of the CR alone.

Further structural information on PA aggregates were obtained by cryogenic transmission electron microscopy (Cryo-TEM) technique. Selected cryo-TEM images, reported in **Figure 3.70**, show that C_{19}-VAGK, C_{19}-K1 and C_{19}-K2 at the concentration of 0.1 wt% present a fibrillar network, in which the mean fiber diameter is 6.07, 5.74 and 7.32 nm, respectively. On the contrary, C_{19}-K3 does not form fibers, but really small clusters.

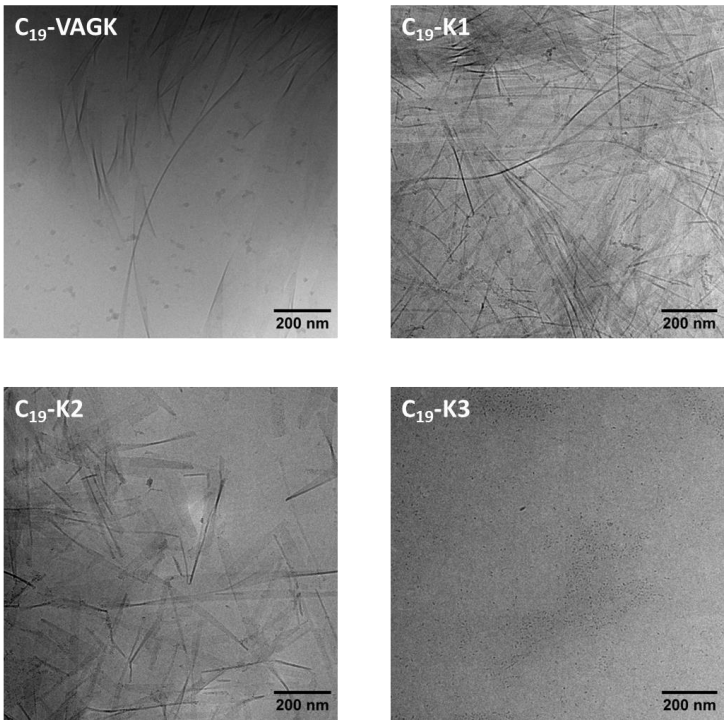

Figure 3.70: Cryo-TEM micrographs for the four peptide sequences at the concentration of 0.1 wt%.

Cryo-TEM imaging was complemented with in situ SAXS measurements for aqueous solutions. The data along with model fits to the form factor of extended nanotape fibrils with a bilayer packing of the molecules are shown in **Figure 3.71**.

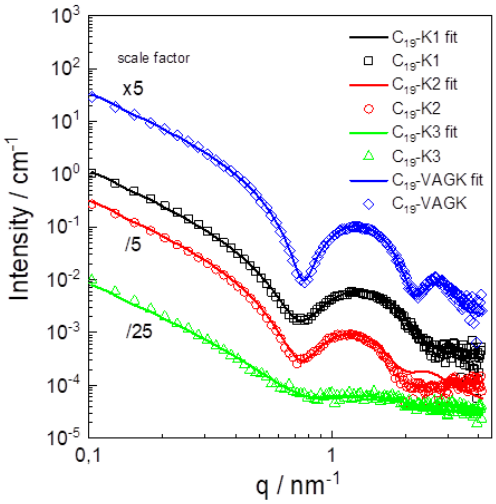

Figure 3.71: SAXS data - measured along with form factor fits (solid lines) discussed in the text with fit parameters listed in **Table 3.13**. Some data sets are scaled by the factors indicated for ease of visualization.

Table 3.13: Parameters extracted from the fitting of the SAXS dataa. All samples were 0.1 wt% aqueous solutions.

	C_{19}-VAGK	**C_{19}-K1**	**C_{19}-K2**	**C_{19}-K3**
$t \pm \Delta t$ [nm]	4.23 ± 0.33	3.73 ± 0.63	4.60 ± 0.75	2.78 ± 1.00
η_{out} [cm^{-1}]	5.0×10^{-4}	2.6×10^{-4}	5.0×10^{-4}	1.3×10^{-4}
σ_{out} [nm]	0.45	0.45	0.19	0.45
η_{in} [cm^{-1}]	4.11×10^{-5}	-8.6×10^{-5}	3.2×10^{-5}	-5.7×10^{-5}
σ_{in} [nm]	0.45	0.45	1.21	0.55
D[b] [nm]	100	100	100	100
C	4.1×10^{-4}	3.0×10^{-4}	$1.\times10^{-4}$	4.0×10^{-4}

[a] Data fitted using form factor of a Gaussian bilayer (all DA series samples) using the software SASfit.

[b] Fixed parameter

Key: Gaussian bilayer: layer thickness t (Gaussian polydispersity Δt), scattering contrast of outer layers η_{out}, and inner layer η_{in}, Gaussian widths σ_{in} and σ_{out} of inner and outer layers respectively, D diameter (width) of layer system. **Background:** constant background, C.

The bilayer packing is consistent with the packing of the C_{19} lipid chains in the hydrophobic interior, with the hydrophilic peptides on the exterior of the layers. The fitting parameters in **Table 3.13** indicate bilayer thicknesses *(t)* in the range 2.8 – 4.6 nm. The estimated molecular lengths are 4.1 nm for C_{19}-K1, C_{19}-K2 and C_{19}-K3 and 3.4 nm for C_{19}-VAGK. Therefore, the values of *t* indicate substantial interdigitation of the molecules within the bilayers in the extended b-sheet fibril structures.

3.4.17 Cell viability studies for cationic lipopeptides

The cytotoxicity of the four lipopeptides was assessed with the HaCat aneuploid immortal keratinocytes cell line. Results, in terms of cell viability (%) after 72h, are reported in **Figure 3.72** and t-test probability values are collected in **Table 3.14.**

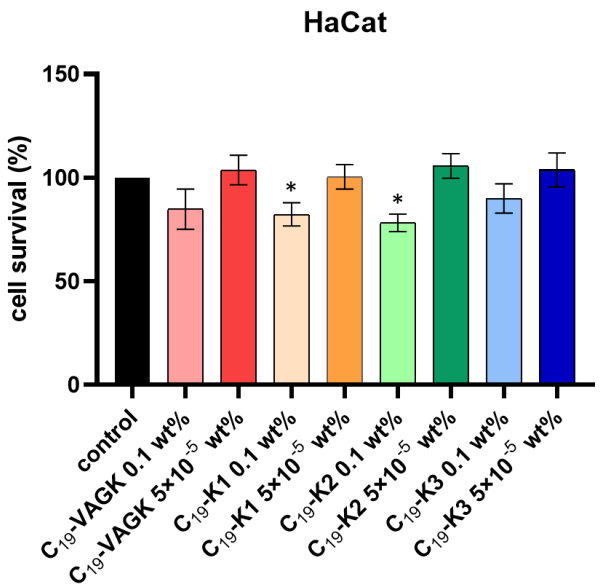

Figure 3.72: Cytotoxicity data from MTT assays obtained after 72 h.

A high cytocompatibility is observed when cells are treated with peptide solutions at concentrations below the CAC (5×10^{-5} wt%). The percentage of cell viability is even slightly higher than the control (103.7±5.8 %, 100.4±4.9%, 105.6±4.8% and 103.8±6.7% for C_{19}-VAGK, C_{19}-K1, C_{19}-K2 and C_{19}-K3, respectively) with no significant differences from sample to sample. For more concentrated solutions (0.1 wt%, higher than the CAC), a reduction in HaCat survival percentage is observed for all the tested lipopeptides. However, since the cell viability is around 80% for all the samples (84.8±7.9 %, 82.3±4.5%, 78.2±3.5% and 90.0±5.8% for C_{19}-VAGK, C_{19}-K1, C_{19}-K2 and C_{19}-K3, respectively), it can be concluded that even the aggregates can be considered biocompatible on the tested cell line after 72h of incubation.

Table 3.11: Statistical significance t-test p values for HaCat cells after 72h.

T-test	P value
Control vs. C_{19}-VAGK 0.1 wt%	0.1139
Control vs. C_{19}-VAGK 5×10^{-5} wt%	0.4599
Control vs. C_{19}-K1 0.1 wt%	0.0316
Control vs. C_{19}-K1 5×10^{-5} wt%	0.9084
Control vs. C_{19}-K2 0.1 wt%	0.0125
Control vs. C_{19}-K2 5×10^{-5} wt%	0.2403
Control vs. C_{19}-K3 0.1 wt%	0.1358
Control vs. C_{19}-K3 5×10^{-5} wt%	0.5097

3.4.18 Hydrogelation test, structural and rheological characterization

We investigated the potential ability of the four PAs to gel at 2 wt% upon addition of PBS. As clearly indicated by the inverted test tube in **Figure 3.73A**, hydrogels are not formed. However, after 24 hours at room temperature the formation of a self-supporting hydrogel for C_{19}-VAGK can be observed when the concentration is increased up to 5 wt% (**Figure 3.73B**). No syneresis phenomena were detected after a week, indicating that water is well confined in the supramolecular architecture. On the contrary, no gel was observed for the longer K1, K2 and K3 variants (**Figure 3.73B**). The capability of tetrapeptide PA respect to the hexapeptides PAs can be justified by its slightly major tendency to self-aggregate, also testified by its lower CAC value. Fluorescence images collected on air-dried C_{19}-VAGK xerogel, stained with Thioflavin T (ThT), show the typical emission in the green spectral region (**Figure 3.73C**), thus indicating the presence of β-sheet structures. Moreover, FTIR measurement carried out on C_{19}-VAGK based hydrogel confirmed the structural organization previously found for the sample in solution, thus indicating that the peptide secondary structure is kept upon increase of the concentration from 0.5 to 5 wt% (**Figure 3.73D**). To further confirm the gel state for the C_{19}-VAGK solution, a rheological study was performed. A time sweep measurement (1000 s, frequency ν=1.0 Hz and 0.1 % strain, **Figure 3.73E**) was performed on a self-supporting sample (5.0 wt%), reporting data in terms of G' (storage modulus) and G''(loss modulus). A tanδ (G'/G'') value higher than 1 indicates the formation of a hydrogel matrix. C_{19}-VAGK gel possesses values of G'=104 Pa and G''=21, respectively, indicating soft mechanical properties, thus comparable with other peptide-based hydrogels.

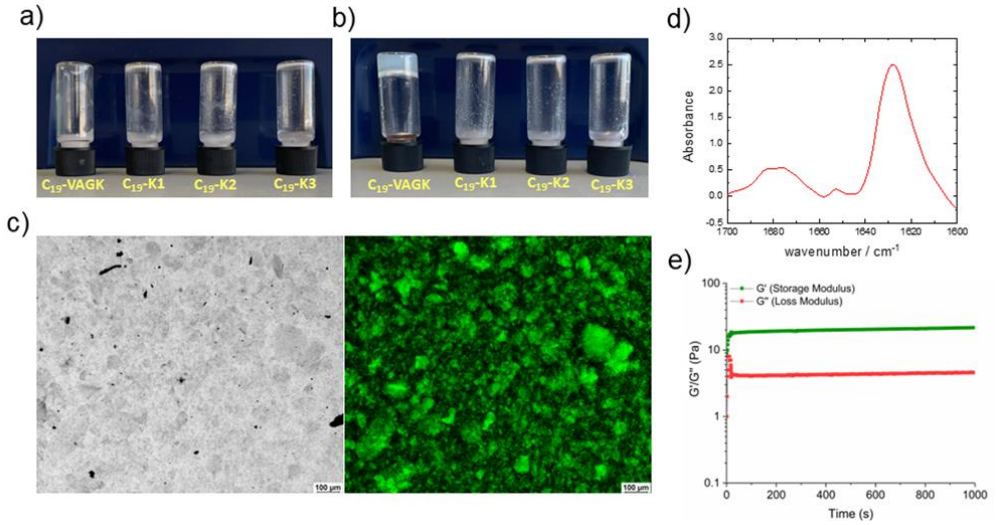

Figure 3.73: C_{19}-VAGK gel characterization: Inverted test tube at 2 wt% (A) and 5 wt% (B). (C) ThT assays: fluorescence and optical images of C_{19}-VAGK drop-casted on glass slide, air-dried and stained with the ThT solution. Sample is imaged in the bright field and in the spectral regions of the GFP (Green Fluorescent Protein, λ_{exc} = 488 nm, λ_{em} = 507 nm). Scale bar = 50 μm. (D) FTIR spectrum (Amide I region) of the C_{19}-VAGK gel at 5%wt. (E) Rheological analysis of peptide: time sweep showing the hydrogel storage modulus (G') and loss modulus (G'').

[115] Berthiaume, F.; Maguire T. J.; Yarmush, M. L. *Annu. Rev. Chem. Biomol. Eng.* **2011**, 2, 403–430.

[116] Laurencin, C. T.; Khan, Y. *Sci. Transl. Med.* **2012**, 4(160), 160ed9.

[117] Langer, R.; Vacanti, J. P. *Science* **1993**, 260(5110), 920–926.

[118] Shevchenko, R. V.; James, S. L.; James, S. E. *J R Soc Interface.* **2010**, 7(43), 229-258.

[119] Chung, C.; Burdick, J. A. *Adv Drug Deliv Rev.* **2008**, 60(2), 243-62.

[120] Gu, X.; Ding, F.; Yang, Y.; Liu, J. *Progress in Neurobiology* **2011**, 93(2), 204-230.

[121] Baguneid, M. S.; Seifalian, A. M.; Salacinski, H. J.; Murray, D.; Hamilton, G.; Walker, M. G. *British Journal of Surgery* **2006**, 93 (3), 282-290.

[122] Heydari, Z.; Najimi, M.; Mirzaei, H.; Shpichka, A.; Ruoss, M.; Farzaneh, Z.; Montazeri, L.; Piryaei, A.; Timashev, P.; Gramignoli, R.; Nussler, A.; Baharvand, H.; Vosough, M. *Cells* **2020**, 9(2), 304.

[123] Amini, A. R.; Laurencin, C. T.; Nukavarapu, S. P. *Crit Rev Biomed Eng.* **2012**, 40(5), 363-408.

[124] Nguyen, A.H.; Marsh, P.; Schmiess-Heine, L.; Burke, P. J.; Lee, A.; Lee, J.; Cao, H. *J Biol Eng* **2019**, 13, 57.

[125] Arshad, M. S.; Javed, M.; Sohaib, M.; Saeed, F.; Imran, A.; Amjad, Z. *Cogent Food & Agriculture* **2017**, 3, 1320814.

[126] Chan, B.P; Leong K. W. *Eur Spine J.* **2008**, 17 (Suppl 4), 467–479.

[127] Gentile, P.; Valeria Chiono, V.; Carmagnola, I.; Hatton, P. V. *Int. J. Mol. Sci.* **2014**, 15(3), 3640-3659.

[128] Liu, S.; Qin, S.; He, M.; Zhou, D.; Qin, Q.; Wange, H. *Composites Part B: Engineering* **2020**, 199, 108238.

[129] Boland, E. D.; Wnek, G. E.; David G.; Simpson, D. G.; Pawlowski, K. J.; Bowlin, G. L. J. Macromol. Sci. A **2001**, 38(12), 1231-1243.

[130] Ding, X.; Zhao, H.; Li, Y.; Lee, A. L.; Li, Z.; Fu, M.; Li, C.; Yang, Y. Y.; Yuan, P. *Adv. Drug Deliv. Rev.* **2020**, 160, 78-104.

[131] Chen, F.; Le, P.; Fernandes-Cunha, G.M.; Heilshorn, S. C.; Myung, D. *Biomaterials* **2020**, 255, 120176.

[132] Wang, J.; Chu, R.; Ni, N.; Nan, G. *Sci. Rep.* **2020**, 10, 2576.

[133] Liu, S. Q.; Tian, Q.; Wang, L.; Hedrick, J. L.; Hui, J. H. P.; Yang, Y. Y.; Ee, P. L. R. *Rapid Commun.* **2010**, 31, 1148-1154.

[134] Diaferia, C.; Netti, F.; Ghosh, M.; Sibillano, T.; Giannini, C.; Morelli, G.; Adler-Abramovich, L.; Accardo, A. *Soft Matter.* **2020**, 16(30), 7006-7017.

[135] Yan, C.; Altunbas, A.; Yucel, T.; Nagarkar, R.P.; Schneider, J. P.; Pochan, D. J. *Soft Matter.* **2010**, 6, 5143-5156.

[136] Liu, Y.; Xu, K.; Chang, Q.; Darabi, M. A.; Lin, B.; Zhong W.; Xing, M. *Adv. Mater.* **2016**, 28, 7758–7767.

[137] Jun, S.; Hong, Y.; Imamura, H.; Ha, B. Y.; Bechhoefer, J.; Chen, P. *Biophys J.* **2004,** 87(2),1249-1259.

[138] Hidenori, Y.; K. Takatoshi, K.; Shuguang, Z. *Proc. Natl. Acad. Sci. USA.* **2005**, 102(24), 8414-8419.

[139] Loo, Y.; Lakshmanan, A.; Ni, M.; Toh, L. L.; Wang, S.; Hauser, C. A. E. *Nano Lett.* **2015**, 15, 6919–6925.

[140] Halperin-Sternfeld, M.; Ghosh, M.; Sevostianov, R.; Grigoriants, I.; Adler-Abramovich, L. *Chem. Commun.* **2017**, 53, 9586-9589.

[141] Netti, F.; Aviv, M.; Dan, Y.; Rudnick-Glick, S.; Halperin-Sternfeld, M.; Adler-Abramovich, L. *Nanoscale* **2022**, 14, 8525-8533.

[142] Shim, J.; Kang, J.; Yun, S. I. *Int. J. Biol. Macromol.* **2021**, 187, 399-408.

[143] Son, G.; Kim, J.; Park, C. B. *ACS Appl. Energy Mater.* **2020**, 3(1), 1215-1221.

[144] Hassan, H.; Martin, A. D.; Thordarson, P. *J. Mater. Chem. B* **2015**, 3, 9269-9276.

[145] Chakraborty, P.; Guterman, T.; Adadi, N.; Yadid, M.; Brosh, T.; Adler-Abramovich, L.; Dvir, T.; Gazit, E. *ACS Nano* **2019**, 13(1), 163-175.

[146] Diaferia, C.; Sibillano, T.; Balasco, N.; Giannini, C.; Roviello, V.; Vitagliano, L.; Morelli, G.; Accardo, A. *Chem. Eur. J.* **2016**, 22(46), 16586-16597.

[147] Rickhoff, J.; Cornelissen, N. V.; Beuse, T.; Rentmeister, A.; Ravoo, B. *J. Chem. Commun.* **2021**, 57, 5913-5916.

[148] Cui, H. G.; Webber, M. J.; Stupp, S. I. *Biopolymers* **2010**, 94(1), 1-18.

[149] Sewald, N.; Jakubke, H.-D. Peptides: Chemistry and Biology. *Wiley-VCH: Weinheim* **2002**.

[150] Lorusso, M.; Pepe, A.; Ibris, N.; Bochicchio, B. *Soft Matter*. **2011**, 7, 6327-6336.

[151] Ruoslahti, E. *Annu. Rev. Cell Dev. Biol.* **1996**, 12, 697-715.

[152] Lutolf, M. P.; Hubbell, J. A. *Nature Biotech.* **2005**, 23(1), 47-55.

[153] Temming, K.; Schiffelers, R. M.; Molema, G.; Kok, R. J. *Drug Resistance Updates* **2005**, 8(6), 381-402.

[154] Samanen, J.; Ali, F.; Romoff, T.; Calvo, R.; Sorenson, E.; Vasko, J.; Storer, B.; Berry, D.; Bennett, D.; Strohsacker, M.; Powers, D.; Stadel, J.; Nichols, A. *J. Med. Chem.* **1991**, 34(10), 3114-3125.

[155] Pierschbacher, M. D.; Ruoslahti, E. *Nature* **1984**, 309, 30-33.

[156] Bertini, I.; Fragai, M.; Luchinat, C.; Parigi, G. *Magn. Reson. Chem.* **2000**, 38, 543-550.

[157] Lakowicz, J.R. (Ed.) Principles of Fluorescence Spectroscopy, 3rd ed.; *Springer: Boston, MA, USA* **2006.**

[158] Mohan Reddy, S.M.; Shanmugam, G.; Duraipandy, N.; Kiran, M.S.; Mandal, A.S. *Soft Matter.* **2015**, 11, 8126–8140.

[159] Sunde, M.; Serpell, L. C.; Bartlam, M.; Fraser, P. E.; Pepys, M. B.; Blake, C. C. F. *J. Mol. Biol.* **1997**, 273, 729.

[160] Giraud, T.; Bouguet-Bonnet, S.; Marchal, P.; Pickaert, G.; Averlant-Petit, M. C.; Stefan, L. *Nanoscale* **2020**, 12, 19905.

[161] Kimmich, R.; Fatkullin, N. Advances in Polymer Science, Vol. 170, *Springer, Berlin, Heidelberg* **2004**.

[162] Collins, C.; Denisin, A.K.; Pruitt, B.L.; Nelson, W.J. *Proc. Natl. Acad. Sci. USA* **2017**, 114, E5835–E5844.

[163] Fientes-Caparros, A. M.; McAulay, K.; Rogers, S. E.; Dalgliesh, M. R.; Adams, D. J. *Molecules* **2019**, 24, 3855.

[164] Di Carlo, M. G.; Minicozzi, V.; Foderà, V.; Militello, V.; Vetri, V.; Morante, S.; Leone, M. *Biophys. Chem.* **2015**, 206, 1-11.

[165] Orsi, S.; Guarnieri, D.; Netti, P.A. *J. Mat. Sci. Mater. Med.* **2010**, 21, 1013–1020.

[166] Jayawarna, V.; Ali, M.; Jowitt, T.; Miller, A. F.; Saiani, A.; Gough, J. E.; Ulijn, R. V. *Adv. Mater.* **2006**, 18, 611–614.

[167] Krittanai, C.; Johnson, W. C. *Anal. Biochem.* **1997**, 253, 57-64.

[168] Calce, E.; Sandomenico, A.; Saviano, M.; Ruvo, M.; De Luca, S. *Amino Acids* **2014**, 46, 1197– 1206.

[169] Bulaj, G.; Kortemme, T.; Goldenberg, D. P. *Biochemistry* **1998**, 37, 8965-8972.

[170] Nair, S. K.; Basu, S.; Sen, B.; Lin, M. H.; Kumar, A. N.; Yuan, Y.; Cullen, P. J.; Sarkar, D. *Sci. Rep.* **2019**, 9, 1072.

[171] Woody, R. W. Circular dichroism of peptides and proteins. In Circular Dichroism. Principles and Applications, Nakanishi, K.; Berova, N.; Woody, R. W. *Eds. VCH: New York* **1994**.

[172] Xing, H. H.; Chin, S. M.; Udumula, V. R.; Krishnaiah, M.; Rodrigues de Almeida, N. R.; Huck-Iriart, C.; Picco, A. S.; Lee, S. R.; Zaldivar, G.; Jackson, K. A.; Tagliazucchi, M.; Stupp, S. I.; CondaSheridan, M. *Biomacromolecules* **2021**, 22, 3274-3283.

[173] Castelletto, V.; Gouveia, R. J.; Connon, C. J.; Hamley, I. W. *Faraday Discuss.* **2013**, 166, 381–397.

[174] Eker, F.; Griebenow, K.; Schweitzer-Stenner, R. *Biochem*. **2004**, 43, 6893–6898.

[175] Del Mercato, L. L.; Pompa, P. P.; Maruccio, G.; Della Torre, A.; Sabella, S.; Tamburro, A. M.; Cingolani, R.; Rinaldi, R. *Sci USA* **2007**, 104(46), 18019-18024

[176] Hamley, I. W.; Dehsorkhi, A.; Castelletto, V. *Chem. Comm.* **2013**, 49, 1850-1852.

[177] McCourt, J. M.; Kewalramani, S.; Gao, C.; Roth, E. W.; Weigand, S. J.; Olvera de la Cruz, M.; Bedzyk, M. J. *ACS Central Sci.* **2022**, 8(8), 1169–1181.

[178] Hamley, I. W. Small-Angle Scattering: Theory, Instrumentation, Data and Applications. *Wiley: Chichester* **2021**.

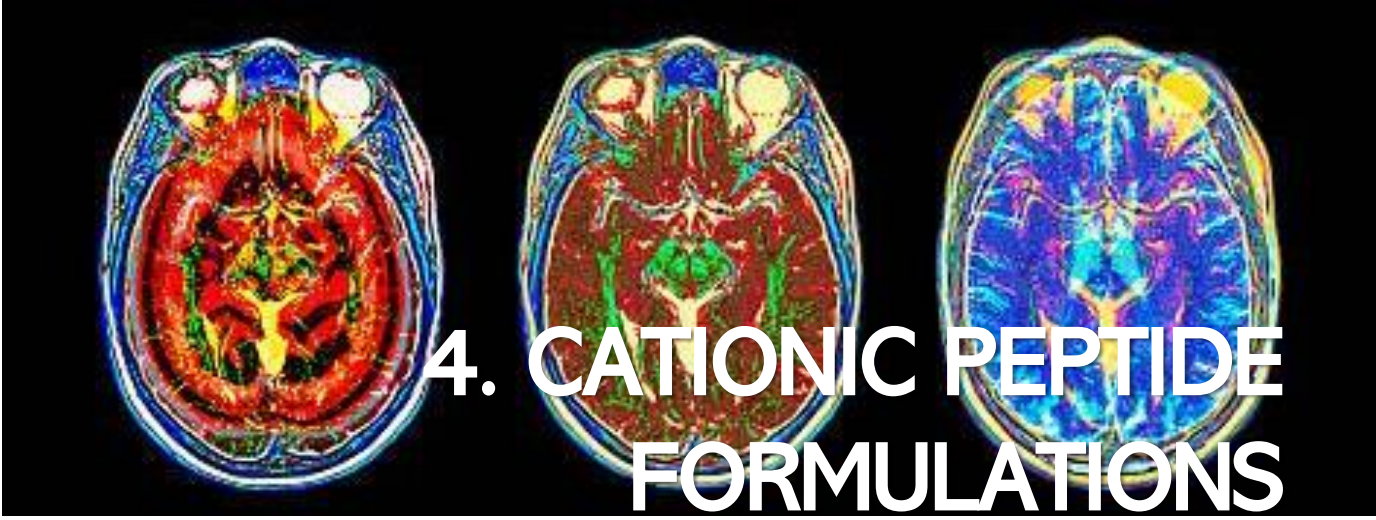

4. CATIONIC PEPTIDE FORMULATIONS FOR THE ENCAPSULATION OF MRI CONTRAST AGENTS

Elisabetta Rosa | University of Naples Federico II | XXXV cycle

4.1 INTRODUCTION

4.1.1 Magnetic Resonance Imaging: principles and contrast agents

Magnetic Resonance Imaging (MRI) has known a fast spread since 1972, when Lauterbur first traced that, by the superimposition of linear field gradients to the static magnetic field during a Nuclear Magnetic Resonance (NMR) experiment, the image of the investigated object can be beamed. [179]. MRI is a powerful, non-invasive, diagnostic technique representing today one of the election methods to image the interior of the human anatomy, widely used for the early detection of tumoral lesions or other physiological alterations of living tissues. The non-ionizing electromagnetic fields it takes advantage of, belong to three different frequency bands: static magnetic field (SMF) and gradient magnetic field (GMF) in the kHz range and pulsed radiofrequency (RF) in the MHz range. [180] A SMF does not vary over time; it is generated by direct current of electricity and, by and of itself, it does not have a frequency (0 Hz). On the contrary, a GMF is produced by a sinusoidally time-varying alternating current; the frequency of the field indicates how many times the sinusoid repeats itself every second. Through pulsed radiofrequency, instead, RF oscillations are inspected at a rate of cycles *per* second. One cycle *per* second corresponds to one Hz. When protons are placed in a magnetic field (like the chamber of the MRI scan) they may align parallel or antiparallel respect to it. Most of the protons will align in a parallel mode, also named “spin up”, which corresponds to a lower energy, thus generating a net parallel magnetization, defined as longitudinal magnetization. In truth, the direction of the alignment is not perfectly parallel with respect to the axis of the external magnetic field, but deviates from it by a certain angle, which causes the protons to oscillate around the axis with a frequency, called the Larmor frequency, depending on the strength of the external magnetic field. The distribution of the proton around their precessional orbits is, at the

equilibrium state, random and, therefore, no net transverse magnetization is generated. The application of an RF pulse oscillating at the Larmor frequency as a secondary magnetic field has the role to force some protons to move to the "spin down" (antiparallel) orientation, so that the net parallel magnetization decreases, and a transverse magnetization is partially induced. When the RF is pulsed at 90 °C, the longitudinal magnetization is nullified, and the positive transverse is used by the system to trace the image. Protons can exploit two processes to "relax", that is to reach again the equilibrium conditions, whose contribution depend on the examined tissue: 1) they can recover the longitudinal magnetization depending on a rate known as T_1 time; 2) they can cause a decay of transverse magnetization through a rate defined as T_2 time. Since the variation in the proton density between tissues is not very relevant, T_1 and T_2 times are the two parameters which mostly affect the MRI acquisitions and by which the contrast is provided, together with a large number of modulable instrument parameters. The quality of this contrast may be enhanced using appropriate contrast agents (CAs), acting by increasing the proton relaxation rates in the tissues where they distribute. [181] They can be classified according to different specific features, such as their chemical and magnetic properties, the route of administration, together with their biodistribution and specific application. Taking into account their chemical composition and the type of contrast they generate, MRI CAs are generally categorized as T_1 or T_2 CAs. [182] Water-soluble complexes of paramagnetic ions like the lanthanide metal gadolinium (Gd(III)), or the transition metal manganese (Mn(II)) are classified as T_1 contrast agents because of their larger effect on tissue T_1 than on T_2, which allows increasing the contrast in T_1-weighted images. Their paramagnetic properties derive from the presence and the number of unpaired electrons: Gd(III) has seven and Mn(II) has five. They provide a positive contrast since the ratio between the longitudinal relaxivity (r_1) and the transversal relaxivity (r_2) is slightly higher than 1. [183] On the contrary

T_2 agents are based on superparamagnetic compounds (generally superparamagnetic (iron oxide) magnetite particles, named as SPIOs), presenting a r_1/r_2 value higher than 10 and giving rise to a negative contrast. [184]

4.1.2 Gadolinium-based T_1 contrast agents

Starting from 1981, when the first contrast-enhanced MRI analyses was carried out by the use of ferric chloride for the imaging of the gastrointestinal tract, [185] many strategies have been explored to increase the sensitivity of this diagnostic technique. Among all the designed, synthesized and tested agents Gd-based CAs are used in about 40% of all MRI exams and in about 60% of neuro MRI exams. This means that about 40 million Gd(III) chelates preparations are administered each year worldwide. The first example of a gadolinium complex as an intravascular diagnostic compound, dates back to 1984. [186] Gadolinium (electron configuration: [Xe] $4f^7 5d^1 6s^2$, atomic number 64), for MRI applications, is used as gadolinium(III) presenting a high magnetic moment, due to the presence of seven unpaired electrons. (**Figure 4.1A**) Gd(III) can be weakly bound to serum proteins and lanthanide hydroxides, derived from salts hydrolysis, can be picked up by the reticuloendothelial system (RES) and accumulate in bones, liver and spleen of the patient, thus explicating a potential toxicity. [187] To overcome this problem, chelation of paramagnetic ions has been introduced, so that the metal complex can be delivered to the kidneys for excretion in its intact form. Gd(III) displays a high coordination number (8-9), making it possible being chelated by high denticity ligands, allowing a high complex stability, maintaining, at the same time, the capability to coordinate one or two water molecules (q = 1 or 2) to the paramagnetic center. This is particularly important considering that the ability of a paramagnetic agent to act as CA for MRI applications is assessed by the determination of its "in vitro" relaxivity (r_{1p}), expressing the

contribution to the observed water proton relaxation rate that the complex gives to a solution in which it is solved in 1 mmol/L concentration, at a measured frequency of 20 MHz. [188]

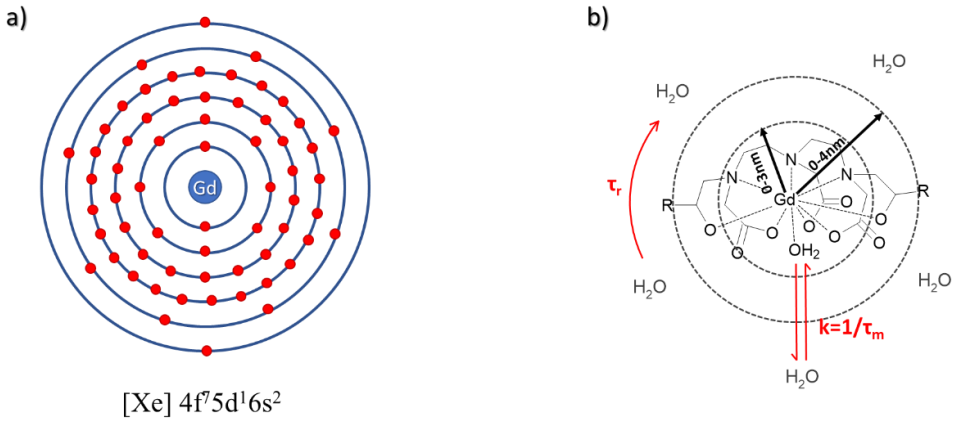

Figure 4.1: (A) Bohr atomic model for gadolinium; (B) parameters that determine the inner-sphere relaxivity

The two factors which mainly contribute to the r_{1p} are the water molecule directly coordinated to the metal and the bulk solvent molecules that express the paramagnetic effect by diffusing around the metal, known as the inner-sphere and the outer-sphere relaxation rate, respectively. Moreover, water molecules belonging to the second-coordination sphere, that are bound through hydrogen bonds to the electronegative acceptor groups of the ligand, also explicit an important effect. [189]. As a consequence, different factors contribute to the overall measured relaxivity (r_1^{obs}), as expressed by *Equation 4.1*. This value is commonly obtained through a Field-Cycling Relaxometer, an NMR instrument in which the r_1 parameter is measured on a range of frequencies between 0.01 – 50 MHz. [190]

$$r_1^{obs} = r_{1\rho}^{IS} + r_{1\rho}^{SS} + r_{1\rho}^{OS} + R_1^W \qquad (4.1)$$

r_1^{IS}, r_1^{SS} and r_1^{OS} indicate the relaxation enhancement in the presence of 1 mmol/L paramagnetic complex of the inner-sphere, the second sphere and the outer-sphere, respectively, while R_1^W represents the relaxation rate of water when the paramagnetic center is absent. [191] The parameters that determine the inner-sphere relaxivity are shown in **Figure 4.1B**. The r_1^{IS} depends, in turn, on the relaxation time (T_{1M}) and the exchange lifetime (τ_m) of the protons of the water molecules (q) in the inner coordination sphere.

$$r_{1\rho}^{IS} = \frac{1.8 \times 10^{-5} q}{T_{1M} + \tau_m} \qquad (4.2)$$

As expressed by *Equation 4.2*, r_1^{IS} reaches the highest value when $T_{1M} > \tau_m$, meaning fast exchange conditions, T_{1M} is as short as possible and there are many water molecules bound to the metal center. However, if q is higher than 2, the thermodynamic stability and the kinetic inertness is compromised. T_{1M} increases with the increase of the sixth power of the distance between the metal centre and the coordinated water protons and it is also influenced by the molecular reorientation time (τ_r) of the complex. The modified Solomon-Bloembergen equations, where c is the molar concentration of the paramagnetic complex, (*Equation 4.3* and *Equation 4.4*) also describe the contribution of the applied magnetic field strength and the electronic relaxation times (τ_{Si}; i = 1, 2) of the unpaired electrons of the metal, to the relaxation time. Other factors influencing the T_{1M} are: the square of the gyromagnetic ratio (γ_I^2), the electron spin quantum number (S=7/2 for Gd(III) ions), the electron g-factor (g), the Bohr magneton (μ_B) and the nuclear and electron Larmor frequencies (ω_I and ω_S, respectively). [192]

$$\frac{1}{T_{1M}} = \frac{2}{15}\left(\frac{\mu_0}{4\pi}\right)\left[\frac{\gamma_I^2 g^2 \mu_B^2 S(S+1)}{r_{GdH}^6}\right] x \left(\frac{7\tau_{c2}}{1+\omega_S^2\tau_{c2}^2} + \frac{3\tau_{c1}}{1+\omega_I^2\tau_{c1}^2}\right) \qquad (4.3)$$

$$\frac{1}{\tau_{ci}} = \frac{1}{\tau_r} + \frac{1}{\tau_m} + \frac{1}{\tau_{Si}} \qquad (4.4)$$

The inner sphere relaxivity in the high magnetic field region is mainly depended upon the reorientation correlation time, τ_r, whose value is influenced by the molecular dimensions of the complex. At the same time, the low magnetic field region is largely influenced by the zero-field value of electronic relaxation time (τ_{S0}) of the complex, which is sensitive to the chemical nature of the coordinating groups and increases with the symmetry of the complex. The τ_m is inversely related to the water exchange rate (k_{ex} = 1/ τ_m) and, it has been evidenced that this value may be long enough to limit relaxation enhancement promoted by Gd(III) complexes. For this reason, it is important to correctly tune the steric environment in the proximity of the metal center.

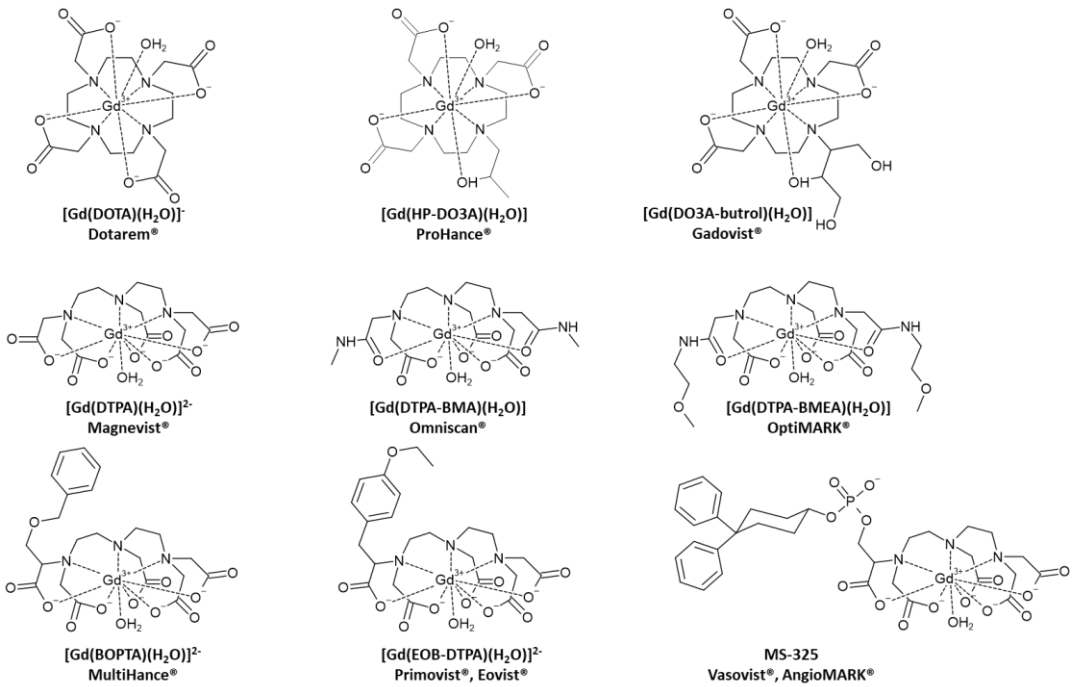

Figure 4.2: Clinically used contrast agents based on Gd(III) complexes

Figure 4.2 shows the Gd-based CA which have entered the commerce since the first gadolinium-based MRI contrast agent, Gd-DTPA (Magnevist®), was approved for clinical use in 1987. These CAs have been used for intravenous or intra-articular administration and may be classified according to their chemical features in:

1. *Ionic and hydrophilic complexes*: Gd(III) diethylenetriamine pentaacetate (Gd-DTPA *or* gadopentate dimeglumine) and Gd(III) 1,4,7,10-tetrazacyclododecane NN'N''N'''-tetra-acetate (Gd-DOTA *or* gadoterate). These CAs are recognized as non-specific agents or extracellular fluid space (EFS) agents. They distribute in the extracellular fluid and elimination occurs *via* glomerular filtration. Their use mostly implies the visualization of brain lesions as a result of disruption of the blood brain barrier.
2. *Nonionic and hydrophilic complexes*: Gd(III) diethylenetriamine pentaacetate-bis(methylamide) (Gd-DTPA-BMA *or* gadodiamide), Gd(III) 1,4,7-triscarboxymethyl-1,4,7,10-tetraazacyclododecane (Gd-HP-DO3A *or* gadoteridol), which is a Gd-DOTA analogue. Their pharmacokinetics properties are similar to their ionic analogues.
3. *Ionic and lipophilic complexes*: Gd(III) benzyl-oxy-methyl derivative of diethyltriamine pentaacetate dimethylglucamine salt (Gd-BOPTA *or* gadobenate dimeglumine) and Gd(III) ethoxybenzyl diethylentriamine pentaacetate (Gd-EOB-DTPA *or* gadoxetate). The introduction of an aromatic ring on the backbone of the DTPA ligand allows increasing the lipophilicity and altering the biodistribution. They have higher affinity for serum albumin, specifically concentrate in hepatocytes, thus presenting liver specificity, and are eliminated partly through the biliary system.

4.1.3 Strategies to improve the safety and the efficiency of gadolinium-based T_1 contrast agents

All these CAs have r_{1p} values around 3-4 mM^{-1} s^{-1} at 20 MHz and 310 K, and 4-5 mM^{-1} s^{-1} at 298K. These low relaxivities implicate high dose administration (typically, 0.1 mmol of Gd *per* kilogram) to allow a good sensitivity of the technique. This evidence may represent a hindrance related to safety of CAs. Indeed, in 2006 a very serious, even lethal disease, the nephrogenic systemic fibrosis (NSF), has been associated with the release of Gd(III) ions after the treatment with CAs of patients with impaired renal clearance. [193,194]

Table 4.1: EMA's opinion on the restrictions on use of linear gadolinium agents in body scans.

Product	Type (formulation)	Recommendation
Artirem / Dotarem (***gadoteric acid***)	macrocyclic (i.v.)	maintain
Artirem / Dotarem (***gadoteric acid***)	macrocyclic (intra-articular)	maintain
Gadovist (***gadobutrol***)	macrocyclic (i.v.)	maintain
Magnevist (***gadopentetic acid***)	linear (intra-articular)	maintain
Magnevist (***gadopentetic acid***)	linear (i.v.)	suspend
Multihance (***gadobenic acid***)	linear (i.v.)	restrict use to liver scans
Omniscan (***gadodiamide***)	linear (i.v.)	suspend
Optimark (***gadoversetamide***)	linear (i.v.)	suspend
Primovist (***gadoxetic acid***)	linear (i.v.)	maintain
Prohance (***gadoteridol***)	macrocyclic (i.v.)	maintain

Moreover, it has been evidenced that gadolinium also accumulate in tissues of healthy patients receiving multiple doses of Gd-bases CAs. [195]. For this reason, in 2017, European Medicinal Agency's (EMA) Committee for Medicinal Products for Human Use (CHMP) has recommended restrictions for some intravenous linear agents in order to prevent any risks that could

potentially be associated with gadolinium brain accumulation. Other CAs can, nowadays, only be used when other agents are not suitable (for example for liver scans). These decisions are summarized in **Table 4.1.**

A strategy proposed to decrease the administered dose, thus improving the safety of these compounds, consists in the maximization of their efficacy in terms of the relaxivity value. According to the Solomon-Bloembergen-Morgan theory, by the optimization of τ_r, τ_m and τ_{Si} parameters, relaxivity of 100 mM^{-1} s^{-1} for a complex with q=1 at 20 MHz may be reached. [192]

To realize this scope, together with the selective activation of the contrast agent, some solutions have been proposed and CAs with improved properties were synthesized and can be classified as follows: [196]

1. *Responsive or activated contrast agents*, also defined as "smart" CAs, comprise compounds that, by reacting to variants like temperature, pH, metal ion concentration, partial pressure of oxygen or enzyme activity, undergo an activation in the distribution site resulting in a change of their relaxivity value. [197,198]
2. *Target selective contrast agents* allow the Gd(III) complex to be selectively delivered by peptides or antibodies on tissues of interest by bioactive molecules such as antibodies or peptides. [199]
3. *Multimeric or macromolecular contrast agents* are compounds composed by a large number of gadolinium complexes combined together where the final relaxivity results from the contribution of each gadolinium ion. [200,201]

Regarding the latter group of CAs, to increase the blood residence time and reduce the extravasation of a Gd(III) complex, an explored strategy is the insertion of substituents able to bind serum proteins. [202] The large molecular size offered by macromolecular Gd(III) chelates like dendrimers, [203] linear polymers, [204] gadofullerenes, [205] gadonanotubes, [206]

or large protein derivatives obtained from the strong interaction in the avidin-biotin or in the β-ciclodextrin-dextran complexes, [207] allows the CA to remain confined to the blood vessel space. (**Figure 4.3**) Micelles and liposomes have been proposed to deliver multiple copies of T_1-CAs, too. [208,209] Due to the size and to the slow reorientation time offered by these nanostructures, each Gd(III) complex embedded in them reaches relaxivity values 2-5-fold higher than the ones associated with the classical low molecular weight (LMW) contrast agents.

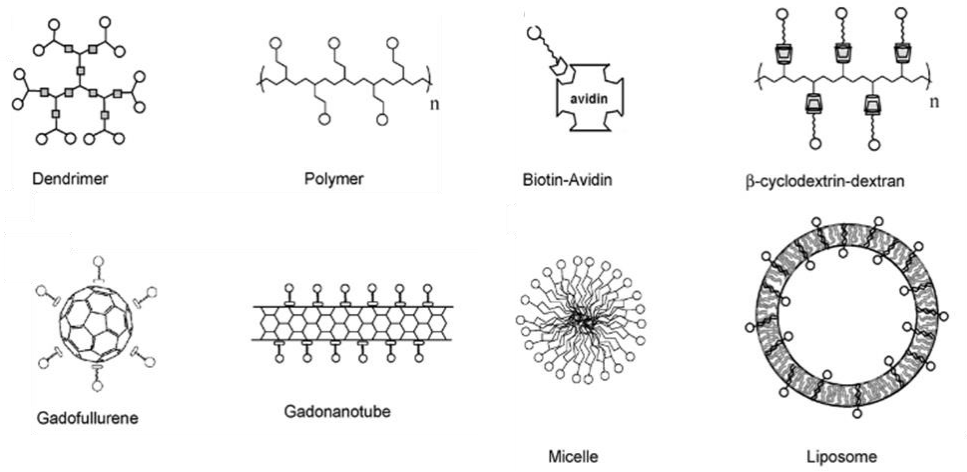

Figure 4.3: Schematic representation of macromolecular adducts

Different strategies have been used to obtain new supramolecular contrast agents:

1. the LMW Gd(III)-complex can be entrapped within the internal compartments of the nanostructure;
2. the LMW Gd(III)-complex can be used to functionalize the external surface of the nanostructure;

3. the LMW Gd(III)-complex can be covalently linked to a hydrophobic portion able to prompt the self-assembly process of the nanostructure.

In this scenario, peptides can be proposed as tools able to suit all the different design approaches, thanks to their tunable properties. [210]

Among all the nanostructures that can be obtained starting from aromatic, amphiphilic or polymeric peptides, soft materials like fibers and hydrogels (HGs) have been recently discovered to provide a significant improvement of the relaxometric behavior. [91,211] This may be ascribed to the high content and high viscosity reached by the water within the peptide network. However, no examples of peptide based nanogel has ever been provided for imaging applications, even though a large spectrum of advantages may be derived from the combination of the high biocompatibility of peptide materials and the possibility of nanogels to be intravenously administered.

4.1.4 Chemical Exchange Saturation Transfer MRI

In the context of the emerging solutions to the concerns about the safety of Gd(III) CAs, a broad interest has focused on Chemical Exchange Saturation Transfer (CEST) imaging as a new MRI contrast approach. The term CEST was first coined in 2000 by Balaban and colleagues at the National Institutes of Health [212] and the technique implies the use of endogenous or exogenous molecular targets containing exchangeable spins. The principle behind this is that the contrast is generated by the continuous application of a radiofrequency pulse at the resonance of the exchangeable spins of the CEST agent. This results in a saturation of the spins which, thanks to the proton exchange, is continuously transferred to the bulk spins, thus generating a saturation of a significant portion of their MRI signal. This allows, by observing the effect on the abundant bulk solvent, the indirect detection of metabolites at low concentration. Contrarily to T_1 and T_2 contrast mechanisms, CEST specifically inquiries molecules carrying

exchangeable protons in a frequency-specific manner, and this request, as inferable, does not interfere with the safety of the agent. Since the CEST contrast is strictly specific for one chemical shift, multiple agents with more than one exchangeable proton, each of one possessing a different chemical shift, can be designed to obtain multi-frequency [213] or multi-color [214] MRI. The simplest mathematical model to describe the CEST process is the two-pool one, where the two pools are represented by the exchangeable proton of the molecule and the bulk water proton, presenting differences is chemical shifts ($\Delta\omega$) and the equilibrium exchange rate (k_{ex}). As inferable, the concentration of the considered protons is significantly different. [215] From an experimental perspective, CEST contrast is determined through the collection of a z spectrum (or CEST spectrum, or Magnetization Transfer (MT) spectrum), where the normalized saturation of water (S_{sat}/S_0) is reported as a function of the irradiation frequency. After irradiation of the water protons, the signal disappears because of direct saturation. In the z spectrum, this frequency is indicated as 0 ppm.

4.1.5 CEST-MRI contrast agents

CEST agents can be classified in three main classes, which are: diamagnetic CEST (DiaCEST), paramagnetic CEST (ParaCEST) and hyperpolarized CEST (HyperCEST). DiaCEST agents exploit natural non-metallic markers, like peptides, sugars and liposomes, and provide a contrast depending on the number and the type of labile protons. [216] ParaCEST agents mainly comprise lanthanide complexes with protons undergoing slow exchange. [217] In this case, the contrast is due to the proton exchange between the protons of then ligand or of the water molecules bound to the metal and bulk water ones. The offset frequencies of these protons are influenced by the presence of the metal ion. Finally, HyperCEST agents represent a particular class of CA acting like cages designed to trap dissolved hyperpolarized materials, which pass in and out of the cage structure

inducing frequency differences in their spins. [218] This type of imaging requires the use of a polarizer, and it has been applied using xenon as solvent instead of water, which can be hyperpolarized to allow adequate detection sensitivity. CEST probes have been proposed for the specific detection of biologically and pathologically relevant molecules like enzymes, [219] inorganic ions, [220] metabolites, [221] glucose/glycogen, [222] peptides or proteins [223] and nucleoside base. [224] From a biomedical point of view, CEST imaging may be used to detect tumors, [225] to monitor gene expression, [226] cell therapy, [227] osteoarthritis and to characterize ischemia, [228] but also to follow the delivery and the release of active pharmaceutical ingredients possessing exchangeable spins. [229] CEST agents have been also investigated for the possibility they offer to label hydrogels, in order to make them detectable by MRI. Among the DiaCEST probes, iodinated CT agents represent a relevant alternative since they have an excellent safety profile ensuring a high clinical transability potential. Their exchangeable protons resonate in a range of frequencies compatible with CEST detection. Iopamidol has been the first iodinated molecule to be considered as CEST-MRI contrast agent [230] for its ability to act as *in vivo* pH reporter. [231]

4.2 OBJECTIVES

To solve the safety problems related to classical T_1-CAs and to improve the sensitivity of the imaging technique, two strategies were pursued by us. First of all, lysine-containing peptide sequences (Ac- and Fmoc-K peptides) [139], working as hydrogelators, were selected as starting models for improving the electrostatic interactions with T_1-CAs like $[Gd(AAZTA)]^-$ and $[Gd(BOPTA)]^{2-}$, containing one and two negative charges, respectively, thus promoting their physical encapsulation. Moreover, a nanogel was also formulated through a submicronization procedure carried out on the best

performing Gd(III) complex loaded HG. The aim was to improve the relaxivity behavior and to reduce the possible *in vivo* transmetallation of gadolinium chelates. Both Gd(III) complexes-loaded hydrogels and nanogels were fully characterized from their structural point of view and their ^{1}H NMR relaxometric behaviour was investigated as a function of the applied magnetic field strength. On the other hand, the possibility of creating new and safer contrast agents for CEST-MRI applications, was pursued by loading iopamidol into the Ac-K1 and Ac-K2 hydrogel networks. The obtained loaded hydrogels were characterized in terms of their structural properties and imaging performances. Their biocompatibility was evaluated *in vitro* and an *in vivo* proof-of-concept of their potential application was provided through intratumor injection of the macroscopic scaffold in Balb/c mice inoculated with TS/a breast cancer cells.

4.3 MATERIALS AND METHODS

Rink amide MBHA (4-methylbenzhydrylamine) resin, protected N^{α}-Fmoc-amino and coupling are commercially available from Calbiochem-Novabiochem (Laufelfingen, Switzerland). All other chemicals were purchased from Merck (Milan, Italy), Fluka (Bucks, Switzerland), or LabScan (Stillorgan, Dublin, Ireland) and they were used as delivered (unless stated otherwise). Peptide solutions were prepared by weight using double distilled water. Sodium chloride, potassium chloride, sodium phosphate dibasic, potassium phosphate monobasic were purchased from Sigma Aldrich (LLC -Merck KGaA, Darmstadt, Germany) and used without further purification. PBS (Phosphate Buffered Saline) was prepared to reach a sodium chloride concentration of 0.137 mol/L and 100 or 10 mmol/L phosphate (pH 7.3 ± 0.1, osmolarity 280 ± 10 mosm/L).

Bracco Imaging S.p.A. kindly provided $[Gd(BOPTA)]^{2-}$ (Gadobenate dimeglumine, MultiHance).

To promote the complexation in $[Gd(DTPA)]^{2-}$ and $[Gd(AAZTA)]^{-}$, Diethylenetriaminepentaacetic acid (DTPA) and 6-amino-6-methylperhydro-1,4-diazepine-*N*,*N*′,*N*″,*N*‴-tetraacetic acid (AAZTA) were dissolved in pure water in the presence of a molar excess of $GdCl_3 \cdot 6H_2O$. [232] The pH of the solution was brought to 6 by adding NaOH 0.1 mol/L and the reaction was left 1h under stirring at room temperature. Then, an increase in pH up to 9.5 promoted the precipitation of unreacted Gd(III), which was removed through filtration. Finally, the pH of solution was corrected to 7 with 0.1 mol/L HCl.

4.3.1 Peptide Synthesis

All the peptide derivatives were synthesized using standard solid-phase peptide synthesis (SPPS) protocols according to Fmoc/tBu strategy as previously described. After the coupling of the six protected amino acids on the solid support (Rink amide MBHA resin, substitution grade 0.73 mmol/g), Fmoc derived peptides (Fmoc-ILVAGK (Fmoc-K1), Fmoc-LIVAGK (Fmoc-K2) and Fmoc-AIVAGK (Fmoc-K3)) were directly cleaved by treating the resin with a TFA (trifluoroacetic acid)/TIS (triisopropylsilane)/ H_2O (92.5/5/2.5 *v/v/v*) mixture for 2 hours. Ac-K1, Ac-K2 and Ac-K3 peptides were subjected first to the removal of the Fmoc group from the last amino acid and then to acetylation of the N-terminus with a solution of pyridine/acetic anhydride (4/4.7 *v/v*) in DMF (two cycles of 10 minutes each). At the end of the treatment, also these peptides were cleaved from the resin as previously described. All the crude peptides were precipitated with cold ether and freeze-dried for three times.

The synthesized sequences were purified using preparative RP-HPLC with a LC8 Shimadzu HPLC system (Shimadzu Corporation, Kyoto, Japan) equipped with a UV lambda-Max Model 481detector, using a Phenomenex

(Torrance, CA, USA) C_{18} column. Elution solvents were H_2O/0.1% TFA (A) and CH_3CN/0.1% TFA (B), with the concentration of (B) increasing from 30 to 80% over 30 min at a flow rate of 20 mL/min. Analytical RP-HPLC-MS analysis confirmed the purity of Ac-K peptides; the system was composed by a Finnigan Surveyor MSQ single quadrupole electrospray ionization detector (Finnigan/Thermo Electron Corporation San Jose, CA, USA), with a C_{18}-Phenomenex column eluting with (A) and (B) at a flow rate of 1 mL/min. During the analysis, a gradient from 5 to 70 % of (B) in 10 minutes was set. Identity of peptides was assessed by MS spectrometry conducted by the use of a LTQ XL Linear Ion Trap Mass Spectrometer, ESI source (**Figures 6.7-6.8**).

Ac-K1: t_R = 11.62 min, MS (ESI+): m/z 640.82 calcd. for $C_{30}H_{56}N_8O_7$: $[M+H^+]$ = 641.4 u.m.a.
Ac-K2 t_R = 11.51 min, MS (ESI+): m/z 640.82 calcd. for $C_{30}H_{56}N_8O_7$: $[M+H^+]$ = 641.5 u.m.a.
Ac-K3: t_R = 10.13 min, MS (ESI+): m/z 598.74 calcd. for $C_{27}H_{50}N_8O_7$: $[M+H^+]$ = 599.4 u.m.a.

4.3.2 Formulation of peptide hydrogels loaded with Gd(III) complexes

Peptide based HGs loaded with $[Gd(BOPTA)]^{2-}$ and $[Gd(DTPA)]^{2-}$ were prepared by solving 6 mg of the lyophilized peptide in 300 µL of bidistilled water (final concentration 2wt%); then 50 µL of an aqueous solution of the Gd(III) complex (at a concentration of 30 mmol/L) was added to the suspension and the sample was sonicated for 5 minutes and left at room temperature till the gel was formed. Since $[Gd(AAZTA)]^-$ presents one less negative charge than the other two linear complexes on its structure (only one), $[Gd(AAZTA)]^-$-loaded HGs were formulated using a different procedure. Briefly, 6 mg of the lyophilized peptide powder were first dissolved into 300 µL of a 5.0 mmol/L aqueous solution of $[Gd(AAZTA)]^-$,

and then 50 µL of 0.1 mol/L phosphate buffer solution were added to better balance electrostatic forces within the HG structure. The final concentration of Gd(III) was 4.28 mmol/L in each hydrogel.

4.3.3 Formulation of peptide hydrogels loaded with iopamidol

6 mg of Ac-K1 or Ac-K2 peptides were solved in 300 µL of a 260 mmol/L water solution of iopamidol and were sonicated for 10 min (final 2 wt%). Then, 50 µL of 100 mmol/L phosphate buffer were added, and mixture was vortexed to let the gel form.

4.3.4 Hydrogel stability studies

An *in vitro* stability assay was performed to evaluate the Gd(III) complex-loaded HGs degradation profile, by determining the percent weight loss of the matrices. 350 µL of freshly formed HGs were weighted (W_o) and then incubated at 37°C with 1.0 mL of Ringer's solution (8.6 mg of NaCl, 0.30 mg of KCl and 0.33 mg of $CaCl_2$). The Ringer's solution was removed after 20 days and HGs were weighted again (W_t). The degradation degree was expressed as percentage ratio (ΔW) between W_o and W_t, calculate by using the following formula:

$$\Delta W = \left(1 - \frac{Wt}{Wo}\right) * 100 \qquad (4.5)$$

4.3.5 Scanning Electron Microscopy (SEM)

Morphological analysis of xerogels, deriving from dehydration of hydrogels loaded with Gd-complexes, was carried out by a field emission scanning electron microscope (PhenomXL, Alfatest). A thin coat of gold and palladium at a current of 25 mA for 75 sec was sputtered on xerogels obtained by letting 10 µL of peptide HG, drop-casted on an aluminum stub, to air-dry. Samples were then introduced into the specimen chamber and the images

were acquired through the Secondary Electron Detector (SED), at an accelerating voltage of 10 kV, spot 3.

4.3.6. Rheological studies

Rheological properties of freshly prepared HGs loaded with a Gd(III) complex or iopamidol were evaluated using a rotational controlled stress rheometer (Malvern Kinexus) using a 15 mm flat-plate geometry (PU20:PL61). Each experiment was performed on 400 µL of sample at 25 °C using a humidity chamber and a gap of 1 mm. To identify the regime of linear viscoelasticity, preliminary dynamic rheological tests were carried out. The viscous elastic region was determined by the strain sweep (0.01-100%) and the oscillatory frequency (0.1-100 Hz). A time-sweep oscillatory evaluation test was then performed for 20 minutes using a constant 0.1% strain and 1 Hz frequency. Results are reported as shear Storage or elastic modulus (G') and shear loss or viscous modulus (G") measured in Pascal (Pa)

4.3.7 Formulation of peptide nanogel loaded with $[Gd(BOPTA)]^{2-}$

The formulation of $[Gd(BOPTA)]^{2-}$-loaded nanogel was achieved through the top-down method previously described. Briefly, 350 µL of a gel disk of Fmoc-K2 HG loaded with the complex (peptide concentration 1.7% wt) was prepared into a silicone mold and then added to 1.650 mL of a water suspension of two surfactants, TWEEN® 85 (Polyoxyethylenesorbitan Trioleate) and SPAN® 85 (Sorbitan trioleate) at a w/w ratio of 89/11 ($2.34 \cdot 10^{-5}$ total mol of surfactants). This surfactant ratio allowed the obtainment of an HLB (Hydrophilic Lipophilic Balance) value of 10. The sample was first homogenized for 5 min at 35.000 min^{-1}, and then subjected to tip-sonication for 5 min at 9 W. The loaded NG fraction was purified from free Gd(III) complex by gel filtration on a pre-packed Sephadex

G-50 column and the amount of encapsulated complex was quantified by inductively coupled plasma-mass spectrometry (ICP-MS).

4.3.8 Dynamic Light Scattering (DLS)

DLS measurements were carried out at room temperature on a Zetasizer Nano ZS (Malvern Instruments, Westborough, MA) to analyze the mean diameter and diffusion coefficient (*D*) of $[Gd(BOPTA)]^{2-}$-filled NG. Instrumental settings for the measurements were: backscatter detector at 173° in automatic modality, room temperature and disposable sizing cuvette as cell. The DLS measurements were carried out in triplicate on aqueous samples. Before the analysis, the NG was subjected to centrifugation at room temperature at 13.000 rpm for 5 minutes.

4.3.9 Circular Dichroism (CD) studies

Far-UV CD spectra of $[Gd(BOPTA)]^{2-}$ loaded Fmoc-K2 nanogel was collected at 25°C with a Jasco J-810 spectropolarimeter equipped with a NesLab RTE111 thermal controller unit. The sample was placed in a 0.5 mm quartz cell. Other experimental settings were: sensitivity = 50 mdeg, scan speed = 50 nm/min, response = 2 sec, time constant = 16 s, bandwidth = 1 nm and data pitch = 1 nm. The final spectrum, collected from 350 to 190 nm, was obtained by averaging three scans, and then subtracting for the blank and adjusting for the concentration.

4.3.10 Relaxometric characterization

A fast-field cycling (FFC) Stelar SmarTracer Relaxometer was used to collect $1/T_1$ ^1H nuclear magnetic relaxation dispersion (NMRD) profiles of Gd(III) complexes loaded HGs and NG. A continuum of magnetic field strengths from 0.00024 to 0.25 T was used. The relaxometer operates under computer control with an absolute uncertainty in $1/T_1$ of ± 1%. A High Field Relaxometer (Stelar), equipped with the HTS-110 3T Metrology cryogen-

free superconducting magnet, was used to obtain additional data in the range 0.5-3.0 T. The standard inversion recovery sequence (20 experiments, 2 scans) with a 90° pulse width of 3.5 μs was used, and the reproducibility of the data was within ±0.5%. The NMRD profiles were collected at 283, 298 and 310 K.

4.3.11 Iopamidol release from hydrogels

350 μL of iopamidol-loaded Ac-K1 HG were prepared, as above described, in a 1.5 mL Eppendorf and then the hydrogel was covered with 700 μL of 10 mmol/L PBS. At well-defined time points (30 min, 1 h, 3 h, 6 h, 9 h, 12 h, 24 h, 36 h, 48 h, 60 h and 72 h), 350 μL of the supernatant were removed from the top of the HG and replaced with an equal amount of fresh PBS. The quantity of iopamidol in each fraction was estimated through UV-vis spectroscopy (λ=240nm). The amount of released iopamidol was plotted over time to obtain the release.

4.3.12 Cells culture

All cell culture media and supplements (RPMI, DMEM, FBS, Glutamine, pen/strep, MycoAlert™ Mycoplasma Detection Kit) were purchased from Lonza Sales AG-EuroClone SpA (Milano, Italy). Experiments were carried out on three different cell lines, which were GL261 (murine glioma), TS/a (murine breast carcinoma), and 3T3-NIH (murine fibroblasts). GL261 and 3T3-NIH cell lines were purchased from ATCC (American Type Culture Collection) and grown in DMEM medium (Dulbecco'modified Eagle medium) supplemented with 10% fetal bovine serum (FBS), previously inactivated by heat treatment, 2 mmol/L glutamine, 100 U/mL penicillin and 100 μg/mL streptomycin. TS/a murine breast cancer cells were obtained from a spontaneous mammary adenocarcinoma arisen in a retired breeder BALB/c female. [233] These cells were grown in RPMI (Roswell Park Memorial Institute) 1064 medium supplemented with 10% heat-inactivated fetal

bovine serum (FBS), 2 mmol/L glutamine, 100 U/mL penicillin and 100 µg/mL streptomycin. All the cells were seeded in 75-cm^2 flasks at density of ca. 2×10^4 cells/cm^2, and the flasks were put in a humidified 5% CO_2 incubator at 37 °C. At confluence, 1 mL of Trypsin-EDTA solution (0.25 % (w/v) Trypsin- 0.53 mmol/L EDTA) was added to detach the cells. All the used cells were found to be negative for mycoplasma after testing with MycoAlert™ Mycoplasma Detection Kit.

4.3.13 Cells viability: MTT assay

The biocompatibility of the iopamidol-loaded hydrogels on GL261, TS/a, and 3T3-NIH cells was tested by performing an elution assay (according to ISO 10993-5 guidelines) on cells cultured in the proper medium previously conditioned by hydrogels. 200 µL of each hydrogel were prepared under sterile conditions; gels were then purified through 2 washes of 2 hours each with 1 mL of complete medium (ratio gel/extracting media 1/5 v/v). At the end of the treatment, gels were then incubated overnight with 1 mL of fresh complete medium. The day after, no medium color change was detected and pink coloration of the gel after the extraction of the medium indicates permeability. MTT (Thiazolyl Blue Tetrazolium Bromide, Sigma Aldrich) assay was performed to evaluate the toxicity of the samples: cells were seeded into 96-well tissue culture plates (10^4 cells for plate) 24 h before the experiment. After this time, they were incubated overnight with complete medium, previously conditioned by the hydrogel. The medium was then removed, cells were washed and re-incubated with fresh medium supplemented with 0.5 mg/mL MTT for 4 h. The MTT containing solution was removed and each plate was treated with 0.1 mL of DMSO for 30 min at room temperature, under gentle agitation, thus allowing solubilization of formazan crystals. The absorbance of the resulting solutions was measured through a 96-multiwell iMark Bio-Rad microplate Reader (λ = 570 nm). The cell viability was calculated as percentage using the following formula:

$$\text{Viable cells } \% = (Abs_T/Abs_{cnt}) \times 100 \qquad (4.6)$$

where Abs_T is the mean absorbance of Treated cells and Abs_{cnt} is the mean absorbance of control untreated cells. MTT assay was repeated four times and data are reported as mean value ± standard deviation.

4.3.14 Animal models

In vivo experiments were carried out on 8-10 weeks female Balb/C mice (Charles River Laboratories, Calco, Italy) which were bred at the Department of Molecular Biotechnology and Health Sciences of the University of Turin, Italy. Mice were kept in standard housing (12 h light/dark cycle) with rodent chow and water available ad libitum. Experiments were performed according to the Amsterdam Protocol on Animal Protection and in conformity with institutional guidelines that are in compliance with national laws (D.L.vo 116/92, D.L.vo 26/2014 and following additions) and international laws and policies (2010/63/EU, EEC Council Directive 86/609, OJL 358, Dec 1987, NIH Guide for the Care and Use of Laboratory Animals, U.S. National Research Council, 1996). For the tumor model preparation, ca. $3x10^5$ TS/a breast cancer cells were suspended in 0.1 mL of PBS and subcutaneously injected in the flank of mice (n = 3 for each tested group). Before the implantation, mice were anesthetized by intramuscular injection of tiletamine/zolazepam (Zoletil 100; Virbac, Milan, Italy) 20 mg/kg plus xylazine (Rompun; Bayer, Milan, Italy) 5 mg/kg by using a 27-G syringe. Changes in tumor size by caliper were monitored weekly. 2 weeks after tumor cells implantation the mean tumour volume is ca. 400±50 mm^3 and experiments were carried out. 50 µL of each hydrogel were intratumorally implanted by using a 27-G syringe and CEST-MR images were recorded. At the end of the experiments, mice were sacrificed by cervical dislocation in agreement with ethical guidelines.

4.3.15 MRI and data analysis

Bruker Avance 300 spectrometer equipped with a Micro 2.5 microimaging probe was used to acquire MR images of phantoms and mice at 7 T. T_{2w} images were acquired by using a standard T_{2w} RARE (Rapid Acquisition with Refocused Echoes) sequence. Experimental settings were: Repetition Time (TR) 5000 ms, Echo Time (TE) 5.5 ms, RARE factor 24, Number of averages 4, 128×128 isotropic acquisition matrix with a FOV of 30 mm and a slice thickness of 1 mm. Z-spectra were acquired by using a typical RARE spin–echo sequence with the following parameters: TE 3 ms, TR 5 s, RARE factor 32, Number of averages 1. An isotropic 64×64 acquisition matrix with a FOV of 30 mm and a slice thickness of 1 mm was used. A saturation scheme, consisting of a continuous rectangular wave pulse 2 s with a radiofrequency intensity of 3 μT, preceded the whole sequence. The range of frequency-offset range investigated was ± 20 ppm. The Z-spectra were interpolated by smoothing splines to identify the zero-offset on a pixel-by-pixel basis of the bulk water and then to assess the correct ST % value over the entire range of investigated frequency offsets. A custom-made analysis algorithm, compiled in Matlab (Mathworks Inc., Natick, MA), was used. CEST effect was calculated through the following formula:

$$ST\% = (1-M_S/M_0)\times 100 \qquad (4.7)$$

where M_S is the intensity of the bulk water NMR signal after the on-resonance saturation on the mobile proton pool of iopamidol ($\Delta\omega$), and M_0 is the intensity of the bulk water NMR signal after the contralateral frequency ($-\Delta\omega$). The resonance of the bulk water protons was set to 0.

4.4 RESULTS AND DISCUSSION

4.4.1 Formulation and characterization of hydrogels loaded with Gd(III) complexes

Due to the presence of a positively charged lysine residue in their sequence, acetyl (Ac-) and fluorenylmethyloxycarbonyl (Fmoc-) K1, K2 and K3 peptide hydrogelators were selected to promote the physical encapsulation of negatively charged T_1-CAs like $[Gd(AAZTA)]^-$ and $[Gd(BOPTA)]^{2-}$ within the network. The choice of these two Gd-complexes arises from the purpose of obtaining both the best encapsulation ratio and the highest relaxivity (r_1) value. To satisfy the first target, two contributes were taken into account: i) the electrostatic interactions between the peptide moieties and the two differently charged Gd(III) complexes and ii) the possibility to establish further interactions between the aromatic groups of the components (π-π stacking interactions between the benzene ring on the backbone of BOPTA ligand with the Fmoc protecting group on the peptide derivatives). The influence of these interactions on the efficacy of the hydrogel as supramolecular CA was studied by comparison of Fmoc-K2 hydrogels loaded alternatively with $[Gd(BOPTA)]^{2-}$ and $[Gd(DTPA)]^{2-}$. $[Gd(AAZTA)]^-$ was chosen because of its high relaxivity value (r_1=6.6 mM^{-1} s^{-1} at 32 MHz and 298 K) as free complex, which is due to the presence of two water molecules coordinated to the metal ion in the inner sphere. For $[Gd(BOPTA)]^{2-}$- and $[Gd(DTPA]^{2-}$-loaded HGs, hydrogel formation was triggered by the simple addiction of 50 µL of the 30 mmol/L complex solution to the 2 wt% peptide one. This effect was ascribed to the presence of two residual negative charges on the complex. On the other hand, $[Gd(AAZTA)]^-$ only presents one negative charge, which was not enough to prompt the gelation in the same conditions experimented with the two other complexes. For this reason, $[Gd(AAZTA)]^-$ loaded HGs formulations were obtained by dissolving the peptide powder in a 5 mmol/L complex solution and then by adding 50 µL

of phosphate buffer to balance the positive charges of the lysine residue. Inverted test tubes experiments were carried out to visualize hydrogel formation (**Figure 4.4**). As observed in the figure, not all the peptides are able to generate self-supporting hydrogels in the presence of one or more complexes: Ac-K3 does not form gels with both complexes and Fmoc-K1 is not able to gel in the presence of $[Gd(AAZTA)]^-$ and seems to form very soft, not completely supporting gels when loaded with $[Gd(BOPTA)]^{2-}$.

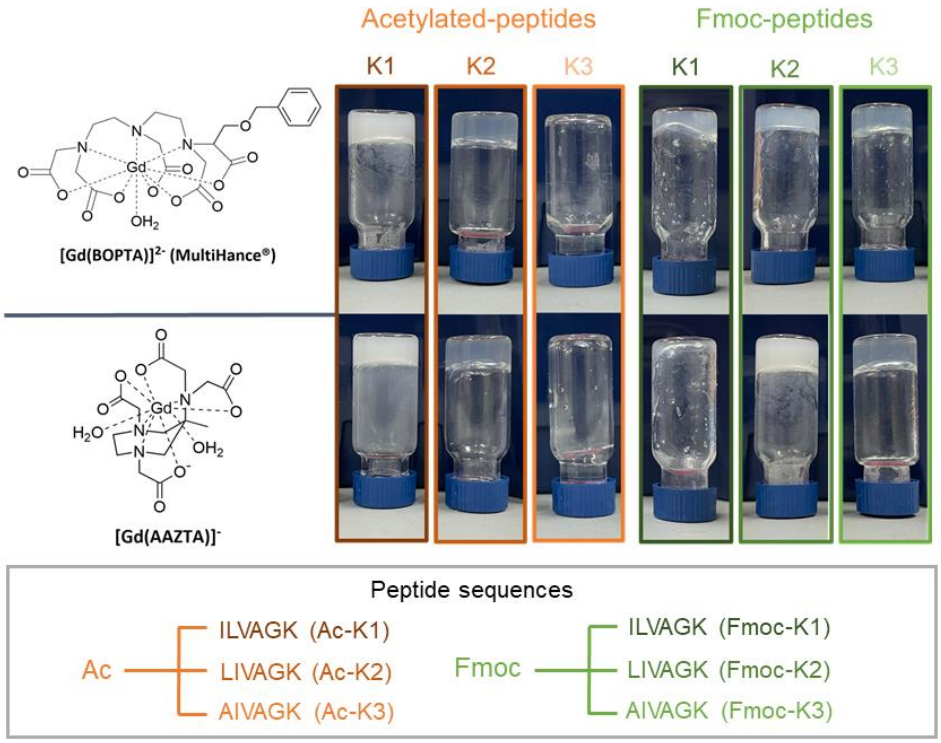

Figure 4.4: Schematic representation of peptide sequences according to the one code letter practice and of $[Gd(BOPTA)]^{2-}$ and $[Gd(AAZTA)]^-$ complexes. The inverted test tube picture is reported for each peptide/complex combination.

The inability of Fmoc-K1 sequence to form a hydrogel network, able to appropriately support the encapsulation of both the complexes, can be explained on the basis of its low storage modulus (G') of 557 Pa as empty

matrix, which identified this peptide as the softer of the series. However, the encapsulation of $[Gd(BOPTA)]^{2-}$ in Fmoc-K1 is not completely forbidden thanks to the occurring interactions between the aromatic ring of the ligand and the Fmoc group.

Table 4.2: Degradation degree, expressed as percentage ratio (ΔW), storage modulus (G'), loss modulus (G'') and Tanδ for the different paramagnetic formulations. Rheological parameters of empty hydrogels are also reported for comparison.

	SAMPLE		ΔW(%)	G' (PA)	G''(PA)	TAN(Δ)
Fmoc-K1	Fmoc-K1		---	557	40	13.9
	Fmoc-K1 $[Gd(BOPTA)]^{2-}$	+	3.74	11	2	5.5
	Fmoc-K1 $[Gd(AAZTA)]^{-}$	+		-	-	-
Fmoc-K2	Fmoc-K2		---	925	89	10.4
	Fmoc-K2 $[Gd(BOPTA)]^{2-}$	+	2.65	57	6	9.5
	Fmoc-K2 $[Gd(AAZTA)]^{-}$	+	4.91	500	102	4.9
	Fmoc-K2 $[Gd(DTPA)]^{2-}$	+	---	36	3	12
Fmoc-K3	Fmoc-K3		---	2526	273	9.2
	Fmoc-K3 $[Gd(BOPTA)]^{2-}$	+	1.08	425	51	8.3
	Fmoc-K3 $[Gd(AAZTA)]^{-}$	+	0.01	4210	508	8.3
Ac-K1	Ac-K1		---	306	40	7.6
	Ac-K1 $[Gd(BOPTA)]^{2-}$	+	0.20	18280	3826	4.8
	Ac-K1 + $[Gd(AAZTA)]^{-}$		0.67	42583	5182	8.2
Ac-K2	Ac-K2		---	2677	192	13.9
	Ac-K2 $[Gd(BOPTA)]^{2-}$	+	7.79	520	102	5.1
	Ac-K2 + $[Gd(AAZTA)]^{-}$		2.81	11018	2304	4.8

On the contrary, the complete inability of Ac-K3 sequence to gel could be probably explained on the basis of the presence of an alanine residue in place of a leucine or an isoleucine, together with the absence of the fluorenyl group. These two chemical differences have been recognized to

hinder a good packaging between the components. The stability of filled HGs was also evaluated over time by incubation with the Ringer's solution at 37°C. After 20 days, their weight loss was evaluated and results, reported in **Table 4.2** as ΔW(%), pointed out that all the hydrogels are stable in the explored conditions (weight loss for all the hydrogels < 7.79%).

4.4.2 Structural characterization of hydrogels loaded with Gd(III) complexes: SEM and Rheology

A structural characterization of hydrogels loaded with the complexes was assessed by Scanning Electron Microscopy (SEM) technique. Micrographs of selected samples (Fmoc-K1, Fmoc-K2 and Fmoc-K3 encapsulating $[Gd(BOPTA)]^{2-}$; **Figure 4.5A-C**) reveal a structuration in fibrillary interconnected networks, which is characteristic of peptide-based hydrogels. This organization was also evidenced for the corresponding empty formulations, letting us to conclude that the insertion of the metal complex does not affect the overall morphology. Similar results were obtained also for all the other loaded hydrogels (data not shown). Rheological analyses were performed to acquire information about the mechanical features of the samples. Results (**Figure 4.5D,E** and **Table 4.2**) are reported in terms of G' (storage modulus), G'' (loss modulus) and tanδ (tangent of the phase angle). All the samples possess value of tanδ > 1 and G' > G''. These results analytically confirm the presence of a gel state and are consistent with materials that behave like an elastic solid. The encapsulation of $[Gd(BOPTA)]^{2-}$ in Fmoc-K matrices generates a sensible decrease of the G' modulus, which, as previously mentioned, is particularly relevant for Fmoc-K1 (around 50-fold decrease). This general trend may be ascribed to the chemical structure of the Gd(III) chelate, whose aromatic ring probably alters the interaction pathways of the peptide component, interfering with Fmoc/Fmoc interactions responsible of the aggregative process. This hypothesis is supported by results obtained with the Ac-K

series, in which an increase in the G' value is observed after the entrapment of $[Gd(BOPTA)]^{2-}$. G' value for Ac-K1 hydrogel is around 60 fold higher for the $[Gd(BOPTA)]^{2-}$ loaded sample than for the empty one.

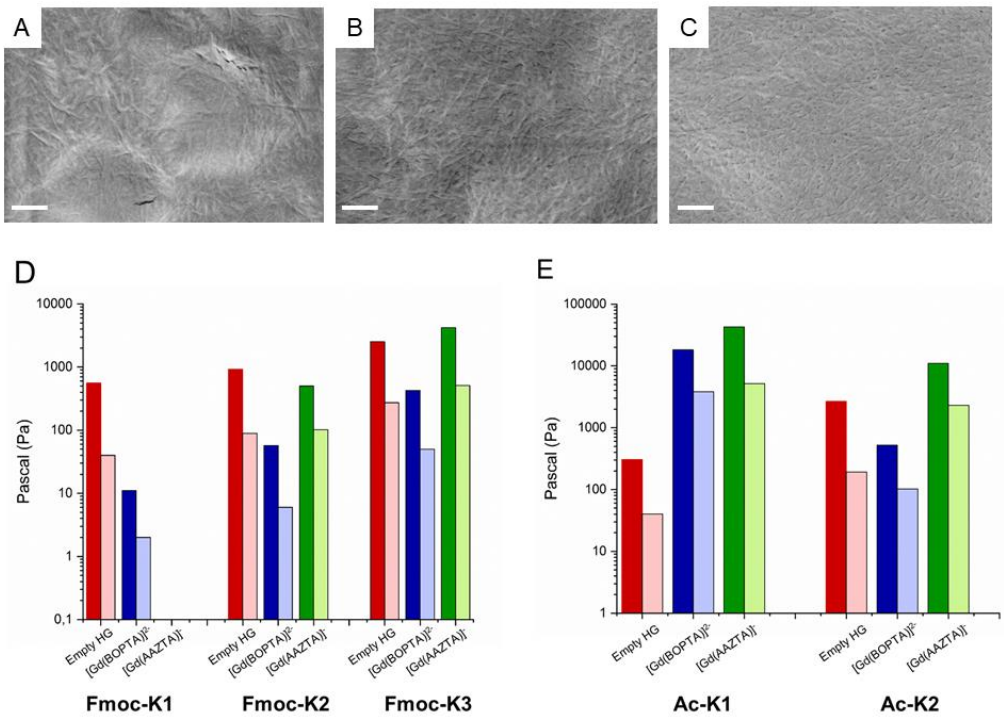

Figure 4.5: Structural characterization of hydrogels filled with Gd-complexes. SEM images of Fmoc-K1 (A), Fmoc-K2 (B), and Fmoc-K3 (C) loaded with $[Gd(BOPTA)]^{2-}$ (scale bar = 500 nm). Histograms summarize rheological results from analysis performed on hydrogels loaded with Gd-complexes. D) Fmoc-peptides; E) Ac-peptides. Graph report both G' (dark bar) and G" (light bar) moduli of each time sweep experiment (20 min, strain of 0.1%, frequency 1 Hz). Values are expressed in Pascal (Pa) in logarithmic scale.

On the contrary, $[Gd(AAZTA)]^{-}$ encapsulation induces an increase of the mechanical rigidity in Fmoc-K3 (G' value from 2526 Pa to 4210 Pa for empty and filled, respectively) and a decrease (~ 2-fold) in Fmoc-K2 (G' value from 500 Pa to 925 Pa). Similarly to $[Gd(BOPTA)]^{2-}$, also $[Gd(AAZTA)]^{-}$

entrapment causes an increase in the G' values in the Ac-K series, especially evident for Ac-K1, where an increase of G' of 140-fold is observed.

4.4.3 Hydrogel loaded with Gd(III) complexes relaxivity studies

The relaxometric properties of the supramolecular CAs were investigated by the measurement of the relaxivity values as a function of the applied magnetic field strength in the 0.01 - 120 MHz range, at three different temperatures (283, 298 and 310 K). Results were then compared to the r_1 values of free chelates in aqueous solution, obtained at 298 K and neutral pH. The ^{1}H NMRD profile of Fmoc-K2+[Gd(BOPTA)]$^{2-}$ showed a field-dependence relaxivity that is typical of matrices containing Gd(III) chelates with restricted mobility, with a marked hump centered around 20 MHz. [234] The π-π stacking interactions occurring between the aromatic group of the BOPTA ligand and the Fmoc-K2 functionality is responsible of both the profile shape and the high r_1 values observed, which is around 5 times higher for the hydrogel than for the free complex, at 20 MHz and 298 K (**Figure 4.6A** and **4.7**). Differently from what is typically observed for negatively charged Gd(III) chelates, the relaxivity of the hydrogel increases with the temperature. [235] This behavior suggests the occurrence of a slow water exchange process, which is probably related to a reduced water diffusion within the peptide network. Relaxometric features of Fmoc-K2+[Gd(DTPA)]$^{2-}$ were investigated to confirm the importance of the aromatic interactions inside the [Gd(BOPTA)]$^{2-}$ loaded matrix. The Fmoc-K2+[Gd(DPTA)]$^{2-}$ hydrogel displayed a ^{1}HNMRD profile with a less pronounced peak at high magnetic fields and lower relaxivity values (**Figure 4.6B** and **4.7**). These differences were ascribed to a weaker interaction of the complex with the peptide matrix. Nevertheless, also for this hydrogel, an increase in relaxivity at 20 MHz and 298 K respect to the free [Gd(DTPA)]$^{2-}$ in aqueous solution was observed (around 3 times higher).

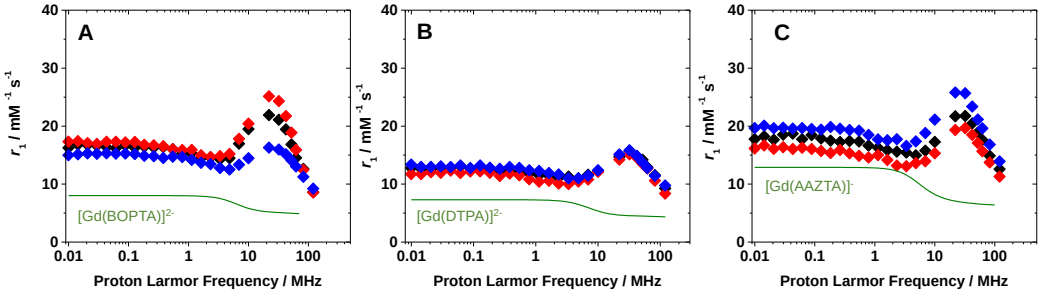

Figure 4.6: ^{1}H NMRD profiles of Fmoc-K2+[Gd(BOPTA)]$^{2-}$ (A), Fmoc-K2+[Gd(DTPA)]$^{2-}$ (B) and Fmoc-K2+[Gd(AAZTA)]$^{-}$ (C) at 283 (blue), 298 (black) and 310 K (red). Profiles of the corresponding chelates in aqueous solution are also reported as solid lines.

Although r_1 does not increase with the temperature, the water exchange regime is still slow and limited by the diffusion processes. ^{1}H NMRD profiles of the Fmoc-K2 peptide hydrogel formulated in the presence of the bis-hydrated [Gd(AAZTA)]$^-$ complex were collected. For this sample, an increment of the r_1 values at 20 MHz with respect to the pure complex was still observed, but the r_1 decreases with increasing temperature, thus demonstrating that the water exchange process is fast enough not to limit relaxivity (**Figure 4.6C**). Some hypotheses were formulated to explain the different water dynamics in the various hydrogels: i) localization of the complexes hydrogel sites characterized by different accessibility to water; ii) differences in the water network organization for the three hydrogels; iii) influences of the mechanical strenght of the matrix loaded with different chelates. One or more of these conditions can occur simultaneously and result from the high complexity of these systems. For this reason, the application of well-known models, describing the paramagnetic relaxation and assessing the molecular parameters responsible for the relaxivity values, has no physical meaning. Moreover, the modification of the peptide hydrogelator sequence can dramatically affect the relaxometric properties of the final hydrogel.

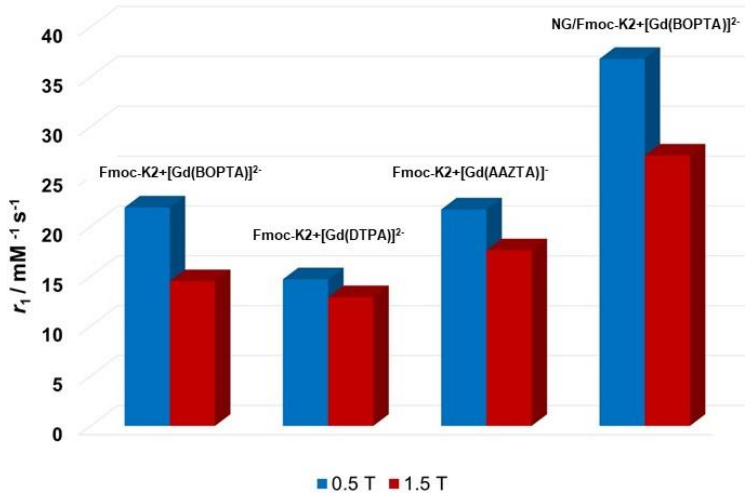

Figure 4.7: Comparison of the r_1 values at 0.5 and 1.5 T (298 K) for Fmoc-K2+[Gd(BOPTA)]$^{2-}$, Fmoc-K2+[Gd(DTPA)]$^{2-}$ and Fmoc-K2+[Gd(AAZTA)]$^{-}$ and NG/Fmoc-K2+[Gd(BOPTA)]$^{2-}$.

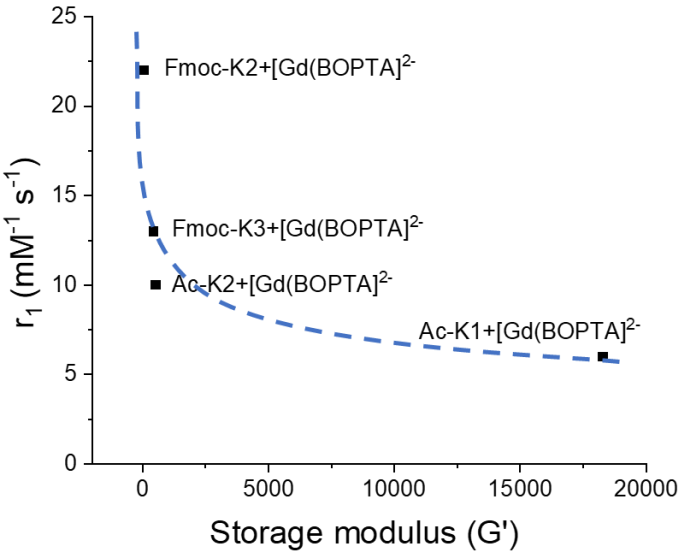

Figure 4.8: Dependence of r_1 values (20 MHz and 298K) with the storage modulus (G') of hydrogels based on [Gd(BOPTA)]$^{2-}$.

Indeed, a marked decrease of r_1 is observed moving from Fmoc-K2 to the more rigid Fmoc-K3 hydrogels loaded with the different complexes (**Figure 4.5**). .A similar tendency is also evident for Ac-K1 and Ac-K2 peptides (**Figure 4.5**). For HGs embedding $[Gd(BOPTA)]^{2-}$, a general decrease of r_1 with increasing of the storage modulus is observed and clearly highlighted in **Figure 4.8**.

4.4.4 Fmoc-K2+$[Gd(BOPTA)]^{2-}$) Nanogel: formulation and structural and relaxivity characterization

Since the best results were obtained with Fmoc-K2+$[Gd(BOPTA)]^{2-}$ hydrogel, the corresponding nanogel was formulated using the top-down approach. The hydrogel was subjected to submicronization carried out in the presence of two commercial surfactants TWEEN® 85 (Polyoxyethylenesorbitan Trioleate) and SPAN® 85 (Sorbitane trioleate), which have the role to stabilize the final suspension. The ratio between TWEEN®85 and SPAN®85 was chosen to be 89/11 w/w, which allowed obtaining an HLB value of 10, previously emerged as the optimal one for similar peptide-based NG formulations. Gd(III)-complex loaded NG was purified from free $[Gd(BOPTA)]^{2-}$ by gel filtration and the encapsulated fraction of the complex (final concentration 0.4 mmol/L) was estimated by inductively coupled plasma-mass spectrometry (ICP-MS). The mean diameter and the polydispersity index of the nanogel, (~190 nm and 0.272, respectively), reported in **Figure 4.9A** and assessed by DLS technique, are compatible with the possibility of a systemic administration. Circular Dichroism (CD) studies were performed to obtain structural information. The shape of the CD profile is comparable to the corresponding Fmoc-K2 hydrogel and upholds that the structuration of the HG is preserved also in its nano-derivative (**Figure 4.9B**). The positive band centered at 212 nm is attributable to $n\rightarrow\pi^*$ transitions occurring in the β-sheet organization, while the one around 250 nm is associated with the π–π^* transition of fluorenyl

moiety. Moreover, the nanogel presents a unique negative band at ~230 nm, which has been demonstrated to be due to the presence of strongly twisted β-sheets in which both the inter-β-sheet distance and the solvent exposure increase. This higher accessibility to water is well justified by the concept of nanogels itself, in which the fibrillary network of HGs is preserved and the surface area increases.

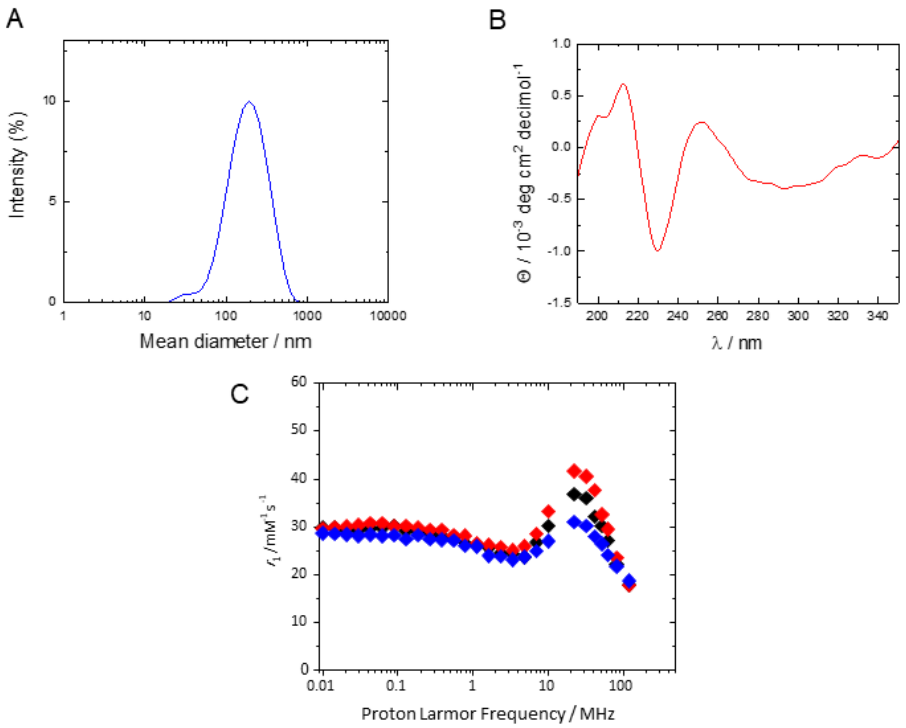

Figure 4.9: Structural and relaxometric characterization of Fmoc-K2 NG loaded with $[Gd(BOPTA)]^{2-}$. (A) CD profile; (B) Dynamic light scattering profile (C) ^{1}H NMRD profile at 283 (blue), 298 (black) and 310 K (red).

The relaxometric behavior of an aqueous suspension of nanogel was investigated. The shape of the ^{1}H NMRD profile and the temperature dependence of the r_1 values are comparable to those observed for the corresponding hydrogel, thus highlighting that a strong limitation of the

mobility of the complex still occurs even after the submicronization process. Furthermore, it has been evidenced a significant increase of the relaxivity value at 20 MHz and 298 K respect to the corresponding hydrogel. This value reaches 36.8 mM^{-1} s^{-1} and provides evidence of a different degree of rotational freedom of the complexes within the polymeric matrix.

4.4.5 Formulation and characterization of hydrogels loaded with iopamidol

Ac-K1 and Ac-K2 hydrogels were selected as matrices for the encapsulation of iopamidol (**Figure 4.10**), an iodinated clinically approved contrast agent for x-ray computed tomography, herein used for its capability to be used as CEST-MRI contrast agent. Indeed, it has been shown that it displays proper signals resonating at 1.5, 4.3 and 5.5 ppm from bulk water signals. The first signal is ascribed to the hydroxyl groups and is pH-independent, while the other two ones belong to the amide protons and thus their CEST contrast is pH-dependent and has been employed for i*n vivo* mapping of extracellular/extravascular pH. Hydrogels were prepared by dissolving peptide powder in a water solution of 260 mmol/L iopamidol and then adding the phosphate buffer to reduce the electrostatic repulsive forces and so to trigger the gelation process (final peptide and iopamidol concentrations 1.7 wt% and 223 mmol/L, respectively). The effect of the physical entrapment of iopamidol in the hydrogel in terms of viscoelastic behavior was evaluated by oscillatory rheological studies. Results are reported as G' (storage modulus) and G'' (loss modulus) in **Figure 4.11A**). An oscillation strain sweep (at a frequency of 1.0 Hz) and a frequency sweep (at 0.1 % strain) tests were carried out. The linear viscoelastic region (LVE region), was found to be in 0.01-2.0 % strain range for the examined hydrogels. The time sweeps were acquired for 20 minutes at frequency of 1.0 Hz and at 0.1 %. The hydrogel state was confirmed by the tanδ (G'/G'') values, exceeding 1 for both the matrices (tanδ Ac-K1 = 3.03 and tanδ Ac-K2 = 5.02).

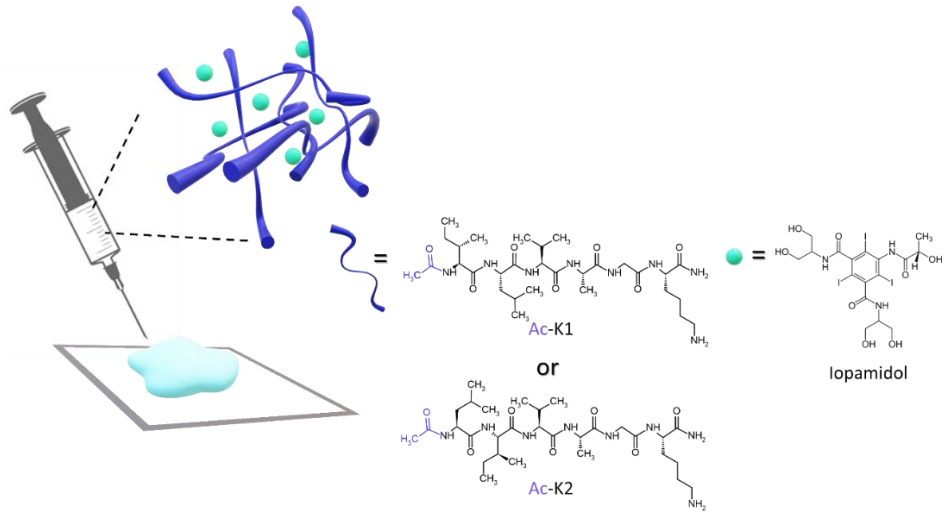

Figure 4.10: Chemical structures of the cationic hexapeptides and iopamidol, used for the formulation of the hydrogels.

Results pointed out that iopamidol-loaded Ac-K2 hydrogel displayed a more pronounced viscoelastic behavior, as also verified comparing the G' values of the two formulations. (G'= 251 Pa/G''= 50 Pa and G'= 203 Pa/G''= 67 Pa for Ac-K2 and Ac-K1, respectively). The generally low G' values are indicative of the soft nature of these matrices and suggest a good suitability for *in vivo* injectable preparations. Moreover, the iopamidol entrapment resulted into a decrease of the rigidity with respect to the empty systems, especially for Ac-K2 based hydrogels (G' values of 306 Pa and 2677 Pa for pure Ac-K1 and Ac-K2 in the same experimental conditions). This effect may be referred to a change in the non-covalent interactions of the fiber entanglement with a consequence decrease of the physical and reversible cross-networking. The injectability of the hydrogels was evaluated as follows: after being extruded on a plastic support through the needle of a 27-G syringe, the metastatic solution was found able to re-form a hydrogel in few minutes, thus demonstrating its self-healing properties (**Figure 4.11B**).

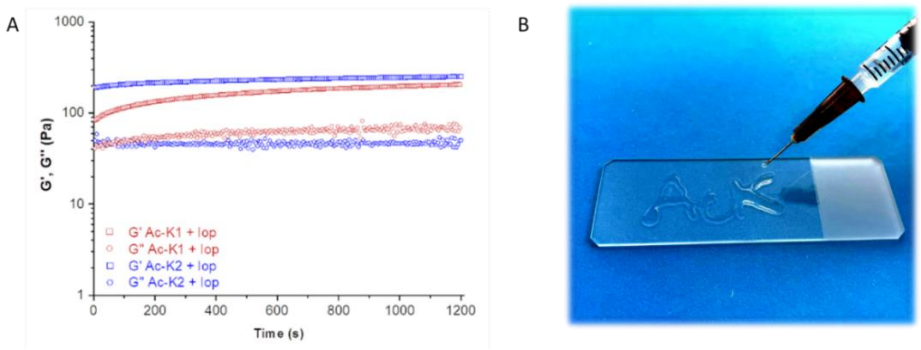

Figure 4.11: (A) Rheological characterization of Ac-K1 and Ac-K2 loaded with iopamidol: time sweep rheological analysis of hydrogels reported as storage modulus (G') and loss modulus (G"); (B) Test of syringability.

4.4.6 *In vitro* release of iopamidol

To study the *in vitro* release of Iopamidol from the most rigid system (Ac-K1 one), the hydrogel was put in contact with phosphate buffer and subjected to repeated sampling of supernatant, which was substituted each time with PBS fresh solution (up to 3 days).

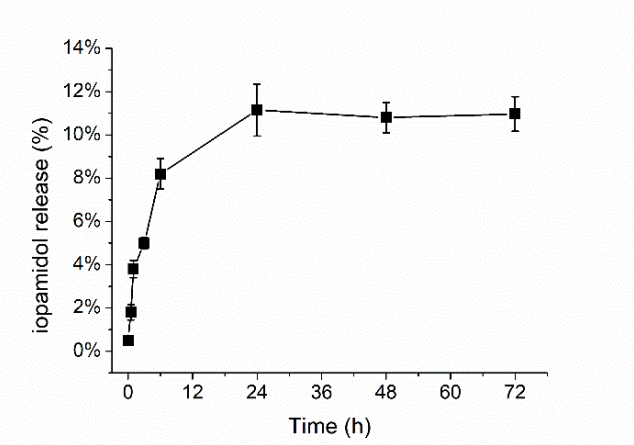

Figure 4.12: In vitro release of iopamidol from Ac-K1 hydrogel. Experimental conditions are reported in Experimental section.

The agent released in each fraction was quantified using UV-vis measurements carried out at λ=240 nm. As reported in **Figure 4.12**, the maximum of release (*ca.* 12%) has been reached after 24 h from the start of the experiment. However, the tested conditions allowed a percentage release that is very far from the 100%, thus suggesting a very stable loading of the molecule. Hence, this system has been demonstrated to be suitable as scaffold for the topic administration of drugs and for monitoring the in *vivo* release.

4.4.7 Cell viability studies for hydrogels loaded with iopamidol

In vitro toxicity of the supramolecular CEST agents was assessed by MTT assay conducted on three cell lines: i) GL261 (murine glioma), ii) TS/a (murine breast carcinoma) and iii) 3T3-NIH (murine fibroblasts). Cells were incubated for 24 h in the presence of cell medium previously conditioned by the hydrogel formulation.

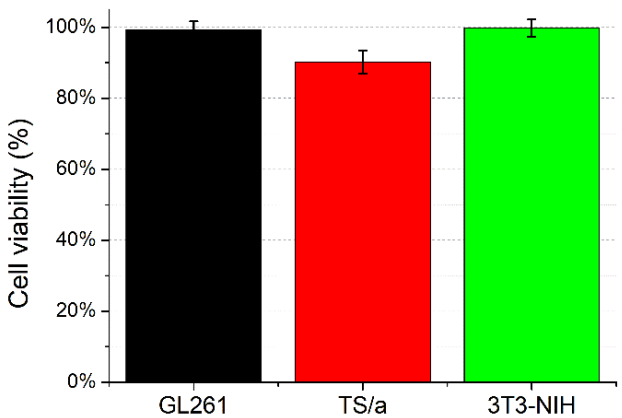

Figure 4.13: Cell viability assessed by MTT assay for GL261, TS/a, and 3T3-NIH cells incubated in presence of culture media conditioned with Ac-K1 (3% *w/v*) hydrogel.

The pre-treatment of the hydrogel with the cell medium allows the release from the matrix of toxic monomers that could affect the safety of the system.

As reported in **Figure 4.13**, Ac-K1 system can be considered no toxic on all the explored cell lines, since cell viability was found to be ca. 100% for GL261 and 3T3-NIH and ca. 90% for TS/a cells. Similar results were obtained for iopamidol-loaded Ac-K2 hydrogel (data not shown).

4.4.8 *In vitro* and *in vivo* imaging of Ac-K hydrogels by CEST-MRI

Z- and ST-spectra of Ac-K1 or Ac-K2 hydrogels loaded with iopamidol are reported in **Figure 4.14**. As shown, Ac-K1 and Ac-K2 hydrogels loaded with iopamidol display the typical CEST pattern of iopamidol, with ST% contrast higher than 50%. The control iopamidol-free Ac-K1 hydrogel does not display any significant CEST contrast. Since the CEST effect is slightly higher for Ac-K1 sample, this formulation was chosen for the following studies. Some differences were evidenced between the iopamidol loaded into the gel matrix and the free molecule: a ST% reduction upon saturation at 1.5 and 5.5 ppm was observed and credited to small changes in the exchange rate of the mobile protons of the agent and/or to the slightly lower pH value of the free iopamidol solution. Indeed, lowering pH narrows the CEST peaks. The *proof of concept* of the feasibility of using these systems *in vivo* has been pursued by intratumoral injection of scaffolds in tumor-bearing Balb/c mice (N=3). For this purpose, TS/A breast cancer cells were subcutaneously injected in the flank mice, which were used for the experiments when tumors reached the volume of *ca.* 400 $\pm$ 50mm^3. At this time, 50 µL of hydrogels were injected in the tumor regions and images have been recorded before and after hydrogel injection. The *wash-out* kinetics of iopamidol from the hydrogel was assessed through CEST-MRI. T_{2w} and CEST images acquired after pre-saturation at 4.2 and 5.5 ppm of a representative mouse treated with the Ac-K1 hydrogel are reported in **Figure 4.15A**. MR images were acquired at variable times from the hydrogel injection, from t=15 min to t=24h. A decrease of ST% is observed over time for the typical iopamidol pH-dependent CEST signals.

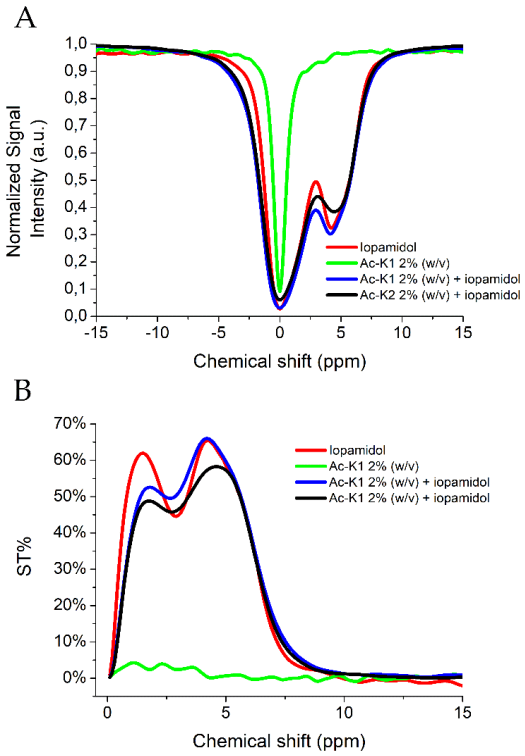

Figure 4.14: Z- (A) and ST%- (B) spectra of Ac-K1 (blue) or Ac-K2 (black) hydrogels loaded with iopamidol (233 mmol/L) at physiological pH compared with iopamidol in solution (red, 260 mmol/L, pH=7.0) or iopamidol-free Ac-K1 hydrogel (green).

ST% spectra and ST% plotted as function of the time are reported in **Figure 4.15B,C**. For the three mice, the signals at 4.2 and 5.5 ppm appear quite similar, while the signal at 1.5 ppm undergoes a higher variability (data not shown). This can be ascribed to the fact that this peak is partially related to iopamidol structure and partially due to endogenous CEST signals (amide, amines, sugars, creatine, etc.), whose *in vivo* variability is high. The exponential decay for the ST signals of Iopamidol at 1.5, 4.2 and 5.5 ppm for the three mice was reported as Mean ± SD in **Figure 4.15D**. A similar decay trend is observed for the two pH-dependent peaks, whereas a slower decay is present for the pH-independent CEST signal at 1.5 ppm.

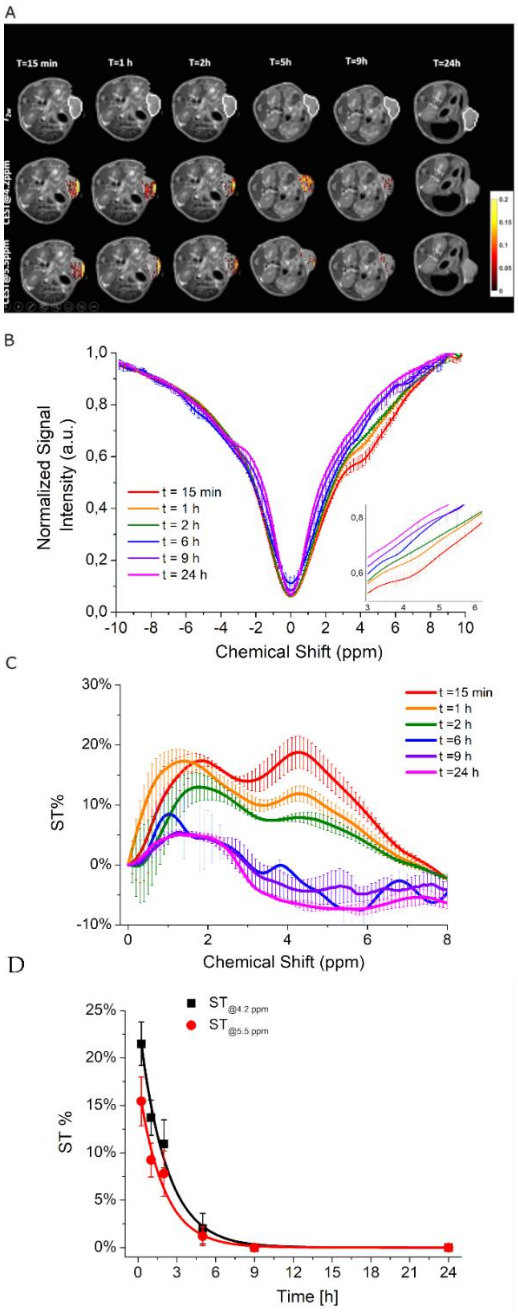

Figure 4.15: (A) T_{2w}, $CEST_{@4.2ppm}$, and $CEST_{@5.5ppm}$ MR images of a representative mouse upon intratumor administration of iopamidol-loaded Ac-K1 hydrogel at different time points (from 15 min to 24 h). (B) Corresponding ST% spectra. (C) ST% at different saturation frequency vs. time of the ROI drawn in the tumour region (mean ± SD for the three analysed mice). (D) exponential decay rate for $CEST_{@4.2ppm}$, and $CEST_{@5.5\ ppm}$ (mean ± SD for the three analysed mice).

[179] Lauterbur, P. C. *Nature* **1973**, 242, 1.

[180] Vijayalaxmi; Fatahi, M.; Speck, O. *Mutation Research* **2015,** 764, 51-63.

[181] Pierre, V. C.; Allen, M. J. Contrast agents for MRI: experimental methods, *RSC* **2018.**

[182] Xiao, Y.; Paudel, R.; Liu, J.; Ma, C.; Zhang, Z.; Zhou, S. *Int. J. Mol. Med.* **2016**, 38, 1319-1326.

[183] Weinmann, H. J.; Mühler, A.; Radüchel, B. Biomedical Magnetic Resonance Imaging and Spectroscopy *John Wiley & Sons Ltd., Chichester* **2000.**

[184] Weissleder, R.; Papisov, M. *Rev. Magn. Reson. Med.* **1992**, 4, 1-20.

[185] Young, I. R.; Clarke, G. J.; Bailes, D. R.; Pennock, J. M.; Doyle, F. H.; Bydder, G. M. *J. Comput. Tomogr.* **1981**, 5, 543-547.

[186] Carr, D. H.; Brown, J.; Bydder, G. M.; Weinmann, H. J.; Speck, U.; Thomas, D. J.; Young, I. R. *Lancet* **1984**, 1, 484-486.

[187] Tweedle, M. F.; Runge, V. M. *Drugs Future* **1992**, 17, 187-190.

[188] Banci, L.; Bertini, I.; Luchinat, C. Nuclear and Electronic *Relaxation, VCH, Weinheim* **1991**.

[189] Botta, M. *Eur. J. Inorg. Chem.* **2000**, 3, 399-407.

[190] Seibert, J. A.; Morin, R. L. *Pediatr. Radiol.* **2011**, 41(5), 573-581.

[191] Peters, A. J.; Huskens, J.; Raber, D. J. *Prog. in NMR Spectrosc.* **1996**, 28, 283-350.

[192] Aime, S.; Botta, M.; Fasano, M.; Terreno, E. *Chem. Soc. Rev.* **1998**, 27, 19-29.

[193] Di Gregorio, E.; Gianolio, E.; Stefania, R.; Barutello, G.; Digilio, G.; Aime, S. *Anal. Chem.* **2013**, 85, 5627-5631.

[194] Marckmann, P.; Skov, L.; Rossen, K.; Dupont, A.; Damholt, M. B.; Heaf, J. G.; Thomsen, H. S. *J. Am. Soc. Nephrol.* **2006**, 17, 2359-2362.

[195] Gianolio, E.; Bardini, P.; Arena, F.; Stefania, R.; Di Gregorio, E.; Iani, R.; Aime, S. *Radiology* **2017**, 285, 839-849.

[196] Accardo, A.; Tesauro, D.; Aloj, L.; Pedone, C.; Morelli, G. Coordination Chemistry Reviews **2009**, 253, 2193-2213.

[197] Que, E. L.; Chang, C. J. *J. Am. Chem. Soc.* **2006**, 128, 15942-15943.

[198] Anelli, P. L.; Bertini, I.; Fragai, M.; Lattuada, L.; Luchinat, C.; Parigi, G. *Eur. J. Inorg. Chem.* **2000**, 625-630.

[199] Bull, S. R.; Guler, M. O.; Bras, R. E.; Maede, T. J.; Stupp, S. I. *Nano Lett.* **2005**, 5, 1-4

[200] Battistini, E.; Gianolio, E.; Gref, R.; Couvreur, P.; Fuzerova, S.; Othman, M.; Aime, S.; Badet, B.; Durand, P. *Chem. Eur. J.* **2008**, 14, 4551-4561.

[201] Aime, S.; Botta, M.; Garino, E.; Geninatti Crich, S.; Giovenzana, G.; Pagliarin, R.; Palmisano, G.; Sisti, M. *Chem. Eur. J.* **2000**, 6, 2609-2617.

[202] Caravan, P.; Cloutier, N. J.; Greenfield, M. T.; McDermid, S. A.; Dunham, S. U.; Bulte, J. W. M.; Amedio Jr., J. C.; Looby, R. J.; Supkowski, R. M.; Horrocks, W. D.; McMurryand, T. J.; Lauffer, R. B. *J. Am. Chem. Soc*. **2002**, 124, 3152.

[203] Bosman, A. W.; Janssen, H. M.; Meijer, E. W. *Chem. Rev.* **1999**, 99, 1665.

[204] Ladd, D. L.; Hollister, R.; Peng, X.; Wei, D.; Wu, G.; Delecki, D.; Snow, R. A.; Toner, J. L.; Kellar, K.; Eck, J.; Desai, V. C.; Raymond, G.; Kinter, L. B.; Desser, T. S.; Rubin, D. L. *Bioconjugate Chem*. **1999**, 10, 361.

[205] Laus, S.; Sitharaman, B.; Toth, E.; Bolskar, R. D.; Helm, L.; Wilson, L. J.; Merbach, A. E. *J. Phys. Chem. C* **2007**, 111, 5633

[206] Hartman, K. B.; Laus, S.; Bolskar, R. D.; Muthupillai, R.; Helm, L. M.; Toth, E.; Merbach, A. E.; Wilson, L. *J. Nano Lett.* **2008**, 8, 415

[207] Geninatti Crich, S.; Barge, A.; Battistini, A. E.; Cabella, C.; Coluccia, S.; Longo, D.; Mainero, V.; Tarone, G.; Aime, S. *J. Biol. Inorg. Chem.* **2005**, 10, 78-86.

[208] Accardo, A.; Tesauro, D.; Roscigno, P.; Gianolio, E.; Paduano, L.; D'Errico, G.; Pedone, C.; Morelli, G. *J Am Chem Soc.* **2004**, 126(10), 3097-3107.

[209] Cittadino, E.; Botta, M.; Tei, L.; Kielar, F.; Stefania, S.; Chiavazza, E.; Aime, S.; Terreno, E. *Chempluschem.* **2013**, 78(7), 712-722.

[210] Diaferia, C.; Gianolio, E.; Accardo, A. *J. Pept. Sci.* **2019**, 25, e3157.

[211] Gallo, E.; Diaferia, C.; Di Gregorio, E.; Morelli, G.; Gianolio, E.; Accardo, A. *Pharmaceuticals (Basel).* **2020**, 13(2), 19.

[212] Ward, K. M.; Aletras, A. H.; Balaban, R. S. *J. Magn. Reson.* **2000**, 143(1), 79-87.

[213] Terreno, E.; Delli Castelli, D.; Aime, S. *Contrast Media Mol. Imaging* **2010**, 5(2), 78–98.

[214] Liu, G.; Moake, M.; Har-el, Y. E.; Long, C. M.; Chan, K. W.; Cardona, A.; Jamil, M.; Walczak, P.; Gilad, A. A.; Sgouros, G.; van Zijl, P. C.; Bulte, J. W.; McMahon, M. T. *Magn. Reson. Med.* 2012, 67 (4), 1106-1113.

[215] Liu, G.; Song, X.; Chan, K. W.; McMahon, M. T. *NMR Biomed.* **2013**, 26(7), 810-828.

[216] Goffeney, N.; Bulte, J. W.; Duyn, J.; Bryant, L. H.; van Zijl, P. C*. J Am Chem Soc.* **2001**, 123, 8628-8629.

[217] Aime, S.; Barge, A.; Delli Castelli, D.; Fedeli, F.; Mortillaro, A.; Nielsen, F. U.; Terreno, E. *Magn Reson Med*. **2002**, 47, 639-648.

[218] Schroder, L.; Lowery, T. J.; Hilty, C.; Wemmer, D. E.; Pines, A. *Science.* **2006**, 314, 446-449.

[219] Li, Y.; Sheth, V. R.; Liu, G.; Pagel. M. D. *Contrast Media Mol. Imaging* **2011**, 6(4), 219-228.

[220] Esqueda, A. C.; Lopez, J. A.; Andreu-de-Riquer, G.; Alvarado-Monzon, J. C.; Ratnakar, J.; Lubag, A. J.; Sherry, A. D.; De Leon-Rodriguez, L. M. *Chem. Soc.* **2009**, 131(32), 11387-11391.

[221] Cai, K.; Haris, M.; Singh, A.; Kogan, F.; Greenberg, J. H.; Hariharan, H.; Detre, J. A.; Reddy, R. *Nat. Med.* **2012**, 18(2), 302-306.

[222] Shah, T.; Lu, L.; Dell, K. M.; Pagel, M. D.; Griswold, M. A.; Flask, C. A. *Magn. Reson. Med.* **2011**, 65(2), 432–437.

[223] Zhou, J.; Payen, J. F.; Wilson, D. A.; Traystman, R. J.; van Zijl, P. C. M. *Nat. Med.* **2003**, 9(8), 1085-1090.

[224] Liu, G.; Liang, Y.; Bar-Shir, A.; Chan, K. W.; Galpoththawela, C. S.; Bernard, S. M.; Tse, T.; Yadav, N. N.; Walczak, P.; McMahon, M. T.; Bulte, J. W.; van Zijl, P. C.; Gilad, A. A. *J. Am. Chem. Soc.* **2011**, 133(41), 16326-16329.

[225] Zhou, J.; Tryggestad, E.; Wen, Z.; Lal, B.; Zhou, T.; Grossman, R.; Wang, S.; Yan, K.; Fu, D. X.; Ford, E.; Tyler, B.; Blakeley, J.; Laterra, J.; van Zijl, P. C. *Nat. Med.* **2011**, 17(1), 130-134.

[226] Gilad, A. A.; McMahon, M. T.; Walczak, P.; Winnard, P. T. Jr; Raman, V.; van Laarhoven, H. W.; Skoglund, C. M.; Bulte, J. W.; van Zijl, P. C*. Nat. Biotechnol.* **2007**, 25(2), 217-219

[227] Lubag, A. J.; De Leon-Rodriguez, L. M.; Burgess, S. C.; Sherry, A. D. *Proc. Natl. Acad. Sci. USA* **2011**, 108(45), 18400-18405.

[228] Sun, P. Z.; Wang, E.; Cheung, J. S. *Neuroimage* **2012**, 60(1), 1-6.

[229] Delli Castelli, D.; Dastru, W.; Terreno, E.; Cittadino, E.; Mainini, F.; Torres, E.; Spadaro, M.; Aime, S. *J. Controlled Release* **2010**, 144(3), 271-279.

[230] Aime, S.; Calabi, L.; Biondi, L.; De Miranda, M.; Ghelli, S.; Paleari, L.; Rebaudengo, C.; Terreno, E. *Magn. Reson. Med.* **2005**, 53, 830-834.

[231] Moon, B. F.; Jones, K. M.; Chen, L. Q.; Liu, P.; Randtke, E. A.; Howison, C. M.; Pagel, M. D. *Contrast Media Mol. Imaging* **2015**, 10, 446-455.

[232] Lalli, D.; Carniato, F.; Tei, L.; Platas-Iglesias, C.; Botta, M. *Inorg. Chem.* **2021**, 61, 496-506.

[233] Nanni, P.; De Giovanni, C.; Lollini, P-L.; Nicoletti, G.; Prodi, G. *Clin Expl Metastasis* **1983**, 1(4), 373-380.

[234] Carniato, F.; Tei, L.; Botta, M.; Ravera, E.; Fragai, M.; Parigi, G.; Luchinat, C. *ACS Appl. Bio Mat.* **2020**, 3(12), 9065-9072.

[235] Caravan, P.; Ellison, J.J.; McMurry, T.J.; Lauffer, R.B. *Chem. Rev.* **1999**, 99, 2293-2352.

5. CONCLUSIONS

The objective of this PhD thesis has been the development of novel peptide based nanosystems to use in various nanomedicine fields. HGs and NGs, formulated starting from peptide building blocks, have been proposed and tested for the delivery of drugs and MRI contrast agents and as scaffolds for tissue engineering scopes. The employment of supramolecular platforms as *in vivo* carriers allows achieving several advantages respect to low molecular weight molecules, mainly represented by the selective target reached through the exploitation of the EPR effect, in addition to the increase in solubility, the decrease in toxicity and the protection of the active principle from biodegradation. Moreover, the delivery strategy has shown to provide an increase in the performances of contrast agents imaging. Hydrogel scaffolds have been shown to properly promote the adhesion and growth of cells for tissue engineering scopes. The choice of peptides as building blocks to provide the self-aggregation into the final biomaterial guarantees high biocompatibility and biodegradability. Peptides also present the great advantage to be highly tunable since the modification of the primary sequence dramatically affects the properties of the supramolecular system. At the end of this study several conclusions can be deduced. Reasonings have been divided into three different paragraphers to better clarify the results that have followed the different intentions at the basis of each research line.

5.1 PEPTIDE BASED NANOGELS: FORMULATION PROCEDURE, CELL INTERNALIZATION AND LOADING CAPABILITY

Over the last years, nanogels have been identified as promising platforms for the delivery of APIs such as drugs, contrast agents and nucleic acids, thanks to their ability to combine the advantages of both hydrogel matrices and nanoparticles. Many studies on polymer-based nanogels have been conducted, whereas only few examples of peptide-based nanogels can be

found in literature until now, and none of them presented, as colloidal suspension, the stability required for a desirable use in clinic. [63,102]

We standardize the formulation procedure of Fmoc-FF nanogels through three different methodologies, by evaluating the effect of the HLB value of the stabilizing agents used to coat the hydrogel nanoparticles. The reverse emulsion technique reported for this hydrogelator [63] was modified by us by the choice of different surfactants. TWEEN®60 and SPAN®60 were used in different ratios and were found able to guarantee good stability over time, after storage in water at room temperature. The freeze-drying step was thus avoided.

Other two methodologies were proposed for the preparation of Fmoc-FF nanogels: top-down and nanogelification in water. Nanoparticles obtained by top-down and W/O emulsion techniques have a diameter of about 200 nm, which is compatible with intravenous administration. Top-down procedure was recognized by us as the one allowing more advantages with respect to the other two. First, it avoids the use of mineral oil during the preparation and consequently, no n-hexane is required, and a higher biocompatibility is guaranteed. Moreover, it consists in less steps and, in the perspective of an industrial translation, an easier procedure presents more advantageous.

Before their feasible clinical employment, the mechanisms of nanogels uptake must be identified. Our studies pointed out that Fmoc-FF nanogels prepared using TWEEN®60 and SPAN®60 as surfactants enter cancer cells via caveolae-mediated endocytosis. This specific penetration mechanism confers them a selectivity towards cell lines overexpressing the protein caveolin1, such as MDA-MB-231 breast cancer cells.

At the best of our knowledge, this is the first peptide-based nanogel that demonstrates selectivity towards a cancer line.

Peptide-based nanogels and also the corresponding hydrogels formulation were tested as potential drug delivery systems. To this scope, doxorubicin

was chosen as anticancer model drug. Fmoc-FF alone or in combination with (FY)3 and PEG_8-(FY)3 at different ratios were chosen as matrices. Due to the porous structure of their inner peptide network, both NGs and HGs allow to efficiently encapsulate Dox. The gelation kinetics (from 24 to 40 minutes) and the drug release kinetics (16–28%, after 72 h) from HGs were found to be clearly influenced by the matrix composition. Analogously, the DLC values (0.137 and 0.093 for pure and mixed NGs, respectively) and the release percentages of Dox (20–40%, after 72 h) in NGs are affected by the net charge. Cytotoxicity assays were carried out on MDA-MB-231 cells, previously found to be selectively targeted from Fmoc-FF NGs. A reduced cell viability (49–57%) was observed for both Dox loaded HGs and NGs. Immunofluorescence assays pointed out a different cellular localization for the Dox delivered by HGs and NGs with respect to the free drug. Indeed, while the free Dox is localized in the nucleus, HGs and NGs allow internalization of the drug at the peri-nuclear level and in the cytoplasm, respectively. All the *in vitro* data we collected suggested a potential *in vivo* use of these peptide platforms for drug delivery applications. In particular, Dox-loaded peptide NGs could be considered as promising valid alternatives to the already available liposomal Dox formulations.

5.2 PEPTIDE SYSTEMS FOR TISSUE ENGINEERING APPLICATIONS.

Peptide-based hydrogels have been widely proposed as tissue engineering scaffolds for their ability to mimic the extracellular matrix and support cell growth. An opportune design of the primary sequence can allow to modify the chemical-physical properties of the system to obtain the desirable features. With the studies here presented, we demonstrated that different strategies can be applied to obtain formulations with appealing mechanical behaviour, biocompatibility and cell adhesion capability. These strategies

can be summarized as follows and have been used, in some cases, in combination:

1) Employment of cationic sequences end-capped, at the N-terminus, with aromatic groups or alkyl chains.
2) Combination of ultra-short hydrogelators with other peptide sequences or other chemical entities (i.e. polymers).
3) Inducible cross-linking of the building blocks to increase the mechanical responsiveness.
4) Use of lipopeptides to promote the aggregative behaviour.

First, K1, K2, and K3 cationic hexapeptides [139] have been end-capped at the N-terminus with both the Fmoc protecting group and the Fmoc-FF hydrogelator. The characterization of these peptide aqueous solutions pointed out that chemical modifications do not hamper the self-assembly. However, only Fmoc derivatives were able to form hydrogels in the experimented conditions, thus demonstrating that the insertion of the FF dipeptide alters the hydrophilic-lipophilic balance recognized as the driving force in the gel formation. The stacking of the fluorenyl groups in the resulting Fmoc-K HGs led to the formation of β-sheet structures with an antiparallel orientation of the β-strands. No toxicity was detected after cell viability assays performed on 3T3 and on HaCat cell lines for all the tested systems. However, only Fmoc-K3 hydrogel is able to support opportune cell adhesion, growth and duplication. This result may be ascribed to the higher rigidity (G' = 2526 Pa) compared to Fmoc-K1 and Fmoc-K2 (G' = 557 and 925 Pa, respectively), probably due to a more efficient packing of the amino acid side chains because of the presence of an Ala residue in place of a Leu or a Ile one. Moreover, in vitro cell studies conducted on Fmoc-K3 hydrogel, showed that this peptide was able to support the formation of highly organized structures, resembling organoids (data non shown). This result will be subjected to further investigations.

The substitution of the aromatic group at the N-terminus of K peptides with a nineteen carbon atoms chain, does not alter the aggregative capability of these peptides. In this context, also a truncate version of the afore mentioned cationic sequence (C_{19}-VAGK) was analyzed and similar results were obtained. In detail, it was shown that, while the peptide component tends to arrange into an α-helix like organization, the voluminous groups inserted at the N-terminus control the aggregation and push towards a β-sheet structuration.

The combination of two or more building blocks has been demonstrated to be an efficient strategy for the preparation of novel hybrid hydrogels with enhanced mechanical and functional properties. [106,140] For this reason, new mixed HGs have been formulated and tested by combining the Fmoc-FF dipeptide with cationic peptide sequences or PEGDA polymers. In some cases, the combination results in the alteration of the equilibrium leading to self-assembly. Indeed, not all of the tested ratios between Fmoc-FF and cationic peptides were able to form self-supporting hydrogels. However, FmocFF-K peptides (FmocFF-K1, FmocFF-K2, and FmocFF-K3), which were not able to gel alone, could form hydrogels in the hybrid formulations. By comparing hydrogels obtained by the only Fmoc-K sequence with hydrogels obtained combining these sequences with Fmoc-FF, no direct correlation can be evidenced between their respective rigidity. Indeed, the scale of G' values, previously found for self-assembled systems, was K1 < K2 < K3, whereas in multicomponent systems the scale is K2 < K1 < K3, with a G' value for K3 (G' = 35 000 Pa) around ten-fold higher with respect to K1 (G' = 3226 Pa) and K2 (G' = 2000 Pa). This difference in the rigidity was ascribed to the complexity of noncovalent interactions originated by peptides inside the fibrillary network. As expected, the dynamic parameters of the water molecules constrained in the peptide scaffold (slow water) are affected by the stiffness of the HG, but a direct comparison is possible only

for analogous series. Also the mixed samples, tested through *in vitro* cell viability assays on the same cell lines previously used, were found to be highly biocompatible. However, the cell adhesion tests highlight that the best formulation is not, as it was expected, the more rigid one, thus suggesting that many parameters are involved in the capability of the matrix to support adhesion.

Mixed peptide-polymer matrices were also tested by combining Fmoc-FF with two different polydisperse diacrylate-capped PEGs (PEGDA, specifically PEGDA 575, PEGDA1, and PEGDA 250, PEGDA2). Hydrogels at different peptide/polymer ratios (1/1, 1/2, 1/5, and 1/10 mol/mol) were obtained through a solvent-switch method. Both the polymer molecular weight and abundance were found to influence the features of the final material in terms of water content, surface topology, stability, and drug release profiles (Napthol Yellow S chosen as model molecule). The supramolecular organization was found to be dictated by Fmoc-FF self-assembling, as assessed by CD, FTIR, and WAXS analysis. By changing the amount of the polymer, different matrices with different mechanical properties could be obtained. This evidence suggests the potential use of these materials in various application areas. Finally, the presence of diacrylate functionalities in the supramolecular Fmoc-FF hydrogel network could be employed to promote a photo-activated cross-linking reaction, thus providing the generation of interpenetrating networks (IPNs) with a higher organization level in the system.

The insertion of Cys residue within a peptide sequence also opens the way to the possibility of a cross-linking process able to change the structural and functional properties of the final product. For this reason, the FYFCFYF peptide and it PEGylated derivative were designed on the basis of previous studies that highlighted the capability of all-aromatic peptides to self-assemble through the generation of a hydrophilic and a hydrophobic

interface. [107] The introduction of a cross-linkable cysteine residue in the wet phase was demonstrated to not hamper the gelification process. Through oxidation and formation of a disulfide bond, more rigid matrices, useful for tissue engineering applications, were obtained (G' from 979 to 3360 Pa). Moreover, the presence of a thiol group could be employed for derivatization of the hydrogel with targeting molecules or APIs.

The capability of lipopeptides alkyl chain to prompt the self-assembling was exploited to drive the aggregation of four RGDS-containing sequences (mG, mW, pG and pW). Results pointed out that all of them exhibit an extended β-sheet arrangement at sufficiently high concentration, above the CAC. A singular morphology was observed for mW derivative, for which helical twisted ribbons closing into nanotubes were detected in clearly resolved cryo-TEM images. It was thus demonstrated that tryptophan residue has a role in the packing, making it more chiral and twisted because of its steric hindrance. However, this effect is modulated by alkyl chain length and balanced by its increase, as it can be deduced from the thinner and more extended, but less twisted, structures formed by pW. Moreover, SAXS analyses showed that mW and pW possess birefringence due to the formation of a lyotropic nematic phase and spontaneous flow alignment of this phase upon delivery into X-ray capillaries was noted. Nematic phase formation is relatively infrequently observed for amyloid systems [236-239] and points to the high persistence length of the nanotube, twisted ribbon and nanotape structures of mW and pW.

Cells viability assays, conducted on L929 fibroblasts and C2C12 myoblast, pointed out that all the lipopeptides are highly biocompatible at concentrations below the CAC, with low variation between the sequences. Hydrogels were found to be generally less toxic that solutions at concentrations above the CAC and below the CGC. The flow alignment observed for lipopeptides is interesting in terms of further research on the

preparation of scaffolds for tissue engineering, using alignment of myoblasts to improve the texture of cultured meat.

5.3 PEPTIDE BASED HYDROGELS AND NANOGELS AS SUPRAMOLECULAR CONTRAST AGENTS FOR MRI AND CEST-MRI APPLICATIONS.

The advent of NSF and brain deposition of Gd(III) has led to increased regulatory scrutiny of T_1-CAs [240]. The efforts that have been put in this thesis to propose safer contrast agents have been mainly two. First of all, Gd-complexes have been physically entrapped within peptide networks to protect them from transmetallation phenomena. On the second hand, CEST-MRI has been explored as new diagnostic technique that, avoiding the use of paramagnetic compounds, assures the safety of contrast agents' administration.

Electrostatic interactions have been exploited to promote the loading of different Gd-complexes like $[Gd(BOPTA)]^{2-}$, $[Gd(DTPA)]^{2-}$, $[Gd(AAZTA)]^{-}$ into the network formed by cationic peptide sequences. The physical encapsulation of the complex was shown to not significantly alter the hydrogel morphology, in which the fibrillary network is kept. Rheological characterization pointed out that the insertion of a Gd (III) complex within the peptide network can allow an increase or a decrease of the rigidity of the matrix as a consequence of the non-covalent interactions (π–π stacking, hydrogen bonding and electrostatic interactions). A significative increase in relaxivity performances was obtained, since the CAs loaded into the macroscopic hydrogel exhibit a r_{1p} value up to five-fold higher than the corresponding free contrast agent. Beyond the typical relaxometric parameters (τ_R, τ_M and q), which affect the relaxivity, the r_{1p} value seems to be influenced by other key factors such as: i) the mechanical properties of the hydrogel, ii) the interactions between the complex and the peptide

matrix and iii) the water accessibility to the complex within the hydrogel. The influence of these parameters must be deeply investigated and optimized to improve the relaxivity performance of the resulting CA. The best performing HG was used as starting point to formulate the correspondent nanogel by a top-down approach. A reduced mobility of the complex into the peptide matrix and a slow regime of the water exchange process was observed for the injectable nanoparticle. The higher relaxivity at 20 MHz and 298 K (r_1 = 36.8 $mM^{-1}\,s^{-1}$) measured for the nanogel with respect to the corresponding hydrogel can be probably attributed to the different degree of rotational freedom of the complexes within nanosized matrix.

The same cationic peptide sequences, end-capped with the acetyl group at the N-terminus, were also used to promote the physical loading of the clinically approved CEST-CA Iopamidol. The self-healing properties of the obtained hydrogels were demonstrated through injectability test. Biocompatibility studies pointed out that both Ac-K1 and Ac-K2 matrices have no side effects neither on in vitro cell cultures nor in mice and are promising for in vivo application as route for topic administration of contrast agents. With this study, it has been reported for the first time that peptide-based hydrogels can be imaged by CEST-MRI, paving the way for the design and development of new optimized systems.

[236] Aggeli, A.; Nyrkova, I. A.; Bell, M.; Harding, R.; Carrick, L.; McLeish, T. C. B.; Semenov, A. N.; Boden, N. *Proc. Nat. Acad. Sci USA* **2001**, 98 (21), 11857-11862.

[237] Hamley, I. W. *Soft Matter* **2010**, 6, 1863-1871. Jung, J.-M.; Mezzenga, R. *Langmuir* **2010**, 26, 504-514.

[238] Nystrom, G.; Mezzenga, R. *Curr. Opin. Colloid Interface Sci.* **2018**, 38, 30-44.

[239] Pelin, J. N. B. D.; Edwards-Gayle, C. J. C.; Castelletto, V.; Aguilar, A. M.; Alves, W. A.; Seitsonen, J.; Ruokolainen, J.; Hamley, I. W. *ACS Appl. Mater. Interfaces* **2020**, 12 (12), 13671-13679.

[240] Wahsner, J.; Gale, E. M.; Rodríguez-Rodríguez, A.; Caravan, P. *Chem. Rev.* **2019**, 119, 957−1057.

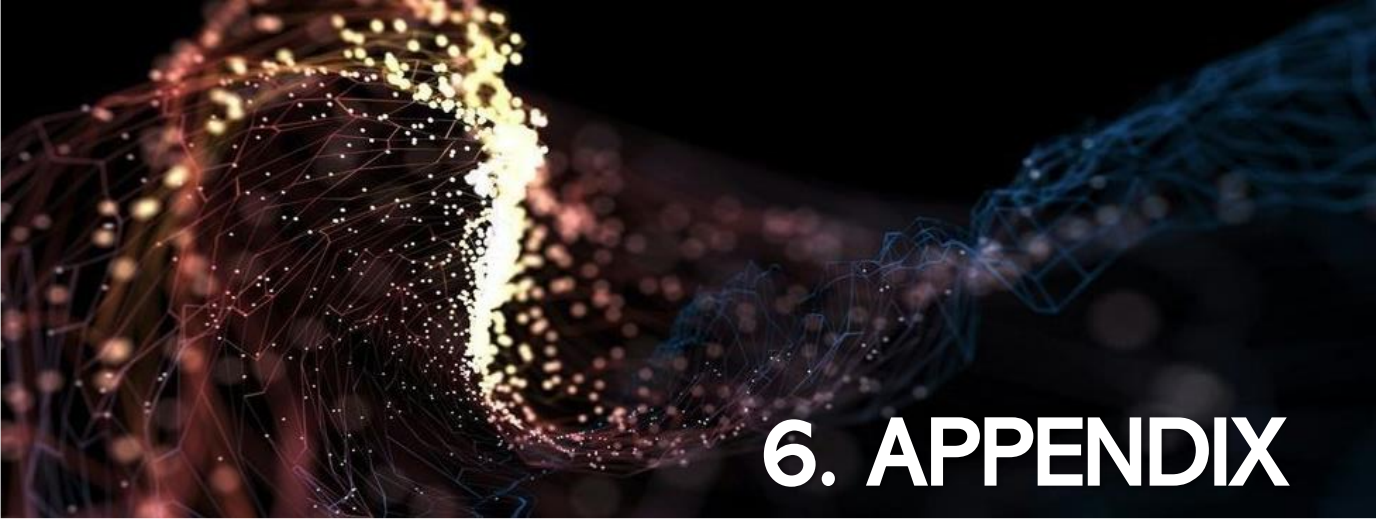

6. APPENDIX

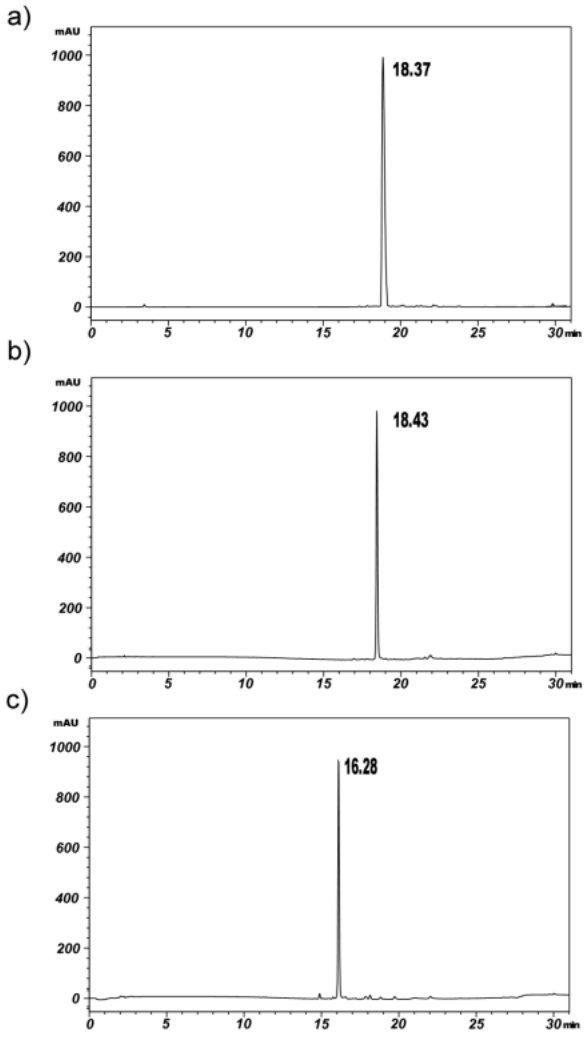

Figure 6.1: RP-HPLC chromatograms for (A) Fmoc-K1, (B) Fmoc-K2 and (C) Fmoc-K3 peptides

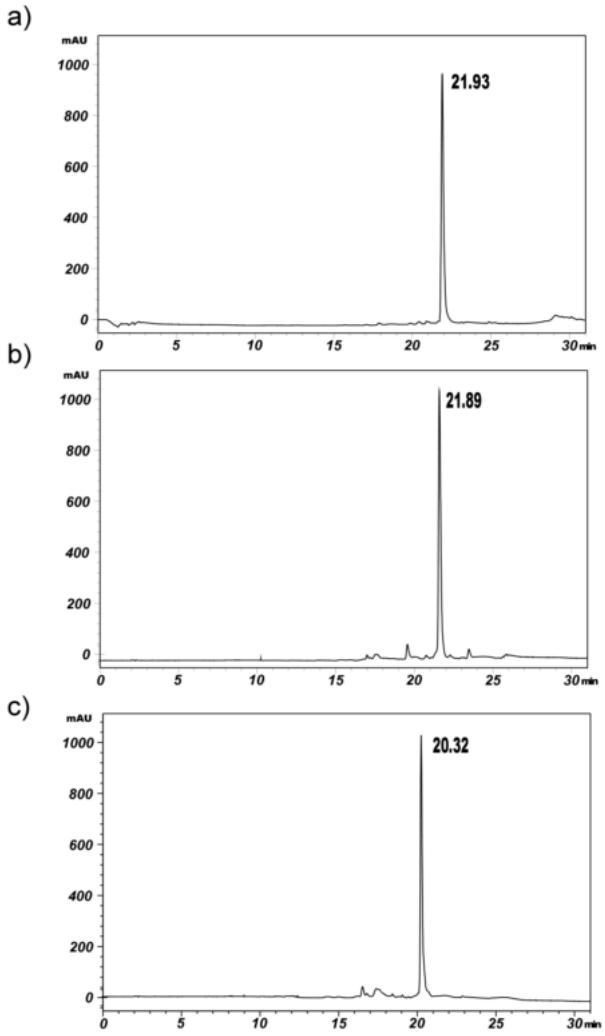

Figure 6.2: RP-HPLC chromatograms for (A) FmocFF-K1, (B) FmocFF-K2 and (C) FmocFF-K3 peptides.

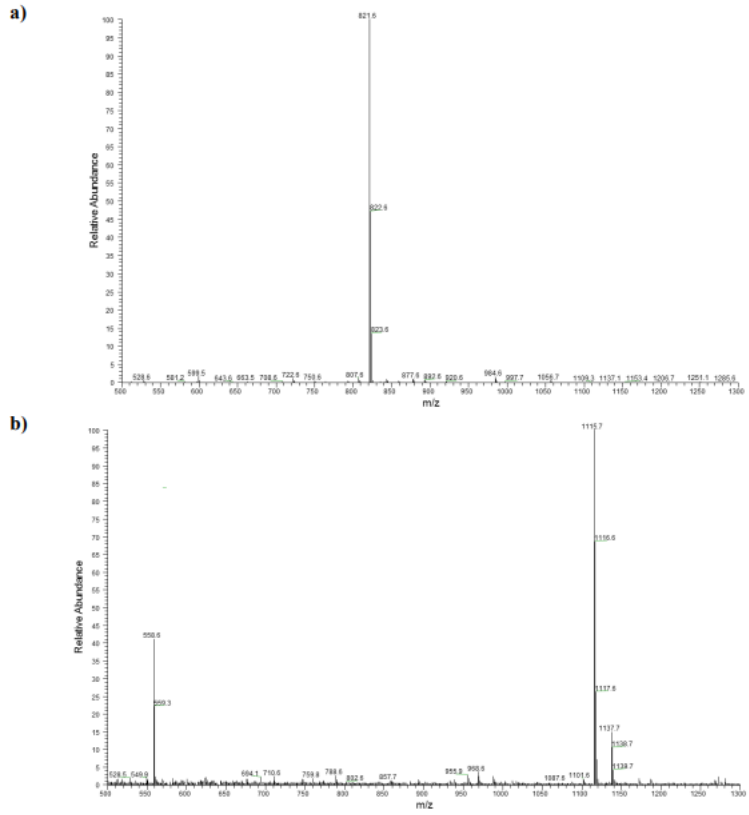

Figure 6.3: ESI mass spectra for (A) Fmoc-K1 and (B) FmocFF-K1 peptides.

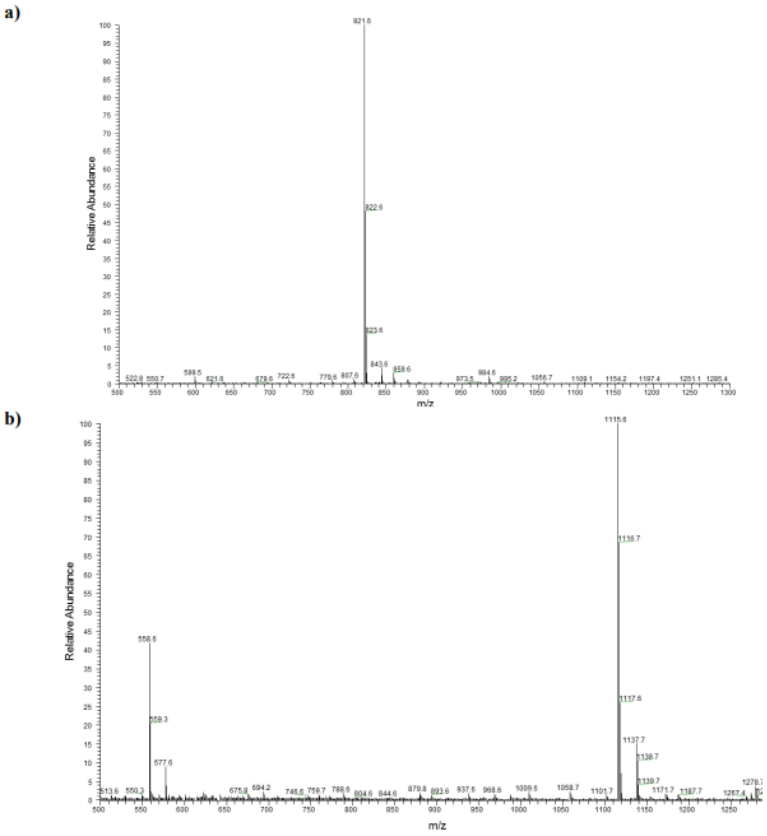

Figure 6.4: ESI mass spectra for (A) Fmoc-K2 and (B) FmocFF-K2 peptides.

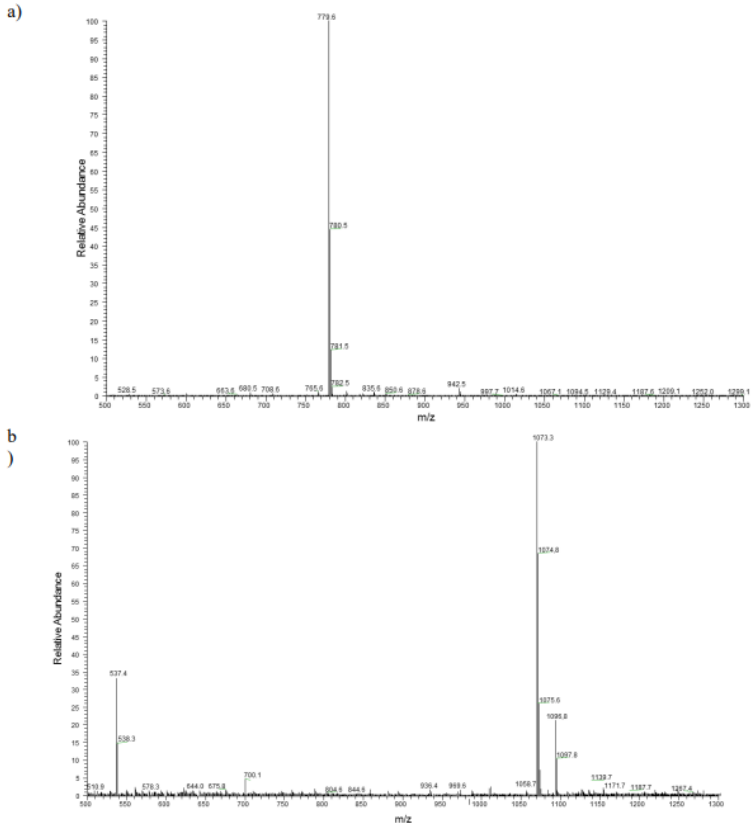

Figure 6.5: ESI mass spectra for (A) Fmoc-K3 and (B) FmocFF-K3 peptides.

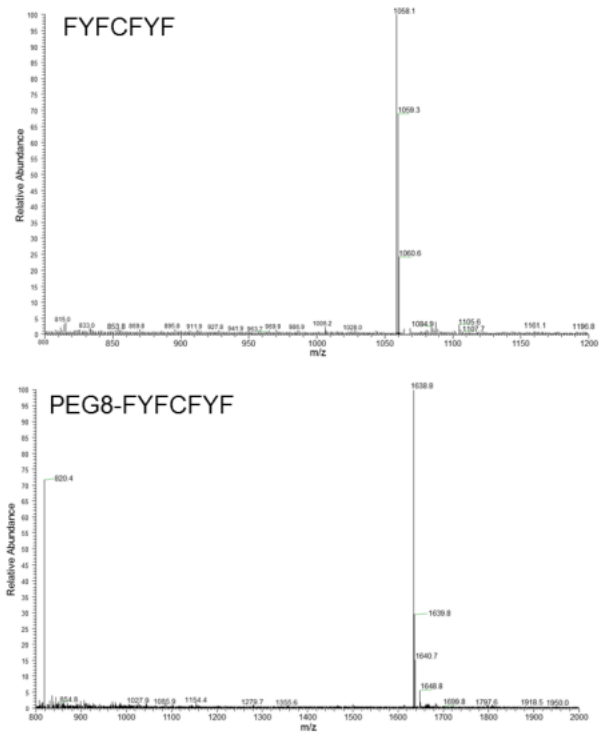

Figure 6.6: ESI mass spectra for both Cys-containing peptides.

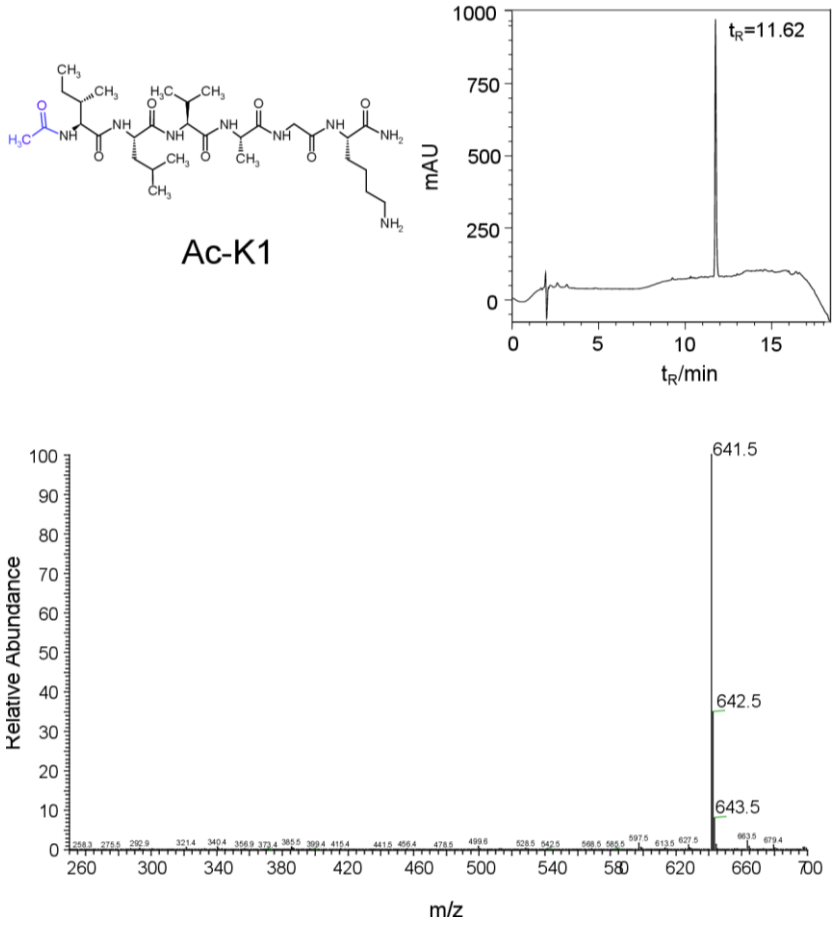

Figure 6.7: Chemical structure of Ac-K1 peptide with the corresponding RP-HPLC chromatogram and ESI mass spectrum

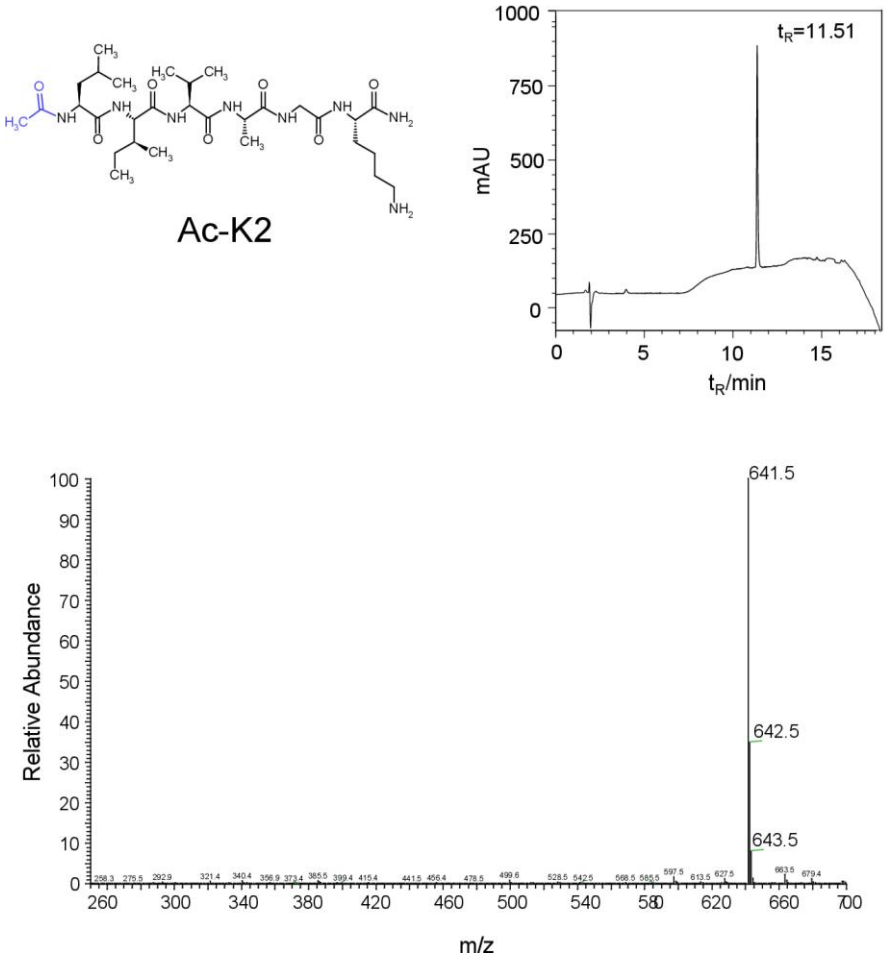

Figure 6.8: Chemical structure of Ac-K2 peptide with the corresponding RP-HPLC chromatogram and ESI mass spectrum

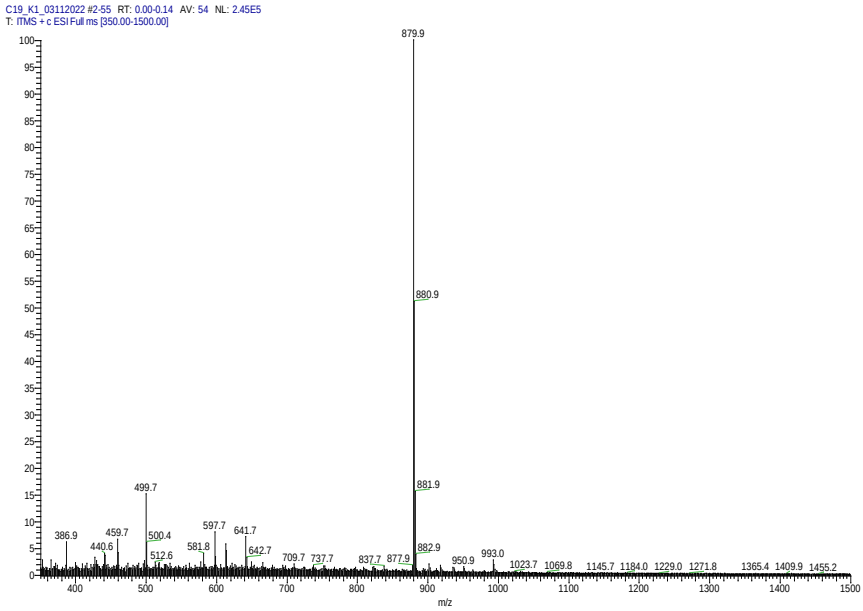

Figure 6.9: ESI mass spectrum for C_{19}-K1

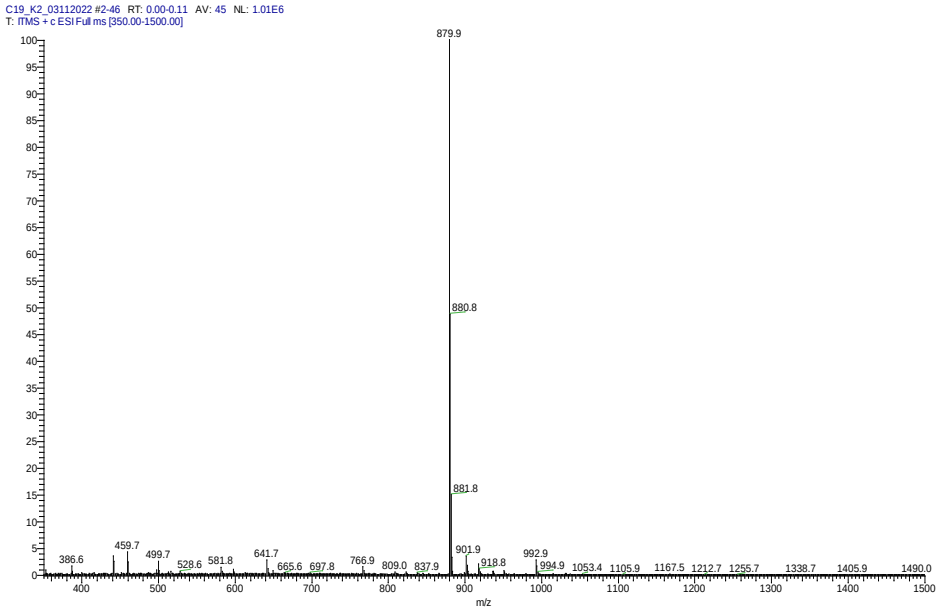

Figure 6.10: ESI mass spectrum for C_{19}-K2

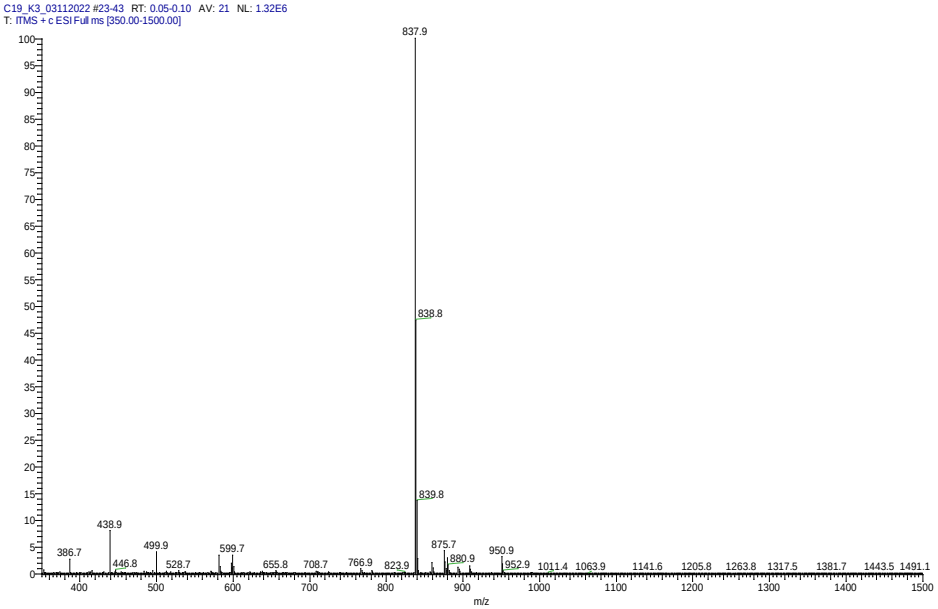

Figure 6.11: ESI mass spectrum for C_{19}-K3

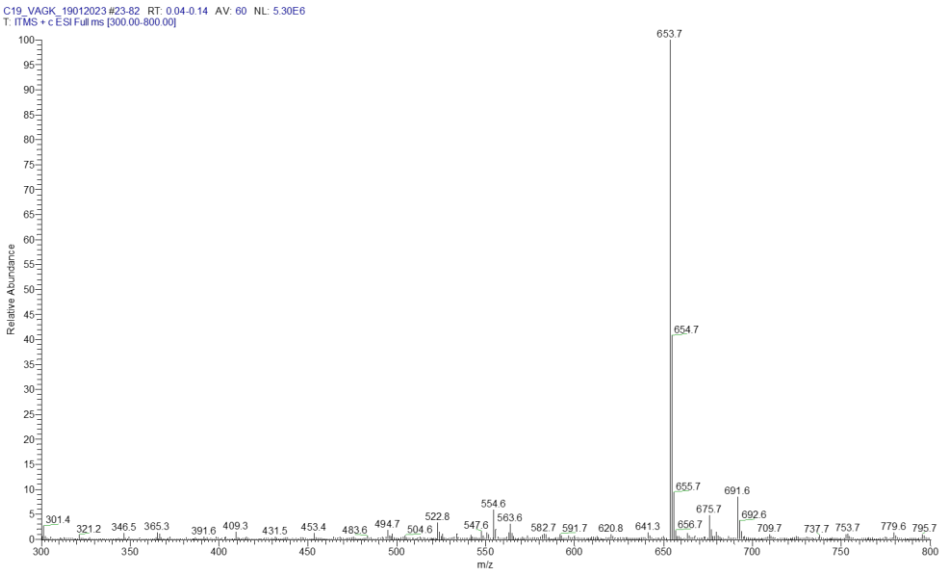

Figure 6.12: ESI mass spectrum for C_{19}-VAGK

7. PUBLISHED ARTICLES

RSC Advances

REVIEW

View Article Online
View Journal | View Issue

Cite this: *RSC Adv.*, 2020, **10**, 27064

Systematic overview of soft materials as a novel frontier for MRI contrast agents

Enrico Gallo,[a] Elisabetta Rosa,[b] Carlo Diaferia,[b] Filomena Rossi,[b] Diego Tesauro[b] and Antonella Accardo *[b]

Received 9th April 2020
Accepted 2nd July 2020

DOI: 10.1039/d0ra03194a

rsc.li/rsc-advances

Magnetic resonance imaging (MRI) is a well-known diagnostic technique used to obtain high quality images in a non-invasive manner. In order to increase the contrast between normal and pathological regions in the human body, positive (T1) or negative (T2) contrast agents (CAs) are commonly intravenously administered. The most efficient class of T1-CAs are based on kinetically stable and thermodynamically inert gadolinium complexes. In the last two decades many novel macro- and supramolecular CAs have been proposed. These approaches have been optimized to increase the performance of the CAs in terms of the relaxivity values and to reduce the administered dose, decreasing the toxicity and giving better safety and pharmacokinetic profiles. The improved performances may also allow further information to be gained on the pathological and physiological state of the human body. The goal of this review is to report a systematic overview of the nanostructurated CAs obtained and developed by manipulating soft materials at the nanometer scale. Specifically, our attention is centered on recent examples of fibers, hydrogels and nanogel formulations, that seem particularly promising for overcoming the problematic issues that have recently pushed the European Medicines Agency (EMA) to withdraw linear CAs from the market.

1. Introduction

Clinical imaging and microscope/fluorescence processing have taken on a valuable role with regards to the methodologies used to produce images of the human body in recent years.[1] These visualization techniques provide benefits and allow a multidimensional evaluation scale, from the imaging of macroscopic anatomical areas and tissues, right down to the microscopic cellular, intra-plasmatic and molecular levels. Consequently, bio-clinical imaging strategies have emerged as some of the most useful devices in healthcare technology for the diagnosis and the treatment of human pathological states (Fig. 1). The evolution of bio-clinical visualizing techniques from radioisotope imaging to more complicated and sensitive methodologies, consisting of computer-assisted tomography (CAT scans), magneto-encephalogram (MEG), positron emission tomography (PET) and ultrasound imaging, has led to innovative improvements in the quality of the healthcare available today.[2] However, every bio-imaging approach available currently suffers from numerous limitations. For instance, the most common limitations of these techniques are the noxious effects of ionizing radiations (X-ray and CAT scan),[3] the damaging impact of radioactivity (in radioscopic techniques),[4] the low sensitivity (*e.g.* magnetic resonance imaging, MRI),[5] the inability to provide resolution smaller than millimeters (as reported for ultrasound imaging)[6] and the general impossibility of differentiating between distinctive pathological compartments (*e.g.* benign and malignant tumors).[7] The urgency of more accurate information about the early cellular and molecular pathological contexts accurately explains the need for extending deep bio-imaging to these organization levels. This understanding may assist the fast detection, screening, diagnosis, and image-guided treatment of life-threatening diseases consisting of cancer, metabolic inborn errors and neurodegenerative diseases. In this direction, nanotechnology could be of great help. Innovative nanomaterials (NMs) and nanostructured platforms (NPs) can help to conquer some of the previously described limitations, combining traditional techniques with modern methods of interest in nanotechnology.[8] In modern science and technology, NMs and NPs have had a revolutionary and radical impact.[9,10] The potential applications of nanoparticles as tracers,[11] markers[12] or contrast agents (CAs)[13] for *in vitro* and *in vivo* optical biological imaging is of remarkable significance. Indeed, nanoparticles can provide several advantages, including tunable physical properties (*e.g.* luminescence and ferromagneticity), a high stability (*e.g.* against photobleaching), the opportunity for targeted delivery, and specific binding through chemical functionalization, multimodality, high sensitivity and selectivity. The aim of this review is to focus

[a]*IRCCS SDN, Via E. Gianturco 113, 80143, Napoli, Italy*
[b]*Department of Pharmacy, Research Centre on Bioactive Peptides (CIRPeB), University of Naples "Federico II", Via Mezzocannone 16, 80134-Naples, Italy. E-mail: antonella.accardo@unina.it*

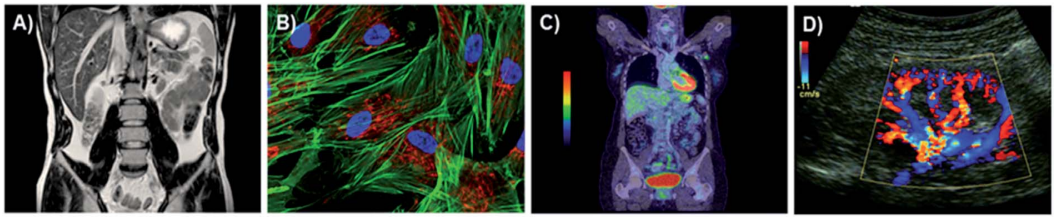

Fig. 1 Techniques: MRI (A), fluorescence (B), PET (C) and SPECT (D).

attention on MRI diagnostic techniques, paying specific attention to the latest soft-based nanomaterials (fibrillary nanostructures, hydrogels and nanogels) proposed as MRI-CAs (see Fig. 2). A description of the advantages of these nanomaterials with respect to the low molecular weight (LMW) ones is also reported. Moreover, in order to give a comprehensive picture of the previously published literature on this specific topic at the end of the review, we report the methodology and the criteria used for the bibliography, explaining all of the consecutive operations related to the identification, screening, eligibility and inclusion steps.

2. Magnetic resonance imaging

Magnetic resonance imaging is a non-invasive medical diagnostic imaging technique presently used to study pathological or other physiological alterations in living tissues, it is used, for example, to reveal and delineate tumor and coronary artery lesions and diseases. MRI signals are generated by the hydrogen nuclei in human tissues. It is worth noting that the human body consists significantly, in part, of water, which is the primary source of the MRI signal in medical imaging applications. MRI signals are generated by measuring parameters associated with the relaxation of hydrogen nuclei. A further magnetic field in the gradient allows retrieval of the spatial information (Fig. 3) in order to obtain 3D MRI-images.[14,15] CAs are widely used to enhance the image resolution in terms of the contrast between normal and abnormal tissues.[16,17] According to the ratio between the two specific parameters, the longitudinal relaxivity (r_1) and transverse relaxivity (r_2), CAs can be classified into two different categories: T1 or T2 CAs. T1 agents generate a positive contrast and are usually based on thermodynamically stable and kinetically inert complexes of paramagnetic ions such as gadolinium.[18] On the other hand, T2 agents generate a negative contrast and are based on paramagnetic compounds such as superparamagnetic iron oxide (SPIO).[19] The parameters of the relaxivity, which represents the efficacy of a contrast agent (CA) at a 1 mM concentration by changing the rate of water proton relaxation, may be used to evaluate the CA performances.[20] The relaxivity of a CA is essentially determined by the molecular reorientation time (τ_R) of the complex and by the exchange lifetime (τ_M) of the water coordinated to the complex. Most of the Gd-complexes used as T1-CAs are based on polydentate chelating agents with a branched or cyclic structure such as diethylenetriaminepentaacetic acid (DTPA) or 1,4,7,10-tetraazacyclododecane-*N*,*N*,*N*,*N*-tetraacetic acid (DOTA). Gd-DTPA (Magnevist®) was the first gadolinium-based MRI-CA; it was authorized for clinical use in 1987. After Magnevist®, a series of other Gd(III) complexes (Gd-DOTA (Dotarem®), Gd-DTPA-BMA (Omniscan®), Gd-HPDO3A (Prohance®), Gd-MS-325

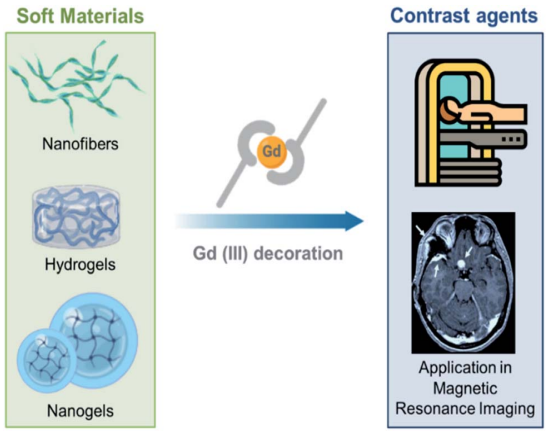

Fig. 2 The class of soft materials includes nanofibers, hydrogels and nanogels. Using appropriate strategies for decoration, these supramolecular aggregates can be functionalized with Gd(III) ions and complexes in order to became suitable for application in MRI as T1-positive contrast agents.

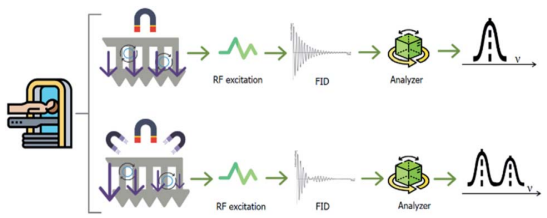

Fig. 3 To obtain an MRI image, the body is located in a uniform magnetic field. Hydrogen nuclei align with the magnetic field and create a net magnetic moment parallel to it. When a radio-frequency pulse (RF excitation) is applied perpendicularly, the net magnetic moment of the nuclei tilts away from the magnetic field. When the RF pulse stops, the nuclei return to the equilibrium initial state (relaxation step). During the relaxation, the nuclei lose energy and a measurable signal, indicated as the free-induction decay (FID), is detected. 3D MRI images can be generated, encoding the FID in each dimension. An additional magnetic field in the gradient changes the FID as a function of the proton 3D position.

(Ablavar®), Gd-DTPA-BMEA (OptiMARK®), EOBDTPA31 (Eovist®) and Gd-BOPTA (Multihance®)) were approved for diagnostic applications. These T1-agents with an LMW have a range of relaxivities between 4 and 5 mM^{-1} s^{-1} at 20 MHz and 310 K. Owing to their LMW, classical Gd-complexes rapidly extravasate after their intravascular administration. This extravasation causes a reduction in the contrast from the neighboring tissues. In contrast, the extravasation phenomenon can be extensively limited using multimeric gadolinium complexes or macromolecular/supramolecular CAs with a molecular weight of more than 30 kDa. Several strategies have been proposed to obtain macromolecular CAs. One of them utilizes the insertion of a hydrophobic substituent capable of binding with high affinity serum proteins such as human serum albumin (*e.g.* Ablavar® and MP-2269)[21] on the Gd-complex. Alternatively, the synthesis of polymeric scaffolds decorated with multiple copies of the CA have been suggested.[22–25] Another approach, explored over recent years, is the non-covalent association between the protein avidin and the Gd-complex–biotin adduct that brings about the formation of a macromolecular system containing four Gd-complexes.[26] An analogous non-covalent approach is the interaction between cyclodextrin and its host ligand.[27] Alternatively, gadofullerenes and gadonanotubes have been proposed as a new generation of high performance CAs for MRI.[28–30] These carbon nanostructures were found to be 20-times more effective than the current clinical CAs with a relaxivity value up to 180 mM^{-1} s^{-1} per gadolinium ion. Beyond the high relaxivity value, these nanosystems exhibit a low *in vivo* dissociation of the metal ion, a decrease in the uptake by the reticulo endothelial system (RES) and an increase in the clearance.[31] All of these macromolecular compounds exhibit an increase in their relaxivity according to the unit dose of the paramagnetic ion. This increase is caused by the coexisting presence of a high number of gadolinium complexes for each molecule and the longer τ_R value with respect to the LMW-CAs, such as Magnevist® or Dotarem®.

More recently, and with the same purpose, supramolecular aggregates, such as micelles and liposomes, have also drawn significant attention as diagnostic agents in nanomedicine.[32] The pharmacological properties of these systems, including the relaxivity, biodistribution and clearance can be simply settled and controlled by modifying their physicochemical properties such as the size, surface charge or membrane composition.[32] These multi-gadolinium CAs can be formulated in agreement with two different procedures: (i) Gd-complexes can be entrapped within the internal compartments of these nanostructures; or (ii) they can be covalently linked to a hydrophobic chain able to self-assemble.[32] In the first method, minimal exchange of the bulk water with the CA could result and the relaxivity of the entrapped paramagnetic species could be noticeable low as a consequence of the low permeability of some lipidic membranes. In the second method, it is important to distinguish between liposomal and micellar aggregates. The micellar structures present in the gadolinium complexes are entirely exposed on the external surface of the aggregate. Otherwise, in liposomes the metal complexes are distributed between their inner and the outer compartments. The assignment of Gd-complexes between the two liposomal layers could be different, and each contribution has to be considered.[33] In this instance, the complexes in the inner layer provide a contribution to the paramagnetic relaxation rate for liposomal structures only with a highly permeable membrane, in which the water exchange rate is very fast. Macro- and supramolecular CAs exhibit a typical NMRD (nuclear magnetic relaxation dispersion) profile with a peak at high frequencies (clinically relevant field strengths). This characteristic peak is caused by the increase in the rotational correlation times. Furthermore, to analyze the data for the longitudinal ^{17}O and ^{1}H relaxation rates, the Solomon–Bloembergen–Morgan model, adapted in agreement with the Lipari–Szabo approach, must be used.[34,35]

This approach differentiates between two statistically independent motions: a rapid local motion of the Gd(III) complex governed by means of a correlation time (τ_l) and a slower global motion of the entire supramolecular construct governed by a correlation time (τ_g). The degree of local to global influence related to the overall motion is established by another model-free parameter (S^2) that can assume a value ranging between 0 and 1. Both τ_l and τ_g can be affected by several structural features of the amphiphilic gadolinium complex, such as the length and the hydrophobicity of the side chain.

3. Gd-CAs based on fibers

Organic and inorganic fibrillary nanostructures have been recently proposed as platforms for biomedical applications.[36,37] Owing to their excellent mechanical strength, high porosity and easy fabrication, fibers could be employed as potential delivery systems of active pharmaceutical ingredients (APIs) such as therapeutic and/or diagnostic agents, for the fabrication of wound dressings and regenerative medicine. In this scenario,

Table 1 Gadolinium complex, relaxivity value at a 1 mM concentration and references for fibrillary nanostructures

System	Gd(III) complex	r_{1p} (mM^{-1} s^{-1})	Ref.
PA 5	Gd-DO3A	16.6 (pH = 4), 13.2 (pH = 10)	40
DOTAMA-PEG_6-F4, DTPAMA-PEG_6-F4	Gd-DOTA, Gd-DTPA	14.0, 14.8	41
FF-DOTAMA-FF	Gd-DOTA	11.5	44
$2NaI_2$	Gd-DOTA	12.3	45
Cha-DOTA/C-Cha (2 : 8 mol mol^{-1}), (8 : 2 mol mol^{-1})	Gd-DOTA	19.5, 17.2	48
PpiX-PEG8-SSSPLGLAK-Ppdf	Gd-DOTA	28.2 (sphere), 51.5 (fiber)	49
SMNs/FMNs	Gd-DOTA	15.6 (sphere), 18.5 (fiber)	51

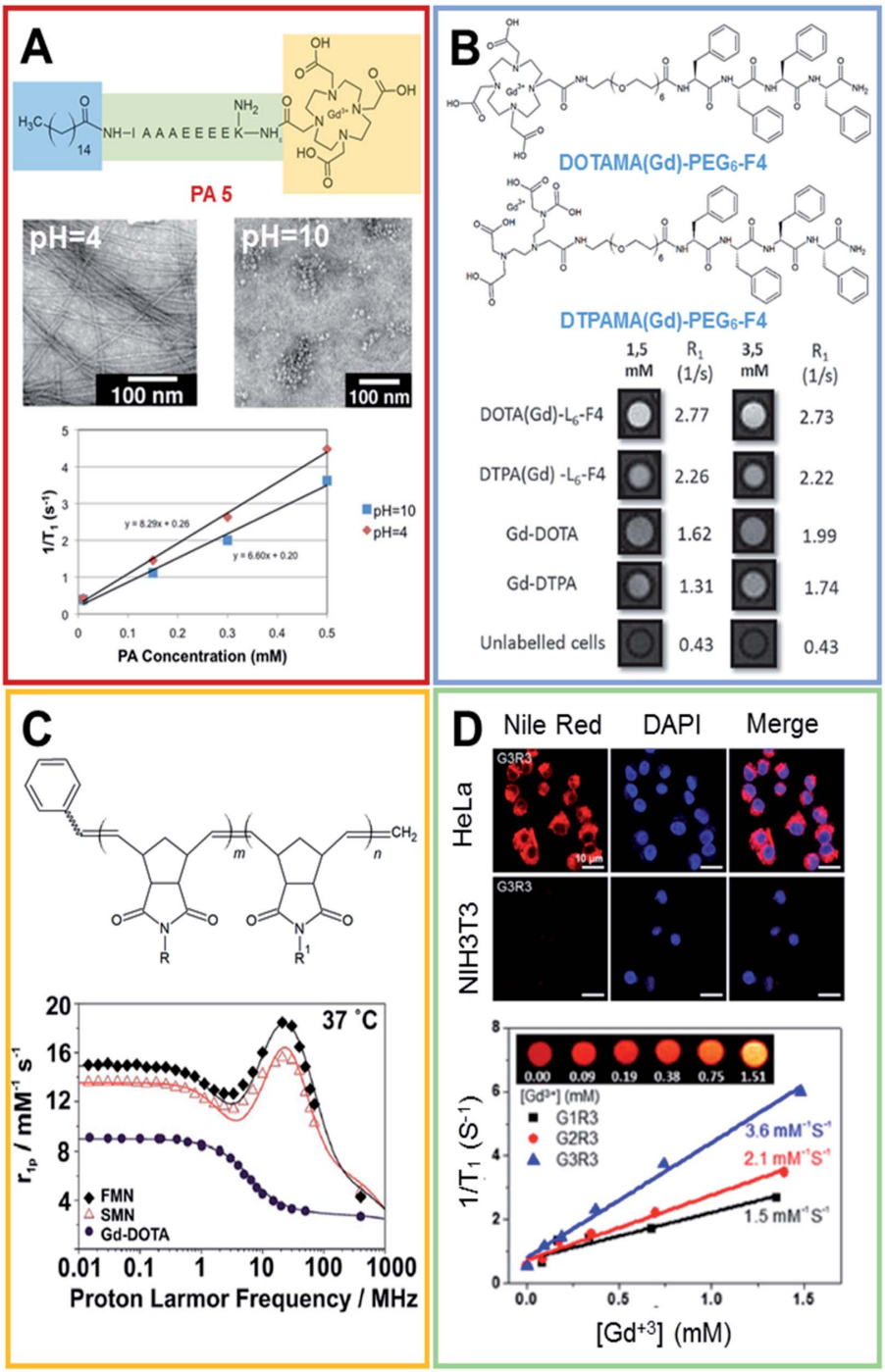

Fig. 4 (A) Chemical formula for the PA 5 compound, the peptide sequence of PA 5 is reported according to the one code letter. TEM images (0.5 mM solution of PA 5) at pH 4.0 (on the left) and 10.0 (on the right). T1 relaxivity graph of PA 5 under basic and acidic conditions (adapted with permission[40] 2012-American Chemical Society). (B) Chemical structure of DOTAMA(Gd)-PEG_6-F4 and DTPAMA(Gd)-PEG_6-F4. T1-weighted MR-images of pellets of the J774A.1 cell line labelled with 1.5 and 3.5 $\times$ 10^{-3} mol L^{-1} of the two Gd-complexes. The relative observed relaxation rates are reported too (reproduced with permission from ref. 41). (C) Chemical structure of Gd^{3+}-containing an amphiphilic block copolymer. R and R′ can be a phenyl group or a modified Gd-DOTA complex (norbornenyl-Gd-DOTA monoamide). ^{1}H NMRD profiles for Gd-DOTA, spherical and fibrillar micellar nanoparticles (reproduced with permission,[51] published by The Royal Society of Chemistry). (D) Laser scanning microscopy images of HeLa and NIH3T3 cells lines treated with Nile red-loaded porous networks of Gd^{3+}-G3R3 (1 h after incubation): left, Nile red (red); middle, nuclei stained with DAPI (blue); and right, merged images. T1 relaxivity plots of Gd^{3+}-chelating nanostructures (0.2 mM) as a function of the Gd^{3+} concentration ([Gd^{3+}]) (4.7 T, 25 °C) and (inset) T1-weighted MR images of Gd^{3+}-G3R3 (adapted with permission,[50] copyright 2017-American Chemical Society).

there are various previously published examples of MRI-CAs based on fibrillary nanostructures (see Table 1). Most of these were obtained for the self-assembly of peptide sequences. Peptides are versatile molecules, which present various advantages such as biocompatibility, a low-cost and synthetic variability. Owing to their appealing features, they have been proposed as antimicrobial/antiviral agents, therapeutic/diagnostic agents, or molecules for achieving passive or active targeting on cells. Moreover, in the last two decades researchers have begun to use peptides as useful functional molecules for obtaining novel biocompatible supramolecular architectures including nanotubes, nanofibers, nanospheres, nanovesicles and hydrogels.[38]

These supramolecular nanostructures can be obtained by self-assembly of several types of peptides, including cyclic and linear peptides, amphiphilic peptides (PAs), and α-helical and β-sheet peptides.[39] In this context, amphiphilic peptides and aromatic peptides were found to self-assemble into well-ordered nanofibers. In 2012 Goldberger *et al.*[40] synthesized a series of self-assembling PA molecules as pH sensitive reversible systems for *in vivo* imaging and drug delivery applications. These PAs, containing a hydrophobic alkyl tail, a β-sheet-forming peptide sequence and a charged amino acid sequence, were found to give a transition from single molecules or spherical micelles into self-assembling nanofibers upon acidification (from pH 7.4 to 6.6). Structural studies showed a fast and reversible transition from the random coil, which corresponds to isolated molecules in solution, to a β-sheet structure that supports the existence of fibers, at a pH of 6.6. By varying the β-sheet propensity of the amino acids in the β-sheet-forming region, the transition pH can be finely modulated. Moreover, it was observed that after the modification of the peptide sequence at the C-terminus with the gadolinium complex [1,4,7-tris(carboxymethylaza)cyclododecane-10-azaacetylamide (Gd-DO3A)] the structural transition occurs at a more acidic pH value (5.7–6.0). This result could probably be ascribed to the steric hindrance and the additional hydrophilicity of DO3A. Relaxivity studies using a 1.5 T magnet showed values of 8.3 and 6.6 mM^{-1} s^{-1} for 500 μM of the product at pH 4 and 10 respectively (Fig. 4A). Recently, Diaferia *et al.*[41,42] developed several examples of aromatic peptide conjugates for use as MRI-CAs. The idea of using aromatic short peptides (containing two or three residues) as building blocks to prompt fiber formation originated from the large amount of published literature on the ultra-short homodipeptide Phe–Phe (FF or F2), a dipeptide identified for the first time by Gazit in 2003 as an aggregating core motif for the Aβ-amyloid peptides (Aβ1-40 and Aβ1-42).[43] This peptide self-organizes efficiently into well-ordered tubular architectures, but according to the experimental conditions (pH, temperature, solvents and preparation methods) it can assemble into nanostructures with a different morphology. Initially, the authors prepared conjugates in which the Gd-complexes (Gd-DTPA or Gd-DOTA) were bound on diphenylalanine (F2) or tetraphenylalanine (F4) using a PEG spacer.[41] Only tetraphenylalanine derivatives, DOTAMA(Gd)-PEG_6-F4 and DTPAMA(Gd)-PEG_6-F4, exhibited the capability to form fibrillary nanoaggregates, in which the peptides were arranged in a β-sheet conformation with an antiparallel alignment along the fiber axis. Relaxivity studies indicated that both the DOTA and the DTPA conjugates exhibited a r_{1p} (~15 mM^{-1} s^{-1} at 20 MHz) three-fold higher than the classical LMW CAs. Analysis of the relaxometric parameters, with particular reference to the τ_R, suggested that the PEG spacer significantly increases the internal motility of the Gd-complexes with respect to the overall fibril-like structures. *In vitro* assays demonstrated the ability of both the nanostructures to enhance the MRI cellular response on the J774A.1 mouse macrophage cell line (Fig. 4B) and their high biocompatibility in the 0.5–5.0 mg mL^{-1} concentration range. In order to improve the relaxivity of these nanostructures, the same authors synthesized novel conjugate analogues in which the position of the Gd-complex in the aromatic sequence[44] and the aromaticity/hydrophobicity of the peptide framework were changed.[45] In the first study they investigated how the change in the position of the Gd-complex from the N-terminus to the center of the F4-motif could affect both the structural and relaxivity properties of the aggregates. The results highlighted that when the Gd-complex is located at the center of the aromatic peptide sequence (FF-DOTAMA(Gd)-FF), there is a reduced tendency to self-assemble and the fibrillary networks only appear above a concentration of 50 mg mL^{-1}. This reduced tendency to self-organize also causes a decrease in the observed relaxivity value (11.5 mM^{-1} s^{-1}).[44] In the second study, the role of the aromaticity on the structural organization and on the relaxometric behavior was studied by replacing the F residue with the non-coded amino acid naphthylalanine (2-Nal).

As expected, the increase in the aromaticity corresponds to a major tendency to self-assemble (critical aggregation concentration ~ 0.1 mg mL^{-1}) and stable amyloid like nanostructures can be observed for Gd-$2Nal_2$ for a concentration of around 1.0 mg mL^{-1}. A further increase in the concentration (above 20 mg mL^{-1}) brought about the formation of a hydrogel such as those of other PEGylated analogues.[46,47] In line with the other systems previously described, these gels exhibited a r_{1p} value of 12.3 mM^{-1} s^{-1} at 20 MHz and a satisfactory capability to encapsulate anticancer drugs, such as doxorubicin. According to this strategy, in 2016 Lee and coworkers proposed a similar multifunctional theranostic nanoplatform, loaded with Gd-complexes and doxorubicin, for application in personalized medicine.[48] These targeted fibrillary nanostructures were obtained by mixing two different peptide monomers: the first one composed of an aggregative motif and the homing peptide octreotide (OCT) and the second one composed of the same aggregative motif and the Gd-DOTA complex. The common motif contains four hydrophobic amino acids (*e.g.* Phe, or cyclo-hexylalanine, Cha) alternating with four lysine residues and a PEG linker with four ethoxylic units. The relaxivity values of the different nanofibers, prepared at several molar ratios, fall in the 17.1–19.5 mM^{-1} s^{-1} range. As expected, the slight differences in the r_1 values are strictly related to the dimensions of the resulting nanostructures. *In vitro* assays carried out on MCF-7 cancer cells overexpressing the SST receptor (SSTR) indicated the capability of targeted theranostic fibrils to selectively deliver doxorubicin, with a very

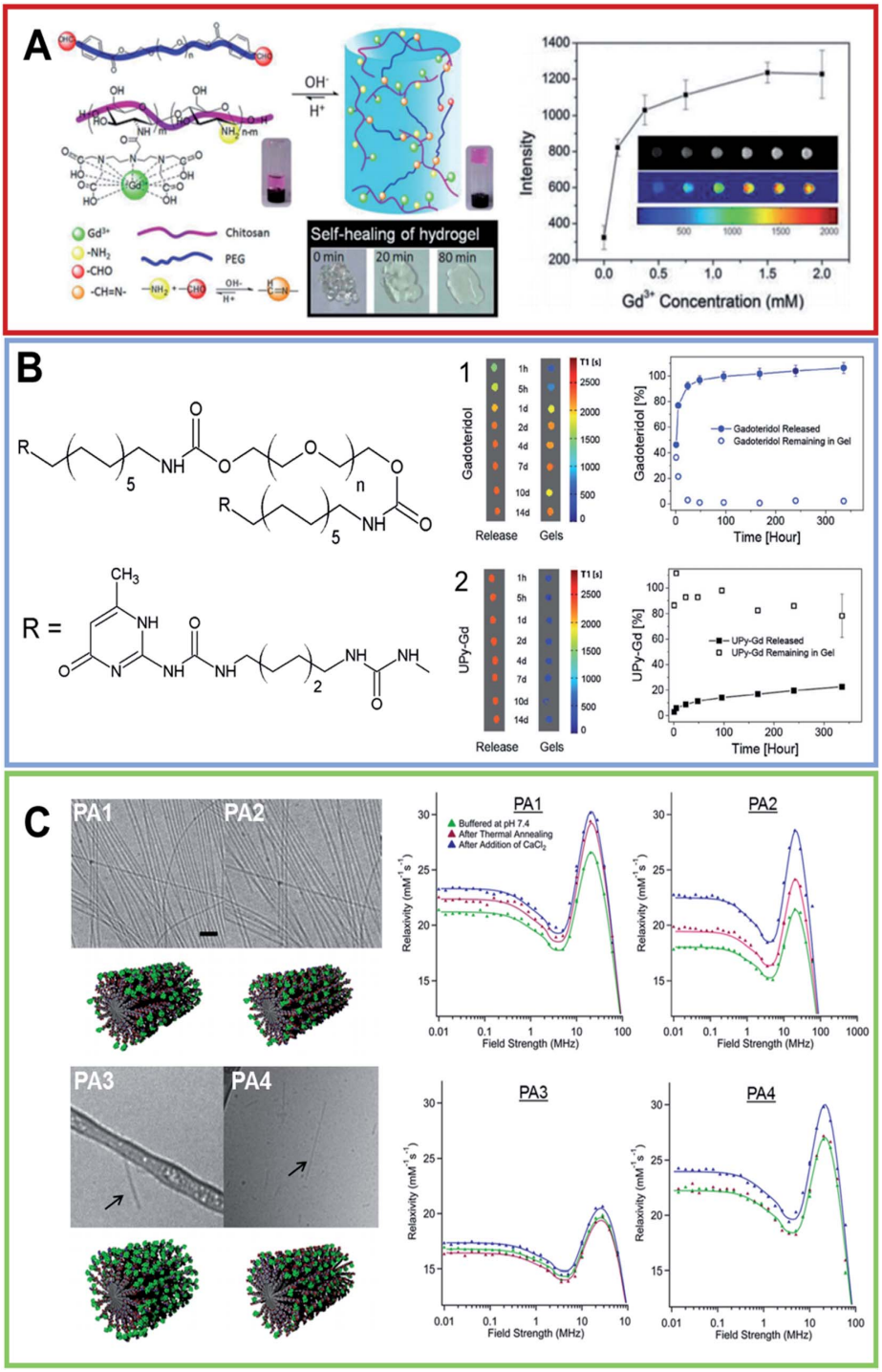

Fig. 5 (A) On the left, schematic illustration of the formation of pH-sensitive injectable hydrogel composed by a modified PEG polymer (blue ribbon) and a DTPA-decorated chitosan (purple ribbon). The hydrogel self-healing feature is reported too. On the right, MRI intensity of the visible hydrogel as a function of the Gd(III) concentration (from ref. 57. Reproduced by permission of The Royal Society of Chemistry). (B) Chemical structure for the bifunctional hydrogelator containing ureidopyrimidinone (UPy). 10 wt% UP-PEG hydrogels T1-weighted 1.5 T MRI scans reported in pseudo-color of the released solution and for the gels. Hydrogels contain either (1) 1×10^{-3} mol L^{-1} Gadoteridol or (2) 1×10^{-3} mol L^{-1} UPy-Gd(III) modified monomers. The relative release curves are reported too (arranged with permission[59]). (C) On the left, Cryo-TEM of PAs conjugates in 10 mmol L^{-1} in Tris buffer after a process of thermal annealing (80 °C for 30 min) and their relative molecular graphical representation. The scale bar represents 200 nm and Gd macrocycles are represented as green elements. On the left, the NMRD profiles for all PAs at three different conditions recorded at 37 °C and a PAs concentration of 2 mmol L^{-1} (adapted with permission,[67] copyright 2014-American Chemical Society).

low toxicity during 24 h of incubation. Another example of a smart theranostic agent based on fibrillary nanostructures was recently proposed by Han *et al.*[49] In this case, the nanostructure was obtained thanks to the self-assembly of PpiX-PEG8-SSSPLGLAK (DOTAMA)-PEG_6-F4 (named as Ppdf-Gd), a monomer containing four different moieties: (i) the polymer-peptide PEG_6-F4 previously described; (ii) a matrix metalloproteinase-2 (MMP-2) responsive chimeric peptide (PLGLA); (iii) the Gd-DOTA complex; and (iv) the photosensitizer protoporphyrin IX (PpiX). Under physiological conditions, the monomer aggregates into spherical nanoparticles having a r_{1p} value of 28.17 mM^{-1} s^{-1}. *In vivo*, the overexpressed MMP-2 hydrolyzes the cleavable peptide sequence, releasing the PEGylated-PpiX fragment, as well as LAK-DOTAMA(Gd)-PEG_6-F4 in the tumor site. Owing to the aromatic stacking interaction among the Phe residues and the hydrogen bond within the peptide chain, this latter fragment self-assembles in long fibers. This sphere-to-fiber transition enhances both the *in vivo* tumor accumulation and the relaxation rate of the Gd-complex (r_{1p} = 51.52 mM^{-1} s^{-1}). The therapeutic efficacy of Ppdf-Gd was assessed in SCC-7 tumor bearing nude mice. The results showed that tumors in the Ppdf-Gd group that underwent light irradiation were significant smaller than other groups. Furthermore, the serum analysis carried out on the blood of mice indicated that the Ppdf-Gd, with and/or without light irradiation, did not cause any toxicity in the liver, kidneys and heart.

In 2017 Lee *et al.* developed supramolecular theranostic nanoagents with antimicrobial activities.[50] These agents, based on the self-assembly of amphiphatic antimicrobial peptides (AMPs), are capable of Gd^{3+} conjugation and tumor-targeting in aqueous solution. In detail, a series of AMPs (G1, G2, G3) consisting of *N*-alkyl/aryl pyrazole (Py) amino acids and arginine (Arg) building blocks were designed. Py and Arg were responsible for upholding the hydrophobicity and positive charge of the peptides. Then, the building block structure was covalently decorated with the addition of tripeptide glycine–histidine–lysine (GHK), for the Gd^{3+} coordination, or linked to cyclic arginine–glycine–aspartic acid (cRGD) (R1, R3), for the recognition of αvβ3 and αvβ5 integrin receptors expressed on tumor cells. Several Gd-complexed co-assembled AMPs (Co-AMPs, G1R1, G2R1, G3R1, G1R3, G2R3, G3R3) were prepared by mixing GHK-AMP and cRGD-AMP peptides of various lengths in deionized water, these peptides were obtained by repeating Py or Arg building units. Co-AMPs were successfully tested as carriers, encapsulating the drug doxorubicin. *In vitro* studies showed a relatively low cytotoxicity in HeLa cells (human tumor cell line), antimicrobial activities against *E. coli* and *S. aureus* and biocompatibility in theranostic treatments (Fig. 4D). Moreover, the r_1 value of Gd^{3+}-G3R3 Co-AMPs (3.6 mM^{-1} s^{-1}) showed the strongest magnetic resonance (MR) signal (Fig. 4D).

Beyond the fibrillary CAs obtained from the self-assembly of PAs and aromatic peptides, there is also an example of supramolecular CAs prepared by direct polymerization of amphiphilic block copolymers, in which the hydrophilic block consists of a modified Gd-DOTA moiety (Fig. 4C).[51] The resulting nanostructures were proposed as promising candidates for the treatment and diagnosis of peritoneal malignancies. The copolymers assemble, leading to two different phases of micellar nanoparticles (MNs): one entirely spherical (SMN) and the other predominantly fibrillar (FMN). The NMRD profiles show enhanced relaxivity over Gd-DOTA (15.6 mM^{-1} s^{-1} and 18.5 mM^{-1} s^{-1} for SMN and FMN respectively), with the same order of magnitude of other nanoparticles and polymer-based systems. *In vivo* preliminary studies, following intraperitoneal injection in mice, indicate that the nanoparticle formulations are retained *in situ* for longer than Gd-DOTA, undergoing less clearance through renal excretion. These data were also confirmed by *ex vivo* analyses.

4. Hydrogels

Hydrogels represent the first class of biomaterials planned for use in the human body, and they have found widespread biomedical applications. Hydrogels are viewed as a three-dimensional network of natural and/or synthetic polymers, having the ability to absorb a large amount of water molecules or biological fluids. The most common constituents include polyvinyl alcohol (PVA), sodium polyacrylate, acrylate polymers and generally copolymers with an abundance of hydrophilic groups. Recently, innovative methods for hydrogel synthesis have extended the field of biomaterials, to concern the unusual aspects of the synthesis of hydrogels, the rewards and limitations, together with particular aspects of synthetic hydrogels such as the composite, biodegradable, superabsorbent and stimuli-sensitive ones.[52,53] They have found application in surgical procedures, as scaffolds for tissue engineering[54] or as the basis for the administration of therapeutic and/or diagnostic agents.[55] Surgical therapies or tissue regenerations can be monitored in real-time, exploiting non-invasive techniques. MRI, indubitably, fulfills these requirements. Despite this interest, few examples of *in vivo* imaging hydrogels based on Gd^{3+}, especially injectable hydrogels, have been reported.

Seliktara *et al.* prepared fluorescence/MRI probes based on two novel hydrogels, in order to identify the host angiogenic response to implants.[56] The Gd-DTPA complex was covalently conjugated to VEGF-bearing biodegradable PEG–fibrinogen hydrogel implants, and they were used to document the *in vivo* degradation and release of bioactive constituents in a stem cell rat implantation model. Hydrogels based on carbohydrates derivatives exhibit many desirable advantages, such as biocompatibility and an easily available feedstock. Moreover, they are pH sensitive, can be injected and are self-healing. These properties allowed the preparation, at room temperature, of hydrogels based on chitosan (CH) and PEG. Zhuo *et al.*, obtained them by mixing, in aqueous solutions, CH functionalized with DTPA and the PEG end-capped with aryl-aldehyde[57] (Fig. 5A). The obtained macromolecular Gd-complex in solution is able to tolerate steam sterilization, and it retains the paramagnetic MRI enhancement contrast effect. The value of the relaxivity is not affected by the covalent bond, showing almost the same value when the complex electrostatically interacts with CH. However, the covalent bond does not allow complex diffusion and the hydrogel can hold back Gd^{3+} ions for 35 d,

according to the *in vivo* tests. Therefore, the gradual loss of intensity is only a result of the hydrogel degradation from the surface to the core of the structure. Consequentially, the shape and global state of the hydrogel can be visualized by a non-invasive MRI, offering a scaffold to monitor long-term reporting of implants. Hydrogels based on enzymatic sensitive carbohydrates were also reported by Hilborn *et al.*[58] They achieved injectable gadolinium-labeled HA, dually functionalized with Gd-DTPA and chemoselective groups. The *in situ* crosslinking of hyaluronic acid (HA) was based on the hydrazone bond. *In vitro* T1-weighted MR images of Gd-labeled hydrogels decreased in function at different time points of degradation. *Ex vivo* MRI confirmed that the resulting hydrogels show noteworthy differences in contrast with the surrounding tissues. At the same time Dankers *et al.*, embedded an ureidopyrimidine modified Gd-DOTA (UPy Gd) complex (Fig. 5B) in an injectable supramolecular ureidopyrimidinone based hydrogel (UPy-PEG).[59] This hydrogel prevents the complex UPy Gd from diffusing, giving a high contrast and precise information on the 3D shape and location, better than Gadoteridol (Prohance®) loaded in UPy-PEG. The UPy-Gd labeled hydrogel is perfectly visible *in vivo* after minimally invasive catheter injection in a beating heart. Despite these results, this supramolecular system has not reached a clinical standard yet. In addition, Parigi *et al.* investigated the Prohance® relaxometric enhancement in HA hydrogels used as a tissue model.[60] This effect can be attributed to a reduced diffusion coefficient in the outer sphere water molecules or by the additional contribution of fast exchanging second-sphere water molecules, with a residence time longer than several hundred nanoseconds. Another class of hydrogels can form self-assembling peptide amphiphiles (PAs). PAs are molecules in which a hydrophilic peptide is covalently bound on a hydrophobic moiety (one or more alkyl chains). The chemical nature of PAs prompts them to self-aggregate in water in highly ordered nanostructures, such as one-dimensional cylindrical micelles.[61] The very close packing of peptide moieties on the nanostructure surface causes their β-sheet arrangement during the self-assembly process. The high biocompatibility and biodegradability of the PAs-based materials suggests their potential employment in nanomedicine as 3D-scaffolds for tissue engineering[62] or as delivery systems for CAs and/or anticancer drugs.[63] In the latter role, the peptide sequence could play both a structural and biological role in the recognition mechanism.[64] One of the first examples of self-assembled MRI-CAs based on PA nanofibers was reported by Stupp and coworkers in 2005, for the *in vivo* detection (migration and degradation) of PA biomaterial based scaffolds.[65] The authors synthesized two branched PAs, both of them containing the palmitic acid as hydrophobic portion, the cyclic DOTA as chelating agent and a peptide sequence as β-sheet inducer (V3A3). Moreover, the two PAs (PACA1 and PACA2) differ for the presence of an additional sequence on V3A3, that is RGDS in PACA1 and C4 in PACA2. The repetition of four cysteins was introduced to achieve the reversible crosslinking of the supramolecular aggregate. Under physiological conditions, Gd-PACA1 forms well-ordered fibers longer than 100 nm and with a width of around 20 nm; whereas uncrosslinked Gd-PACA2 generates spherical micelles (10 nm). Both the nanostructures exhibited relaxivity values higher than the corresponding LMW Gd-complexes (14.7 mM^{-1} s^{-1} for self-assembled Gd-PACA1, 22.8 mM^{-1} s^{-1} for uncrosslinked Gd-PACA2 and 20.8 mM^{-1} s^{-1} for crosslinked Gd-PACA2, respectively). The different r_{1p} observed for the two PAs could be attributed to the different flexibility of the Gd-complex into the supramolecular nanostructure. Indeed, it was observed that the change of position of the chelating agent (close to the alkyl chain) causes a significant increase in the measured relaxivity (21.5 mM^{-1} s^{-1}). In their next study, the same authors used these self-assembled PACA1 nanofibers to dope a PA gel at 1% wt. The PA sequences chosen for the hydrogel preparation were two epitopes typically used for neuronal stem cell differentiation (IKVAV and YIGSR). The resulting hydrogels were non-invasively imaged.[66] The encouraging results prompted the authors to develop four novel DOTAMA(Gd)-PACAs to follow the *in vivo* fate of implanted PA gels in the tibialis anterior muscle of mouse limbs over several days.[67] As for the previously described PAs, all of the PAs contain the V3A3 motif to induce the formation of β-sheet structures plus three glutamic acid residues (E3), that allow an increase of the water solubility and the coordination of divalent cations during the crosslinking with Ca(II) ions. These PAs crosslinked hydrogels, which exhibit a relaxivity value higher than 20 mM^{-1} s^{-1} at 60 MHz, were tested *in vivo* in a mouse model. The results indicated the persistence of the PA gel in the legs over a 4 d period (Fig. 5C).

The other goal pursued by researchers is the delivery of therapeutic and/or diagnostic agents to the desired tissues.[68] From this perspective, several MRI contrast agents containing hydrogels have been formulated in recent years. For example, Cheng *et al.*[69] investigated the theranostic ability of a PEG hydrogel used as a carrier. The effect of Apatinib containing Gd-PEG was studied by injecting this supramolecular structure into a hepatocellular carcinoma model of HepG2 in nude mice. MRI and histomorphology showed that the necrotic area in carcinoma was larger in the Apatinib-Gd-PEG hydrogel treated mouse group, compared with three groups treated with Apatinib, the Gd-PEG hydrogel and saline solution. Moreover, after the treatment, the angiogenesis (VEGF receptor 2) of HepG2 appears to be reduced with respect to the others three groups. Another material with theranostic applications was reported by Yan *et al.*[70] This material, represented by a metallo-folate hydrogel as printable biomaterials, was obtained step by step and has strong mechanical properties. The pterin rings, through hydrogen bonding, form tetramers that evolve into nanofibers by π–π stacking. The zinc ion allows larger-scale fibrils to be achieved that form networks with further crosslinked fibrils. This hydrogel material is able to be doped by Gd^{3+} increasing the value of 1/T1 in the function of the ion concentration. *In vivo* MRI experiments clearly revealed tumor HeLa cells in nude mice.

As an alternative, the PEG network can be crosslinked with bioactive peptides to obtain hydrogels. In this context, Stevens *et al.* developed a multimodal platform system for potential theranostic use in tissue engineering and drug delivery applications.[71] The central moiety of the peptide contains the

heparin binding region amino acid sequence (LRKKLGKA), whereas both the C- and the N-terminus contain a cysteine residue, which assists the hydrogel crosslinking achieved by a Michael addition between the thiol groups of Cys and 4-arm PEG-acrylate. The heparin-binding peptides were further functionalized on the lysine residues with Gd-DOTA. The resulting hydrogel, loaded with cardiac stem cells (CSC), displays mechanical properties resembling cardiac tissue and maintains cell metabolic activity. This platform system improves luciferase-expressing-CSC (CSC-Luc2) retention in the myocardia of mice and shows promising properties for use in further applications enhancing existing cell therapies. In order to improve the MR performance, Chen *et al.* opted to use the Gd(III) ion to generate the formation of supramolecular nanofibers and hydrogels.[72] In this case, hydrogelations were achieved by adding the Gd^{3+} ion to the nanofiber dispersion of the sequence naphthalene-GFFYGRGD or naphthalene-GFFYGRGE. The formation of supramolecular nanostructures improves the longitudinal relaxivity of the contrast agent up to 58.9 mM^{-1} s^{-1}. This large enhancement of the r_1 value could be applied *in vitro* for enzyme detection in aqueous solutions and cell lysates. In our opinion, these hydrogels may be very toxic *in vivo* because of the gadolinium ion loss owing to the peptide hydrolysis. In 2020, Accardo *et al.* developed novel supramolecular MRI diagnostic agents, based on the self-assembly of poly-aromatic peptide sequences.[73] These diagnostic agents [DTPA-PEG8-(FY)3 and DOTA-PEG8-(FY)3] contain two functional regions: a chelating agent (DTPA or DOTA), for the Gd^{3+} complexation, and a peptide-polymer [PEG8-(FY)3] able to form self-supporting and stable soft hydrogels at a concentration of 0.5–1.0% wt. Structural characterization suggested that the insertion of the chelating agent on the peptide building block sequence does not significantly change its aggregation properties. Indeed, both the peptide conjugates self-assemble into highly ordered tree-like multi-branch nanostructures, dominated by antiparallel β-sheet structures, and able to gelificate between 0.5 and 1.0% wt. According to the previously studied systems, relaxivity values of these fibrillary aggregates were found to be approximately 12 mM^{-1} s^{-1} at 20 MHz. Moreover, *in vitro* studies, on the metastasizing TS/A mouse mammary adenocarcinoma cell line, showed a good cytocompatibility of the nanostructures, even at high concentrations.

5. Nanogels

In recent years, researchers have turned their attention to new types of nanosized hydrophilic structures, to solve the problems associated with the use of Gd-based CAs in MRI studies. One of the proposed supramolecular systems is represented by hydrogel nanoparticles, usually named nanogels. These nanostructures are based on biocompatible polymers able to hold a large amount of water on their framework. These molecules can very quickly exchange with coordinated water increasing the relaxivity values per Gd complex embedded in the nanostructure. Moreover, inside these systems Gd-complexes are more stable, avoiding transmetallation reactions with endogenous ions, which are responsible for the toxicity of these CAs. Indeed, the release of Gd^{3+} ions has been related, in patients with impaired renal clearance values, to a very dangerous, and sometimes lethal, pathology called nephrogenic systemic fibrosis (NSF).[74] Moreover, a growing concern is derived from the evidence of a gradual accumulation of Gd^{3+} ions in the bones and in the brain of patients undergoing continuous administration of Gd-CAs over several years, even if they have normal renal clearance values.[75] The research has moved in different directions for the synthesis of these nanostructures. We can distinguish three main classes of nanogels: (i) nanogels in which the LMW Gd-complex is physically encapsulated; (ii) nanogels in which the Gd-complex is covalently bound, and (iii) nanogels in which the paramagnetic ion is used to prompt gel crosslinking. As expected, the relaxivity value of each nanosystem is strongly affected by the synthetic strategy used.

5.1 Gd complex encapsulated in nanogels

Gd-complexes can be directly encapsulated into nanogel structures. The first example of this was reported in 2011 by Keppler *et al.*,[76] who synthesized lectin-Gd-loaded CH nanogels with a prolonged clearance time. Tomato lectin (Lycopersicon esculentum agglutinin (LEA)) was chosen owing to its capacity to specifically bind the polysaccharide side chains of human endothelial cells. The LEA-DTPA conjugate was prepared by covalent coupling to the carboxyl groups of latex nanoparticles, and then complexed with gadolinium ions. LEA-DTPA-Gd conjugates were then encapsulated into CH hydrogel nanoparticles and assembled by the reverse microemulsion method. In order to evaluate the different loading capacities and MRI characteristics, spherical nanoparticles of different sizes (50–250 nm) were formulated by varying the concentrations of reactants. The large amount of Gd-DTPA encapsulated in a single nanosphere permits the detection of a strong MRI signal. Successively, in 2012 Chuburu *et al.* realized a new and straightforward formulation of gadolinium-loaded NPs, based on an ionotropic gelation process, for use as T1/T2 dual-mode contrast agents.[77] In this study, Gd-DOTA was encapsulated in CH/HA based nanoparticles, with a mean diameter between 235 and 284 nm. The release kinetics of the encapsulated CA, evaluated in PBS, detected no significant release after 3 d. The nanogels presented a r_1 and r_2 value of 72.3 and 177.5 mM^{-1} s^{-1} respectively, at a concentration of 1 mM and at 60 MHz. *In vitro* studies were carried out to measure the mitochondrial enzyme activity of C6 glioma cells, and showed no nanoparticle toxicity even at high concentrations. Two years later, the same research group tuned the composition of the previously synthesized Gd-NPs. They also compared two different approaches to incorporate Gd-CAs by physical gelation within CH-NPs.[78] According to the first procedure, CH-NPs were constituted of a single polymer network incorporating Gd-DOTP or MS325. In the second protocol, CH-NPs were composed of a hybrid polymer network (CH, solubilized in a citric acid solution, was left to react with HA and sodium tripolyphosphate, TPP). The formation of the polyelectrolyte complexes induced the gelation process; then Gd-DOTP or MS325 was incorporated into the polyanion phase. Relaxivity studies highlighted enhancements in both the r_1 and

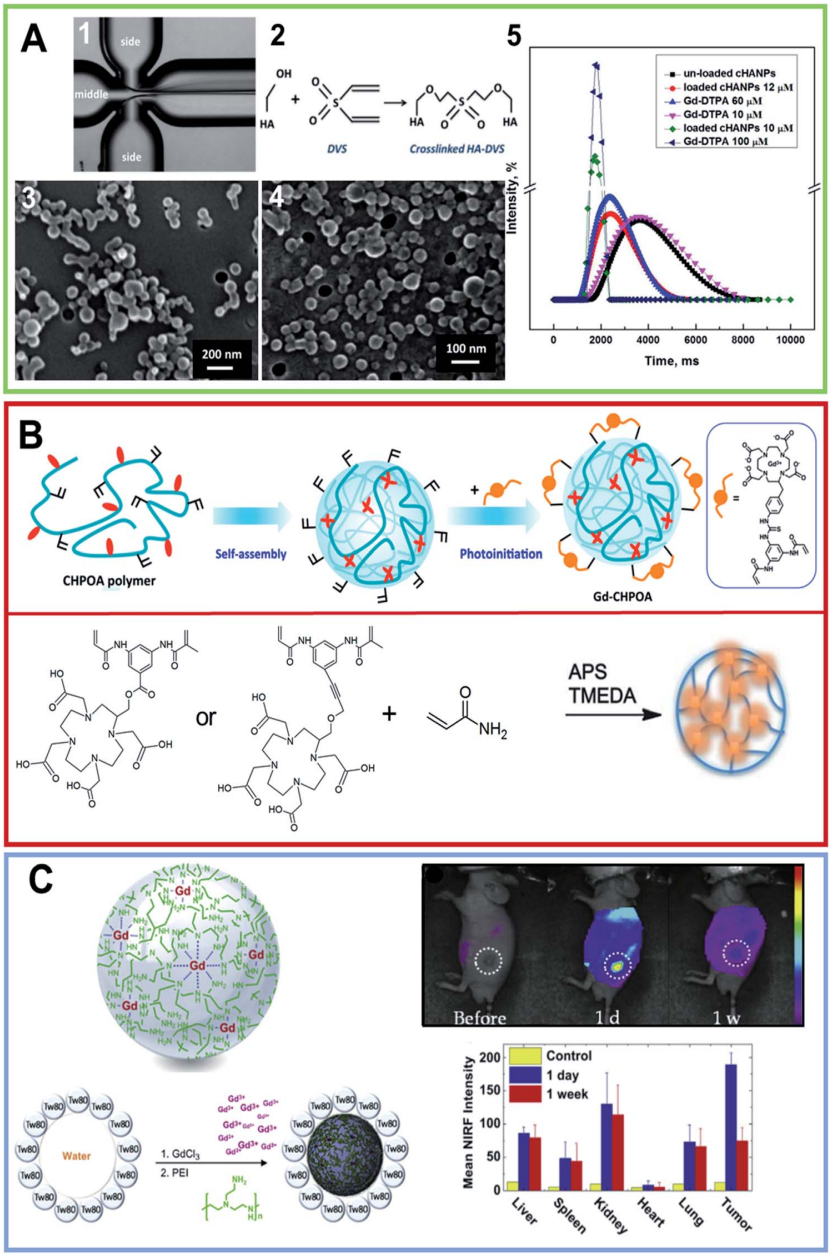

Fig. 6 (A) (1) Optical fluorescence microscopy photo of flow-focusing pattern used for obtaining the nanogel formulation using a microfluidic approach. (2) Schematic crosslinking reaction involving HA hydroxyl groups with DVS. FE-SEM images of crosslinked HA nanoparticles (cHANPs) in aqueous solution in (3) 0.8% v/v of DVS added in the middle channel and (4) 4% v/v of DVS added in the side channels. (5) *In vitro* relaxation time distribution reported for: Gd-DTPA in water solution at (purple line) 10 μmol L^{-1}, (light blue line) 60 μmol L^{-1} and (blue) 100 μmol L^{-1}; un-loaded cHANPs (black line). Also reported are the loaded HA nanoparticles at standard conditions obtained using (red line) 4% v/v DVS in the side channels, at pH 12.3, reported at 12 μmol L^{-1} of Gd-DTPA, (green line) 0.8% v/v DVS and Cspan80 tensioactive 0.5% v/v in the middle channel, reported at Gd-DTPA of 10 μM (reproduced with permission[83]). (B) Upper row, nanogel formulation obtained by self-assembling of a cholesterol and acryloyl-modified polysaccharide pullulan (CHPOA). The photoinduced crosslinkage of the acryloyl groups on the nanogel surface of the DOTA-Gd modified chelating agent (GdCHPOA) allows the creation of T1 MRI contrast agents (adapted with permission,[89] copyright 2015-American Chemical Society). Lower row: chemical structure of two macrocyclic DOTA-based crosslinkers. Polymers were converted in polyacrylamide-based nanogels using an inverse emulsion process *via* ammonium persulfate (APS) as the initiator and by adding tetramethylethylenediamine (TMEDA) to control the radical polymerization rate (arranged from ref. 88. Reproduced by permission of The Royal Society of Chemistry). (C) Graphical representation of the functional metal–organic coordinated nanogels (GdNGs) obtained using the branched poly(ethyleneimine) (PEI) polymer *via* the colloidal reverse microemulsion method. On the right, *in vivo* NIRF images of the SCC7 tumor-bearing mouse before and after tail vein injection (1 d and 1 week) of the GdNGs and the biodistribution of the GdNGs, obtained by NIRF signals from the dissected organs and tumors before (control) and after injection (reproduced with permission[93]).

r_2 values. They appeared to be more important for Gd-DOTP, indicating that the first sphere relaxation effects provide a minor contribution to the relaxivity enhancement, which is mainly ruled by the second sphere contribution. Indeed, the gain in relaxivity was more important for hydrogels that corresponded to the hybrid polymer network, owing to the high number of water molecules involved in the network. These results indicated a direct relationship between the relaxivity performance and the hydrogel matrix composition. Finally, *in vitro* studies showed no toxicity against primary fibroblast cells, in accordance with the results of the MTT assay. Later, the same group also designed and synthesized CH/TPP/HA nanohydrogels loaded with gadolinium complexes, for long-term MRI of lymph nodes (LNs).[79] These Gd-DOTA loaded nanohydrogels were prepared according to the previously employed ionotropic gelation process. In order to obtain NPs with a diameter of less than 100 nm, able to be drained to LNs, CH with molecular weights of 51 kDa (CH51) and 37 kDa (CH37) were used. Beyond the molecular weight of CH, for the formulations the authors also varied several experimental conditions such as the nature of the acid (citric/acetic acid) used for CH solubilization and the CH/TPP ratio (from 0.5 to 12), whereas the HA concentration was kept constant. The results highlighted that the decrease of the CH molecular weight, as well as the CH/TPP ratio, did not induce a decrease in the nano-object size, but only the nanoparticle density in the nanosuspensions (the low CH/TPP led to an increase in the particle density). Moreover, the results indicated the effect of the different acids on the number of formed nanoparticles. Therefore, the amount of Gd-DOTA encapsulated inside nanohydrogels was reduced when using LMW CH. The relaxivity measurements of the resulting nanomaterials indicated their good ability to increase the r_1 longitudinal relaxation rates and the MRI efficiency at 1.5 T. Preliminary cytotoxicity studies, on the SVEC4-10 murine lymph node endothelial cell line, highlighted the good biocompatibility of the nanohydrogels. Very recently, Dinischiotu *et al.*, in collaboration with Chuburu's group, thoroughly investigated the biocompatibility of these CH/TPP/HA nanogels prepared at two different concentrations of CH (2.5 and 1.5 mg mL^{-1}) and loaded with Gd-DOTP or Gd-DOTA complexes.[80] Quantification of the gadolinium ions highlighted the better loading capability of the formulations containing 2.5 mg mL^{-1} of CH. The CH concentration, type of acid or gadolinium contrast agent did not affect the cell survival profiles and the LDH release in SVEC4-10 murine lymph node endothelial cells. Moreover, none of the tested nanogels induced changes in the Nrf-2 protein expression. Another example of CH nanoparticles conjugated with gadolinium *meso*-tetrakis(4-pyridyl)porphyrin [Gd(TPyP)] was described in 2015 by Korri-Youssoufi *et al.*[81] In this study, nanogels were prepared by ionic gelation using bulk LMW and medium molecular weight (MW) CH with different degrees of deacetylation. Gd(TPyP) loaded CH nanoparticles were realized *via* passive absorption by adding various quantities of Gd(TPyP) to CH nanoparticles. The longitudinal and transverse relaxivities of the Gd(TPyP) nanoparticles in aqueous solution have been evaluated, showing a value of 38.35 mM^{-1} s^{-1} for r_1, higher than that of free Gd(TPyP) and commercial Gd-DOTA. On the other hand, the r_2 value in water was found to be 33.43 mM^{-1} s^{-1}, lower compared with free Gd(TPyP), this is probably due to the greater solubility of the compound in water.

In 2018 Ardestani *et al.* reported the synthesis and characterization of a new theranostic CH-carbon dot quantum hybrid nanogel functionalized with dimeglumine gadopentetate.[82] The preparation of the nanoparticles, with an average size of 140 nm, was achieved by adding CH, EDTA and finally glutaraldehyde in sequence, to carbon quantum dots. *In vitro* studies, using normal kidney, HEK-293 and MCF-7 breast cell lines, demonstrated the ability of the nanogel-drug to enter the cell, which appears to be five times more likely than the drug alone, especially for HEK-293. According to the MTT assay and the apoptosis–necrosis test, the nanogel showed less toxicity than the free drug.

PCR quantitative analysis revealed an increase in the Bcl-2 gene expression, followed by a decrease in the Bax expression on the MCF-7 cell line. In addition to several examples of nanogels prepared using the ionotropic gelation process, nanogels can be prepared using a microfluidic flow-focusing platform.[83] In this approach crosslinked HA nanogels entrapping Gd-DTPA were synthesized using divinyl sulfone (DVS) as a crosslinking agent.[83,84] DVS was alternately injected into the middle microfluidic channel or into the side channels and the role played by the concentration, pH and hydrophilic–lipophilic balance (HLB) of the selected surfactants was monitored (Fig. 6A). An increase in the DVS concentration (from 0.6 to 1% v/v) enabled an increase in the encapsulation efficiency and loading capability of the resulting nanoparticles. In the second approach, smaller nanoparticles (~40 nm) were formed, under standard flow conditions and at a pH equal to 12.3, by adding DVS up to 4% v/v to the side channels. Optimizing the process parameters and the crosslinking reaction, a T1 of 1562 mM^{-1} s^{-1} was achieved with 10 μM of the Gd-loaded nanoparticles suspension. A year later, the same group described a process that could be used to produce nanoparticles, encapsulated with both Gd-DTPA and a dye for dual imaging applications. The nanoparticles presented a CH core and an outer shell of HA, consisting of double crosslinking obtained using TPP and DVS.[85] The crosslinkers were used in reverse, specifically TPP to the coacervant phase and DVS to the aqueous phase. Different gradients of temperature were tested and the pH was controlled and kept at a value ranging from 4.5–5 to minimize the time of the coacervation step. Stability studies, performed at various pH values, highlighted the peculiar and interesting pH-sensitive behavior of the nanovectors. MRI studies showed that, during the crosslinking, a relaxation rate T1 of 1720 ms was achieved for a suspension of 20 μM of Gd-loaded nanoparticles. *In vitro* cytotoxicity studies on the adenocarcinoma human alveolar basal epithelial cell line (A549) revealed that, in a range between 200 and 100 μg mL^{-1}, the nanoparticles showed no detectable toxicity. Several specific dyes, Cy5, Atto 633, FITC, were alternately added to the aqueous phase at concentrations ranging from 0.1 to 1 mg mL^{-1} for *in vivo* optical imaging. Gd-loaded nanoparticles appeared capable of maintaining their cargo of CA, and therefore their boosted relaxometric properties.

Wu *et al.* designed and synthesized thermally responsive hydrogel–lipid-hybrid nanoparticulate (HLN), in which stable Gd-hydrogel nanoparticles were loaded into a solid lipid nanoparticle matrix that prevented T1-weighted contrast signal enhancement. Poly(*N*-isopropylacrylamide-coacrylamide) (NIPAM-*co*-AM) nanogels (with a mean diameter lower than 15 nm) were prepared using bisallylamidodiethylenetriaminetriacetic acid, a novel crosslinker able to chelate Gd(III) ions.[86] This supramolecular aggregate provides a very innovative application as a thermometric window for the Gd(III) hydrogel. Increasing the temperature, the melting of the matrix lipid releases the Gd-hydrogel nanoparticles, enhancing the contrast signal. When the temperature was further raised above the volume phase transition temperature of the hydrogel nanoparticles, they collapsed and provided an 'on–off' signal diminution. Both the 'off–on' and the 'on–off' transition temperature could be tuned by changing the lipid matrix and altering the NIPAM/AM ratio in the hydrogel, respectively.

5.2 Covalently bound Gd complexes

Gd-complexes can also be covalently bound on the nanogel, as an alternative. The chemical anchorage of the Gd-complex on the nanogels can occur in distinct ways. One of the simplest strategies is the design and synthesis of a Gd-complex containing a monomer able to generate nanogels under specific experimental self-assembling conditions. Another strategy, is based instead on the employment the gadolinium complexes directly as crosslinker agents during the generation of nanogels. This strategy allows the entire nanoparticle to incorporated into the CA, keeping the nanogel surface available for functionalization with other compounds (for example with targeting molecules). Alternatively, the preparation of the Gd-nanogel can be achieved by covalently binding the metal complex onto the nanogel after preparation. A summary of the nanogels prepared by using these approaches and their structural and relaxometric properties are reported in Table 2. According to the first strategy, based on the self-assembly of a Gd-complex containing monomer, in 2015, Zhu *et al.* synthesized nanospheres based on a derivative of HA functionalized with a DTPA(Gd) complex (HA-Gd-DTPA) as a novel lymphatic system.[87] The self-assembled HA-Gd-DTPA nanospheres exhibited an average hydrodynamic size of around 300 nm. The relaxivity studies showed that the nanoformulation led to a r_1 value of 11.35 mM^{-1} s^{-1} when measured using a 3 T MRI scanner. Preliminary *in vitro* studies, performed on L929 cells, indicated a cell viability of around 90% for cells incubated for 12 h at a dose of 1.5 mg mL^{-1}. Moreover, *in vivo* studies on rabbits demonstrated that the nanospheres had a lymphographic effect superior to that of Magnevist®. Thanks to their dimensions and targeting capabilities, these nanostructures could be used as lymphatic system-specific CAs. Using a completely different strategy, in which the gadolinium complexes (*e.g.* DTPA or DOTA) act as crosslinker agents in the generation of nanogels, Almutairi *et al.* formulated three nanogels of polyacrylamide (PAA).[88] In detail, they synthesized one crosslinker starting from the DTPA chelating agent and two others crosslinkers starting from DOTA. After coordination with gadolinium, the three crosslinker agents [1Gd(III), 2Gd(III) and 3Gd(III)] were used to prepare the PAA/1Gd(III), PAA/2Gd(III) and PAA/3Gd(III) nanogels, through the inverse emulsion process (Fig. 6B). As expected, the obtained nanogels, with a mean diameter ranging between 50 and 85 nm, allowed prolonged circulation and were found to be thermodynamically and kinetically more inert than Magnevist® *versus* transmetallation with Zn^{2+} in phosphate buffer. The incorporation of 1Gd(III) into the PAA based nanogels allowed an increase in the relaxivity up to 9.7 mM^{-1} s^{-1} at 60 MHz and 37 °C. In the same way, the DOTA-based crosslinkers 2Gd(III) and 3Gd(III) showed higher relaxivities than Dotarem® (4.3 and 5.0 mM^{-1} s^{-1} respectively, at 60 MHz and 37 °C), and the nanogels formed revealed an increase in the r_{1p} values up to 17.6 and 14.8 mM^{-1} s^{-1}, respectively. The increase in relaxivity probably depends on the rigidity of the system after crosslinking. Nevertheless, the interesting relaxometric properties of these nanogels, their formulation, and the use of *in situ* on emulsion polymerization, was not highly reproducible. Moreover, the surfactants required for their preparation are difficult

Table 2 Gadolinium complex, synthetic approach used to prepare nanoparticle hydrogels, mean diameter of nanogels, relaxivity value at a 1 mM concentration and references

System	Gd(III) complex	Synthetic approach	Mean diameter (nm)	r_{1p} (mM^{-1} s^{-1})	# ref.
HA-Gd-DTPA	Gd-DTPA	Self-assembly of the Gd-derivative	300	11.4[a]	87
PAA/1Gd(III)	Gd-DTPA	Inverse emulsion using Gd-complex as crosslinker	50 < *d* < 85	9.7[b]	88
PAA/2Gd(III)	Gd-DOTA			17.6	
PAA/3Gd(III)	Gd-DOTA			14.8	
Gd-CHPOA	Gd-DOTA	Photoinitiation using Gd-complex as crosslinker	65	24.1[b]	89
POEMA/AEMA/EGDMA	Gd-DTPA	Free radical polymerization and post-functionalization with Gd-complex	10	20.8[c]	90
VCL/VOU	NH_2-DOTA(Gd)-GA	Precipitation and post-functionalization with Gd-complex	180	6.85[c]	91
Dex-PGMA	Gd-DTPA	Graft polymerization and post-functionalization Gd-complex	185	44.4[a]	92

[a] The relaxivity value was recorded at 3.0 T. [b] The relaxivity value was recorded at 1.41 T. [c] The relaxivity value was recorded at 0.5 T.

to remove. To overcome these drawbacks, in 2015 the same authors explored an alternative synthetic approach based on photoinitiation.[89] In this procedure, a cholesterol and acryloyl-modified polysaccharide pullulan (CHPOA) polymer, characterized by a high biocompatibility, and an ability to self-assemble into nanogels through hydrophobic interactions amongst the cholesterol moieties was formulated. Then, thanks to the photoinitiation, Gd-chelating DOTA crosslinkers were reacted with the acryloyl groups (Fig. 6B). The resulting nanogels, having a mean diameter of 65 nm, present a high colloidal and high Gd-chelating stability. Moreover, they have a longitudinal (T1) relaxivity value (24.1 mM^{-1} s^{-1} at 1.41 T) that is higher than the nanogels previously obtained. These Gd-chelating pullulan nanogels (Gd-CHPOA) caused no organ dysfunction for up to 3 months after intravenous injection in mice.

Beyond the crosslinking approach, there are three examples in the literature of Gd-nanogels obtained using a post-functionalization method in which the Gd-complex is covalently bound on the preformed nanogel. The first example in this direction was reported by Gillies *et al.* in 2013.[90] They obtained very small nanogels, with a mean diameter of 10 nm, using a free radical polymerization approach by starting from poly(ethylene glycol) methyl ether methacrylate (POEMA) and *N*-(2-aminoethyl) methacrylamide hydrochloride (AEMA) as monomers for the preparation. Moreover, ethylene glycol dimethacrylate (EGDMA) was used as a crosslinking agent and benzoyl peroxide was employed as an initiator. POEMA was selected by the authors owing to its hydrophilicity, it should provide a significant enhancement in the water accessible to the nanogel, and in turn increase the relaxivity value of the nanosystem. Moreover, the pendant amine functionalities on AEMA were derivatized with an isothiocyanate derivative of DTPA and, finally, gadolinium coordination was achieved. The obtained nanogel had r_1 values of 20.8 and 17.5 mM^{-1} s^{-1} at 20 and 60 MHz, respectively. The nanogel, injected in mice, showed an enhanced contrast and vascular circulation compared to Magnevist®. Later, a new example of a nanogel for MRI purposes was prepared by Shi *et al.* by post-functionalizing poly(*N*-vinylcaprolactam) (VCL) nanogels with the DOTA(Gd) derivative, NH_2-DOTA(Gd)-GA.[91] In the first step the authors achieved the synthesis of the nanogel *via* precipitation polymerization of VCL with acrylic acid (Aac) and with the degradable crosslinker 3,9-divinyl-2,4,8,10-tetraoxaspiro-[5,5]-undecane (VOU). Then, the surface of the PVCL nanogels was covalently modified with the Gd-complex on the carboxylic groups. The size distributions of the nanogel before and after modification with NH_2-DOTA(Gd)-GA did not show any significant differences and had an average diameter around 180 nm. Relaxivity values, at different gadolinium concentrations, were constants with an average r_1 value of 6.85 mM^{-1} s^{-1} measured with a 0.5 T MRI scanner. Moreover, viability assays carried out on HeLa cells treated with PVCL-Gd nanogels (NGs) with various Gd loadings (10–300 μM), demonstrated the good cytocompatibility of the formulation, with a cell viability of more than 70%. Finally, the PVCL-NGs were found to be able to enhance the MR imaging of cancer cells and of subcutaneous tumor models *in vivo* with an increase in the MR signal-to-noise ratio (SNR) compared to Magnevist®. In the same year, Dou *et al.* synthesized dextran-poly(glycidyl methacrylate) (Dex-PGMA) nano-suitcases *via* a graft copolymerization induced self-assembly (GISA) approach.[92] Then, these nano-suitcases were modified with hydrazine groups in order to afford non-covalent interactions between the hydrazine group and the carboxylic groups of Gd-DTPA. The amount of the Gd-complex in the nano-suitcases, estimated using inductively coupled plasma atomic emission spectroscopy (ICP-AES), was 22.6% wt. The dimensions of the Dex-PGMA-Gd(III) hybrid nanosystems (~185 nm in aqueous solution) are suitable for lymph node accumulation. Moreover, the obtained nanostructure had a very high value of relaxivity, with a r_1 and r_2 relaxivity values of 44.4 and 9.54 mM^{-1} s^{-1} at 3.0 T. Owing to the low r_2/r_1 ratio (~0.21), the Dex-PGMA-Gd(III) nano-suitcases can be considered as potentially positive CAs. As expected, based on their dimensions, these aggregates were found to be able to accumulate the Gd-complex *in vivo* in the lymph nodes of rats and provide strong MR-signals.

5.3 Crosslinked by Gd ions

Gadolinium or others paramagnetic ions, such as manganese, were also directly used as crosslinker agents during nanogel formation. For example, Kim *et al.* developed Gd^{3+} ions coordinated to branched PEI nanogels (GdNGs).[93] The non-crystalline elastic polymer nanogel, that was randomly crosslinked was obtained by mixing the PEI chains with Gd^{3+} ions in aqueous solution (Fig. 6C). Owing to random crosslinking of flexible polymer chains, the resulting nanogel presents an irregular gelation with the core and overall hydrodynamic sizes of approximately 65 and 160 nm and a high elasticity, with an apparent Young's modulus of 3.0 MPa. In contrast to common T1-enhancing gadolinium complexes, Gd-NGs showed the capability of enhancing the negative T2 contrast (r_2 = 82.6 mM^{-1} s^{-1}). Gd-NGs manifested strong intracellular entry into SCC7 (squamous cell carcinoma) cells with no apparent toxicity, suggesting that toxic Gd^{3+} ions are solidly trapped in the PEI network. Owing to their features, these nanogels showed a long blood circulation time as opposed to the rapid system clearance of common nanohybrids that usually undergo sequestration and filtration by the RES. *In vivo* studies, carried out in mice, demonstrated efficient systemic targeting and dual-modality (magnetic resonance/fluorescence) visualization of the tumor area (Fig. 6C). Successively, in 2017 Warszyński *et al.* synthesized another example of a theranostic nanogel, in which alginate gel nanoparticles have been prepared using the reverse microemulsion and physical crosslinking method prompted by Gd(III) ions.[94] The nanogel surface was then modified using the layer-by-layer (LbL) technique using natural polyelectrolytes: CH as the polycation with a zeta potential (ζ) value of +45 mV and alginate (ALG) as the polyanion with ζ −35 mV. The structural characterization of the LbL modified Gd-NG (5 layers) determined the average size and a ζ value of 110 nm and −30 mV, respectively in a 0.015 M NaCl solution. *In vitro* studies indicated that no statistically significant toxic effects were found for both the non-modified and LbL modified nanogels on

the human neuroblastoma cell line SH-SY5Y. Moreover, Gd-NGs were found able to significantly reduce the T1 relaxation time relative to the control samples. At the same time, Leal *et al.* synthesized a highly efficient crosslinked NG based on another paramagnetic ion, the manganese, incorporated into a pH sensitive polymeric hydrogel matrix, composed of 4-vinylpyridine (4-VP) and divinylbenzene (DVB) monomers.[95] The Mn chelate nanogel switches on as a dual MRI contrast agent upon a change in the pH, being able to produce both positive and negative contrast on T1- and T2-weighted MR images. The relaxivities, r_2 and r_1, for the Mn-NG at pH 3.8 were 19.6 and 10.6 mM^{-1} s^{-1}, respectively, at a low magnetic field (1.5 T). This nanoswitch presents the characteristics of a T1 CA with an r_2/r_1 ratio of 1.8. In contrast, at a high magnetic field (9.4 T), the hydrogel behaves as a T2 CA with relaxivity values of 306.3 and 14.6 mM^{-1} s^{-1}, respectively. *In vitro* studies, carried out on the rat glioma cell line C6 cell, showed a high viability with a cell survival value of above 80%.

6. Conclusion

Magnetic resonance imaging CAs based on Gd-complexes are employed in approximately 40% of clinical examinations used to visualize small tumor lesions. Even if highly accurate, MRI modality suffers because of its low sensitivity and LMW-CAs rapidly extravasate after their administration. For these reasons, in the last two decades many macro- and supramolecular multimeric gadolinium complexes (dendrimers, polymers, carbon nanostructures, micelles and liposomes) have been designed to increase their performance and to reduce the administered dose. One of the most promising applications of these nanostructures is the possibility of combining two or more diagnostic agents. In this context, in recent years several examples of nanoparticles have been proposed for simultaneous visualization using different diagnostic techniques.[96–98] However, research on novel supramolecular systems such as fibers, hydrogels and nanogels has become particularly relevant after the European Medicines Agency (EMA) decided to withdraw contrast agents based on linear chelators from the market as they were considered to not be sufficiently stable in relation to the *in vivo* release of toxic Gd(III) ions. Supramolecular systems have been identified as innovative vehicles for CAs that are able to significantly increase their relaxivity values. Indeed, it was observed that nanogels that encapsulate LMW-CAs have very high relaxivity values (up to 100 mM^{-1} s^{-1}). On the other hand, it can be observed that nanostructures in which the Gd-complex is covalently bound exhibit lower relaxivity values. The reasons for these differences, in terms of the performance, are not yet completely clear. The availability of high-relaxivity nanosystems could provide the answer to the urgent need for reducing the clinical dose. This strategy could allow long-term adverse health effects to be minimized owing to the *in vivo* metal deposition. Moreover, the capability of the supramolecular nanostructures to shield Gd-complexes from transmetallation reactions may prevent unwanted biotransformation, which are the basis of *in vivo* metal accumulation. Obviously, the preparation and exploitation of these supramolecular Gd-CAs is not trivial. For this reason, this strategy should be the preferred method only if it is strictly necessary. Identification of the structural parameters that affect the performance of the supramolecular CA could allow novel soft materials to be designed for use in the clinic in the future.

7. Methodology

A systematic literature review was performed according to PRISMA (Preferred Reporting Items for Systematic Reviews and Meta-Analyses) criteria. Scientific contributions were critically selected *via* consecutive operations, related to identification, screening, eligibility and inclusion steps (see Scheme 1). Published studies were correlated to the selected topic and were identified using an electronic search in SciFinder Scholar web database, that includes PubMed, Caplus and Medline. A systematic literature review was performed using English keywords and refining procedures were applied. The operators "OR" and "AND" were used in order to obtain an inclusive and restrictive outcome. SciFinder Scholar web database was first questioned using the "MRI contrast agent" query, producing 14 012 results. A consecutive refinement with "gadolinium" produced 5610 outcomes. Removing duplicates, non-English languages, and selecting only journal, review book and letter contributions, gradually decrease the number of results from 4474 to 4105, and finally to 3514. These latter outcomes were further analyzed using the following keywords: fiber (29 results), hydrogel (21 results), hydrogel nanoparticle (10 results), nanogel (6 results), nanohydrogel (2 results), and chitosan nanoparticles (42 results). The articles related to CEST contrast agents, nanocomposites, micelles and gadolinium oxide were excluded. A manual search in the reference list of the eligible products was performed in order to identify additional relevant

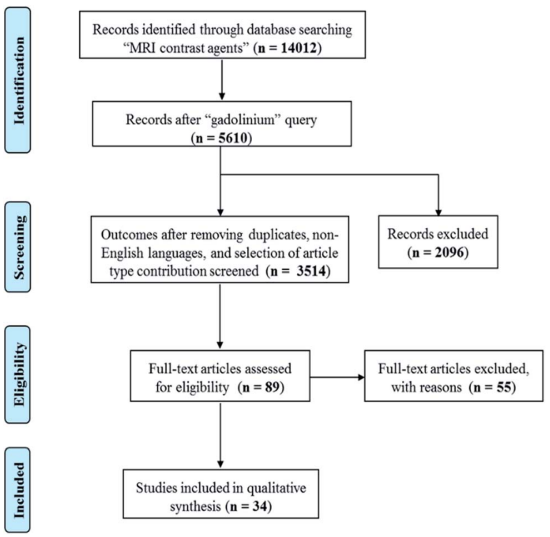

Scheme 1 Scheme describing the systematic literature review performed according to PRISMA (Preferred Reporting Items for Systematic Reviews and Meta-Analyses) criteria.

papers, in case they were missed in the online searches. The clear identification of the relevant literature data was performed including the title, abstract and full-text reading procedures. The research provided 9 results about fibers, 14 regarding hydrogels and 20 about nanogels.

Conflicts of interest

There are no conflicts to declare.

Acknowledgements

This work was supported by the PRIN-2017A2KEPL project and by the grant from Regione Campania-POR Campania FESR 2014/2020 "Combattere la resistenza tumorale: piattaforma integrata multidisciplinare per un approccio tecnologico innovativo alle oncoterapie-Campania Oncoterapie" (Project No. B61G18000470007).

Notes and references

1 A. R. Kherlopian, T. Song, Q. Duan, M. A. Neimark, M. J. Po, J. K. Gohagan and A. F. Laine, *BMC Syst. Biol.*, 2008, **2**, 74–92.
2 R. Salzer, *Biomedical imaging: principles and applications*, John Wiley & Sons, Inc., Hoboken, NJ USA, 2012.
3 E. C. Lin, *Mayo Clin. Proc.*, 2010, **85**, 1142–1146.
4 J. A. Seibert and R. L. Morin, *Pediatr. Radiol.*, 2011, **41**, 573–581.
5 F. A. Gallagher, *Clin. Radiol.*, 2010, **65**, 557–566.
6 A. Ng and J. Swanevelder, *Cont. Educ. Anaesth. Crit. Care Pain*, 2011, **11**, 186–192.
7 N. Ji, *Neuron*, 2014, **83**, 1242–1254.
8 S. K. Nune, P. Gunda, P. K. Thallapally, Y. Y. Lin, M. Laird Forrest and C. J. Berkland, *Expert Opin. Drug Delivery*, 2009, **6**, 1175–1194.
9 M. A. Farrukh, *Functionalized nanomaterials*, InTech-Open Access Publisher, London, UK, 2016.
10 T. H. LaBean, *Nature*, 2009, **459**, 331–332.
11 A. P. Khandhar, P. Keselman, S. J. Kemp, R. M. Ferguson, P. W. Goodwill, S. M. Conolly and K. M. Krishnan, *Nanoscale*, 2017, **9**, 1299–1306.
12 X. Huang, R. O'Connor and E. A. Kwizera, *Nanotheranostics*, 2017, **1**, 80–102.
13 R. Cheheltani, R. M. Ezzibdeh, P. Chhour, K. Pulaparthi, J. Kim, M. Jurcova, J. C. Hsu, C. Blundell, H. I. Litt, V. A. Ferrari, H. R. Allcock, C. M. Sehgal and D. P. Cormode, *Biomaterials*, 2016, **102**, 87–97.
14 I. R. Young, *Methods in biomedical magnetic resonance imaging and spectroscopy*, John Wiley & Sons, Inc., Chichester, UK, 2012.
15 P. A. Rinck, *Magnetic resonance in medicine*, ABW Wissenschaftsverlag GmbH, Berlin, Germany, 2003.
16 V. C. Pierre and M. J. Allen, *Contrast agents for MRI: experimental methods*, RSC, Croydon, UK, 2018.
17 A. Merbach, L. Helm and E. Toth, *The chemistry of contrast agents in medical magnetic resonance imaging*, John Wiley & Sons, Inc., Hoboken, NJ USA, 2013.
18 S. Laurent, C. Henoumont, D. Stanicki, S. Boutry, E. Lipani, S. Belaid, R. N. Muller and L. V. Elst, *MRI Contrast agents: from molecules to particles*, Springer, Singapore, 2017.
19 C. Corot and D. Warlin, *Wiley Interdiscip. Rev.: Nanomed. Nanobiotechnol.*, 2013, **5**, 411–422.
20 S. Aime, E. Gianolio and A. Viale, in *Paramagnetism in experimental biomolecular NMR*, ed. C. Luchinat, G. Parigi and E. Ravera, RCS, Cambridge, UK, 2018, pp. 189–218.
21 P. Caravan, N. J. Cloutier, M. T. Greenfield, S. A. McDermid, S. U. Dunham, J. W. Bulte, J. C. Amedio Jr, R. J. Looby, R. M. Supkowski, W. D. Horrocks Jr, T. J. McMurry and R. B. Lauffer, *J. Am. Chem. Soc.*, 2002, **124**, 3152–3162.
22 A. W. Bosman, H. M. Janssen and E. W. Meijer, *Chem. Rev.*, 1999, **99**, 1665–1688.
23 D. L. Ladd, R. Hollister, X. Peng, D. Wei, G. Wu, D. Delecki, R. A. Snow, J. L. Toner, K. Kellar, J. Eck, V. C. Desai, G. Raymond, L. B. Kinter, T. S. Desser and D. L. Rubin, *Bioconjugate Chem.*, 1999, **10**, 361–370.
24 C. Diaferia, E. Gianolio and A. Accardo, *J. Pept. Sci.*, 2019, **25**, 3157.
25 T. S. Desser, D. L. Rubin, H. Muller, G. L. McIntire, E. R. Bacon and K. R. Hollister, *Acad. Radiol.*, 1999, **6**, 112–118.
26 A. Dirksen, S. Langereis, B. F. M. de Waal, M. H. P. van Genderen, T. M. Hackeng and E. W. Meijer, *Chem. Commun.*, 2005, 2811–2813.
27 S. Aime, E. Gianolio, E. Terreno, I. Menegotto, C. Bracco, L. Milone and G. Cravotto, *Magn. Reson. Chem.*, 2003, **41**, 800–805.
28 B. Sitharaman and L. J. Wilson, *J. Biomed. Nanotechnol.*, 2007, **3**, 342–352.
29 P. P. Fatouros and M. D. Shultz, *Nanomedicine*, 2013, **8**, 1853–1864.
30 R. Sethi, Y. Mackeyev and L. J. Wilson, *Inorg. Chim. Acta*, 2012, **393**, 165–172.
31 K. B. Hartman, S. Laus, R. D. Bolskar, R. Muthupillai, L. Helm, E. Toth, A. E. Merbach and L. J. Wilson, *Nano Lett.*, 2008, **8**, 415–419.
32 A. Accardo, D. Tesauro, L. Aloj, C. Pedone and G. Morelli, *Coord. Chem. Rev.*, 2009, **253**, 2193–2213.
33 E. Cittadino, M. Botta, L. Tei, F. Kielar, R. Stefania, E. Chiavazza, S. Aime and E. Terreno, *ChemPlusChem*, 2013, **78**, 712–722.
34 G. Lipari and A. Szabo, *J. Am. Chem. Soc.*, 1982, **104**, 4546–4559.
35 G. Lipari and A. Szabo, *J. Am. Chem. Soc.*, 1982, **104**, 4559–4570.
36 T. Fan, X. Yu, B. Shen and L. Sun, *J. Nanomater.*, 2017, **9**, 1–16.
37 Y. Wang, J. Chou, Y. Sun, S. Wen, S. Vasilescu and H. Zhang, *Mater. Sci. Eng., C*, 2019, **101**, 650–659.
38 J. J. Panda and V. S. Chauhan, *Polym. Chem.*, 2014, **5**, 4418–4436.
39 D. Tesauro, A. Accardo, C. Diaferia, V. Milano, J. Guillon, L. Ronga and F. Rossi, *Molecules*, 2019, **24**, 351–378.
40 A. Ghosh, M. Haverick, K. Stump, X. Yang, M. F. Tweedle and J. E. Goldberger, *J. Am. Chem. Soc.*, 2012, **134**, 3647–3650.

41 C. Diaferia, E. Gianolio, P. Palladino, F. Arena, C. Boffa, G. Morelli and A. Accardo, *Adv. Funct. Mater.*, 2015, **25**, 7003–7016.
42 C. Diaferia, E. Gianolio, A. Accardo and G. Morelli, *J. Pept. Sci.*, 2017, **23**, 122–130.
43 M. Reches and E. Gazit, *Science*, 2003, **300**, 625–627.
44 C. Diaferia, F. A. Mercurio, C. Giannini, T. Sibillano, G. Morelli, M. Leone and A. Accardo, *Sci. Rep.*, 2016, **6**, 26638.
45 C. Diaferia, E. Gianolio, T. Sibillano, F. A. Mercurio, M. Leone, C. Giannini, N. Balasco, L. Vitagliano, G. Morelli and A. Accardo, *Sci. Rep.*, 2017, **7**, 307–321.
46 C. Diaferia, N. Balasco, T. Sibillano, M. Ghosh, L. Adler-Abramovich, C. Giannini, L. Vitagliano, G. Morelli and A. Accardo, *Chem.–Eur. J.*, 2018, **24**, 6804–6817.
47 J. Huang, C. L. Hastings, G. P. Duffy, H. M. Kelly, J. Raeburn, D. J. Adams and A. Heise, *Biomacromolecules*, 2013, **14**, 200–206.
48 I. Kim, E. H. Han, J. Ryu, Y. J. Min, H. Ahn, Y. H. Chung and E. Lee, *Biomacromolecules*, 2016, **17**, 3234–3243.
49 J. Zhang, Y. Mu, Z. Ma, K. Han and H. Han, *Biomaterials*, 2018, **182**, 269–278.
50 I. Kim, S. Jin, E. Han, E. Ko, M. Ahn, W. Bang, J. Bang and E. Lee, *Biomacromolecules*, 2017, **18**, 3600–3610.
51 L. M. Randolph, C. L. M. LeGuyader, M. E. Hahn, C. M. Andolina, J. P. Patterson, R. F. Mattrey, J. E. Millstone, M. Botta, M. Scadeng and N. C. Gianneschi, *Chem. Sci.*, 2016, **7**, 4230–4236.
52 J. Radhakrishnan, A. Subramanian, U. M. Krishnan and S. Sethuraman, *Biomacromolecules*, 2017, **18**, 1–26.
53 A. Dasgupta, J. H. Mondal and D. Das, *RSC Adv.*, 2013, **3**, 9117–9149.
54 R. Langer and J. P. Vacanti, *Science*, 1993, **260**, 920–926.
55 J. Li and D. J. Mooney, *Nat. Rev. Mater.*, 2016, **1**, 16071.
56 A. Berdichevski, H. S. Yameen, H. Dafni, M. Neeman and D. Seliktara, *Proc. Natl. Acad. Sci. U. S. A.*, 2015, **112**, 5147–5152.
57 J. Liu, K. Wang, J. Luan, Z. Wen, L. Wang, Z. Liu, G. Wu and R. Zhuo, *J. Mater. Chem. B*, 2016, **4**, 1343–1353.
58 D. Bermejo-Velasco, W. Dou, A. Heerschap, D. Ossipov and J. Hilborn, *Carbohydr. Polym.*, 2018, **197**, 641–648.
59 M. H. Bakker, C. C. S. Tseng, H. M. Keizer, P. R. Seevinck, H. M. Janssen, F. J. Van Slochteren, S. A. Chamuleau and P. Y. W. Dankers, *Adv. Healthcare Mater.*, 2018, **7**, 1701139.
60 M. Fragai, E. Ravera, F. Tedoldi, C. Luchinat and G. Parigi, *ChemPhysChem*, 2019, **20**, 2204–2209.
61 A. Dasgupta and D. Das, *Langmuir*, 2019, **35**, 10704–10724.
62 M. J. Webber, J. A. Kessler and S. I. Stupp, *J. Intern. Med.*, 2010, **267**, 71–88.
63 A. Altunbas and D. J. Pochan, *Top. Curr. Chem.*, 2012, **310**, 135–167.
64 A. Accardo, D. Tesauro and G. Morelli, *Polym. J.*, 2013, **45**, 481–493.
65 S. R. Bull, M. O. Guler, R. E. Bras, T. J. Meade and S. I. Stupp, *Nano Lett.*, 2005, **5**, 1–4.
66 S. R. Bull, M. O. Guler, R. E. Bras, P. N. Venkatasubramanian, S. I. Stupp and T. J. Meade, *Bioconjugate Chem.*, 2005, **16**, 1343–1348.
67 A. T. Preslar, G. Parigi, M. T. McClendon, S. S. Sefick, T. Y. Moyer, C. R. Haney, E. A. Waters, K. W. MacRenaris, C. Luchinat, S. I. Stupp and T. J. Meade, *ACS Nano*, 2014, **8**, 7325–7332.
68 D. Qureshi, S. K. Nayak, S. Maji, A. Anis, D. Kim and K. Pal, *Eur. Polym. J.*, 2019, **120**, 109220.
69 Z. Liu, C. Wang, G. Wu and J. Cheng, *Biochem. Biophys. Res. Commun.*, 2019, **509**, 529–534.
70 K. Liu, S. Zang, R. Xue, J. Yang, L. Wang, J. Huang and Y. Yan, *ACS Appl. Mater. Interfaces*, 2018, **10**, 4530–4539.
71 A. T. Speidel, D. J. Stuckey, L. W. Chow, L. H. Jackson, M. Noseda, M. Abreu Paiva, M. D. Schneider and M. M. Stevens, *ACS Cent. Sci.*, 2017, **3**, 338–348.
72 Y. Hua, G. Pu, C. Ou, X. Zhang, L. Wang, J. Sun, Z. Yang and M. Chen, *Sci. Rep.*, 2017, **7**, 40172.
73 E. Gallo, C. Diaferia, E. D. Gregorio, G. Morelli, E. Gianolio and A. Accardo, *Pharmaceuticals*, 2020, **13**, 19.
74 P. Marckmann, L. Skov, K. Rossen, A. Dupont, M. B. Damholt, J. G. Heaf and H. S. Thomsen, *J. Am. Soc. Nephrol.*, 2006, **17**, 2359–2362.
75 E. Gianolio, P. Bardini, F. Arena, R. Stefania, E. Di Gregorio, R. Iani and S. Aime, *Radiology*, 2017, **285**, 839–849.
76 I. Pashkunova-Martic, C. Kremser, M. Galanski, V. Arion, P. Debbage, W. Jaschke and B. Keppler, *Mol. Imaging Biol.*, 2011, **13**, 16–24.
77 T. Courant, V. G. Roullin, C. Cadiou, M. Callewaert, M. C. Andry, C. Portefaix, C. Hoeffel, M. C. de Goltstein, M. Port, S. Laurent, L. V. Elst, R. Muller, M. Molinari and F. Chuburu, *Angew. Chem., Int. Ed. Engl.*, 2012, **51**, 9119–9122.
78 M. Callewaert, V. G. Roullin, C. Cadiou, E. Millart, L. Van Gulik, M. C. Andry, C. Portefaix, C. Hoeffel, S. Laurent, L. V. Elst, R. Muller, M. Molinari and F. Chuburu, *J. Mater. Chem. B*, 2014, **2**, 6397–6405.
79 G. Rigaux, C. V. Gheran, M. Callewaert, C. Cadiou, S. N. Voicu, A. Dinischiotu, M. C. Andry, L. V. Elst, S. Laurent, R. N. Muller, A. Berquand, M. Molinari, S. Huclier-Markai and F. Chuburu, *Nanotechnology*, 2017, **28**, 055705.
80 C. V. Gheran, G. Rigaux, M. Callewaert, A. Berquand, M. Molinari, F. Chuburu, S. N. Voicu and A. Dinischiotu, *Nanomaterials*, 2018, **8**, 201.
81 T. Jahanbin, H. Sauriat-Dorizon, P. Spearman, S. Benderbous and H. Korri-Youssoufi, *Mater. Sci. Eng., C*, 2015, **52**, 325–332.
82 V. V. Boroujeni, H. Hejazinia, S. E. S. Ebrahimi, M. P. Hamedani and M. S. Ardestani, *J. Pharm. Res.*, 2018, **7**, 153–159.
83 M. Russo, P. Bevilacqua, P. A. Netti and E. Torino, *Sci. Rep.*, 2016, **6**, 37906.
84 M. Russo, P. Bevilacqua, P. A. Netti and E. Torino, *Mol. Imaging*, 2017, **16**, 1–3.
85 D. Vecchione, A. M. Grimaldi, E. Forte, P. Bevilacqua, P. A. Netti and E. Torino, *Sci. Rep.*, 2017, **7**, 45121.

86 A. J. Shuhendler, R. Staruch, W. Oakden, C. R. Gordijo, A. M. Rauth, G. J. Stanisz, R. Chopra and X. Y. Wu, *J. Controlled Release*, 2012, **157**, 478–484.
87 G. Wu, H. Zhang, Z. Zhan, Q. R. Lu, J. Cheng, J. Xu and J. Zhu, *Chin. J. Chem.*, 2015, **33**, 1153–1158.
88 J. Lux, M. Chan, L. V. Elst, E. Schopf, E. Mahmoud, S. Laurent and A. Almutairi, *J. Mater. Chem. B*, 2013, **1**, 6359–6364.
89 M. Chan, J. Lux, T. Nishimura, K. Akiyoshi and A. Almutairi, *Biomacromolecules*, 2015, **16**, 2964–2971.
90 A. Soleimani, F. Martinez, V. Economopoulos, P. J. Foster, T. J. Scholl and E. R. Gillies, *J. Mater. Chem. B*, 2013, **1**, 1027–1034.
91 W. Sun, S. Thies, J. Zhang, C. Peng, G. Tang, M. Shen, A. Pich and X. Shi, *ACS Appl. Mater. Interfaces*, 2017, **9**, 3411–3418.
92 H. Wang, T. T. Dai, B. L. Lu, S. L. Li, Q. Lu, V. Mukwaya and H. J. Dou, *Chin. J. Polym. Sci.*, 2018, **36**, 391–398.
93 C. K. Lim, A. Singh, J. Heo, D. Kim, K. E. Lee, H. Jeon, J. Koh, I. C. Kwon and S. Kim, *Biomaterials*, 2013, **34**, 6846–6852.
94 K. Podgórna, K. Szczepanowicz, M. Piotrowski, M. Gajdošová, F. Štěpánek and P. Warszyński, *Colloids Surf., B*, 2017, **153**, 183–189.
95 C. Caro, M. L. García-Martín and M. P. Leal, *Biomacromolecules*, 2017, **18**, 1617–1623.
96 X. Zhao, L. Zeng, N. Hosmane, Y. Gong and A. Wu, *Chin. Chem. Lett.*, 2019, **30**, 87–89.
97 Y. Zhang, H. Huang, H. Fu, M. Zhao, Z. Wu, Y. Dong, H. Li, Y. Duan and Y. Sun, *RSC Adv.*, 2019, **9**, 33302–33309.
98 J. Qin, G. Liang, B. Feng, G. Wang, N. Wu, Y. Deng, A. A. Elzatahry, A. Alghamdi, Y. Zhao and J. Wei, *Chin. Chem. Lett.*, 2020, DOI: 10.1016/j.cclet.2020.05.021.

molecules

MDPI

Article

Stable Formulations of Peptide-Based Nanogels

Elisabetta Rosa [1], Carlo Diaferia [1], Enrico Gallo [2], Giancarlo Morelli [1] and Antonella Accardo [1,*]

[1] Department of Pharmacy and Interuniversity Research Centre on Bioactive Peptides (CIRPeB), University of Naples "Federico II", via Mezzocannone 16, 80134 Naples, Italy; elisabetta.rosa@unina.it (E.R.); carlo.diaferia@unina.it (C.D.); gmorelli@unina.it (G.M.)

[2] IRCCS SDN, Via E. Gianturco 113, 80143 Naples, Italy; enrico.gallo@synlab.it

* Correspondence: antonella.accardo@unina.it; Tel.: +39-081-2532045

Academic Editor: Paula A. C. Gomes
Received: 22 June 2020; Accepted: 27 July 2020; Published: 29 July 2020

Abstract: Recently, nanogels have been identified as innovative formulations for enlarging the application of hydrogels (HGs) in the area of drug delivery or in diagnostic imaging. Nanogels are HGs-based aggregates with sizes in the range of nanometers and formulated in order to obtain injectable preparations. Regardless of the advantages offered by peptides in a hydrogel preparation, until now, only a few examples of peptide-based nanogels (PBNs) have been developed. Here, we describe the preparation of stable PBNs based on Fmoc-Phe-Phe-OH using three different methods, namely water/oil emulsion (W/O), top-down, and nanogelling in water. The effect of the hydrophilic–lipophilic balance (HLB) in the formulation was also evaluated in terms of size and stability. The resulting nanogels were found to encapsulate the anticancer drug doxorubicin, chosen as the model drug, with a drug loading comparable with those of the liposomes.

Keywords: peptide-based nanogels; inverse emulsion; nanogel formulation; hydrogel nanoparticles; diagnostic imaging; peptide aggregates; doxorubicin

1. Introduction

In the last few years, the design and the formulation of hydrogel materials (HGs) have attracted a great deal of interest in biomedical areas [1,2]. Hydrogels are three-dimensional (3D) structures formed by chemically or physically crosslinked polymeric networks which can confine a large amount of water. Because of their unique structural and mechanical properties and their high biocompatibility, HGs have been proposed as innovative materials for different biomedical applications such as tissue engineering [3–6] and delivery systems of active pharmaceutical ingredients (APIs), including drugs [7] or diagnostic agents [8]. Nanosized structures, including micelles [9], nanoparticles [10], nanofibers [11], and liposomes [12] are particularly suitable for this purpose. Indeed, they overcome some problematic issues and limitations related to the in vivo bioavailability, biodisponibility, toxicity, and instability of drugs. Hydrogel nanoparticles, also named nanogels, seem to be particularly appealing for this purpose. They combine the advantages of traditional HGs and nanosized particles. Nanogels are aggregates in the submicron range scale composed of an interior hydrogel-like network (core) stabilized by an external surfactant coating (shell). Their physical colloidal form is compatible with needle injection. The large surface area is accessible for multivalent bioconjugation, meanwhile, the interior network can work as a reservoir for additional incorporation of biomolecules. Moreover, the small size of these formulations generally leads to simple renal clearance, increased penetration through tissue barriers, and good stability for prolonged circulation in the blood stream. Analogously to HGs, nanogels can be prepared by the self-assembly of biocompatible and biodegradable polymers such as chitosan (CS) [13], hyaluronic acid (HA) [14], and dextran [15] according to different technological

approaches including microfluidic [16] micromolding [17] and photolithographic techniques [18]. However, most of these processes require extreme conditions of pH and temperature and some of them require the use of crosslinking agents, which are not completely biocompatible. In order to overcome these limitations, peptide-based nanogels (PBNs) could represent an innovative tool. In the literature, so far, there are only two examples of peptide-based nanogels. The first example describes the preparation of the nanogels by the inverse emulsion technique [19] and the other example describes a top-down methodology. On the one hand, the inverse emulsion technique consists of the formation of a water-in-oil (W/O) emulsion via homogenization of an aqueous phase containing the Fmoc-Phe-Phe-OH (Fmoc-FF, N^{α}-9-fluorenylmethoxycarbonyl-diphenylalanine) peptide with an oily phase containing a surfactant as a stabilizer. This methodology is very often used for the formulation of polymeric nanogels [20]. On the other hand, the top-down methodology involves the formulation of nanogel particles using a α,β-dehydrophenylalanine (ΔPhe) containing dipeptide, H-Phe-ΔPhe-OH (phenylalanine-α,β-dehydrophenylalanine) [21]. Successively, preformed H-Phe-ΔPhe-OH gels are sonicated with a microprobe, obtaining a formulation with an average hydrodynamic radius (r_H) of 150 nm. However, in this formulation a certain degree of particle instability, probably due to the absence of surfactant protective shell, was noticed with an increase of the radius up to 350 nm, after 60 h. By starting from the awareness that in vitro and in vivo stability represents an essential requirement for the development of biomedical nanosystems, we exploited three different methodologies (see Figure 1) to achieve a stable and reproducible formulation of peptide-based nanogels. The peptide chosen for nanogel preparation is the ultrashort Fmoc-FF peptide. It is well known that many short and ultrashort peptide sequences can spontaneously self-assemble into HGs, as a consequence of physical and noncovalent interactions, thus, avoiding the employment of crosslinking agents [22–24]. Among these peptides, one of the most studied is Fmoc-FF. It was identified simultaneously by Ulijn's [25] and Gazit's groups [26], in 2006. This simple building block, utilizing a β-sheet motif, efficiently assembles into nanostructured fibrous hydrogels under physiological conditions. Structural studies have been carried out on this dipeptide and some of its analogues, resulting in an extensive comprehension of the self-assembling mechanism [27–30]. However, it was observed that the mechanical properties of the resulting gel were deeply affected by the preparation method (pH and the solvent switch method [25,26]) and by the final solution conditions (pH and salt content) [31]. Because of a series of interesting features (such as a certain stability degree across a broad range of pH and temperatures, the presence of hollow cavities in the supramolecular architecture, and mechanical rigidity), Fmoc-FF hydrogel was also proposed as a potential scaffold material for tissue engineering or as a drug delivery system [5,26]. The methods we investigated for preparation of the Fmoc-FF-based nanogels are as follows: (A) the water-in-oil emulsion technique (or reverse emulsion technique, W/O); (B) the top-down methodology; and (C) a novel modified procedure designed by us and named "nanogelling in water". In the inverse emulsion method, we focused our attention on the stabilizing capacity of the surfactant chosen for the nanogel preparation, basing our reasoning on the hydrophilic–lipophilic balance (HLB). This parameter, proposed by Griffin between the late 1940s and early 1950s [32,33] allows one to predict the stability of an aqueous phase in the oily phase, or vice versa. A comparison of results obtained using these three different methods in terms of size, stability, and feasibility, is reported. Moreover, the capability of the resulting PBNs to encapsulate drugs was checked by using doxorubicin as the model drug and the loading capability, in terms of drug loading content, was compared to that of the liposomal doxorubicin formulations currently in clinical use.

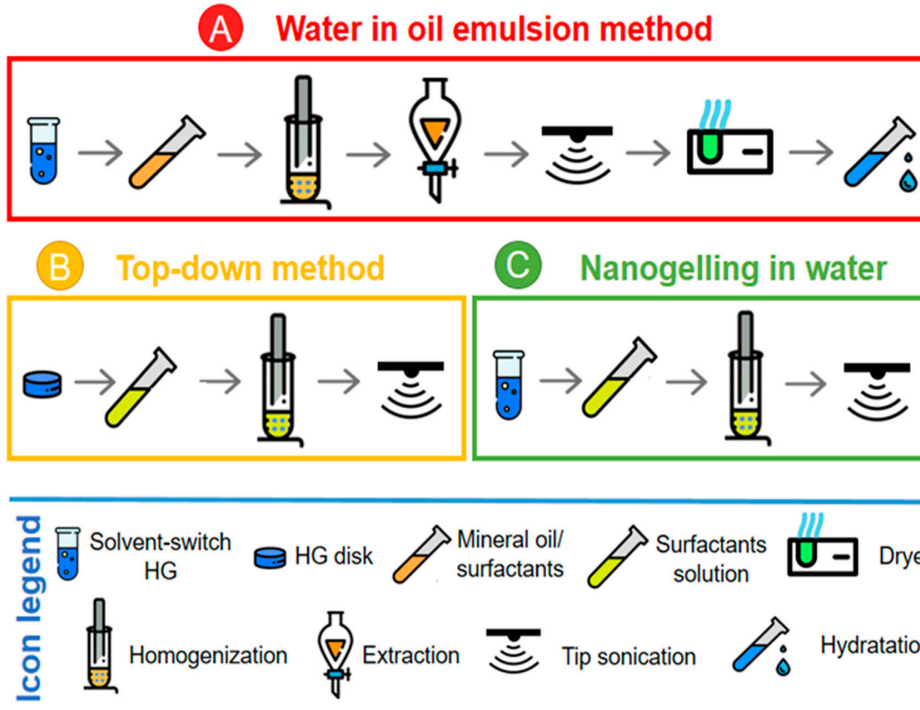

Figure 1. Icons graphical representation of the three different strategies for the nanogel formulation. (**A**) Water-in-oil emulsion methodology; (**B**) Top-down method; and (**C**) Nanogelling in water approach. Each step is identified using an icon of which the legend is reported too.

2. Results

2.1. Nanogel Formulation Methodologies

PBNs were prepared using Fmoc-FF peptide (Figure 2) which is well-known for its capability to self-assemble into macroscopic HGs [22,23]. Fmoc-FF-based nanogels were formulated according to the following three different preparation procedures (Figure 1): (A) water-in-oil inverse emulsion technique (W/O emulsion), (B) top-down approach, and (C) nanogelling in water. The inverse emulsion technique consists of the formation of a water-in-oil emulsion assisted by a mechanical homogenization step. The emulsion is achieved between an aqueous phase containing the gelling DMSO/H_2O peptide solution and an organic phase consisting of a mineral oil, in which one or more stabilizing surfactants are dispersed. This method was previously proposed by Gazit's group for fabrication of Fmoc-FF hydrogel nanoparticles coated using d-α-tocopheryl polyethylene glycol 1000 succinate (E-TPGS, Figure 2) surfactant as the stabilizing agent [24]. According to the reported experimental protocol, we prepared six nanogel formulations (see Table 1), all of them containing the same amount of Fmoc-FF (10 mg/mL, final gel at 0.25 %wt) and a different percentage of two biocompatible surfactants, TWEEN® 60 (polyethylene glycol sorbitan monostearate, see Figure 2) and SPAN® 60 (sorbitan stearate, see Figure 2). The combination of this couple of surfactants allows obtaining different HLB values (4.7 < HLB < 14.9) as indicated in Table 2. The HLB is equal to the molecular weight (MW) of the hydrophilic part of the surfactant divided by the molecular weight of the lipophilic part, multiplied by 20. It is a dimensionless quantity that can take values between 0 and 20.

$$HLB = \frac{MW\ hydrophilic\ part}{MW\ lipophilc\ part} \times 20$$

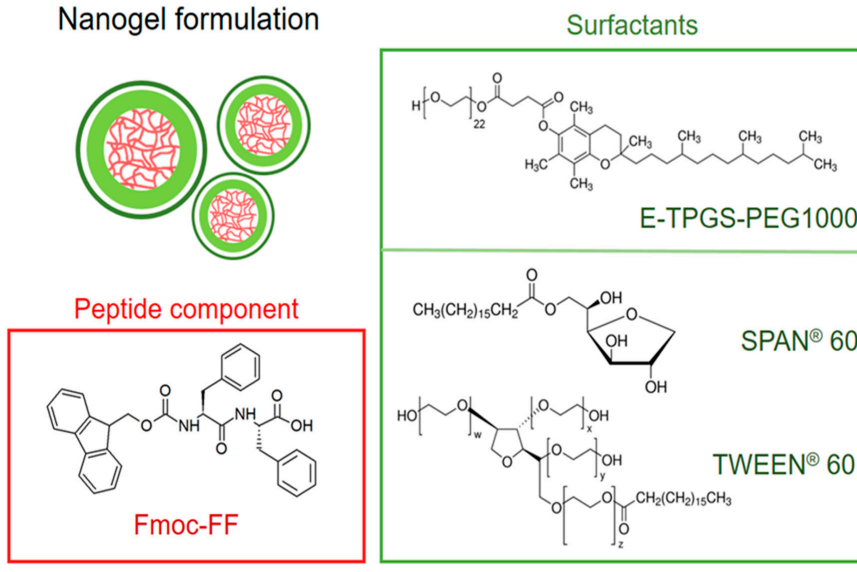

Figure 2. Chemical formulas of components used for the peptide-based nanogel formulation. Internal core (red) is formed by Fmoc-Phe-Phe-OH (Fmoc-FF). External surfactants shell (green) was formulated using d-α-tocopherol polyethylene glycol 1000 succinate (E-TPGS-PEG1000) or mixing SPAN® 60 (sorbitan monostearate) and TWEEN® 60 (polyethylene glycol sorbitan monostearate) in different ratios.

Table 1. Structural characterization (mean diameter, polydispersity index (PDI), and zeta potential) of Fmoc-FF nanogels prepared according to the three methods.

Method	HLB	Mean Diameter (nm) ± S.D.	PDI	Mean Diameter (nm) ± S.D. After 30 gg	ζ mV± S.D.
W/O emulsion	4.7	163 ± 87	0.180	189 ± 89	−40.2 ± 0.3
W/O emulsion	6	205 ± 85	0.174	241 ± 91	−40.9 ± 1.5
W/O emulsion	8	217 ± 93	0.201	249 ± 102	−30.4 ± 0.9
W/O emulsion	10	204 ± 115	0.192	224 ± 109	−27.4 ± 1.0
W/O emulsion	12 [a]	d_1 = 161± 42 d_2 = 721 ± 230	0.168 0.264	d_1 = 243 ± 117 d_2 = 1844 ± 560	−29.5 ± 1.0
W/O emulsion	14.9	242 ± 100	0.208	332± 183	−27.2 ± 1.0
Top-down	10	174 ± 82	0.176	202 ± 97	−24.0 ± 0.1
Nanogelling in water	10	d_1 = 61 ± 18 d_2 = 358 ± 186	0.132 0.210	D_1 = 98 ± 43 d_2 = 407 ± 235	−16.6 ±0.6
Top-down/Dox	10 [a]	242 ± 102	0.190	—	−30.2 ± 0.3

[a] Two populations of aggregates (indicated as d_1 and d_2) were found for the W/O emulsion HLB 12 and for nanogelling in water HLB 10.

This approach permitted us to study the relationship between the HLB value and the structural properties of each formulation in terms of size, stability, and feasibility. The total amount of TWEEN® 60 and SPAN® 60 was 3×10^{-5} mol in all the nanogels, with respect to 1.86×10^{-5} mol of the Fmoc-FF (10 mg/mL). This ratio was chosen in order to assure a complete coating of the peptide core in the resulting nanoparticles. From the experimental point of view, 1 mL of the Fmoc-FF hydrogel, during its opaque-to-limpid transition step, was transferred into the mineral oil containing the two surfactants. The resulting suspension was mechanically homogenized for 5 min (at 35,000 rpm), and then the oily phase was extracted with n-hexane.

We also explored the possibility of preparing the PBNs according to a modified version of the "top-down" methodology, previously described by Chauhan et al. [23]. Their method for preparing Phe-ΔPhe-based nanogels consisted of the progressive reduction in size of preformed hydrogels into an aqueous solution. In our approach, Fmoc-FF hydrogels were produced in macroscopic discs using silicone molds, and then they were unpacked into an aqueous solution of surfactants (TWEEN®/SPAN®

at 58/42 ratio, HLB = 10), using in sequence the homogenizer and the tip sonicator. Analogously to the W/O emulsion, also in this procedure, the amount of Fmoc-FF and of the surfactants were 10 mg/mL and 3×10^{-5} mol, respectively.

Beyond these two methods previously reported in the literature, nanogels were also formulated by a third procedure, which we named "nanogelling in water", in which the peptide hydrogel was added to an aqueous solution of the stabilizing agents before the gelling procedure was completed. This methodology is very similar to the W/O emulsion method, but it avoids the use of mineral oil and, as a consequence, the use of n-hexane during the extraction step.

2.2. Nanogel Characterization

The dimensions of PBNs prepared according the previously procedures at different HLB values and their stability over the time were assessed by dynamic light scattering (DLS). Structural data (mean diameter, polydispersity index, PDI, and zeta potential) for all the samples are collected in Table 1. In Figure 3 are reported the intensity correlation functions for three HLB values (4.7, 10, and 14.9) that represent the two extreme HLB conditions and the middle condition.

The DLS intensity profile of the three freshly prepared formulations were reported, as well as reported after one month. From the comparison of the mean diameter values (ranged between ~160 and ~240 nm) in Table 1 and of the intensity correlation functions in Figure 3, it seems that there is a direct correlation between the HLB value and the size of nanogels. This consideration is fully supported by the DLS measurements carried out on pure SPAN® 60 and TWEEN® 60 aggregates prepared with the same procedure without Fmoc-FF. Indeed, pure SPAN® 60 and TWEEN® 60 aggregates exhibit a hydrodynamic radius of 205 ± 111 and 310 ± 158 nm, respectively (see Figure 4A). These values are slightly higher (~20%) with respect to the values measured for the corresponding Fmoc-FF nanogels, thus, indicating that attractive interactions occur between the hydrophobic portion of the surfactants and the Fmoc-FF peptide.

Moreover, all the formulations, independent of the HLB value, present a shelf stability at room temperature up to a month, even if they showed slightly more uneven profiles at DLS analysis. For example, nanogels with an HLB value of 10 increased their size from 204 to 224 nm (around 10% with respect to the initial size). A similar behavior was also observed for the other formulations.

This result can be explained considering the Z potential values measured for the nanogel formulations (see Table 1). Indeed, all the formulations present a negative value which ranged between −27 and −41 eV. Instead, as shown in Figure 4B, we reported the intensity profile of nanogels prepared according to the others two procedures and with an HLB = 10. From the inspection of Figure 4B we observe that the top-down methodology results in formation of nanostructures that are slightly smaller (174 ± 82 nm) than those obtained with the W/O emulsion technique, whereas the nanogelling in water methodology provides larger objects (358 ± 186 nm). Moreover, all the nanostructures preserve high stability up to one month.

Table 2. Hydrophilic–lipophilic balance (HLB) values obtained combining different percentages of SPAN® 60 and TWEEN® 60.

Emulsifier Blend		HLB
SPAN® 60	TWEEN® 60	
100%	0%	4.7
87%	13%	6
68%	32%	8
48%	52%	10
28%	72%	12
6%	94%	14
0%	100%	14.9

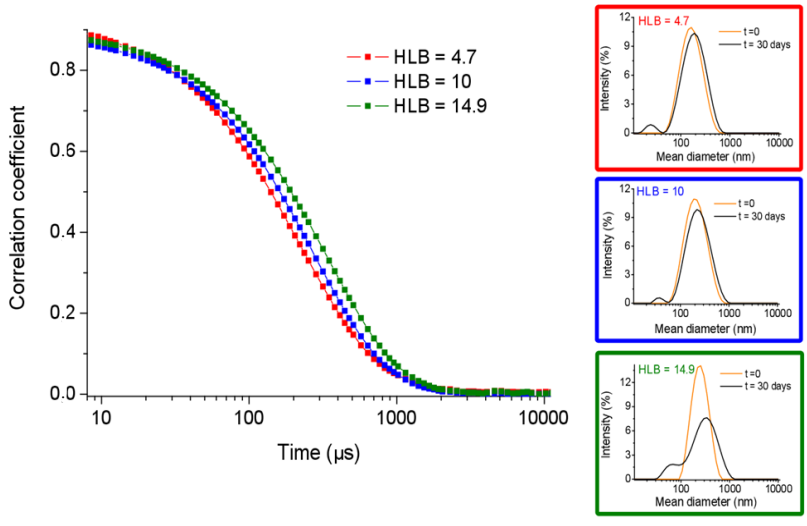

Figure 3. Intensity correlation functions for Fmoc-FF nanogels prepared according to the inverse emulsion at three different HLB values (4.7, 10, and 14.9). On the right, the dynamic light scattering (DLS) profiles for these formulations freshly prepared and after one month.

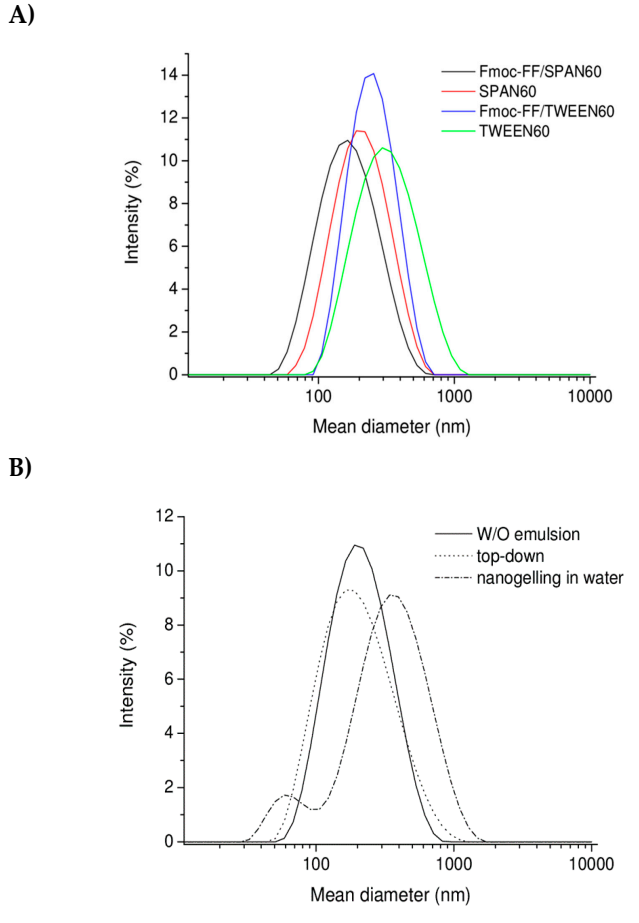

Figure 4. DLS profiles. (**A**) For Fmoc-FF/SPAN®60 (HLB = 4.7) and Fmoc-FF/TWEEN®60 (HLB = 14.9) as compared with the corresponding aggregates lacking the dipeptide; (**B**) For Fmoc-FF nanogels prepared according to W/O emulsion, top-down, and nanogelling in water methods (HLB = 10).

Aggregation properties and secondary structuration of Fmoc-FF-based nanogels were also characterized by fluorescence and circular dichroism (CD) spectroscopies. Because of the structural role of intermolecular aromatic interactions in gelation, fluorescence spectroscopy has been previously employed to understand the molecular organization of Fmoc-FF building blocks in HG formulations [34,35]. It was observed that the fluorescence emission peak λem = 313 nm) of the fluorenyl moiety in its monomeric form could undergo to a red shift in its aggregated form. The wavelength of the fluorenyl moiety, in its associated form, could provide information on the mutual arrangement occurring in the aggregate. A comparison of the fluorescence spectrum of Fmoc-FF nanogel prepared according to the top-down technique with the spectrum of the macroscopic Fmoc-FF hydrogel is reported in Figure 5A.

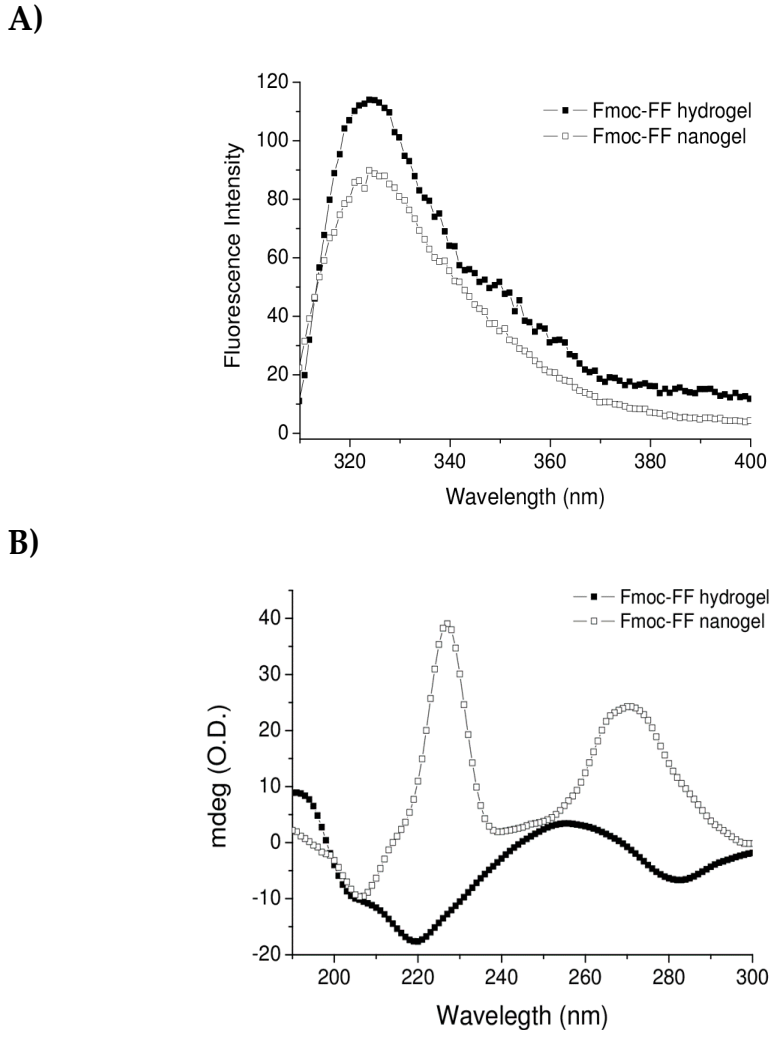

Figure 5. Structural characterization of nanogels prepared by inverse emulsion method. Fluorescence spectrum (**A**) and circular dichroism (CD) spectrum (**B**) of Fmoc-FF nanogel formulation as compared with fluorescence and CD spectra of Fmoc-FF hydrogel.

As previously reported for other Fmoc-containing aggregates, [34,35], the spectrum of the peptide hydrogel exhibits a maximum at 325 nm, indicating an anti-parallel staking of two fluorenyl moieties. Analogously, it can be noted that the fluorescence spectrum of the nanogel formulation is well superimposable with the spectrum of the hydrogel. This result proves that Fmoc-FF in the nanogel

preparation keeps its ability to generate π–π interactions between the fluorenyl moieties, and that the nanosized formulation does not alter the organization at the molecular level.

Further structural information on nanogels was achieved by CD characterization. This spectroscopic methodology has been commonly applied to investigate the secondary structuration of proteins and peptide-based materials [36–38]. Indeed, secondary structural types, including α-helix, β-sheet, and random coil, generate distinctive CD spectra. Thus, by comparing the dichroic behaviors of different systems of interest, CD allows one to visualize homologies or differences in secondary structure. The CD spectrum for nanogel formulation (top-down technique) is compared with the spectrum of macroscopic Fmoc-FF hydrogel (black squares) and reported in Figure 5B. The spectra are both characterized by two leading signals. The first signal is located in the 220–230 nm region (221 and 228 nm for Fmoc-FF hydrogel and nanogel, respectively) and it is generally referred to as indicative of β-sheet structuration of the peptide building block in the supramolecular system [39,40]. This signal is negative for Fmoc-FF hydrogel and positive and more intense for nanogel formulation. The dichroic inversion can be attributed to a global different chiral environment in the nanogel as compared with the Fmoc-FF hydrogel. However, this tri-dimensional surrounding does not alter the fundamental β-sheet organization of the Fmoc-FF-based nanogel. Instead, the second signal, which can be considered to be the typical signature of the Fmoc moiety, is a broad band centered at 259 nm for the hydrogel material and it is red shifted at 270 nm for nanogel [25]. The bathochromic effect can be a consequence of a different dielectric constant in the nanogel core covered by surfactants with respect to the macroscopic nude hydrogel. It is worthwhile noting that the two samples also differ in their physical state, and thus the scattering phenomena could also contribute to the red-shifted behavior [41].

2.3. Drug Loading and Release

In order to assess the capability of the Fmoc-FF-based nanogels to encapsulate active pharmaceutical ingredients (APIs), nanogels were loaded with doxorubicin (Dox), a well-known water-soluble anticancer drug. Dox belongs to the anthracycline family and works as a DNA intercalating agent and as an inhibitor of topoisomerase II [42], and due to its high cardiotoxicity, Dox can be administered as a liposomal formulation in patients with cardiac compliance. PEGylated liposomal doxorubicin is commercially available as Doxil® (Caelyx® in Europe). FDA approved Doxil, in 1995, for the following: (1) AIDS-related Kaposi's sarcoma (KS); (2) relapsed ovarian cancer, after platinum-based treatment; (3) metastatic breast cancer with cardiac risk; and (4) multiple myeloma in combination with bortezomib (Velcade®). In the latter formulation, Doxil is encapsulated in liposomes using a well-known method based on a sulfate ammonium gradient [43].

Analogously, we formulated Dox-loaded nanogels, according to the top-down methodology, in the absence or in the presence of the sulfate ammonium gradient. The amount of Dox used was chosen in order to obtain a drug loading content (DLC) of 0.250. After the loading, the free drug was removed from nanogels encapsulating doxorubicin using size exclusion chromatography. The size and the zeta potential of the Dox-loaded nanogels were 241.5 nm and −30.2, respectively. The DLC of both of the PBNs was estimated by UV-Vis spectroscopy. Because of the soft nature of the hydrogel disk which was prepared in the ammonium sulfate solution, the resulting encapsulation degree was found to be extremely low (data not shown). On the contrary, in the absence of salt, the measured DLC (0.137) was found to be comparable with that of the not PEGylated liposomal Dox formulation, Myocet (0.127), and slightly lower than that of the PEGylated formulation, Doxil (0.250).

The release profile of doxorubicin from nanogels was studied within 72 h, using a dialysis membrane immersed in phosphate buffer at 37 °C. We assumed that the crossing of the free Dox through the dialysis membrane occurred quickly, thus, the overall release of the free drug from the PBNs to the dialysis bag medium could be considered to be rate determining for the process. The amount of Dox released was evaluated by fluorescence spectroscopy, and the releasing profile is reported in Figure 6, as a percentage of released Dox on the total one previously encapsulated in the nanogel. Doxorubicin release (%) for Fmoc-FF nanogel is around 20% after 72 h, with the most part

(~50%) released during the first 8–12 h. This value is significantly lower with respect to the release (80% after 55 h) previously observed by Gazit's group for Fmoc-FF nanogel prepared using E-TPGS surfactant [19].

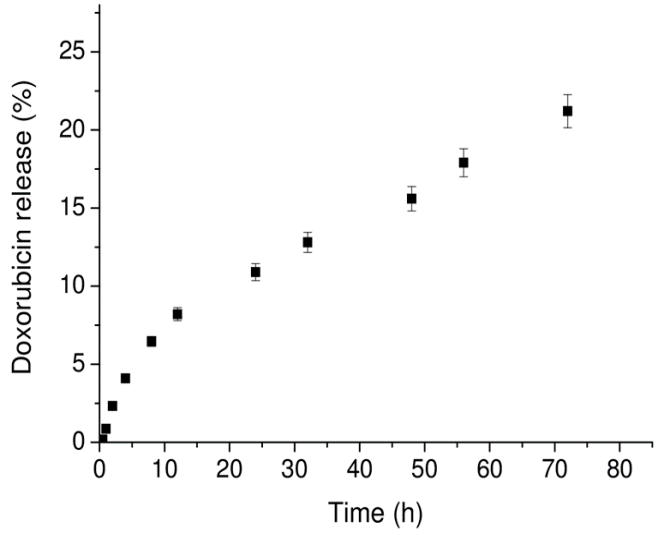

Figure 6. Doxorubicin release profile by Fmoc-FF PBNs. The amount of Dox released was estimated by fluorescence spectroscopy at 590 nm.

3. Discussion

In the literature, there are only two examples of peptide-based nanogels reported, i.e., the first example concerning the preparation of nanogels using the inverse W/O emulsion technique and the other example concerning a top-down methodology. In this study, we started trying to reproduce nanogels according to the reverse emulsion technique described by Gazit et al., in which the authors used Fmoc-FF peptide as a hydrogelator and E-TPGS, a derivative of the vitamin E, as the stabilizing agent. PEGylated Vitamin E-TPGS was selected due to its remarkable biocompatibility, biodegradability, and low immunogenicity profiles. After their preparation, the authors chose to lyophilize Fmoc-FF nanogels and to resuspend them at the time of use. According to this procedure, we obtained nanoparticles with a mean diameter of ≈250 nm and we traced their stability over the time. The DLS measurements highlighted a significant increase in the size of nanogels (mean diameter around 1000 nm) after the first 24 h from their preparation, thus, indicating that the lyophilization step was indispensable when this formulation procedure was used.

In order to avoid lyophilization, we tried to develop novel and more stable PBN formulations. In this context, we focused our attention on the surfactant stabilizing capacity. Our reasoning was based on the HLB parameter, proposed by Griffin between the late 1940s and early 1950s. To obtain a water-in-oil emulsion, the HLB value of the surfactant should be between three and six, but the E-TPGS has an HLB value of 13.2. It must be said that, in the reverse emulsion method, the two phases are physically and chemically different. Although for the formation of the emulsion it is necessary to obtain stabilization of the aqueous phase in the oily phase, after the extraction of the mineral oil and the rehydration, the system needs to be stabilized in water. For this reason, the first choice was to use an HLB value of 10, which was in the middle of the proposed scale of values. Indeed, surfactants with HLB > 10 are good O/W emulsion stabilizer, whereas surfactants with HLB < 10 are good W/O emulsion stabilizer.

We chose SPAN® 60 and TWEEN® 60 as the surfactants. SPAN® 60 is a hydrophilic neutral surfactant which has an HLB value of 4.7 while TWEEN® 60 is a lipophilic neutral surfactant which has an HLB value of 14.9. By mixing these surfactants in different proportions, it is possible to obtain all the HLB values ranged between 4.7 and 14.9, as described in Table 2. As already mentioned, assuming

that an HLB value of 10 could be the most suitable for the stabilization of the formulations, we started to prepare Fmoc-FF nanogels, through the reverse emulsion method, using a mixture of SPAN® 60 and TWEEN® 60 for an HLB = 10. The mean diameter measured for these nanogels, freshly prepared, and after one month in solution at room temperature, was 204 and 224 nm, respectively. The slight increase (around 10%) of the nanoparticles over the time indicates good shelf stability. This result points out that it is possible to avoid the freeze-drying step by choosing an appropriate surfactant. According to the W/O emulsion methodology, we prepared others PBN formulations using different ratios of SPAN® 60 and TWEEN® 60, as reported in Table 1. All the formulations exhibited good stability, even if they showed slightly more uneven profiles at DLS analysis. Surprisingly, we obtained a high stability, also at HLB values comparable or even higher than 13.2, which corresponds to the HLB value of E-TPGS. We suppose this happens because HLB is a parameter that expresses the correlation between the molecular weight of the hydrophilic and the lipophilic parts and provides an indication of the intrinsic tendency of the surfactant to preferentially place itself in the aqueous or oily phase of the emulsion.

However, HLB does not provide information about the stabilizing properties of one surfactant related with another one. Indeed, TWEEN® 60 and E-TPGS have almost comparable HLB values, by presenting a similar number of ethylene glycol groups (polyethylene glycol chains and PEG chains) and a similar length of hydrophobic alkyl chains. Nevertheless, the best polysorbate stabilization capability could be ascribed to the distribution of the PEG chains on different OH groups in TWEEN® 60. This structural feature probably confers conformational freedom to the PEG chain that can orientate themselves towards the aqueous phase, undergoing less folding. Furthermore, it is possible to observe a moderate linear dependence between the nanogel size and the HLB value, since the smaller dimensions are obtained at lower HLB values.

The structural characterization, carried out by fluorescence and CD spectroscopies, highlighted that the inner structure of the Fmoc-FF hydrogel is maintained also in the nanogel formulations. After choosing the best mixture of surfactants, Fmoc-FF nanogels were also prepared according to the other two methods, i.e., the "top-down" and the "nanogelling in water" methods. The top-down method consists of adding the preformed Fmoc-FF hydrogel to an aqueous surfactant solution; whereas the nanogelling in water method is a variant of the inverse emulsion, in which the hydrogel is added to an aqueous solution of stabilizing agents (lacking the mineral oil) before the gelling procedure is completed. The structural characterization highlighted that both methods resulted in obtaining a stable formulation. However, the mean diameter of aggregates prepared by the nanogelling in water method (~360 nm) is two-fold those of the top-down and W/O emulsion methods (204 and 174 nm, respectively). These results suggest that stability is not significantly affected by the preparation method, whereas it seems that the stabilizing agents play a determinant role. The resulting Fmoc-FF-based nanogels were found to be able to encapsulate the model drug doxorubicin with a DLC value comparable to the commercially available liposomal formulations.

4. Materials and Methods

Lyophilized Fmoc-FF powder was purchased from Bachem (Bubendorf, Switzerland). TWEEN® 60, SPAN® 60, oil mineral, and all other chemicals were purchased from Sigma-Aldrich, Fluka (Bucks, Switzerland) or LabScan (Stillorgan, Dublin, Ireland) and were used as received unless otherwise stated. All solutions were obtained by weight using doubly distilled water as a solvent. The effective peptide concentrations in solution were spectroscopically determined by UV-Vis measurements on a nanodrop 2000c spectrophotometer (Thermo Fisher Scientific Inc., Wilmington, DE, USA) equipped with a 1.0 cm quartz cuvette (Hellma) using as molar absorptivity (ε) the values of 7800 mol^{-1} L cm^{-1} at 301 nm.

4.1. Nanogel Formulations

4.1.1. Water-in-Oil Emulsion Technique

One milliliter of Fmoc-FF hydrogel at a concentration of 1 %wt was prepared attending the solvent switch method. Briefly, 10 mg of Fmoc-FF were solubilized in 100 µL of dimethyl sulfoxide (DMSO), and then rehydrated with 900 µL of sterilized water. The gel formation was added to a solution of surfactants in 9 mL of mineral oil. Surfactants were alternatively E-TPGS (3×10^{-5} mol) or a TWEEN® 60/SPAN® 60 mixture (3×10^{-5} mol), at different ratios (*w/w*), as reported in Table 2. The resulting suspension was subjected to homogenization at 35,000 min^{-1} for 5 min. Then, the emulsion was stirred at 4 °C, for 3 h, and then the oily phase extracted three times by centrifugation with 6 mL of n-hexane. The product of the extraction was dried under vacuum for 3 h, and then resuspended into 4 mL of sterilized water. This suspension was sonicated using a tip sonicator for 5 min at 9 W.

4.1.2. Top-Down Methodology

One milliliter of Fmoc-FF hydrogel was prepared according to the switch method. The peptide in the DMSO/water mixture was transferred into a silicone mold before the gelification process was completed in order to obtain a gel disk. This disk was added to 4 mL of an aqueous filtered solution of TWEEN® 60/SPAN® 60 at a w/w ratio of 52/48 (3×10^{-5} mol) and the resulting suspension was homogenized at 35,000 min^{-1} for 5 min, and then tip sonicated for 5 min at 9 W.

4.1.3. Nanogelling in Water

Fmoc-FF hydrogel 1% wt, prepared in accordance with the solvent switch method, was added into 4 mL of an aqueous filtered solution of TWEEN® 60 and SPAN® 60 surfactants (52/48 *w/w* and 3×10^{-5} mol) before the gelling process was completed. The resulting suspension underwent the same procedure previously described consisting of homogenization at 35,000 min^{-1} for 5 min and tip sonication for 5 min at 9 W.

4.2. DLS Measurements

Hydrodynamic radii (RH) diffusion coefficients (D) and the zeta potential (ζ) of all the peptide nanogel formulations were measured by dynamic light scattering (DLS) using a Zetasizer Nano ZS (Malvern Instruments, Westborough, MA, USA). Instrumental settings for the measurements were a backscatter detector at 173° in automatic modality, room temperature, and disposable sizing cuvette as cell. The DLS measurements, in triplicate, were carried out on aqueous samples after centrifugation at room temperature at 13,000 rpm, for 5 min. Data of ζ were collected as the average of 20 measurements.

4.3. Fluorescence Measurements

Fluorescence spectra of Fmoc-FF-based nanogels and Fmoc-FF-based hydrogels were recorded at room temperature with a spectrofluorophotometer Jasco (Model FP-750, Japan) with the test sample in a quartz cell with 1.0 cm path length. The other settings were as follows: excitation and emission bandwidths = 5 nm, recording speed = 125 nm/min, and excitation wavelength = 280 nm.

4.4. Circular Dichroism

Far-UV CD spectra of aqueous solution of nanogels and hydrogels at the same peptide concentration were collected with a Jasco J-810 spectropolarimeter (Japan) equipped with a NesLab RTE111 thermal controller unit using a 0.1 mm quartz cell at 25 °C. The spectra of samples were recorded from 280 to 190 nm. Other experimental settings were as follows: scan speed = 10 nm/min, sensitivity = 50 mdeg, time constant = 16 s, and bandwidth = 1 nm. Each spectrum was obtained by averaging three scans and corrected for the blank.

4.5. Doxorubicin Loading

Dox-loaded nanogels were prepared according to the top-down methodology previously described, with or without the sulfate ammonium gradient. In the classical top-down methodology, a disk of Fmoc-FF hydrogel loaded with Dox was prepared as previously reported, adding the stock solution of Fmoc-FF in DMSO (100 mg/mL) to 900 µL of an aqueous solution of Dox (0.0141 mol L^{-1}) in order to reach a drug weight/lipid weight ratio of 0.250. The hydrogel disk was smashed into 4 mL of an aqueous solution of TWEEN® 60/SPAN® 60 by homogenization and sonication. The other Dox-loaded nanogels were prepared using the top-down approach, modified according to the well-assessed ammonium sulfate gradient method [43]. Briefly, empty Fmoc-FF nanogel (HLB = 10) were prepared, as previously described, in a 250 mM sulfate ammonium solution (pH = 5.5). The nanogel solution was eluted on a Sephadex G-50 column pre-equilibrated with HEPES buffer (10 mM) at pH 7.4, then 57.4 µL of doxorubicin from an aqueous stock solution (1.18×10^{-2} mol/L) were added to 500 µL of nanogel in order to reach a drug weight/lipid weight ratio of 0.250. The suspension was stirred alternatively for 30 min or overnight at room temperature. For both the preparation, unloaded Dox was removed from the nanogel solution by gel filtration on a pre-packed column Sephadex G-50. The Dox concentration was determined by UV-Vis spectroscopy using calibration curves obtained by measuring absorbance at λ = 480 nm. The drug loading content (DLC, defined as the weight ratio of encapsulated Doxo versus the amphiphilic molecules forming nanogels) was quantified by subtraction of the amount of removed Dox from the total amount of loaded Dox.

4.6. Drug Release

The in vitro Dox release from nanogels was measured using a dialysis method [44]. Briefly, 1.0 mL of nanogels loaded with Dox were prepared as previously described and immediately transferred into a dialysis bag (MW cut-off = 3500 Da). Then, it was placed into 20 mL of phosphate buffer and incubated under stirring for 72 h, at 37 °C. Then, 2 mL of the dialyzed solution were replaced with an equal amount of fresh solution at different time points. The extent of drug release was estimated by fluorescence spectroscopy as a percentage of the ratio between the amount of released drug and of the total drug previously loaded into the nanogel. The amount of released Dox was evaluated using a titration curve. For the fluorescence measurements, the excitation wavelength was settled at 480 nm, and the emission spectrum recorded between 490 and 700 nm.

5. Conclusions

In recent years, nanogels have been identified as interesting platforms for the delivery of APIs (such as drugs, contrast agents, nucleic acids, and so on). Although there is a large number of studies on polymer-based nanogels, only a few studies have been reported on peptide-based nanogels until now. This is probably related to the difficulty associated with obtaining a stable form indispensable for their commercialization and their use in the pharmaceutical field.

We prepared peptide nanogel formulations based on the well-known hydrogelator Fmoc-FF using three different methods. In these preparations we evaluated the effect of the HLB value of the stabilizing agent used to coat the hydrogel nanoparticles. We proposed a modification of the inverse emulsion technique and the top-down methodology mainly by changing the surfactants. Indeed, we used a mixture of TWEEN® 60 and SPAN® 60 which were able to guarantee good stability over time, after storage in water at room temperature. In this way, the freeze-drying step could be avoided.

Furthermore, we proposed a new formulation method for the preparation of Fmoc-FF nanogels, named nanogelification in water. Nanoparticles obtained by top-down and W/O emulsion have a diameter of about 200 nm, which is desirable for any clinical applications. However, it is worthwhile noting that the top-down methodology exhibits several advantages with respect to the W/O emulsion method. First, the top-down method avoids the use of mineral oil during the preparation. Consequently, the extraction of the nanogel solution with organic solvents such as n-hexane can also be avoided.

Moreover, the top-down method requires a minor number of steps during the preparation. The easy procedure, conjointly with the high biocompatibility, are useful characteristics in the perspective to optimize and simplify their industrial fabrication. Moreover, this method is also compatible with procedures to encapsulate anticancer drugs. Even if there is a long way to carry nanogel from bench to bedside for drug delivery applications [45], the use of peptide-based nanogels could contribute to shortening the development phases and the results reported here give a good perspective for the use of PBNs as a new drug delivery system.

Author Contributions: All the author discussed the results and wrote the paper in close collaboration with each other. Conceptualization, A.A., C.D., and G.M.; methodology, E.R, C.D., and E.G.; validation, A.A. and E.R.; experimental analysis, E.R. and A.A.; investigation, A.A. and C.D.; data curation and image preparation, C.D., A.A., and E.G.; writing—original draft preparation and writing—review and editing, E.R., C.D., E.G., G.M., and A.A.; supervision, project administration, and funding acquisition, A.A. All authors have read and agreed to the published version of the manuscript.

Funding: This research was funded by PRIN-2017A2KEPL.

Conflicts of Interest: The authors declare no conflict of interest.

References

1. Chai, Q.; Jiao, Y.; Yu, X. Hydrogels for biomedical applications: Their characteristics and the mechanisms behind them. *Gels* **2017**, *3*, 6. [CrossRef] [PubMed]
2. Kirschning, A.; Dibbert, N.; Dräger, G. Chemical functionalization of polysaccharides towards biocompatible hydrogels for biomedical applications. *Chem. Eur. J.* **2018**, *24*, 1231–1240. [CrossRef] [PubMed]
3. Diaferia, C.; Gogh, M.; Sibillano, T.; Gallo, E.; Stornaiuolo, M.; Giannini, C.; Morelli, G.; Adler-Abramovich, L.; Accardo, A. Fmoc-FF and hexapeptide-based multicomponent hydrogels as scaffold materials. *Soft Matter* **2019**, *15*, 487–496. [CrossRef] [PubMed]
4. Jayawarna, V.; Richardson, S.M.; Hirst, A.R.; Hodson, N.W.; Saiani, A.; Gough, J.E.; Ulijn, R.V. Introducing chemical functionality in Fmoc-peptide gels for cell culture. *Acta Biomater.* **2009**, *5*, 934–943. [CrossRef]
5. Jayawarna, V.; Ali, M.; Jowitt, T.A.; Miller, A.F.; Saiani, A.; Gough, J.E.; Ulijn, R.V. Nanostructured Hydrogels for Three-Dimensional Cell Culture Through Self-Assembly of Fluorenylmethoxycarbonyl–Dipeptides. *Adv. Mater.* **2006**, *18*, 611–614. [CrossRef]
6. Worthington, P.; Pochan, D.J.; Langhans, S.A. Peptide hydrogels-versatile matrices for 3D cell culture in cancer medicine. *Front. Oncol.* **2015**, *5*, 92. [CrossRef]
7. Nummelin, S.; Liljeström, V.; Saarikoski, E.; Ropponen, J.; Nykänen, A.; Linko, V.; Seppälä, J.; Hirvonen, J.; Ikkala, O.; Bimbo, L.M.; et al. Self-assembly of amphiphilic janus dendrimers into mechanically robust supramolecular hydrogels for sustained drug release. *Chem. Eur. J.* **2015**, *21*, 14433–14439. [CrossRef]
8. Jung, I.Y.; Kim, J.S.; Choi, B.R.; Lee, K.; Lee, H. Hydrogel based biosensors for in vitro diagnostics of biochemicals, Proteins, and Genes. *Adv Healt. Mater.* **2017**, *6*, 1601475. [CrossRef]
9. Tanbour, R.; Martins, A.M.; Pitt, W.G.; Husseini, G.A. Drug delivery systems based on polymeric micelles and ultrasound: A review. *Curr. Pharm. Des.* **2016**, *22*, 2796–2807. [CrossRef]
10. Baudino, T.A. Targeted cancer therapy: The next generation of cancer treatment. *Curr. Drug Discov. Technol.* **2015**, *12*, 3–20. [CrossRef]
11. Kenawy, E.; Abdel-Hay, F.I.; El-Newehy, M.H.; Wnek, G.E. Processing of polymer nanofibers through electrospinning as drug delivery systems. *Mater. Chem. Phys.* **2009**, *113*, 296–302. [CrossRef]
12. Ringhieri, P.; Avitabile, C.; Saviano, M.; Morelli, G.; Romanelli, A.; Accardo, A. The influence of liposomal formulation on the incorporation and retention of PNA oligomers. *Colloid Surf. B* **2016**, *145*, 462–469. [CrossRef] [PubMed]
13. Pérez-Álvarez, L.; Laza, J.M.; Álvarez-Bautista, A. Covalently and ionically crosslinked chitosan nanogels for drug delivery. *Curr. Pharm. Des.* **2016**, *22*, 3380–3398. [CrossRef] [PubMed]
14. Sagbas Suner, S.; Ari, B.; Onder, F.C.; Ozpolat, B.; Ay, M.; Sahiner, N. Hyaluronic acid and hyaluronic acid: Sucrose nanogels for hydrophobiccancer drug delivery. *Int. J. Biol. Macromol.* **2019**, *126*, 1150–1157. [CrossRef]

15. Curcio, M.; Diaz-Gomez, L.; Cirillo, G.; Concheiro, A.; Iemma, F.; Alvarez-Lorenzo, C. pH/redox dual-sensitive dextran nanogels for enhanced intracellular drug delivery. *Eur. J. Pharm. Biopharm.* **2017**, *117*, 324–332. [CrossRef]
16. Sugiura, S.; Oda, T.; Izumida, Y.; Aoyagi, Y.; Satake, M.; Ochiai, A.; Ohkohchi, N.; Nakajima, M. Size control of calcium alginate beads containing living cells using micro-nozzle array. *Biomaterials* **2005**, *26*, 3327–3331. [CrossRef]
17. Yeh, J.; Ling, Y.; Karp, J.M.; Gantz, J.; Chandawarkar, A.; Eng, G.; Blumling, J.; Langer, R.; Khademhosseini, A. Micromolding of shape-controlled, harvestable cell-laden hydrogels. *Biomaterials* **2006**, *27*, 5391–5398. [CrossRef]
18. Rolland, J.P.; Maynor, B.W.; Euliss, L.E.; Exner, A.E.; Denison, G.M.; De Simone, J.M. Direct fabrication and harvesting of monodisperse, shape-specific nanobiomaterials. *J. Am. Chem. Soc.* **2005**, *127*, 10096–10100. [CrossRef]
19. Ischakov, R.; Adler-Abramovich, L.; Buzhansky, L.; Shekhter, T.; Gazit, E. Peptide-based hydrogel nanoparticles as effective drug delivery agents. *Bioorg. Med. Chem.* **2013**, *21*, 3517–3522. [CrossRef]
20. Raghupathi, K.; Eron, S.J.; Anson, F.; Hardy, J.A.; Thayumanavan, S. Utilizing inverse emulsion polymerization to generate responsive nanogels for cytosolic protein delivery. *Mol. Pharm.* **2017**, *14*, 4515–4524. [CrossRef]
21. Panda, J.J.; Kaul, A.; Kumar, S.; Alam, S.; Mishra, A.K.; Kundu, G.C.; Chauhan, V.S. Modified dipeptide-based nanoparticles: Vehicles for targeted tumor drug delivery. *Nanomedicine* **2013**, *8*, 1927–1942. [CrossRef] [PubMed]
22. Diaferia, C.; Balasco, N.; Sibillano, T.; Gogh, M.; Adler-Abramovich, L.; Giannini, C.; Vitagliano, L.; Morelli, G.; Accardo, A. Amyloid-like fibrillary morphology originated by tyrosine-containing aromatic hexapeptides. *Chem. Eur. J.* **2018**, *24*, 6804–6817. [CrossRef] [PubMed]
23. Gao, J.; Tang, C.; Elsawy, M.A.; Smith, A.M.; Miller, A.F.; Saiani, A. Controlling self-assembling peptide hydrogel properties through network topology. *Biomacromolecules* **2017**, *18*, 826–834. [CrossRef] [PubMed]
24. Garcia, A.M.; Lavendomme, R.; Kralj, S.; Kurbasic, M.; Bellotto, O.; Cringoli, M.C.; Semeraro, S.; Bandiera, A.; De Zorzi, R.; Marchesan, S. Self-Assembly of an Amino Acid Derivative into an Antimicrobial Hydrogel Biomaterial. *Chem. Eur. J.* **2020**, *26*, 1880–1886. [CrossRef] [PubMed]
25. Smith, A.M.; Williams, R.J.; Tang, C.; Coppo, P.; Collins, R.F.; Turner, M.L.; Saiani, A.; Ulijn, R.V. Fmoc-diphenylalanine self-assembles to a hydrogel via a novel architecture based on π-π interlocked β-sheets. *Adv. Mater.* **2008**, *20*, 37–41. [CrossRef]
26. Mahler, A.; Reches, M.; Rechter, M.; Cohen, S.; Gazit, E. Rigid, self-assembled hydrogel composed of a modified aromatic dipeptide. *Adv. Mater.* **2006**, *18*, 1365–1370. [CrossRef]
27. Tang, C.; Smith, A.M.; Collins, R.F.; Ulijn, R.V.; Saiani, A. Fmoc-Diphenylalanine Self-Assembly Mechanism Induces Apparent pKa Shifts. *Langmuir* **2009**, *25*, 9447–9453. [CrossRef]
28. Tang, C.; Ulijn, R.V.; Saiani, A. Effect of Glycine Substitution on Fmoc–Diphenylalanine Self-Assembly and Gelation Properties. *Langmuir* **2011**, *27*, 14438–14449. [CrossRef]
29. Tang, C.; Ulijn, R.V.; Saiani, A. Self-assembly and gelation properties of glycine/leucine Fmoc-dipeptides. *Eur. Phys. J. E* **2013**, *36*, 111. [CrossRef]
30. Arakawa, H.; Takeda, K.; Higashi, S.L.; Shibata, A.; Kitamura, Y.; Ikeda, M. Self-assembly and hydrogel formation ability of Fmoc-dipeptides comprising α-methyl-L-phenylalanine. *Polym. J.* **2020**, *52*, 923–930. [CrossRef]
31. Raeburn, J.; Pont, G.; Chen, L.; Cesbron, Y.; Lévy, R.; Adams, D.J. Fmoc-diphenylalanine hydrogels: Understanding the variability in reported mechanical properties. *Soft Matter* **2012**, *8*, 1168. [CrossRef]
32. Griffin, W.C. Classification of surface-active agents by "HLB". *J. Soc. Cosmet. Chem.* **1949**, *1*, 311–326.
33. Griffin, W.C. Calculation of HLB values of non-ionic surfactants. *J. Soc. Cosmet. Chem.* **1954**, *5*, 249–256.
34. Yang, Z.; Wang, L.; Wang, J.; Gao, P.; Xu, B. Phenyl groups in supramolecular nanofibers confer hydrogels with high elasticity and rapid recovery. *J. Mater. Chem.* **2010**, *20*, 2128–2132. [CrossRef]
35. Raddy, S.M.M.; Shanmugam, G.; Duraipandi, N.; Kiran, M.S.; Mandal, A.B. An additional fluorenylmethoxycarbonyl (Fmoc) moiety in di-Fmoc-functionalized *L*-lysine induces pH-controlled ambidextrous gelation with significant advantages. *Soft Matter* **2015**, *11*, 8126–8140. [CrossRef] [PubMed]
36. Greenfield, N.J. Using circular dichroism spectra to estimate protein secondary structure. *Nat. Protoc.* **2006**, *1*, 2876–2890. [CrossRef] [PubMed]

37. Diaferia, C.; Balasco, N.; Sibillano, T.; Giannini, C.; Vitagliano, L.; Morelli, G.; Accardo, A. Structural characterization of self-assembled tetra-tryptophan based nanostructures: Variations on a common theme. *ChemPhysChem* **2018**, *19*, 1635–1642. [CrossRef]
38. Diaferia, C.; Roviello, V.; Morelli, G.; Accardo, A. Self-assembly of PEGylated diphenylalanines into photoluminescent fibrillary aggregates. *ChemPhysChem* **2019**, *20*, 2774–2782. [CrossRef]
39. Castelletto, V.; Hamley, I.W. Self-assembly of a model amphiphilic phenylalanine peptide/polyethylene glycol block copolymer in aqueous solution. *Biophys. Chem.* **2009**, *141*, 169–174. [CrossRef]
40. Diaferia, C.; Balasco, N.; Altamura, D.; Sibillano, T.; Gallo, E.; Roviello, V.; Giannini, C.; Morelli, G.; Vitagliano, L.; Accardo, A. Assembly modes of hexaphenylalanine variants as function of the charge states of their terminal ends. *Soft Matter* **2018**, *14*, 8219–8230. [CrossRef]
41. Miles, A.J.; Wallace, B.A. Circular dichroism spectroscopy of membrane proteins. *Chem. Soc. Rev.* **2016**, *45*, 4859–4872. [CrossRef] [PubMed]
42. Marinello, J.; Delcuratolo, M.; Capranico, G. Anthracyclines as topoisomerase II poisons: From early studies to new perspectives. *Int. J. Mol. Sci.* **2018**, *19*, 3480. [CrossRef] [PubMed]
43. Fritze, A.; Hens, F.; Kimpfler, A.; Schubert, R.; Peschka-Süss, R. Remote loading of doxorubicin into liposomes driven by a transmembrane phosphate gradient. *Biochim. Biophys. Acta Biomembr.* **2006**, *1758*, 1633–1640. [CrossRef] [PubMed]
44. Falciani, C.; Accardo, A.; Brunetti, J.; Tesauro, D.; Lelli, B.; Pini, A.; Bracci, L.; Morelli, G. Target-selective drug delivery through liposomes labeled with oligobranched neurotensin peptides. *ChemMedChem* **2011**, *6*, 678–685. [CrossRef] [PubMed]
45. Soni, K.S.; Desale, S.S.; Bronich, T.K. Nanogels: An overview of properties, biomedical applications and obstacles to clinical translation. *J. Control. Release* **2016**, *240*, 109–126. [CrossRef]

Sample Availability: Samples of the formulation are available from the authors.

International Journal of Nanomedicine

Dovepress

open access to scientific and medical research

Open Access Full Text Article

ORIGINAL RESEARCH

Peptide-Based Hydrogels and Nanogels for Delivery of Doxorubicin

This article was published in the following Dove Press journal:
International Journal of Nanomedicine

Enrico Gallo[1]
Carlo Diaferia[2]
Elisabetta Rosa[2]
Giovanni Smaldone[1]
Giancarlo Morelli[2]
Antonella Accardo[2]

[1]IRCCS SDN, Naples, 80143, Italy; [2]Department of Pharmacy and Research Centre on Bioactive Peptides (CIRPeB), University of Naples "Federico II", Naples, 80134, Italy

Introduction: The clinical use of the antitumoral drug doxorubicin (Dox) is reduced by its dose-limiting toxicity, related to cardiotoxic side effects and myelosuppression. In order to overcome these drawbacks, here we describe the synthesis, the structural characterization and the in vitro cytotoxicity assays of hydrogels (HGs) and nanogels (NGs) based on short peptide sequences loaded with Dox or with its liposomal formulation, Doxil.

Methods: Fmoc-FF alone or in combination with (FY)3 or PEG8-(FY)3 peptides, at two different ratios (1/1 and 2/1 v/v), were used for HGs and NGs formulations. HGs were prepared according to the "solvent-switch" method, whereas NGs were obtained through HG submicronition by the top-down methodology in presence of TWEEN®60 and SPAN®60 as stabilizing agents. HGs gelation kinetics were assessed by Circular Dichroism (CD). Stability and size of NGs were studied using Dynamic Light Scattering (DLS) measurements. Cell viability of empty and filled Dox HGs and NGs was evaluated on MDA-MB-231 breast cancer cells. Moreover, cell internalization of the drug was evaluated using immunofluorescence assays.

Results: Dox filled hydrogels exhibit a high drug loading content (DLC=0.440), without syneresis after 10 days. Gelation kinetics (20–40 min) and the drug release (16–28%) over time of HGs were found dependent on relative peptide composition. Dox filled NGs exhibit a DLC of 0.137 and a low drug release (20–40%) after 72 h. Empty HGs and NGs show a high cell viability (>95%), whereas Dox loaded ones significantly reduce cell viability after 24 h (49–57%) and 72 h (7–25%) of incubation, respectively. Immunofluorescence assays evidenced a different cell localization for Dox delivered through HGs and NGs with respect to the free drug.

Discussion: A modulation of the Dox release can be obtained by changing the ratios of the peptide components. The different cellular localization of the drug loaded into HGs and NGs suggests an alternative internalization mechanism. The high DLC, the low drug release and preliminary in vitro results suggest a potential employment of peptide-based HGs and NGs as drug delivery tools.

Keywords: hydrogels, nanogels, drug delivery, peptide materials, doxorubicin, in vitro assays

Introduction

Nowadays, cancer remains one of the leading causes of mortality worldwide, affecting more than 10 million new patients every year. Among cancerous diseases, breast cancer is the most common one for women in the United States with more than 200,000 newly diagnosed cases for year.[1] Current treatment options include surgical resection, radiation, and chemotherapy. Chemotherapeutic regime establishes the treatment of patients with drugs (doxorubicin, docetaxel, paclitaxel, and tamoxifen) alone or in combination.[2] Doxorubicin (Dox), also known as Adriamycin, is a natural antitumor antibiotic of the anthracycline class, which

Correspondence: Antonella Accardo
Department of Pharmacy and Research Centre on Bioactive Peptides (CIRPeB), University of Naples "Federico II", Via Mezzocannone 16, Naples, 80134, Italy
Tel +39 0812532045
Fax +39 0812536642
Email antonella.accardo@unina.it

submit your manuscript | www.dovepress.com
DovePress
http://doi.org/10.2147/IJN.S296272

works as DNA intercalating agent and as an inhibitor of topoisomerase II.[3] Despite its therapeutic potentiality, clinical use of Dox is hampered by its dose-limiting toxicity, represented by myelosuppression and cardiotoxic side effects, which cause increased cardiovascular risks.[4] In addition, Dox-mediated cardiotoxicity was found to be cumulative and dose-dependent, with heart suffering from the very first dose and then with accumulative damage for each following anthracycline cycle.[5,6] In order to overcome these drawbacks, Dox encapsulating nanoformulations has been proposed as an alternative strategy for its administration. Currently, two doxorubicin liposomal formulations, Caelyx®/Doxil® and Myocet®, and their bioequivalent formulations, are available in the clinic.[7,8] The liposomal spatial confinement of Dox allows altering biodistribution of the drug, minimizing its toxicity, increasing the half-life and the therapeutic index and improving the pharmaceutical profile, thus leading to increased patient compliance.[9,10]

In the last years, other typologies of nanosized structures, including polymer-based aggregates,[11] nanofibers,[12] nanodisks,[13] gold nanoparticles,[14] graphene and graphene oxide[15,16] and hydrogels (HGs), were evaluated and studied as novel Dox-delivery tools. HGs are self-supporting materials, structured as supramolecular hydrophilic networks associated with the construction of space-spanning structures characterized by a non-Newtonian behavior. The hydrophilic nature of HGs constituents allows entrapping a high volume of biological fluids and water during the swelling process.[17] 3D-connectivity in physical cross-linked HGs is related to aggregation/interaction of molecules, cooperating through non-covalent interactions or via chemical irreversible bonds. Due to their unique structure, HGs have been exploited as versatile tools for many different biomedical applications (such as 3D-extracellular matrices for wound healing systems,[18] cell support for tissue engineering and regeneration,[19,20] protein mimetics,[21] ophthalmic compatible materials,[22] and drug delivery systems[23]). Submicronization of HGs by top-down methodologies gives the possibility to generate smaller hydrogel particles with a size in the nano-range.[24] These hydrogel nanoparticles, named nanogels (NGs), combine the same hydrated inner network of hydrogels with the size of injectable nanoparticles, such as micelles and liposomes.[25] Due to their size, nanogel formulations could achieve a fast renal clearance, a feasible penetration through tissue barriers and a prolonged circulation time in the blood stream.

Hydrogels and nanogels can be prepared using synthetic[26–28] or natural polymers[29–32] or peptide sequences.[33,34] With respect to polymers, peptides exhibit several advantages such as high biocompatibility, biodegradability and tunability. Fmoc-FF (N^{α}-fluorenylmethyloxycarbonyl diphenylalanine) hydrogelator (Figure 1) represents one of the most studied peptide sequences for hydrogels formulation, thanks to its capability to gelificate under physiological conditions, required for biomedical applications.[35–37] Recently, we have described the preparation of pure Fmoc-FF and mixed Fmoc-FF/(FY)3 and Fmoc-FF/PEG_8-(FY)3 (at 2/1 or 1/1, v/v) hydrogels.[38] PEG_8-(FY)3 and (FY)3 are the PEGylated and the non-PEGylated versions of the (FY)3 hexapeptide, this latter containing as peptide framework the alternation of three tyrosine (Y) and three phenylalanine (F) residues.[39] The rheological characterization of the mixed gels pointed out that the presence of PEG and its relative amount into the mixed gel causes a slowing down of the gelation kinetic and a decrease of the gel rigidity. This different behavior was attributed to the high flexibility and conformational freedom of the PEG chain in the mixed hydrogel. Independently of their composition, all the gels showed an in vitro cell viability higher than 95% after 24 h of incubation, thus suggesting their potential applications in the biomedical field.

Here we describe the Dox loading capability of hydrogels and nanogels (both pure and mixed) and their drug release properties over time. We also report the in vitro cytotoxicity of both empty and Dox filled HGs and NGs on MDA-MB-231 breast cancer cell line representative of Triple Negative Breast Cancer (TNBC), the most aggressive breast cancer subtype.[40] These results are compared with empty and Dox filled nanogel formulations,[41] obtained sub-micronizing hydrogels by a top-down method. We also checked the capability of peptide-based hydrogels to encapsulate supramolecular nanodrugs and we studied their effective cytotoxicity on cells. For instance, as nanodrug we chose the liposomal doxorubicin formulation Doxil. This strategy could allow to obtain a composite drug delivery platform for a multi-stage delivery of Dox.

Materials and Methods

Protected N^{α}-Fmoc-amino acid derivatives, coupling reagents, and Rink amide MBHA (4-methylbenzhydrylamine) resin

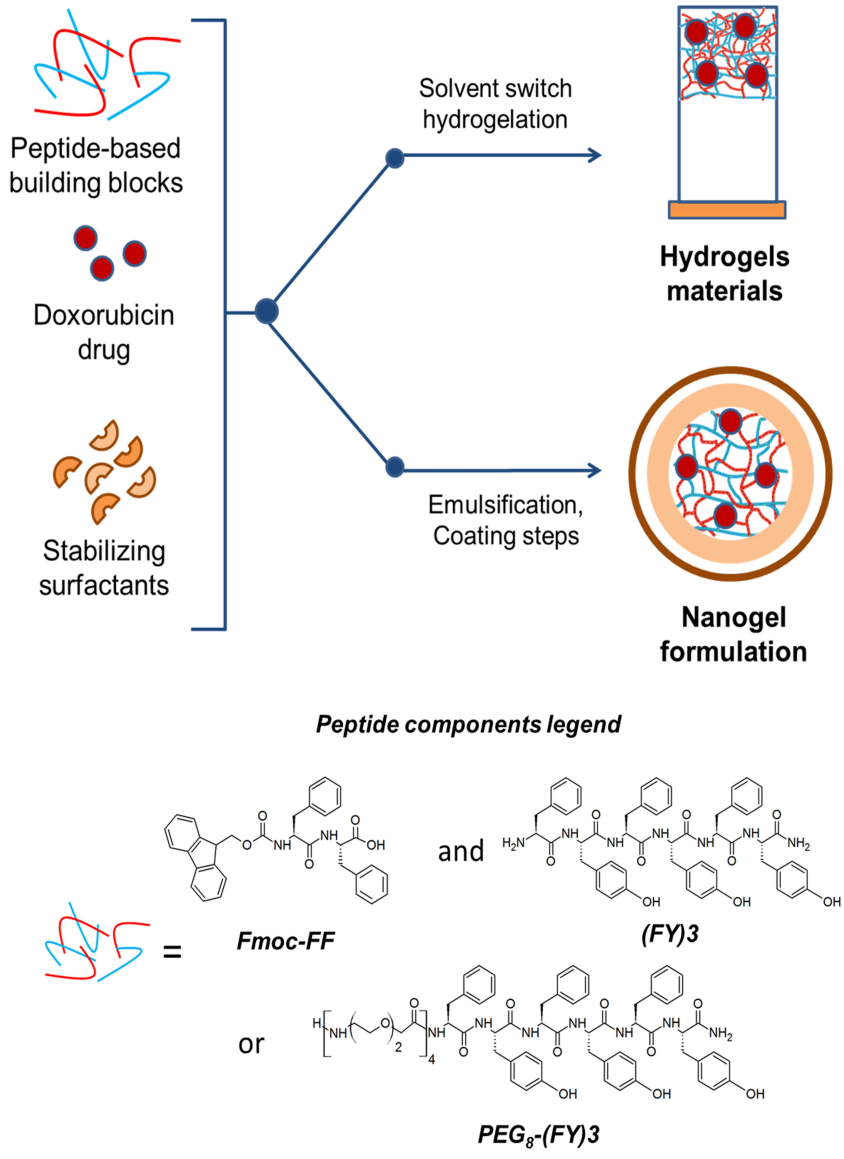

Figure 1 Schematic representation of components and methodologies for the formulation of HGs and NGs. Chemical formulas for peptide-based components are reported in the legend.

were purchased from Calbiochem-Novabiochem (Laufelfingen, Switzerland). The monodisperse Fmoc-8-amino-3,6-dioxaoctanoic acid (Fmoc- AdOO-OH, PEG2) was purchased from Neosystem (Strasbourg, France). Lyophilized Fmoc-FF powder was purchased from Bachem (Bubendorf, Switzerland). Doxorubicin chlorohydrate (Dox. HCl) was purchased from Sigma Aldrich (Milan, Italy). Pegylated liposomal Dox (commercial name of Doxil) vials were kindly gifted by the Italian Cancer Institute in Naples (Italy) "Fondazione G. Pascale". TWEEN®60, SPAN®60, and all other chemicals and solvents were purchased from Sigma-Aldrich, Fluka (Bucks, Switzerland) or LabScan (Stillorgan, Dublin, Ireland) and were used as received unless otherwise stated. All solutions were obtained by weight using doubly distilled water as a solvent. UV-Vis spectra were recorded on a Thermo Fisher Scientific Inc (Wilmington, Delaware USA) Nanodrop 2000c, equipped with a 1.0 cm quartz cuvette (Hellma).

Peptide Synthesis

(FY)3 and its PEGylated analogue PEG_8-(FY)3 peptide derivative were synthesized by peptide solid phase

synthesis (SPPS) procedures with a Fmoc/tBu chemistry approach as previously described[39,42,43] and purified by RP-HPLC chromatography.

Hydrogels and Nanogels Formulation

Pure Fmoc-FF hydrogel and mixed Fmoc-FF/PEG_8-(FY)3 and Fmoc-FF/(FY)3 hydrogels (1/1 or 2/1, v/v) were prepared as previously described using the "solvent-switch method"[44] to a final concentration of 0.5 wt%.[38] Briefly, each peptide component (Fmoc-FF, (FY)3 and PEG_8-(FY)3) was dissolved in dimethyl sulfoxide (DMSO) to a final concentration of 100 mg/mL. Pure Fmoc-FF hydrogel (400 µL) was obtained by diluting 20 µL of the Fmoc-FF stock solution with 380 µL of double distilled water under stirring (5 seconds). Preparation of all the mixed hydrogels was achieved analogously, by combining the peptides stock solutions at the desired volume/volume ratios. Pure and mixed nanogel formulations were prepared as previously described according to the top-down method.[41] Briefly, the gel disk obtained into a silicone mold was homogenized at 35,000 min^{-1} for 5 min into 4 mL of an aqueous solution containing TWEEN 60/SPAN 60 at a w/w ratio of 52/48 (3.10^{-5} mol) for pure Fmoc-FF NGs and only TWEEN 60 (3.10^{-5} mol) for mixed Fmoc-FF/(FY)3 NGs. The resulting suspensions were then tip sonicated for 5 min at 9 W.

Doxorubicin Filled Hydrogels and Nanogels

Dox filled hydrogels were prepared as described above by adding 380 µL of an aqueous Dox solution at a concentration of $4.0.10^{-3}$ mol L^{-1} to the peptide stock solutions. Dox filled nanogels were prepared according to the top-down methodology as previously described.[41] Shorty, a disk of pure or mixed hydrogel loaded with Dox was prepared adding the stock solution of peptide (100 mg/mL) to 900 µL of an aqueous solution of Dox (0.018 mol L^{-1}), which allows to reach a drug weight/lipid weight ratio of 0.250. Then, the hydrogel disk was homogenized, and tip sonicated into 4 mL of TWEEN 60/SPAN 60 mixture or TWEEN 60, according to the empty formulation. Purification of Dox filled nanogels from free Dox was achieved by gel filtration on a pre-packed column Sephadex G-50. The drug loading content (DLC), defined as $g_{Dox\ encapsulated}/g_{(surfactant+peptide)}$, was quantified by subtraction of the free Dox from the total amount of loaded Dox. The Dox concentration was determined by UV-Vis spectroscopy using calibration curves obtained by measuring absorbance at λ = 480 nm.

Doxil Filled Hydrogels

Doxil filled hydrogels were prepared analogously to Dox filled ones, by adding 380 µL of the commercial Doxil solution opportunely diluted in order to achieve the same Dox concentration ($4.0.10^{-3}$ mol L^{-1}) that was in the HGs.

Circular Dichroism (CD)

Far-UV CD spectra of Dox filled hydrogels and nanogels were collected on a Jasco J-810 spectropolarimeter equipped with a NesLab RTE111 thermal controller unit at 25°C. 100 µL of a hydrated DMSO stock solution (immediately after its generation) were placed on a 0.1 mm quartz cell. The measurements were recorded as function of the time (every 8 minutes) in the range of wavelength between 300 and 200 nm. Other experimental settings were: scan speed = 50 nm min^{-1}, sensitivity = 10 mdeg, time constant = 16 s, bandwidth = 1 nm. Each spectrum was obtained by averaging three scans. All the spectra are reported in optical density (O.D.).

Confocal Analysis

For confocal microscopy, Dox filled hydrogels were drop-casted and spread on a glass slide, air-dried at room temperature, and examined by confocal microscopy. Confocal images were obtained with a Leica TCS-SMD-SP5 confocal microscope (λ_{exc} = 488 nm and λ_{em} = 505–600 nm). 0.8-µm thick optical slices were acquired with a 63× or 40×/1.4 NA objective.

Dynamic Light Scattering (DLS) Measurements

Mean diameters and diffusion coefficients (D) of empty and Dox filled NGs were estimated by DLS using a Zetasizer Nano ZS (Malvern Instruments, Westborough, MA). Instrumental settings for the measurements are a backscatter detector at 173° in automatic modality, room temperature and disposable sizing cuvette as cell. DLS measurements in triplicate were carried out on aqueous samples after centrifugation at room temperature at 13,000 rpm for 5 minutes.

Dox Release from Hydrogels and Nanogels

Dox and Doxil release from hydrogels were evaluated in a conic tube (1.5 mL) using 400 µL of drug filled hydrogels (0.5% wt) adding, on the top of them, 800 µL of 0.100 mol L^{-1} phosphate buffer. At each time-point, 400 µL of this solution was removed and replaced with an equal fresh aliquot. Released Dox was quantified by UV-Vis spectrum of the supernatant at 480 nm. All the release experiments were performed in triplicates. The extent of Dox release was reported as percentage of the ratio between the amount of released drug and the total quantity of drug initially loaded into hydrogels. Dox release from nanogels was achieved using the well-known dialysis method.[45] Briefly, Dox loaded nanogel suspension (1.0 mL) was placed into a dialysis bag (MW cut-off = 3500 Da). This bag was immersed under stirring for 72 h, at 37°C into 20 mL of phosphate buffer. Then, 2 mL of the dialyzed solution was replaced with an equal amount of fresh solution at different time points. Fluorescence measurements of each fraction of the dialyzed solution were recorded at room temperature with a spectrofluorophotometer Jasco (Model FP-750, Japan) in a quartz cell with 1.0 cm path length. The other settings were as follows: excitation and emission bandwidths = 5 nm, recording speed = 125 nm/min, and excitation wavelength = 480 nm, emission range from 490 to 700 nm. The amount of doxorubicin contained in each fraction was estimated using an analytical titration curve previously recorded for the free Dox in the same spectral range. Analogously to HGs, Dox release profile from NGs was reported as percentage of released drug/total drug loaded into NGs.

Cell Line

Human breast cancer cell line MDA-MB-231 was obtained from IRCCS-SDN Biobank (10.5334/ojb.26) and growth in Dulbecco's Modified Medium (DMEM) supplemented with 10% fetal bovine serum (FBS) and 1% GlutaMAX. Cells were incubated at 37°C and 5% CO_2 and seeded in T-25 culture flasks.

Cell Viability Evaluation by MTT

For MTT assays (Sigma Aldrich, Germany), MDA-MB-231 cells were seeded in 24-well plates at a density of 50 × 10^4 per well. After 24 h free Dox at 1µmol L^{-1}, nanogels and hydrogels (these latter preformed into a hollow plastic chamber sealed at one end with a porous membrane) were added to the wells. Cells were treated with the hydrogels for 24 h and with nanogel solutions for 72 h. At the end of the treatment, cell viability was assessed by the MTT assay. For the IC_{50} determination of Dox, MDA-MB-231 cells were seeded in 24-well plates at a density of 50 × 10^4 per well and treated with different concentrations (0.25, 0.5, 1, 2 and 4 µmol L^{-1}) of Dox for 24 h. At the end of the treatment, cell viability was assessed by the MTT assay. In brief, MTT, dissolved in DMEM in the absence of phenol red (Sigma-Aldrich), was added to the cells at a final concentration of 0.5 mg/mL. After 4 h incubation at 37°C, the culture medium was removed, and the resulting formazan salts were dissolved by adding isopropanol containing 0.1 mol L^{-1} HCl and 10% Triton-X100. Absorbance values of blue formazan were determined at 490 nm using an automatic plate reader (EL 800, Biotek). Cell survival was expressed as percentage of viable cells in the presence of hydrogels or nanogels, compared to control cells grown in their absence. MTT assay was repeated twice with similar results.

Immunofluorescence Experiments

MDA-MB-231 cells were treated for 24 h with 1µmol L^{-1} free Dox or 1.13 mmol L^{-1} Dox loaded Fmoc-FF/(FY)3 hydrogels and Fmoc-FF/(FY)3 nanogels. Cells were fixed at -20 °C for 15 minutes with a -80 °C pre-cooled solution of methanol/acetone (1/1, v/v). Subsequently, cells were subjected to blocking with solution of 3% (w/v) BSA in PBS pH 7.4 at room temperature (RT). Anti B-actin (A2228, Sigma Aldrich) monoclonal antibody was diluted 1:200 in a solution of PBS + 1% (w/v) BSA and then all slides were incubated for 4 h at + 4°C. After three washing steps in PBS for 5 minutes each, FITC-conjugated anti-mouse secondary antibody (ab7064, Abcam, UK) diluted 1:400 in a solution of PBS + 1% (w/v) BSA was incubated for 1 h at 4°C in the dark. After additional three washing steps in PBS, a solution of 4′,6-Diamidino-2-Phenylindole, Dihydrochloride (DAPI, Thermo Fischer Scientific D1306) diluted 35,000-fold in PBS was used and it was left to act for 10 minutes at RT in the dark to color the nuclei. Images were obtained using an automated upright microscope system (Leica DM5500 B) coupled with Leica Cytovision software.

Statistical Analyses

All statistical analyses were performed using the Graphpad Prism 6 (Graphpad Software, Graphpad Holdings, LLC, CA, USA). Numbers of biological and/or technical replicates, as well as a description of the statistical parameters, are stated in the figure legends. All experimental images

are representative of at least two independent experiments. For statistical significance, a p–value less than 0.05 was considered, unless otherwise specified.

Results and Discussion

Classical administrations of active pharmaceutical ingredients (APIs) are affected by issues related to systemic toxicity, drug chemical instability and repeated dosing requirement. As previously mentioned, HGs offer convenient drug delivery approaches, allowing them to overcome these drawbacks thanks to their tunable features, modular degradability and easy formulation. Macroscopically, hydrogel-based materials belong to two different categories based on their size: hydrogels (HGs) and nanogels (NGs). The specific size-feature determines the route of administration: transepithelial drug delivery or in situ gelation process of implants for HGs and systemic, oral and pulmonary administration of APIs for nanogels.[46] The knowledge about the encapsulation procedures, the efficiency of drugs loading, and the cytotoxicity profiles can steer the development of efficient vehicles. For instance, swollen HGs matrices can be loaded in different ways, acting at macroscopic level, on the fibrillary network, the mesh size or at molecular scales. Moreover, the drug release can be differently modulated according to covalent or non-covalent approaches, in which drug molecules are chemically bound on the HG matrix by stable or cleavable linkers, or they can establish electrostatic interactions with HGs building blocks. These different drug loading strategies could affect the experimental conditions of preparation (eg, solvents, pH and salt content) and in turn the biological profile of the resulting vehicle. In this perspective, comparative studies on analogies and differences between HGs and NGs may assume a great importance.

Formulation and Characterization of Dox Filled HGs

HGs filled with the anticancer drug Dox were prepared according to the "solvent-switch" method.[41] This method consists of the addition of an aqueous solution of Dox directly into the stock peptide solution (100 mg/mL in DMSO). After few seconds of vortex, the resulting opaque metastable mixture is vertically incubated at room temperature until the formation of a limpid, translucent self-supportive hydrogel. Dox filled hydrogels Fmoc-FF/(FY)3 and Fmoc-FF/PEG_8-(FY)3 at two different ratios (1/1 or 2/1, v/v) were successfully formulated. Instead, in the same experimental conditions, Dox filled Fmoc-FF hydrogel appears not completely homogenous (see Figure S1). On the other hand, we observed a progressive improvement of the hydrogel homogeneity by increasing the amount (up to 0.018 mol L^{-1}) of Dox to encapsulate (Figure S1). This behavior could be attributed to a shield effect of the charges occurring between the drug and the peptidic matrix. Although Dox filled Fmoc-FF hydrogel can be prepared, the Dox concentration is too high compared with mixed HGs and, for this reason, we did not further focus our attention on this sample. For mixed HGs, no syneresis was detected after 10 days. This specific no water-loss is an important advantage offered by HGs, thus allowing a precise modulation of water-soluble drug loaded in the system. According to this experimental evidence, we can assume that all the Dox was efficiently and quantitatively entrapped in the hydrogel matrix.

The resulting Dox filled hydrogels were further characterized in their xerogel form by confocal microscopy. Confocal images of one sample (Fmoc-FF/(FY)3, 1/1) are reported in Figure 2A and B. These images clearly show the characteristic intricate network of entangled fibers,[47] and their red color suggests the tight interaction of Dox with the network constituents. The amount of drug we were able to encapsulate in mixed HGs was 2.32 mg/mL. This quantity corresponds to a drug loading content (DLC) of 0.440 and to an encapsulation ratio (ER%, defined as the weight percentage of drug encapsulated in the HG on the total drug added during preparation) of 100%, respectively. This high encapsulation degree can be explained as consequence of the electrostatic interactions between the positive charge on the drug and the negative one present on the C-terminus of the Fmoc-FF peptide. Analogously to free Dox, also Doxil was efficiently encapsulated into mixed hydrogels at the same drug concentration. This is surprising due to the negative Z potential value (see Figure S2) we measured for Doxil ($\zeta \sim -11$ mV) into the experimental conditions ([Dox] =1.13 mmol L^{-1}) used to achieve the encapsulation into the hydrogel.

A macroscopic evaluation of the gelation kinetics for mixed drug-filled hydrogels can be done by simply following the opaque-to-transparent optic transition. As previously observed for the corresponding empty systems, a different time (between 20 and 40 minutes) is required for the gelation process of each mixed hydrogel.[38] In particular, we observed a more rapid formation for mixed HGs containing PEG_8-(FY)3 (24 and 30 minutes for 2/1

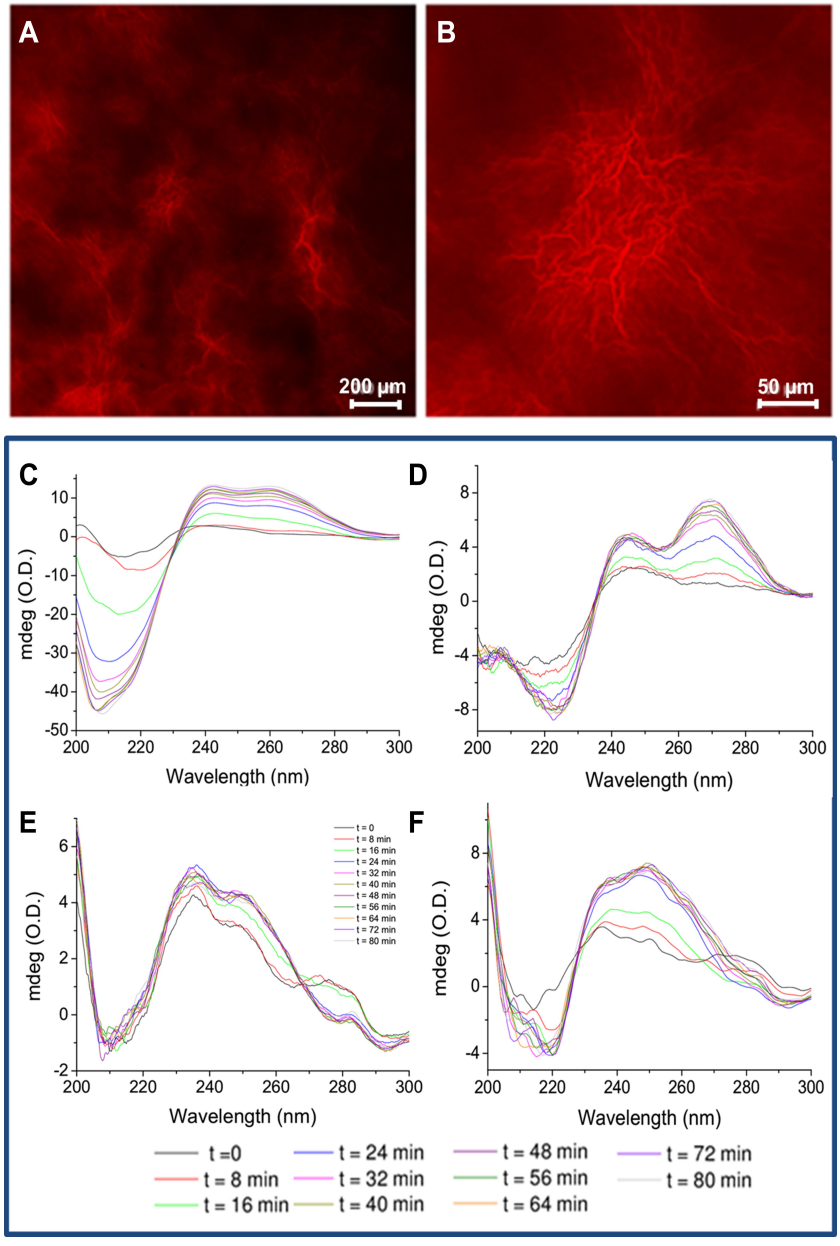

Figure 2 Characterization of mixed HGs. (**A** and **B**) Confocal microscopy image of Fmoc-FF/(FY)3 (1/1) xerogel loaded with Dox. Scale bar 200 (**A**) and 50 µm (**B**), respectively. CD spectrum of Fmoc-FF/(FY)3 (1/1) loaded with Dox in the visible region between 600 and 400 nm. CD spectra of DOX filled co-assembled hydrogels Fmoc-FF/(FY)3 (2/1) (**C**) Fmoc-FF/(FY)3 (1/1) (**D**) Fmoc-FF/PEG_8-(FY)3 (2/1) (**E**) and Fmoc-FF/PEG_8-(FY)3 (1/1) (**F**) as function of the time.

and 1/1, respectively) with respect to those containing (FY)3 (35 and 40 minutes for 2/1 and 1/1, respectively). Analogously to empty matrices, the gelation kinetics of Dox filled HGs is faster by increasing the amount of the Fmoc-FF. This result may be ascribable to the capability of Fmoc-FF to gelificate in a very quick time (~2 min).[35] On the contrary, we observe a faster gelation for HGs containing PEG in respect to HGs lacking polymer. This result is probably due to the additional interactions occurring between the hydrophilic PEG structure and the hydrophilic daunosamine moiety of Dox. As an alternative, gelation kinetics of hydrogels can be more accurately determined by following other structural or mechanical transitions occurring over time, related to alteration of UV-Vis absorbance, storage modulus (G') or the dichroic signal.[48] In this perspective, we recorded the CD spectra of Dox filled

hydrogels at several time points in the spectral region between 300 and 200 nm (see Figure 2C–F). From the inspection of all the CD spectra, it clearly appears an evolution of the dichroic signal towards a stable state, in which we can assume that the HG has reached its final arrangement. The co-existence of several conformational states in the solution is also confirmed by isosbestic points between 220 and 240 nm and around 267 nm for PEG_8-(FY)3 containing HGs. By plotting the optical density (OD) in the relative minima for each sample, we were able to extrapolate the gelation times (see Figure S3). These times, evaluated from the CD measurements, were found in good agreement with the gelation times observed following the transition from the opaque to limpid form.

Formulation and Characterization of Dox Filled NGs

The preparation of pure Fmoc-FF and mixed nanogels loaded with Dox was achieved according to the top-down methodology.[41] In this approach, macroscopic discs of hydrogels (1.0%wt) loaded with Dox (0.018 mol L^{-1}) were prepared into silicone molds according to the above-described protocol. Successively, these discs were homogenized into an aqueous solution of TWEEN®60 (polyethylene glycol sorbitan monostearate) and SPAN®60 (Sorbitan stearate) as stabilizing agents. The combination of this couple of surfactants permits to achieve a hydrophilic/lipophilic balance (HLB) value ranged between 4.7 and 14.9. Due to the similar behavior exhibited by the four mixed HG formulations in terms of DLC and stability, we decided to prepare only one of the four mixed formulations, ie, Fmoc-FF/(FY)3 (1/1, v/v). The best Dox filled NG formulations, in terms of size and stability, were obtained using TWEEN®60/SPAN®60 at 58/42 ratio (HLB= 10) or at 100/0 ratio (HLB= 14.9) for pure Fmoc-FF and mixed Fmoc-FF/(FY)3 (1/1, v/v), respectively. Indeed, contrarily to the pure Fmoc-FF formulation, the mixed one was found unstable when prepared with a value of HLB = 10. The resulting suspensions, further submicronized using tip sonicator, were purified from free drug using size exclusion chromatography. The red coloration of purified formulations macroscopically suggested the incorporation of the anthracycline in the NGs vehicle. Due to its spectroscopic features (λ_{abs} = 480 nm; λ_{em} = 560, 590 nm), the amount of Dox encapsulated was analytically monitored and evaluated by UV-Vis spectroscopy, by checking the absorbance in the maximum at λ_{abs}= 480 nm. DLC and ER% values for pure Fmoc-FF nanogel were 0.137% and 63%, respectively. This DLC value is similar to that of the commercially available liposomal formulations Myocet (DLC=0.127) and Doxil (DLC=0.250). Therefore, the insertion of (FY)3 peptide in the preparation causes a slight decrease of both the DLC (0.093) and the ER% (45%) with respect to the pure formulation. The lower encapsulation degree observed for mixed NGs versus pure ones can be explained considering the different amount of the net negative charge present in the two nanogels. Indeed, the peptide (FY)3 has an amidated C-terminus, significantly less acidic compared to the carboxylic one, and a basic non protected N-terminal amino group that can support a positive charge after protonation. This latter phenomenon contributes to the reduction of the total negative charge in the inner sphere of NGs, which determines lower attractive forces between the drug and the peptide system. The size of empty and filled Fmoc-FF/(FY)3 NGs, measured by Dynamic Light Scattering (DLS), was 168 and 214 nm, respectively (see Figure 3). This increase in size (~22%) is comparable to the increase of dimensions previously observed for empty (174 nm) and filled (241 nm) Fmoc-FF NGs.

Drug Release from HGs and NGs

Drug release from both hydrogels and nanogels was evaluated in 0.100 mol L^{-1} phosphate buffer solution up to 72 hours and the corresponding release profiles are reported in Figure 4A and B, respectively. Two different procedures were used for determination of Dox release from hydrogels and nanogels. In the first case, Dox or Doxil filled hydrogels, prepared into a conic tube, were directly put in contact with a double volume of physiological solution,

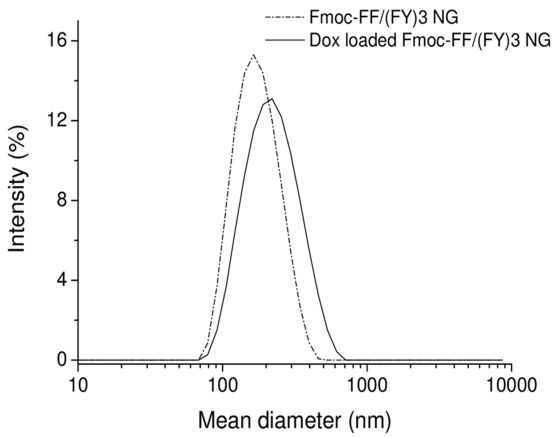

Figure 3 DLS profiles for empty and Dox filled Fmoc-FF/(FY)3 (1/1, v/v) nanogels prepared according to the top-down method.

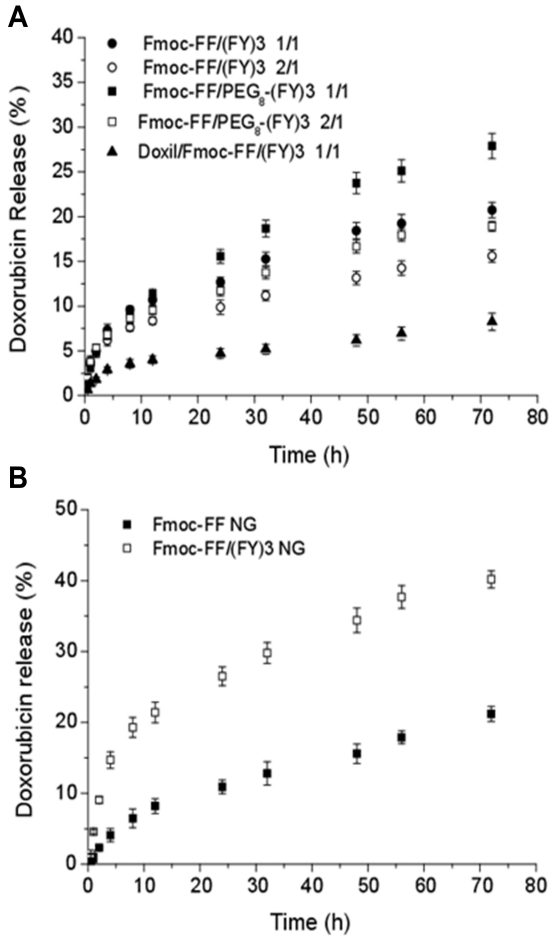

Figure 4 Drug release profiles for: (**A**) multicomponent Fmoc-FF/(FY)3 and Fmoc-FF/PEG8-(FY)3 hydrogels up 72 hours; (**B**) pure Fmoc-FF and mixed Fmoc-FF/(FY)3 (1/1, v/v) nanogels.

cyclically replaced with a fresh one. Instead, in the second case, the release of Dox from nanogels was studied using a dialysis membrane immersed in phosphate buffer at 37° C. We assumed that the crossing of the free Dox through the dialysis membrane occurred quickly, thus, the overall release of the free drug from the peptide-based nanostructures to the dialysis bag medium could be considered to be rate determining for the process. The API release from the systems was considered undergone to a diffusion process. The Dox amount released was estimated by UV-Vis (at λ_{abs}= 480 nm) or by fluorescence spectroscopies (at λ_{em}= 590 nm) for HGs and NGs, respectively. The extent of drug was reported as a percentage of the ratio between the amount of released drug and the total drug initially loaded. From the inspection of Figure 4A, we can observe a similar release profile for all the Dox filled hydrogels during the first 24 hours. However, after 72 hours, each mixed gel exhibits a different release, with the lowest one for Fmoc-FF/(FY)3 (2/1) (16%). A low drug release (21%) was also observed for the other mixed HGs Fmoc-FF/(FY)3 (1/1). The same trend was also observed for the PEG_8-(FY)3 containing hydrogels with a release of 19% and 28% for 2/1 and 1/1 ratios, respectively. These results agree with our expectations that PEGylation of the peptide could affect the rigidity and permeability of the hydrogels matrix and, in turn, the drug release. As expected, the amount of drug released from the hydrogel encapsulating Doxil (~8.5%) was lower than the drug released from the corresponding hydrogel (21%). In Figure 4B is reported the Dox release (%), which after 72 h, is around 20% and 40% for pure Fmoc-FF and mixed Fmoc-FF/(FY)3 (1/1, v/v) nanogels, respectively. Analogously to HGs, also for NGs the drug release is more appreciable during the first 8–12 h. The higher release observed for mixed NGs with respect to pure ones can be interpreted as a direct consequence of the lower electrostatic interactions occurring between the NG and the drug.

Cytotoxicity Assays

Cytotoxicity of mixed Fmoc-FF/(FY)3 (1/1, v/v) hydrogel encapsulating Dox or its liposomal formulation Doxil, at the same Dox concentration, was evaluated after 24 hours of incubation on MDA-MB-231 breast cancer cell line, using MTT assay. The cytotoxicity of the free drug, as well as of the empty hydrogels, was studied in the same conditions. HGs preparation was directly achieved into the hollow plastic chamber sealed at one end with a porous membrane. This experimental setting for hydrogels allows to mimic its conditions of utilization, in which this biocompatible support loaded with the chemotherapeutic agent is grafted at the level of the tumor lesion, where a controlled and constant drug release is achieved. During our experiments, hydrogels remain in contact with the cells for all the duration of the treatment. As shown in Figure 5A, the cell viability of empty hydrogels was found to be more than 95%. This percentage of cell survival is similar to that previously observed by us for Fmoc-FF and Fmoc-FF/(FY)3 hydrogels co-incubated with the Chinese Hamster Ovarian (CHO) cell line.[38] Dox loaded hydrogels significantly reduced viability of MDA-MB-231 cells after only 24 h of incubation (49%) as well as free Dox at a concentration of 1μmol L^{-1} (55%). This Dox concentration corresponds to its IC_{50} on MDA-MB-231 cells (see Supplementary Figure S4). Due to its lower drug release,

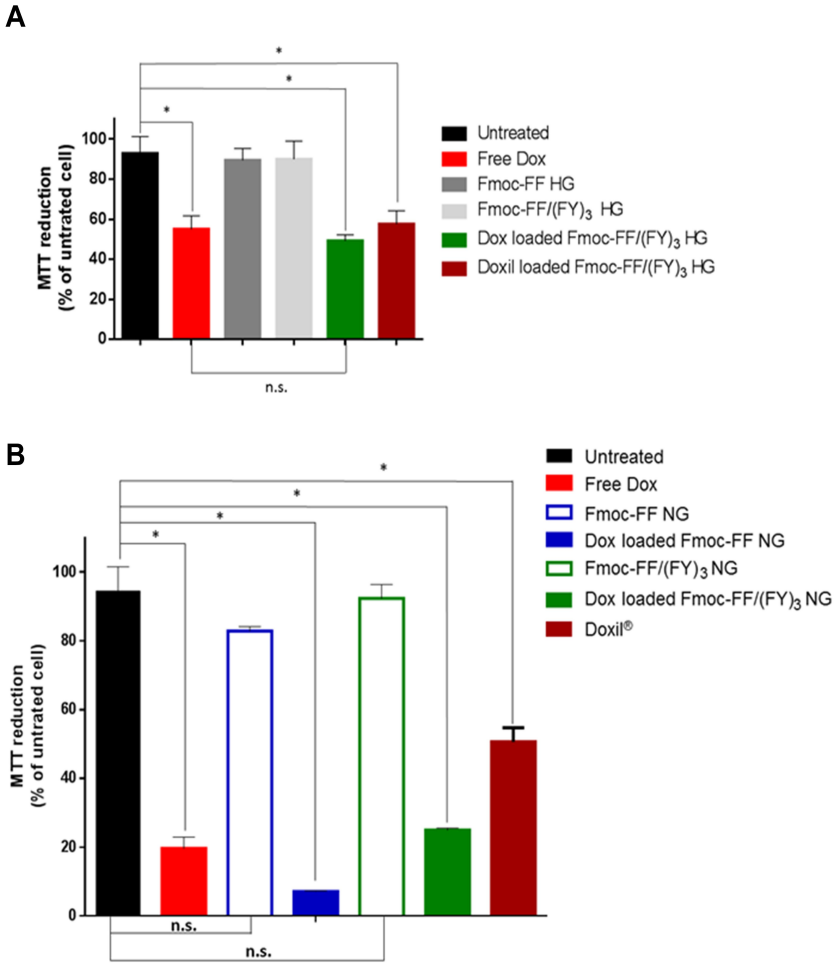

Figure 5 MDA-MB-231 cell survival after doxorubicin treatments. (**A**) MTT assay was conducted on MDA-MB-231 cells treated for 24 h with 1μmol·L^{-1} of free Dox (red bar), empty Fmoc-FF HG (gray bar), empty Fmoc-FF/(FY)3 (1/1, v/v) HG (light gray bar), mixed Fmoc-FF/(FY)3 (1/1, v/v) HG loaded with Dox (green bar) and loaded with Doxil (burgundy bar) in comparison with untreated cells (black bar). Cell survival was expressed as percentage of viable cells in the presence of hydrogels, compared to control cells grown in their absence. (**B**) MTT assay was conducted on MDA-MB-231 cells treated for 72h with 1μmol·L^{-1} of free Dox (red bar), empty Fmoc-FF NG (blue empty bar), empty Fmoc-FF/(FY)3 (1/1, v/v) NG (green empty bar), Dox loaded Fmoc-FF nanogels (blue fill bar), Dox loaded mixed Fmoc-FF/(FY)3 (1/1, v/v) NG (green fill bar) and Doxil (burgundy bar) in comparison with untreated cells (black bar). Cell survival was expressed as percentage of viable cells in the presence of hydrogels and nanogels compared to control cells grown in their absence (Error represents SD of four independent experiments. *p-value<0,05. Mann-Withey *t*-test).
Abbreviation: n.s., not significant.

hydrogels encapsulating Doxil showed a slightly lower cytotoxicity, with a cell viability of 57%.

On the other hand, Figure 5B reports the cell viability of the same cell line treated with pure Fmoc-FF and mixed Fmoc-FF(FY)$_3$ nanogels, empty or loaded with the drug, in comparison to free Dox and Doxil. Initially, we evaluated the cytotoxicity of empty nanogels as function of the total peptide concentration at three different time points (24, 48 and 72 h). We observed that there is a significant decrease in the cell viability during the first 48 h of incubation with nanogels. After this time of incubation, cell viability improves during the next 24 h (see Figure S5). This effect may be due to a temporary inhibition of the cell cycle induced by nanogels. Based on these results, cytotoxicity of NGs encapsulating Dox was checked after 72 h of incubation. Analogously to HGs, Dox loaded nanogels are able to significantly reduce breast cancer cells viability, with a cell viability of 7% and 25% for pure and mixed hydrogels, respectively. The higher cytotoxicity of pure HG with respect to the mixed one is probably attributable to the intrinsic toxicity of the empty gel.

Determination of the Cellular Uptake by Immunofluorescence

The intracellular internalization of Dox loaded HGs and NGs was assessed using immunofluorescence analysis on

MDA-MB-231 cells treated for 24 h. Internalization of free Dox and Doxil are also reported for comparison. As indicated by the overlapping of red fluorescence associated to Dox with blue signal associated to DAPI (nucleus), the free drug can internalize into the nucleus after 24 h of incubation at 37°C (Figure 6A). Differently, Dox loaded Fmoc-FF/(FY)3 mixed hydrogel induces the internalization of Dox at peri-nuclear level since Dox signal is not perfectly overlapped with DAPI, but it is also partially detectable in the cytoplasm together with the green Actin signal (Figure 6B). The same behavior was previously observed for other liposomal Dox formulations.[49,50] At the same time, doxorubicin conveyed through the nanogels remains in the cytoplasm of treated cells (Figure 6C), whereas by using Doxil the drug diffuses equally between the cytoplasm and the nucleus (Figure 6D). The different intracellular distribution of the drug in Figure 6 suggests an internalization mechanism alternative to the diffusion for the drug delivered by supramolecular systems like HGs, NGs and liposomes. One of the most accredited hypotheses is that nanogels are able to bind themselves primarily to the cellular membrane and then to enter the tumor cell via the endocytosis pathway.[51,52]

Conclusion

The administration of drugs is often affected by several issues related to systemic toxicity, chemical instability and repeated dosing requirement. Hydrogels and nanogels can represent alternative drug delivery vehicles to conventional supramolecular structures, such as vesicles, liposomes and nanostructures already developed and in clinical use. Indeed, macroscopic tridimensional HG networks could allow

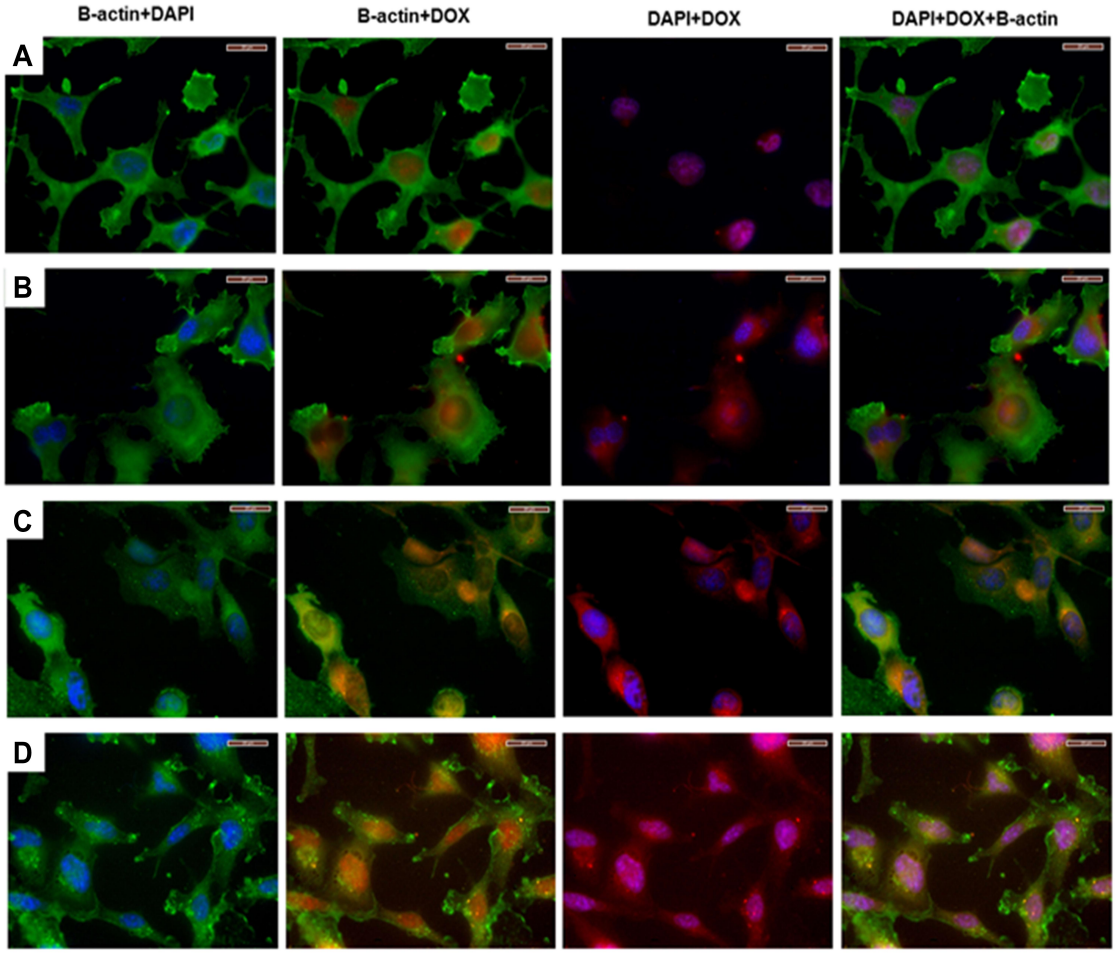

Figure 6 Immunofluorescence assay on cells. MDA-MB-231 cells treated with: (**A**) free Dox; (**B**) Dox loaded mixed Fmoc-FF/(FY)3 (1/1, v/v) HG; (**C**) Dox loaded Fmoc-FF/$(FY)_3$ (1/1, v/v) NGs and (**D**) Doxil. Column I corresponds to Nuclei (DAPI, blue) and B-actin (FITC, green) staining. Column II corresponds to II β-actin (FITC, green) and doxorubicin (red) staining. Column III corresponds to Nuclei (DAPI, blue) and doxorubicin (red) staining. Column IV corresponds to Overlapping of FITC, PE and DAPI channels. Magnification 63×. Scale bars 20 μm.

transepithelial drug delivery or in situ gelation process for the formation of implants, whereas nanosized nanogels could be used for systemic, oral and pulmonary administration of drugs. Due to their high biocompatibility, good biodegradability and tunability, short or ultra-short peptides represent potential attractive alternatives for preparation of HGs and NGs with respect to natural and synthetic polymers. The peptide-based HGs and NGs here formulated are obtained by using the well-known hydrogelator Fmoc-FF alone or in combination with (FY)3 peptide or its PEGylated analogue PEG_8-(FY)3 at two different ratios. NGs were prepared starting from the corresponding HGs using a top-down approach in which the macroscopic hydrogel is submicronized and stabilized with commercially available biocompatible surfactants. Due to the common structure of their inner peptidic network, both NGs and HGs allow to efficiently encapsulate Dox. The gelation kinetics (from 24 to 40 minutes) and the drug release (16–28%, after 72 h) from hydrogels are clearly influenced by the hydrogel peptide composition. Analogously, the DLC values (0.137 and 0.093 for pure and mixed NGs, respectively) and the release percentages (20–40%, after 72 h) in NGs are affected by their composition in terms of net charges. Cytotoxicity assays carried out on MDA-MB-231 breast cancer cell line pointed out a high cell viability (>95%) for empty HGs and NGs, and a reduced cell viability (49–57%) for Dox loaded HGs and NGs. Moreover, immunofluorescence assays show a different cellular localization for the Dox delivered by HGs and NGs with respect to the free Dox. Indeed, contrarily to the free Dox, localized in the nucleus, HGs and NGs allow internalization of the drug at the peri-nuclear level and in the cytoplasm, respectively. This result suggests a different internalization mechanism and a different intracellular distribution and Dox release between free Dox and Dox loaded in hydrogels/nanogels. All the in vitro data we collected and analyzed for pure Fmoc-FF and mixed Fmoc-FF/(FY)3 nanogels loaded with Dox suggest their potential use in vivo, by systemic administration, to deliver the cytotoxic drug on tumor tissues and cells. Thanks to its characteristics the new Dox loaded peptide supramolecular systems here described could be considered as promising valid alternatives to the already available liposomal Dox formulations.

Acknowledgments

This work was supported by the Italian Ministry of Health-Ricerca Corrente project, by the PRIN-2017A2KEPL project and by the grant from Regione Campania-POR Campania FESR 2014/2020 “Combattere la resistenza tumorale: piattaforma integrata multidisciplinare per un approccio tecnologico innovativo alle oncoterapie-Campania Oncoterapie” (Project No. B61G18000470007).

Disclosure

The authors report no conflicts of interest in this work.

References

1. Siegel RL, Miller KD, Jemal A. Cancer statistics, 2020. *CA Cancer J Clin*. 2020;70(1):7–30. doi:10.3322/caac.21590
2. Poustchi F, Amani H, Ahmadian Z, et al. Combination therapy of killing diseases by injectable hydrogels: from concept to medical applications. *Adv Healthcare Mater*. 2020;2001571.
3. McGowan JV, Chung R, Maulik A, Piotrowska I, Walker JM, Yellon DM. Anthracycline chemotherapy and cardiotoxicity. *Cardiovasc Drugs Ther*. 2017;31(1):63–75. doi:10.1007/s10557-016-6711-0
4. Carvalho C, Santos R, Cardoso S, et al. Doxorubicin: the good, the bad and the ugly effect. *Curr Med Chem*. 2009;16(25):3267–3285. doi:10.2174/092986709788803312
5. Falcone G, Filippelli W, Mazzarella B, et al. Cardiotoxicity of doxorubicin: effects of 21-aminosteroids. *Life Sci*. 1998;63(17):1525–1532. doi:10.1016/S0024-3205(98)00419-6
6. Unverferth DV, Fertel RH, Talley RL, Magorien RD, Balcerzak SP. The effect of first-dose doxorubicin on the cyclic nucleotide levels of the human myocardium. *Toxicol Appl Pharmacol*. 1981;60(1):151–154. doi:10.1016/0041-008X(81)90145-9
7. Falciani C, Accardo A, Brunetti J, et al. Target-selective drug delivery through liposomes labeled with oligobranched neurotensin peptides. *ChemMedChem*. 2011;6(4):678–685. doi:10.1002/cmdc.201000463
8. Nik ME, Malaekeh-Nikouei B, Amin B, et al. Liposomal formulation of galbanic acid improved therapeutic efficacy of PEGylated liposomal doxorubicin in mouse colon carcinoma. *Sci Rep*. 2019;9(1):9527. doi:10.1038/s41598-019-45974-7
9. Joniec A, Sek S, Krysinski P. Magnetoliposomes as potential carriers of doxorubicin to tumours. *Chem Eur J*. 2016;22(49):17715–17724. doi:10.1002/chem.201602809
10. Haghiralsadat F, Amoabediny G, Sheikhha MH, et al. New liposomal doxorubicin nanoformulation for osteosarcoma: drug release kinetic study based on thermo and pH sensitivity. *Chem Biol Drug Des*. 2017;90(3):368–379. doi:10.1111/cbdd.12953
11. Lipowska-Kur SR, Trzebicka B, Dworak A, Dworak A. Preparation and characterization of doxorubicin nanocarriers based on thermo-responsive oligo(ethylene glycol) methyl ether methacrylate polymer-drug conjugates. *Eur Pol J*. 2018;109:391–401. doi:10.1016/j.eurpolymj.2018.10.008
12. Diaferia C, Gianolio E, Sibillano T, et al. Cross-beta nanostructures based on dinaphthylalanine Gd-conjugates loaded with doxorubicin. *Sci Rep*. 2017;7(1):307. doi:10.1038/s41598-017-00332-3
13. Jiang T, Zhang C, Sun W, et al. Doxorubicin encapsulated in TPGS-modified 2D-nanodisks overcomes multidrug resistance. *Chem Eur J*. 2020;26(11):2470–2477. doi:10.1002/chem.201905097
14. Saini M, Ghosh S, Kumar V, Roy P, Sadhu KK. Selective release of doxorubicin from cucurbit[8]uril stabilized gold supra-pyramid host at pH of small intestine. *Chem Eur J*. 2020;26(66):15150–15158. doi:10.1002/chem.202002048
15. Hashemzadeh H, Raissi H. Understanding loading, diffusion and releasing of doxorubicin and paclitaxel dual delivery in graphene and graphene oxide carriers as highly efficient drug delivery systems. *Appl Surf Sci*. 2020;500:144220. doi:10.1016/j.apsusc.2019.144220
16. Alinejad A, Raissi H, Hashemzadeh H. Development and evaluation of a pH-responsive and water-soluble drug delivery system based on smart polymer coating of graphene nanosheets: an in silico study. *RSC Adv*. 2020;10(52):31106. doi:10.1039/D0RA06705A

17. Okay O. General properties of hydrogels. In: Gerlach G, Arndt K-F, editors. *Hydrogel Sensors and Actuators. Engineering and Technology*. 2010:1–14.
18. Martino MM, Tortelli F, Mochizuki M, et al. Engineering the growth factor microenvironment with fibronectin domains to promote wound and bone tissue healing. *Sci Transl Med*. 2011;3(100):100ra89. doi:10.1126/scitranslmed.3002614
19. Hosoyama K, Lazurko C, Muñoz M, McTiernan CD, Alarcon EI. Peptide-based functional biomaterials for soft-tissue repair. *Front Bioeng Biotechnol*. 2019;7:205. doi:10.3389/fbioe.2019.00205
20. Klotz BJ, Oosterhoff LA, Utomo L, et al. A versatile biosynthetic hydrogel platform for engineering of tissue analogues. *Adv Health Mater*. 2019;8(19):1900979. doi:10.1002/adhm.201900979
21. Singh N, Kumar M, Miravet JF, Ulijn RV, Escuder B. Peptide-based molecular hydrogels as supramolecular protein mimics. *Chem Eur J*. 2016;23(5):981–993. doi:10.1002/chem.201602624
22. Alvarez-Lorenzo C, Anguiano-Igea S, Varela-García A, Vivero-Lopez M, Concheir A. Bioinspired hydrogels for drug-eluting contact lenses. *Acta Biomater*. 2019;84:49–62. doi:10.1016/j.actbio.2018.11.020
23. Karcher J, Pianowski ZL. Photocontrol of drug release from supramolecular hydrogels with green light. *Chem Eur J*. 2018;24 (45):11605–11610. doi:10.1002/chem.201802205
24. Daly AC, Riley L, Segura T, Burdick JA. Hydrogel microparticles for biomedical applications. *Nat Rev Mater*. 2020;5:20–43.
25. Lübtow MM, Lorson T, Gröber-Becker F-K, Luxenhofer R, Luxenhofer R. Combining ultra-high drug-loaded micelles and injectable hydrogel drug depots for prolonged drug release. *Macromol Chem Phys*. 2020;221(1):1900341. doi:10.1002/macp.201900341
26. Argentiere S, Blasi L, Ciccarella G, Barbarella G, Cingolani R, Gigli G. Synthesis of poly(acrylic acid) nanogels and application in loading and release of an oligothiophene fluorophore and its bovine serum albumin conjugate. *Macromol Symp*. 2009;281(1):69–76. doi:10.1002/masy.200950709
27. Dong L, Wang S-J, Zhao X-R, Zhu Y-F, Yu J-K. 3D-printed poly(ε-caprolactone) scaffold integrated with cell-laden chitosan hydrogels for bone tissue engineering. *Sci Rep*. 2017;7(1):13421. doi:10.1038/s41598-017-13838-7
28. Das D, Das R, Mandal J, Ghosh A, Pal S. Dextrin crosslinked with poly(lactic acid): a novel hydrogel for controlled drug release application. *J Appl Polym Sci*. 2014;131(7). doi:10.1002/APP.40039
29. Neves MI, Araújo M, Moroni L, da Silva RMP, Barrias CC. Glycosaminoglycan-inspired biomaterials for the development of bioactive hydrogel networks. *Molecules*. 2020;25(4):978. doi:10.3390/molecules25040978
30. Suner SS, Ari B, Onder FC, Ozpolat B, Ay M, Sahine N. Hyaluronic acid and hyaluronic acid: sucrose nanogels for hydrophobic cancer drug delivery. *Int J Biol Macromol*. 2019;1(126):1150–1157. doi:10.1016/j.ijbiomac.2019.01.021
31. Wang H, Qian J, Ding F. Recent advances in engineered chitosan-based nanogels for biomedical applications. *J Mater Chem B*. 2017;5(34):6986–7007. doi:10.1039/C7TB01624G
32. Dibbert N, Krause A, Rios-Camacho J-C, Gruh I, Kirschning A, Dräger G. A synthetic toolbox for the in situ formation of functionalized homo- and heteropolysaccharide-based hydrogel libraries. *Chem Eur J*. 2016;22 (52):18777–18786. doi:10.1002/chem.201603748
33. Echalier C, Jebors C, Laconde G, et al. Sol–gel synthesis of collagen-inspired peptide hydrogel. *Mater Today*. 2017;20(2):59–66. doi:10.1016/j.mattod.2017.02.001
34. Ghosh M, Bera S, Schiffmann S, Shimon LJW, Adler-Abramovich L. Collagen-inspired helical peptide co-assembly forms a rigid hydrogel with twisted polyproline II architecture. *ACS Nano*. 2020;14 (8):9990–10000. doi:10.1021/acsnano.0c03085
35. Smith AM, Williams RJ, Tang C, et al. Fmoc-diphenylalanine self assembles to a hydrogel via a novel architecture based on π–π interlocked β-sheets. *Adv Mater*. 2008;20(1):37–41. doi:10.1002/adma.200701221
36. Diaferia C, Morelli G, Accardo A. Fmoc-diphenylalanine as a suitable building block for the preparation of hybrid materials and their potential applications. *J Mater Chem B*. 2019;7(34):5142–5155. doi:10.1039/C9TB01043B
37. Mahler A, Reches M, Rechter M, Cohen S, Gazit E. Rigid, self-assembled hydrogel composed of a modified aromatic dipeptide. *Adv Mater*. 2006;18(11):1365–1370. doi:10.1002/adma.200501765
38. Diaferia C, Ghosh M, Sibillato T, et al. Fmoc-FF and hexapeptide-based multicomponent hydrogels as scaffold materials. *Soft Matter*. 2019;15(3):487–496. doi:10.1039/C8SM02366B
39. Diaferia C, Balasco N, Sibillano T, et al. Amyloid-like fibrillary morphology originated by tyrosine-containing aromatic hexapeptides. *Chem Eur J*. 2018;24(26):6804–6817. doi:10.1002/chem.201800351
40. Foulkes WD, Smith IE, Reis-Filho JS. Triple-negative breast cancer. *N Engl J Med*. 2010;363(20):1938–1948. doi:10.1056/NEJMra1001389
41. Rosa E, Diaferia C, Gallo E, Morelli G, Accardo A. Stable formulations of peptide-based nanogels. *Molecules*. 2020;25(15):3455. doi:10.3390/molecules25153455
42. Diaferia C, Balasco N, Altamura D, et al. Assembly modes of hexaphenylalanine variants as function of the charge states of their terminal ends. *Soft Matter*. 2018;14(40):8219–8230. doi:10.1039/C8SM01441H
43. Diaferia C, Netti F, Ghosh M, et al. Bi-functional peptide-based 3D hydrogel-scaffolds. *Soft Matter*. 2020;16(30):7006–7017. doi:10.1039/D0SM00825G
44. Raeburn J, Mendoza-Cuenca C, Cattoz BN, et al. The effect of solvent choice on the gelation and final hydrogel properties of Fmoc-diphenylalanine. *Soft Matter*. 2015;11(5):927–935. doi:10.1039/C4SM02256D
45. Ringhieri P, Iannitti R, Nardon C, et al. Target selective micelles for bombesin receptors incorporating. Au(III)-dithiocarbamato complexes. *Int J Pharm*. 2014;473(1–2):194–202. doi:10.1016/j.ijpharm.2014.07.014
46. Li J, Mooney DJ. Designing hydrogels for controlled drug delivery. *Nat Rev Mater*. 2016;1:16071.
47. Tang JD, Mura C, Lampe KJ. Stimuli-responsive, pentapeptide, nanofiber hydrogel for tissue engineering. *J Am Chem Soc*. 2019;141(12):4886–4899. doi:10.1021/jacs.8b13363
48. Ghosg M, Halperin-Sternfeld M, Grigoriants I, Lee J, Nam KT, Adler-Abramovich L. Arginine-presenting peptide hydrogels decorated with hydroxyapatite as biomimetic scaffolds for bone regeneration. *Biomacromol*. 2017;18(11):3541–3550. doi:10.1021/acs.biomac.7b00876
49. Accardo A, Arena F, Gianolio E, et al. Diolein based nanostructures as targeted theranostics. *J Biomed Nanotechnol*. 2016;12 (5):1076–1088. doi:10.1166/jbn.2016.2212
50. Tarallo R, Accardo A, Falanga A, et al. Clickable functionalization of liposomes with the gH625 peptide from Herpes simplex virus type I for intracellular drug delivery. *Chem Eur J*. 2011;17 (45):12659–12668. doi:10.1002/chem.201101425
51. Zhang H, Pei M, Liu P. pH-activated surface charge-reversal double-crosslinked hyaluronic acid nanogels with feather keratin as multifunctional crosslinker for tumor-targeting DOX delivery. *Int J Biol Macromol*. 2020;150:1104–1112. doi:10.1016/j.ijbiomac.2019.10.116
52. Chen X, Zhang X, Guo Y, et al. Smart supramolecular "trojan horse"-inspired nanogels for realizing light-triggered nuclear drug influx in drug-resistant cancer cells. *Adv Funct Mater*. 2019;29(13):1807772. doi:10.1002/adfm.201807772

biomedicines

MDPI

Article

Self-Supporting Hydrogels Based on Fmoc-Derivatized Cationic Hexapeptides for Potential Biomedical Applications

Carlo Diaferia [1,†], Elisabetta Rosa [1,†], Enrico Gallo [2], Giovanni Smaldone [2], Mariano Stornaiuolo [1], Giancarlo Morelli [1] and Antonella Accardo [1,*]

[1] Department of Pharmacy and Research Centre on Bioactive Peptides (CIRPeB), University of Naples "Federico II", 80134 Naples, Italy; carlo.diaferia@unina.it (C.D.); elisabetta.rosa@unina.it (E.R.); mariano.stornaiuolo@unina.it (M.S.); gmorelli@unina.it (G.M.)

[2] IRCCS SDN, Via Gianturco 113, 80143 Naples, Italy; enrico.gallo@synlab.it (E.G.); giovanni.smaldone@synlab.it (G.S.)

* Correspondence: antonella.accardo@unina.it; Tel.: +39-081-2532045

† These Authors contributed equally to this work.

Abstract: Peptide-based hydrogels (PHGs) are biocompatible materials suitable for biological, biomedical, and biotechnological applications, such as drug delivery and diagnostic tools for imaging. Recently, a novel class of synthetic hydrogel-forming amphiphilic cationic peptides (referred to as series K), containing an aliphatic region and a Lys residue, was proposed as a scaffold for bioprinting applications. here, we report the synthesis of six analogues of the series K, in which the acetyl group at the N-terminus is replaced by aromatic portions, such as the Fmoc protecting group or the Fmoc-FF hydrogelator. The tendency of all peptides to self-assemble and to gel in aqueous solution was investigated using a set of biophysical techniques. The structural characterization pointed out that only the Fmoc-derivatives of series K keep their capability to gel. Among them, Fmoc-K3 hydrogel, which is the more rigid one (G′ = 2526 Pa), acts as potential material for tissue engineering, fully supporting cell adhesion, survival, and duplication. These results describe a gelification process, allowed only by the correct balancing among aggregation forces within the peptide sequences (e.g., van der Waals, hydrogen bonding, and π–π stacking).

Keywords: peptide hydrogel; tissue engineering; Fmoc peptides; peptide materials; self-assembling; tissue engineering

Citation: Diaferia, C.; Rosa, E.; Gallo, E.; Smaldone, G.; Stornaiuolo, M.; Morelli, G.; Accardo, A. Self-Supporting Hydrogels Based on Fmoc-Derivatized Cationic Hexapeptides for Potential Biomedical Applications. *Biomedicines* **2021**, *9*, 678. https://doi.org/10.3390/biomedicines9060678

Academic Editors: Elvira De Giglio and Maria A. Bonifacio

Received: 28 May 2021
Accepted: 12 June 2021
Published: 15 June 2021

1. Introduction

Peptide-based hydrogels (PHGs) are soft materials formed by water-swollen networks (up to 99% water) with a no-Newtonian fluid behavior and self-supporting features [1–3]. Compared to polymeric gels, PHGs display different advantages, including chemical and physical responsiveness to stimuli, intrinsic biocompatibility of their molecular constituents, chemical accessibility, tunability, and the generation of a physiologically relevant environment for in vitro experiments [4–6]. In virtue of these features, PHGs have been proposed for many applications, such as formulation of membranes and coatings [7], generation of components for sensors [8,9] and optimization of tools for delivery of drugs and/or diagnostic agents [10–12]. Moreover, in the last years, PHG materials have emerged as promising options for cell culture and bioink, since they mimic salient elements of native extracellular matrices (ECMs) and possess mechanics similar to those of many biological tissues [13]. Since self-assembling peptides may represent an innovative solution to problems encountered with the use of bioink materials for 3D cell culture, different peptide categories have been screened for this scope [14,15]. Specifically, their spontaneous aggregation in nanofibrillar structures allow avoiding the use of UV-mediated crosslinking or chemical polymerization, which are formulative steps that might damage printed cells or alter their biological features [16].

Recently, a novel class of synthetic hydrogel-forming amphiphilic cationic peptides was proposed as a scaffold for bioprinting applications [17]. The primary sequences, formed by tri-, tetra- or hexapeptides acetylated, and amidated on their termini, consist of an aliphatic region (containing Gly, Ala, Val, Leu, and/or Ile) followed by a Lys residue at the C-terminus [17]. In these peptides, self-aggregation in elongated and unbranched fibers is prompted by the establishment of hydrogen bonds and van der Waals hydrophobic interactions between the amphiphilic monomers. Successively, these fibrillary structures mutually contact to form the macroscopical PHG. The water trapped within the matrix can protect cells from dehydration during the printing process. Among the investigated sequences, the best gelling properties at low concentrations were observed for three hexapeptides (here indicated as K1, K2, and K3), consisting of a succession of five aliphatic amino acids followed by the positively charged one. Moreover, the preparation of the hydrogel in phosphate buffer solution allows a decrease of the critical gelation concentration (CGC) and a higher rigidity of the resulting hydrogel with a storage modulus (G′) value up to 40 kPa [17].

Here, we describe the synthesis of K1, K2, and K3 peptides modified at their N-terminus with the fluorenylmethyloxycarbonyl (Fmoc) protecting group or with two Phe residues and the Fmoc group (see Figure 1). The basis behind the modification of K-peptides with the aromatic fluorenyl group arises from the knowledge that aromatic groups (such as Fmoc or naphthyl one) can deeply affect aggregation and gelation properties of short or ultrashort peptide sequences [18–21]. Indeed, in these derivatives, the hydrogelation is simplified by the establishment of additional stabilization effect (π–π stacking) due to the long-range aromaticity of these molecules. Moreover, the aromatic dipeptide FmocFF is a well-known low molecular weight hydrogelator able to form self-supporting hydrogels under physiological conditions [3,22–26].

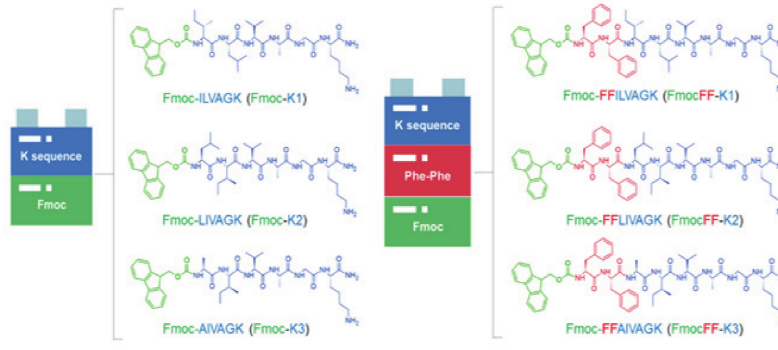

Figure 1. Schematic representation of Fmoc-K1, Fmoc-K2, and Fmoc-K3 peptides, and of their corresponding analogues containing the FF motif between the Fmoc protecting group and K1, K2, and K3 peptides. The sequences of the three peptides are reported in the figure according to the one letter code.

The effective capability of the six peptides to spontaneously assemble in supramolecular aggregates, such as fibers and hydrogels, was evaluated using a set of biophysical techniques (fluorescence, circular dichroism, Fourier transform infrared, Congo Red assay, scanning electron microscopy). The mechanical properties of the resulting hydrogels were also evaluated by rheological studies. Finally, the potential employment of these hydrogels as extracellular matrices was tested by cytotoxicity and cell adhesion assays on 3T3 fibroblast and on haCat cell lines.

2. Materials and Methods

Protected N^{α}-Fmoc-amino acid derivatives, coupling reagents, and Rink amide MBHA (4-methylbenzhydrylamine) resin are commercially available from Calbiochem-Novabiochem (Laufelfingen, Switzerland). All other chemical products are commercially

available from Merck (Milan, Italy), Fluka (Bucks, Switzerland), or Labscan (Stillorgan, Dublin, Ireland), and unless stated otherwise, they were used as delivered. Peptide solutions were prepared by weight using double distilled water. Preparative RP-HPLC was carried out using an LC8 Shimadzu hPLC system (Shimadzu Corporation, Kyoto, Japan) equipped with a UV lambda-Max Model 481detector, using a Phenomenex (Torrance, CA, USA) C18 column. Elution solvents were h_2O/0.1% TFA (A) and CH_3CN/0.1% TFA (B) from 30 to 80% over 30 min at a flow rate of 20 mL/min. The purity of the products was assessed by analytical RP-HPLC analysis performed by using Finnigan Surveyor MSQ single quadrupole electrospray ionization (Finnigan/Thermo Electron Corporation San Jose, CA, USA), with a C18-Phenomenex column eluting with h_2O/0.1% TFA (A) and CH_3CN/0.1% TFA (B) from 20 to 80% over 20 min at a flow rate of 200 µL/min. Identity of peptides was assessed by MS spectrometry using a LTQ XL Linear Ion Trap Mass Spectrometer, ESI source.

2.1. Peptide Solid Phase Synthesis

All peptide derivatives were synthesized according to standard SPPS (solid-phase peptide synthesis) procedures using the Fmoc/tBu strategy [27]. The Rink amide MBHA resin (substitution 0.71 mmol/g) was selected as the solid-phase support to provide amidated peptides at the C-terminus. Each peptide was synthetized using a scale of 0.20 mmol in DMF. The resin was allowed to swell for 30 min in the reactor, and then the Fmoc group was deprotected by treating the resin with 30% (*v*/*v*) piperidine in DMF (two cycles of 10 min). The coupling of each amino acid was performed by adding a 2-fold molar excess of the protected Fmoc-amino acid, with equimolar amounts of 1-hydroxybenzotriazole (HOBt), benzotriazol-1-yl-oxytris-pyrrolidino-phosphonium (PyBOP), and a 4-fold molar excess of diisopropylethylamine (DIPEA) in DMF/NMP. All couplings were performed twice for 40 min. At the end of the synthesis, crude peptides were fully cleaved from the resin with a TFA (trifluoroacetic acid)/TIS (triisopropylsilane)/H_2O (92.5/5/2.5 *v*/*v*/*v*) mixture at room temperature for 3 h. All the peptides were precipitated with cold ether and freeze-dried for three times. The purification of the crude products was carried out by RP-HPLC. Mass spectra confirmed the identity of the products (see Table 1 for analytical data of peptides).

Table 1. Formula, theoretical and experimentally found molecular weight (MW) and retention time of investigated peptides.

Peptide	Formula	MWcalc. (a.m.u.)	MWdeter. (a.m.u.)	t_R (min)
Fmoc-K1	$C_{43}H_{64}N_8O_8$	821.01	821.6	18.37
Fmoc-K2	$C_{43}H_{64}N_8O_8$	821.01	821.6	18.43
Fmoc-K3	$C_{40}H_{58}N_8O_8$	778.93	779.6	16.28
FmocFF-K1	$C_{61}H_{82}N_{10}O_{10}$	1115.36	1115.7	21.93
FmocFF-K2	$C_{61}H_{82}N_{10}O_{10}$	1115.36	1115.6	21.89
FmocFF-K3	$C_{58}H_{76}N_{10}O_{10}$	1073.28	1073.3	20.32

2.2. Preparation of Peptide Solutions

Peptide solutions were prepared by dissolving 10 mg of each lyophilized peptide in 1.0 mL of water. These suspensions were sonicated for 30 min at room temperature; after centrifugation (5 min at 13,000 rpm), the concentration was spectroscopically determined on UV–Vis Thermo Fisher Scientific Inc. (Wilmington, DE, USA) NanoDrop 2000 c spectrophotometer equipped with a 1.0 cm quartz cuvette (Hellma). The quantification of the concentration was assessed using the molar absorptivity (ε) of 7800 M^{-1} cm^{-1} for Fmoc group at λ = 301 nm.

2.3. Preparation of Peptide Hydrogels

Hydrogel preparation was achieved by initially dissolving peptides in 300 µL of water at 2 wt% and then by adding 50 µL of 0.100 mol/L phosphate buffer. The hydrogel formation was macroscopically verified by the inverted test tube.

2.4. Peptide Characterization in Solution

2.4.1. Fluorescence Studies

Fluorescence measurements were recorded at room temperature with a spectrofluorometer Jasco (Model FP-750) placing the sample in a quartz cell with 1.0 cm path length. The other settings were excitation and emission bandwidths = 5 nm; recording speed = 125 nm/min, and automatic selection of the time constant. Fluorescence spectra of each peptide solution at the maximum of solubility for each peptide were recorded exciting the samples at 257 and 301 nm. The determination of the critical aggregation concentration (CAC) values for all the peptide sequences was assessed by fluorescence titration of the dye 8-anilino-1-naphthalene sulfonic acid ammonium salt (ANS) with increasing amounts of the peptide solution [28]. The fluorescence spectra were recorded between 360 and 550 nm exciting the samples at 350 nm. The measurements were performed by adding small aliquots of peptide derivatives in 1 mL of 20 µm ANS water solution. At the end of the titration, the blank was subtracted. Fluorescence spectra were corrected for the blank and adjusted for the dilution.

2.4.2. Circular Dichroism (CD) Studies

Far-UV CD spectra in aqueous solution at 1.0 mg/mL for Fmoc-K derivatives and at the maximum solubility for FmocFF-K analogues (0.51, 0.25, and 0.34 mg/mL for K1, K2, and K3, respectively) were collected with a Jasco J-810 spectropolarimeter equipped with a Neslab RTE111 thermal controller unit using a 0.1 mm quartz cell at 25 °C. The spectra of samples at several concentrations were recorded from 320 to 190 nm. Other experimental settings were: scan speed = 50 nm/min, sensitivity = 50 mdeg, time constant = 16 s, bandwidth = 1 nm, response = 2 s and data pitch = 1 nm. Each spectrum was obtained by averaging three scans and corrected for the blank. here, Θrepresents the mean residue ellipticity (MRE), i.e., the ellipticity per mole of peptide divided by the number of amide bonds in the peptide sequences.

2.4.3. Fourier Transform Infrared Spectroscopy (FTIR)

Fourier transform infrared spectra of all the peptides solubilized at the maximum concentration were collected on a Jasco FT/IR 4100 spectrometer (Easton, MD, USA) in an attenuated total reflection (ATR) mode and using a Ge single-crystal at a resolution of 4 cm^{-1}. A total of 100 scans for each sample were recorded with a rate of 2 $mm \cdot s^{-1}$ against a KBr background. After collection in transmission mode, spectra were converted to emission.

2.4.4. Congo Red (CR) Assay

Congo Red spectroscopic assay was carried out by UV/Vis measurements; 10 µL of a water solution of CR (0.3 $mg \cdot mL^{-1}$) were freshly prepared and added to 200 µL of preformed gel. The resulting mixture was vortexed for 30 s and then sonicated for 15 min at room temperature.

At the end of the homogenization process, a further aliquot of water (200 µL) was added to the gel and then the suspension was measured at the UV–Vis, recording the spectrum between 400 and 700 nm at room temperature. Analogously, it was also recorded the spectrum of the CR alone at the same final concentration.

2.5. Hydrogel Characterization

2.5.1. Scanning Electron Microscopy (SEM)

Morphological analysis of xerogels was carried out by field emission scanning electron microscope (PhenomXL, Alfatest); 10 µL of peptide hydrogel were drop-casted on an aluminum stub and air-dried. A thin coat of gold and palladium was sputtered at a current of 25 mA for 75 s. The sputter-coated samples were then introduced into the specimen chamber and the images were acquired at an accelerating voltage of 10 kV, spot 3, through the Secondary Electron Detector (SED).

2.5.2. Swelling and Stability Studies

The swelling ratios of hydrogels were measured by adding 1.5 mL of doubly distilled water to each hydrogel sample (0.50 wt%, V = 400 µL) and subsequently incubating them at 30 °C overnight. Fully swollen hydrogels were weighed (Ws) immediately after the removal of excess water. Then, the hydrogels were freeze-dried and weighed again (Wd). The swelling behavior was expressed, according to Equation (1), as the swelling ratio q, which is the ratio between the weight of the swollen sample (Ws) and the weight of the freeze-dried hydrogel (Wd)

$$q = ((Ws - Wd))/Wd\ \% \quad (1)$$

In vitro hydrogel degradation assay was performed by adding a fixed amount (1.5 mL) of Ringer's solution (12.9 mg of NaCl, 0.45 mg of KCl and 0.48 mg of $CaCl_2$) to the preformed hydrogels and by placing them in an oven at 37 °C for 40 days. hydrogels were weighed before the addition of the Ringer's solution (Wo) and after its removal (Wt). The weight loss ratio (ΔW) was calculated as percentage according to Equation (2)

$$\Delta W = ((Wo - Wt))/Wo\ \% \quad (2)$$

2.5.3. Rheological Studies

Rheological properties of cationic hydrogels were evaluated using a rotational controlled stress rheometer (Malvern Kinexus) using a 15 mm flat-plate geometry (PU20:PL61). Freshly prepared hydrogel sample (400 µL) at a concentration of 2.0 wt% was tested. Each experiment was performed at 25 °C using a humidity chamber and a gap of 1 mm. Preliminary dynamic rheological tests were carried out in order to identify the regime of linear viscoelasticity. The viscous elastic region was determined by the oscillatory frequency (0.1–100 hz) and the strain sweep (0.01–100%). A time-sweep oscillatory evaluation test (using a constant 0.1% strain and 1 hz frequency) was then performed for 20 min. Results are reported in Pascal (Pa) as shear Storage or elastic modulus (G') and shear loss or viscous modulus (G").

2.6. In Vitro Assays

2.6.1. Cell Line

Aneuploid immortal keratinocyte cell line haCat and mouse pre-adipocyte cell line 3T3-L1 were obtained from IRCCS-SDN Biobank (10.5334/ojb.26) and grown in Dulbecco's Modified Medium (DMEM) supplemented with 10% fetal bovine serum (FBS) and 1% GlutaMAX. Cells were incubated at 37 °C and 5% CO_2 and seeded in 100 mm culture dishes.

2.6.2. Cell Viability Evaluation

For the adhesion test, 3T3-L1 cells were seeded in 96-well plates at a density of 0.5×10^4 cells per well. Before seeding, each well was filled with the indicated hydrogels; 16 h after seeding, cells were stained with Acridine Orange/Propidium Iodide stain. Cell adhesion was reported as % of adherent viable cell (fluorescing green) on total plated cells. Viability upon adhesion was reported as % viable cells and total adherent cells. Duplication rate was reported as the ratio between viable cells upon 48 h from seeding and the number of viable adherent cells upon 16 h from seeding. In order to test the toxicity of hydrogels conditioned media, we used MTS assay, (CellTiter 96® AQueous

One Solution Cell Proliferation Assay, Promega, Italy). For MTS assays, haCat and 3T3-L1 cells were seeded in 96-well plates at a density of 0.7×10^4 cells per well. To obtain the conditioned media, hydrogels formed in a hollow plastic chamber sealed at one end with a porous membrane, were incubated with 2 mL of completed DMEM medium for 16 h in sterile condition at RT [23]. No color change of the media was detected following the incubation and the tested pH value (7.5–7.8) was suitable for culturing added to the wells. The conditioned media were used to grow the cells for 24, 48, and 72 h. At the end of the treatment, cell viability was assessed by the MTS assay. In brief, MTS was added to the cells at a final concentration of 0.5 mg/mL. After 30 min of incubation at 37 °C, the samples were analyzed using the VICTOR Nivo (Perkin Elmer, Buckinghamshire, UK) at 490 nm absorbance. Cell survival was expressed as percentage of viable cells in the presence of hydrogels, compared to control cells grown in their absence. MTS assay was repeated twice with similar results.

3. Results and Discussion

3.1. Synthesis and Fluorescence Characterization

The Fmoc-K1, Fmoc-K2, and Fmoc-K3 peptides, and their analogues, FmocFF-K1, FmocFF-K2, and FmocFF-K3, in which the FF motif is interposed between the Fmoc group and the peptide sequence, are schematically depicted in Figure 1. All the peptides were synthetized according to the standard solid phase peptide synthesis procedures. Peptides, cleaved from the polymeric support, were purified by RP-HPLC chromatography and their identity was assessed by LC–MS (see Figures S1–S5 and Table 1).

Due to their different sequence, each peptide has a different water solubility (see Table 2). As expected, the three peptides containing the FF motif exhibit a lower solubility (~3-fold lower) than their analogues lacking of it. The capability of peptides to self-assemble was initially checked by fluorescence spectroscopy, recording the emission spectra at the maximum concentration of the peptide. Peptides containing the FF motif were excited at both 257 and 301 nm, which corresponded to the excitation wavelength of phenyl and the Fmoc group, respectively, whereas peptides lacking FF were excited only at 301 nm. All the peptide derivatives, upon excitation at 301 nm, have an emission peak at 328 nm, red-shifted of 15 nm, with respect to the peak at 313 nm, which is expected for the monomeric form (see Figure S6) [29,30].

Table 2. Water solubility, logP values, water solubility, storage modulus (G′) and loss modulus (G″) of the investigated peptides.

Peptide	Water Solubility (mg/mL)	logP	G′ (Pa)	G″(Pa)
Fmoc-K1	1.24	4.30 ± 0.84	557	40
Fmoc-K2	2.56	4.30 ± 0.84	925	89
Fmoc-K3	3.21	2.89 ± 0.84	2526	273
FmocFF-K1	0.508	7.47 ± 0.90	—	—
FmocFF-K2	0.253	7.47 ± 0.90	—	—
FmocFF-K3	0.345	6.06 ± 0.90	—	—

This red shift is usually detected when an antiparallel stacking of the fluorenyl groups occurs. An analogous emission peak at 328 nm is also detected for samples excited at 257 nm, thus indicating the occurrence of a Förster resonance energy transfer (FRET) phenomenon between the phenyl and fluorenyl groups [31]. In addition, peptide derivatives containing the FF motif also exhibit a broad peak around 460 nm that indicates further stacking phenomena with consequent excimer formation [29,30].

Moreover, we also evaluated the critical aggregation concentration (CAC) value of the peptides using the well-assessed fluorescence method based on the titration of the fluorophore, 8-anilinonaphthalene-1-sulfonate ammonium salt (ANS), with increasing amounts of peptide. The characteristic of the ANS is its capability to emit fluorescence between 460 and 480 nm only in the presence of a hydrophobic environment, such as the

inner micellar core [32] or the aliphatic/aromatic interface of peptide nanostructures [33]. The CAC value is easily extrapolated from the break points of the graphics in Figure 2. The graph shows the behavior of each peptide derivative in the presence or in the absence of the FF motif. All the determined values are in the range $1.16 \cdot 10^{-6} < CAC < 3.39 \cdot 10^{-5}$ mol·L^{-1}. As expected, the peptide sequences containing the two aromatic amino acids exhibit lower CAC values. This behavior is obviously related to the logP values theoretically estimated by ACD/3D Viewer and reported in Table 2.

Peptide	CAC (mol/L)	CAC (μg/mL)
Fmoc-K1	$3.39 \cdot 10^{-5}$	27.8
FmocFF-K1	$1.16 \cdot 10^{-5}$	12.9
Fmoc-K2	$1.23 \cdot 10^{-5}$	10.0
FmocFF-K2	$5.98 \cdot 10^{-6}$	6.53
Fmoc-K3	$2.34 \cdot 10^{-5}$	18.2
FmocFF-K3	$1.83 \cdot 10^{-5}$	11.5

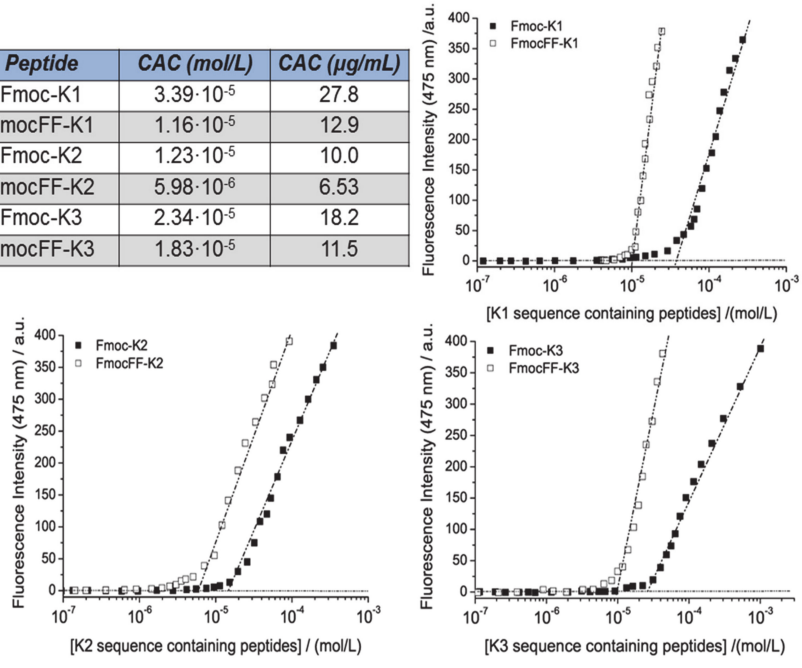

Figure 2. CAC determination. Fluorescence intensity of the ANS fluorophore at 470 nm versus the concentration of each peptide. CAC values, calculated from the break points, are reported in the Table (expressed in mol/L and in μg/mL).

3.2. Secondary Structural Characterization in Solution

The secondary structure of all the peptides in water was investigated by circular dichroism (CD), Fourier transform infrared (FTIR), and Congo Red (CR) assays (Figures 3 and 4). These investigations are classically used to establish the presence of β-sheets (with parallel or antiparallel β-strands) in fibrillary peptide nanostructures [34,35]. CD spectra of all the peptides were recorded between 320 and 190 nm and the corresponding dichroic signals are reported in Figure 3. Spectra of Fmoc-K1, Fmoc-K2, and Fmoc-K3 in Figure 3a were recorded at a concentration of 1.0 mg/mL, whereas spectra of their FF containing derivatives in Figure 3b are relative to the maximum solubility of peptides in water. Regardless of their primary peptide sequence, CD spectra of Fmoc-K1, Fmoc-K2, and Fmoc-K3 show a similar dichroic signature with two well distinct regions.

The first one, ranged between 212 and 220 nm, is dominated by a maximum, attributable to $n \rightarrow \pi^*$ transitions occurring in the β-sheet structure and the second one, extended from 250 and 310 nm, is associated with the π–π^* transition of fluorenyl absorption [30]. In particular, the signal around 305 nm is indicative of the coupling of fluorenyl chromophores in the hydrogels.

The peak around 305 nm is more pronounced for Fmoc-K3 peptide, thus suggesting a better overlapping of Fmoc groups [36]. On the other hand, absorption bands in the region of 250–295 nm are generated by the transfer the chirality to fluorenyl moieties [30]. Analogously, the three peptides containing the FF motif exhibit a similar dichroic behavior. however, in these peptides we observe a minimum at 220 nm in place of a

maximum.This inversion of the CD signal is symptomatic of an apparent inversion of the amino acid configuration caused by a different orientation of the amino acids due to intramolecular interactions occurring in the final 3D supramolecular network. Moreover, a red shift of the signals is observed in the CD spectrum of FmocFF-K3 respect to K1 and K2 analogues. This red shift could be probably attributed to the major aggregation occurring in K3 peptide sequence (see below).

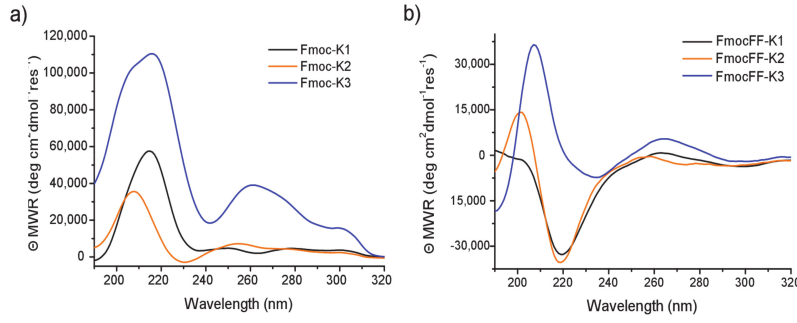

Figure 3. CD spectra of peptide solutions: (**a**) Fmoc-K1, Fmoc-K2, and Fmoc-K3 at 1.0 mg/mL, (**b**) FmocFF-K1, FmocFF-K2, and FmocFF-K3 at the maximum concentration of each peptide. All the spectra are recorded between 350 and 190 nm.

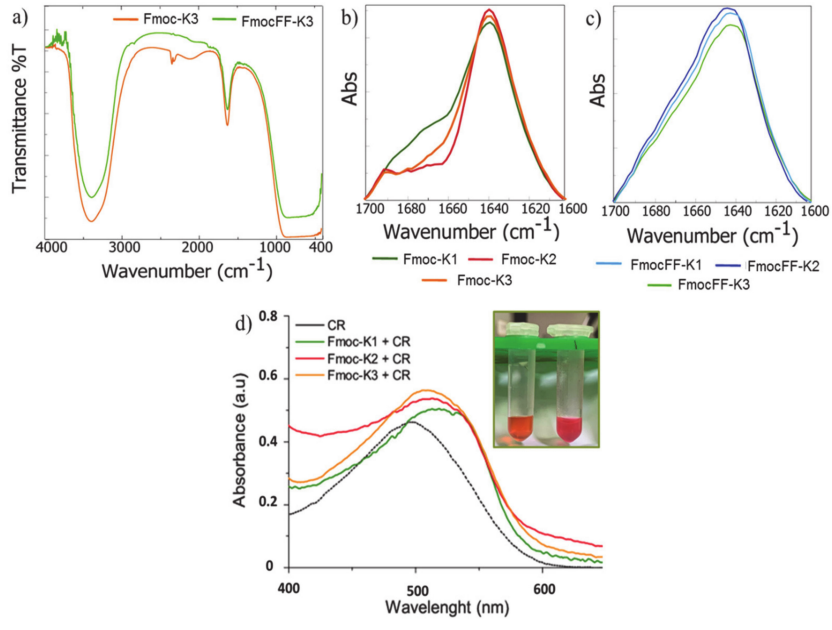

Figure 4. (**a**) FTIR spectra of Fmoc-K3 and Fmoc-FFK3. Absorbance deconvolution in the amide I region for: Fmoc-K1, Fmoc-K2, and Fmoc-K3 (**b**) and for FmocFF-K1, FmocFF-K2, and FmocFF-K3 (**c**). UV–Vis spectra of CR alone and co-incubated with hydrogels of the three Fmoc-K derivatives. (**d**) Macroscopical appearance of CR and Fmoc-K3+CR is reported in the insert.

Further information on the secondary structure of self-assembled peptides were obtained by recording FTIR spectra on the peptide solution at the maximum concentration of the peptide. As exemplificative case, in Figure 4a are reported the IR spectra for Fmoc-K3 and its diphenylalanine containing analogue FmocFF-K3. Similar profiles were recorded for all the other peptides (data not shown). From the spectra examination, a common transmittance profile of aggregates is observed.

IR profiles are characterized by two main signals: the first one localized at 3405 cm^{-1} in the amide A region (~3500–3300 cm^{-1}) and the second one at 1640 cm^{-1} in the amide I region (ranged from 1700 to 1600 cm^{-1}). The band at 3405 cm^{-1} is attributed to NH stretching vibrations polarized along the N-H bond and to the asymmetric and symmetric O–H stretching between bulk water and nanostructures, thus suggesting a strong inter and intramolecular hydrogen bonds network.Generated by C=O stretching vibration and usually used to presume the secondary arrangement of peptide building blocks, the band at 1640 cm^{-1} is referred to β-sheet elements of secondary structure. The spectral deconvolutions of this signal (Figure 4b,c) suggest that all the peptides contain β-sheet arrangements due to the presence of a dominant peak at 1640 cm^{-1}.Moreover, only for Fmoc-K1, Fmoc-K2, and Fmoc-K3 an additional weak band (centered at 1675 cm^{-1}) can be detectable. This spectral signature, typically observed for an antiparallel orientation of the β-strands in assemblies, is absent in the FmocFF-K derivatives, suggesting that the insertion of diphenylalanine interferes with the antiparallel arrangement.

The presence of β-sheet structures can be also deduced from the spectroscopic Congo Red (CR) assay. CR, the water-soluble sodium salt of benzidinediazo-bis-1-naphthylamine-4-sulfonic acid, selectively stains β-sheet nanofibers formed during supramolecular hydrogelation [37]. Specifically, CR interaction with nanostructures induces a characteristic increase in the dye absorption, coupled to a red shift of the absorbance peak from 490 to ~530 nm. From the experimental point of view, 200 µL of Fmoc-K hydrogels (2.0 wt%) containing a final concentration of 20 µmol/L of CR, were prepared and the spectroscopic properties of the resulting gels were investigated.

When hydrogels were prepared in the presence of CR, we observed a significant and immediate color variation of the dye in the gel compared to the CR alone (insert of Figure 4d). Moreover, the absorbance spectra of the three PHGs appear red-shifted (λ = 530 nm) respect to the CR alone (λ = 490 nm), thus supporting the hypothesis that hydrogel matrices contain a β-sheet structuration of the Fmoc-K monomers.

3.3. Structural Characterization of the Hydrogels

According to the literature, [17] we initially tried to trigger the formation of peptide hydrogels by adding 0.1 mmol/L phosphate buffer to a 2 wt% aqueous suspension of each cationic peptide. As demonstrated by the inverted test tube in Figure 5a, only the three peptides lacking of FF motif were able to gel. This result indicates that the insertion of the Fmoc group does not alter the capability of K1, K2, and K3 sequences to assemble, whereas the combination of the Fmoc with the FF motif on the N-terminus of the peptide causes the loss of interactions and hampers hydrogel formation. FmocFF hydrogelator self-assemble according to the "solvent switch" method, when a very concentrated peptide solution (100 mg/mL) in DMSO [22] or in hFIP (1,1,1,3,3,3-hexafluoro-2-isopropanol) [24] is diluted in water at the final concentration of 0.5 wt%. We thus tried to prepare 3D self-supporting hydrogels of FmocFF-K1, FmocFF-K2, and FmocFF-K3 by the solvent switch method using alternatively hFIP or DMSO.

Contrarily to our expectations, no hydrogel formation was observed in these experimental conditions. This result suggests that the aromatic/aliphatic balance in the peptide analogues could play a key role in the gel formation. hydrogels are matrices able to absorb water and swell in the media without dissolving [38]. The calculated degree of swelling (q) was 55.2%, 56.6%, and 54.3% for Fmoc-K1, Fmoc-K2, and Fmoc-K3, respectively. The q values are reciprocally comparable in the Fmoc-K series, thus suggesting that there is not a significant effect of the primary peptide sequence in terms of q value. These swelling degrees are substantially higher respect to whose found for FmocFF and for other mixed peptide hydrogels containing aromatic residues (around 40%) [23]. This result points out that probably in the proposed Fmoc-K PHGs the physical crosslink network is weaker compared to other peptide-based matrices. As consequence, it can be supposed that the porosity of Fmoc-K hydrogels is higher and so the affordable space for solvent adsorption increases.

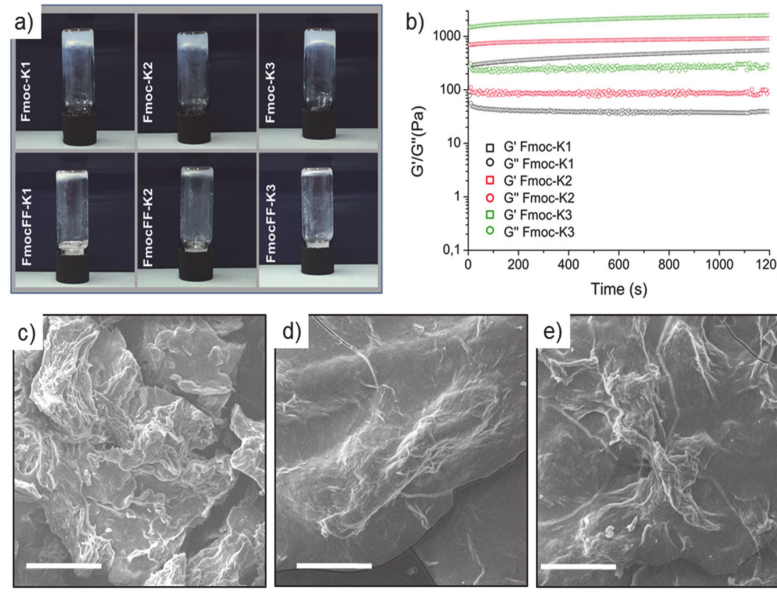

Figure 5. Three-dimensional (3D) hydrogel characterization. (**a**) Inverted test tubes of peptides at a concentration of 2.0 wt% in 14 mM phosphate buffer solution. (**b**) hydrogel rheological analysis: time sweep rheological analysis of Fmoc-K hydrogels reported as storage modulus (G′) and loss modulus (G″). SEM micro-photos of Fmoc-K1 (**c**), Fmoc-K2 (**d**), and Fmoc-K3 (**e**). Scale bars are 30 μm, 2700×.

Morphological and viscoelastic characterization of the three hydrogels was achieved by scanning electron microscopy (SEM) and rheology, respectively (see Figure 5b,c). SEM micro-photos of peptides showed a dense and wavy fibrillar tight network in the hydrogels.

For the determination and the mutual comparison of the viscoelastic behavior of hGs, rheological measurements were carried out using a rotational controlled stress rheometer. Figure 5b reports, in terms of G′ (storage modulus) and G″ (loss modulus), the time sweeps oscillatory profiles (1.0 hz and 0.1% strain, 20 min) of preformed 2.0 wt% PHGs. Data were acquired after a preliminary parameter evaluation, identified via dynamic oscillation strain sweep (at a frequency of 1 hz), and dynamic frequency sweep (at 0.1% strain) for all the gels. The linear viscoelastic region (LVE region) was in the range of 0.01–4.2% strain for all the samples. The rheological analysis analytically confirmed the viscoelastic features of samples, with G′ values higher than G″ ones (see Table 2) for all the tested matrices and tan δ ratios (G′/G″) of 13.9, 10.4, and 9.25 for Fmoc-K1, Fmoc-K2, and Fmoc-K3, respectively. The higher tan δ ratios for Fmoc-K1 indicates a more dissipative feature for this peptide-based hydrogel. however, Fmoc-K1 is less rigid (G′ = 557 Pa) with respect to Fmoc-K2 (G′ = 925 Pa) and Fmoc-K3 (G′ = 2526 Pa). Looking at the differences in the primary sequence, the more rigid behavior of Fmoc-K3 may be ascribed to an improved monomer packaging probably promoted by the substitution of Leu residue with the smaller Ala one. In addition, G′ values are significantly lower than the ones associated to analogues lacking of Fmoc decoration (G′ moduli around 40 KPa in similar conditions) [17]. For this reason, the net decrease of stiffness for Fmoc-K hGs is again ascribed to the chemical modification. It can be supposed that the introduction of the Fmoc group perturbs the forces (van der Waals interactions and the hydrogen bonding) governing the aggregation in K1, K2, and K3 peptides.

As potential tissue engineering matrices, PHG materials would be directly exposed to biological fluids. According to this consideration, the degradation test was performed to evaluate the matrices stability in an in vivo mimetic environment. The biological setting was mimed, incubating the hydrogels with Ringer's solution at 37 °C for 20 days [38]. The stability, reported as ΔW, calculated using Equation (2), was estimated as weight loss. ΔW values determined for Fmoc-K1, Fmoc-K2, and Fmoc-K3 were 43.2, 39.7, and 41.8%, respec-

tively. In comparison to other FmocFF peptide-based hydrogels [23], all tested samples undergo faster and more remarkable degradation. This behavior is probably ascribable to the less rigid nature of Fmoc-K hGs. As an alternative, it can also be hypothesized that the large amount of salt in the Ringer's solution could improve the solubility of K peptides and, in turn, accelerate the loss of 3D-organization of the matrix. It is worth it to note that an efficient in vivo degradation by biological fluids of hydrogels in their single components could allow achieving a rapid excretion of the matrix, which means a high biocompatibility.

3.4. Biological Assays

To test the ability of the three hydrogels to support in vitro growth of eukaryotic cells, we culture 3T3-L1 (mouse fibroblast) cells on Fmoc-K1, K2, and K3. As first, we measured the number of cells able to adhere to hydrogels. An efficient cell adhesion is necessary for an optimal growth of the culture, and growth-supports un-favoring cell adhesion cause cell cycle arrest and induce apoptosis. As shown in Figure 6a, cells were plated on pre-casted hydrogels and adhesion efficiency was measured 16 h upon seeding. Compared to cells plated in the absence of hydrogels, Fmoc-K1 and Fmoc-K2 disfavored cell adhesion, allowing cell attachment to 20 ± 3%, 36 ± 8% of the seeded cells, respectively.

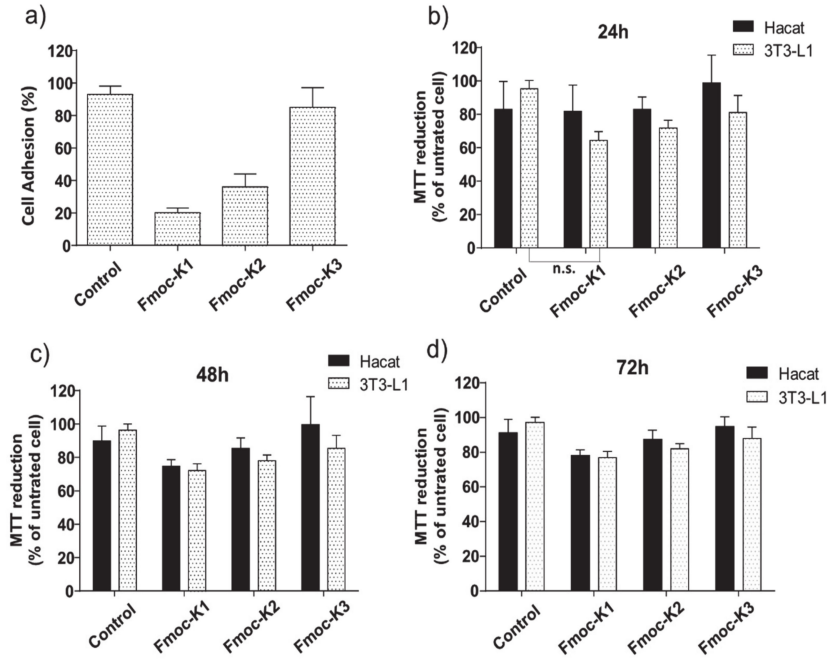

Figure 6. In vitro biological assays. (**a**) Cell adhesion on pre-casted hydrogels. (**b**–**d**) Compatibility of hydrogels with eukaryotic cell culture. The 3T3-L1 cells were seeded on the indicated hydrogel pre-casted in 96-well plates. Cell adhesion (% of adherent viable cell), viability upon adhesion (% viable cells upon plating), duplication rate for the indicated hydrogels are reported as mean ± SD of at least three replicates. MTT assay conducted on haCat (black bars) and 3T3-L1 (dotted white bars) cell lines treated for 24 h (**b**), 48 h (**c**), and 72 h (**d**) with Fmoc-K1, Fmoc-K2, and Fmoc-K3 hydrogels conditioned media. Cell survival was expressed as percentage of viable cells in the presence of conditioned media, compared to control cells grown in their absence. Error represent SD of three independent experiments. n.s. = not significant, Mann–Whitney *t*-test.

On the contrary, cells plated on Fmoc-K3 were able to adhere with a much higher efficiency, 85 ± 12%, a value statistically similar to cells attachment on tissue culture plasticware (93 ± 5%). The different capability of the three peptides to support the cell adhesion could be explained taking in account their different stiffness. Indeed, it was

previously observed that more rigid gels are able to support more efficiently the cell adhesion respect to soft ones [39,40].

Notwithstanding, independently from their ability to favor adhesion, the cytotoxicity of the three supports was minimal, with Fmoc-K1, K2, and K3 hydrogel inducing cell death in 9 ± 3, 11 ± 2, and 3 ± 1% of the attached cells after 24 h from plating, respectively. Cells that were able to adhere on any of the three tested hydrogels remained thus viable, at least for up to 72 h (92 ± 3, 95 ± 3, 94 ± 3% cell viability for Fmoc-K1, K2, and K3, respectively). In addition, while Fmoc-K3 allowed cell duplication (duplication rate 1.7 ± 0.2) with a rate similar to cell plated in the absence of hydrogel (duplication rate 1.9 ± 0.1), we could measure cell growth impairment for cell growing on Fmoc-K1 and -K2 hydrogels (duplication rate 0.4 ± 0.1 and 1.2 ± 0.2, respectively).

To verify if growth arrest was due to chemicals released by Fmoc-K1 and -K2 hydrogels in the cell culture, we tested the cytotoxicity of a conditioned medium collected upon incubation for 16 h with the three hydrogels. As shown in Figure 6, none of the conditioned media exerted cytotoxicity on 3T3-L1 cells or on haCat (human fibroblast) cells up to 72 h. We could measure a minimal cytotoxic effect after 24 h of culturing 3T3-L1 cells in the presence of Fmoc-K1 hydrogel conditioned medium (viability above 70%).

However, such reduction in viability is not significant when compared to control cells (Figure 6, Mann–Whitney t-test). In general, Fmoc-K1, Fmoc-K2 discourage cell adhesion and slow down cell growth of 3T3-L1 cells. however, cell growth impairment does not depend on the toxicity of the hydrogels themselves. On the contrary, Fmoc-K3 promotes cell attachment and favors cell duplication supporting cell growth on the hydrogel support.

4. Conclusions

Structural, morphological, and functional properties of PHGs are deeply affected by the amino acid composition of their peptide sequence. Furthermore, the modification of one or both the peptide termini can affect the complex interplay of forces and interactions occurring in the supramolecular network. In this contest, we evaluated the effect caused by the derivatization of the N-terminus in K1, K2, and K3 hexapeptides with aromatic portions, such as the Fmoc protecting group or the hydrogelator FmocFF. The structural characterization highlighted that these chemical modifications do not hamper the self-assembly of the peptides in aqueous solution. however, the simultaneous insertion of both the Fmoc group and of the FF motif causes the loss of key interactions for the hydrogel formation. This experimental evidence points out the importance to correctly balance the forces in order to gain the aggregation, and that, in some cases, the coexistence of portions with different chemical features (e.g., aromatic and aliphatic groups) in the same peptide sequence can disadvantage the self-assembly. On the other hand, the three Fmoc-derivatives (Fmoc-K1, Fmoc-K2, and Fmoc-K3) keep their capability to gel. In the resulting hydrogels, due to the stacking of the fluorenyl group, peptides assemble into β-sheet structures with an antiparallel orientation of the β-strands. In vitro cell viability assays performed on 3T3 and on haCat cell lines indicate that none of the hydrogels release toxic molecules impairing the cell growth. however, only Fmoc-K3 hydrogel is able to act as a cell growth matrix and fully support cell adhesion, survival, and duplication. The better capability of Fmoc-K3 to support the cell adhesion can probably be attributed to the higher rigidity (G′ = 2526 Pa) compared to Fmoc-K1 and Fmoc-K2 (G′ = 557 and 925 Pa, respectively). The major stiffness of K3 could be due to a more compact packing of the amino acid side chains because of the presence of an Ala residue in place of a Leu one. All the results lead to potential employment of the Fmoc-K3 derivative as a novel material for biomedical applications.

Supplementary Materials: The following are available online at https://www.mdpi.com/article/10.3390/biomedicines9060678/s1, Figures S1 and S2: RP-HPLC chromatograms of peptides; Figures S3–S5: ESI mass spectra of peptides; Figure S6: Fluorescence spectra of peptides.

Author Contributions: Conceptualization, C.D., M.S., and A.A.; methodology, G.S., C.D., E.G., and E.R.; formal analysis, C.D., G.S.; investigation, E.R., E.G., G.S.; resources, G.M.; data curation, A.A. and M.S.; writing—original draft preparation, A.A. and M.S.; writing—review and editing, C.D. and G.M.; visualization, E.R., E.G., and G.S.; supervision, A.A. and M.S.; funding acquisition, G.M. All authors have read and agreed to the published version of the manuscript.

Funding: This research was supported by a grant from Regione Campania-POR Campania FESR 2014/2020 "Combattere la resistenza tumorale: piattaforma integrata multidisciplinare per un approccio tecnologico innovativo alle oncoterapie-Campania Oncoterapie" (project no. B61G18000470007) and the Italian ministry of health-Ricerca Corrente project.

Institutional Review Board Statement: Not applicable.

Informed Consent Statement: Not applicable.

Data Availability Statement: Author agree with MDPI Research Data Policies.

Acknowledgments: The authors thank Chiara Cassiano for technical support in acquiring mass spectra.

Conflicts of Interest: The authors declare no conflict of interest.

References

1. Cascone, S.; Lamberti, G. hydrogel-based commercial products for biomedical applications: A review. *Int. J. Pharm.* **2020**, *573*, 118803. [CrossRef] [PubMed]
2. Cho, I.S.; Ooya, T. Cell-Encapsulating hydrogel Puzzle: Polyrotaxane-Based Self-Healing hydrogels. *Chem. Eur. J.* **2020**, *26*, 913. [CrossRef] [PubMed]
3. Diaferia, C.; Morelli, G.; Accardo, A. Fmoc-diphenylalanine as a suitable building block for the preparation of hybrid materials and their potential applications. *J. Mater. Chem. B* **2019**, *7*, 5142–5155. [CrossRef]
4. Mart, R.J.; Osborne, R.D.; Stevens, M.M.; Ulijn, R.V. Peptide-based stimuli-responsive biomaterials. *Soft Matter* **2006**, *2*, 822–835. [CrossRef] [PubMed]
5. Sahoo, J.K.; Nazareth, C.; VandenBerga, M.A.; Webber, M.J. Self-assembly of amphiphilic tripeptides with sequence-dependent nanostructure. *Biomater. Sci.* **2017**, *5*, 1526–1530. [CrossRef] [PubMed]
6. Sahoo, J.K.; Nazareth, C.; VandenBerga, M.A.; Webber, M.J. Aromatic identity, electronic substitution, and sequence in amphiphilic tripeptide self-assembly. *Soft Matter* **2018**, *14*, 9168–9174. [CrossRef]
7. Malizos, K.; Blauth, M.; Danita, A.; Capuano, N.; Mezzoprete, R.; Logoluso, N.; Drago, L.; Romanò, C.L. Fast-resorbable antibiotic-loaded hydrogel coating to reduce post-surgical infection after internal osteosynthesis: A multicenter randomized controlled trial. *J. Orthop. Traumat.* **2017**, *18*, 159–169. [CrossRef] [PubMed]
8. Chen, B.; Wang, W.; Yan, X.; Li, S.; Jiang, S.; Liu, S.; Ma, X.; Yu, X. highly Tough, Stretchable, Self-Adhesive and Strain-Sensitive DNA-Inspired hydrogels for Monitoring human Motion. *Chem. Eur. J.* **2020**, *26*, 11604–11613. [CrossRef] [PubMed]
9. Bhat, A.; Amanor-Boadu, J.M.; Guiseppi-Elie, A. Toward Impedimetric Measurement of Acidosis with a pH-Responsive hydrogel Sensor. *ACS Sens.* **2020**, *5*, 500–509. [CrossRef]
10. Vashist, A.; Vashist, A.; Gupta, Y.K.; Ahmad, S. Recent advances in hydrogel based drug delivery systems for the human body. *J. Mater. Chem. B* **2014**, *2*, 147–166. [CrossRef]
11. Gallo, E.; Diaferia, C.; Rosa, E.; Smaldone, G.; Morelli, G.; Accardo, A. Peptide-Based hydrogels and Nanogels for Delivery of Doxorubicin. *Int. J. Nanomed.* **2021**, *16*, 1617–1630. [CrossRef]
12. Leganés Bayón, J.; Sánchez-Migallón, A.; Díaz-Ortiz, Á.; Castillo, C.A.; Ballesteros-Yáñez, I.; Merino, S.; Vázquez, E. On-Demand hydrophobic Drug Release Based on Microwave-Responsive Graphene hydrogel Scaffolds. *Chem. Eur. J.* **2020**, *26*, 17069–17080. [CrossRef]
13. Ding, X.; Zhao, h.; Li, Y.; Lingzhi Lee, A.; Li, Z.; Fu, M.; Li, C.; Yang, Y.Y.; Yuan, P. Synthetic peptide hydrogels as 3D scaffolds for tissue engineering. *Adv. Drug Deliv. Rev.* **2020**, *160*, 78–104. [CrossRef]
14. Gungor-Ozkerim, P.S.; Inci, I.; Zhang, Y.S.; Khademhosseini, A.; Dokmeci, M.R. Bioinks for 3D bioprinting: An overview. *Biomater. Sci.* **2018**, *6*, 915–946. [CrossRef]
15. Heidarian, P.; Kouzani, A.Z.; Kaynak, A.; Paulino, M.; Nasri-Nasrabadi, B. Dynamic hydrogels and Polymers as Inks for Three-Dimensional Printing. *ACS Biomater. Sci. Eng.* **2019**, *5*, 2688–2707. [CrossRef]
16. Li, J.; Xing, R.; Bai, S.; Yan, X. Recent advances of self-assembling peptide-based hydrogels for biomedical applications. *Soft Matter* **2019**, *15*, 1704–1715. [CrossRef]
17. Loo, Y.; Lakshmanan, A.; Ni, M.; Toh, L.L.; Wang, S.; hauser, C.A.E. Peptide Bioink: Self-Assembling Nanofibrous Scaffolds for Three-Dimensional Organotypic Cultures. *Nano Lett.* **2015**, *15*, 6919–6925. [CrossRef]
18. Fleming, S.; Ulijn, R.V. Design of nanostructures based on aromatic peptide amphiphiles. *Chem. Soc. Rev.* **2014**, *43*, 8150–8177. [CrossRef]
19. Dasgupta, A.; Mondal, J.H.; Das, D. Peptide hydrogels. *RSC Adv.* **2013**, *3*, 9117–9149. [CrossRef]

20. Fichman, G.; Gazit, E. Self-assembly of short peptides to form hydrogels: Design of building blocks, physical properties and technological applications. *Acta Biomater.* **2014**, *10*, 1671–1682. [CrossRef]
21. Kaur, h.; Sharma, P.; Patel, N.; Pal, V.K.; Roy, S. Accessing highly Tunable Nanostructured hydrogels in a Short Ionic Complementary Peptide Sequence via pH Trigger. *Langmuir* **2020**, *36*, 12107–12120. [CrossRef]
22. Mahler, A.; Reches, M.; Rechter, M.; Cohen, S.; Gazit, E. Rigid, Self-Assembled hydrogel Composed of a Modified Aromatic Dipeptide. *Adv. Mater.* **2006**, *18*, 1365–1370. [CrossRef]
23. Diaferia, C.; Ghosh, M.; Sibillano, T.; Gallo, E.; Stornaiuolo, M.; Giannini, C.; Morelli, G.; Adler-Abramovich, L.; Accardo, A. Fmoc-FF and hexapeptide-based multicomponent hydrogels as scaffold materials. *Soft Matter* **2019**, *15*, 487–496. [CrossRef]
24. Jayawarna, V.; Ali, M.; Jowitt, T.A.; Miller, A.F.; Saiani, A.; Gough, J.E.; Ulijn, R.V. Nanostructured hydrogels for Three-Dimensional Cell Culture Through Self-Assembly of Fluorenylmethoxycarbonyl-Dipeptides. *Adv. Mater.* **2006**, *18*, 611–614. [CrossRef]
25. Halperin-Sternfeld, M.; Ghosh, M.; Sevostianov, R.; Grigoriants, I.; Adler-Abramovich, L. Molecular co-assembly as a strategy for synergistic improvement of the mechanical properties of hydrogels. *Chem. Commun.* **2017**, *53*, 9586–9589. [CrossRef]
26. Chakraborty, P.; Tang, Y.; Guterman, T.; Arnon, Z.A.; Yao, Y.; Wei, G.; Gazit, E. Co-Assembly between Fmoc Diphenylalanine and Diphenylalanine within a 3D Fibrous Viscous Network Confers Atypical Curvature and Branching. *Angew. Chem. Int. Ed. Engl.* **2020**, *59*, 23731–23739. [CrossRef]
27. Palombo, J.M. Solid-phase peptide synthesis: An overview focused on the preparation of biologically relevant peptides. *RSC Adv.* **2014**, *4*, 32658–32672. [CrossRef]
28. Birdi, K.S.; Singh, h.N.; Dalsager, S.U. Interaction of ionic micelles with the hydrophobic fluorescent probe 1-anilino-8-naphthalenesulfonate. *J. Phys. Chem.* **1979**, *83*, 2733–2737. [CrossRef]
29. Yang, Z.; Wang, L.; Wang, J.; Gao, P.; Xu, B. Phenyl groups in supramolecular nanofibers confer hydrogels with high elasticity and rapid recovery. *J. Mater. Chem.* **2010**, *20*, 2128–2132. [CrossRef]
30. Mohan Reddy, S.M.; Shanmugam, G.; Duraipandy, N.; Kiran, M.S.; Mandal, A.S. An additional fluorenylmethoxycarbonyl (Fmoc) moiety in di-Fmoc-functionalized l-lysine induces pH-controlled ambidextrous gelation with significant advantages. *Soft Matter* **2015**, *11*, 8126–8140. [CrossRef] [PubMed]
31. Lakowicz, J.R. (Ed.) *Principles of Fluorescence Spectroscopy*, 3rd ed.; Springer: Boston, MA, USA, 2006.
32. Accardo, A.; Morisco, A.; Palladino, P.; Palumbo, R.; Tesauro, D.; Morelli, G. Amphiphilic CCK peptides assembled in supramolecular aggregates: Structural investigations and in vitro studies. *Mol. BioSyst.* **2011**, *7*, 862–870. [CrossRef]
33. Diaferia, C.; Sibillano, T.; Balasco, N.; Giannini, C.; Roviello, V.; Vitagliano, L.; Morelli, G.; Accardo, A. hierarchical Analysis of Self-Assembled PEGylated hexaphenylalanine Photoluminescent Nanostructures. *Chem. Eur. J.* **2016**, *22*, 16586–16597. [CrossRef]
34. Castelletto, V.; hamley, I.W. Self-assembly of a model amphiphilic phenylalanine peptide/polyethylene glycol block copolymer in aqueous solution. *Biophys. Chem.* **2009**, *141*, 169–174. [CrossRef]
35. Krysmann, M.J.; Castelletto, V.; Kelarakis, A.; hamley, I.W.; hule, R.A.; Pochan, D.J. Self-assembly and hydrogelation of an amyloid peptide fragment. *Biochemistry* **2008**, *47*, 4597–4605. [CrossRef]
36. Sahoo, J.K.; Roy, S.; Javid, N.; Duncan, K.; Aitken, L.; Ulijn, R.V. Pathway-dependent gold nanoparticle formation by biocatalytic self-assembly. *Nanoscale* **2017**, *9*, 12330–12334. [CrossRef]
37. Gallo, E.; Diaferia, C.; Di Gregorio, E.; Morelli, G.; Gianolio, E.; Accardo, A. Peptide-Based Soft hydrogels Modified with Gadolinium Complexes as MRI Contrast Agents. *Pharmaceuticals* **2020**, *13*, 19. [CrossRef]
38. Chronopoulou, L.; Margheritelli, S.; Toumia, Y.; Paradossi, G.; Bordi, F.; Sennato, S.; Palocci, C. Biosynthesis and Characterization of Cross-Linked Fmoc Peptide-Based hydrogels for Drug Delivery Applications. *Gels* **2015**, *1*, 179–193. [CrossRef]
39. Collins, C.; Denisin, A.K.; Pruitt, B.L.; Nelson, W.J. Changes in E-cadherin rigidity sensing regulate cell adhesion. *Proc. Natl. Acad. Sci. USA* **2017**, *114*, E5835–E5844. [CrossRef]
40. Barber-Pérez, N.; Georgiadou, M.; Guzmán, C.; Isomursu, A.; hamidi, h.; Ivaska, J. Mechano-responsiveness of fibrillar adhesions on stiffness-gradient gels. *J. Cell Sci.* **2020**, *133*, jcs242909. [CrossRef]

The Introduction of a Cysteine Residue Modulates The Mechanical Properties of Aromatic-Based Solid Aggregates and Self-Supporting Hydrogels

Carlo Diaferia,[a] Elisabetta Rosa,[a] Nicole Balasco,[b] Teresa Sibillano,[c] Giancarlo Morelli,[a] Cinzia Giannini,[c] Luigi Vitagliano,[b] and Antonella Accardo*[a]

Abstract: Peptide-based hydrogels, originated by multiscale self-assembling phenomenon, have been proposed as multivalent tools in different technological areas. Structural studies and molecular dynamics simulations pointed out the capability of completely aromatic peptides to gelificate if hydrophilic and hydrophobic forces are opportunely balanced. Here, the effect produced by the introduction of a Cys residue in the heteroaromatic sequence of (FY)3 and in its PEGylated variant was evaluated. The physicochemical characterization indicates that both FYFCFYF and PEG8-FYFCFYF are able to self-assemble in supramolecular nanostructures whose basic cross-β motif resembles the one detected in the ancestor (FY)3 assemblies. However, gelification occurs only for FYFCFYF at a concentration of 1.5 wt%. After cross-linking of cysteine residues, the hydrogel undergoes to an improvement of the rigidity compared to the parent (FY)3 assemblies as suggested by the storage modulus (G') that increases from 970 to 3360 Pa. The mechanical properties of FYFCFYF are compatible with its potential application in bone tissue regeneration. Moreover, the avalaibility of a Cys residue in the middle of the peptide sequence could allow the hydrogel derivatization with targeting moieties or with biologically relevant molecules.

Introduction

Amino acids and peptides are crucial entities in biological systems, covering functional and structural roles. Due to their biocompatibility, easy accessibility and well-known chemistry, they have been widely used as constitutive and versatile elements for the generation of supramolecular architectures, including nanofibers, nanodots, plates, film and hydrogels (HGs).[1] These latter materials drew increasing interest during the last decade due to their large range of applications.[2] For instance, they have found use as drug reservoir,[3] healthcare tools[4] and scaffolds for tissue engineering.[5] Peptides based HGs share a common gelation mechanism, driven by physical and no-covalent cross linking network formation in which monomers mutually interact via aromatic stacking, hydrogen bonding and water exclusion effect. As consequence of these molecular interactions, solvated amyloid-like fibrils are formed. The subsequent complex fibrils entanglement promotes the formation of a tridimensional supramolecular network that generates the gel, restricting flow of solvent and imprinting the non-Newtonian behaviour of the final material. Fmoc N-terminally protected mono-, di- and tripeptides and peptide amphiphiles (PAs) are some examples of peptide monomers used as constitutive elements for HGs matrices generation.[6] These monomers can differently arrange in well-known structural motifs, for example β-hairpin, β-sheet and α-helix. It was observed that the appropriate modulation of the peptide primary sequence can allow controlling the morphology, the structural and the functional properties of the hydrogel.[6] One of the most used strategy consists in using primary sequences containing an alternation of charged/apolar amino acids.[7] In these peptide sequences, HGs formation can be prompted by the protonation/deprotonation state of charged amino acids (such as Lys, Arg, Glu or Asp). Structurally, it was recently observed that the presence of negatively or positively charged amino acids in the peptide sequence, characterized by an alternation of polar and apolar residues, is not essential for aggregation and gelation.[8] Noteworthy examples in this context are represented by the peptides PEG8-(FY)3[9] and by its analogues (Nal-Dopa)3, (Nal-Y)3, (F-Dopa)3 and PEG8-(Nal-Y)3 [where Dopa = dopamine, Nal = naphthylalanine, PEG = polyethylene glycol], which are able to self-assemble in self-supporting hydrogels at a concentration of 1.0% wt.[10] The

[a] Dr. C. Diaferia, E. Rosa, Prof. G. Morelli, Prof. A. Accardo
Department of Pharmacy and Research Centre on Bioactive Peptides (CIRPeB)
University of Naples "Federico II"
Via Mezzocannone 16, Naples, 80134 (Italy)
E-mail: antonella.accardo@unina.it

[b] Dr. N. Balasco, Dr. L. Vitagliano
Institute of Biostructures and Bioimaging (IBB), CNR
Via Mezzocannone 16, 80134, Naples (Italy)

[c] Dr. T. Sibillano, Dr. C. Giannini
Institute of Crystallography (IC), CNR
Via Amendola 122, 70126 Bari (Italy)

Supporting information for this article is available on the WWW under https://doi.org/10.1002/chem.202102007

structural characterization of the resulting HGs highlighted the organization in β-sheet fibrillary networks with an antiparallel orientation of peptide sequences. Wide angle X-ray scattering (WAXS) data, collected on solid fibers of (FY)3, combined with molecular dynamics (MD) simulations studies allowed to identify the essential structural elements that are at the basis of the assembly. The proposed model indicates the presence of two well distinct interfaces: a hydrophobic and highly rigid one generated by the interactions between phenyl rings of Phe residues, and a hydrophilic one caused by interacting Tyr side chains of facing strands.[9] Analogously, peptide derivatives, in which Phe and Tyr aromatic residues are replaced with non-coded ones like Nal and Dopa, exhibit propensity to gelificate under specific experimental conditions. The derivatization of this class of peptides with a PEG moiety was found to cause an increase or a decrease of their propensity to gelificate.[10]

This result suggests the key role played by the hydrophilic/hydrophobic balance in the gel formation. In order to further investigate this class of aromatic peptide hydrogelators, we designed a novel peptide analogue in which the (FY)3 motif was modified into a heptapeptide sequence, inserting a cysteine residue (C) in the middle of its primary sequence. Moreover, to elucidate the effect of the PEG decoration on the aggregation behaviour, the resulting peptide FYFCFYF was also derivatized with a monodisperse PEG moiety containing eight oxoethylenic units (PEG8-FYFCFYF). Due to its thiol group, the cysteine residue may be chemically treated to prompt cross-link in peptidic and polymeric hydrogels. Aggregation properties of these Cys-containing peptides were fully investigated using a set of biophysical techniques. Gelification features were analysed and mechanical properties of the resulting gels, before and after cross-linking, were also characterized by rheology.

Results and Discussion

Chemical formulas of the peptide FYFCFYF and of its PEGylated variant (PEG8-FYFCFYF) characterized in the present study are reported in Figure 1. Both peptides were designed modifying the (FY)3 sequence, by inserting a cysteine residue (C) in the middle of the heteroaromatic sequence. The position of the Cys amino acid was chosen in order to generate a symmetrical disposition of the aromatic residues and to locate it into the structural centre of the resulting nanostructures (Figure 1). With respect to other polar neutral residues (e.g. serine or glutamine), the Cys modification makes possible the generation of additional chemical cross linking via thiol (SH) oxidation. This approach allows the introduction of a tunable and reversible functionality without a radical modification of the non-covalent pathway network. The Cys-Cys disulfide bridge formation was scrutinized also in its impact on the mechanical properties of the biomaterials formed by the proposed peptides.

Molecular modelling and dynamics

In order to gain insights into the aggregation propensity of FYFCFYF, we preliminary performed computational studies on the putative assemblies formed by this peptide. A molecular model of the peptide FYFCFYF, which also constitutes the structural spine of PEG8-FYFCFYF, was generated by exploiting the information derived from the structural characterization of the related (FY)3 peptide assemblies.[9,11] In particular, an individual β-sheet was generated by assuming an antiparallel association of their β-strands. The alternative orientation between the consecutive residues within the strands produces in the β-sheet an apolar and a polar surface made by either Phe or Tyr/Cys side chains, respectively. The juxtaposition of two β-sheets, through the association of their apolar surfaces, generated a potential basic element of the FYFCFYF system.

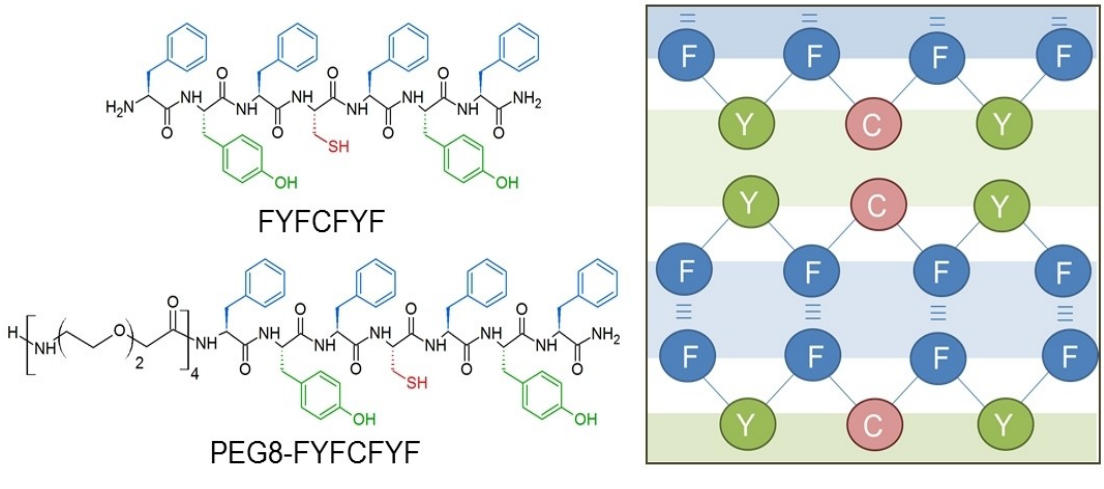

Figure 1. Chemical structure of FYFCFYF and PEG8-FYFCFYF cysteine containing peptides. Schematic representation of the double interfaces supposed organization: green region indicates the hydrophilic interface; blue one identifies the hydrophobic interface.

The three-dimensional representation of this starting model, containing two fifty-stranded β-sheets (FYFCFYF_ST50_SH2), is illustrated in Figure S1a. The stability and the dynamics of this model was evaluated by MD simulations. A 500 ns simulation of the FYFCFYF_ST50_SH2 system indicates that the initial model undergoes a significant structural rearrangement. As indicated by the gyration radius and by the root mean square deviation (RMSD) values of the trajectory structures *versus* the initial model, an equilibrated region is reached only after 250 ns of the simulation (Figures S2a and S2b). Although the secondary β-structure of the assembly is well preserved in the entire simulation timescale, a clear twisting of the two-sheet model is observed (Figure 2a). Notably, the inter-sheet distance (~11 Å) is also well preserved in the simulation, further

confirming the stability and the relative rigidity of the assembly (Figure 2b). The inspection of the side chain flexibility (Figure S3a) and their rotameric states (Figure S3b) provides insights into the basis of the particular stability and rigidity of the assembly. Indeed, recurrent and preserved rotameric states are detected for the inter-strand interacting side chains with the alternation of strands with residues either in the trans or gauche χ1 state. The alternation of the side chains also assures the interactions that stabilized the hydrophobic interface.

These analyses were expanded by considering an assembly formed by four ten-stranded β-sheets (see Methods for details) containing both hydrophobic and hydrophilic interfaces (FYFCFYF_ST10_SH4, Figure S1b). The MD characterization of FYFCFYF_ST10_SH4 clearly indicates that the stability detected for FYFCFYF_ST50_SH2 extends to larger assemblies without being significantly affected by the presence of a hydrophilic interface (Figures S4). As shown in Figure 3b, the inter-sheet distance found for the hydrophilic interface resembles that detected for the hydrophobic ones (~11 Å). As observed for FYFCFYF_ST50_SH2, also the side chains of FYFCFYF_ST10_SH4 are endowed with a remarkable rigidity (Figures S5a and S5b). This is particularly evident for the internal β-sheets within this four-sheet model. The inspection of the distances between the side chains of the Cys residues located in facing sheets within the hydrophilic interface indicates that the sulphur atoms may come as close as 3.5 Å, the minimal distance expected on the basis of their van der Waals radius (~1.8 Å) (Figure S6).

Based on this observation, we verified the possibility of having Cys residues in their oxidized state in this assembly. To this aim, we considered a variant of FYFCFYF_ST10_SH4 in which the Cys residues at the hydrophilic interface were involved in the formation of Cys-Cys disulphide bonds

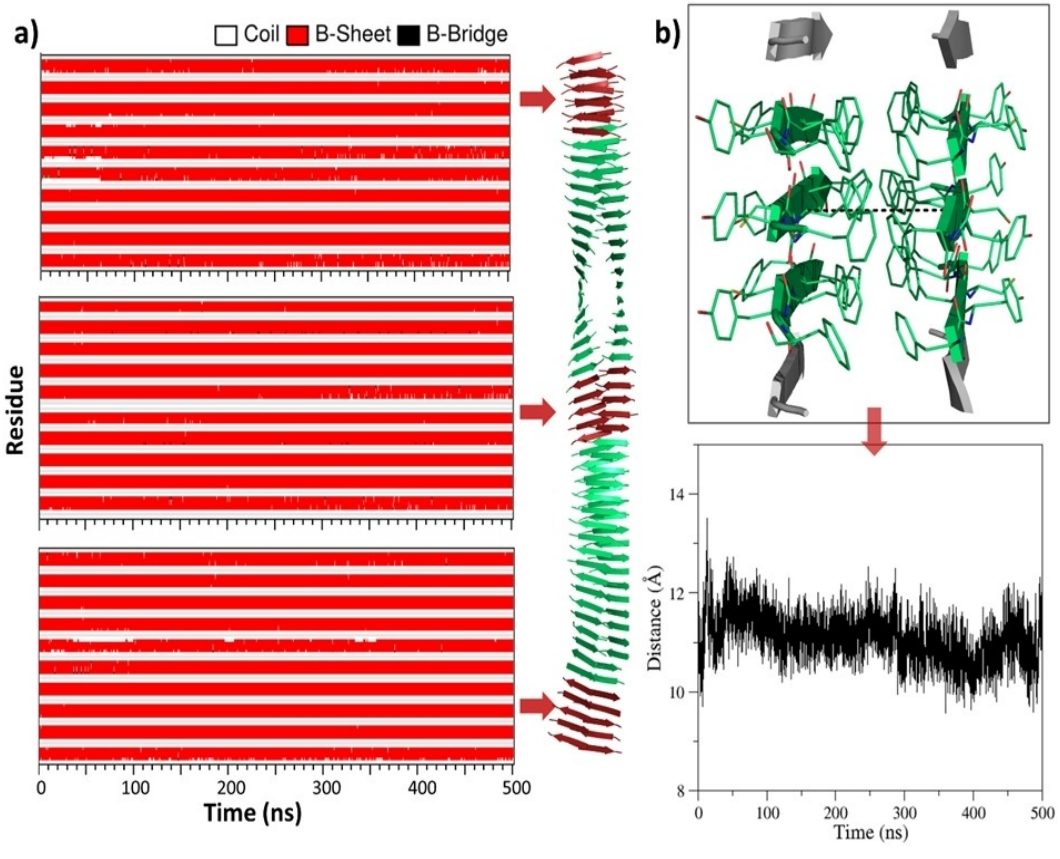

Figure 2. a) Time evolution of secondary structure in the MD simulation carried out starting from the flat model of FYFCFYF_ST50_SH2. Secondary structure is reported only for the strands belonging to the central region and to both terminal ends that are shown in red in the average structure computed in the trajectory region 250–500 ns. b) Time evolution of the distance between two representative C^{α} atoms of the facing sheets along the MD trajectory.

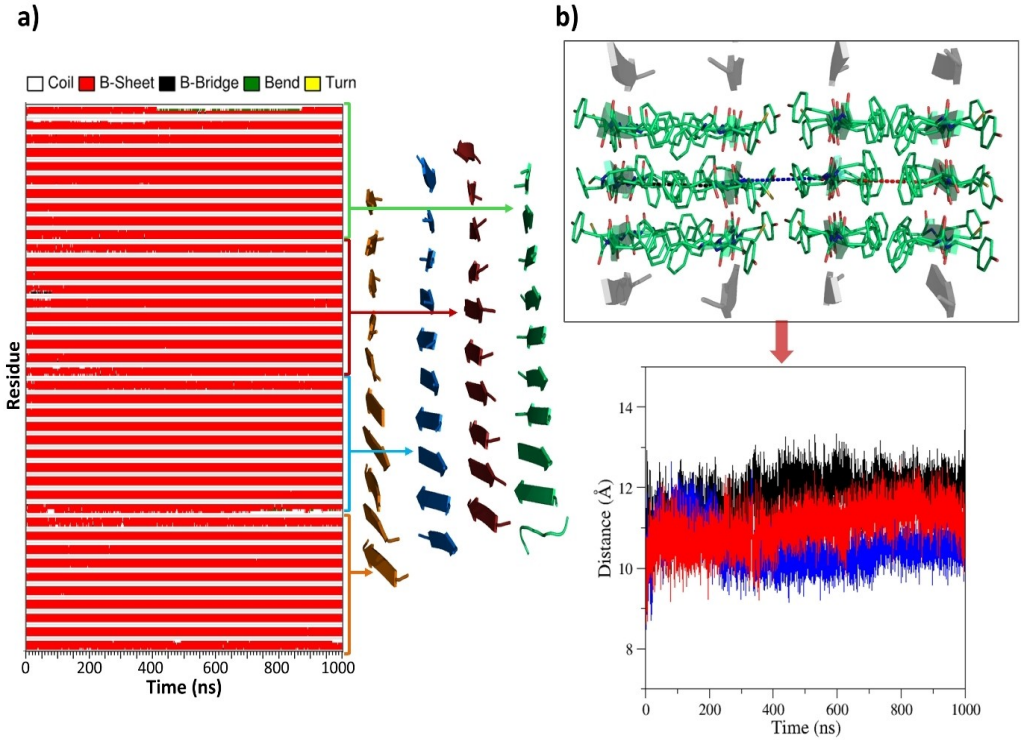

Figure 3. a) Time evolution of secondary structure in the MD simulation carried out starting from the flat model of FYFCFYF_ST10_SH4. The average structure computed in the trajectory region 500–1000 ns is also shown. b) Time evolution of the distances between two representative Cα atoms of the facing sheets along the MD trajectory.

(FYFCFYF_ST10_SH4 SS) (Figure S1c). A one μs MD simulation clearly indicates that the presence of the disulphide bridge is fully compatible with the formation of β-rich assemblies of FYFCFYF (Figures S7 and S4). Also, the inter-sheet distances detected in FYFCFYF_ST10_SH4 SS are very similar to those detected in FYFCFYF_ST10_SH4 (Figure 4).

Collectively, the present findings indicate that FYFCFYF peptide forms pretty stable β-sheet assemblies in which both the hydrophobic and the hydrophilic interface are rather rigid. These assemblies may be formed with the Cys residues either in its reduced or oxidized state.

Peptide synthesis and aggregation

Both the peptide derivatives were synthetized using solid phase peptide synthesis protocols (SPPS) with Fmoc/OtBu strategy. After their purification by RP-HPLC chromatography, peptides were characterized by ESI mass spectrometry (see Figure S8). The log*P* values, estimated using the ACD Lab ChemSketch software, predict the intrinsic water solubility of peptides. Due to the presence of the ethoxylic moieties, PEG8-FYFCFYF (log*P* = 3.57 ± 1.05) shows a 40-fold higher water solubility (~ 10.0 mg/mL) compared to FYFCFYF (log*P* = 7.57 ± 0.92; water solubility of 0.240 mg/mL). A diametric behaviour was noted using the organic solvent 1,1,1,3,3,3-hexafluoro-isopropan-2-ol (HFIP).[11a,12] Indeed, in HFIP the peptide FYFCFYF is highly soluble (up to 200 mg/mL), whereas PEG8-FYFCFYF is moderately soluble (up to 5 mg/mL). According to their different solubility, peptide solutions were prepared using two approaches: PEG8-FYFCFYF solutions were prepared by a direct dissolution of the lyophilized powder in water, whereas FYFCFYF ones were obtained by dilution in water of a HFIP stock solution (100 mg/mL). Then, the organic solvent was removed using N2 flow. Peptide concentration was then analytically quantified using UV-Vis spectroscopy. Preliminarily, we evaluated the capability of both the peptides to aggregate in solution (at 2.0 mg/mL) using the Dynamic Light Scattering (DLS) technique. As expected, DLS profiles of both Cys-containing peptides exhibit a monomodal distribution (see Figure S9a), with a mean diameter of 164 and 197 nm for PEGylated and unPEGylated derivatives, respectively. This result indicates that aggregation phenomena occur in solution at the investigated concentrations. The formation of nanoarchitectures was further investigated by fluorescence spectroscopy. Despite the presence of four Phe residues in the peptides, their self-assembling propensity cannot be evaluated by simply considering the Phe excimer formation. Indeed, from the inspection of Figure S9b, it can be observed that a FRET (Förster resonance energy transfer) phenomenon occurs between the aromatic

chains of Phe and Tyr residues, which work as the donor and the acceptor, respectively.The evidence of the FRET

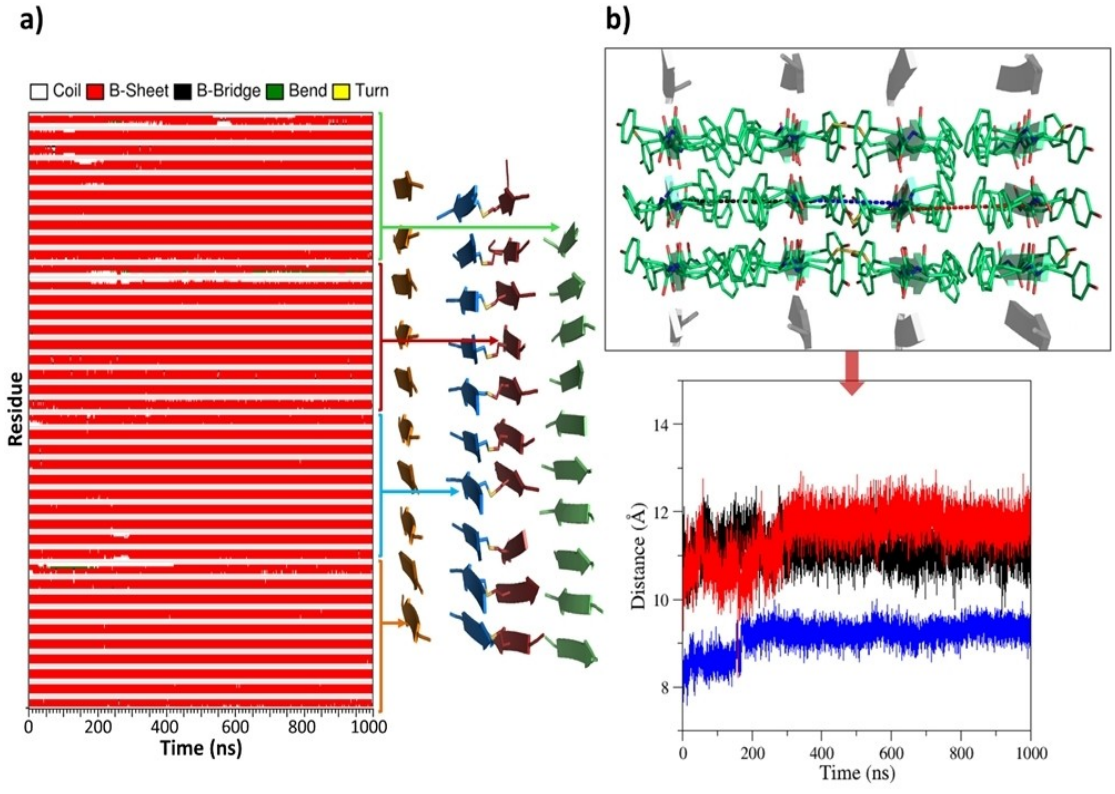

Figure 4. a) Time evolution of secondary structure in the MD simulation carried out starting from the flat model of FYFCFYF_ST10_SH4 SS. The average structure computed in the trajectory region 500–1000 ns is also shown. b) Time evolution of the distances between two representative C^{α} atoms of the facing sheets along the MD trajectoryi.

phenomenon is well proved by the superimposition of the emission profiles recorded for PEG-FYFCFYF (0.005 mg/mL) upon excitation at 257 and 275 nm, which correspond to the absorbance wavelength of Phe and Tyr, respectively. Hence, fluorescence spectra of peptide solutions at different concentrations were acquired exciting samples at the wavelength of the Tyr. From the inspection of the spectra, it can be observed an emission peak at 305 nm, whose intensity decreases upon increasing the concentration (Figure S10a). This behaviour, due to quenching phenomena occurring at high peptide concentration, was previously observed for other aromatic peptides such as PEGylated and unPEGylated (FY)3, Y4 and F6 derivatives.[9,11b, 13] By further diluting the peptide solution below 0.05 mg/mL, we also observed the appearance of another more intense peak centred at 340 nm (Figure S10b). The presence of this additional peak suggests the existence of different equilibria in solution.

A more accurate determination of the critical aggregation concentration (CAC) was achieved by fluorescence titration method previously used also for micelles[14] or self-assembled peptide aggregates.[15] CAC values are graphically extrapolated in the break point of the titration graph, this latter obtained plotting the fluorescence intensity of ANS in the maximum at 475 nm as function of the peptide concentration. CAC evaluation experiments for both Cys-containing peptides are reported in Figure 5a, and the values are $9.09 \cdot 10^{-5}$ mol/L (94.1 μg/mL) and $1.50 \cdot 10^{-5}$ mol/L (24.2 μg/mL) for FYFCFYF and PEG8-FYFCFYF, respectively. A similar trend in the CAC values was previously observed for the PEG8-(FY)3/(FY)3 sequences, which had a CAC value of $1.50 \cdot 10^{-5}$ and $5.98 \cdot 10^{-5}$ mol/L.[9] This consideration points out the importance of the PEG moiety in the promotion of the molecular interactions that drive the aggregation mechanism. It is worth noting that the CAC value of PEG8-FYFCFYF corresponds exactly to the CAC of PEG8-(FY)3, thus suggesting that the insertion of a Cys residue at the centre of the peptide primary structure does not affect the aggregation propensity of the PEGylated variant. On the other hand, a slight increase of the CAC value can be noticed for FYFCFYF respect to (FY)3. This increase could be probably attributed to an interference of the Cys residue with the mechanism of hydrophobic collapse driving the self-assembling phenomenon.

Secondary structure characterization

In order to characterize and analyse the supramolecular behaviour of PEG8-FYFCFYF and FYFCFYF assemblies, spectroscopic techniques such as Circular Dichroism (CD) and FTIR

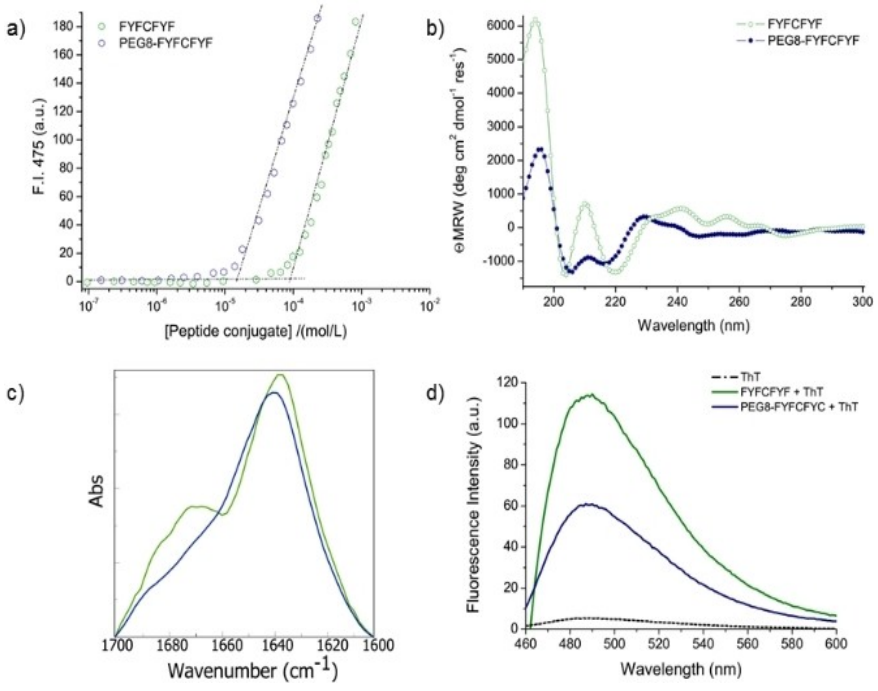

Figure 5. Characterization of peptide aggregates in solution. a) Fluorescence intensity of the ANS fluorophore at 475 nm *versus* the concentration of each peptide. CAC values are calculated from the visual break points. b) CD spectra of peptide solutions at a concentration of 1.0 mg/mL. All the spectra are recorded between 300 and 190 nm. c) Absorbance deconvolution of FTIR spectra in the amide I region for FYFCFYF and PEG8-FYFCFYF. d) Fluorescence spectra of ThT coincubated with each peptide derivative after the subtraction of the peptide self-fluorescence. The spectrum of ThT alone is also reported for comparison.

were used.[16] A CD spectrum covers both the far and the near UV region, where the spectrum is dominated by the amide chromophores and lateral chains of aromatic residues and cysteine absorbance, respectively. CD spectra of both Cys-containing peptide samples at 1.0 mg/mL were recorded between 190 and 300 nm (see Figure 5b). Differing only for the N-terminus PEGylation, both CD spectra share a common profile, with a maximum at 195 nm (indicative of $\pi\rightarrow\pi^*$ transitions), a relative maximum at 210 nm and two minima located at ~204 nm and at 221 or 217 nm for FYFCFYF and PEG8-FYFCFYF, respectively. Signals at 221 and 217 nm are attributed to the $n\rightarrow\pi^*$ transition. The region 240–300 nm is characterized by multiple signals, attributed to contribution of aromatic and thiol side chains.[17] The presence of β structures, which well agrees with the computational modelling of the peptide described in the previous sections, is confirmed by the broad negative band around 215–225 nm and a significant positive band at 195 nm.[18] The β structuration preferentially appears in the FYFCFYF peptide derivative with respect to the PEGylated analogue. The secondary structure characterization was furthermore executed using FTIR spectroscopy. The absorbance spectral deconvolution of the amide I region (1700-1600 cm^{-1}) for both FYFCFYF (green line) and PEG8-FYFCYFY (blue line) at 2.0 mg/mL are reported in Figure 5c. This spectral window is specifically sensible to peptide secondary structuration.[19] Deconvolution profiles for both the peptides are dominated by a principal band located at 1637 and 1640 cm^{-1} for FYFCFYF and PEG8-FYFCFYF, respectively. In the spectrum of FYFCFYF, the association of the band at 1637 cm^{-1}, with an additional signal at 1675 cm^{-1}, indicates the presence of β-sheet secondary structure with an antiparallel orientation of strands. The 1675 cm^{-1} signal may be imputed to the presence of β-turn structure too. However, it is almost implausible that very short peptides, such as the proposed heptapeptide, can arrange into β-turn. In addition, the primary sequence is lacking of β-turn prone residues, such as Gly and Pro.

The inspection of FTIR results is indicative of a predominant tendency for the unPEGylated peptide to adopt a β-sheet conformation with respect to PEG8-FYFCFYF, thus indicating a certain impact of the PEG polymer on the supramolecular organization. The structuration in β-sheet rich aggregates was further confirmed qualitatively using Thioflavin T (ThT) spectroscopic assays. ThT is a dye endowed with a cationic benzothiazole structure that adopts a stabilized conformation when bound to aggregates thus inducing an enhancement and a shift of the fluorescence emission peak from 445 to 482 nm.[20] The fluorescence spectra of both Cys-peptides (10 mg/mL) upon excitation at $\lambda = 450$ nm in a 50 μmol/L solution of ThT are reported in Figure 5d. In both the spectra, subtracted from the self-fluorescence of the peptide, a peak at 482 nm is clearly visible. The emission peak appears more intense for FYFCFYF.

The higher ThT emission of FYFCFYF respect to PEG8-FYFCFYF can be explained taking into account the different molar concentration of the two peptides. Indeed, both the samples have been studied at a concentration of 10 mg/mL that corresponds to 9.7 and 6.2 mmol/L for unPEGylated and PEGylated peptides, respectively.

Taking advantage from a different molecular dye-aggregate mechanism of interaction with respect to ANS, thus avoiding some kind of dye-aggregates and dye-monomers interactions, the characteristic fluorescence behaviour of ThT allowed us to estimate again the CACs (Figure S11). The extrapolated values via ThT titration ($1.22 \cdot 10^{-4}$ mol/L, 126 μg/mL for FYFCFYF; $1.81 \cdot 10^{-5}$ mol/L, 19.1 μg/mL for PEG8-FYFCFYF) are in line with CACs obtained using ANS, thus supporting the evidence of aggregation propensity in the found concentration ranges.

All these results are in good agreement with the FTIR analysis, which highlighted a higher grade of β-sheet organization for unPEGylated derivative with respect to PEG8-FYFCFYF.

Wide-angle X-ray scattering (WAXS)

The FYFCFYF fibril in Figure 6a, obtained by the stretch frame method, was characterized through WAXS investigation. The 2D WAXS data, reported in Figure 6b, show several continuous diffraction rings, which indicate the absence of a clear preferred orientation within the illuminated volume of the fiber. The collected 2D WAXS pattern, once centred and calibrated, and radially folded into a 1D profile (Figure 6c), reveals that the diffraction pattern has main peaks at $q_1 = 0.58$ Å^{-1} ($d_1 = 10.8$ Å) and $q_3 = 1.32$ Å^{-1} ($d_3 = 4.75$ Å) that are in agreement with the structural models described in Figure 4, and explained as the inter-sheet distance detected in the trajectory structures and the inter-strand distance within each sheet, respectively. Two additional peaks were found at $q_2 = 1.05$ Å^{-1} ($d_2 = 6.0$ Å), and $q4 = 1.53$ Å^{-1} ($d_4 = 4.0$ Å^{-1}) too. The 1D WAXS azimuthal profile in Figure 6d indicates a slight preferred orientation mainly for the peak at $q_1 = 0.58$ Å^{-1} that typically identifies the equatorial direction, i.e. the direction perpendicular to the fiber axis.

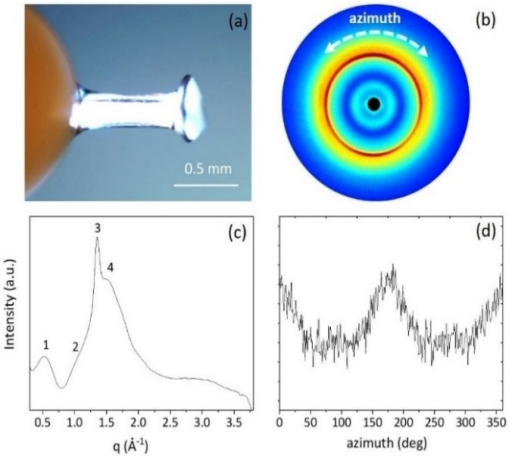

Figure 6. a) Image of the investigated FYFCFYF dried fiber (scale bar = 0.5 mm); b) 2D WAXS data of the FYFCFYF fiber; c) radial integrated 1D WAXS profile; d) intensity distribution along the azimuth of the equatorial peak at $q_1 = 0.58$ Å^{-1} peak.

Gel formation and oxidation

Interconnected fibers network can generate self-supporting hydrogels as a consequence of additional physical cross-linking phenomena or chemical modifications. In the specific case of peptide-based HGs, these materials are formed by further entanglement of supramolecular fibrillary structures, which can be induced by increasing the total sample concentration, and as a consequence, the number of fibers and their mutual contacts.[21] During the preparation of FYFCFYF solutions, we observed a viscosity degree that increases proportionally to the peptide concentration. Hence, we studied the capability of the two peptides to gelificate using the inverted test tube in the range of concentration between 0.25 and 2.0 wt%. As reported in Figure S12, the critical gelation concentration (CGC) for FYFCFYF can be identified in the range 0.5 wt% < CGC < 1.0 wt %. On the contrary, PEG8-FYFCFYF was not able to gelificate (data not shown). These evidences indicate a completely opposite behaviour of Cys-containing peptides respect to the ancestor peptide (FY)3, which gelificates only in its PEGylated form.[9] However, the characterization of others analogues of (FY)3 and PEG8-(FY)3 [*eg.* (F-Dopa)3 and (Nal-Dopa)3 and their PEGylated versions PEG8-(F-Dopa)3 and PEG8-(Nal-Dopa)3] highlighted a diametrically opposed behavior respect to (FY)3.[10] All these evidences point out the importance of the hydrophilic/hydrophobic balance in the peptide sequence in the gelification process. Moreover, it is possible that the Cys side chain plays a role in the confinement and retention of water molecules in the gel. The stability of the FYFCFYF hydrogel (macroscopically evaluated in terms of homogeneity, opacity and reproducibility) and its capability to hold water (as difference between the weight of the matrix before and after an incubation in water overnight at room temperature) were evaluated by the swelling value q (See Equation (1)).[22] Results indicate that hydrogels at 1.0 wt% have a partial instability after the incubation in term of matric homogeneity and opacity and lower $q = 15$%, meanwhile a swelling value of 29% and 33% was measured for 1.5 and 2.0 wt% samples, respectively. The shelf stability was also evaluated via inverted test tube. The 1.0 wt% samples resulted less stable (20 days) respect to the samples at 1.5 wt% (up to 40 days) and to the samples at 2.0 wt % (up to 65 days), which did not report visible modification of the matrices. These evidences suggested us that the increase of concentration can improve the hydrogel stability. In addition, no syneresis was noted for 1.5 wt% and 2.0 wt% HGs, meanwhile for the 1.0 wt% sample the expulsion of water (~15%) occurs after five days from the preparation.

In order to further improve the hydrogel stability, we tried to generate additional chemical networks in the supramolecular material by preparing HGs in presence of ammonium bicarbon-

ate (NH_4HCO_3, AmBic) at different concentrations (10.0, 6.0, 5.0, 2.0 and 1.0 mmol/L). The AmBic has been used in several peptide synthesis protocols for achieving the air oxidation of Cysteine residues with consequential formation of disulphide bonds.[23] The preparation of FYFCFYF hydrogels in presence of AmBic, at different concentrations, has a different impact on both macroscopical aspect and on kinetics of HGs formation. Indeed, using AmBic solution at a concentration of 10 mmol/L, it is noted an inhomogeneous HG formation; meanwhile self-supporting and translucent HGs were formed using a concentration of 1.0, 2.0 or 6.0 mmol/L. It was also observed a different correlation between the AmBic concentration and the gelation kinetics, with a gelation time of 35 and 45 minutes for a concentration of 2.0 and 1.0 mmol/L, respectively and an instantaneous gelation for a concentration of 6.0 mmol/L. The disulphide bond formation was experimentally checked by ESI-MS analysis (Figure S13a), which shows the prevalent presence of dimeric species.

The formation of an additional chemical network affects also on the CGC and swelling features. Indeed, the sample prepared in the presence of 6.0 mmol/L AmBic exhibits a moderate decrease of the critical gelation concentration (0.25 wt% < CGC < 0.50 wt%) and an increase of the swelling ratio (q up to 34% and 40% for 1.5 and 2.0 wt% samples, respectively) and of the shelf stability (up to three months). The efficiency of oxidation procedure was evaluated using the well-assessed Ellman's test.[24] Ellman's reagent (5,5′-dithio-bis-(2-nitrobenzoic acid)) also known as DTNB, is a chromogenic compound used to quantify free sulfhydryl groups in solution. DTNB has an oxidizing disulphide bond that, in the presence of free thiols, undergoes reduction, releasing one molecule of 5-thio-2-nitrobenzoic acid (TNB, yellow) and a mixed disulphide as products. Thus, free thiol concentration can be indirectly determined by TNB UV-Vis absorption at 412 nm. The reaction mechanism is reported in Figure S13b. The DTNB solution added in FYFCFYF gel aliquot immediately becomes more coloured with respect to oxidized gel (see insert in Figure 7).

The β-sheet structuration seems not to be altered by the matrix preparation via AmBic. This evidence is supported by the positive response of both HGs to Congo Red ((3,3-([1,1′-biphenyl]-4,4′-diyl)-bis(4-aminonaphthalene-1-sulfonic acid) sodium salt, CR) spectroscopic assay[25] and to the FTIR analysis. UV-Vis spectra of Cys-containing HGs (1.5 wt%), pure or prepared using AmBic and co-incubated with CR, are reported in Figures 7b and 7c in comparison with the spectrum of the CR alone. Both the samples exhibit a bathochromic shift of the CR maximum from 480 to ~540 nm, as clearly visible from the spectrum subtraction, thus indicating a retention of the β-sheet secondary structuration after Cys oxidation.

Scanning electron microscopy (SEM) characterization

Morphological characterization of hydrogels before and after oxidation was assessed by Scanning Electron Microscopy (SEM).

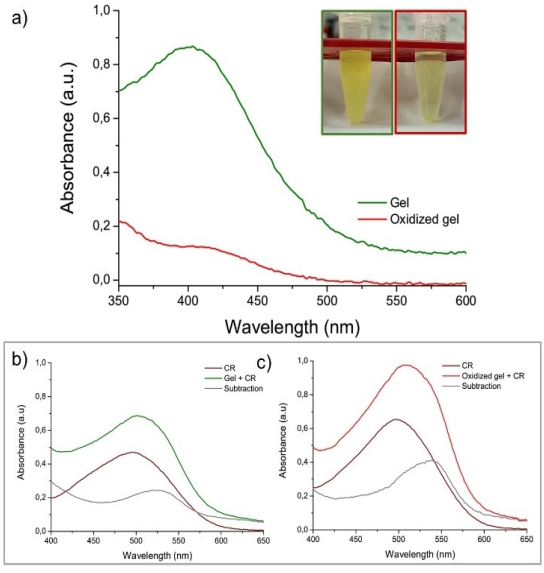

Figure 7. UV-Vis spectra of oxidized and not oxidized peptide hydrogels co-incubated with the Hellman's reagent (DTNB). Macroscopical appearance of hydrogels analyzed by UV-Vis are reported in the insert. Absorbance spectra of CR alone or coincubated with hydrogels before (b) and after the oxidation (c). The subtraction of spectra is also reported.

Selected SEM microphotos of peptide xerogels are reported in Figure 8.

Contrarily to the parental (FY)3 hexapeptide[9] and to the other analogues containing DOPA and Nal residues in place of Tyr and Phe ones,[10] FYFCFYF hydrogel does not show a dense network of interconnected fibres, but mesoscopic fibrillary clusters that interact themselves by intermolecular forces. This kind of organization is typically observed in solid-like colloidal gels.[26] After the disulphide bridge formation an increase of clusters can be observed in the SEM microphotos, even if it can be not excluded the effect due to the increase of the ionic strength caused by AmBic.

Rheological studies

The viscoelastic behaviour and mechanical features of FYFCFYF gels have been evaluated via rheological studies, reporting the results as G′ (Storage modulus) and G″ (Loss modulus). For this scope, time sweeps oscillatory measurements (1.0 Hz and 0.1% strain) were carried out on FYFCFYF gel at a concentration of 1.5 wt%; the oxidized version was prepared at the same concentration using 6 mmol/L AmBic.

Results were collected after preliminary evaluation of the optimal measurement parameters, these identified according to dynamic oscillation strain sweep (at a frequency of 1 Hz) and dynamic frequency sweep (at 0.1% strain) for both the tested gels (Figure S12).

The linear viscoelastic region (LVE region), indicating the range of strain in which the rheological tests can be carried out

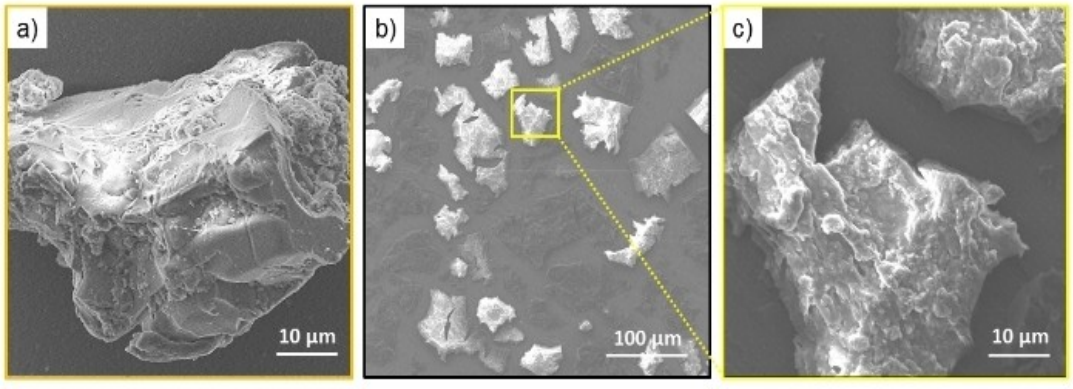

Figure 8. SEM microphotos of FYFCFYF xerogels before (a) and after oxydation (b,c).

without destroying the structure of the sample, was identified in the 0.03-3.0% range of the strain sweep diagram for both hydrogelated matrices. G′ and G″ time sweep profiles in Figure 9, acquired for 20 minutes at a frequency of 1 Hz and at 0.1% strain, evidence values of G′ higher than G″, thus analytically confirming the gel state of the samples.[27] FYFCFYF gel possesses a couple of value of G′ = 970 Pa and G″ = 71 (tan δ = 13.6). These values point out that the Cys-containing peptide is able to produce a matrix ten time more rigid if compared with the ancestor hydrogel PEG8-(FY)3 (G′ ~ 100 Pa).

After AmBic oxidation, G′ and G″ moduli values increase to 3360 Pa and 273 Pa, respectively (tan δ = 12.3). This increase is symptomatic of an efficient improvement of the mechanical rigidity. The enhancement of stiffness is also detectable by an increase of the breakage point of strain (from 22% to 40%) and of frequency (from 25 Hz to 50 Hz) (see Figure S14).

This result points out the capability of disulphide bonds to enlarge the network of interactions, thus generating an accentuated viscoelastic response of the material.

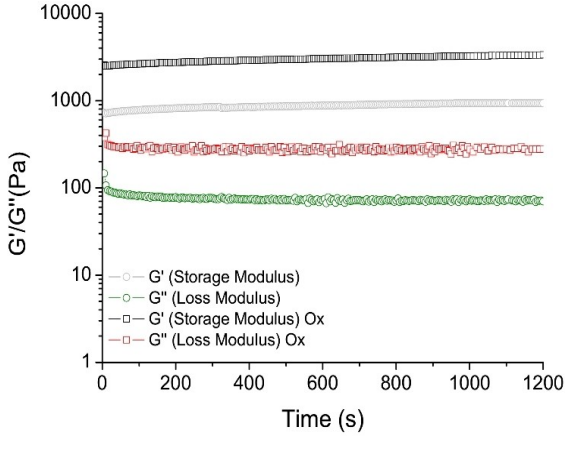

Figure 9. Time sweep (20 minutes) for FYFCFYF gel and for FYFCFYF oxidized one. Rheological analysis is reported in terms of G′ (Storage modulus) and G″ (Loss modulus).

Conclusions

In virtue of their high biocompatibility, biodegradability and to their adjustable mechanical properties, peptide-based HGs have been proposed for a myriad of applications in different biomedical[28] and biotechnological areas.[29]

Due to their similar structure with native extracellular matrix (ECM), as well as their mechanics similar to those of many biological tissues, HGs have emerged as promising scaffolds in tissue regeneration[30] and bioink.[31] Moreover, the efficiency to answer to external stimuli (such as variation of pH, temperature and salt content) and the target ability of some peptide sequences make peptide-based HGs suitable carriers for the delivery of drugs and/or diagnostic agents.[32] Furthermore, due to their capability to rapidly undergo to sol-gel transition under the high shear rate; PHGs have been also proposed as injectable materials.[33] In this scenario, the research has been focused in the last years in the design and synthesis of novel peptide building blocks able to generate hydrogels. The capability of completely aromatic peptides [(F-Dopa)3, (Nal-Y)3 and (Nal-Dopa)3] and of their PEGylated derivatives [PEG8-(FY)3 and PEG8-(Nal-Y)3] to self-assemble into self-supporting hydrogels has been recently demonstrated.[9,10] MD simulations studies suggested that the aggregation and the gelification of these peptides are due to the presence of two interfaces: a wet and a dry one. Since the use of cross-linking of peptides and proteins in amyloid-like nanostructures via disulphide bond formation is progressively becoming a powerful tool for modulating their structural and functional properties,[34] we here evaluated the impact of such a modification on (FY)3-based assemblies. Our investigations demonstrate that the introduction of a cross-linkable cysteine residue in the wet interface of the peptide (FY)3 does not hamper the gelification process. Moreover, the cross-linking of cysteine residues generates a more rigid hydrogel, potentially useful for bone tissue regeneration. Moreover, the presence of a Cys residue in the middle of the peptide sequence could be employed for derivatization of the hydrogel with targeting moieties or with biologically relevant molecules such as drugs and/or diagnostic agents.

Experimental Section

Materials: Protected N^{α}-Fmoc-amino acids (Fmoc-Cys(Trt)-OH, Fmoc-Phe-OH and Fmoc-Tyr(OtBu)-OH), coupling reagents and Rink amide MBHA (4-methylbenzhydrylamine) resin were purchased from Calbiochem-Novabiochem (Laufelfingen, Switzerland). The monodisperse Fmoc-8-amino-3,6-dioxaoctanoic acid, [Fmoc-AdOO-OH, PEG2] was purchased from Neosystem (Strasbourg, France). All other chemical reagents, 1,1,1,3,3,3-hexafluoropropan-2-ol (HFIP), 8-anilino-1-naphthalene sulfonic acid ammonium salt (ANS), thioflavin T (ThT) and 5,5′-dithio-bis-(2-nitrobenzoic acid, DTNB), are commercially available on Merck (Milan, Italy), Fluka (Bucks, Switzerland) or LabScan (Stillorgan, Dublin, Ireland). All of them were used as received unless otherwise stated. Purifications were carried out on a LC8 Shimadzu HPLC system (Shimadzu Corporation, Kyoto, Japan) equipped with a UV lambda-Max Model 481detector using Phenomenex (Torrance, CA) C18 column. Elution solvents are H_2O/0.1% TFA (A) and CH_3CN/0.1% TFA (B), from 20% to 70% over 30 minutes at 20 mL/min flow rate. Purity of products was assessed using analytical HPLC (Agilent), column: C18-Phenomenex eluted with an H_2O/0.1% TFA (A) and CH_3CN/0.1% TFA (B) from 20% to 80% over 20 minutes at 1 mL/min flow rate. Identity of peptides was checked by MS analyses on LTQ XL™ linear ion trap mass spectrometer LTQ-XL with an HESI sorgent (Finnigan Surveyor MSQ single quadrupole electrospray ionization (Finnigan/Thermo Electron Corporation San Jose, CA).

Molecular modeling and dynamics

Systems and notations: Three-dimensional models of FYFCFYF aggregates were generated following the procedure we previously reported.[11] A single sheet model of FYFCFYF was generated using as template the structure of the hexapeptide fragment KLVFFA of the amyloid-beta peptide II (Protein Data Bank entry 3OW9).[35] Starting from this structure, we generated a model composed of a single fifty-stranded β-sheet. A steric zipper model was then produced through the association of a pair of these sheets using the organization of the KLVFFA peptide in the crystalline state (FYFCFYF_ST50_SH2). Taking into account the hydrophobicity/hydrophilicity of Tyr and Phe residues, the two-sheet model was built by locating the Phe side chains at the dry interface leaving Tyr and Cys residues solvent exposed. A more complex system was generated by considering four ten-stranded β-sheets (FYFCFYF_ST10_SH4). As shown in Figure S1, this assembly is endowed with two different steric zipper interfaces: two hydrophobic ones composed of Phe side chains and a hydrophilic one made of Tyr/Cys residues. In addition, in this model two surfaces made by Tyr/Cys residues are solvent exposed. Finally, a variant of FYFCFYF_ST10_SH4 in which the Cys residues in the hydrophilic interface form Cys-Cys disulfide bonds was also characterized (FYFCFYF_ST10_SH4 SS).

Molecular dynamics protocol: The GROMACS software[36] was used to perform MD simulations on the models we generated (FYFCFYF_ST50_SH2, FYFCFYF_ST10_SH4 and FYFCFYF_ST10_SH4 SS). Amber03 and TIP3P were used as force field and water model, respectively. The systems were solvated with water molecules in triclinic boxes. Cl^- counterions were added to balance charges. MD parameters of the simulations (box dimensions, number of water molecules and ions) are reported in Table S1. Electrostatic interactions were computed by means of the particle-mesh Ewald (PME) method with a grid spacing of 1.2 Å and a relative tolerance of 10^{-6}. A 10 Å cut-off was applied for the Lennard-Jones (LJ) interactions. The LINCS algorithm was used for constraining bond lengths. The systems were initially energy minimized using steepest descent (50,000 steps) and then equilibrated in two phases. In the first step, systems were heated to 300 K temperature for 500 ps (NVT). Then, the pressure was equilibrated at the value of 1 atm for 500 ps (NpT). The Velocity Rescaling and Parrinello-Rahman algorithms were used to control temperature and pressure, respectively. The MD production runs were carried out at constant temperature (300 K) and pressure (1 atm) with a time step of 2 fs. The analysis of trajectory structures was performed by using the VMD program[37] and GROMACS tools. The achievement of an adequate convergence in the production runs was checked by calculating the root mean square inner product (RMSIP) values between the two halves of the equilibrated trajectories (Table S1).

Peptide synthesis: Peptides FYFCFYF and PEG8-FYFCFYF were synthesized according to the solid phase peptide synthesis (SPPS) procedure previously optimized and reported.[9] Briefly, Rink amide MBHA resin (substitution 0.73 mmol/g, 0.25 mmol) was allowed to swell in N, N-dimethylformamide (DMF) for 35 minutes. Then, peptide sequences were progressively elongated by coupling the Fmoc-protected amino acids and the Fmoc-monodisperse oxothylene spacer twice in DMF. Each coupling was performed using active ester strategy and using a reaction time of 45 min in presence of HOBt (Hydroxybenzotriazole), HBTU ((2-(1H-benzotriazol-1-yl)-1,1,3,3-tetramethyluronium hexafluorophosphate) and DIPEA (N,N-Diisopropylethylamine or Hünig's base reagent) as coupling activating agents. Peptides were cleaved from the resin by treatment with a TFA (trifluoroacetic acid) solution containing TIS (triisopropylsilane), EDT (1,2-Ethanedithiol) and water at 92.5%, 2.5%, 2.5% and 2.5% v/v/v/v at room temperature for 3 h. Crude products were precipitated with ice-cold ethyl ether, dissolved in H_2O/CH_3CN and lyophilized for three times. After lyophilization, both the peptides were purified by reverse phase high pressure liquid chromatography (RP-HPLC). Chemical identity of the pure products was verified and assessed by ESI mass spectrometry and analytical RP-HPLC chromatography.

FYFCFYF characterization: $t_R = 13.65$ min, MS (ESI^+): m/z 1035.2 *calcd.* for $C_{57}H_{62}N_8O_9S$: $[M+Na^+] = 1058.1$.

PEG8-FYFCFYF characterization: $t_R = 12.90$ min, MS (ESI^+): m/z 1615.8 *calcd.* for $C_{81}H_{106}N_{12}O_{21}S$: $[M+Na^+] = 1638.8$; $[M+Na^+]/2 = 820.4$.

Preparation of aqueous peptide solutions: Sample solutions of FYFCFYF were prepared using a HFIP as co-solvent. A 100 mg/mL solution was prepared and then diluted in water. The organic solvent was removed using N_2 flow. Peptide solutions of PEG8-FYFCFYF were prepared by simply dissolving the lyophilized powders in water at the desired concentration, and sonicating them for 30 minutes. The concentration of the solutions was spectroscopically determined by absorbance on UV-Vis Thermo Fisher Scientific Inc (Wilmington, Delaware USA) Nanodrop 2000c spectrophotometer equipped with a 1.0 cm

quartz cuvette (Hellma) using a molar absorptivity (ε) of 3210 M^{-1} cm^{-1} for both the peptides.

Dynamic Light Scattering (DLS) measurements: The hydrodynamic diameter of peptide aggregates were measured by DLS, carried out on a Zetasizer Nano ZS instrument (Malvern Instruments, Westborough, MA) employing a 173 backscatter detector. Other instrumental initial settings, optimized automatically by the instrument, were: measurement position point = 4.54 mm; attenuator = 7; temperature = 25 °C; cell = 1.0 mL disposable sizing cuvette. DLS measurements were carried out in triplicate on aqueous samples at 2.0 mg/mL after a centrifugation step operated at room temperature at 13000 rpm for 4 minutes.

Fluorescence studies: The determination of the critical aggregate concentration (CAC) for the peptides was assessed by a fluorescence spectroscopy method, in which the two fluorescent dyes ANS (8-anilino-1-naphthalene sulfonic acid ammonium salt) and Thioflavin T are titrated with the peptide solution. In details, the experiment was carried out by adding small aliquots of peptide derivatives in 200 μL of 20 μmol/L ANS water solution or in 200 μL of 50 μmol/L ThT water solution The emission spectra were recorded at room temperature with a spectrofluorophotometer Jasco (Model FP-750) and the sample was located in a quartz cell with 1.0 cm path length. The others setting are: excitation and emission bandwidths = 5 nm; recording speed = 125 nm/min and automatic selection of the time constant, and λ_{ex} = 350 nm (for ANS) and λ_{ex} = 450 (for ThT). Spectra were then corrected for the blank and adjusted for dilution. Fluorescence emission spectra of FYFCFYF and PEG8-FYFCFYF at several peptide concentrations (0.05, 0.1, 0.25, 0.5, 1.0, 2.0, 4.0 and 10 mg/mL) were also recorded by exciting samples both at λ_{ex} = 257 and λ_{ex} = 276 nm.

Circular Dichroism: Far-UV CD spectra of FYFCFYF and PEG8-FYFCFYF peptides were collected with a Jasco J-810 spectropolarimeter equipped with a NesLab RTE111 thermal controller unit using a 0.1 mm quartz cell at 25 °C. The spectra were recorded from 300 to 190 nm on water solutions of samples at 1.0 mg/mL. Other experimental settings were: scan speed = 10 nm/min, sensitivity = 50 mdeg, time constant = 16 s, bandwidth = 1 nm. Each spectrum was obtained by averaging three scans and corrected for the blank. Here Θ represents the mean residue ellipticity (MRE), i.e. the ellipticity per mole of peptide divided by the number of amide bonds in the peptide sequences.

Fourier Transform Infrared spectroscopy (FTIR): FTIR spectra of both the peptides solubilized at a concentration of 2.0 mg/mL were collected on a Jasco FT/IR 4100 spectrometer (Easton, MD) in an attenuated total reflection (ATR) mode and using a Ge single-crystal at a resolution of 4 cm^{-1}. Each spectrum was obtained by recording a total of 120 scans with a rate of 2 mm/s against a KBr background. After collection in transmission mode, spectra were converted directly in their deconvolution in emission.

Thioflavin T (ThT) spectroscopic assay: Cys-containing peptide conjugates were studied using Thioflavin T (ThT). Fluorescence spectra of an aqueous solution of ThT (50 μM) before and after the addition of peptide derivatives (10.0 mg/mL) was recorded at 25 °C after the peptide addition into the cuvette. Samples were excited at 450 nm and fluorescence emission spectra were recorded between 460 and 600 nm. Spectra are reported after subtraction of ThT and peptide aggregates alone.

Wide Angle X-Ray Scattering (WAXS): FYFCFYF fiber (Figure 6a) was prepared from stalks using the "stretch-frame" method.[38] 2D WAXS data were collected at the X-ray Micro-Imaging Laboratory (XMI–L@b), equipped with a Fr–E+ SuperBright rotating anode table-top microsource (Cu K_α, λ = 0.15405 nm, 2475 W), a multilayer focusing optics (Confocal Max-Flux; CMF 15–105) and a three-pinholes camera (Rigaku SMAX-3000). An image plate (IP) Raxia detector with 100 μm pixel size and off-line reader was placed at around 10 cm from the sample to acquire the data. Once acquired, the 2D WAXS data were centered, calibrated by means of the Si NIST standard reference material (SRM 640b) and folded into 1D WAXS radial profiles.[39]

FYFCFYF hydrogel preparations: A volume of 400 μL of peptide HG was prepared via dilution in water at different final concentration of a HFIP stock solutions (200, 100 or 50 mg/mL). The HG is immediately formed after the addition of water to the organic solvent. The oxidized HG was prepared by hydrating the organic solvent with NH_4HCO_3 ammonium bicarbonate (AmBic) solutions (10.0, 6.0, 5.0, 2.0 and 1.0 mmol/L).[23] In all the preparations, HFIP was gently removed using N_2 flow, avoiding any physical stress.

Swelling test: The swelling ratio of hydrogels (q) was evaluated by adding 1.4 mL of doubly distilled water to each sample of 400 mL at different concentrations. After an overnight incubation at room temperature, swollen matrices were weighed (W_s) immediately after the removal of aqueous medium. Then, the samples were freeze-dried and weighed again (W_d). The swelling behavior was expressed, according to Equation (1), as the swelling ratio q that corresponds to the ratio between the weight of the swollen sample (W_s) and the weight of the freeze-dried hydrogel (W_d):

$$q = \frac{(Ws - Wd)}{Wd}\% \quad (1)$$

Ellman's Test: The test was conducted using the chromogenic reagent 5,5′-dithiobis-(2-nitrobenzoic) acid (DTNB) to determine the free sulfhydryl groups in gels, in normal or oxidizing conditions. The DTNB was prepared at 2.0 mmol/L in a 50 mmol/L sodium acetate solution (stock A). A solution of Tris·HCl at a concentration of 1.0 mol/L was adjusted to pH = 8.0 (stock B). Reagent solution (stock C) was obtained by mixing 50 μL of stock A, 100 μL of stock B and 840 μL of H_2O. 20 μL of gels were added to 980 μL of stock C. Samples were vortexed, properly diluted and incubated at room temperature for 10 minutes. Then, free thiols were indirectly quantified via UV-Vis measurements at 412 nm ($\varepsilon = 13600\ cm^{-1}\cdot mol^{-1}\cdot L$), acquiring the spectrum of the formed 5-thio-2-nitrobenzoic ion (TNB) yellow solutions.

Scanning Electron Microscopy (SEM): Morphological analysis of xerogels was carried out by field emission scanning

electron microscope (PhenomXL, Alfatest). 10 μL of peptide hydrogel were drop-casted on an aluminium stub and air-dried. A thin coat of gold and palladium was sputtered at a current of 25 mA for 75 sec. The sputter coated samples were then introduced into the specimen chamber and the images were acquired at an accelerating voltage of 10 kV, spot 3, through the Secondary Electron Detector (SED).

Rheological characterization: The rheological properties of the gels were evaluated using a rotational controlled stress rheometer (Malvern Kinexus) using a 15 mm flat-plate geometry (PU20:PL61). Freshly prepared hydrogel sample (400 μL) at a concentration of 1.5 wt% was used. Each experiment was performed at 25 °C using a humidity chamber and a gap of 1 mm. Preliminary dynamic rheological tests were carried out in order to identify the regime of linear viscoelasticity. The viscous elastic region was determined by oscillatory frequency (0.1–100 Hz) and strain sweep (0.01–100 %). Then a time-sweep oscillatory evaluation test (using a constant 0.1 % strain and 1 Hz frequency) was performed for 20 minutes. Results are reported in Pascal (Pa) as shear Storage or elastic modulus (G′) and the Shear loss or viscous modulus (G″).

Acknowledgements

This research was supported by the grant from Regione Campania-POR Campania FESR 2014/2020 "Combattere la resistenza tumorale: piattaforma integrate multidisciplinare per un approccio tecnologico innovativo alle oncoterapie-Campania Oncoterapie" (Project No. B61G18000470007). Open Access Funding provided by the University of Naples "Federico II" within the CRUI-CARE Agreement. The authors thank Dr. Chiara Cassiano for technical support in aquiring the ESI mass spectra. Open Access Funding provided by Universita degli Studi di Napoli Federico II within the CRUI-CARE Agreement.

Conflict of Interest

The authors declare no conflict of interest.

Keywords: aromatic peptides · cysteine oxidation · hydrogels · peptide materials · self-assembling

[1] a) J. Shi, G. Fichman, J. P. Schneider, *Angew. Chem. Int. Ed.* **2018**, 57,11188–11192; b) S. Díaz, I. Insua, G. Bhak, J. Montenegro, *Chem. Eur. J.* **2020**, *26*, 14765–14770; c) E. Gallo, C. Diaferia, N. Balasco, T. Sibillato, V. Roviello, C. Giannini, L. Vitagliano, G. Morelli, A. Accardo, *Sci. Rep.* **2021**, *11*, 2470; d) G. Wei, Z. Su, N. P. Reynolds, P. Arosio, I. W. Hamley, E. Gazit, R. Mezzenga, *Chem. Soc. Rev.* **2017**, *46*, 4661–4708; e) N. Singh, M. Kumar, J. F. Miravet, R. V. Ulijn, B. Escuder, *Chem. Eur. J.* **2016**, *23*, 981–993.

[2] Mb Bahram, N. Mohseni, M. Moghtader, in *An introduction to hydrogels and some recent applications in: emerging concepts in analysis and applications of hydrogels*. (Ed. Sutapa Biswas Majee) IntechOpen **2016**.

[3] R. Al-Kasasbeh, A. J. Brady, A. J. Courtenay, E. Larrañeta, M. T. C. McCrudden, D. O'Kane, S. Liggett, R. F. Donnelly, *Drug Del. Transl. Res.* **2020**, *10*, 690–705.

[4] B. Mirani, E. Pagan, B. Currie, M. A. Siddiqui, R. Hosseinzadeh, P. Mostafalu, Y. S. Zhang, A. Ghahary, M. Akbar, *Adv. Healthcare Mater.* **2017**, *6*, 1700718.

[5] a) Y. J. He, M. F. Santana, A. Staneviciute, M. B. Pimentel, F. Yang, J. Goes, K. Kawaji, M. K. Vaicik, R. Abdulhadi, N. Hibino, G. Papavasiliou, *Adv. Healthcare Mater.* **2021**, *10*, 2001706; b) J. D. Tang, C. Mura, K. J. Lampe, *J. Am. Chem. Soc.* **2019**, *141*, 12, 4886–4899; c) A. Serafina, C. Murphya, M. C. Rubio, M. N. Collins, *Mater. Sci. Eng. C* **2021**, *122*, 111927.

[6] a) C. Liu, Q. Zhang, S. Zhu, H. Liu, J. Chen, *RSC Adv.* **2019**, *9*, 28299–28311; b) A. M. Garcia, R. Lavendomme, S. Kralj, M. Kurbasic, O. Bellotto, M. C. Cringoli, S. Semeraro, A. Bandiera, R. De Zorzi, S. Marchesan, *Chem. Eur. J.* **2020**, *26*, 1880–1886; c) Z. Yang, H. Xu, X. Zhao, *Adv. Sci.* **2020**, *7*, 1903718; d) M. Rivas, L. J. del Valle, C. Alemán, J. Puiggalí, *Gels* **2019**, *5*, 14; e) N. Falcone, H.-B. Kraatz, *Chem. Eur. J.* **2018**, *24*, 14316–14328; f) L. M. De Leon Rodriguez, Y. Hemar, J. Cornish, M. A. Brimble, *Chem. Soc. Rev.* **2016**, *45*, 4797–4824; g) S. Basak, N. Nandi, S. Paul, I. W. Hamley, A. Banerjee, *Chem. Commun.* **2017**, *53*, 5910–5913; h) L. A. Estroff, A. D. Hamilton, *Chem. Rev.* **2004**, *104*, 3, 1201–1218; i) H. He, W. Tan, J. Guo, M. Yi, A. N. Shy, B. Xu, *Chem. Rev.* **2020**, *120*, 9994–10078.

[7] a) I. M. Geisler, J. P. Schneider, *Adv. Funct. Mater.* **2012**, *22*, 529–537; b) J. Mangelschots, M. Bibian, J. Gardiner, L. Waddington, Y. Van Wanseele, A. Van Eeckhaut, M. M. Diaz Acevedo, B. Van Mele, A. Madder, R. Hoogenboom, S. Ballet, *Biomacromolecules* **2016**, *17*, 437–445; c) Y. Qi, H. Min, A. Mujeeb, Y. Zhang, X. Han, X. Zhao, G. J. Anderson, Y. Zhao, G. Nie, *ACS Appl. Mater. Interfaces* **2018**, *10*, 6972–6981; d) F. Raza, Y. Zhu, L. Chen, X. You, J. Zhang, A. Khan, M. W. Khan, M. Hasnat, H. Zafar, J. Wu, L. Ge, *Biomater. Sci.* **2019**, *7*, 2023–2036.

[8] N. Balasco, C. Diaferia, G. Morelli, L. Vitagliano, A. Accardo, *Front. Biol.* **2021**, *9*, 641372.

[9] C. Diaferia, N. Balasco, T. Sibillano, M. Ghosh, L. Alder-Abramovich, C. Giannini, L. Vitagliano, G. Morelli, A. Accardo, *Chem. Eur. J.* **2018**, *24*, 6804–6817.

[10] C. Diaferia, F. Netti, M. Ghosh, T. Sibillano, C. Giannini, G. Morelli, L. Adler-Abramovich, A. Accardo, *Soft Matter* **2020**, *16*, 7006–7017.

[11] a) C. Diaferia, N. Balasco, D. Altamura, T. Sibillano, E. Gallo, V. Roviello, C. Giannini, G. Morelli, L. Vitagliano, A. Accardo, *Soft Matter* **2018**, *14*, 8219–8230; b) C. Diaferia, T. Sibillano, N. Balasco, C. Giannini, V. Roviello, L. Vitagliano, G. Morelli, A. Accardo, *Chem. Eur. J.* **2016**, *22*, 16586–16597.

[12] a) P. S. Zelenovskiy, A. O. Davydov, A. S. Krylov, A. L. Kholkin, *J. Raman Spectrosc.* **2017**, *48*, 1401–1405; b) R. Bucci, P. Das, F. Iannuzzi, M. Feligioni, R. Gandolfi, M. L. Gelmi, M. Reches, S. Pellegrino, *Org. Biomol. Chem.* **2017**, *15*, 6773–6779; c) A. Gemma, E. Mayans, G. Ballano, J. Torras, A. Díaz, A. I. Jiménez, J. Puiggalí, C. Cativiela, C. Alemán, *Phys. Chem. Chem. Phys.* **2017**, *19*, 27038–27051.

[13] a) C. Diaferia, T. Sibillano, D. Altamura, V. Roviello, L. Vitagliano, C. Giannini, G. Morelli, A. Accardo, *Chem. Eur. J.* **2017**, *23*, 14039–14048.

[14] A. Accardo, A. Morisco, P. Palladino, R. Palumbo, D. Tesauro, G. Morelli, *Mol. BioSyst.* **2011**, *7*, 862–870.

[15] a) C. Diaferia, N. Balasco, T. Sibillano, C. Giannini, L. Vitagliano, G. Morelli, A. Accardo, *ChemPhysChem* **2018**, *19*, 1635–1642; b) C. Diaferia, V. Roviello, G. Morelli, A. Accardo, *ChemPhysChem* **2019**, *20*, 2774–2782.

[16] A. Micsonai, F. Wien, L. Kernya, Y.-H. Lee, Y. Goto, M. Réfrégiers, J. Kardos, *PNAS* **2015**, *112*, E3095-E3103.

[17] a) J. Nan, X.-P. Yan, *Chem. Eur. J.* **2010**, *16*, 423–427; b) C. Krittanai, W. C. Johnson, *Anal. Biochem.* **1997**, 253, 57–64.

[18] V. Castelletto, I. W. Hamley, *Biophys. Chem.* **2009**, *141*, 169–174.

[19] A. Barth, *Biochim. Biophys. Acta* **2007**, *1767*, 1073–1101.

[20] a) M. G. Di Carlo, V. Minicozzi, V. Foderà, V. Militello, V. Vetri, S. Morante, M. Leone, *Biophys. Chem.* **2015**, *206*, 1–11; b) K. G. Malmos, L. M. Blancas-Mejia, B. Weber, J. Buchner, M. Ramirez-Alvarado, H. Naiki, D. Otzen, *Amyloid* **2017**, *24*, 1–16.

[21] E. K. Johnson, D. J. Adams, P. J. Cameron, *J. Mater. Chem.* **2011**, *21*, 2024–2027.

[22] L. Chronopoulou, S. Margheritelli, Y. Toumia, G. Paradossi, F. Bordi, S. Sennato, C. Palocci, *Gels* **2015**, *1*, 179–193.

[23] a) E. Calce, A. Sandomenico, M. Saviano, M. Ruvo, S. De Luca, *Amino Acids* **2014**, *46*, 1197–1206; b) Y. Zhang, K. Schulten, M. Gruebele, P. S. Bansal, D. Wilson, N. L. Daly, *Biophys. J.* **2016**, *110*, 1744–1752.

[24] a) G. Bulaj, T. Kortemme, D. P. Goldenberg, *Biochemistry* **1998**, *37*, 8965–8972; b) G. L. Ellman, *Arch. Biochem. Biophys.* **1959**, *82*, 70–77.

[25] a) E. I. Yakupova, L. G. Bobyleva, I. M. Vikhlyantsev, A. G. Bobylev, *Biosci. Rep.* **2019**, *39*, BSR20181415; b) M. Mie, M. Oomuro, E. Kobatake, *Polymer J.* **2013**, *45*, 504–508.

[26] S. K. Nair, S. Basu, B. Sen, M.-H. Lin, A. N. Kumar, Y. Yuan, P. J. Cullen, D. Sarkar, *Sci. Rep.* **2019**, *9*, 1072.
[27] S. R. Raghavan, B. H. Cipriano, **2006**, Gel formation: phase diagrams using tabletop rheology and calorimetry, in: Weiss R. G., Terech P. (eds) *Molecular Gels*, Springer, Dordrecht.
[28] S. Sankar, K. O'Neill, M. Bagot D'Arc, F. R. M. Buffier, E. Aleksi, M. Fan, N. Matsuda, E. S. Gil, L. Spirio, *Front. Biol.* **2021**, *9*, 679525.
[29] a) K. Fu, H. Wu, Z. Su, *Biotechnol. Adv.* **2021**, *49*, 107752; b) C. Gong, S. Sun, Y. Zhang, L. Sun, Z. Su, A. Wu, G. Wei, *Nanoscale* **2019**, *11*, 4147–4182; c) W. Zhang, D. Lin, H. Wang, J. Li, G. U. Nienhaus, Z. Su, G. Wei, L. Shang, *Bioconjugate Chem.* **2017**, *28*, 2224–2229.
[30] a) R. Agarwal, A. J. García, *Adv. Drug Delivery Rev.* **2015**, *94*, 53–62, 14; b) C. Diaferia, E. Rosa, E. Gallo, G. Smaldone, M. Stornaiuolo, G. Morelli, A. Accardo, *Biomedicine* **2021**, *9*, 678.
[31] a) P. S. Gungor-Ozkerim, I. Inci, Y. S. Zhang, A. Khademhosseini, M. R. Dokmeci, *Biomater. Sci.* **2018**, *6*, 915–946; b) P. Heidarian, A. Z. Kouzani, A. Kaynak, M. Paulino, B. Nasri-Nasrabadi, *ACS Biomater. Sci. Eng.* **2019**, *5*, 2688–2707; c) Y. Loo, A. Lakshmanan, M. Ni, L. L. Toh, S. Wang, C. A. E. Hauser, *Nano Lett.* **2015**, *15*, 6919–6925.
[32] a) A. Altunbas, D. J. Pochan, T. Deming (Ed.), *Peptide-Based Materials*, Springer, Berlin Heidelberg, Berlin, Heidelberg, **2012**, 135–167; b) L. Mei, K. Xu, Z. Zhai, S. He, T. Zhu, W. Zhong, *Org. Biomol. Chem.* **2019**, *17*, 3853–3860; c) C. Diaferia, E. Rosa, A. Accardo, G. Morelli, *J. Pept. Sci.* **2021**, e3301.
[33] a) W. L. Dissanayaka, K. M. Hargreaves, L. Jin, L. P. Samaranayake, C. Zhang, *Tissue Eng. A* **2015**, *21*, 550–563; b) P. K. Nguyen, W. Gao, S. D. Patel, Z. Siddiqui, S. Weiner, E. Shimizu, B. Sarkar, V. A. Kumar, *ACS Omega* **2018**, *3*, 5980–5987; c) Y. Zhang, H. Zhang, Q. Zou, R. Xing, T. Jiao, X. Yan, *J. Mater. Chem. B* **2018**, *6*, 7335–7342.
[34] a) D. Korouski, I. K. Lednev, *Int. J. Biomed. Nanosci. Nanotechnol.* **2011**, *2*, 167–176; b) Z. Ridgway, X. Zhang, A. G. Wong, A. Abedini, A. M. Schmidt, D. P. Raleigh, *Biochem.* **2018**, *57*, 3065–3074; c) R. González-Castro, M. A. Gómez-Lim, F. Plisson, *ChemPhysChem* **2020**, *22*, 961–973; d) V. Cabra, E. Vázquez-Contreras, A. Moreno, R. Arreguin-Espinosa, *Biochim. Biophys. Acta* **2008**, *1784*, 1028–1036.
[35] J. P. Colletier, A. Laganowsky, M. Landau, M. Zhao, A. B. Soriaga, L. Goldschmidt, D. Flot, D. Cascio, M. R. Sawaya, D. Eisenberg, *Proc. Natl. Acad. Sci. USA* **2011**, *108*, 16938–16943.
[36] D. VanDer Spoel, E. Lindahl, B. Hess, G. Groenhof, A. E. Mark, H. J. Berendsen, *J. Comput. Chem.* **2005**, *26*, 1701–1718.
[37] W. Humphrey, A. Dalke, K. Schulten, *J. Mol. Graphics* **1996**, *14*, 33–38.
[38] M. Sunde, L. C. Serpell, M. Bartlam, P. E. Fraser, M. B. Pepys, C. C. Blake, *J. Mol. Biol.* **1997**, *273*, 729–739.
[39] a) D. Altamura, R. Lassandro, F. A. Vittoria, L. De Caro, D. Siliqi, M. Ladisa, C. Giannini, *J. Appl. Crystallogr.* **2012**, *45*, 869–873; b) T. Sibillano, L. De Caro, D. Altamura, D. Siliqi, M. Ramella, F. Boccafoschi, G. Ciasca, G. Campi, L. Tirinato, E. Di Fabrizio, C. Giannini, *Sci. Rep.* **2014**, *4*, 6985.

Manuscript received: June 7, 2021
Accepted manuscript online: September 9, 2021
Version of record online: October 1, 2021

Received: 26 September 2020 | Revised: 14 January 2021 | Accepted: 15 January 2021

DOI: 10.1002/psc.3301

SPECIAL ISSUE REVIEW

Journal of PeptideScience WILEY

Peptide-based hydrogels as delivery systems for doxorubicin

Carlo Diaferia | Elisabetta Rosa | Antonella Accardo | Giancarlo Morelli

Department of Pharmacy, Research Centre on Bioactive Peptides (CIRPeB), University of Naples "Federico II", Naples, 80134, Italy

Correspondence
Giancarlo Morelli, Department of Pharmacy, Research Centre on Bioactive Peptides (CIRPeB), University of Naples "Federico II", Via Mezzocannone 16, 80134 Naples, Italy.
Email: gmorelli@unina.it

Funding information
Regione Campania - POR Campania FESR 2014/2020, Grant/Award Number: B61G18000470007; Italian Minister of Education, University and Research, Grant/Award Number: PRIN-2017A2KEPL

Hydrogels (HGs) and nanogels (NGs) have been recently identified as innovative supramolecular materials for many applications in biomedical field such as in tissue engineering, optoelectronic, and local delivery of active pharmaceutical ingredients (APIs). Due to their in vivo biocompatibility, synthetic accessibility, low cost, and tunability, peptides have been used as suitable building blocks for preparation of HGs and NGs formulations. Peptide HGs have shown an outstanding potential to deliver small drugs, protein therapeutics, or diagnostic probes, maintaining the efficacy of their loaded molecules, preventing degradation phenomena, and responding to external physicochemical stimuli. In this review, we discuss the possible use of peptide-based HGs and NGs as vehicles for the delivery of the anticancer drug doxorubicin (Dox). This anthracycline is clinically used for leukemia, stomach, lung, ovarian, breast, and bladder cancer therapy. The loading of Dox into supramolecular systems (liposomes, micelles, hydrogels, and nanogels) allows reducing its cardiotoxicity. According to a primary sequence classification of the constituent peptide, doxorubicin-loaded systems are here classified in short and ultra-short peptide-based HGs, RGD, or RADA-peptide-based HGs and peptide-based NGs.

KEYWORDS
anticancer drug, doxorubicin, drug delivery, peptide hydrogels, peptide materials, peptide self-assembling

1 | INTRODUCTION

Natural and synthetic peptides are largely utilized in biomedical and biotechnological fields as therapeutic and diagnostic tools. They present a series of advantages from the high synthetic accessibility (low cost, well-assessed synthetic process, tunability of the peptide sequence, suitability of functional groups for derivatization, and functionalization) to their noteworthy in vitro and in vivo biocompatibily.[1] Due to the high biocompatibility, peptides recently achieved resounding success in the drug delivery field.[2–4] Moreover, the specific feature of peptides to organize themselves in ordered secondary, tertiary, and quaternary structures,[1] not accessible to polymers and small organic molecules, has also promoted the design of novel nanomaterials for nanomedicine smart applications.[5–7] In this context, different classes of peptides (including cyclic peptides,[8] ultra-short sequences,[9] and amphiphilic peptide-polymer derivatives[10]) have been proposed as native building blocks for generating nanostructured aggregates. Peptide-based supramolecular systems showed a wide morphological heterogeneity, including fibers,[11] ribbons,[12] nanorods,[13] films,[14] and nanospheres.[15] Moreover, the possibility of modifying the primary sequence of these building blocks with non-coded amino acids or decorating them with drugs or fluorophores allows to hugely expand the number of potential application areas.[16,17]

For example, aggregate systems of peptides have been exploited for the development of supramolecular diagnostic tools,[18] for tissue engineering,[19] for water treatment,[20] and for optoelectronic scopes.[21] Some of them have evidenced interesting functional properties including the stimuli responsiveness and the reversibility.[22,23] Moreover, self-assembling lipid conjugated amphiphilic peptides have been developed for their ability to form nanostructures (NSs) such as nanotubes, micelles, and liposomes.[24–26] These NSs have been studied for selective targeting delivery of contrast agents and drugs, especially doxorubicin. The alkyl chains stabilize the NS, the exposed

https://doi.org/10.1002/psc.3301

peptide targets specific receptors overexpressed on the cell membrane, and the contrast agent and/or the drug remain encapsulated in the NS. Finally, conjugation of the doxorubicin to self-assembling peptides has been employed to deliver the drug on target sites, in a selective way.[27]

In material science applications, numerous studies highlighted the possibility to use self-assembling peptides for generating self-supporting hydrogels (HGs)[28] and nanogels (NGs).[29] HGs are an interesting group of implantable non-Newtonian materials formed by a large amount of water blocked in a tridimensional (3D) hydrophilic network. They are characterized by an excellent biocompatibility profile attributed to the high water content (generally in the range of 75%–99%).[30,31] The high water content and the viscoelastic behavior allow mimicking the extracellular matrices (ECMs) and tissue properties. For this reason, HGs are actually studied as ideal candidates for tissue engineering applications.[32] The possibility to produce HGs differing in size, dimensions, structure, and function allows improving the HGs applications in pharmaceutical area, including drug delivery.[33] NGs, identified also as HG nanoparticles, are examples of colloidal formulations in the submicron scale obtained by micronization of the 3D HG network. They are structured as an external surfactant coating (shell), which stabilizes an interior core of HG-like structure. The physical colloidal form of NGs is compatible with their intravenous injection via needle. Similarly to HGs matrices, the NG interior core can act as a drug reservoir for incorporation of active pharmaceutical ingredients (APIs).[34]

Within this context, HGs and NGs delivery tools can generate therapeutically beneficial outcomes with respect to classical administration routes, providing physical and chemical protection of the encapsulated drug and a spatiotemporal control on its release. These supramolecular preparations can also easily encapsulate different classes of APIs, either hydrophilic or hydrophobic, including small molecules,[35] active peptides,[36] proteins,[37] and cells.[38] In addition, HGs and NGs can allow a release in a programmable manner, producing modified pharmacokinetics profiles. Moreover, the NGs size feature generally was found compatible with simple renal clearance, improved barrier penetration, and good shelf stability and prolonged effect of circulation in the blood stream.[39]

In this review, we report about peptide-based HGs and NGs for the delivery of one of the most important chemotherapeutic drugs, doxorubicin (Dox, see chemical formula in Figure 1). Dox, also known as adriamycin, is a natural antitumor antibiotic used to treat several types of cancers. It is clinically applied for leukemia, stomach, lung, breast, ovarian, and bladder cancer therapy.[40] Cytotoxicity and activity effects are related to the interference with DNA/RNA replication and to topoisomerase II inhibition. However, the use of this drug is partially limited by dose-limiting toxicities. A myelosuppression and a cardio toxic side effects were detected, thus exposing cancer survivor to increased cardiovascular risks. To overcome these issues, doxorubicin has been incorporated in liposomes and some liposomal products of this drug (Myocet, Doxil, and Caelyx) are on the market and in clinical use for tumor therapy. Moreover, other products based on the liposomal doxorubicin modified with targeting agents, such as peptides and antibodies, are in development to enhance the efficacy of the drugs with a simultaneous reduction of side effects.[25,41,42]

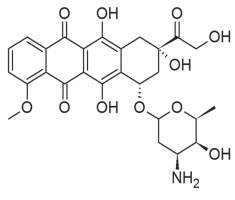

FIGURE 1 Chemical structure of the anthracycline drug doxorubicin

Encapsulation in HG matrices or in NGs represent a feasible strategy, alternative to liposomal doxorubicin, for increasing the Dox maneuverability in chemotropic treatments, reducing accumulation and related cardiac side effects. In this review, systems are classified, according to a primary sequence classification of the constituent peptide, in short and ultra-short peptide-based HGs, RGD-, and RADA-peptide-based HGs. The peptide-based NGs formulations encapsulating Dox are also reported.

2 | ULTRA-SHORT AND SHORT PEPTIDE-BASED HGS

Short and ultra-short peptides are well-known for their ability to aggregate in solution according to a self-assembling mechanism that leads to the formation of nanofibrous and HG materials. The most studied ultra-short peptide is the aromatic homodimer diphenylalanine (FF), identified for the first time by Gazit as the smallest peptide able to promote the aggregation of the $A\beta^{1-42}$ in oligomers, protofibrils, and finally into amyloid plaques. Since its identification in 2003,[43] the self-assembling properties of this homodimer have been deeply investigated.[44,45] It was observed that FF and its congeners are able to self-organize into a large variety of NSs from nanotubes to nanofibrils, vesicles, and HGs.[46–48] The morphological variability of NSs depends on the experimental procedure adopted for their preparation such as the polarity of the solvent,[49] the pH value or temperature,[50] and by chemical modifications of the aromatic homodimer, including the addition/modification of residues in the sequence, and/or modification of peptide termini.[51,52]

Recently, several examples of the HGs based on FF peptide[53] and on its analogues[54] have emerged in literature as potential carriers for the delivery of Dox. Figures 2 and 3 display peptide the composition of HGs proposed for the in vitro and in vivo doxorubicin delivery. The first example in this sense was reported by Chieh et al. in 2015.[58] They prepared peptide-based supramolecular HGs loaded with Dox by using an innovative electrostatic and cross-linking approach, in which naphthyl-Phe-Phe-Cys (Nap-FFC, Figure 2A) oligopeptides are mixed to gold nanoparticles (AuNPs) and calcium ions (Ca^{2+}). The peptide was designed by starting from Nap-FF building block that is able to spontaneously self-assemble in water in HGs.[59] The presence of few components improves the mechanical stability of the gel through the

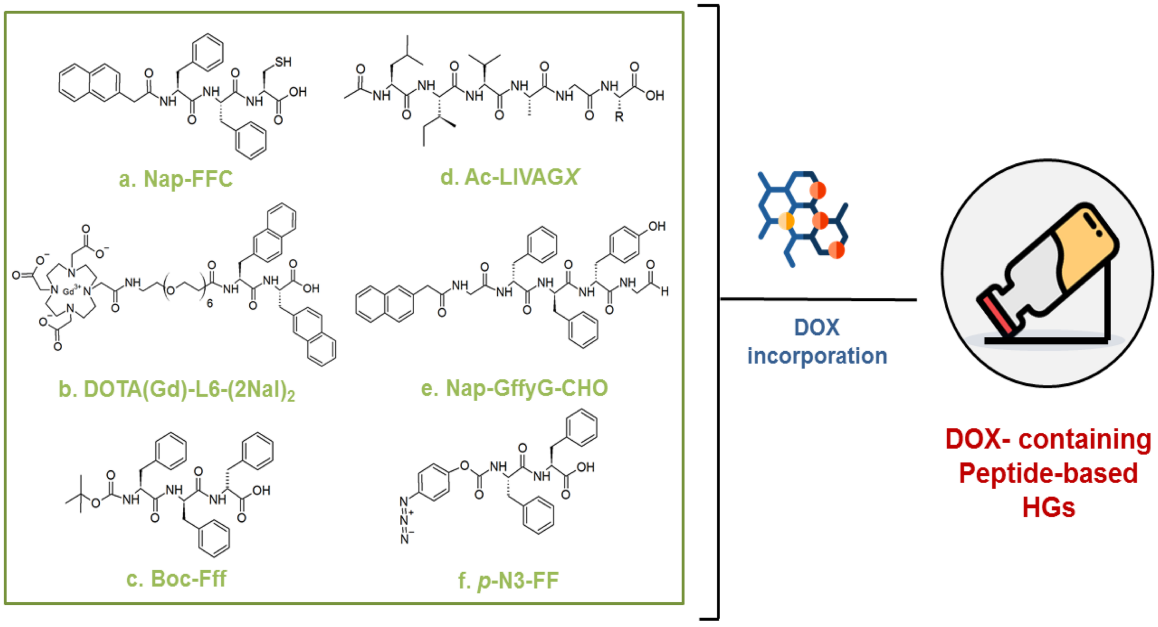

FIGURE 2 (A–F) Chemical structure of building blocks used for generating Dox-encapsulating peptide-based (HGs) hydrogels

formation of a densely entangled fibrous network of peptide multimers. The dense agglomeration is probably due to presence of Ca^{2+} ions and to the interaction of the peptide with gold nanoparticles. The presence of AuNPs and Ca^{2+} can strengthen the prepared HG by doubling the diameter of NapFFC nanofibers, allowing the formation of stronger frameworks and slowing the release of components. The authors demonstrated that the bioinspired NapFFC-AuNP HG supports the growth of HeLa cells and exhibits high cell viability in assays in which cells are incubated with HG at a concentration of 500 μM for 72 h. As expected, the Dox-loaded HG allows an increase of the cytotoxicity.

At the same time, our research group has studied the aggregation and gelation properties of different peptides sequences based on FF or FY motifs modified with the polyethylene glycol polymer (PEG) moiety and eventually capped with metal chelators.[54,60–63] Among these studies, we described the synthesis, the structural characterization and the relaxometric behavior of a novel water-soluble fibers that generate HG for molecular resonance imaging (MRI).[64] This HG is based on a dipeptide containing the non-coded residue 2-naphthylalanine (2Nal) and modified with a gadolinium complex. The peptide conjugate DOTA (Gd)-L6-$(2Nal)_2$ (L6 = ethoxylic linker, see Figure 2B) can self-assemble in long fibrillary NSs in water solution. Circular dichroism (CD) and Fourier-transform infrared (FTIR) spectroscopies indicate a β-sheet secondary structure with an antiparallel orientation of single strands. As confirmed by molecular modeling studies, the three-dimensional structure of the peptide spine in the aggregates is composed by extended β-sheet motifs stabilized by hydrophobic interactions and hydrogen bonds. The high relaxivity of these nanoaggregates (12.3 mM^{-1} s^{-1} at 20 MHz) and their capability to encapsulate Dox suggest potential application as supramolecular theranostic agents.

Simultaneously, Basu et al. created soft biocompatible materials filled with Dox for cancer drug release at physiological pH and temperature.[65] Remarkably, the modulation of stiffness and proteolytic stability of these HGs have been achieved by replacing one or more *L*-Phe residues in a Boc-Phe-Phe-Phe-OH tripeptide by *D*-Phe (*f*) residue(s) and by changing the position of the *D*-residue in the tripeptide. Their studies demonstrated that the incorporation and the location of *D*-residues could determine the mechanical stability of the gel and its drug release capacity. Similarly, the number and position of *D*-amino acid residues seem deeply govern the proteolytic stability of the resulting gel. After trying all possible combinations of *D*- and *L*- amino acids, the authors identified Boc-*L*-Phe-*D*-Phe-*D*-Phe-OH (Boc-Fff, Figure 2C) as the most efficient gelator molecule. in vitro studies pointed out the very low toxicity of this peptide gelator towards cancerous cells and the capability of Dox-loaded gel to kill breast cancer cells more efficiently than the free Dox alone. Analogously, Chan et al. also demonstrated that single-molecular changes on a tripeptide can dramatically affect final self-assembling and hydrogelation properties.[66] In details, the authors investigated the C-terminal modification on two ultra-short peptide backbones, that is, acetylated-Leu-Ile-Val-Ala-Gly-Xaa (Ac-LIVAGX, Figure 2D) and acetylated-Ile-Val-Xaa (Xaa = His, Arg, Asn). The resultant HGs have varying stiffness and yield stress, depending on the backbone and C-terminal residue, as revealed by rheological studies. By using visible spectroscopy-based elution studies, they also evaluated how the C-terminal residue can influence the rate and extent of drug elution. Comparative studies on three different small molecules drugs (naltrexone, methotrexate, and doxorubicin) pointed out that both rate and extent of drug elution can be also partially affected by the shape of the drug. Based on the elution assays, field emission scanning electron microscope (FESEM),

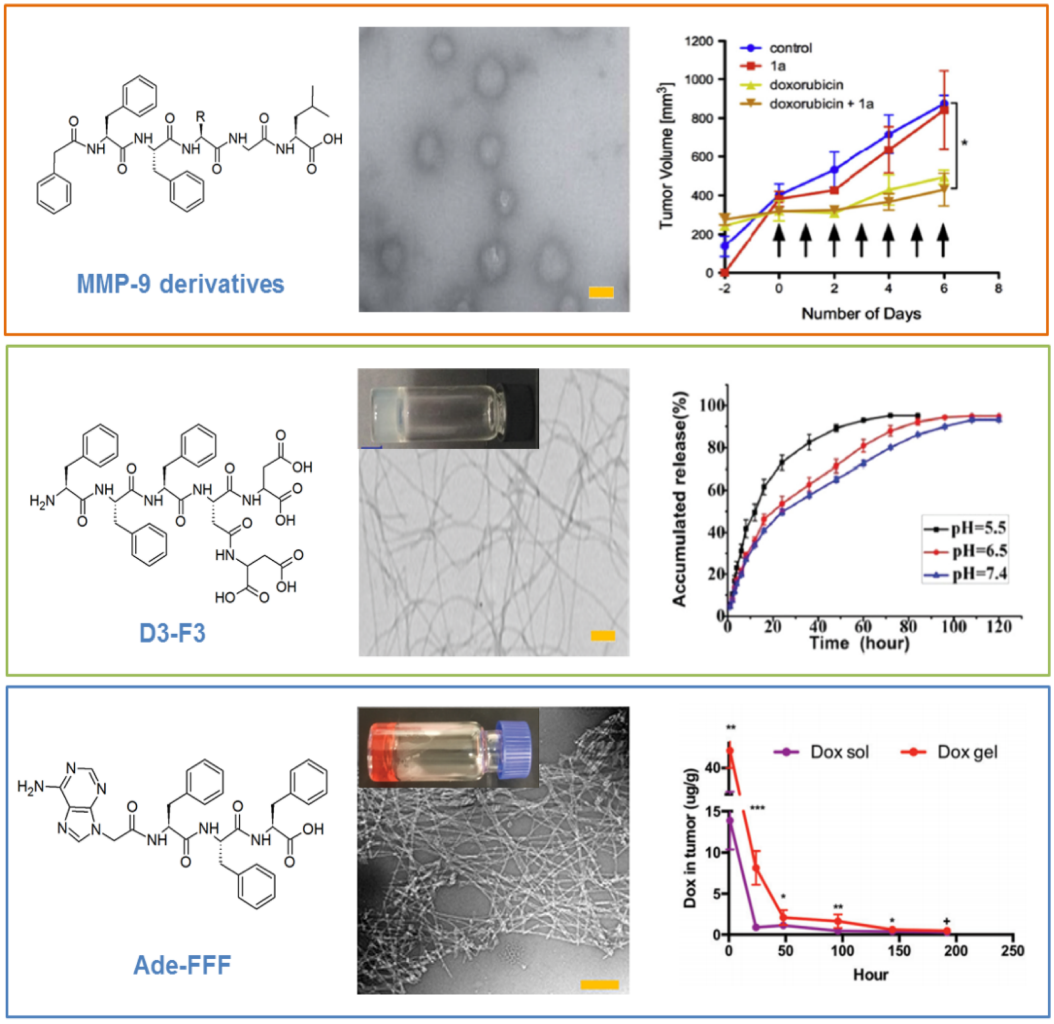

FIGURE 3 Orange panel (from left to right): chemical formula of MMP-9 derivatives, transmission electron microscopy (TEM) of spherical aggregates and MMPSense680™ reporting on metalloproteinase (MMP) activity in vivo in a subcutaneous tumor of MDA-MB-231-luc-D3H2LN. Green panel (from left to right): chemical structure of D3F3 hydrogel building block, TEM and resulting macroscopic gel (inset), and release curve of Dox as function of the pH value. Blue panel (from left to right): chemical formula of Ade-FFF, TEM microphotos and 3D Dox-loaded HGs matrices (inset), and comparison between the biodistribution of the Dox solution and the Dox gel in cancer tissue. Scale bar represents 200 nm. The figure was adapted from other studies[55–57]

and infrared spectroscopy, the authors propose models for the peptide fibril–drug interaction. They also studied the hemolytic effect of empty HGs and cytotoxicity of both empty and filled Dox HGs on human adipose-derived mesenchymal stem cells. Their results indicated a high cytocompatibility of the peptide HG on cells and that Dox can fully intercalate within the peptide fibril structure.

Later, Wang et al. reported another example of HG based on a peptide modified at C-terminus with an aldehyde function.[67] The HG was prepared via an enzyme-dependent self-assembly process, in which the phosphorylated peptide Nap-Gly-*D*-Phe-*D*-Phe-*D*-pTyr-CHO (Nap-GffyG-CHO, Figure 2E) is the precursor of the hydrogelator obtained after the action of the alkaline phosphatase enzyme. The resulting HG showed ultra-stable properties in highly basic or acidic aqueous solutions. Moreover, the hydrogelator forms Schiff bases by interaction between amine group on Dox and aldehyde group on Nap-Gly-*D*-Phe-*D*-Phe-*D*-Tyr-CHO. Owing to the pH-responsive properties of Schiff bases, the HG was identified as a potential vehicle for the controlled release of drugs containing amine groups. In this scenario, the recent paper from Dadhwal et al. reported the first use of a strain-promoted alkene-azide 1,3-dipolar cycloaddition that can trigger the dissolution of an HG.[68] Using an ultra-short aryl azide-capped peptide HG (formed by *p*-N3-FF, Figure 2F), they demonstrated that upon click-type reaction with trans-cyclooctene, the HG undergoes a gel–sol transition and subsequent release of the encapsulated Dox (with a release of 87% over 10 h compared with 13%–14% in the non-triggered control experiments).

All the studies described until this section show the in vitro potentiality of short peptides as building blocks for formulation of cargo HGs. However, only the three following studies evaluate their effective in vivo ability towards cancer disease. In the first study, the authors designed and synthetized novel enzyme-responsive vehicle for the local delivery of Dox for application in cancer therapy. They are based on a series of FF peptide analogues having a common formula (xFFyG, where x is either glycine or phenylacetyl group and y is leucine or alanine). These peptide sequences spontaneously self-assemble into micelles and undergo to enzymatic cleavage in proximity of ECM-metalloproteinases (MMPs), overexpressed in many types of cancer.[55] Due to the different amphiphilic balances in the cleaved peptide, a structural transition from micelles to fibrillary NSs occurs. These fibrillary HGs, generated at the sites of MMP-9 overexpression, are highly biocompatible in vitro and can be used as carriers for Dox in vivo. Studies performed on xenograft mouse model showed that some peptide HGs have a significant higher inhibition effect respect to the free Dox.

Successively, in 2019, Zhong's group designed and synthesized a novel fork peptide, D3F3 (see Figure 3, green panel) that transforms into an HG through crosslinking induced by high concentration of zinc ions.[56] Because the concentration of zinc ions necessary to promove gelation falls into the physiological range of the prostate tissue, the peptide-based drug delivery system (DDS) could be injected, and only when it reaches the prostate the tissue-specific self-assembly process starts. D3F3 HGs exhibited an optimal gelation time, satisfactory mechanical strength (also enhanced after incorporation of Dox) as well as excellent thixotropic properties. The DDS brings doxorubicin in the prostate 24 h after the injection, making possible local sustained release.

In addition, the peptide materials demonstrated no cytotoxicity against normal fibroblast cells, and no damage was observed to the prostate tissue of rats. It is worth to note that the Dox-HG system exhibited higher anticancer efficacy (IC_{50} = 9.30 μg/ml) respect to free Dox (IC_{50} = 12.46 μg/ml) on prostate cancer cells DU-145. Therefore, the study could be considered the base for the future design of tissue-specific DDSs that are activated by cationic ions, and the system could be further developed to incorporate other active drugs utilized in prostate cancer therapy, with an increase of the pharmaceutical potency and simultaneous reduction of side effects.

Finally, in 2020, the Suggs's group published a study describing a Dox-loaded HG based on triphenylalanine peptide modified with adenosine on its N-terminus (Ade-FFF, Figure 3, blue panel).[57] Due to non-covalent interactions between peptide groups as well as π–π stacking and Watson–Crick interactions via complementary nucleobases, this nucleotide-peptide self-assembles into HGs with a fibrillary structure. Beyond the well-known advantages of peptide biomaterials, these HGs interacting with DNA exhibited specific benefits for biomedical applications. Ade-FFF nucleo-peptide HGs were able to load a high concentration of Dox (1 mM) and demonstrated continuous release under in vitro degradation conditions. Moreover, an in vivo study in tumor-bearing mouse model to evaluate the delivery of Dox by Ade-FFF HGs was also reported. Results indicated that Dox-containing HGs are able to reduce the tumor growth and demonstrated a greater apoptosis-mediated cell death in the tumor as evidenced by caspase-3 expression. Pharmacokinetic studies and biodistribution profile also confirmed the observation that Dox delivery by an Ade-FFF HG improves sustained delivery in the local tumor site. All the experimental evidence reported in this study highlight the potential employment of these self-assembled nucleo-peptides in biomedicine.

3 | RGD CONTAINING PEPTIDES

Another class of peptide HGs studied as potential vehicles for the delivery of Dox are peptide analogues of the RGD one. RGD (sequence reported in Figure 4) is a well-known peptide sequence able to recognize $\alpha_v\beta_3$ integrin receptors on angiogenic endothelial cells that are overexpressed in many solid tumors (colon cancer, brain cancer, prostate cancer, and others).[73] The first example in this sense was reported in 2015 by Xue et al.[69] The authors described the synthesis of Nap-GFFYGRGD peptide composed of a common self-assembling motif GFFYG derivatized with a naphthalene group on its N-terminus and the RGD sequence. This peptide is able to spontaneously form supramolecular nanofibers in aqueous solution and cross-linked HGs in presence of different amounts of Dox (Figure 4, orange panel). These doxorubicin-peptide HGs allowed a sustained release of the drug at 37°C with a release of 95%, 52%, and 38% during the first 72 h for gels with 0.1, 0.2, and 0.3 *equiv*. of doxorubicin, respectively. Moreover, these gels exhibited an in vitro cytotoxicity comparable with the free doxorubicin on HeLa and MCF-7 cancer cells thus suggesting that the anticancer activity of drug is not affected by the gel.

Similarly to this study, Mei et al. proposed other RGD-derived peptide conjugates (GFFYGRGDH*n* with *n* = 0–2, named 1-RGD, 1-RGDH, and 1-RGDHH, respectively) that to co-assemble into HGs in the presence of 0.1 equivalents of doxorubicin (Figure 4, green panel). It was observed that the supramolecular network of fibers in the HG matrix is reinforced by electrostatic interactions occurring between the peptide and the drug with a decrease of the minimum gelation concentration (from 1.2 to 0.8 wt %) and an increase of the G′ value.[70] Dox-loaded HGs exhibited viscoelastic and shear-thinning properties typical of injectable HGs. Furthermore, the DOX release was pH-responsive with an accelerated drug release in the pH range 6.5–5.5 (14.5% and 27.7%, respectively). This trend is due to the loss of electrostatic interactions because of the histidine protonation under acidic conditions. Moreover, DOX-peptide hybrid HGs were more efficient than the free drug in inhibiting the growth of A549, MCF-7, and HeLa. This result was attributed to the capability of the peptide HG to mediate the cellular entry of the drug through an integrin receptor-mediated endocytosis. At the same time, the same authors also reported the formulation of DOX-peptide hybrid HG based on the self-assembly of IDM-GFFYGRGDH (IDM-1), containing the RGD analogue GFFYGRGDH and the non-steroidal anti-inflammatory drug indomethacin (*IDM*) that inhibits the production of

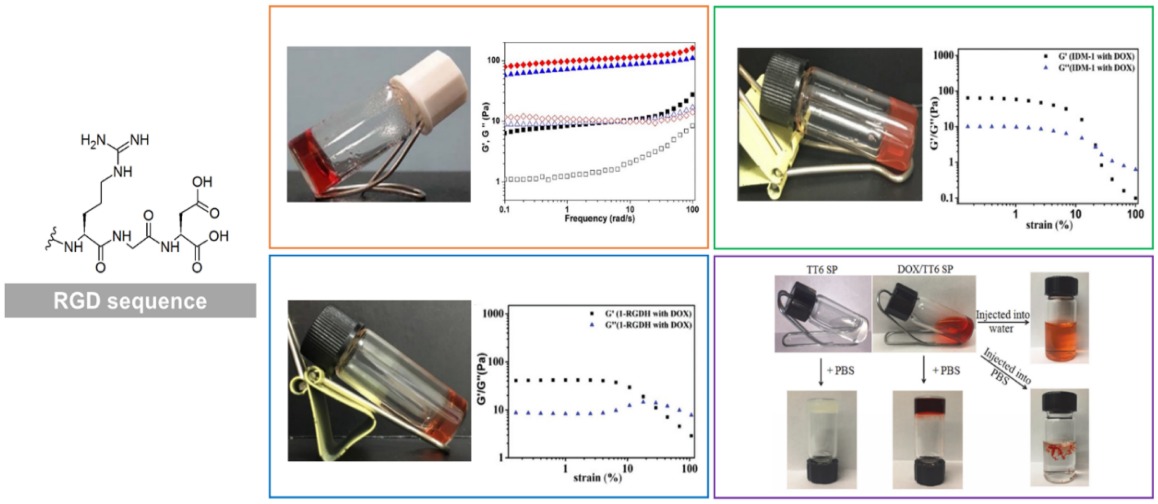

FIGURE 4 Examples of peptide-based hydrogels (HGs) containing RGD sequence. Orange panel: macroscopic photo of Nap-GFFYGRGD gel formed by adding 0.1 equiv. of Dox and rheological analysis in dynamic frequency sweep (strain of 0.5%) for gels adding different amounts of Dox (diamonds: 0.3 equiv., triangles: 0.2 equiv., squares: 0.1 equiv., filled symbols: G′ and open symbols: G″). Green panel: optical images of 1-RGDH/DOX hydrogel HGs at 1 wt % after the addition of 0.4 mol/L imidazole and dynamic strain sweep of 1-RGDH hybrid hydrogels (1 wt % gel containing 0.1 equiv. of DOX). Blue panel: macroscopic photo of 1.5 wt % IDM-1/Dox gel and dynamic strain sweep rheological analysis of IDM-1 hydrogels (2 wt %, 0.1 equiv. DOX). Violet panel: Gelation process tests for TT6 SP and DOX/TT6 SP solution in different aqueous media. The figure was adapted from other studies.[69–72] PBS, phosphate-buffered saline

prostaglandins (Figure 4, blue panel).[71] The co-delivery of IDM and DOX in these hybrid HGs allows achieving a synergistic inhibition of cancer cell growth.

Recently, Wang et al. reported the synthesis of an amphiphilic construct in which two camptothecin (CPT) drug units are covalently bound onto a cyclic iRGD peptide through a biodegradable disulfanylethyl carbonate linker (etcSS).[72] This amphiphilic construct self-assembles into tubular supramolecular polymers (SPs) in water and in 3D-HGs in phosphate buffer with a critical gelation concentration ranged between 1.5 and 2 mM (Figure 4, violet panel). The resulting hollow NS (TT6-SPs) allows for encapsulation of another therapeutic agent, either curcumin or DOX for combination therapies.

The iRGD sequence, which selectively recognizes the integrin receptors, allows tumor penetration and cellular internalization of the drug-loaded nanovector. This cellular environment prompts the breakdown of the disulfide linkage between the peptide and the CPT and the consequent release of CPT in its free drug form. Cytotoxicity of the Dox-loaded HGs in comparison with that of free CPT and of the empty HG was assessed on U-87 brain cancer cell line. Results highlighted that empty HG and free CPT have similar IC_{50} values (217.9 and 199.4 nM, respectively) thus indicating that the activity of CPT is not affected by its conjugation to the cyclic peptide. As expected, a significant increase of cytotoxicity (IC_{50} = 38.3 nM) was observed for Dox-loaded HG. Moreover, the complete set of in vitro and in vivo studies pointed out the capability of these polymeric HGs to improve tumor retention (after 45 days, approximately 35% of the HG still remains in the injection site), tissue penetration, and sustained release, and in turn to allow tumor regression, inhibition of tumor metastasis, and recurrence.

4 | PEPTIDES CONTAINING RADA SEQUENCE

Another sequence recently proposed as decoration for peptide-based building block for generating versatile supramolecular materials is the Ac-$(RADA)_4$-$CONH_2$ peptide (sequence reported in Figure 5). This sequence, alternating charged and hydrophobic residues, promotes the adaptation of a β-strand conformation in which the hydrophobic alanine residues remain on one side of the strand while hydrophilic amino acids (such as arginine and glutamic acid) are exposed on the other side. Upon self-assembly, β-strands arrange into an ordered nanofiber structure composed of two stacked β-sheets, which are further stabilized by a hydrophobic core formed by alanine side chains. Due to their features, the resulting supramolecular materials have been proposed as building blocks for several applications in biomedicine: as a host for small and large molecules, as biomaterial in tissue engineering, and finally as a carrier for chemotherapeutic agents.[77,78]

In this context, Fatouros's group recently employed this peptide as hydrogelator for the local co-delivery of Dox and/or curcumin (CUR) and verified the in vitro ability of the HG in apoptosis of cells from human glioblastoma.[74] Then, the same authors studied the potential employment of this gel in the treatment of neck and head cancer.[75] Morphological studies, carried out using SEM technique, revealed that the Ac-$(RADA)_4$-$CONH_2$ HG contains an entangled nanofiber network. Moreover, rheological analysis showed that the more hydrophobic CUR drug allows the obtainment of a stiffer HG compared with Ac-$(RADA)_4$-$CONH_2$ and Ac-$(RADA)_4$-$CONH_2$-DOX. This different mechanical behavior was attributed by the authors to the interaction of CUR drug with the hydrophobic region present in

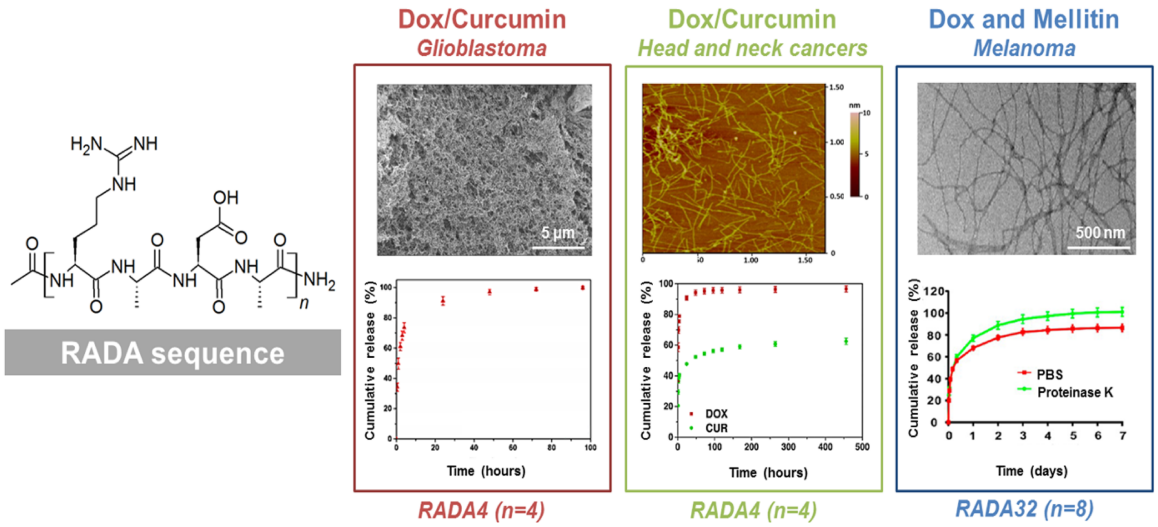

FIGURE 5 Examples of peptide-based hydrogels (HGs) containing RADA sequence. Red panel: scanning electron micrograph (SEM) of the hydrogel formed by Ac-$(RADA)_4$-$CONH_2$ peptide sequence and Dox release from the HGs matrices. Green panel: atomic force microscopy (AFM) of Ac-$(RADA)_4$-$CONH_2$ peptide Solutions A prior- and B post-drug loading with CUR and DOX at final drug concentrations of 222 and 5 mg/ml, respectively. The figure was adapted from other studies.[74–76] PBS, phosphate-buffered saline

the peptide nanofibers. in vitro release studies showed a complete DOX release from Ac-$(RADA)_4$-$CONH_2$ within 4 days and a prolonged release for Ac-$(RADA)_4$-$CONH_2$-CUR over 20 days. An increased cellular uptake and a higher cytotoxic effect were observed for Ac-$(RADA)_4$-$CONH_2$-DOX, compared with free DOX. Higher levels of early apoptosis were observed for the cells treated with the Ac-$(RADA)_4$-$CONH_2$-CUR, compared with CUR solution. In conclusions, the obtained findings highlight the potential advantage of the in-situ depot forming Ac-$(RADA)_4$-$CONH_2$ HG for the local delivery of both water-soluble and insoluble chemotherapeutic drugs. The dual loaded peptide HG enabled control over the rate of drug release based on their aqueous solubility. in vitro assays pointed out a significantly enhanced growth inhibitory effect in cells treated with HG formulations containing a combination of the two drugs respect to the combination of CUR and Dox in solution. The synergistic pharmacological effect of selected HG formulations was clearly confirmed in vivo the antitumor efficacy of the drug-loaded peptide HG was also verified in HSC-3 cell-xenografts. Finally, the safety of the topically administered HG formulation was highlighted by labeling assay analyses of major organs. Overall, results demonstrated the therapeutic utility of the dual drug-loaded peptide HG as an appropriate approach for the local treatment of head and neck cancer.

At the same time, Yang and co-workers studied and reported the formulation of an injectable melittin-RADA32 hybrid peptide HG (MRD) loaded with DOX, as potent chemo-immunotherapeutic agent against melanoma through the active regulation of tumor microenvironments (TMEs).[76] In this hybrid peptide, the RADA sequence is covalently conjugated to the melittin peptide, a cationic sequence (GIGAVLKVLTTGLPALISWIKRKRQQ) derived from bee venom. It disrupts the membranes and, thus, has strong in vivo hemolysis effect. Therefore, there are a lot of problems for in vivo applications of this peptide. MRD HG is based on an interweaving nanofiber structure; it exhibits excellent biocompatibility and controlled drug release properties both in vitro and in vivo, and it is able to kill melanoma cells. Their results indicated that a single-dose injection of MRD HG retards the growth of primary melanoma tumors by more than 95% with concomitant recruitment of activated natural killer cells in the tumors. Furthermore, MRD HG can activate dendritic cells of draining lymph nodes and produce active, cytotoxic T cells to further protect the cells against remaining tumors, providing potent anticancer efficacy against subcutaneous and metastatic tumors in vivo. Owing to its abilities to perform controlled drug release, regulate innate immune cells, direct anticancer and immune-stimulating capabilities, and reshape immunosuppressive TMEs, MRD HG may serve as a powerful tool for anticancer applications.

5 | PEPTIDE-BASED NGS

HG nanoparticles, also commonly named NGs, have recently attracted a growing interest as delivery systems of bioactive ingredients. They allow fusing the advantages of classical HGs and nanosized particles (e.g., liposomes, micelles, and nanoparticles). Due to their submicron range scale, they are compatible with needle injection and allow overcoming some problematic issues related to the drug administration such as the in vivo bioavailability, bio-disponibility, toxicity, and deactivation. Moreover, in vivo studies evidenced a high penetration through tissue barriers, a prolonged circulation in the blood stream, beyond their capability to be easily cleared from kidneys. Despite their advantages, only few examples of Dox-loaded peptide-based NGs have been reported until now (see Figure 6). The first example of peptide-based nanogel (PBN) was described in 2013 by Ischakov

et al.[79] They described an NG formulation based on Fmoc-FF dipeptide using the inverse emulsion technique. In particular, the water-in-oil emulsion was prepared by homogenizing an aqueous solution of Fmoc-FF peptide and a mineral oil, in which the stabilizing surfactant E-TPGS (d-α-tocopheryl polyethylene glycol 1000 succinate) is dispersed (Figure 6, green panel). The resulting nanoparticles, with an average size of 225 nm, were simultaneously loaded with a diagnostic agent (e.g., gold nanoparticles) and an anticancer drug (e.g., Dox or 5-flourouracil [5-Fu]). As expected also in this case, the release kinetics of the drugs are affected by their chemical structure, molecular weight, and hydrophobicity. Recently, Rosa et al. reported another example of Fmoc-FF based NGs encapsulating Dox, in which the peptide building block is prepared using a different couple of stabilizing agents that are TWEEN®60 (polyethylene glycol sorbitan monostearate) and SPAN®60 (sorbitan stearate).[80] The combination of this couple of surfactants allows achieving a scale of hydrophilic–lipophilic

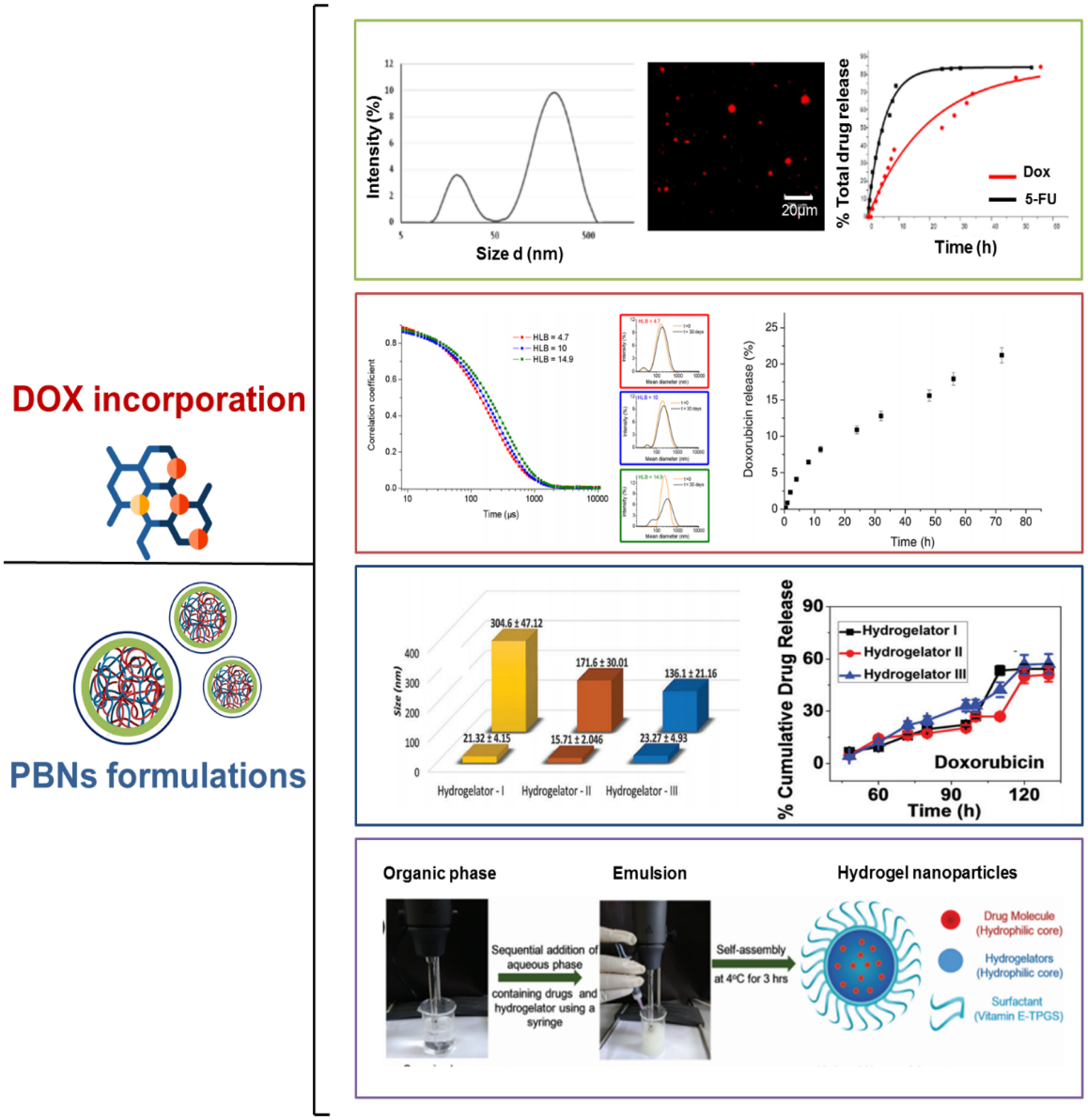

FIGURE 6 Peptide-based nanogel (PBN) formulations as cargo systems for Dox. Green panel: dynamic light scattering (DLS) for Fmoc-FF/E-TPGS stabilized nanogels. DLS reports two populations: 21.5 ± 1.3 and 225.9 ± 0.8 nm. Confocal microscopy of Dox-containing PBNs and release profiles for Dox and 5-FU as function of the time. Red panel: DLS correlation function of Fmoc-FF/TWEEN®60/SPAN®60 stabilized nanogels as function of hydrophilic–lipophilic balance (HLB) value and release time profile of Dox. Blue panel: histogram bimodal nanoparticle dimensions obtained from zeta-size measurements for amphiphilic peptides (named Hydrogelators I, II, and III) and Dox release study. Violet panel: inverse emulsion methodology for obtaining hydrogel nanoparticles of Hydrogelators I, II, and III. The figure was adapted from other studies[79–82]

balance (HLB) values ranged 4.7 < HLB < 14.9. NGs were prepared according three experimental procedures, namely, water/oil emulsion (W/O), top-down, and nanogelling in water, respectively. The structural characterization highlighted that NGs have an average size ranged between 170 and 240 nm and keep the inner structure of the initial Fmoc-FF HG formulation (Figure 6, red panel). These NGs demonstrated the ability to encapsulate an amount of Dox comparable with that of the commercially available liposomal formulations Myocet® and Doxil®. The percentage of Dox released was of approximately 20% after 72 h, significantly lower respect to the release (80% after 55 h) previously observed by Gazit's group for Fmoc-FF NG prepared using E-TPGS surfactant. Other two examples of PBNs were reported by Mehra et al. (Figure 6, blue and violet panels).[81,82] Initially, they reported the formulation of a series of NGs prepared using amphiphilic peptide (PA) analogues with the general formula Me–$(CH_2)_{14}$–CO–NH–CH(X)–COOH, where X = CH_2Ph in hydrogelators I (*L*-Phe) and II (*D*-Phe) and X = CH_2Ph(OH) in hydrogelator III (*L*-Tyr). Successively, the same authors reported the synthesis of others PAs having analogous general formula, but with a shorter alkyl chain [–$(CH_2)_8$–] with respect to the first series [–$(CH_2)_{12}$–]. Structural characterization of self-assembled HGs, initially obtained by self-assembling of PAs, evidenced the presence of nanofibers with a β-sheet conformation. Due to their mechanical properties (thermoreversibility, injectability, and high mechanical strength), low in vitro cytotoxicity and high resistance towards proteolytic degradation, these HGs could be considered as promising vehicles to selectively transport drugs to a targeted site. In this perspective, the corresponding NG formulation was prepared using E-TPGS in agreement with the inverse emulsion technique previously reported by Gazit's group, and the resulting nanoparticles were loaded with two different anticancer drugs: 5-fluoro uracil and Dox. As expected, it was observed that under physiological conditions, the release of the two drugs is strictly related to their physicochemical parameters.

6 | MISCELLANEA

Beyond the previously described classes of peptides, other few peptide sequences have been exploited for the preparation of Dox-loaded HGs. According a chronologic criterion, a brief description of these sparse examples is here reported. In 2011, in a pioneering paper, Zarzhitsky and Rapaport[83] studied the interaction between the amphiphilic β-sheet Pro-Asp-(Phe-Asp)$_5$-Pro peptide and the mildly amphiphilic chemotherapeutic drug Dox. The adsorption of the drug to the interface of phosphate-buffered saline (PBS) solution is enhanced by the presence of the amphiphilic peptide. Over the time and in buffered ionic solutions, Dox tends to self-associate into molecular forms that appear to be more hydrophobic and have higher interaction propensity with peptides arranged in the β-sheet conformation (see Figure 7, green panel). HGs with high concentrations of Dox loaded are obtained; they slowly release fractions of Dox in the time giving cytotoxicity to SaOS2 cells. The study demonstrates that due to the electrostatic forces and to the hydrophobic interactions, the amphiphilic peptide HG may act as an efficient and controllable carrier of the anticancer drug Dox.

Successively, the KLD12 peptide (Ac-KLDLKLDLKLDL, schematically represented in Figure 7) with its alternating ionic hydrophilic and hydrophobic amino acids has been reported to spontaneously form stable β-sheet structures in aqueous solution, then promoting HG formation. In 2004, David's group developed injectable in situ-forming HG formulations based on self-assembled KLD motifs to control the delivery of doxorubicin and/or a Smac-derived pro-apoptotic peptide (SDPP) for cancer therapy.[84] The core KLD peptide ([KLDL]3) was separated into two β-sheet peptides by a spacer containing three or four glycine residues or four glycines and one phenylalanine. They found that analogously KLD-based HGs could effectively load Dox and SDPP within the HG network. The insertion of a single aromatic amino acid (F) into 4G sequence of the spacer caused a faster gelation (in few seconds) of the peptide sequence (i.e., KLDLKLGGGGFDLKLDLKL). Moreover, the resulting HG was found very effective at controlling the release of the loaded molecules and inhibiting tumor cell growth in vitro.

Recently, another peptide sequence named Max8 (VKVKVKVKV^{D}PPTKVEVKVKV-NH_2) was employed for generating a composite system for the treatment of solid tumors through both first-line and consolidation chemotherapy. This supramolecular material is composed by an HG matrix able to suspend gemcitabine (GEM) and modified graphene oxide (GO) nanoparticles loaded with Dox.[85] The resulting composite material exhibits high loading of the two drugs and an optimal with a ratio of 10/1 between GEM and Dox that assure a synergistic combination of drugs. Moreover, the optimized formulation showed a faster kinetic release for GEM (47-fold rate) with respect to Dox (18.9% over 72 h and 31.4% over 4 weeks). The resulting HG demonstrated a high therapeutic efficacy on the triple-negative breast cancer cell line (MDA-MB-231). Indeed, they afforded a remarkable combination index (CI = 0.093 ± 0.001), considerably lower than the combination of free drug Dox-GEM (CI = 0.396 ± 0.034) in the same conditions in terms of concentration and molar ratio.

7 | CONCLUSIONS

Classical administration of anticancer drugs (such as doxorubicin) is seriously compromised by issues related to its in vivo bioavailability and biodegradability, systemic toxicity, and repeated dosing requirement. These concerns can be partially overcome by encapsulating the drug into nanostructured systems. For instance, this strategy allows increasing the Dox use in tumor therapy, by enhancing the efficacy of the drug with a simultaneous reduction of side effects such as the related cardiac risk. Liposomal doxorubicin is clinically used for several years for the therapy of several human tumors. Peptide-based HGs and NGs seem a promising alternative to liposomes for the delivery of doxorubicin. Due to their unique features such as the inner structure, the high water content, low drug release profiles, and mechanical properties, HGs have been recently proposed for transepithelial drug

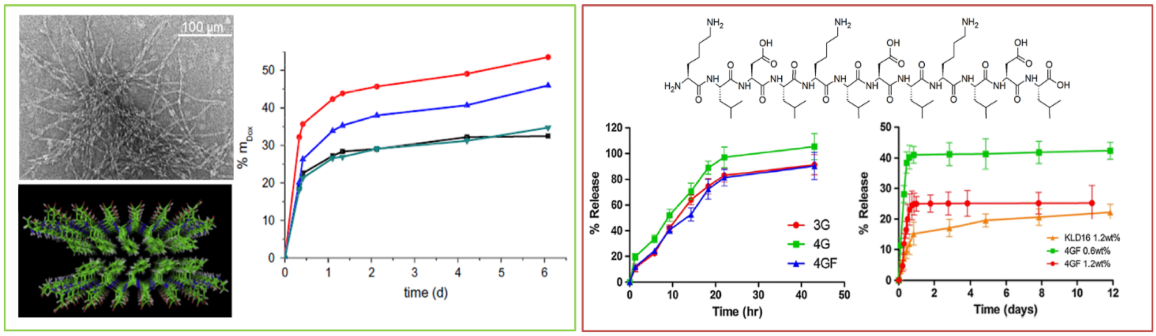

FIGURE 7 Green panel: transmission electron microscopy (TEM) image of Dox-loaded Pro-Asp-(Phe-Asp)5-Pro hydrogel and computational structure along the fibril long axis of bilayer formed by the amphiphilic β-strands; on the right, percentage of Dox released from 5% w/v hydrogels loaded with different amounts of drug. Red panel: schematic representation of (KLDL)3 peptide sequence and the comparison between the in vitro release profiles of (KLDL)3-based hydrogel and other based on peptide analogues. The figure was adapted from Zarzhitsky and Rapaport[83] and Yishay-Safranchika et al.[84]

administration or for in situ gelation process of drug containing implants. Moreover, their inner porous structure (with a diameter ranged between 1 and 10 μm) leaves envisage the possibility to further encapsulate supramolecular nanodrugs (such as liposomes or micelles). This strategy could allow obtaining a composite drug delivery platform for a multi-stage delivery of doxorubicin. On the other hand, submicronization of HGs by top-down methodologies could allow obtaining HG nanosized particles compatible with a systemic, oral, and pulmonary administration of the drug. Due to their size, NG formulations could achieve a fast renal clearance, a feasible penetration through tissue barriers, and a prolonged circulation time in the blood stream. Several studies, here reported, indicate good loading properties and efficient releasing mechanism for several classes of peptides, such as short and ultra-short FF containing peptides, RGD-, and RADA-based peptides, structured in HGs or in NGs. However, this research is still in a starting phase, and several steps should be done to arrive to the clinical use of peptide-based HGs or NGs for doxorubicin administration. For instance, investigations on relationship occurring between the inner structure of HGs/NGs and the amount of drug encapsulated/released could permit to obtain more efficient DDSs. In non-covalent approaches, the drug encapsulation and release are highly dependent by electrostatic or hydrophobic interactions established between the drug and the HG/NG building blocks. As an alternative, drug molecules can be covalently bound on the HG/NG matrix by stable or cleavable linkers. It is worth nothing that the formulation strategy (e.g., solvents, pH, and salt content used during the preparation) could in turn affect the biodistribution and the pharmacological profile of the resulting supramolecular drug. Another important issue to assess before their exploitation for clinical applications is the intrinsic toxicity related to the in vitro and in vivo administration of building blocks forming these macroscopic and nanoscopic systems.

ACKNOWLEDGEMENTS

This research was funded by the Italian Minister of Education, University and Research (PRIN-2017A2KEPL) and by the *Regione Campania* - *POR Campania* FESR 2014/2020 "Combattere la resistenza tumorale: piattaforma integrata multidisciplinare per un approccio tecnologico innovativo alle oncoterapie-Campania Oncoterapie" (Project No. B61G18000470007).

ORCID

Carlo Diaferia https://orcid.org/0000-0002-9273-0136
Elisabetta Rosa https://orcid.org/0000-0001-9273-5589
Antonella Accardo https://orcid.org/0000-0002-7899-2359
Giancarlo Morelli https://orcid.org/0000-0002-5791-3690

REFERENCES

1. Tesauro D, Accardo A, Diaferia C, et al. Peptide-based drug-delivery systems in biotechnological applications: recent advances and perspectives. *Molecules*. 2019;24(2):351.
2. Ebaston TM, Rozovsky A, Zaporozhets A, et al. Peptide-driven targeted drug-delivery system comprising turn-on near-infrared fluorescent xanthene–cyanine reporter for real-time monitoring of drug release. *ChemMedChem*. 2019;14(19):1727-1734.
3. Falcone N, Kraatz H-B. Supramolecular assembly of peptide and metallopeptide gelators and their stimuli-responsive properties in biomedical applications. *Chem a Eur J*. 2018;24(54):14316-14328.
4. Sis MJ, Webber MJ. Drug delivery with designed peptide assemblies. *Trends Pharm Sci*. 2019;40(10):747-762.
5. Tena-Solsona M, Nanda J, Díaz-Oltra S, Chotera GA, Escuder AB. Emergent catalytic behavior of self-assembled low molecular weight peptide-based aggregates and hydrogels. *Chem a Eur J*. 2016;22(19):6687-6694.
6. Edwards-Gaylea CJC, Hamley IW. Self-assembly of bioactive peptides, peptide conjugates, and peptide mimetic materials. *Org Biomol Chem*. 2017;15(28):5867-5876.
7. Avitabile A, Diaferia C, Della Ventura B, et al. Self-assembling of Fmoc-GC peptide nucleic acid dimers into highly fluorescent aggregates. *Chem a Eur J*. 2018;24(18):4729-4735.
8. Insua I, Montenegro J. 1D to 2D self assembly of cyclic peptides. *J am Chem Soc*. 2020;142(1):300-307.
9. Mayans E, Ballano G, Casanovas J, et al. Hierarchical self-assembly of di-, tri- and tetraphenylalanine peptides capped with two fluorenyl functionalities: from polymorphs to dendrites. *Soft Matter*. 2016;12(24):5475-5488.

10. Diaferia C, Roviello V, Morelli G, Accardo A. Self-assembly of PEGylated diphenylalanines into photoluminescent fibrillary aggregates. *ChemPhysChem*. 2019;20(21):2774-2782.
11. Pizzi A, Catalano L, Demitri N, Dichiarante V, Terraneo G, Metrangolo P. Halogen bonding as a key interaction in the self-assembly of iodinated diphenylalanine peptides. *Pept Sci*. 2019;112 (1):1-10.
12. Mayans E, Casanovas J, Gil AM, et al. Diversity and hierarchy in supramolecular assemblies of triphenylalanine: from laminated helical ribbons to toroids. *Langmuir*. 2017;33(16):4036-4048.
13. Li Q, Dai L, Yang Y, Li J. Controlled rod nanostructured assembly of diphenylalanine and their optical waveguide properties, films and nanospheres. *ACS Nano*. 2015;9(3):2689-2695.
14. Apter B, Fainberg B, Handelman A, et al. Long-range fluorescence propagation in amyloidogenic β-sheet films and fibers. *Adv Opt Mater*. 2020;8(9):2000056.
15. Matsuura K, Mizuguchi Y, Kimizuka N. Peptide nanospheres self-assembled from a modified β-annulus peptide of Sesbania mosaic virus. *Pep Sci*. 2016;106(4):470-475.
16. Diaferia C, Netti F, Ghosh M, et al. Bi-functional peptide-based 3D hydrogel-scaffolds. *Soft Matter*. 2020;16(30):7006-7017.
17. Bucci R, Das P, Iannuzzi F, et al. Self-assembling of an amphipathic ααβ-tripeptide into cationic spherical particles for intracellular delivery. *Org Biomol Chem*. 2017;15(32):6773-6779.
18. Diaferia C, Gianolio E, Accardo A, Morelli G. Gadolinium containing telechelic PEG-polymers end-capped by di-phenylalanine motives as potential supramolecular MRI contrast agents. *J Pep Sci*. 2017;23(2): 122-130.
19. Hosoyama K, Lazurko C, Muñoz M, McTiernan CD, Alarcon EI. Peptide-based functional biomaterials for soft-tissue repair. *Front Bioeng Biotechnol*. 2019;7:205.
20. Basak S, Nandi N, Paul S, Hamley IW, Banerjee A. A tripeptide-based self-shrinking hydrogel for wastewater treatment: removal of toxic organic dyes and lead (Pb^{2+}) ions. *Chem Commun*. 2017;53(43):5910-5913.
21. Handelman A, Lapshina N, Apter B, Rosenman G. Peptide integrated optics. *Adv Mater*. 2018;30(5):1705776.
22. Mart RJ, Osborne RD, Stevens MM, Uljin RV. Peptide-based stimuli-responsive biomaterials. *Soft Matter*. 2006;2(10):822-835.
23. Gobeaux F, Wien F. Reversible assembly of a drug peptide into amyloid fibrils: a dynamic circular dichroism study. *Langmuir*. 2018;34(24): 7180-7191.
24. Dehsorkhi A, Castelletto V, Hamley IW. Self-assembling amphiphilic peptides. *J Pept Sc*. 2014;20(7):453-467.
25. Accardo A, Morelli G. Peptide-targeted liposomes for selective drug delivery: advantages and problematic issues. *Biopolymers*. 2015;104 (5):462-479.
26. Accardo A, Mansi R, Morisco A, et al. Peptide modified nanocarriers for selective targeting of bombesin receptors. *Mol Biosyst*. 2010;6(5): 878-887.
27. Wang Y, Cheetham AG, Angacian G, Su H, Xie L, Cui H. Peptide–drug conjugates as effective prodrug strategies for targeted delivery. *Adv Drug Deliv Rev*. 2017;110-111:112-126.
28. Yadav N, Chauhan MK, Chauhan VS. Short to ultrashort peptide-based hydrogels as a platform for biomedical applications. *Biomater Sci*. 2020;8(1):84-100.
29. Panda JJ, Kaul A, Kumar S, et al. Modified dipeptide-based nanoparticles: vehicles for targeted tumor drug delivery. *Nanomedicine*. 2013;8(12):1927-1942.
30. Estroff LA, Hamilton AD. Water gelation by small organic molecules. *Chem Rev*. 2004;104(3):1201-1218.
31. Du X, Zhou J, Shi J, Xu B. Supramolecular hydrogelators and hydrogels: from soft matter to molecular biomaterials. *Chem Rev*. 2015;115 (24):13165-13307.
32. Kumar D, Workman VL, O'Brien M, et al. Peptide hydrogels—a tissue engineering strategy for the prevention of oesophageal strictures. *Adv Funct Mater*. 2017;27(38):1702424.
33. Li J, Mooney DJ. Designing hydrogels for controlled drug delivery. *Nat Rev Mater*. 2016;1(12):16071.
34. Li L, Fu L, Ai X, Zhang J, Zhou J. Design and fabrication of temperature-sensitive nanogels with controlled drug release properties for enhanced photothermal sterilization. *Chem a Eur J*. 2017;23 (72):8180-18186.
35. López C, Ximenis M, Orvay F, Rotger C, Costa A. Supramolecular hydrogels based on minimalist amphiphilic squaramide–squaramates for controlled release of zwitterionic biomolecules. *Chem a Eur J*. 2017;23(31):7590-7594.
36. Doostmohammadi M, Ameri A, Mohammadinejad R, et al. Hydrogels for peptide hormones delivery: therapeutic and tissue engineering applications. *Drug des Devel Ther*. 2019;13:3405-3418.
37. Sotirios Koutsopoulosa LDU, Nagaia Y, Zhang S. Controlled release of functional proteins through designer self-assembling peptide nanofiber hydrogel scaffold. *Proc Natl Acad Sci U S a*. 2009;106(12): 4623-4628.
38. Cho IS, Ooya T. Cell-encapsulating hydrogel puzzle: polyrotaxane-based self-healing. *Chem a Eur J*. 2019;26(4):913-920.
39. Men Y, Peng S, Yang P, et al. Biodegradable zwitterionic nanogels with long circulation for antitumor drug delivery. *ACS Appl Mater Interfaces*. 2018;10(28):23509-23521.
40. McGowan JV, Chung R, Maulik A, Piotrowska I, Walker JM, Yellon DM. Anthracycline chemotherapy and cardiotoxicity. *Cardiovasc Drugs Ther*. 2017;31(1):63-75.
41. Accardo A, Salsano G, Morisco A, et al. Peptide-modified liposomes for selective targeting of bombesin receptors overexpressed by cancer cells: a potential theranostic agent. *Int Journ of Nanomedicine*. 2012;7:2007-2017.
42. Accardo A, Diaferia C, Mannucci S, et al. Easy formulation of liposomal doxorubicin modified with a bombesin peptide analogue for selective targeting of GRP receptors overexpressed by cancer cells. *Drug Deliv Transl Res*. 2019;9(1):215-226.
43. Reches M, Gazit E. Casting metal nanowires within discrete self-assembled peptide nanotubes. *Science*. 2003;300(5619): 625-627.
44. Görbitz CH. Nanotube formation by hydrophobic dipeptides. *Chem a Eur J*. 2001;7(23):5153-5159.
45. Silva RF, Araujo DR, Silva ER, Ando RA, Alves WA. L-diphenylalanine microtubes as a potential drug-delivery system: characterization, release kinetics, and cytotoxicity. *Langmuir*. 2013;29(32):10205-10212.
46. Pellach M, Mondal S, Shimon LJW, Alder-Abramovich L, Buzhansky L, Gazit E. Molecular engineering of self-assembling diphenylalanine analogues results in the formation of distinctive microstructures. *Chem Mater*. 2016;28(12):4341-4348.
47. Diaferia C, Balasco N, Altamura D, et al. Assembly modes of hexaphenylalanine variants as function of the charge states of their terminal ends. *Soft Matter*. 2018;14(40):8219-8230.
48. Fuentes E, Boháčová K, Fuentes-Caparrós AM, et al. PAINT-ing fluorenylmethoxycarbonyl (Fmoc)-diphenylalanine hydrogels. *Chem a Eur J*. 2020;24(44):9869-9873.
49. Mayans E, Ballano G, Sendros J, et al. Effect of solvent choice on the self-assembly properties of a diphenylalanine amphiphile stabilized by an ion pair. *ChemPhysChem*. 2017;18(14):1888-1896.
50. Tomara D, Chaudharya S, Jena KC. Self-assembly of L-phenylalanine amino acid: electrostatic induced hindrance of fibril formation. *RSC Adv*. 2019;9(22):12596-12605.
51. Diaferia C, Balasco N, Sibillano T, et al. Structural characterization of self-assembled tetra-tryptophan based nanostructures: variations on a common theme. *ChemPhysChem*. 2018;19(13):1635-1642.

52. Martin DA, Wojciechowski JP, Robinson AB, et al. Controlling self-assembly of diphenylalanine peptides at high pH using heterocyclic capping groups. *Sci Rep*. 2017;7(1):43947.
53. Basavalingappa V, Guterman T, Tang Y, et al. Expanding the functional scope of the Fmoc-diphenylalanine hydrogelator by introducing a rigidifying and chemically active urea backbone modification. *Adv Sci*. 2019;6:190021.
54. Diaferia C, Balasco N, Sibillano T, et al. Amyloid-likefibrillary morphology originated by tyrosine-containing aromatic hexapeptides. *Chem a Eur J*. 2018;24(26):6804-6817.
55. Kalafatovic D, Nobis M, Son J, Anderson KI, Ulijn RV. MMP-9 triggered self-assembly of doxorubicin nanofiber depots halts tumor growth. *Biomaterials*. 2016;98:192-202.
56. Tao M, Liu J, He S, Xu K, Zhong W. In situ hydrogelation of forky peptides in prostate tissue for drug delivery. *Soft Matter*. 2019;15(20):4200-4207.
57. Baek K, Noblett AD, Ren P, Suggs LJ. Self-assembled nucleotripeptide hydrogels provide local and sustained doxorubicin release. *Biomater Sci*. 2020;8(11):3130-3137.
58. Chieh C, Meng-Che T, Chung-Shu W, Turibius F-HK. New synthesis route of hydrogel through a bioinspired supramolecular approach: gelation, binding interaction, and in vitro dressing. *ACS Appl Mater Interfaces*. 2015;7:19306-19315.
59. Zhang Y, Kuang Y, Gao Y, Xu B. Versatile small-molecule motifs for self-assembly in water and the formation of biofunctional Supramolecular hydrogels. *Langmuir*. 2011;27(2):529-537.
60. Gallo E, Diaferia C, Di Gregorio E, Morelli G, Gianolio E, Accardo A. Peptide-based soft hydrogels modified with gadolinium complexes as MRI contrast agent. *Pharmaceuticals*. 2020;13(2):19.
61. Avitabile C, Diaferia C, Roviello V, et al. Fluorescence and morphology of self-assembled nucleobases and their diphenylalanine hybrid aggregates. *Chem a Eur J*. 2019;25(65):14850-14857.
62. Diaferia C, Gosh M, Sibillano T, et al. Fmoc-FF and hexapeptide-based multicomponent hydrogels as scaffold materials. *Soft Matter*. 2019;15(3):487-496.
63. Diaferia C, Sibillano T, Altamura D, et al. Structural characterization of PEGylated hexaphenylalanine nanostructures exhibiting green photoluminescence emission. *Chem a Eur J*. 2017;23(56):14039-14048.
64. Diaferia C, Gianolio E, Sibillano T, et al. Cross-beta nanostructures based on dinaphthylalanine Gd-conjugates loaded with doxorubicin. *Sci Rep*. 2017;7(1):307.
65. Basu K, Baral A, Basak S, et al. Peptide based hydrogels for cancer drug release: modulation of stiffness, drug release and proteolytic stability of hydrogels by incorporating *D*-amino acid residue(s). *Chem Commun*. 2016;52(28):5045-5048.
66. Chan KA, Lee WH, Ni M, Loo Y, Hauser CAE. C-terminal residue of ultrashort peptides impacts on molecular self-assembly, hydrogelation, and interaction with small-molecule drugs. *Sci Rep*. 2018;8(1):17127.
67. Wang Y, Zhang Y, Li X, Li C, Yang Z, Wang L. A peptide-based supramolecular hydrogel for controlled delivery of amine drugs. *Chem Asian J*. 2018;13(22):3460-3463.
68. Dadhwal S, Fairhall GM, Goswami SK, Hook S, Gamble AB. Alkene–Azide 1,3-dipolar cycloaddition as a trigger for ultrashort peptide hydrogel dissolution. *Chem Asian J*. 2019;14(8):1143-1150.
69. Xue Q, Ren H, Xu C, et al. Nanospheres of doxorubicin as cross-linkers for a supramolecular hydrogelation. *Sci Rep*. 2015;5(1):8764.
70. Mei L, Xu K, Zhai Z, He S, Zhu T, Zhong W. Doxorubicin-reinforced supramolecular hydrogels of RGD-derived peptide conjugates for pH responsive drug delivery. *Org Biomol Chem*. 2019;17(15):3853-3860.
71. Mei L, He S, Liu Z, Xu K, Zhong W. Co-assembled supramolecular hydrogels of doxorubicin and indomethacin-derived peptide conjugates for synergistic inhibition of cancer cell growth. *Chem Commun*. 2019;55(30):4411-4414.
72. Wang F, Su H, Lin R, et al. Supramolecular tubustecan hydrogel as chemotherapeutic carrier to improve tumor penetration and local treatment efficacy. *ACS Nano*. 2020;14(8):10083-10094.
73. Wang G, Wang Z, Li C, et al. RGD peptide-modified, paclitaxel prodrug-based, dual-drugs loaded, and redox-sensitive lipid-polymer nanoparticles for the enhanced lung cancer therapy. *Biomed Pharmacother*. 2018;106:275-284.
74. Karavasili C, Panteris E, Vizirianakis IS, Koutsopoulos S, Fatouros DG. Chemotherapeutic delivery from a self-assembling peptide nanofiber hydrogel for the management of glioblastoma. *Pharm Res*. 2018;35(8):166.
75. Karavasili C, Andreadis DA, Katsamenis OL, et al. Synergistic antitumor potency of a self-assembling peptide hydrogel for the local co-delivery of doxorubicin and curcumin in the treatment of head and neck cancer. *Mol Pharm*. 2019;16(6):2326-2341.
76. Jin H, Wan C, Zou Z, et al. Tumor ablation and therapeutic immunity induction by an injectable peptide hydrogel. *ACS Nano*. 2018;12(4):3295-3310.
77. Biscaglia F, Ripani G, Rajendran S, et al. Gold nanoparticle aggregates functionalized with cyclic RGD peptides for targeting and imaging of colorectal cancer cells. *ACS Appl Nano Mater*. 2019;2(10):6436-6444.
78. Di Pietro P, Zaccaro L, Comegna D, et al. Silver nanoparticles functionalized with a fluorescent cyclic RGD peptide: a versatile integrin targeting platform for cells and bacteria. *RSC Adv*. 2016;6(113):112381-112392.
79. Ischakov R, Adler-Abramovich L, Buzhansky L, Shekhter T, Gazit E. Peptide-based hydrogel nanoparticles as effective drug delivery agents. *Bioorg Med Chem*. 2013;21(12):3517-3522.
80. Rosa E, Diaferia C, Gallo E, Morelli G, Accardo A. Stable formulation of peptide based nanogels. *Molecules*. 2020;25(15):3455.
81. Mehra RR, Tiwari P, Basu A, DuttKonar A. In search of bioinspired hydrogels from amphiphilic peptides: a template for nanoparticle stabilization for the sustained release of anticancer drugs. *New J Chem*. 2019;43(29):11666-11678.
82. Mehra RR, Basu A, Christman RM, et al. Mechanoresponsive, proteolytically stable and biocompatible supergelators from ultra-short enantiomeric peptides with sustained drug release propensity. *New J Chem*. 2020;44:6346-6354.
83. Zarzhitsky S, Rapaport H. The interactions between doxorubicin and amphiphilic and acidic β-sheet peptides towards drug delivery hydrogels. *JColl Interf Sci*. 2011;360(2):525-531.
84. Yishay-Safranchika E, Golana M, David A. Controlled release of doxorubicin and Smac-derived pro-apoptotic peptide from self-assembled KLD-based peptide hydrogels. *Polym Adv Technol*. 2014;25(5):539-544.
85. Schneible JD, Shi K, Young AT, et al. Modified graphene oxide (GO) particles in peptide hydrogels: a hybrid system enabling scheduled delivery of synergistic combinations of chemotherapeutics. *J Mater Chem B*. 2020;8(17):3852-3868.

AUTHOR BIOGRAPHIES

Dr. Carlo Diaferia received his MD in medicinal chemistry and pharmaceutical technology at University of Naples "Federico II" in 2014, completing in 2018, at the same University, his PhD in Drug Science. He currently works at the Department of Pharmacy, University of Naples "Federico II". Carlo's research activities deals with peptide synthesis and chemical decoration, supramolecular chemistry and nanotechnology. Studying

aggregation and formulation optimization, he proposed different classes of peptide-based materials for the development of nanoplatforms for application in MRI diagnostic, therapy, drug delivery systems (DDS), optoelectronic components and healthcare. He is member of ItPS (Italian Peptide Society).

Elisabetta Rosa received her MD in medicinal chemistry and pharmaceutical technology at University of Naples "Federico II" in 2019. She is currently a PhD student in Drug Science at the Department of Pharmacy, University of Naples "Federico II". Her research mainly concerns the synthesis of self-assembling peptide dervatives to obtain novel peptide-based materials (in particular hydrogels and nanogels) for application in drug-delivery, Magnetic Resonance Imaging (MRI) and tissue-engineering. She is member of ItPS (Italian Peptide Society).

Prof. Antonella Accardo obtained her PhD in Biotechnological Science in the field of supramolecular contrast agents and peptide chemistry at the University of Naples "Federico II" in 2005. She is presently associate Professor in Chemistry at the Department of Pharmacy of the University of Naples "Federico II". Her research interests lie in the synthesis of peptide derivatives and formulation of micelles and liposomes as target selective contrast agents in MRI and as drug delivery systems (DDS) for cancer diagnosis and therapy. She also focuses on the development of novel peptide based materials (nanofibers, hydrogels and nanogel) and on the investigation of their structural and functional properties.

Prof. Giancarlo Morelli is full professor of Chemistry at the Department of Pharmacy of the University of Naples "Federico II". He is Director of the Research Center on Bioactive Peptides (CIRPeB) and President of the Italian Peptide Society (ItPS). His research interests lie in peptide chemistry and in the development of peptide based supramolecular aggregates for target delivery of contrast agents and drugs.

How to cite this article: Diaferia C, Rosa E, Accardo A, Morelli G. Peptide-based hydrogels as delivery systems for doxorubicin. *J Pep Sci*. 2022;28(1):e3301. doi:10.1002/psc.3301

International Journal of
Molecular Sciences

MDPI

Article

Preparation and In Vitro Evaluation of RITUXfab-Decorated Lipoplexes to Improve Delivery of siRNA Targeting C1858T PTPN22 Variant in B Lymphocytes

Andrea Arena [1,†], Eugenia Belcastro [1,†], Antonella Accardo [2], Annamaria Sandomenico [3], Olivia Pagliarosi [1], Elisabetta Rosa [2], Stefania Petrini [4], Libenzio Adrian Conti [4], Ezio Giorda [5], Tiziana Corsetti [6], Riccardo Schiaffini [7], Giancarlo Morelli [2] and Alessandra Fierabracci [1,*]

1 Infectivology and Clinical Trials Research Department, Bambino Gesù Children's Hospital, Scientific Institute for Research, Hospitalization and Healthcare (IRCCS), 00146 Rome, Italy; aarena026@gmail.com (A.A.); eugenia.belcastro@opbg.net (E.B.); olivia.pagliarosi@opbg.net (O.P.)
2 Research Centre on Bioactive Peptides (CIRPeB), Department of Pharmacy, University of Naples Federico II, 80134 Naples, Italy; antonella.accardo@unina.it (A.A.); elisabetta.rosa@unina.it (E.R.); gmorelli@unina.it (G.M.)
3 Institute of Biostructures and Bioimaging (IBB), National Research Council (CNR), 80134 Naples, Italy; sandomenico@cnr.it
4 Confocal Microscopy Core Facility, Research Laboratories, Bambino Gesù Children's Hospital, Scientific Institute for Research, Hospitalization and Healthcare (IRCCS), 00146 Rome, Italy; stefania.petrini@opbg.net (S.P.); libenzioadrian.conti@opbg.net (L.A.C.)
5 Research Laboratories, Bambino Gesù Children's Hospital, Scientific Institute for Research, Hospitalization and Healthcare (IRCCS), 00146 Rome, Italy; ezio.giorda@opbg.net
6 Unit of Hospital Pharmacy, Bambino Gesù Children's Hospital, Scientific Institute for Research, Hospitalization and Healthcare (IRCCS), 00165 Rome, Italy; tiziana.corsetti@opbg.net
7 Diabetes and Growth Pathology Unit, Bambino Gesù Children's Hospital, Scientific Institute for Research, Hospitalization and Healthcare (IRCCS), 00165 Rome, Italy; riccardo.schiaffini@opbg.net
* Correspondence: alessandra.fierabracci@opbg.net; Tel.: +39-06-6859-2656
† These authors contributed equally to this work.

Abstract: Autoimmune endocrine disorders, such as type 1 diabetes (T1D) and thyroiditis, at present are treated with only hormone replacement therapy. This emphasizes the need to identify personalized effective immunotherapeutic strategies targeting T and B lymphocytes. Among the genetic variants associated with several autoimmune disorders, the C1858T polymorphism of the protein tyrosine phosphatase non-receptor type 22 (*PTPN22*) gene, encoding for Lyp variant R620W, affects the innate and adaptive immunity. We previously exploited a novel personalized immunotherapeutic approach based on siRNA delivered by liposomes (lipoplexes) that selectively inhibit variant allele expression. In this manuscript, we improved lipoplexes carrying siRNA for variant C1858T by functionalizing them with Fab of Rituximab antibody ($Ritux_{Fab}$-Lipoplex) to specifically target B lymphocytes in autoimmune conditions, such as T1D. $Ritux_{Fab}$-Lipoplexes specifically bind to B lymphocytes of the human Raji cell line and of human PBMC of healthy donors. $Ritux_{Fab}$-Lipoplexes have impact on the function of B lymphocytes of T1D patients upon CpG stimulation showing a higher inhibitory effect on total cell proliferation and IgM+ plasma cell differentiation than the not functionalized ones. These results might open new pathways of applicability of $Ritux_{Fab}$-Lipoplexes, such as personalized immunotherapy, to other autoimmune disorders, where B lymphocytes are the prevalent pathogenic immunocytes.

Keywords: T1D; autoimmune disease; functionalized lipoplexes; rituximab; immunotherapy; variant PTPN22

check for updates

Citation: Arena, A.; Belcastro, E.; Accardo, A.; Sandomenico, A.; Pagliarosi, O.; Rosa, E.; Petrini, S.; Conti, L.A.; Giorda, E.; Corsetti, T.; et al. Preparation and In Vitro Evaluation of RITUXfab-Decorated Lipoplexes to Improve Delivery of siRNA Targeting C1858T PTPN22 Variant in B Lymphocytes. *Int. J. Mol. Sci.* **2022**, *23*, 408. https://doi.org/10.3390/ijms23010408

Academic Editor: Arcangelo Liso

Received: 1 December 2021
Accepted: 27 December 2021
Published: 30 December 2021

Publisher's Note: MDPI stays neutral with regard to jurisdictional claims in published maps and institutional affiliations.

1. Introduction

Autoimmune diseases encompass a broad category of tissue-targeted conditions including organ-specific ones, often affecting endocrine glands like insulin-dependent

diabetes mellitus (type 1 diabetes, T1D) and thyroiditis, and non-organ specific ones like systemic lupus erythematosus (SLE), vasculitides, rheumatoid arthritis (RA) and systemic sclerosis (SS) [1]. The incidence of autoimmune diseases is increasing worldwide [2]. With reference to endocrine autoimmunity and T1D, the latter especially occurs in children below the age of five [3]. It is generally recognized that autoimmunity is caused by autoreactive effector cells, that is, autoreactive T lymphocytes for T1D whilst autoreactive B lymphocytes play a major role in SLE. Pathogenic T cell precursors result from the defective process of immunological tolerance that takes place in the thymus in perinatal age under the influence of genetic susceptibility and epigenetic modifications and it is triggered by putative exogenous and endogenous environmental agents (i.e., the microbiome) [4,5]. Nevertheless, the onset of clinical disease is caused by still unknown eliciting antigens that may be different from those which generate the tolerance breakdown and act after a long preclinical period.

Complexity and heterogeneity are the hallmarks of this category of disorders; therefore, this emphasizes the need to identify more effective strategies for their personalized prevention and treatment. At present, the only available treatment for endocrine organ-specific autoimmune disorders is the substitutive administration of the deficient hormone. Therefore, a theoretical advance is the contribution that an immunotherapeutic strategy, by halting the pathogenetic mechanism of disease, may add to preserve the hormonal cells from the autoimmune attack of autoreactive T cells [6].

Several approaches targeting the immune system have already been experimented with, but without success, especially for the treatment of T1D since insulin-independence was not achieved in diabetic patients [7,8]. Indeed, these approaches in particular explored the possibility to target T lymphocytes, the main pathogenic effectors.

B lymphocytes are also important targets in autoimmunity because they give rise to autoantibody-producing plasma cells and induce CD4+ T cell differentiation by antigen presentation. Moreover, they regulate the organization of the lymphoid system architecture and play a role in co-stimulation, controlling the function of dendritic cells and the secretion of soluble factors, that is, proinflammatory cytokines tumor necrosis factor alpha (TNF-α), interleukin (IL)-8 and IL-6 [9]. Therefore, B cell modulating therapies in B cell-mediated autoimmune diseases were attempted in order to maintain immune surveillance, eliminate effector B lymphocytes and stimulate regulatory B cells (B-regs) [10]. These strategies have employed Rituximab [11] and anti-CD20 antibodies of a new generation, that is, anti-CD19, -CD22, chimeric autoantibody receptor T (CAAR-T) cells and inhibitors of B cell receptor activation [9]. With variable applications to specific autoimmune conditions, these treatments had limited efficacy or generated adverse effects since they also affected the B-regs cellular subset or halted the humoral antigen recall response thus enhancing risk [12].

In light of the foregoing, tailored approaches of 'personalized medicine' should be attempted especially on the basis of disease susceptibility under genetic influence. With the advent of genome-wide linkage, candidate gene and genome-wide association studies [13], in addition to human leucocytes antigens, several single nucleotide polymorphisms (SNPs) were discovered to contribute to autoimmunity etiopathogenesis [14,15]. In citing examples of candidate common susceptibility genes involved in immune regulation, cytotoxic T lymphocyte-associated antigen 4 (CTLA4) suppresses T cell activation [16], forkhead box P3 (FOXP3) is involved in the differentiation of T regulatory cells (T-regs), the IL-2 receptor alpha/CD25 gene also affects the development and the function of T-regs, and the TNF-α gene, located on chromosome 6p21.3, is at the basis of the increased risk for the association of T1D and autoimmune thyroid disease (rev. in [15]). Among the others, protein tyrosine phosphatase non-receptor type 22 (*PTPN22*), encoding for the lymphoid tyrosine phosphatase (Lyp), affects the TCR signaling pathway. The C1858T polymorphism of *PTPN22*, which replaces the amino acid Arg (R) 620 with Trp (W) (R620W), encodes for a more active phosphatase, namely Lyp variant R620W. This is a potent inhibitor of T cell activation involved in several autoimmune diseases [17,18]. The variant is supposed to

have important effects at the level of thymocyte tolerization [18]. In particular, the C1858T allelic variant represents a genetic risk factor for T1D [17,19–21], Graves' disease [22], the association of T1D and autoimmune thyroid disease known as autoimmune polyglandular syndrome type 3 variant (APS3v) (rev. in [6]) and myasthenia gravis [23]. Even for non-organ specific autoimmune diseases of complex pathogenesis, the association with the *PTPN22* polymorphism was observed in Caucasians, that is, SLE (rev. in [20,24]), Wegener's granulomatosis [25] and RA patients [18,26].

We provided evidence that the C1858T *PTPN22* gene polymorphism [6,18] could be a relevant target for immunomodulation in the treatment of C1858T patients affected by an autoimmune disease, that is, T1D [6,27]. In particular, we demonstrated the possibility of achieving target down-modulation of variant C1858T *PTPN22* gene by delivering siRNA molecules with liposomes to peripheral blood mononuclear cells (PBMC) in culture [6]. Strategies can be implemented to improve the targeted delivery of lipoplexes to specific immunotypes playing a major role in the autoimmune disease pathogenesis. On a theoretical basis, this can be unraveled by using monoclonal antibodies that drive nanoparticles to T or B lymphocytes through Food and Drug Administration (FDA) approved humanized monoclonal antibodies (MoAbs) [28–30]. In light of the foregoing, the aim of this manuscript was to evaluate the possibility of generating functionalized lipoplexes with Fab of anti-CD20 (Rituximab) [30] in order to target B lymphocytes in autoimmune diseases.

2. Results

2.1. Preparation of Proteolytic Fab' Fragment

Fragment antigen binding (Fab) of Rituximab ($Ritux_{Fab}$) was prepared by reduction of the $F(ab')_2$ of Rituximab ($Ritux_{Fab2}$) obtained by a standard proteolytic cleavage with pepsin. Analytical size exclusion chromatography (SEC)-HPLC showed that both $Ritux_{Fab2}$ and $Ritux_{Fab}$ were purified to homogeneity (purity over 95%, Supplementary Figure S1A,B). Sodium dodecyl sulphate–polyacrylamide gel electrophoresis (SDS-PAGE) analysis showed that $Ritux_{Fab2}$ and $Ritux_{Fab}$ had an apparent molecular mass of ~150 kDa and ~50 kDa in native conditions, respectively (Figure 1).

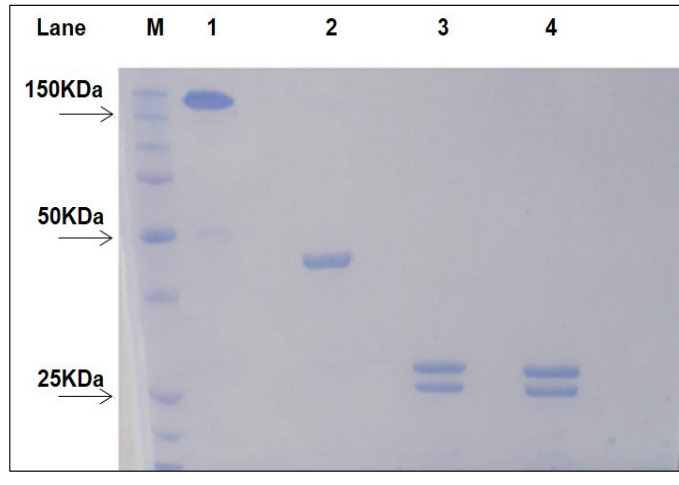

Figure 1. SDS-PAGE of purified $Ritux_{Fab2}$ and $Ritux_{Fab.}$ The two samples were loaded under non-reducing and reducing (lanes 3–4) conditions, respectively. Lane 1: non reduced $Ritux_{Fab2}$; Lane 2: non reduced $Ritux_{Fab}$; Lane 3: reduced $Ritux_{Fab2}$; Lane 4: reduced $Ritux_{Fab}$; Lane M: Protein Precision Blue MW Marker (Biorad) used as reference.

Upon reduction, the products were stained as two bands at about 25 kDa and 23 kDa, corresponding to the heavy (HC) and light chains (LC), respectively. The sequences of the LC and HC (residues 1–238) of Rituximab are reported in Figure 2 (https://go.drugbank.com/drugs/DB00073, accessed on 10 November 2021). The HC was cut by pepsin at the

C-terminus of L238 leaving, after the reduction of $F(ab)_2$, cysteine 230 and cysteine 233 side chains as free thiols. $Ritux_{Fab2}$ and $Ritux_{Fab}$ were analyzed by liquid chromatography coupled with electrospray ionization ion-traptime-of-flight mass spectrometry (LC-ESI-TOF-MS) after extensive reduction. The chromatogram showed the two distinct chains eluted at different retention times according to their hydrophobicity (LC and HC eluted at 13.9 and 14.8 min (min), respectively) (Supplementary Figure S2A). Deconvolution of mass/charge spectra of the separated chains revealed that both experimental molecular weights (MWs) were in agreement with those calculated (average MW), considering the partial reformation of the intradomain disulphide bridges. For the LC, an experimental MW of 23,035.82 Da (Supplementary Figure S2B), which was comparable to the calculated value of 23,038.33 Da, was observed. The Δmass of −2.51 Da suggested that the two intramolecular bridges were partially reformed. For the HC, an experimental MW of 25,154.86 Da (Supplementary Figure S2C), which is comparable to the calculated value of 25,175.53 Da (Δmass = −20.67 Da), was observed. In this case, the N-terminal glutamine was fully converted to pyroglutamic acid (Δmass = −17.03 Da) and the two intramolecular bridges were almost fully reformed (Δmass = −4.0 Da). Considering these modifications, the calculated MW was 25,154.50 Da and the Δmass with the experimental value was only = −0.36 Da. In order to confirm the occurrence of free cysteines in the hinge region of the HC a reaction of alkylation with 4-[(isopropylaminomethyl] phenylamine (IAM) (Δmass = +57.02 Da) was also performed on the $Ritux_{Fab}$ in native conditions and the MW was again evaluated by LC-ESI-TOF analysis under reducing conditions. The HC was detected as three main species corresponding to the polypeptide modified with one, two or three IAMs, with the double modified chain being the prevailing species. The MWs of the three species were: HC+1 IAM, experimental MW 25,211.06 Da, calculated MW 25,211.50 Da; HC+2 IAM, experimental MW 25,268.54 Da, calculated MW 25,268.52 Da; HC+3 IAM, experimental MW 25,325.33 Da, calculated MW 25,325.52 Da. The presence of the triple modified HC was likely due to an alkylation occurring after reduction. The fluorescein isothiocyanate (FITC)-labelled $Ritux_{Fab}$ was also characterized by LC-ESI-TOF analysis under reducing conditions. The MW of the LC was detected as two main species corresponding to the unmodified polypeptide (experimental MW 23,035.75 Da) and to the single modified product (experimental MW 23,425.60 Da, Δmass = +389.38 Da). The HC was identified as three main species corresponding to the unlabeled HC (experimental MW 25,155.25 Da), and to the single and double FITC-modified HC (experimental MWs: 25,544.42 Da, Δmass = +389.38 Da; 25,933.81 Da, Δmass = +778.56 Da).

>Rituximab light chain chimeric

QIVLSQSPAILSASPGEKVTMTCRASSSVSYIHWFQQKPGSSPKPWIYATSNLASGVPVRFSGSGSGTSYSLTISRV
EAEDAATYYCQQWTSNPPTFGGGTKLEIKRTVAAPSVFIFPPSDEQLKSGTASVVCLLNNFYPREAKVQWKVDNA
LQSGNSQESVTEQDSKDSTYSLSSTLTLSKADYEKHKVYACEVTHQGLSSPVTKSFNRGEC

>Rituximab heavy chain chimeric after pepsinolysis

QVQLQQPGAELVKPGASVKMSCKASGYTFTSYNMHWVKQTPGRGLEWIGAIYPGNGDTSYNQKFKGKATLTA
DKSSSTAYMQLSSLTSEDSAVYYCARSTYYGGDWYFNVWGAGTTVTVSAASTKGPSVFPLAPSSKSTSGGTAALG
CLVKDYFPEPVTVSWNSGALTSGVHTFPAVLQSSGLYSLSSVVTVPSSSLGTQTYICNVNHKPSNTKVDKKAEPKS
CDKTHTCPPCPAPEL

Figure 2. Aminoacidic sequence of intact LC and HC of Rituximab as cut following pepsin hydrolysis. Cysteine involved in intrachain disulfide bridges are underlined and reported in red. C224 of the HC and C213 of the LC that connect the chains are reported in bold green. The free cysteines present in the Fab' hinge region in the HC are in bold blue.

2.2. Circular Dichroism (CD) Structural Characterization

CD analysis was performed on $Ritux_{Fab2}$ and $Ritux_{Fab}$ fragments to evaluate proper folding in terms of secondary structure and stability. CD spectra recorded in the far-

UV region (Figure 3A–C) showed that fragments adopted a classical β-sheet secondary structure according to the Ig-like folding, with a negative band at 219 nm and a positive one at 205 nm. Thermal denaturation performed by monitoring the CD signal at 218 nm from 20 °C to 95 °C revealed a melting temperature (Tm) of 75 °C for Ritux$_{Fab2}$ and 74 °C for Ritux$_{Fab}$ (Figure 3B–D). The data suggested that the proteolytic fragments retain a correct folding and stability comparable to that of the whole antibody.

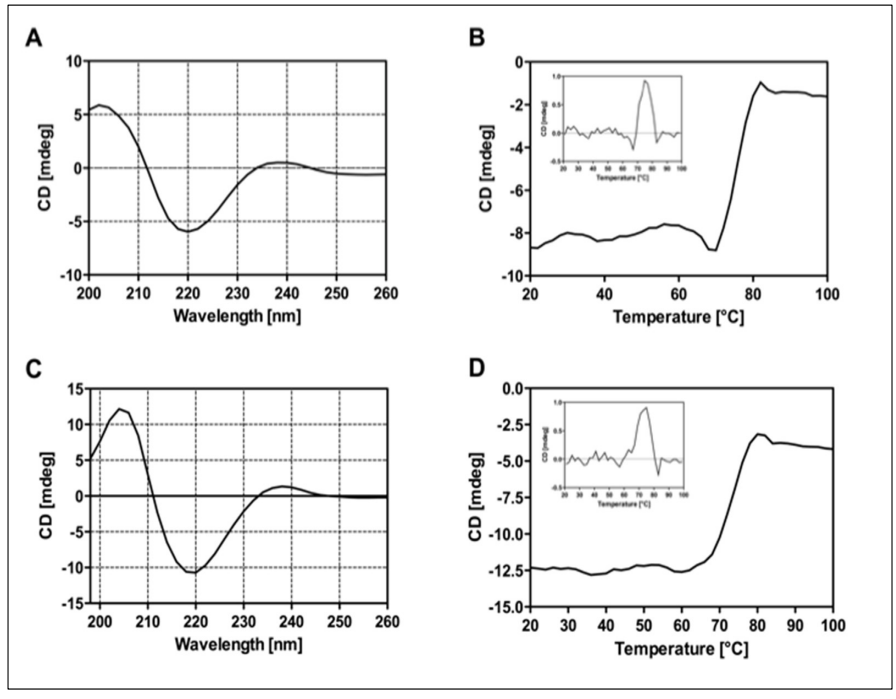

Figure 3. Panel of CD analyses. Far-UV spectra of Ritux$_{Fab2}$ (**A**) and Ritux$_{Fab}$ (**C**) recorded at the concentration of 4 μM at 20 °C. Denaturation curves were collected between 20 °C and 95 °C monitoring the CD signal at 218 nm. Ritux$_{Fab\ 2}$ (**B**) and Ritux$_{Fab}$ (**D**).

2.3. Lipoplex Formulation and DLS Characterization

Cationic liposomes were prepared using commercial phospholipid, 1,2-Dioleoyl-sn-glycero-3-phosphoethanolamine (DOPE), N-[1-(2,3-Dioleoyloxy)propyl]-N,N,N-trimethylammonium chloride (DOTAP), 1,2-distearoyl-sn-glycero-3-phosphoethanolamine-N-[maleimide(polyethylene glycol)-2000] (ammonium salt) (DSPE-PEG2000-Maleimide) (DOPE/DOTAP/DSPE-PEG2000-Maleimide) in 47.5/47.5/5 molar ratio. Briefly, the lipidic film prepared in chloroform was hydrated in phosphate buffer saline (PBS) at pH 7.4. Then, the suspension was sonicated for 30 min and extruded 10-times through a 0.1 μm polycarbonate membrane. Lipoplexes were prepared incubating the liposomal solution with siRNA at room temperature (RT) for 3 h (h). In this preparation, the amount of siRNA was 3.2 μM. Targeted Ritux$_{Fab}$-Lipoplexes were obtained by functionalizing the lipoplex with Ritux$_{Fab.}$ The coupling reaction was obtained by reacting overnight (ON), under nitrogen, the Fab' thiol function with the maleimide group, according to the Michael addition reaction. Functionalized lipoplex were purified from free Fab' by gel filtration. All the aggregates were structurally characterized by dynamic light scattering (DLS) technique. Intensity profiles of liposomal preparation are reported in Figure 4. From the inspection of the figure, it can be observed that all the distributions are monomodal with one slow diffusion mode around 150 nm. Moreover, no significant changes in the size of aggregates were observed after functionalization of the lipoplex surface with Fab'. Fluorescent lipoplexes were obtained by inserting lipophilic dye (such as Rho-PE) in the liposome formulation and functionalizing the liposomal surface with a small amount of Ritux$_{Fab}$-FITC.

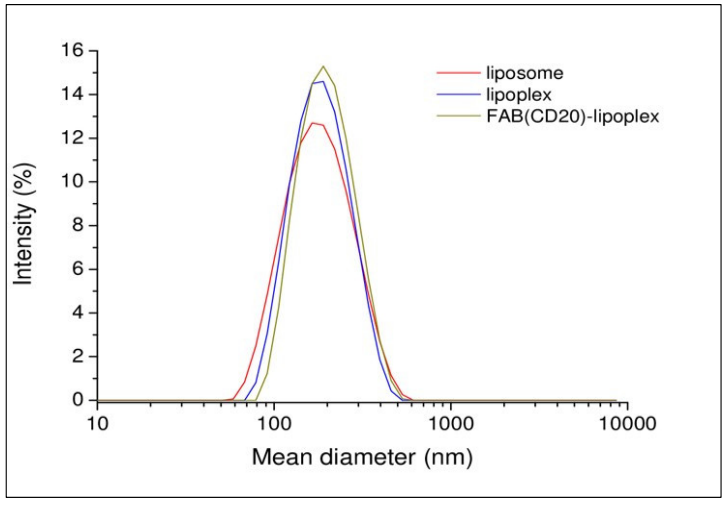

Figure 4. Intensity profiles of liposomal formulations.

2.4. Rituxfab and Liposomes Functionalized with Rituxfab Specifically Bind to Raji Cells

Flow cytometry analysis (FACS) detected specific reactivity FITC-Rituxfab to B lymphocytes of the Raji cell line (human B lymphocyte; Burkitt's lymphoma) as revealed by mean fluorescence intensity (MFI) values (Figure 5B). Further, the mixture composed of liposomes functionalized with Rituxfab/FITC-Rituxfab (90/10 mol/mol) binded efficiently and with high specificity to cells of the B lymphoma Raji cell line (Figure 5C, Supplementary Figure S3).

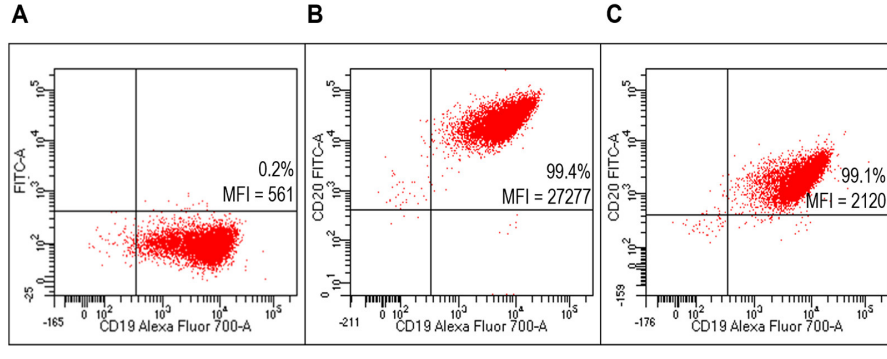

Figure 5. Evaluation of FITC-Rituxfab functionalized liposomes on Raji cells (B-cell lymphoma line). Representative FACS profiles indicating the MFI values of FITC-Rituxfab among Raji cells. Cells were stained with the anti-CD19-Alexa Fluor 700 (**A**) and FITC-Rituxfab (**B**) or liposomes functionalized with Rituxfab/FITC-Rituxfab (90/10 mol/mol) (**C**).

2.5. Rituxfab and Liposomes Functionalized with Rituxfab Specifically Bind to B Lymphocytes within Human PBMC

FACS analysis detected specific reactivity of FITC-Rituxfab to B lymphocytes within the human PBMC pool from healthy donors (HD) (Figure 6B, Supplementary Figure S4). Further, the mixture composed of liposomes functionalized with Rituxfab/FITC-Rituxfab (90/10 mol/mol) binded efficiently and with high specificity to B lymphocytes within the same pool (Figure 6C). Reactivity of FITC-Rituxfab was also revealed on B lymphocytes by confocal microscopy analysis (Figure 7).

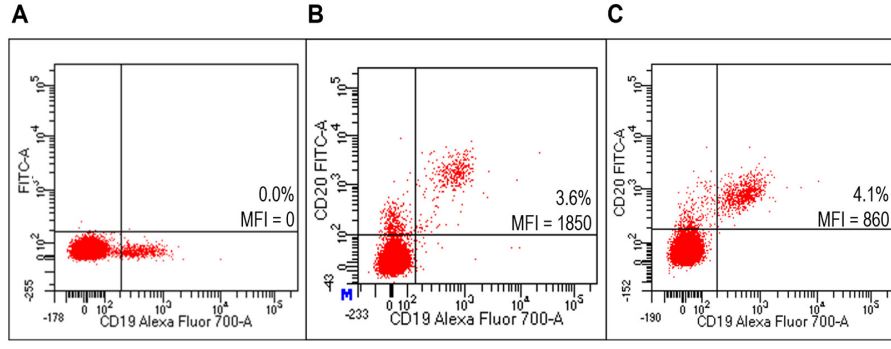

Figure 6. Evaluation of liposomes derivatized with FITC-Ritux$_{Fab}$ on HD PBMC. Representative FACS profiles indicating the MFI values of FITC-Ritux$_{Fab}$ labelled among HD PBMC. Cells were stained with the anti-CD19-Alexa Fluor700 (**A**) and FITC-Ritux$_{Fab}$ (**B**) or combination of liposomes functionalized with Ritux$_{Fab}$/FITC-Ritux$_{Fab}$ (90/10 mol/mol) (**C**).

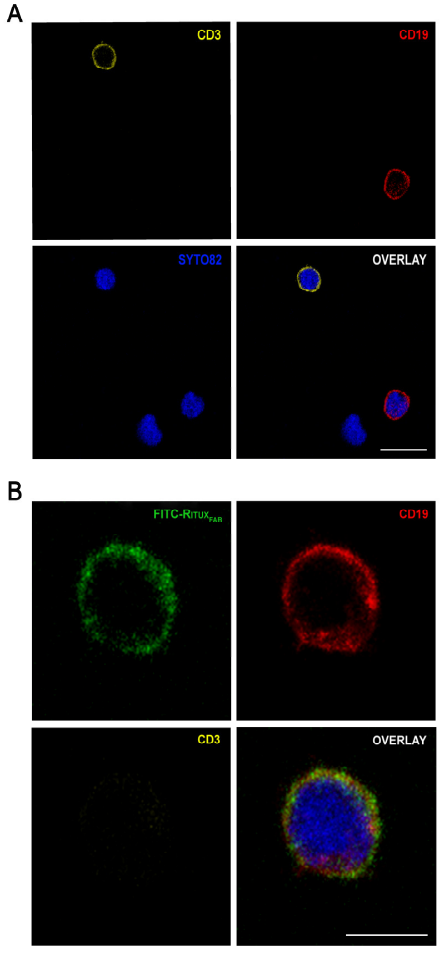

Figure 7. Confocal microscopy analysis of FITC-Ritux$_{Fab}$ in HD PBMC. Images show the expression of CD3+ (pseudocolored in orange, upper left panel) and CD19+ (red, upper right panel) cells (**A**) and the presence of FITC-Ritux$_{Fab}$ (green, upper left panel) in CD19+ (red, upper right panel) cells and the simultaneous absence in CD3+ (orange, lower left panel) (**B**) among lymphocytes within the human PBMC pool from HD. Cell nuclei are counterstained with SYTO™82 dye (pseudocolored in blue). Scale bars = 10 μm (**A**) and 5 μm (**B**).

2.6. Targeted Lipoplexes Specifically Bind to Human B Lymphocytes

Lipoplexes functionalized with FITC-Ritux$_{Fab}$ specifically binded to Raji cells (Figure 8C) compared to unlabeled lipoplex (Figure 8A). They also specifically binded to B lymphocytes within the human HD PBMC pool (Figure 9C).

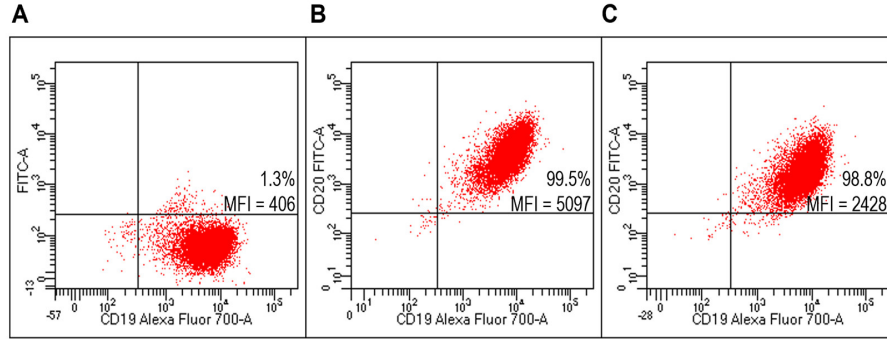

Figure 8. Evaluation of targeted lipoplexes on Raji cell line. Representative FACS profiles indicating the percentages of Fab(CD20)-FITC+ among Raji cells after staining with unlabeled and untargeted lipoplex (**A**), FITC-Ritux$_{Fab}$ (**B**) or targeted lipoplex (**C**).

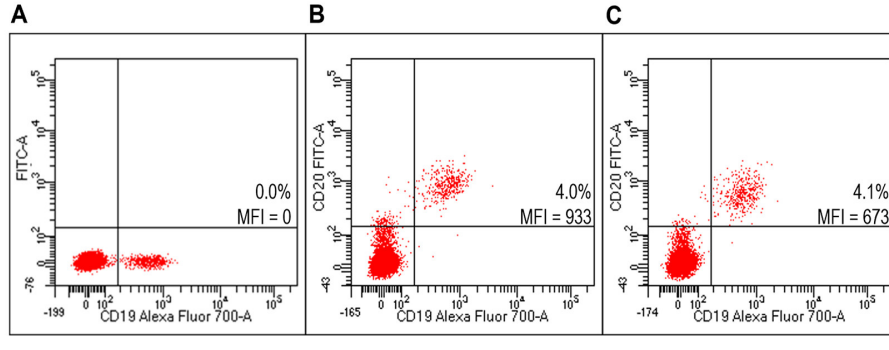

Figure 9. Evaluation of targeted lipoplexes on HD PBMC. Representative FACS profiles indicating the percentages of Fab(CD20)-FITC+ among lymphocytes after staining with unlabeled and untargeted lipoplex (**A**), FITC-Ritux$_{Fab}$ (**B**) or FITC-Ritux$_{Fab}$ lipoplexes (**C**).

By using targeted lipoplex labeled with 1,2-dioleoyl-sn-glycero-3-phosphoethanolamine-N-(7-nitro-2-1,3-benzoxadiazol-4-yl) (ammonium salt) (NBD-PE) fluorophore, we verified their specific MFI fold increase of binding to CD19+ cells on the Raji human cell line (Supplementary Figure S5) and on B lymphocytes within HD PBMC (Supplementary Figure S6) than using the corresponding untargeted lipoplexes.

2.7. Effect of Functionalized Lipoplexes on CpG—Stimulated B Lymphocytes within Human PBMC

The B cell phenotypes of the PBMC from T1D patients carrying the C1858T *PTPN22* variant after treatment of targeted and untargeted lipoplexes at 80 and 100 pmols of siRNA were analyzed after 4 days of CpG oligodeoxynucleotides stimulus (Figure 10). A significant decrease in the proliferative response (calculated as ratio of proliferation of CD19+ cells over unstimulated cells (RPMI)) was observed with targeted lipoplexes with both doses (Figure 10A).

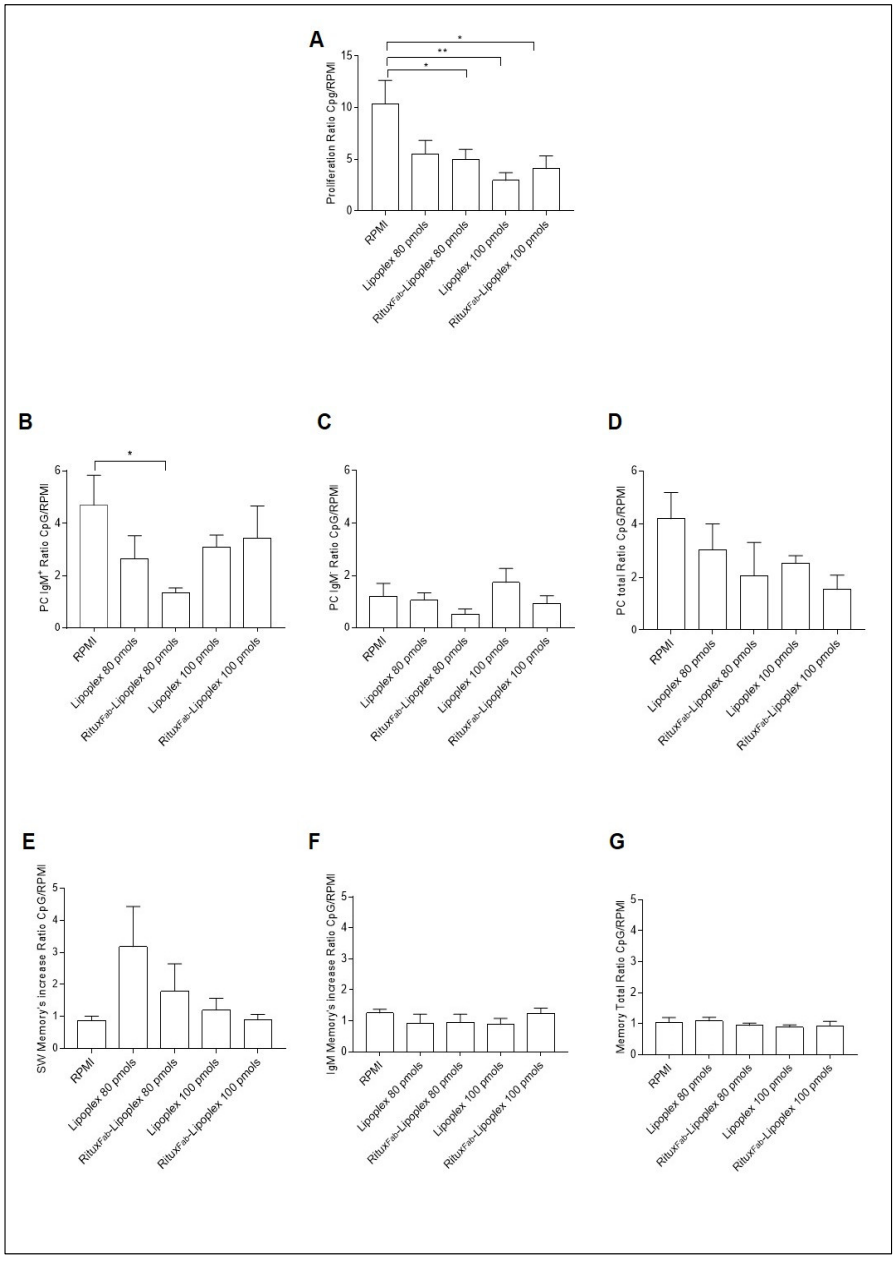

Figure 10. B cell phenotype after 4 days of CpG stimulation in T1D patients carrying the C1858T *PTPN22* variant after treatment with lipoplex and $Ritux_{Fab}$-Lipoplex at different doses. Ratio of proliferation of CpG stimulated over unstimulated CMFDA-labelled CD19+ cells (**A**), ratio of plasma cells from IgM+ (**B**), IgM− (**C**) and total (**D**) memory B cells. Ratio of switched memory (SW) B cell (**E**), IgM+ memory B cells (**F**) and total memory B cells (**G**). Data are expressed as mean ± SEM of $n = 5$. * $p < 0.05$, ** $p < 0.01$.

Regarding the specific immunophenotype, the ratio of plasma cells from IgM+ memory B cells showed a higher inhibitory effect with lipoplex at the respective concentration (Figure 10B).

3. Discussion

In this manuscript, we provided evidence of the feasibility of exposing Fab of a MoAb, that is, Rituximab on lipoplexes delivering siRNA against the C1858T *PTPN22* variant.

Indeed, functionalized lipoplexes bound themselves with high specificity to B lymphocytes of the human Raji cell line and within the PBMC pool. Remarkably, as revealed by FACS analysis, $Ritux_{Fab}$ -functionalized lipoplexes exhibited a higher fold increase of binding to B lymphocytes of the human Raji cell line and of PBMC than not functionalized lipoplexes. This evidence suggests that functionalization does not affect the biofunctionality of $Ritux_{Fab}$.

To complete the functional evaluation of $Ritux_{Fab}$-Lipoplexes, we also unraveled whether they could have a significant effect on the function of B lymphocytes with respect to unfunctionalized lipoplex in comparison to lipoplex following CpG stimulation in PBMC of an exemplary autoimmune disease, that is, T1D. Indeed, we previously observed altered B cell homeostasis and Toll-Like receptor 9-driven response in T1D carriers of the *PTPN22* C1858T allelic variant [31,32]. Data demonstrated that the IgM+ memory B cells were significantly increased in heterozygous (1858C/1858T) T1D patients compared to C/C individuals and in the groups of individuals who were heterozygous for the variant compared to C/C individuals [31]. As regards the functionalization of nanosystems like polymeric micelles and liposomes with antibodies [33] or other homing entities [34] has been widely described as a suitable strategy to achieve an "active targeting" towards specific tissues/cells overexpressing receptors, thus avoiding side effects on healthy tissues [35]. Indeed, we could demonstrate a significant higher inhibitory effect of $Ritux_{Fab}$-Lipoplexes than not functionalized ones on total B lymphocytes proliferation and IgM+ plasma cell differentiation.

The results of this investigation open future pathways to improving the specific delivery and effect of lipoplexes on immunocytes that play a pathogenetic role in different autoimmune conditions. From this initial evidence, certainly more advanced procedures could be exploited in the future to foster functionalization of lipoplexes by exposing Fab of Rituximab to increase B lymphocytes binding and consequently increase functional effect. This investigation also opens the pathway to functionalized lipoplexes with other FDA approved MoAb including anti-CD3 Teplixumab or Otelixizumab [28,29] for specific targeting of T lymphocytes in T cell-mediated diseases such as T1D.

Additional FDA-approved MoAb could be theoretically used for lipoplexes functionalization for their specific targeting delivery. As regards the integrin heterodimer leukocyte function, associated antigen-1 (LFA-1, CD11a) is a classic adhesion molecule that facilitates T and antigen-presenting cells interaction as well as functioning in activation and trafficking of leukocytes [36]. Antagonism of LFA-1 with MoAb, either alone or in combination with other agents, can induce regulatory tolerance in vivo. Efalizumab, a new generation humanized anti-LFA-1 MoAb, offers at present some promises for clinical application in immunotherapy [37]. LFA-3 (CD58) is a receptor found on the membrane of nearly all human cells. Its interaction with the counter-receptor CD2 generates effective cell–cell adhesion and it is responsible for a costimulatory signal to enhance T lymphocytes responses or modulate anergy/apoptosis. This evidence suggests that it may have therapeutic applications [38]. Alefacept is a chimeric fusion protein composed of CD2-binding portion of LFA3 linked to the Fc region of human IgG1 (LFA3-Fc). Alefacept MoAb was designed to inhibit the activation of memory T lymphocytes that contribute to chronic inflammation in psoriasis [39].

In conclusion, the present findings indicate the efficiency of functionalized lipoplexes with Fab anti-CD20 (Rituximab) to specifically target B lymphocytes in autoimmune conditions, such as T1D. These results propel future investigations of the applicability of $Ritux_{Fab}$ functionalized lipoplexes, such as personalized immunotherapy, to other autoimmune disorders, where B lymphocytes are the prevalent pathogenic immunocytes such as SLE.

4. Materials and Methods

4.1. Preparation of Rituximab F(ab')2 and Fab'

$Ritux_{Fab2}$ (CD20, ~100 kDa) was prepared by treatment with pepsin (porcine gastric mucosa pepsin, Sigma-Aldrich, Milan, Italy) using a 20/1 antibody/pepsin ratio (*w*/*w*). The reaction was performed in 100 mM acetate buffer pH 4.0, containing 10 mM ethylenedi-

aminetetraacetic acid (EDTA). After incubation for 16 h at 37 °C, the mixture was purified by SEC on a Superdex S200 column using PBS solution (Sigma-Aldrich) as running buffer [40]. $Ritux_{Fab2}$ was efficiently reduced to Fab' ($Ritux_{Fab}$, ~50 kDa) by treatment for 2 h at 37 °C with 10 mM β-mercaptoethylamine (MEA) in presence of 2 mM EDTA. After reduction, $Ritux_{Fab}$ was again purified by SEC on a Superdex S200 gel filtration column in PBS buffer. Fractions containing $Ritux_{Fab2}$ and $Ritux_{Fab}$ were analyzed by 12% SDS-PAGE under native and reducing conditions. The concentrations were determined spectrophotometrically on a Nanodrop 2000C instrument (ThermoFisher instruments, Milan, Italy) using a ε_{280nm}= 166,060 M^{-1} cm^{-1} for $Ritux_{Fab2}$ and a ε_{280nm}= 83,030 M^{-1} cm^{-1} for $Ritux_{Fab}$.

4.2. Antibody Fragments Labelling with FITC

$Ritux_{Fab2}$ was randomly labeled with FITC (Sigma Aldrich) by reacting the protein with 10-fold excess FITC in 50 mM $NaHCO_3$ pH 8.0 for 1 h at RT. The product, named FITC-$Ritux_{Fab2}$, was extensively dialyzed against PBS buffer at 4 °C, reduced with MEA to obtain FITC-$Ritux_{Fab}$ and then purified by SEC on a Superdex S200 gel filtration column. The concentration of FITC-$Ritux_{Fab}$ was determined spectrophotometrically on a Nanodrop 2000C instrument using a ε_{495nm} = 70,000 M^{-1} cm^{-1}. The presence of FITC was also evaluated by LC-ESI-TOF-MS analyses.

4.3. Analytical Characterization of $Ritux_{Fab2}$ and $Ritux_{Fab}$

Analytical SEC analyses were performed using a Biosep-SEC 2000 column (300 mm × 7.80 mm Phenomenex) in 50 mM phosphate 100 mM NaCl pH 7.5 applying a flow rate of 0.6 mL/min. UV detection was performed at 215 nm. After reduction and alkylation, the products were identified by LC-ESI-TOF analyses using a C4 BioBasic column (50 mm × 2.1 mm, ThermoFisher Scientific, Monza, Italy) connected to a LC-ESI-TOF MS system from Agilent (Cernusco sul Naviglio, Italy). Separations were obtained at 0.2 mL/min using as solvent A 0.05% *v*/*v* trifluoroacetic acid (TFA) in water and as solvent B 0.05% *v*/*v* TFA in acetonitrile applying a linear gradient from 25% to 65% solvent B in 20 min. The mass analyzer was set to operate in positive ion scan mode with mass scanning from 100 to 3200 *m*/*z*. The ion source was upgraded from the original Agilent Jet Stream (AJS) source to the dual-sprayer version for improved reference mass delivery. Nitrogen was used as drying and nebulizer gas. The instrument acquired data using the following parameters: drying gas temperature, 325 °C; drying gas flow, 10 L/min; nebulizer, 20 psi (pound per square inch) sheath gas temperature, 400 °C; sheath gas flow, 11 L/min; VCap. 3500 V; nozzle, 0 V; fragmentor, 200 V, skimmer, 65 V and octapole RF Vpp was 750. The instrument was set to extended dynamic range mode (2 GHz). Tuning and calibration were performed before sample running. Data collection and integration were performed using MassHunter workstation software (version B.05.00, Agilent Technologies, Santa Clara, CA, USA). Data were stored in both centroid and profile formats during acquisition. A constant flow of Agilent TOF reference solution through the reference nebulizer allowed the system to continuously correct for mass drift by using two independent reference lock-mass ions, purine (*m*/*z* 119.03632) and HP-922 (*m*/*z* 922.000725), to ensure mass accuracy and reproducibility. Target compounds were detected, and the data analyzed and reported using the Agilent MassHunter Qualitative software (Agilent Technologies, Santa Clara, CA, USA).

4.4. Structural Characterization of $Ritux_{Fab2}$ and $Ritux_{Fab}$ by CD

CD spectra were recorded on $Ritux_{Fab2}$ and $Ritux_{Fab}$ using a JASCO J-810 spectropolarimeter (Jasco, Cremella, Italy), equipped with a thermostated cell holder (Peltier system) to change the temperature in a controlled way and interfaced with a Neslab RTE-110 water bath. Far-UV CD spectra were recorded in quartz cuvettes 110-QS with 1.0 mm optical path length (Hellma; Mullheim, Baden, Germany) at a concentration of about 4 μM in 20 mM PBS, pH 7.5, at 20 °C. Spectra were collected in the wavelength range between 198 and 280 nm at a scanning speed of 50 nm/min, with a data pitch of 0.2 nm, a band width of 1 nm, a response of 4 s (sec) and a standard sensitivity. Thermal denaturation

experiments were performed by monitoring changes in ellipticity at 218 nm by exposure to increasing temperatures between 20 °C and 95 °C, while heating at 60 °C/h (1 °C/min). Melting points were determined by the method of the first derivative. Four independent spectra for each sample were recorded, averaged and smoothed using the Spectra Manager software, version 1.53. Final spectra were corrected by subtracting the corresponding baseline spectrum obtained under identical conditions.

4.5. Liposome Formulation

DOPE, DOTAP, DSPE-PEG2000-Maleimide and NBD-PE were purchased from Avanti Polar Lipids (Alabaster, AL, USA).

All solutions were prepared by weight and buffered at pH 7.4 using 100 mM PBS and the pH was controlled using pH meter MeterLab PHM220. Mixed liposomes DOTAP/DOPE/DSPEPEG2000-Maleimeide (47.5/47.5/5 molar ratio) were prepared by dissolving the required amounts of phospholipids in 1 mL of chloroform. Subsequently, the organic solvent was removed under a stream of nitrogen gas to obtain a homogeneous film on the wall of the vial. Any trace of the solvent was then removed, keeping the vial under vacuum for 15 min. Then, the dry lipid film was hydrated with 1.0 mL of 100 mM PBS and sonicated in an ultrasound bath for 30 min. The liposomal suspension (at a concentration of 800 µM) was extruded 10 times at RT, using a thermobarrel extruder system (Northern Lipids Inc., Vancouver, BC, Canada) under nitrogen through a polycarbonate membrane (Nucleopore Track Membrane 25 mm, Whatman, Brentford, UK) having 0.1 µm pore size. Lipoplex was prepared by adding 500 µL of a siRNA solution (5.2 µM in 0.1 mM buffer) to 500 µL of the liposome suspension. The resulting mixture was stirred at RT for 3 h. Successively, lipoplex suspension was shared in two vials: the first aliquot was diluted with an equal amount of buffer in order to obtain a final siRNA concentration of 1.3 µM (untargeted lipoplex); the second aliquot was functionalized with $Ritux_{Fab}$ or $Ritux_{Fab}$/FITC-$Ritux_{Fab}$ (90/10, mol/mol) mixture (targeted lipoplex). 0.1 equivalents of $Ritux_{Fab}$ (~0.5 mg/mL) with respect to the maleimide function were added to the liposomal suspension and the reaction was left ON. The unreacted $Ritux_{Fab}$ was removed from the lipoplex by using Sepharose CL-4B column, pre-equilibrated with 0.1 M PBS. Nude liposomes were functionalized with $Ritux_{Fab}$ according to the same procedure used for lipoplex. Liposome formulations for cytofluorimetric analysis were prepared following the same procedure described above, adding the fluorescent phospholipid NBD-PE dye to the lipid solution, during the preparation of the lipid film.

4.6. DLS Measurements

Mean diameter of liposomes and lipoplexes before and after functionalization with $Ritux_{Fab}$ was measured by DLS using a Zetasizer Nano ZS 326 (Malvern Instruments, Westborough, MA, USA). Instrumental settings for the measurements are a backscatter detector at 173° in automatic modality, temperature of 25 °C and disposable sizing cuvette as cell. DLS measurements in triplicate were carried out on aqueous samples after centrifugation at RT at 13,000 rpm for 5 min.

4.7. siRNA Design

Authentic siRNA sequences were designed to specifically target C1858T *PTPN22* gene variant (Rosetta Inpharmatics, Sigma-Aldrich, Saint Louis, MO, USA). The siRNA sequences, sense/antisense (s/a) duplexes were different for mRNA target affinity and did not comprise backbone modifications as previously reported (Italian Patent 102018000005182 released on 26 June 2020. PCT/IT2019/050095 filed on 8 May 2019) [6].

4.8. Cell Culture

PBMC were separated by Ficoll–Hypaque (Histopaque, Sigma-Aldrich, Milan, Italy) from sodium heparinized venous blood samples (5–10 mL) belonging to recruited T1D patients and HD. Subsequently, PBMC were frozen in liquid nitrogen according to standard protocols [31]. The Raji human B lymphocyte cell line (Burkitt's lymphoma) was

obtained from American Type Culture Collection (ATCC CCL-86). Liquid nitrogen frozen cells were thawed and grown in RPMI-1640 Medium (Gibco^{TM}, ThermoFisher Scientific, Waltham, MA, USA) supplemented with 10% fetal bovine serum (FBS, GE Healthcare Life Sciences, Logan, UT, USA), 2 mM L-glutamine (EuroClone S.p.A., Milan, Italy) and 1% penicillin/streptomycin (pen/strep) (EuroClone) according to established protocols [41]. Cells were incubated at 37 °C and in 5% CO_2 at a density of between 0.1 and 1 × 10^6/mL. Cells viability was determined by trypan blue dye staining. Cultures with more than 90% cell viability were used for the experiments.

4.9. FACS Analysis

4.9.1. Cytofluorimetric Analysis of Raji Cell Line and Human PBMC

Cryopreserved PBMC were quickly thawed in pre-warmed RPMI-1640 Medium (Gibco^{TM}) supplemented with 10% FBS (GE Healthcare Life Sciences), 2 mM L-glutamine (EuroClone) and 1% pen/strep (EuroClone) and centrifuged at 1200 rpm for 5 min at RT according to established protocols [31]. Cell pellets of T1D patients, HD and Raji cell line of approximately 5 × 10^5 cells were allocated for each staining condition.

In two different subsequent experiments (*vide infra*) of binding analysis, cells were stained with FITC-Ritux$_{Fab}$ and liposomal suspensions composed of Ritux$_{Fab}$/FITC-Ritux$_{Fab}$ (90/10 mol/mol). Then, the binding of FITC labelled lipoplexes functionalized with Ritux$_{Fab}$ was verified.

4.9.2. Binding of Ritux$_{Fab}$ and the Liposomal Suspensions Derivatized with Ritux$_{Fab}$/FITC-RituxF$_{ab}$ (90/10 mol/mol)

Cell pellets of Raji cells and human PBMC were incubated with a directly conjugated mouse anti-human MoAb CD19- Brilliant Ultraviolet 737 (BUV737, Clone SJ25C1; BD Biosciences, San Jose, CA, USA) at 1:20 dilution for 20 min at 4 °C in the dark. Cells were then washed in 500 µL of PBS containing 2% FBS (FACS medium, EuroClone) by centrifugation at 1200 rpm for 5 min, then incubated with 20 µL of Fab(CD20)-FITC or the mixture of liposomes decorated with Ritux$_{Fab}$/FITC-Ritux$_{Fab}$ (90/10) for 20 min at 4 °C in the dark. After incubation, the non-binding lipoplexes were aspirated carefully by fine needle, then cells were washed in 500 µL of FACS medium by centrifugation at 1200 rpm for 5 min. Data were acquired using the BD LSR Fortessa X-20 flow-cytometer (Becton and Dickinson (BD Biosciences) and analyzed by using FACSDiva software (BD Biosciences). Dead cells were excluded from analysis by side/forward scatter (SSC/FSC) gating. A minimum of fifty thousand gated events on living cells were collected per dataset.

4.9.3. Binding Assays of Ritux$_{Fab}$-Lipoplexes

Cell pellets of Raji cells and human PBMC were incubated with 50 µL of either lipoplexes or Ritux$_{Fab}$-Lipoplexes labelled with FITC for 30 min at 4 °C in the dark. To further unravel that the functionalization enriches the binding of lipoplexes to B lymphocytes, the same pellets were also incubated with lipoplexes labelled with the lipophilic fluorophore NBD-PE located in the inner lipid bilayer. In detail, 50 µL of NBD-PE labelled lipoplexes were incubated for 30 and 60 min at 4 °C in the dark. In both procedures after incubation, the non-binding lipoplexes were aspirated carefully by fine needle and then the cells were washed in 500 µL of FACS medium by centrifugation at 1200 rpm for 5 min.

4.10. Confocal Microscopy Analysis of Ritux$_{Fab}$ Binding to Human B Lymphocytes within PBMC

Cell pellets of PBMC from one healthy donor were incubated with 20 µL of FITC-Ritux$_{Fab}$ (2 mg/mL) for 30 min at 4 °C in the dark. After the incubation, the non-binding lipoplexes were aspirated by fine needle and then the cells were washed in 1 mL of PBS buffer for two times by centrifugation at 700 rpm for 5 min and fixed with paraformaldehyde 4% (*w*/*v*) (Sigma-Aldrich) for 10 min. Fixed cell suspensions were distributed drop wise onto positive charged microscope slides (Super Frost plus, Menzel-Glaser, Germany)

and dried at 37 °C. After rehydration in PBS, cells were incubated with blocking solution PBS supplemented with bovine serum albumin (Sigma-Aldrich) 5% (*w*/*v*) for 30 min at RT.

Cells were subsequently incubated with primary mouse anti-human MoAb CD3 BV510 (Clone UCHT1, 1:30 dilution, BD Biosciences) for 60 min at RT or with primary mouse anti-human MoAb CD19 (Clone HIB19, 1:10 dilution, BD Biosciences) ON at 4 °C followed, after washing, by goat anti-mouse AlexaFluor 647 secondary antibody (1:400 dilution, ThermoFisher Scientific) for 1 h at RT. Another set of cells was double stained by combining the same antibodies. After washing with PBS, cells were incubated with SYTO™82 Orange Fluorescent dye (1:1000 dilution, ThermoFisher Scientific) for 10 min at RT to counterstain nuclei. Thereafter, cells were washed with PBS and mounted in PBS 40%/glycerol 60% solution and cover-slipped before being evaluated by Leica TCS AOBS-SP8X laser-scanning confocal microscope (Leica Microsystems, Mannheim, Germany) equipped with tunable white light laser (WLL, 470–670 nm of wavelength) source, 405 nm diode laser, 3 PMT, 2 HyD detectors and an acousto-optical beam splitter (AOBS) that allowed the separation of multiple fluorescences, using a 63× (1.42 NA oil) objective. Optical single sections were acquired with a scanning mode format of 512 × 512 pixels, sampling speed of 400 Hz (pixel size of 0.103 µm), and Z-reconstructions of serial single optical sections were carried out with an electronic zoom at 3.5. Fluorochromes unmixing was performed by acquisition of automated-sequential collection of multi-channel images, in order to reduce spectral crosstalk between channels.

4.11. Functional Assay on CpG—Stimulated B Lymphocytes

In order to verify the functional effect of Fab functionalized lipoplexes, we tested them on a functional assay in which PBMC of an autoimmune condition, that is, T1D were challenged with CpG oligodeoxynucleotides (Hycult Biotechnology, Uden, The Netherlands).

4.11.1. Human Patients PBMC

PBMC of eight T1D patients heterozygous carriers of the C1858T *PTPN22* variant were recruited from the Endocrinology Division at Bambino Gesù Children's Hospital. All patients were recruited during long-term disease. The mean age at onset of disease was 8.9 years (age range 2–12.7), and the mean disease duration was 9.8 years (age range 4.4–19.2). The mean age at referral of the patients was 18.7 years (age range 11.6–31.1; two females, six males) (Table 1). Diabetics' demographic and clinical characteristics are shown in Table 1. The patients' sera were assayed for glutamic acid decarboxylase (GADA, isoform 65), protein tyrosine phosphatase insulinoma-associated antigen 2 (IA2) and anti-insulin (IAA) antibodies (Abs) by radioimmunoassay, for Abs to thyroglobulin (Tg), thyroperoxidase (TPO) and transglutaminase (tTGA) by chemiluminescence (ADVIA Centaur analyzer, Siemens Healthcare, Germany) and to parietal cells (PCA) and adrenal cortex by indirect immunofluorescence (IFL). The T1D patients presented associated autoimmune disorders, that is, autoimmune thyroid disease (Graves' disease) (patient number (N°) 4) and vitiligo (patient N° 8) (Table 1).

All recruited patients were unrelated. All subjects entered the study after written informed consent was obtained. The investigation was approved by the local Institutional Review Board (IRB) of Bambino Gesù Children's Hospital, which regulates human samples usage for experimental studies (Study protocol no. RF-2019-12369889); all procedures followed were in accordance with institutional guidelines. The informed consent was obtained from the next of kin in case of children. Consent on behalf of children was written. Participant consent was recorded using a paper-based inventory system. The IRB approved the consent procedure.

Table 1. Demographic, genetic and clinical characteristics of patients of the present study.

Patient	Gender	Age of Disease Onset (Years)	Age at Referral (Years)	Duration of Disease (Years)	Autoimm-ne Disorders	*PTPN22* Genotype	Islet Related AABs	Other AABs
1	M	11.1	19.4	8.3	T1D	1858C/1858T	GADA **5.3 U/mL**; IAA **11%**; IA2 **29 U/mL**	tTGA 0.2 U/mL; TPO 40.5 U/mL; Tg < 20.0 UI/mL
2	M	8.6	18.1	9.5	T1D	1858C/1858T	GADA 0.3 U/mL; IAA **8%**; IA2 **2.0 U/mL**	tTGA 0.2 U/mL; TPO 40.3 U/mL; Tg 17.3 U/mL
3	M	10.5	18	7.5	T1D	1858C/1858T	GADA **16 U/mL**; IAA 4.1%; IA2 **2.0 U/mL**	tTGA 0.2 U/mL; TPO < 28.0 U/mL; Tg < 20.0 UI/mL
4	M	11.9	31.1	19.2	Graves' disease T1D	1858C/1858T		tTGA 0.4 U/mL; TPO > **1300 U/mL**; Tg > **2500 U/mL**;
5	M	12.7	18.9	6.3	T1D	1858C/1858T	GADA **5.3 U/mL**; IAA **22%**; IA2 **2.3 U/mL**	tTGA < 1.9 CU; TPO < 28.0 U/mL; Tg < 20.0 UI/mL
6	F	2	15.8	13.7	T1D	1858C/1858T	GADA **18.6 U/mL**; IAA **67.0%;** IA2 0.1 U/mL	tTGA 0.20 U/mL; TPO 19.9 U/mL; Tg 15.2 U/mL
7	M	7.1	11.6	4.4	T1D	1858C/1858T	GADA**12.2 U/mL**; IAA **7.4%**; IA2 **2.7 U/mL**	tTGA 1.9 CU; TPO 30.11 U/mL; Tg < 20.0 UI/mL
8	F	7.2	16.7	9.5	T1D Vitiligo	1858C/1858T	GADA **1.8 U/mL**; IAA 2.4%; IA2 **15 U/mL**	tTGA 0.2 U/mL; TPO 35.9 U/mL; Tg < 20.0 UI/mL

4.11.2. Stimulation of PBMC with CpG and Proliferation Assay

Liquid-nitrogen frozen PBMC from T1D patients were quickly thawed as previously described [31]. Cells were centrifuged at 1200 rpm for 5 min at RT and seeded in 48-well plates (flat bottom, Falcon, Corning, NY, USA) at a density of 1.5×10^6 per well in a final volume of 250 µL of FBS-free RPMI 1640 medium containing L-glutamine (2 mM) and treated with different doses of lipoplex and $Ritux_{Fab}$-Lipoplex (80 and 100 pmols of siRNA). After approximately 16 h (ON) of transfection, cells were washed in complete RPMI by 1200 rpm centrifugation for 5 min at RT.

Before stimulation, PBMC were labeled with 5-chloromethylfluorescein diacetate (CMFDA) (CellTracker, Invitrogen, Molecular Probes, Eugene, OR, USA) at a final concentration of 0.1 mg/mL and cultured at 7.5×10^5 cells per well in 96-well plates (Falcon, Labware BD Biosciences, Oxnard, CA, USA) in complete RPMI 1640 medium supplemented with 10% FBS (Hyclone, South Logan, UT, USA), L-glutamine (2 mM) and 1% pen/strep. The cells were stimulated with human CpG at a concentration of 5 mg/mL and supplemented with IL-2 (25 IU/mL, Sigma Aldrich) according to established protocol [31]. IL-2 was added to the cultures because we found that it improved cell survival in cryopreserved pathological samples without altering cell function. The cells were incubated for 4 days at 37 °C in a humidified atmosphere containing 5% CO_2. In parallel, basal PBMC cultures were set up by incubating PBMC from the same individual with complete medium plus IL-2 as a control. After 4 days of CpG stimulation, PBMC were harvested from the culture plates and washed by centrifugation at 1200 rpm for 5 min at RT in FACS medium. To identify B cell subsets, single-cell suspensions were stained with the appropriate combination of the following directly conjugated MoAbs: CD19-BUV 737 (1:20 dilution; BD Biosciences), CD38-PECy7 (1:90 dilution; BD Biosciences), CD27-PE (1:20 dilution; BD Biosciences) and IgM-Alexa Fluor 647 (1:400 dilution; Jackson ImmunoResearch, West Baltimore Pike, PA, USA). Cells were incubated for 20 min in the dark at 4 °C. After labelling, cells were washed by centrifugation at 1200 rpm for 5 min at 4 °C in FACS medium. Data were acquired using BD LSR Fortessa X-20 flow-cytometer (BD Biosciences) and analyzed by using FACSDiva software (BD Biosciences). Dead cells were excluded from the analysis by side/forward scatter gating. A minimum of fifty thousand gated events on living cells were collected per dataset.

4.12. Statistical Analysis

Values are expressed as means ± SEM. Differences between each test condition were assessed by one-way ANOVA followed by Bonferroni and Dunnett's multiple comparison tests, for the functional assay on T1D PBMC. Differences between CD19+/Ritux$_{Fab}$ and CD19+/FITC-Ritux$_{Fab}$ cells were assessed by the unpaired Mann–Whitney *t*-test, for the binding of FITC-Ritux$_{Fab}$ functionalized liposome to Raji cells and lipoplexes functionalized with Ritux$_{Fab}$/FITC-Ritux$_{Fab}$ (90/10 mol/mol) to HD PBMC experiments. Differences between CD19+/Lipoplex-NBD PE+ and CD19+/Ritux$_{Fab}$-Lipoplex-NBD PE+ cells were determined by the unpaired Mann–Whitney *t*-test, for the binding of functionalized NBD PE-lipoplexes to Raji cells and human B lymphocytes within the PBMC pool. The statistical study was performed with GraphPad Prism (version 7, San Diego, CA, USA). The difference was considered statistically significant at $p < 0.05$.

5. Patents

Italian Patent 102018000005182 released on 26 June 2020. PCT/IT2019/050095 filed on 8 May 2019. Inventor: Dr. Alessandra Fierabracci. Property: Bambino Gesù Children's Hospital, IRCCS, Rome, Italy.

Supplementary Materials: The following supporting information can be downloaded at: https://www.mdpi.com/article/10.3390/ijms23010408/s1.

Author Contributions: A.F., G.M. Conceptualization; A.A. (Andrea Arena), E.B. Data curation; E.B., A.A. (Andrea Arena), S.P., L.A.C., E.G. Formal analysis; A.F. Funding acquisition; A.F., E.B., A.A. (Andrea Arena), O.P., A.A. (Antonella Accardo), A.S. Investigation; A.F., E.B., A.A. (Andrea Arena), A.A. (Antonella Accardo), A.S., E.R. Methodology; A.F. Project administration; A.F., R.S., G.M., E.G., S.P., A.A. (Antonella Accardo), T.C. Resources; E.B., A.A. (Andrea Arena), S.P., L.A.C., E.G. Software; A.F., G.M. Supervision; A.F., G.M. Validation; E.B., A.A. (Andrea Arena), A.F., G.M, A.A. (Antonella Accardo), A.S., E.G. Visualization; A.F., A.A. (Andrea Arena), G.M, A.A. (Antonella Accardo), A.S. Writing—original draft; A.F., E.B., G.M., A.A. (Antonella Accardo), A.S. Writing—review & editing. A.A. (Andrea Arena), E.B. contributed equally to this work. All authors have read and agreed to the published version of the manuscript.

Funding: This work was supported by the Italian Ministry of Health Ricerca Finalizzata RF-2019-12369889 to A.F.

Institutional Review Board Statement: The study was conducted according to the guidelines of the Declaration of Helsinki, and approved by the Institutional Review Board of Bambino Gesù Children's Hospital, which regulates human samples usage for experimental studies (Study protocol n°. RF-2019-12369889).

Informed Consent Statement: The informed consent was obtained from the next of kin in case of children. Consent on behalf of children was written. Participant consent was recorded using a paper-based inventory system. The Institutional Review Board approved the consent procedure.

Data Availability Statement: The original contributions presented in the study are included in the article/Supplementary Materials; further inquiries can be directed to the corresponding author.

Acknowledgments: We thank Giuseppe Bianco (Unit of Hospital Pharmacy, Bambino Gesù Children's Hospital, IRCCS, Rome, Italy) for providing Rituximab.

Conflicts of Interest: The authors declare no conflict of interest.

References

1. Sanz, I.; Lund, F. Complexity and heterogeneity-the defining features of autoimmune disease. *Curr. Opin. Immunol.* **2019**, *61*, iii–vi. [CrossRef] [PubMed]
2. Kahaly, G.J.; Frommer, L. Autoimmune polyglandular diseases. *Best Pract. Res. Clin. Endocrinol. Metab.* **2019**, *33*, 101344. [CrossRef]
3. Norris, J.M.; Johnson, R.K.; Stene, L.C. Type 1 diabetes-early life origins and changing epidemiology. *Lancet Diabetes Endocrinol.* **2020**, *8*, 226–238. [CrossRef]

4. Gianchecchi, E.; Fierabracci, A. Recent Advances on Microbiota Involvement in the Pathogenesis of Autoimmunity. *Int. J. Mol. Sci.* **2019**, *20*, 283. [CrossRef] [PubMed]
5. Fierabracci, A. Unravelling the role of infectious agents in the pathogenesis of human autoimmunity: The hypothesis of the retroviral involvement revisited. *Curr. Mol. Med.* **2009**, *9*, 1024–1033. [CrossRef]
6. Pellegrino, M.; Ceccacci, F.; Petrini, S.; Scipioni, A.; De Santis, S.; Cappa, M.; Mancini, G.; Fierabracci, A. Exploiting novel tailored immunotherapies of type 1 diabetes: Short interfering RNA delivered by cationic liposomes enables efficient down-regulation of variant PTPN22 gene in T lymphocytes. *Nanomedicine* **2019**, *18*, 371–379. [CrossRef]
7. Woittiez, N.J.; Roep, B.O. Impact of disease heterogeneity on treatment efficacy of immunotherapy in type 1 diabetes: Different shades of gray. *Immunotherapy* **2015**, *7*, 163–174. [CrossRef]
8. Atkinson, M.A.; Ogle, G.D. Improving diabetes care in resource-poor countries: Challenges and opportunities. *Lancet Diabetes Endocrinol.* **2013**, *1*, 268–270. [CrossRef]
9. Musette, P.; Bouaziz, J.D.; Musette, P.B. Cell Modulation Strategies in Autoimmune Diseases: New Concepts. *Front. Immunol.* **2018**, *9*, 622. [CrossRef]
10. Wortel, C.M.; Heidt, S. Regulatory B cells: Phenotype, function and role in transplantation. *Transpl. Immunol.* **2017**, *41*, 1–9. [CrossRef]
11. Berghen, N.; Vulsteke, J.B.; Westhovens, R.; Lenaerts, J.; De Langhe, E. Rituximab in systemic autoimmune rheumatic diseases: Indications and practical use. *Acta Clin. Belg.* **2019**, *74*, 272–279. [CrossRef]
12. Van der Kolk, L.E.; Baars, J.W.; Prins, M.H.; van Oers, M.H. Rituximab treatment results in impaired secondary humoral immune responsiveness. *Blood* **2002**, *100*, 2257–2259. [CrossRef]
13. Lessard, C.J.; Ice, J.A.; Adrianto, I.; Wiley, G.B.; Kelly, J.A.; Gaffney, P.M.; Montgomery, C.G.; Moser, K.L. The genomics of autoimmune disease in the era of genome-wide association studies and beyond. *Autoimmun. Rev.* **2012**, *11*, 267–275.
14. Tobón, G.J.; Pers, J.O.; Cañas, C.A.; Rojas-Villarraga, A.; Youinou, P.; Anaya, J.M. Are autoimmune diseases predictable? *Autoimmun. Rev.* **2012**, *11*, 259–266. [CrossRef] [PubMed]
15. Fierabracci, A.; Milillo, A.; Locatelli, F.; Fruci, D. The putative role of endoplasmaticreticulum aminopeptidases in autoimmunity: Insights from genome-wide association studies. *Autoimmun. Rev.* **2012**, *12*, 281–288. [CrossRef] [PubMed]
16. Wang, K.; Zhu, Q.; Lu, Y.; Lu, H.; Zhang, F.; Wang, X.; Fan, Y. CTLA-4+49 G/a polymorphism confers autoimmune disease risk: An updated meta-analysis. *Genet. Test. Mol. Biomark.* **2017**, *21*, 222–227. [CrossRef] [PubMed]
17. Vang, T.; Congia, M.; Macis, M.D.; Musumeci, L.; Orrú, V.; Zavattari, P.; Nika, K.; Tautz, L.; Taskén, K.; Cucca, F.; et al. Autoimmune associated lymphoid tyrosine phosphatase is a gain-of-function variant. *Nat. Genet.* **2005**, *37*, 1317–1319. [CrossRef] [PubMed]
18. Gianchecchi, E.; Palombi, M.; Fierabracci, A. The putative role of the C1858T polymorphism of protein tyrosine phosphatase PTPN22 gene in autoimmunity. *Autoimmun. Rev.* **2013**, *12*, 717–725. [CrossRef] [PubMed]
19. Bottini, N.; Musumeci, L.; Alonso, A.; Rahmouni, S.; Nika, K.; Rostamkhani, M.; MacMurray, J.; Meloni, G.F.; Lucarelli, P.; Pellecchia, M.; et al. A functional variant of lymphoid tyrosine phosphatase is associated with type I diabetes. *Nat. Genet.* **2004**, *36*, 337–338. [CrossRef]
20. Bottini, N.; Vang, T.; Cucca, F.; Mustelin, T. Role of PTPN22 in type 1 diabetes and other autoimmune diseases. *Semin. Immunol.* **2006**, *18*, 207–213. [CrossRef]
21. Zheng, W.; She, J.X. Genetic association between a lymphoid tyrosine phosphatase PTPN22) and type 1 diabetes. *Diabetes* **2005**, *54*, 906–908. [CrossRef]
22. Velaga, M.R.; Wilson, V.; Jennings, C.E.; Owen, C.J.; Herington, S.; Donaldson, P.T.; Ball, S.G.; James, R.A.; Quinton, R.; Perros, P.; et al. The codon 620 tryptophan allele of the lymphoid tyrosine phosphatase (LYP) gene is a major determinant of Graves' disease. *J. Clin. Endocrinol. Metab.* **2004**, *89*, 5862–5865. [CrossRef]
23. Vandiedonck, C.; Capdevielle, C.; Giraud, M.; Krumeich, S.; Jais, J.P.; Eymard, B.; Tranchant, C.; Gajdos, P.; Garchon, H.J. Association of the PTPN22*R620W polymorphism with autoimmune myasthenia gravis. *Ann. Neurol.* **2006**, *59*, 404–407. [CrossRef]
24. Ferreira, R.C.; Castro Dopico, X.; Oliveira, J.J.; Rainbow, D.B.; Yang, J.H.; Trzupek, D.; Todd, S.A.; McNeill, M.; Steri, M.; Orrù, V.; et al. Chronic Immune Activation in Systemic Lupus Erythematosus and the Autoimmune PTPN22 Trp620 Risk Allele Drive the Expansion of FOXP3+ Regulatory T Cells and PD-1 Expression. *Front. Immunol.* **2019**, *10*, 2606.
25. Jagiello, P.; Aries, P.; Arning, L.; Wagenleiter, S.E.; Csernok, E.; Hellmich, B.; Gross, W.L.; Epplen, J.T. The PTPN22 620W allele is a risk factor for Wegener's granulomatosis. *Arthritis Rheum* **2005**, *52*, 4039–4043. [CrossRef] [PubMed]
26. Begovich, A.B.; Carlton, V.E.H.; Honigberg, L.A.; Schrodi, S.J.; Chokkalingam, A.P.; Alexander, H.C.; Ardlie, K.J.; Huang, Q.; Smith, A.M.; Spoerke, J.M.; et al. A missense single-nucleotide polymorphismin a gene encoding a protein tyrosine phosphatase (PTPN22) is associated with rheumatoid arthritis. *Am. J. Hum. Genet.* **2004**, *75*, 330–337. [CrossRef] [PubMed]
27. Perri, V.; Pellegrino, M.; Ceccacci, F.; Scipioni, A.; Petrini, S.; Gianchecchi, E.; Lo Russo, A.; De Santis, S.; Mancini, G.; Fierabracci, A. Use of short interfering RNA delivered by cationic liposomes to enable efficient down-regulation of PTPN22 gene in human T lymphocytes. *PLoS ONE* **2017**, *12*, e0175784. [CrossRef] [PubMed]
28. Gaglia, J.; Kissler, S. Anti-CD3 Antibody for the Prevention of Type 1 Diabetes: A Story of Perseverance. *Biochemistry* **2019**, *58*, 4107–4111. [CrossRef] [PubMed]

29. Herold, K.C.; Bundy, B.N.; Long, S.A.; Bluestone, J.A.; DiMeglio, L.A.; Dufort, M.J.; Gitelman, S.E.; Gottlieb, P.A.; Krischer, J.P.; Linsley, P.S.; et al. An Anti-CD3 Antibody, Teplizumab, in Relatives at Risk for Type 1 Diabetes. *New Engl. J. Med.* **2019**, *381*, 603–613. [CrossRef]
30. Crickx, E.; Weill, J.C.; Reynaud, C.A.; Mahévas, M. Anti-CD20-mediated B-cell depletion in autoimmune diseases: Successes, failures and future perspectives. *Kidney Int.* **2020**, *97*, 885–893. [CrossRef]
31. Gianchecchi, E.; Crinò, A.; Giorda, E.; Luciano, R.; Perri, V.; Lorusso, A.; Cappa, M.; Rosado, M.M.R.; Fierabracci, A. Altered B cell homeostasis and toll-like receptor 9-driven response in type 1 diabetes carriers of the C1858T PTPN22 allelic variant: Implications in the disease pathogenesis. *PLoS ONE* **2014**, *9*, 110755. [CrossRef]
32. Rieck, M.; Arechiga, A.; Onengut-Gumuscu, S.; Greenbaum, C.; Concannon, P.; Buckner, J.H. Genetic variation in PTPN22 corresponds to altered function of T and B lymphocytes. *J. Immunol.* **2007**, *179*, 4704–4710. [CrossRef]
33. Kennedy, P.J.; Sousa, F.; Ferreira, D.; Pereira, C.; Nestor, M.; Oliveira, C.; Granja, P.L.; Sarmento, B. Fab-conjugated PLGA nanoparticles effectively target cancer cells expressing human CD44v6. *Acta Biomater.* **2018**, *81*, 208–218. [CrossRef]
34. Accardo, A.; Tesauro, D.; Morelli, G. Peptide-based targeting strategies for simultaneous imaging and therapy with nanovectors. *Polym. J.* **2013**, *45*, 481–493. [CrossRef]
35. Bae, Y.H.; Park, K. Targeted drug delivery to tumors: Myths, reality and possibility. *J. Control Release* **2011**, *153*, 198–205. [CrossRef]
36. Nicolls, M.R.; Gill, R.G. LFA-1 (CD11a) as a therapeutic target. *Am. J. Transplant.* **2006**, *6*, 27–36. [CrossRef]
37. Talamonti, M.; Spallone, G.; Di Stefani, A.; Costanzo, A.; Chimenti, S. Efalizumab. *Expert Opin Drug Saf.* **2011**, *10*, 239–251. [CrossRef]
38. Brown, M.H.; Cantrell, D.A.; Brattsand, G.; Crumpton, M.J.; Gullberg, M. The CD2 antigen associates with the T-cell antigen receptor CD3 antigen complex on the surface of human T lymphocytes. *Nature* **1989**, *339*, 551–553. [CrossRef] [PubMed]
39. Heffernan, M.P.; Leonardi, C.L. Alefacept for psoriasis. *Semin. Cutan Med. Surg.* **2010**, *29*, 53–55. [CrossRef] [PubMed]
40. Selis, F.; Focà, G.; Sandomenico, A.; Marra, C.; Di Mauro, C.; Saccani Jotti, G.; Scaramuzza, S.; Politano, A.; Sanna, R.; Ruvo, M.; et al. Pegylated Trastuzumab Fragments Acquire an Increased in Vivo Stability but Show a Largely Reduced Affinity for the Target Antigen. *Int. J. Mol. Sci.* **2016**, *17*, 491. [CrossRef] [PubMed]
41. Rich, S.A.; Bose, M.; Tempst, P.; Rudofs, U.H. Purification, Microsequencing, and Immunolocalization of p36, a New Interferon-α-induced Protein That Is Associated with Human Lupus Inclusions. *J. Biol. Chem.* **1996**, *271*, 1118–1126. [CrossRef] [PubMed]

pubs.acs.org/Biomac

Article

Cell Adhesion Motif-Functionalized Lipopeptides: Nanostructure and Selective Myoblast Cytocompatibility

Elisabetta Rosa, Lucas de Mello, Valeria Castelletto, Mark L. Dallas, Antonella Accardo, Jani Seitsonen, and Ian W. Hamley*

Cite This: *Biomacromolecules* 2023, 24, 213−224

Read Online

ACCESS | Metrics & More | Article Recommendations | Supporting Information

ABSTRACT: The conformation and self-assembly of four lipopeptides, peptide amphiphiles comprising peptides conjugated to lipid chains, in aqueous solution have been examined. The peptide sequence in all four lipopeptides contains the integrin cell adhesion RGDS motif, and the cytocompatibility of the lipopeptides is also analyzed. Lipopeptides have either tetradecyl (C_{14}, myristyl) or hexadecyl (C_{16}, palmitoyl) lipid chains and peptide sequence WGGRGDS or GGGRGDS, that is, with either a tryptophan-containing WGG or triglycine GGG tripeptide spacer between the bioactive peptide motif and the alkyl chain. All four lipopeptides self-assemble above a critical aggregation concentration (CAC), determined through several comparative methods using circular dichroism (CD) and fluorescence. Spectroscopic methods [CD and Fourier transform infrared (FTIR) spectroscopy] show the presence of β-sheet structures, consistent with the extended nanotape, helical ribbon, and nanotube structures observed by cryogenic transmission electron microscopy (cryo-TEM). The high-quality cryo-TEM images clearly show the coexistence of helically twisted ribbon and nanotube structures for C_{14}-WGGRGDS, which highlight the mechanism of nanotube formation by the closure of the ribbons. Small-angle X-ray scattering shows that the nanotapes comprise highly interdigitated peptide bilayers, which are also present in the walls of the nanotubes. Hydrogel formation was observed at sufficiently high concentrations or could be induced by a heat/cool protocol at lower concentrations. Birefringence due to nematic phase formation was observed for several of the lipopeptides, along with spontaneous flow alignment of the lyotropic liquid crystal structure in capillaries. Cell viability assays were performed using both L929 fibroblasts and C2C12 myoblasts to examine the potential uses of the lipopeptides in tissue engineering, with a specific focus on application to cultured (lab-grown) meat, based on myoblast cytocompatibility. Indeed, significantly higher cytocompatibility of myoblasts was observed for all four lipopeptides compared to that for fibroblasts, in particular at a lipopeptide concentration below the CAC. Cytocompatibility could also be improved using hydrogels as cell supports for fibroblasts or myoblasts. Our work highlights that precision control of peptide sequences using bulky aromatic residues within "linker sequences" along with alkyl chain selection can be used to tune the self-assembled nanostructure. In addition, the RGDS-based lipopeptides show promise as materials for tissue engineering, especially those of muscle precursor cells.

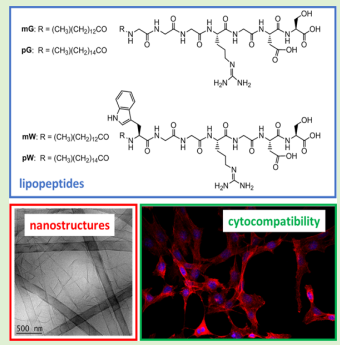

INTRODUCTION

The integrin cell adhesion peptides RGD and RGDS are minimal units of a domain present in proteins such as fibrinogen, fibronectin, and vitronectin.[1,2] These sequences have been extensively used in the development of synthetic bionanomaterials for applications in cell growth and differentiation or tissue scaffolding[3−12] and for the delivery of therapeutics.[13−15] The RGDS tetrapeptide has antithrombolytic activity resulting from the inhibition of platelet aggregation due to the fibrinogen recognition sequence.[16,17] The RGD and RGDS motifs have been incorporated into lipopeptides, one type of peptide amphiphile (PA).[6,9,18−30] In some reports, the RGDS tetrapeptide is purported to have enhanced bioactivity compared to RGD due to the additional serine residue.[31−35] The self-assembly of materials containing RGD-peptide sequences has been reviewed elsewhere.[11,35]

Lipopeptides comprise a peptide sequence attached to one or more alkyl chains. This confers amphiphilicity and leads to self-assembly, often into extended fibril structures, although other morphologies can be accessed through appropriate molecular design. The remarkable self-assembly properties of lipopeptides have been reviewed elsewhere.[36−43] Lipidation is also a practical strategy used to enhance the stability of peptide therapeutics in vivo,[44,45] and extended fibril structures with a lipid core enable the presentation of peptide motifs at high density on the surface, potentially enhancing bioactivity.[40,42,46]

Received: September 1, 2022
Revised: November 23, 2022
Published: December 15, 2022

https://doi.org/10.1021/acs.biomac.2c01068
Biomacromolecules 2023, 24, 213−224

Scheme 1. Structures of Lipopeptides Studied

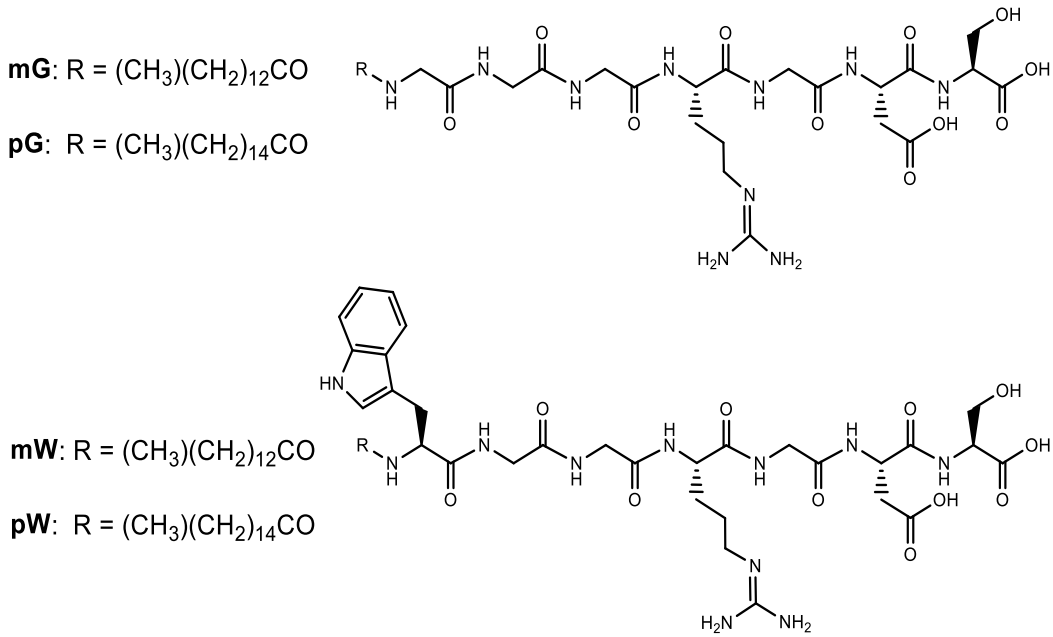

Lipopeptides self-assemble in solution into a range of nanostructures of which elongated nanostructures (fibrils and nanotapes) are the most commonly reported, although micelles and vesicles have also been observed in a few cases.[36−43] Remarkably, some lipopeptides form nanotubes in which the nanotube wall comprises molecular bilayers (i.e., with a peptide coating on both the inner and outer surface). This mode of self-assembly results from the closure of helical ribbon structures arising from the twisting of lipopeptide nanotapes.[47−50] This has also been observed for certain unlipidated amyloid peptides.[48,49,51−63] Other types of peptide nanotubes can also form via distinct mechanisms including the direct packing of cyclic peptides,[64,65] from coiled-coil oligomerization of parallel arrays of α-helical peptides into hollow-core aggregates,[66−68] from packing of α-helices perpendicular to the nanotube wall in a so-called "cross-α" nanotube architecture,[69−71] or others.[72−78] The mode of self-assembly of lipopeptides depends on a variety of molecular features including peptide sequence (charge and its distribution, placement of bulky residues, etc.) and lipid chain length. This is exploited herein, in a comparison of four lipopeptides with two different peptide sequences (but retaining the same bioactive RGDS motif) and two different lipid chains, both of sufficient length (above C_{12}[79]) to lead to amphiphilicity and hence self-assembly. Due to the remarkable range of self-assembled structures of lipopeptides and their diversity of activities, there is great interest in the use of these bioinspired/bioderived materials for applications in nanotechnology, nanobiotechnology, and nanomedicine.

Here, we investigate the effect of the sequence and alkyl chain length on the self-assembly and cytocompatibility of lipopeptides bearing a bioactive C-terminal RGDS (arginine−glycine−aspartic acid−serine) cell adhesion motif sequence. The RGDS sequence is linked to the alkyl chain via a spacer, either GGG or WGG; that is, the N-terminal residue comprises either just the simple (nonchiral) glycine (G) or with one G replaced with bulky aromatic tryptophan (W). In the latter case, tryptophan can also serve as a fluorescence reporter. We also compare the behaviors of lipopeptides bearing myristyl (tetradecyl, C_{14}) or palmitoyl (hexadecyl, C_{16}) lipid chains. The structures of the lipopeptides are shown in Scheme 1. The Hamley group previously studied the self-assembly of C_{16}-GGGRGDS (pG) in comparison with C_{16}-GGGRGD,[24] and their mixtures with C_{16}-ETTES, the latter serving as a negatively charged diluent in our development of supports for tissue engineering.[80] This work has subsequently led to the development of bioactuators for corneal tissue engineering (curved cornea-shaped stromal tissue equivalents)[28] and RGD-terminated lipopeptides which also incorporate matrix metalloprotease substrate sequences have also been used in the development of protease-responsive self-releasing tissue as part of a project to create a biomimetic cornea.[81,82] Lipopeptides C_{16}-GGGRGDS and C_{16}-GGGRGD both self-assemble into nanotapes with an internal bilayer structure.[24] We also investigated the interaction of C_{16}-GGGRGDS with apolipoprotein-AI.[83]

Here, we find that self-assembly can be tuned by the incorporation of a bulky residue (tryptophan) and/or by adjustment of the lipid chain length. We also carefully examined the cytocompatibility of the lipopeptides comparing the fibroblast and myoblast cell lines. Although both cell types are used in tissue engineering and regenerative medicine, myoblasts are precursors of muscle cells and are of particular current interest in the Hamley laboratory for a project on new biomaterials for cultured (synthetic) meat. The production of cultured meat involves the in vitro generation of muscle cells from myoblasts.[84−87] Tissue engineering of skeletal muscle or cardiac muscle also relies on myoblast cytocompatibility.[88−92] Previous work has demonstrated the use of lipopeptides in tissue engineering of smooth muscle cells with enhanced cytocompatibility and/or bioactivity,[93−99] although, to the best of our knowledge, the compatibility of lipopeptides with myoblasts has not been demonstrated. This is of interest since

https://doi.org/10.1021/acs.biomac.2c01068
Biomacromolecules 2023, 24, 213−224

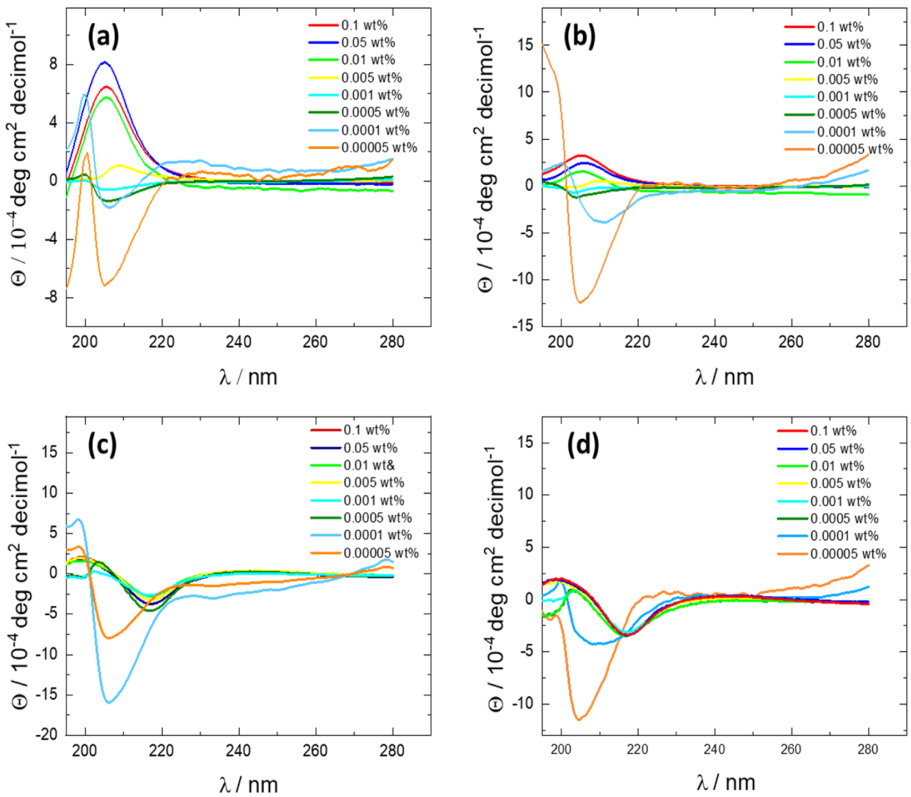

Figure 1. CD spectra at the concentrations indicated for (a) mG, (b) pG, (c) mW, and (d) pW.

the use of myoblasts may be advantageous in controlling the differentiation process and ultimate cell morphology.

EXPERIMENTAL SECTION

Materials. Peptides were obtained from Peptide Synthetics (Peptide Protein Research), Farnham, UK, as trifluoroacetic acid (TFA) salts with >95% purity as confirmed by reverse phase-high-performance liquid chromatography (RP-HPLC). Molar masses by electrospray ionization mass spectrometry are 814.94 g mol^{-1} (C_{14}-GGGRGDS, mG), 842.98 g mol^{-1} (C_{16}-GGGRGDS, pG), 943.68 g mol^{-1} (C_{14}-WGGRGDS, mW), and 971.72 g mol^{-1} (C_{16}-WGGRGDS, pW).

Sample Preparation. All the peptide solutions were prepared by dissolving the peptides at different concentrations in a phosphate-buffered saline (PBS) solution at 10 mmol L^{-1} at pH = 7.4.

CD Spectroscopy. Far-UV circular dichroism (CD) spectra were collected using a Chirascan spectropolarimeter (Applied Photophysics, Leatherhead, UK) equipped with a thermal controller. Peptides solved in PBS were placed in 0.1 or 10 mm quartz cells depending on their concentration (5×10^{-5}, 1×10^{-4}, 5×10^{-4}, 1×10^{-3}, 5×10^{-3}, 1×10^{-2}, 5×10^{-2}, 1×10^{-1}, and 5×10^{-1} and 1 wt %). Spectra were recorded from 280 to 195 nm. Other experimental settings were 0.5 nm step, 1 nm bandwidth, and 1 s collection time per step. Each spectrum was obtained by averaging three scans and correcting for the blank. The critical aggregation concentrations (CACs) of the peptides were obtained by plotting the molar ellipticity at the wavelength of maximum ellipticity, λ_{max}, as a function of the concentration.

Fourier Transform Infrared (FTIR) Spectroscopy. A Thermo-Scientific Nicolet iS5 instrument equipped with a DTGS detector, with a Specac Pearl liquid cell with CaF_2 plates to fix the sample, was used to collect the spectra of peptides at the concentration of 0.1, 0.5, and 1 wt % for mG and pG and 0.1 and 0.5 wt % for mW and pW. A total of 128 scans for each sample were recorded over the range of 900−4000 cm^{-1}.

Polarized Optical Microscopy. A drop of the peptide solution was placed on a microscope slide and stained with a 1 wt % Congo red aqueous solution. Congo red is a dye which shows apple-green birefringence when staining amyloid β-sheet structures.[100−102] After covering the sample with a microscope coverslip, it was observed through the crossed polarizers of an Olympus BX41 polarized microscope. Images were captured using a Canon G2 digital camera fitted to the microscope.

Fluorescence Spectroscopy. Fluorescence experiments were carried out using a 10.0 mm × 5.0 mm quartz cell in a Varian Model Cary Eclipse spectrofluorometer. Excitation and emission bandwidths of 2.5 nm were used as experimental settings. The temperature was set at 20 °C for all the experiments.

The CAC for all the peptides was assessed by fluorescence experiments with thioflavin T (ThT), a cationic benzothiazole dye that shows enhanced fluorescence around 485 nm upon binding to amyloid fibers.[101−104] Peptide solutions at different concentrations were prepared by dissolving the peptide powder in a PBS solution of ThT, concentration 50 μmmol L^{-1}. Samples were excited at 450 nm, and fluorescence emission spectra were recorded between 460 and 600 nm.

Emission spectra for mW and pW at different concentrations were collected from 290 to 500 nm after excitation at 280 nm. The self-fluorescence properties were studied by exciting the peptides at a range of wavelengths between 350 and 580 nm.

Small-Angle X-ray Scattering. Small-angle X-ray scattering experiments were performed on beamline SWING at the SOLEIL synchrotron (Gif-sur-Yvette, France).[105] Solution samples were delivered to a quartz capillary under vacuum in the X-ray beam using a BioSAXS setup. Gels were loaded into a plastic support sandwiched between two polyimide foils held in place by a metal frame. Data were collected using an in-vacuum EigerX-4M detector, with an X-ray wavelength of 1.033 Å at two sample-to-detector

https://doi.org/10.1021/acs.biomac.2c01068
Biomacromolecules 2023, 24, 213−224

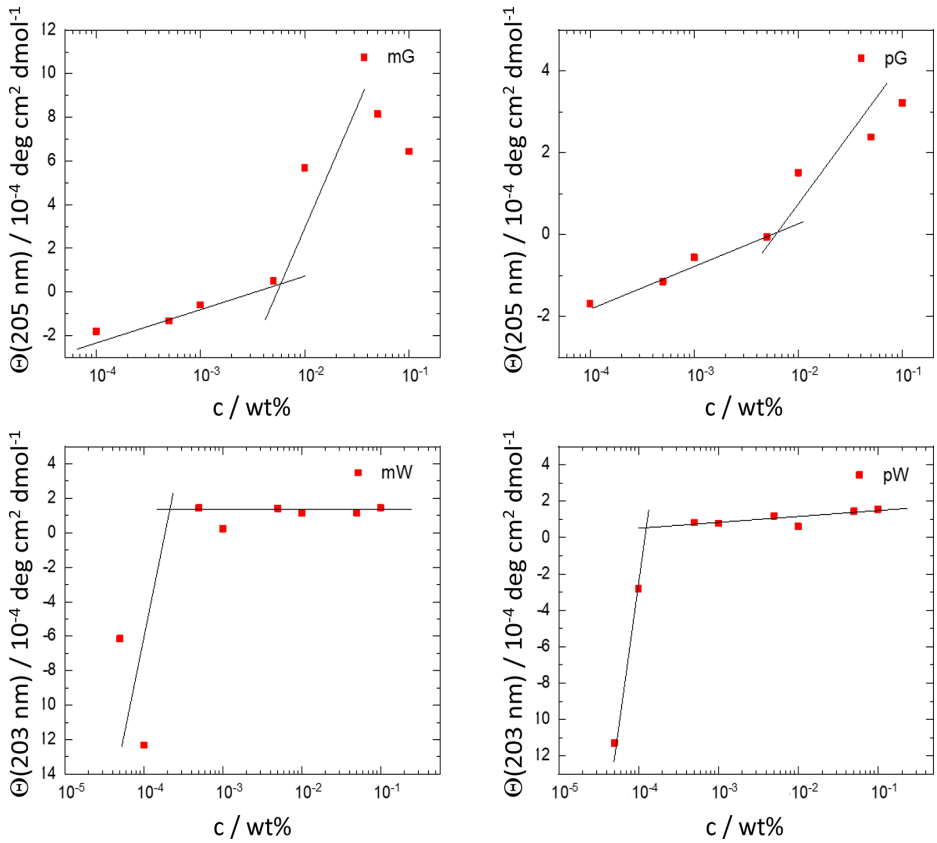

Figure 2. Determination of CAC values from concentration-dependent discontinuities in molar ellipticity values (at 205 nm for mG and pG and 203 nm for mW and pW).

distances, 6.217 and 0.517 m. Data were reduced to one-dimensional form (except the raw two-dimensional patterns where anisotropy was observed) and averaged and background-subtracted using the software Foxtrot.[105]

Cryogenic-TEM. Imaging was carried out using a field emission cryoelectron microscope (JEOL JEM-3200FSC), operating at 200 kV. Images were taken in bright field mode and using zero loss energy filtering (omega type) with a slit width of 20 eV. Micrographs were recorded using a Gatan Ultrascan 4000 CCD camera. The specimen temperature was maintained at −187 °C during the imaging. Vitrified specimens were prepared using an automated FEI Vitrobot device using Quantifoil 3.5/1 holey carbon copper grids with a hole size of 3.5 μm. Just prior to use, grids were plasma-cleaned using a Gatan Solarus 9500 plasma cleaner and then transferred into the environmental chamber of a FEI Vitrobot at room temperature and 100% humidity. Thereafter, 3 μL of the sample solution was applied on the grid and it was blotted twice for 5 s and then vitrified in a 1/1 mixture of liquid ethane and propane at a temperature of −180 °C. The grids with the vitrified sample solution were maintained at liquid nitrogen temperature and then cryotransferred to the microscope.

Cell Lines. L929 murine fibroblast and C2C12 immortalized mouse myoblast cell lines (both from ECACC General Cell Collection) were grown in Dulbecco's modified Eagle's medium (DMEM) supplemented with 10% fetal bovine serum, 20 mM HEPES, and 1% GlutaMAX. The cells were maintained at pH 7.4, 37 °C, and 5% CO_2 in 25 cm^2 cell culture flasks.

Cytotoxicity Assays. Cells were seeded in 96-well plates at a density of 0.6 × 10^4 cells per well. Cells were then treated with peptides dissolved in the medium at the concentrations of 0.1 and 1 × 10^{-4} wt %. To test cytocompatibility in the presence of the hydrogels, wells were filled with 1 wt % mG and pG hydrogels before seeding. At the end of the treatment (after 24 or 72 h), cell viability was assessed using an MTT [3-(4, 5-dimethylthiazolyl-2)-2, 5-diphenyltetrazolium bromide] assay. In brief, after the removal of the culture medium, MTT, dissolved in DMEM at a concentration of 0.5 mg/mL, was added to the cells and incubated for 4 h at 37 °C. The resulting formazan crystals were dissolved by adding dimethyl sulfoxide. Absorbance values of blue formazan were determined at 560 nm using an automatic plate reader. Cell survival was expressed as a percentage of viable cells in the presence of peptides, compared to control cells grown in their absence. The assay was repeated three times, and the results were averaged. Statistical significance was tested using multiple Welch's *t*-tests. All analyses were conducted using Prism 7.

RESULTS AND DISCUSSION

Secondary Structure and CAC. The secondary structure of the four lipopeptides was probed in PBS solutions using CD and FTIR spectroscopy. At lower concentrations, all the peptides present a random coil organization, confirmed by the shape of the CD spectra (Figure 1), characterized by a minimum at 205 nm. At the highest concentrations, for mG and pG, the CD spectra are dominated by a positive band with a maximum centered at 205 nm, while for mW and pW spectra, a characteristic of β-sheet structures is observed,[106−108] with a negative band centered at 216 nm and a positive band centered at 203 nm. The CD spectra of elongated PA nanostructures typically present positive bands due to β-sheets at ∼200−205 nm and negative ones around 220 nm, associated with $\pi \rightarrow \pi^*$ and $n \rightarrow \pi^*$ transitions, respectively. However, it is possible to find some cases in which the signal around 220 nm is only weakly or not detectable in non-aromatic PAs.[109] The lack of the typical

https://doi.org/10.1021/acs.biomac.2c01068
Biomacromolecules 2023, 24, 213−224

negative CD band can be due to overlap with the absorption region of other groups such as arginine, as previously observed for PAs containing the RGD sequence.[24] Although mG and pG do not show typical β-sheet CD profiles above the CAC (they lack a minimum near 216 nm), the presence of β-sheet structures was confirmed by FTIR spectroscopy to be discussed shortly, as well as the observation of extended nanostructures by cryogenic-TEM (cryo-TEM) and small-angle X-ray scattering (SAXS) (vide infra).

To check the consistency of different methods of determining CAC values, we compared data from previously employed fluorescence probes and tryptophan fluorescence methods with less widely used analysis of discontinuities in CD spectra. The former are sensitive to changes in the local environment of the fluorophore upon aggregation (e.g., the formation of hydrophobic domains), whereas the latter is sensitive to the secondary structure of the peptide, which may also change in the self-assembled state. It should also be noted that analysis of CD spectra or W fluorescence avoids the use of added probe molecules, which could potentially influence aggregation properties. Considering CD first, the CACs were initially estimated by plotting the molar ellipticity of the first positive maximum near 205 nm as a function of the concentration. The data is shown in Figure 2. The CACs determined from the intersection point of linear extrapolations of the data were found to be $(6.02 \pm 0.03) \times 10^{-3}$ wt %, $(6.49 \pm 0.08) \times 10^{-3}$ wt %, $(2.16 \pm 0.05) \times 10^{-4}$ wt %, and $(1.26 \pm 0.03) \times 10^{-4}$ wt % for mG, pG, mW, and pW, respectively.

For comparison, the CAC was also obtained for the two tryptophan-containing lipopeptides from W self-fluorescence measurements. Emission spectra of the two tryptophan-containing peptides were collected at different concentrations after excitation at 280 nm. At higher concentrations, an emission peak at 320 nm is visible. This shift indicates that tryptophan is located in a hydrophobic environment.[110−112] By plotting the fluorescence intensity at 320 nm as a function of the concentration (Figure S1), the concentration at the break point (corresponding to the CAC) was found to be $(2.16 \pm 0.05) \times 10^{-4}$ wt % for mW and $(3.75 \pm 0.04) \times 10^{-4}$ wt % for pW. These data are consistent with those obtained with the CD studies. For all the peptides, the CAC was also determined by collecting emission spectra of the amyloid-sensitive dye ThT in the presence of increasing amounts of the lipopeptide. Plotting the fluorescence intensity at 482 nm as a function of the concentration (Figure S2) leads to CAC values of $(4.59 \pm 0.05) \times 10^{-3}$ wt %, $(2.87 \pm 0.04) \times 10^{-3}$ wt %, $(3.10 \pm 0.07) \times 10^{-3}$ wt %, and $(3.55 \pm 0.08) \times 10^{-3}$ wt % for mG, pG, mW, and pW, respectively. The values for mG and pG are in good agreement with those obtained from the analysis of CD spectra; however, the values for mW and pW are significantly (by about an order of magnitude) higher than those from CD or tryptophan fluorescence. This is ascribed to interference between ThT and W fluorescence (e.g., resonance energy transfer), and also, it is well documented that W in its aggregated form can exhibit a weak emission that can overlap with the spectral region of ThT-aggregates (450−480 nm). These findings suggest that measurements using ThT fluorescence in the presence of peptides containing tryptophan should be used with caution. The CAC values obtained from the different methods are compared in Table S2.

The value of the CAC for pG may be compared to the previously reported CAC value determined from ThT fluorescence, CAC = 4.7×10^{-3} wt %.[24] The value reported here is reassuringly consistent with that obtained from a separate measurement on a different batch of the sample, and we also highlight the consistent value obtained from ThT and CD for mG and pG.

Further information on the secondary structure of self-assembled peptides was obtained from FTIR spectroscopy. FTIR spectra were measured for 0.1 and 1 wt % mG and pG and 0.1 and 0.5 wt % mW and pW. Spectra are plotted in the region of the amide I region, from 1700 and 1600 cm^{-1}, as this is used to characterize the secondary structure of peptides.[45,101,113−116] The FTIR spectra shown in Figures 3 and

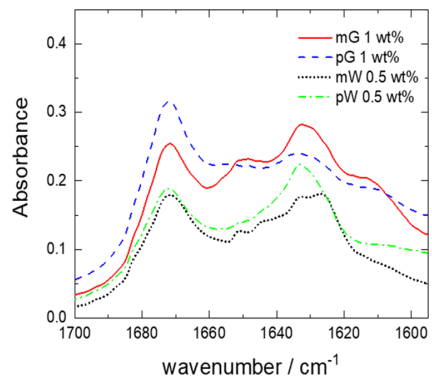

Figure 3. FTIR spectra at the concentrations indicated.

S3 for the four lipopeptides suggest that solutions of all of them contain a significant β-sheet structure because of the presence of bands at 1631 (and 1612 cm^{-1}) for mG and pG and 1633 and 1626 cm^{-1} for mW and pW.[45,101,113,115,116] The peak at 1672 cm^{-1} is attributed to the TFA counterions bound to cationic residues in the peptide[114,117,118] (here: arginine). A minor α-helix component can be observed for all the peptides, as shown by the band centered at 1651 cm^{-1}, while the spectra for mG and pG also contain a minor random coil component, which gives rise to the peak at 1644 cm^{-1}. The presence of β-sheet peaks in the FTIR spectra for mG and pG indicates that this structure forms at a higher concentration (1 wt % used for FTIR measurements) than those studied by CD (Figure 1a,b).

It is known that β-sheet aggregates can undergo self-fluorescence.[119−121] Self-fluorescence of the two myristoyl-modified peptides (mW and mG) at a concentration of 0.05 wt % was tested by exciting the sample in a range of wavelengths between 350 and 580 nm. A self-fluorescence phenomenon is visible after excitation between 380 and 400 nm (Figure S4).

Self-Assembly and Gelation. Cryo-TEM was used to image self-assembled nanostructures in aqueous solution. The images for 0.1 wt % solutions are shown in Figure 4 (additional selected images are presented in Figure S5) and show that mG forms twisted nanotape structures which notably comprise arrays of individual filaments. A similar structure is observed for pG, although with a less pronounced filament structure within the nanotapes. The nanostructures in a solution of mW and pW are distinct from those of the two glycine-containing lipopeptides. Remarkably, mW forms right-handed twisted helical ribbons coexisting with closed nanotubes (in which the wrapped helical ribbon structure can still be seen within the walls) (Figure 4c). The mean diameter of the nanotubes is (178 ± 25) nm with a wall thickness of less than 10 nm. The coexistence of helical ribbons and nanotubes provides visual evidence for the mechanism of nanotube formation via the

https://doi.org/10.1021/acs.biomac.2c01068
Biomacromolecules 2023, 24, 213−224

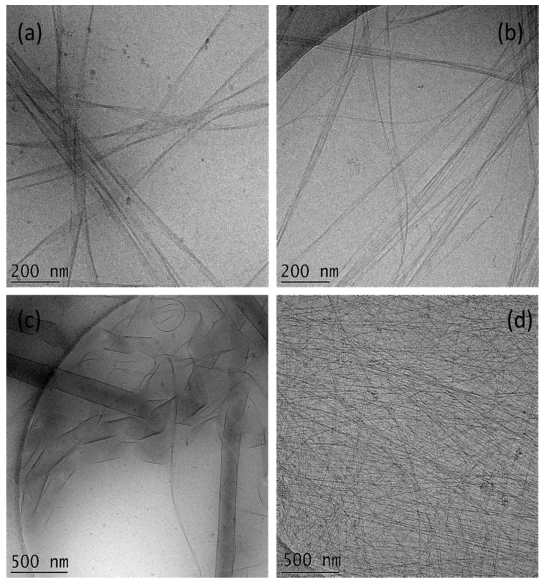

Figure 4. Cryo-TEM images from 0.1 wt % solutions (a) mG, (b) pG, (c) mW, and (d) pW.

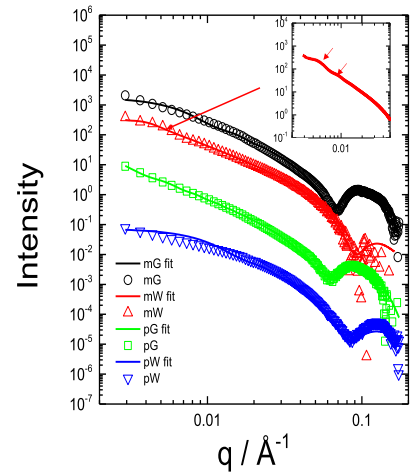

Figure 5. SAXS data from solutions (every fifth data point shown and curves shifted for ease of visualization, along with the model form factor fits described in the text). Inset: data for mW at low q on an expanded intensity scale (and with all data points shown along with form factor fit) to show form factor oscillations resulting from the nanotube structure. The solution concentrations and form factor fit parameters are listed in Table S1.

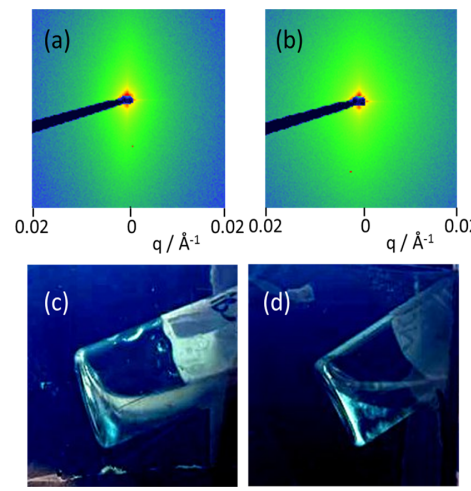

Figure 6. Data showing nematic phase formation by mW and pW (0.5 wt % solutions). Spontaneous alignment in SAXS patterns due to flow in capillaries: (a) mW and (b) pW. Images of solutions in vials between crossed polarizers: (c) mW and (d) pW.

closure of helical ribbon structures. This process has been reported previously for several lipopeptide systems[47,48,57,60,122,123] and shows that nanotube walls comprise layers of lipopeptide molecules arranged perpendicular to the tube walls. The Cryo-TEM images for the sample pW (e.g., Figure 4d) show that it forms a dense network of long intertwined thin fibers with a mean diameter of 4.0 nm. The cryo-TEM images show that the presence of tryptophan in mW and pW significantly alters the molecular packing compared to nonchiral and flexible glycine in mG and pG, and this in turn influences the nanostructure.

Cryo-TEM was complemented with SAXS which provides quantitative information on the shape and dimensions of self-assembled nanostructures via analysis of the form factor.[124] SAXS data for solutions of the four lipopeptides is shown in Figure 5. Consistent with cryo-TEM, the form factors for mG, pG, and pW can be fitted using form factors of nanotapes with an internal bilayer structure (hydrophobic lipid and peptide sublayers). The fit parameters are listed in Table S1. The bilayer thickness is in the range of 35−46 Å. Considering the estimated molecular lengths for myristyl-conjugated heptapeptides (42 Å) or palmitoyl-conjugated heptapeptides (44 Å), these values indicate highly interdigitated bilayers and/or regions where residues are not in extended β-sheet conformation. As revealed by cryo-TEM, mW exhibits unique self-assembly behavior into helical ribbons coexisting with nanotubes. The SAXS form factor data could be fitted using a simple model of nanotubes (i.e., a cylindrical shell), as shown in Figure 5. The fit parameters in Table S1 indicate a nanotube radius of 750 Å, consistent with the cryo-TEM image in Figure 4c. The nanotube wall thickness is 64 Å; that is, it comprises a bilayer (of partly interdigitated molecules), this also being consistent with cryo-TEM.

Two-dimensional SAXS patterns (Figure 6a,b) show that mW and pW solutions (0.5 wt %) show strong anisotropy at low wavenumber q, indicating that the samples comprise nematic phases which align under flow (some anisotropy was also observed for the corresponding solution of mG). This feature was also confirmed by the macroscopic birefringence examined for samples placed in glass vials between crossed polarizers (Figure 6c,d).

The gelation capability of each peptide was tested at a concentration of 1 wt % in PBS. Samples were prepared by simply dissolving the peptide powder in PBS. After 10 min of sonication, as shown from an inverted test tube study (Figure 7), only mG and pG were able to form self-supporting hydrogels. This behavior can potentially be explained considering the less hydrophobic nature of the Gly residue compared to Trp. Moreover, a Gly residue has a lower steric hindrance compared to Trp, thus allowing a better packing of peptide side chains. These features could enable the formation of a more hydrophilic interface within the peptide network, with the capability to retain larger amounts of water.

https://doi.org/10.1021/acs.biomac.2c01068
Biomacromolecules 2023, 24, 213−224

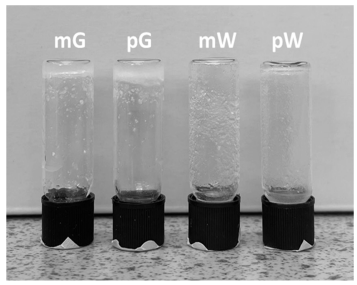

Figure 7. Tube inversion test showing hydrogel formation in 1 wt % PBS solutions of mG and pG.

Cryo-TEM images collected for the hydrogels of mG and pG are shown in Figure S6. These show that mG forms aligned straight nanotapes (apparently comprising parallel filaments as in the nanostructures in solution, Figure 4a) with a mean thickness of 13.6 nm. The hydrogel of pG contains twisted nanotapes (Figure S6b), again a structure similar to that observed in solution at 0.1 wt % (Figure 4b). The cryo-TEM images for the hydrogels thus confirm that these comprise similar nanotape structures to those formed in solution. This is also supported by the SAXS data for hydrogels shown in Figure S7a which have similar form factor profiles to those shown for the solution data in Figure 5.

Spontaneously formed hydrogels of 1 wt % mG and pG and 0.5 wt % mW and pW suspensions were stained with a Congo red solution and then visualized by optical microscopy (Figure S8). Under cross-polarized light, all of them exhibit characteristic green birefringence, suggesting an amyloid-like organization. SAXS data was measured for hydrogels of mW and pW (Figure S7b), and the form factor features are similar to those measured in solution, which indicates that the hydrogels and suspensions are formed from a network of entangled fibrils.

CD spectra collected for mG and pG hydrogels (Figure S9) have a similar shape to those for solutions above the CAC, with a positive band at 205 nm (Figure 1). By rotating the samples to four different positions, the CD profile was not found to differ (data not shown). This result excludes the presence of artifacts such as contributions from linear dichroism and confirms the homogeneity of the hydrogels.

In addition to spontaneous hydrogel formation at 1 wt % of mG and pG, it was possible to produce hydrogels after heat treatment (to 60 °C, followed by cooling to room temperature and leaving the sample for 24 h) for lower-concentration samples (0.5 wt %). Images of inverted tubes are shown in Figure S10, while Figures S11 and S12 show the corresponding FTIR and CD spectra. The inverted tube test showed that all four peptides form hydrogels, although the gel of pW was very soft and not self-supporting. The FTIR spectra measured for hydrogels formed after heating 0.5 wt % peptide solutions (Figure S11) reveal that a β-sheet organization is preserved for all the samples, as attested by the peaks at 1632 cm^{-1} for mG, 1629 cm^{-1} for pG, 1632 and 1624 cm^{-1} for mW, and 1636 and 1623 cm^{-1} for pW. The peaks at 1651, 1649, and 1652 cm^{-1}

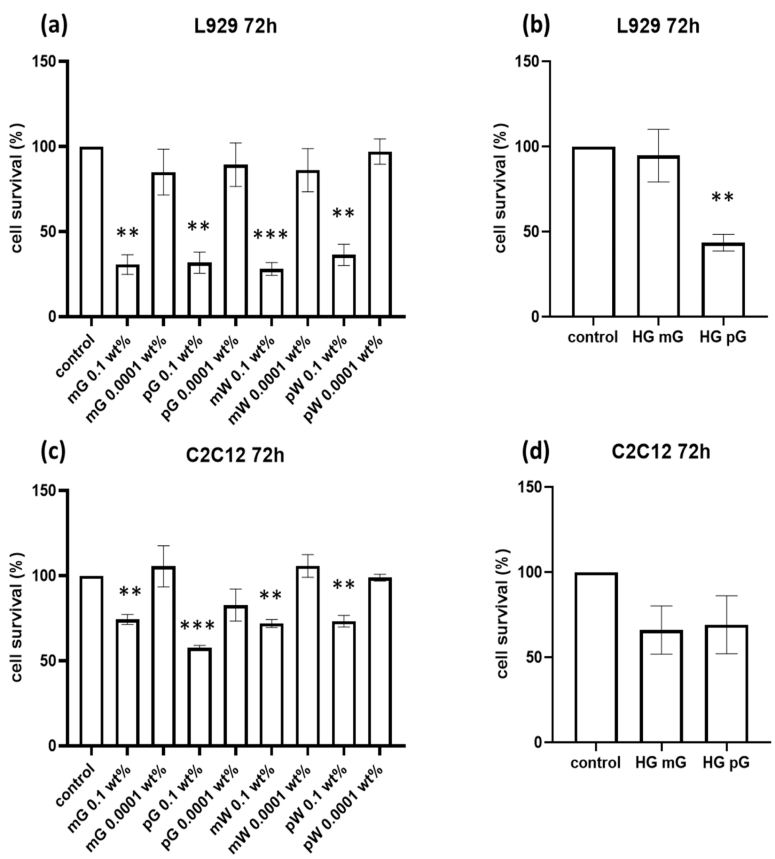

Figure 8. Cytotoxicity data from MTT assays obtained after 72 h. (a) L929 cells in solution, (b) L929 cells on hydrogels, (c) C2C12 cells in solution, and (d) C2C12 cells on hydrogels.

https://doi.org/10.1021/acs.biomac.2c01068
Biomacromolecules 2023, 24, 213−224

reveal a minor α-helix component for mG, mW, and pW, respectively. The peaks at 1647, 1643, and 1646 cm^{-1}, observed for pG, mW, and pW, show that a minor component of unordered peptide is present. The CD spectra for the heat-treated hydrogels (Figure S12) also show similar features to those for the solutions and spontaneously formed hydrogels discussed above.

Cytocompatibility. The cytotoxicity of peptides was assessed using MTT assays on L929 murine fibroblast and C2C12 immortalized mouse myoblast cell lines. The results obtained after 72 h of cell culture are shown in Figure 8. Additional data obtained after 24 h is shown in Figure S13. The *t*-test probability values are presented in Tables S3 and S4. The data in Figure 8a for L929 fibroblasts show that the cell viability is high (there was no significant difference when compared with the control groups) on all plates containing the lower lipopeptide concentration (1×10^{-4} wt %) solutions, with no significant difference from sample to sample. However, at 0.1 wt % (i.e., well above the CAC for all samples), the cell viability is significantly reduced to 30.7 ± 4.7%, 31.8 ± 5.1%, 28.1 ± 3.1%, and 36.3 ± 5.1% for mG, pG, mW, and pW respectively. These results suggest that self-assembled aggregates are not well tolerated, while monomers are. It is notable that the cytotoxicity of peptides at 0.1 wt % on L929 murine fibroblast is higher than that on C2C12 myoblasts. The cytotoxicity observed follows the trend observed after 24 h (Figure S13a), with significant cytotoxicity for the 0.1 wt % solution plates, with higher percentage cell viabilities for samples incubated with lower concentrations. The relative observed cytotoxicity was lower after 24 h incubation when compared with 72 h of incubation.

For L929 cells in contact with hydrogels (1 wt %), remarkably no significant cytotoxicity was observed for mG (cell survival of 92.6 ± 8.8% at 24 h and of 94.6 ± 12.6% at 72 h) (Figures 8b and S13b), but there was a notable reduction in cell viability for pG. Surprisingly, the cytotoxicity at this concentration is lower for both the peptides than for 0.1 wt % solutions, indicating that hydrogels are more cytocompatible than solutions, even with a higher lipopeptide content.

Cell viability measurements with C2C12 myoblasts revealed notable improvements in cytocompatibility at higher peptide concentrations as shown in Figure 8c. While the 0.1 wt % peptide-coated plates are somewhat cytotoxic, the cell viability is better than that observed for L929 fibroblasts by a factor of 2 or more, after 72 h. The cell viability was 84.4 ± 9.6%, 86.0 ± 6.8%, 72.3 ± 10.2%, and 73.3 ± 2.8% for mG, pG, mW, and pW, respectively. After 24 h, there is no significant cytotoxicity even for the higher concentration of lipopeptides (Figure S13c), with the exception of pW. The solutions prepared with 1×10^{-4} wt % lipopeptide showed minimal cytotoxicity, as for the L929 fibroblasts. Hydrogels were reasonably well tolerated by C2C12 cells (Figures 8d and S13d), with no substantial difference between mG and pG gels, in contrast to the superior cytocompatibility of mG gels with L929 fibroblasts.

CONCLUSIONS

In summary, all four lipopeptides form extended β-sheet nanostructures at sufficiently high concentrations. The CAC was determined from CD measurements from discontinuities as a function of the concentration of the ellipticity of the positive band at 205 nm, associated with the β-sheet structure. For the two tryptophan-containing peptides, the CAC obtained from intrinsic W fluorescence was in good agreement with that determined by analysis of molar ellipticity. This was not the case using ThT dye due to interference between tryptophan and ThT fluorescence; however, the ThT fluorescence probe did give consistent CAC values for mG and pG. FTIR spectra reveal a predominant β-sheet structure for all four lipopeptides. Self-fluorescence due to amyloid aggregation was observed for mG and pG.

Cryo-TEM and SAXS were used to elucidate self-assembled nanostructures. Both mG and pG form twisted nanotape structures, the cryo-TEM images showing that these comprise individual filaments that aggregate side by side to form tapes. SAXS form factor data can be fitted using a bilayer form factor which represents the nanotape electron density profile by three Gaussian functions,[125] one for the electron-poor hydrophobic lipid interior and the other two representing the hydrophilic and more electron-rich peptide surfaces. Unexpectedly and in contrast to the other lipopeptides, mW forms helical twisted ribbons which can be seen to close into nanotubes in clearly resolved cryo-TEM images. Oscillations in the SAXS form factor were used to determine the average nanotube radius, which was in good agreement with that obtained from the cryo-TEM images. Lipopeptide pW forms a dense network of fibrils with a different morphology to those of mG and pG, although the SAXS data could still be fitted using a bilayer form factor model. Both mW and pW show birefringence due to lyotropic nematic phase formation and spontaneous flow alignment of this phase upon delivery into X-ray capillaries was noted. Nematic phase formation is relatively infrequently observed for amyloid systems[126−130] and points to the high persistence length of the nanotube, twisted ribbon, and nanotape structures of mW and pW.

The distinct structures formed by mW and pW highlight the effect of the bulky and chiral tryptophan residue compared to glycine in the nanostructure formation of the four lipopeptides. The tryptophan residue is likely to lead to a locally more chiral and twisted packing, but this is modulated by alkyl chain length. The highest degree of twist of β-sheet structures is observed for mW, whereas pW appears to form thinner and more extended but less twisted structures. Therefore, both the N-terminal residue and the alkyl chain length influence molecular packing and self-assembly. Even a small difference of two methyl groups in the lipid chain substantially influences aggregation. Our work shows that the incorporation of tryptophan residues at the lipid−peptide junction can be used to tune self-assembly, as well as providing a useful fluorescence tag for aggregation studies.

The cell assays indicate that all lipopeptides show good cytocompatibility at lower lipopeptide concentrations (below the CAC). In addition, there are only minor differences from sample to sample. This is despite differences in self-assembled nanostructure noted above, in particular the tendency for mW to form nanotubes. Another notable trend was the generally greater tolerance for hydrogels than solution coatings, even though the former were prepared with a higher lipopeptide concentration. One reason for this may be the contact surface between the peptides and hydrogels. The cells seeded on the hydrogels are predominantly located on the surface, whereas the ones incubated with liquid solutions are totally enveloped by the medium containing lipopeptide. The content of free lipopeptide in the medium may differ between hydrogels and solutions. Cell viability data reveal a significant difference in the tolerance of lipopeptide coatings for C2C12 myoblasts compared to L929 fibroblasts at higher concentrations (0.1 wt

https://doi.org/10.1021/acs.biomac.2c01068
Biomacromolecules 2023, 24, 213−224

%, well above the determined CAC values) for all lipopeptides. This selective improvement in cytocompatibility is promising for future applications of self-assembled (and monomeric) lipopeptide coatings in muscular tissue engineering, especially relevant to the production of cultured meat. It is not uncommon to observe multiple responses for the same compound between different cell lines, be it related to metabolic activity, cytotoxicity, proliferation, or cell adhesion. This effect was also observed previously in other RGDS-based molecules, with different levels of cell adhesion and cytotoxicity for the same molecule for distinct cell types.[34,131,132]

A possible explanation for the increased cytotoxicity in fibroblasts is the fact that soluble RGD-peptides may trigger apoptosis by the inhibition of vitronectin and fibronectin domains, promoting cell detachment and leading to anoikis, a type of programmed cell death that occurs in anchorage-dependent cells upon detachment from the surrounding extracellular matrix or substrate, an effect that has already been observed for fibroblasts.[32,133,134]

The observation of fibril textures for the lipopeptides (which in several cases show spontaneous flow alignment) is particularly interesting in terms of further research underway on the preparation of aligned scaffolds for tissue engineering[135] using the alignment of myoblasts to improve the texture of cultured meat.

■ ASSOCIATED CONTENT

Supporting Information

The Supporting Information is available free of charge at https://pubs.acs.org/doi/10.1021/acs.biomac.2c01068.

HPLC data, SAXS data fit parameters, fluorescence data, FTIR spectra, additional cryo-TEM images, SAXS and CD data for hydrogels, polarized optical microscopy images, images of heat-treated hydrogels, and cytotoxicity data from MTT assays obtained after 24 h (PDF)

■ AUTHOR INFORMATION

Corresponding Author

Ian W. Hamley − *School of Chemistry, Pharmacy and Food Biosciences, University of Reading, Berkshire RG6 6AD, U.K.*; orcid.org/0000-0002-4549-0926; Email: I.W.Hamley@reading.ac.uk

Authors

Elisabetta Rosa − *School of Chemistry, Pharmacy and Food Biosciences, University of Reading, Berkshire RG6 6AD, U.K.; Department of Pharmacy and Research Centre on Bioactive Peptides (CIRPeB), University of Naples "Federico II", Naples 80131, Italy*

Lucas de Mello − *School of Chemistry, Pharmacy and Food Biosciences, University of Reading, Berkshire RG6 6AD, U.K.; Departamento de Biofísica, Universidade Federal de São Paulo, São Paulo 04023-062, Brazil*

Valeria Castelletto − *School of Chemistry, Pharmacy and Food Biosciences, University of Reading, Berkshire RG6 6AD, U.K.*; orcid.org/0000-0002-3705-0162

Mark L. Dallas − *School of Chemistry, Pharmacy and Food Biosciences, University of Reading, Berkshire RG6 6AD, U.K.*

Antonella Accardo − *Department of Pharmacy and Research Centre on Bioactive Peptides (CIRPeB), University of Naples "Federico II", Naples 80131, Italy*

Jani Seitsonen − *Nanomicroscopy Center, Aalto University, Espoo FIN-02150, Finland*

Complete contact information is available at: https://pubs.acs.org/10.1021/acs.biomac.2c01068

Notes

The authors declare no competing financial interest.

■ ACKNOWLEDGMENTS

This work was supported by EPSRC Fellowship grant EP/V053396/1 to I.W.H. The synchrotron SAXS beamtime at the SOLEIL (proposal no. 20211309) and the support of Thomas Bizien during the measurements are acknowledged. We thank Nada Aljuaid and Madonna Mitry for assistance with cell culture. We acknowledge access to instruments of the Chemical Analysis Facility at the University of Reading. L.D.M. acknowledges FAPESP grant number 19/20907-7 and Fellowship 2021/10092-6, linked to FAPESP scholarship 2019/19719-1.

■ REFERENCES

(1) Ruoslahti, E.; Pierschbacher, M. D. Arg-Gly-Asp: A versatile cell recognition signal. *Cell* **1986**, *44*, 517−518.

(2) Ruoslahti, E. RGD and other recognition sequences for integrins. *Annu. Rev. Cell Dev. Biol.* **1996**, *12*, 697−715.

(3) Hartgerink, J. D.; Beniash, E.; Stupp, S. I. Self-assembly and mineralization of peptide-amphiphile nanofibers. *Science* **2001**, *294*, 1684−1688.

(4) Hartgerink, J. D.; Beniash, E.; Stupp, S. I. Peptide-amphiphile nanofibers: A versatile scaffold for the preparation of self-assembling materials. *Proc. Natl. Acad. Sci. U.S.A.* **2002**, *99*, 5133−5138.

(5) Lutolf, M. P.; Hubbell, J. A. Synthetic biomaterials as instructive extracellular microenvironments for morphogenesis in tissue engineering. *Nat. Biotechnol.* **2005**, *23*, 47−55.

(6) Guler, M. O.; Hsu, L.; Soukasene, S.; Harrington, D. A.; Hulvat, J. F.; Stupp, S. I. Presentation of RGDS epitopes on self-assembled nanofibers of branched peptide amphiphiles. *Biomacromolecules* **2006**, *7*, 1855−1863.

(7) Storrie, H.; Guler, M. O.; Abu-Amara, S. N.; Volberg, T.; Rao, M.; Geiger, B.; Stupp, S. I. Supramolecular crafting of cell adhesion. *Biomaterials* **2007**, *28*, 4608−4618.

(8) Place, E. S.; Evans, N. D.; Stevens, M. M. Complexity in biomaterials for tissue engineering. *Nat. Mater.* **2009**, *8*, 457−470.

(9) Gouveia, R. M.; Jones, R. R.; Hamley, I. W.; Connon, C. J. The bioactivity of composite Fmoc-RGDS-collagen gels. *Biomater. Sci.* **2014**, *2*, 1222−1229.

(10) Castelletto, V.; Gouveia, R. M.; Connon, C. J.; Hamley, I. W.; Seitsonen, J.; Nykänen, A.; Ruokolainen, J. Alanine-rich amphiphilic peptide containing the RGD cell adhesion motif: a coating material for human fibroblast attachment and culture. *Biomater. Sci.* **2014**, *2*, 362−369.

(11) Hamley, I. W. Small Bioactive Peptides for Biomaterials Design and Therapeutics. *Chem. Rev.* **2017**, *117*, 14015−14041.

(12) Marin, D.; Marchesan, S. Self-Assembled Peptide Nanostructures for ECM Biomimicry. *Nanomaterials* **2022**, *12*, 2147.

(13) Temming, K.; Schiffelers, R. M.; Molema, G.; Kok, R. J. RGD-based strategies for selective delivery of therapeutics and imaging agents to the tumour vasculature. *Drug Resistance Updates* **2005**, *8*, 381−402.

(14) Danhier, F.; Le Breton, A.; Préat, V. RGD-Based Strategies to Target Alpha(v) Beta(3) Integrin in Cancer Therapy and Diagnosis. *Mol. Pharmacol.* **2012**, *9*, 2961−2973.

(15) Diaferia, C.; Rosa, E.; Accardo, A.; Morelli, G. Peptide-based hydrogels as delivery systems for doxorubicin. *J. Pept. Sci.* **2022**, *28*, No. e3301.

(16) Samanen, J.; Ali, F.; Romoff, T.; Calvo, R.; Sorenson, E.; Vasko, J.; Storer, B.; Berry, D.; Bennett, D.; Strohsacker, M.; Powers, D.; Stadel, J.; Nichols, A. Development of a small RGD peptide fibrinogen receptor antagonist with potent antiaggregatory activity in vitro. *J. Med. Chem.* **1991**, *34*, 3114−3125.
(17) Alig, L.; Edenhofer, A.; Hadvary, P.; Huerzeler, M.; Knopp, D.; Mueller, M.; Steiner, B.; Trzeciak, A.; Weller, T. Low molecular weight, non-peptide fibrinogen receptor antagonists. *J. Med. Chem.* **1992**, *35*, 4393−4407.
(18) Muraoka, T.; Koh, C.-Y.; Cui, H.; Stupp, S. I. Light-Triggered Bioactivity in Three Dimensions. *Angew. Chem., Int. Ed. Engl.* **2009**, *48*, 5946−5949.
(19) Webber, M. J.; Tongers, J.; Renault, M.-A.; Roncalli, J. G.; Losordo, D. W.; Stupp, S. I. Development of bioactive peptide amphiphiles for therapeutic cell delivery. *Acta Biomater.* **2010**, *6*, 3−11.
(20) Jin, Y.; Xu, X.-D.; Chen, C.-S.; Cheng, S.-X.; Zhang, X.-Z.; Zhuo, R.-X. Bioactive Amphiphilic Peptide Derivatives with pH Triggered Morphology and Structure. *Macromol. Rapid Commun.* **2008**, *29*, 1726−1731.
(21) Cheng, G.; Castelletto, V.; Moulton, C. M.; Newby, G. E.; Hamley, I. W. Hydrogelation and Self-Assembly of Fmoc-Tripeptides: Unexpected Influence of Sequence on Self-Assembled Fibril Structure, and Hydrogel Modulus and Anisotropy. *Langmuir* **2010**, *26*, 4990−4998.
(22) Cheng, G.; Castelletto, V.; Jones, R.; Connon, C. J.; Hamley, I. W. Hydrogelation of Self-Assembling RGD-Based Peptides. *Soft Matter* **2011**, *7*, 1326−1333.
(23) Castelletto, V.; Moulton, C. M.; Cheng, G.; Hamley, I. W.; Hicks, M. R.; Rodger, A.; López-Pérez, D. E.; Revilla-López, G.; Alemán, C. Self-Assembly of Fmoc-Tetrapeptides Based on the RGDS Cell Adhesion Motif. *Soft Matter* **2011**, *7*, 11405−11415.
(24) Castelletto, V.; Gouveia, R. J.; Connon, C. J.; Hamley, I. W. New RGD-peptide amphiphile mixtures containing a negatively charged diluent. *Faraday Discuss.* **2013**, *166*, 381−397.
(25) Uzunalli, G.; Soran, Z.; Erkal, T. S.; Dagdas, Y. S.; Dinc, E.; Hondur, A. M.; Bilgihan, K.; Aydin, B.; Guler, M. O.; Tekinay, A. B. Bioactive self-assembled peptide nanofibers for corneal stroma regeneration. *Acta Biomater.* **2014**, *10*, 1156−1166.
(26) Sur, S.; Tantakitti, F.; Matson, J. B.; Stupp, S. I. Epitope topography controls bioactivity in supramolecular nanofibers. *Biomater. Sci.* **2015**, *3*, 520−532.
(27) Ozkan, A. D.; Tekinay, A. B.; Guler, M. O.; Tekin, E. D. Effects of temperature, pH and counterions on the stability of peptide amphiphile nanofiber structures. *RSC Adv.* **2016**, *6*, 104201−104214.
(28) Miotto, M.; Gouveia, R. M.; Ionescu, A. M.; Figueiredo, F.; Hamley, I. W.; Connon, C. J. 4D Corneal Tissue Engineering: Achieving Time-Dependent Tissue Self-Curvature through Localized Control of Cell Actuators. *Adv. Funct. Mater.* **2019**, *29*, 1807334.
(29) Li, Y.; Yin, P.; Wu, K.; Wang, X.; Song, Y. Self-Assembly of a Multi-Functional Hydrogel from a Branched Peptide Amphiphile and Its Effects on Bone Marrow Mesenchymal Stem Cells. *J. Biomater. Tissue Eng.* **2020**, *10*, 1731−1737.
(30) Xiong, Q.; Stupp, S. I.; Schatz, G. C. Molecular Insight into the β-Sheet Twist and Related Morphology of Self-Assembled Peptide Amphiphile Ribbons. *J. Phys. Chem. Lett.* **2021**, *12*, 11238−11244.
(31) Pierschbacher, M. D.; Ruoslahti, E. Cell attachment activity of fibronectin can be duplicated by small synthetic fragments of the molecule. *Nature* **1984**, *309*, 30−33.
(32) Pierschbacher, M. D.; Ruoslahti, E. Influence of stereochemistry of the sequence Arg-Gly-Asp-Xaa on binding specificity in cell adhesion. *J. Biol. Chem.* **1987**, *262*, 17294−17298.
(33) Ruoslahti, E.; Pierschbacher, M. D. New Perspectives in Cell Adhesion: RGD and Integrins. *Science* **1987**, *238*, 491−497.
(34) Hirano, Y.; Okuno, M.; Hayashi, T.; Goto, K.; Nakajima, A. Cell-attachment activities of surface immobilized oligopeptides RGD, RGDS, RGDV, RGDT, and YIGSR toward five cell lines. *J. Biomater. Sci., Polym. Ed.* **1993**, *4*, 235−243.
(35) Hersel, U.; Dahmen, C.; Kessler, H. RGD modified polymers: biomaterials for stimulated cell adhesion and beyond. *Biomater* **2003**, *24*, 4385−4415.
(36) Löwik, D. W. P. M.; van Hest, J. C. M. Peptide based amphiphiles. *Chem. Soc. Rev.* **2004**, *33*, 234−245.
(37) Cui, H. G.; Webber, M. J.; Stupp, S. I. Self-Assembly of Peptide Amphiphiles: From Molecules to Nanostructures to Biomaterials. *Biopolymers* **2010**, *94*, 1−18.
(38) Versluis, F.; Marsden, H. R.; Kros, A. Power struggles in peptide-amphiphile nanostructures. *Chem. Soc. Rev.* **2010**, *39*, 3434−3444.
(39) Hamley, I. W. Self-Assembly of Amphiphilic Peptides. *Soft Matter* **2011**, *7*, 4122−4138.
(40) Matson, J. B.; Zha, R. H.; Stupp, S. I. Peptide self-assembly for crafting functional biological materials. *Curr. Opin. Solid State Mater. Sci.* **2011**, *15*, 225−235.
(41) Trent, A.; Marullo, R.; Lin, B.; Black, M.; Tirrell, M. Structural properties of soluble peptide amphiphile micelles. *Soft Matter* **2011**, *7*, 9572−9582.
(42) Matson, J. B.; Stupp, S. I. Self-assembling peptide scaffolds for regenerative medicine. *Chem. Commun.* **2012**, *48*, 26−33.
(43) Hamley, I. W. Lipopeptides: from self-assembly to bioactivity. *Chem. Commun.* **2015**, *51*, 8574−8583.
(44) Sewald, N.; Jakubke, H.-D., *Peptides: Chemistry and Biology*. Wiley-VCH: Weinheim, 2002.
(45) Hamley, I. W., *Introduction to Peptide Science*. Wiley: Chichester, 2020.
(46) Sato, K.; Hendricks, M. P.; Palmer, L. C.; Stupp, S. I. Peptide supramolecular materials for therapeutics. *Chem. Soc. Rev.* **2018**, *47*, 7539−7551.
(47) Ziserman, L.; Lee, H. Y.; Raghavan, S. R.; Mor, A.; Danino, D. Unraveling the Mechanism of Nanotube Formation by Chiral Self-Assembly of Amphiphiles. *J. Am. Chem. Soc.* **2011**, *133*, 2511−2517.
(48) Hamley, I. W.; Dehsorkhi, A.; Castelletto, V.; Furzeland, S.; Atkins, D.; Seitsonen, J.; Ruokolainen, J. Reversible helical unwinding transition of a self-assembling peptide amphiphile. *Soft Matter* **2013**, *9*, 9290−9293.
(49) Hamley, I. W. Peptide Nanotubes. *Angew. Chem., Int. Ed. Engl.* **2014**, *53*, 6866−6881.
(50) Miller, J. G.; Hughes, S. A.; Modlin, C.; Conticello, V. P. Structures of synthetic helical filaments and tubes based on peptide and peptido-mimetic polymers. *Q. Rev. Biophys.* **2022**, *55*, 1−39.
(51) Aggeli, A.; Bell, M.; Boden, N.; Keen, J. N.; Knowles, P. F.; McLeish, T. C. B.; Pitkeathly, M.; Radford, S. E. Responsive gels formed by the spontaneous self-assembly of peptides into polymeric β-sheet tapes. *Nature* **1997**, *386*, 259−262.
(52) Lu, K.; Jacob, J.; Thiyagarajan, P.; Conticello, V. P.; Lynn, D. G. Exploiting Amyloid Fibril Lamination for Nanotube Self-Assembly. *J. Am. Chem. Soc.* **2003**, *125*, 6391−6393.
(53) Krysmann, M. J.; Castelletto, V.; McKendrick, J. M. E.; Clifton, I. W.; Harris, C.; King, P. J. F.; King, S. M. Self-Assembly of Peptide Nanotubes in an Organic Solvent. *Langmuir* **2008**, *24*, 8158−8162.
(54) Mehta, A. K.; Lu, K.; Childers, W. S.; Liang, S.; Dublin, J.; Dong, J. P.; Snyder, S. V.; Pingali, P.; Thiyagarajan, D. G.; Lynn, D. G. Facial symmetry in protein self-assembly. *J. Am. Chem. Soc.* **2008**, *130*, 9829−9835.
(55) Scanlon, S.; Aggeli, A. Self-assembling peptide nanotubes. *Nano Today* **2008**, *3*, 22−30.
(56) Xu, H.; Wang, Y. M.; Ge, X.; Han, S. Y.; Wang, S. J.; Zhou, P.; Shan, H. H.; Zhao, X. B.; Lu, J. A. R. Twisted Nanotubes Formed from Ultrashort Amphiphilic Peptide I3K and Their Templating for the Fabrication of Silica Nanotubes. *Chem. Mater.* **2010**, *22*, 5165−5173.
(57) Adamcik, J.; Castelletto, V.; Bolisetty, I. W.; Hamley, R.; Mezzenga, R. Direct Observation of Time-Resolved Polymorphic States in the Self-Assembly of End-Capped Heptapeptides. *Angew. Chem., Int. Ed. Engl.* **2011**, *50*, 5495−5498.
(58) Madine, J.; Davies, H. A.; Shaw, C.; Hamley, I. W.; Middleton, D. A. Fibrils and nanotubes assembled from a modified amyloid-β

https://doi.org/10.1021/acs.biomac.2c01068
Biomacromolecules 2023, 24, 213−224

peptide fragment differ in the packing of the same β-sheet building blocks. *Chem. Commun.* **2012**, *48*, 2976−2978.
(59) Middleton, D. A.; Madine, J.; Castelletto, V.; Hamley, I. W. New insights into the molecular architecture of a peptide nanotube using FTIR and solid-state NMR combined with sample alignment. *Angew. Chem., Int. Ed. Engl.* **2013**, *52*, 10537−10540.
(60) Hamley, I. W.; Dehsorkhi, A.; Castelletto, V. Self-Assembled Arginine-Coated Peptide Nanosheets in Water. *Chem. Commun.* **2013**, *49*, 1850−1852.
(61) Rüter, A.; Kuczera, S.; Stenhammar, J.; Zinn, T.; Narayanan, T.; Olsson, U. Tube to ribbon transition in a self-assembling model peptide system. *Phys. Chem. Chem. Phys.* **2020**, *22*, 18320−18327.
(62) Zhao, Y. R.; Hu, X. Z.; Zhang, L. M.; Wang, D.; King, S. M.; Rogers, S. E.; Wang, J. Q.; Lu, J. R.; Xu, H. Monolayer wall nanotubes self-assembled from short peptide bolaamphiphiles. *J. Colloid Interface Sci.* **2021**, *583*, 553−562.
(63) Ma, X. Y.; Zhao, Y. R.; He, C. Y.; Zhou, X.; Qi, H.; Wang, Y.; Chen, C. X.; Wang, D.; Li, J.; Ke, Y. B.; Wang, J. Q.; Xu, H. Ordered Packing of β-Sheet Nanofibrils into Nanotubes: Multi-hierarchical Assembly of Designed Short Peptides. *Nano Lett.* **2021**, *21*, 10199−10207.
(64) Ghadiri, M. R.; Granja, J. R.; Buehler, L. K. Artificial Transmembrane Ion Channels from Self-Assembling Peptide Nanotubes. *Nature* **1994**, *369*, 301−304.
(65) Hartgerink, J. D.; Granja, J. R.; Milligan, R. A.; Ghadiri, M. R. Self-assembling peptide nanotubes. *J. Am. Chem. Soc.* **1996**, *118*, 43−50.
(66) Xu, C. F.; Liu, R.; Mehta, A. K.; Guerrero-Ferreira, R. C.; Wright, E. R.; Dunin-Horkawicz, S.; Morris, K.; Serpell, L. C.; Zuo, X. B.; Wall, J. S.; Conticello, V. P. Rational Design of Helical Nanotubes from Self-Assembly of Coiled-Coil Lock Washers. *J. Am. Chem. Soc.* **2013**, *135*, 15565−15578.
(67) Burgess, N. C.; Sharp, T. H.; Thomas, F.; Wood, C. W.; Thomson, A. R.; Zaccai, N. R.; Brady, R. L.; Serpell, L. C.; Woolfson, D. N. Modular Design of Self-Assembling Peptide-Based Nanotubes. *J. Am. Chem. Soc.* **2015**, *137*, 10554−10562.
(68) Wu, Y. Y.; Norberg, P. K.; Reap, E. A.; Congdon, K. L.; Fries, C. N.; Kelly, S. H.; Sampson, J. H.; Conticello, V. P.; Collier, J. H. A Supramolecular Vaccine Platform Based on α-Helical Peptide Nanofibers. *ACS Biomater. Sci. Eng.* **2017**, *3*, 3128−3132.
(69) Castelletto, V.; Seitsonen, J.; Ruokolainen, J.; Piras, C.; Cramer, R.; Edwards-Gayle, C. J. C.; Hamley, I. W. Peptide Nanotubes Self-Assembled from Leucine-Rich Alpha Helical Surfactant-Like Peptides. *Chem. Commun.* **2020**, *56*, 11977−11980.
(70) Castelletto, V.; Seitsonen, J.; Ruokolainen, J.; Hamley, I. W. Alpha Helical Surfactant-Like Peptides Self-Assemble Into pH-Dependent Nanostructures. *Soft Matter* **2020**, *17*, 3096−3104.
(71) Wang, F. B.; Gnewou, O.; Modlin, C.; Beltran, L. C.; Xu, C. F.; Su, Z. L.; Juneja, P.; Grigoryan, G.; Egelman, E. H.; Conticello, V. P. Structural analysis of cross α-helical nanotubes provides insight into the designability of filamentous peptide nanomaterials. *Nat. Commun.* **2021**, *12*, 407.
(72) Valéry, C.; Paternostre, M.; Robert, B.; Gulik-Krzywicki, T.; Narayanan, T.; Dedieu, J. C.; Keller, G.; Torres, M. L.; Cherif-Cheikh, R.; Calvo, P.; Artzner, F. Biomimetic organization: Octapeptide self-assembly into nanotubes of viral capsid-like dimension. *Proc. Natl. Acad. Sci. U.S.A.* **2003**, *100*, 10258−10262.
(73) Valéry, C.; Artzner, F.; Robert, B.; Gulick, T.; Keller, G.; Grabielle-Madelmont, C.; Torres, M. L.; Cherif-Cheikh, R.; Paternostre, M. Self-association process of a peptide in solution: From beta-sheet filaments to large embedded nanotubes. *Biophys. J.* **2004**, *86*, 2484−2501.
(74) Tarabout, C.; Roux, S.; Gobeaux, F.; Fay, N.; Pouget, E.; Meriadec, C.; Ligeti, M.; Thomas, D.; IJsselstijn, M.; Besselievre, F.; Buisson, D. A.; Verbavatz, J. M.; Petitjean, M.; Valéry, C.; Perrin, L.; Rousseau, B.; Artzner, F.; Paternostre, M.; Cintrat, J. C. Control of peptide nanotube diameter by chemical modifications of an aromatic residue involved in a single close contact. *Proc. Natl. Acad. Sci. U.S.A.* **2011**, *108*, 7679−7684.
(75) Reches, M.; Gazit, E. Casting metal nanowires within discrete self-assembled peptide nanotubes. *Science* **2003**, *300*, 625−627.
(76) Reches, M.; Gazit, E. Self-assembly of peptide nanotubes and amyloid-like structures by charged-termini-capped diphenylalanine peptide analogues. *Israel J. Chem.* **2005**, *45*, 363−371.
(77) Reches, M.; Gazit, E. Controlled patterning of aligned self-assembled peptide nanotubes. *Nat. Nanotechnol.* **2006**, *1*, 195−200.
(78) Tian, Y.; Polzer, F. B.; Zhang, H. V.; Kiick, K. L.; Saven, J. G.; Pochan, D. J. Nanotubes, Plates, and Needles: Pathway-Dependent Self-Assembly of Computationally Designed Peptides. *Biomacromolecules* **2018**, *19*, 4286−4298.
(79) Löwik, D. W. P. M.; Garcia-Hartjes, J.; Meijer, J. T.; van Hest, J. C. M. Tuning secondary structure and self-assembly of amphiphilic peptides. *Langmuir* **2005**, *21*, 524−526.
(80) Gouveia, R. M.; Castelletto, V.; Alcock, S. G.; Hamley, I. W.; Connon, C. J. Bioactive films produced from self-assembling peptide amphiphiles as versatile substrates for tuning cell adhesion and tissue architecture in serum-free conditions. *J. Mater. Chem. B* **2013**, *1*, 6157−6169.
(81) Gouveia, R. M.; Castelletto, V.; Hamley, C. J.; Connon, I. W. New Self-Assembling Multifunctional Templates for the Biofabrication and Controlled Self-Release of Cultured Tissue. *Tissue Eng., Part A* **2015**, *21*, 1772−1784.
(82) Gouveia, R. M.; Hamley, I. W.; Connon, C. J. Bio-fabrication and physiological self-release of tissue equivalents using smart peptide amphiphile templates. *J. Mater. Sci.: Mater. Med.* **2015**, *26*, 242.
(83) Castelletto, V.; Hamley, I. W.; Reza, M.; Ruokolainen, J. Interactions between lipid-free apolipoprotein-AI and a lipopeptide incorporating the RGDS cell adhesion motif. *Nanoscale* **2015**, *7*, 171−178.
(84) Bhat, Z. F.; Fayaz, H. Prospectus of cultured meat-advancing meat alternatives. *J. Food Sci. Technol.* **2011**, *48*, 125−140.
(85) Post, M. J.; Levenberg, S.; Kaplan, D. L.; Genovese, N.; Fu, J. A.; Bryant, C. J.; Negowetti, N.; Verzijden, K.; Moutsatsou, P. Scientific, sustainability and regulatory challenges of cultured meat. *Nat. Food* **2020**, *1*, 403−415.
(86) Shaikh, S.; Lee, E.; Ahmad, K.; Ahmad, S. S.; Chun, H.; Lim, J.; Lee, Y.; Choi, I. Cell Types Used for Cultured Meat Production and the Importance of Myokines. *Foods* **2021**, *10*, 2318.
(87) Seah, J. S. H.; Singh, S.; Tan, L. P.; Choudhury, D. Scaffolds for the manufacture of cultured meat. *Crit. Rev. Biotechnol.* **2022**, *42*, 311−323.
(88) Dorfman, J.; Duong, M.; Zibaitis, A.; Pelletier, M. P.; Shum-Tim, D.; Li, C.; Chiu, R. C. J. Myocardial tissue engineering with autologous myoblast implantation. *J. Thorac. Cardiovasc. Surg.* **1998**, *116*, 744−751.
(89) Bach, A. D.; Beier, J. P.; Stern-Staeter, J.; Horch, R. E. Skeletal muscle tissue engineering. *J. Cell. Mol. Med.* **2004**, *8*, 413−422.
(90) Jawad, H.; Ali, N. N.; Lyon, A. R.; Chen, Q. Z.; Harding, S. E.; Boccaccini, A. R. Myocardial tissue engineering: a review. *J. Tissue Eng. Regener. Med.* **2007**, *1*, 327−342.
(91) Ostrovidov, S.; Hosseini, V.; Ahadian, S.; Fujie, T.; Parthiban, S. P.; Ramalingam, M.; Bae, H.; Kaji, H.; Khademhosseini, A. Skeletal Muscle Tissue Engineering: Methods to Form Skeletal Myotubes and Their Applications. *Tissue Eng., Part B* **2014**, *20*, 403−436.
(92) Frontera, W. R.; Ochala, J. Skeletal Muscle: A Brief Review of Structure and Function. *Calcif. Tissue Int.* **2015**, *96*, 183−195.
(93) Harrington, D. A.; Cheng, E. Y.; Guler, M. O.; Lee, L. K.; Donovan, J. L.; Claussen, R. C.; Stupp, S. I. Branched peptide-amphiphiles as self-assembling coatings for tissue engineering scaffolds. *J. Biomed. Mater. Res., Part A* **2006**, *78*, 157−167.
(94) Kushwaha, M.; Anderson, J. M.; Bosworth, C. A.; Andukuri, A.; Minor, W. P.; Lancaster, J. R.; Anderson, P. G.; Brott, B. C.; Jun, H. W. A nitric oxide releasing, self assembled peptide amphiphile matrix that mimics native endothelium for coating implantable cardiovascular devices. *Biomater* **2010**, *31*, 1502−1508.
(95) Ceylan, H.; Tekinay, A. B.; Guler, M. O. Selective adhesion and growth of vascular endothelial cells on bioactive peptide nanofiber functionalized stainless steel surface. *Biomater* **2011**, *32*, 8797−8805.

https://doi.org/10.1021/acs.biomac.2c01068
Biomacromolecules 2023, 24, 213−224

(96) Angeloni, N. L.; Bond, C. W.; Tang, Y.; Harrington, D. A.; Zhang, S. M.; Stupp, S. I.; McKenna, K. E.; Podlasek, C. A. Regeneration of the cavernous nerve by Sonic hedgehog using aligned peptide amphiphile nanofibers. *Biomater* **2011**, *32*, 1091−1101.
(97) Stupp, S. I.; Palmer, L. C. Supramolecular Chemistry and Self-Assembly in Organic Materials Design. *Chem. Mater.* **2014**, *26*, 507−518.
(98) Perez, C. M. R.; Stephanopoulos, N.; Sur, S.; Lee, S. S.; Newcomb, C.; Stupp, S. I. The Powerful Functions of Peptide-Based Bioactive Matrices for Regenerative Medicine. *Ann. Biomed. Eng.* **2015**, *43*, 501−514.
(99) Eren Cimenci, C. E.; Uzunalli, G.; Uysal, O.; Yergoz, F.; Karaca Umay, E. K.; Guler, M. O.; Tekinay, A. B. Laminin mimetic peptide nanofibers regenerate acute muscle defect. *Acta Biomater.* **2017**, *60*, 190−200.
(100) Klunk, W. E.; Jacob, R. F.; Mason, R. P. [19] Quantifying amyloid by congo red spectral shift assay. *Methods Enzymol.* **1999**, *309*, 285−305.
(101) Hamley, I. W. Peptide Fibrillization. *Angew. Chem., Int. Ed. Engl.* **2007**, *46*, 8128−8147.
(102) Buell, A. K.; Dobson, C. M.; Knowles, T. P. J.; Welland, M. E. Interactions between Amyloidophilic Dyes and Their Relevance to Studies of Amyloid Inhibitors. *Biophys. J.* **2010**, *99*, 3492−3497.
(103) Levine, H. Thioflavine T interaction with synthetic Alzheimer's diseaseβ-amyloid peptides: Detection of amyloid aggregation in solution. *Protein Sci.* **1993**, *2*, 404−410.
(104) LeVine, H., [18] Quantification of β-sheet amyloid fibril structures with thioflavin T. In *Methods Enzymol.*, Wetzel, R., Ed. Academic Press: San Diego, 1999; Vol. *309*, pp 274-284. DOI: 10.1016/s0076-6879(99)09020-5
(105) Thureau, A.; Roblin, P.; Pérez, J. BioSAXS on the SWING beamline at Synchrotron SOLEIL. *J. Appl. Cryst.* **2021**, *54*, 1698−1710.
(106) Woody, R. W., Circular dichroism of peptides and proteins. In *Circular Dichroism. Principles and Applications*, Nakanishi, K.; Berova, N.; Woody, R. W., Eds. VCH: New York, 1994; pp 473−496.
(107) Rodger, A.; Nordén, B. *Circular Dichroism and Linear Dichroism*; Oxford University Press: Oxford, 1997.
(108) Nordén, B.; Rodger, A.; Dafforn, T. R. *Linear Dichroism and Circular Dichroism: A Textbook on Polarized-Light Spectroscopy*; RSC: Cambridge, 2010.
(109) Xing, H. H.; Chin, S. M.; Udumula, V. R.; Krishnaiah, M.; Rodrigues de Almeida, N. R.; Huck-Iriart, C.; Picco, A. S.; Lee, S. R.; Zaldivar, G.; Jackson, K. A.; Tagliazucchi, M.; Stupp, S. I.; Conda-Sheridan, M. Control of Peptide Amphiphile Supramolecular Nanostructures by Isosteric Replacements. *Biomacromolecules* **2021**, *22*, 3274−3283.
(110) Lakowicz, J. R., *Principles of Fluorescence Spectroscopy*, 2nd ed.; Kluwer: New York, 1999.
(111) Vivian, J. T.; Callis, P. R. Mechanisms of tryptophan fluorescence shifts in proteins. *Biophys. J.* **2001**, *80*, 2093−2109.
(112) Castelletto, V.; Edwards-Gayle, C. J. C.; Hamley, I. W.; Pelin, J. N. B. D.; Alves, W. A.; Aguilar, A. M.; Seitsonen, J.; Ruokolainen, J. Self-Assembly of a Catalytically Active Lipopeptide and its Incorporation into Cubosomes. *ACS Appl. Bio Mater.* **2019**, *2*, 3639−3647.
(113) Stuart, B. *Biological Applications of Infrared Spectroscopy*; Wiley: Chichester, 1997.
(114) Pelton, J. T.; McLean, L. R. Spectroscopic methods for analysis of protein secondary structure. *Analyt. Biochem.* **2000**, *277*, 167−176.
(115) Barth, A.; Zscherp, C. What vibrations tell about proteins. *Q. Rev. Biophys.* **2002**, *35*, 369−430.
(116) Barth, A. Infrared spectroscopy of proteins. *Biochim. Biophys. Acta, Bioenerg.* **2007**, *1767*, 1073−1101.
(117) Gaussier, H.; Morency, H.; Lavoie, M. C.; Subirade, M. Replacement of trifluoroacetic acid with HCl in the hydrophobic purification steps of pediocin PA-1: A structural effect. *Appl. Environ. Microbiol.* **2002**, *68*, 4803−4808.
(118) Eker, F.; Griebenow, K.; Schweitzer-Stenner, R. Aβ1-28 Fragment of the Amyloid Peptide Predominantly Adopts a Polyproline II Conformation in an Acidic Solution. *Biochem* **2004**, *43*, 6893−6898.
(119) del Mercato, L. L.; Pompa, P. P.; Maruccio, G.; Torre, A.; Sabella, S.; Tamburro, A. M.; Cingolani, R.; Rinaldi, R. Charge transport and intrinsic fluorescence in amyloid-like fibrils. *Proc. Natl. Acad. Sci. U.S.A.* **2007**, *104*, 18019−18024.
(120) Handelman, A.; Natan, A.; Rosenman, G. Structural and optical properties of short peptides: nanotubes-to-nanofibers phase transformation. *J. Pept. Sci.* **2014**, *20*, 487−493.
(121) Diaferia, C.; Sibillano, T.; Altamura, D.; Roviello, V.; Vitagliano, L.; Giannini, C.; Morelli, G.; Accardo, A. Structural Characterization of PEGylated Hexaphenylalanine Nanostructures Exhibiting Green Photoluminescence Emission. *Chem.—Eur. J.* **2017**, *23*, 14039−14048.
(122) Dehsorkhi, A.; Hamley, I. W.; Seitsonen, J.; Ruokolainen, J. Tuning Self-Assembled Nanostructures Through Enzymatic Degradation of a Peptide Amphiphile. *Langmuir* **2013**, *29*, 6665−6672.
(123) McCourt, J. M.; Kewalramani, S.; Gao, C.; Roth, E. W.; Weigand, S. J.; Olvera de la Cruz, M.; Bedzyk, M. J. Electrostatic control of shape selection and nanoscale structure in chiral molecular assemblies. *ACS Cent. Sci.* **2022**, *8*, 1169−1181.
(124) Hamley, I. W. *Small-Angle Scattering: Theory, Instrumentation, Data and Applications*; Wiley: Chichester, 2021.
(125) Pabst, G.; Rappolt, M.; Amenitsch, H.; Laggner, P. Structural information from multilamellar liposomes at full hydration: Full$q$-range fitting with high quality x-ray data. *Phys. Rev. E* **2000**, *62*, 4000−4009.
(126) Aggeli, A.; Nyrkova, I. A.; Bell, M.; Harding, R.; Carrick, L.; McLeish, T. C. B.; Semenov, A. N.; Boden, N. Hierarchical self-assembly of chiral rod-like molecules as a model for peptide β-sheet tapes, ribbons, fibrils, and fibers. *Proc. Natl. Acad. Sci. U.S.A.* **2001**, *98*, 11857−11862.
(127) Hamley, I. W. Liquid Crystal Phase Formation by Biopolymers. *Soft Matter* **2010**, *6*, 1863−1871.
(128) Jung, J.-M.; Mezzenga, R. Liquid Crystalline Phase Behavior of Protein Fibers in Water: Experiments versus Theory. *Langmuir* **2010**, *26*, 504−514.
(129) Nyström, G.; Mezzenga, R. Liquid crystalline filamentous biological colloids: Analogies and differences. *Curr. Opin. Colloid Interface Sci.* **2018**, *38*, 30−44.
(130) Pelin, J. N. B. D.; Edwards-Gayle, C. J. C.; Castelletto, V.; Aguilar, A. M.; Alves, W. A.; Seitsonen, J.; Ruokolainen, J.; Hamley, I. W. Self-Assembly, Nematic Phase Formation, and Organocatalytic Behavior of a Proline-Functionalized Lipopeptide. *ACS Appl. Mater. Interfaces* **2020**, *12*, 13671−13679.
(131) Balacheva, A.; Iliev, I.; Detcheva, R.; Dzimbova, T.; Pajpanova, T.; Golovinsky, E. In vitro assessment of the cytotoxic effects of novel RGD analogues. *BioDiscovery* **2012**, *4*, No. e8931.
(132) Kafi, M. A.; El-Said, W. A.; Kim, T. H.; Choi, J. W. Cell adhesion, spreading, and proliferation on surface functionalized with RGD nanopillar arrays. *Biomaterials* **2012**, *33*, 731−739.
(133) Verderio, E. A. M.; Telci, D.; Okoye, A.; Melino, G.; Griffin, M. A novel RGD-independent cell adhesion pathway mediated by fibronectin-bound tissue transglutaminase rescues cells from anoikis. *J. Biol. Chem.* **2003**, *278*, 42604−42614.
(134) Frisch, S. M.; Screaton, R. A. Anoikis mechanisms. *Curr. Opin. Cell Biol.* **2001**, *13*, 555−562.
(135) Beachley, V.; Katsanevakis, E.; Zhang, N.; Wen, X. J. Highly Aligned Polymer Nanofiber Structures: Fabrication and Applications in Tissue Engineering. *Adv. Polym. Sci.* **2012**, *246*, 171−212.

Macromolecular Bioscience
www.mbs-journal.de

Multicomponent Hydrogel Matrices of Fmoc-FF and Cationic Peptides for Application in Tissue Engineering

*Elisabetta Rosa, Carlo Diaferia, Eliana Gianolio, Teresa Sibillano, Enrico Gallo, Giovanni Smaldone, Mariano Stornaiuolo, Cinzia Giannini, Giancarlo Morelli, and Antonella Accardo**

In the last years, peptide-based hydrogels are being increasingly used as suitable matrices for biomedical and pharmaceutical applications, including drug delivery and tissue engineering. Recently, the synthesis and the gelation properties of a small library of cationic peptides, containing a Lys residue at the C-terminus and derivatized with an Fmoc group or with the fluorenyl methoxycarbonyl-diphenylalanine (FmocFF) at the N-terminus are derived. Here, it is demonstrated that the combination of these peptides with the well-known hydrogelator FmocFF, in different weight/weight ratios, allows the achievement of seven novel self-sorted hydrogels, which share similar peptide organization of their supramolecular matrix. Rheological and relaxometric characterization highlight a different mechanical rigidity and water mobility in the gels as demonstrated by the storage modulus values (200 Pa < *G'* < 35 000 Pa) and by relaxometry, respectively. In vitro studies demonstrate that most of the tested mixed hydrogels do not disturb significantly the cell viability (>95%) over 72 h of treatment. Moreover, in virtue to its capability to strongly favor adhesion, spreading and duplication of 3T3-L1 cells, one of the tested hydrogel may be eligible as synthetic extracellular matrix.

1. Introduction

In the area of supramolecular chemistry, peptide-based materials represent an up-and-coming multivalent biotechnological tool, with fascinating applications in optoelectronics,[1] green chemistry,[2] diagnostics,[3] energy harvesting,[4] and healthcare.[5] Among the vast class of peptide-based materials, peptide-based hydrogels (P-HGs) are accorded a prominent place.[6] Hydrogels are 3D matrices characterized by a non-Newtonian behavior able to confine a high content of water, entrapped in the material as a consequence of noncovalent interactions. P-HGs present a final 3D organization similar to polymeric hydrogels. However, such final conformation is achieved as a consequence of a peculiar multiscale aggregating process, which involves supramolecular interactions between nanohelices or nanofibers, generated by self-assembly of the peptide sequences.[7] Most importantly, the formation of these matrices does not require the employment of biologically toxic cross-linking agents. Further benefits of P-HGs include reproducibility, transparency, injectability, and easy cellular harvesting.

In the last years, P-HGs have been thus proposed for many different biological and pharmaceutical applications including drug delivery[8] and tissue engineering.[9] In this contest, the Fmoc-diphenylalanine (FmocFF, Fmoc = fluorenyl methoxycarbonyl) derivative, first identified in 2006,[10] has been extensively studied, alone or in combination with other chemical entities, as scaffold for generation of biocompatible extracellular matrices in physiological conditions.[6b] Recently, a library of synthetic cationic peptides, composed of an aliphatic portion of tri-, tetra-, and hexapeptides (including Gly, Ala, Val, Leu, and Ile) and a Lys residue at the C-terminus, has been proposed for the fabrication of innovative bioink materials.[11] All the sequences are acetylated and amidated on their termini. Among the library components, the hexapeptides (named K1, K2, and K3) showed the best gelling properties with low critical gelation concentration and high mechanical rigidity (storage modulus *G'* value ≈40 000 Pa). We have also demonstrated that K1, K2, and K3 peptides, protected at the N-terminus with the Fmoc group in place of the acetyl one keep their capability to gel, even if with a decrease of the stiffness (*G'* values around 500–2500 Pa).[12] On the contrary, the addition of

E. Rosa, C. Diaferia, M. Stornaiuolo, G. Morelli, A. Accardo
Department of Pharmacy and Research Centre on Bioactive Peptides (CIRPeB)
University of Naples "Federico II"
Via Mezzocannone 16, Naples 80134, Italy
E-mail: antonella.accardo@unina.it
E. Gianolio
Department of Molecular Biotechnologies and Health Science
University of Turin
Via Nizza 52, Turin 10125, Italy
T. Sibillano, C. Giannini
Institute of Crystallography (IC)
CNR
Via Amendola 122, Bari 70126, Italy
E. Gallo, G. Smaldone
IRCCS Synlab SDN
Via E. Gianturco 113, Naples 80143, Italy

DOI: 10.1002/mabi.202200128

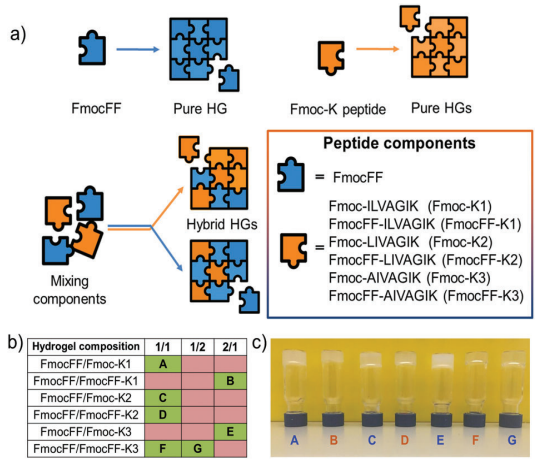

Hydrogel composition	1/1	1/2	2/1
FmocFF/Fmoc-K1	A		
FmocFF/FmocFF-K1			B
FmocFF/Fmoc-K2	C		
FmocFF/FmocFF-K2	D		
FmocFF/Fmoc-K3			E
FmocFF/FmocFF-K3	F	G	

Figure 1. a) Graphical representation of the molecular strategy used to generate hybrid FmocFF/Fmoc-K hydrogels and peptide components. b) Table with all the 18 evaluated combination in terms of weight/weight (w/w) ratio and one letter identification (A–G, green cells) for HGs samples. c) Inverted test tubes of the seven P-HGs samples showing self-supporting 3D mixed hydrogels.

two Phe residues between the Fmoc group and the cationic peptides (FmocFF-K1, FmocFF-K2, and FmocFF-K3) seems to completely inhibit the formation of the hydrogel, thus highlighting the importance of balancing the chemical features within the sequence, to gain synergistic and not divergent interactions between the components.[12]

In order to obtain novel hydrogels with enhanced properties, here we describe the preparation and the characterization of hybrid P-HGs in which the cationic peptides previously studied (see **Figure 1**) have been mixed with the FmocFF hydrogelator. Indeed, due to the different chemical nature of each single component, this co-assembly resulted to be a well-assessed strategy to modulate the physical and the morphological features of the final macroscopic objects.[13] Different weight/weight ratios (2:1, 1:1, and 1:2, w/w) have been analyzed. The aggregative behavior of the hybrid HGs was evaluated using a set of biophysical techniques (fluorescence, circular dichroism (CD), Fourier transform infrared (FT-IR), Congo Red (CR) assay, scanning electron microscopy (SEM), and Wide angle X-ray scattering (WAXS)). The effect caused by the introduction of the FF portion on the aggregation was also evaluated. An analysis of the rheological and relaxometric properties (through the measure of water longitudinal relaxation rate ($R_1 = 1/T_1$) as a function of applied magnetic field) of the obtained hydrogels was also carried out to explore their mechanical behavior and the mobility of the water in the fibrillary network. Cytotoxicity and cell adhesion assays on 3T3 fibroblast and on HaCat cell lines were used to explore the potential application of these hybrid hydrogels as extracellular matrices.

2. Results and Discussion

2.1. Preparation of Multicomponent Hydrogels and Their Stability

The capability of cationic peptides (Figure 1) to gel in combination with FmocFF was checked according to the "solvent-switch" method.[14] In details, each peptide was separately dissolved in dimethylsulfoxide (DMSO, 100 mg mL^{-1}). Then, these resulting stock solutions were properly mixed at different volumetric ratios (2/1, 1/1, and 1/2 v/v), obtaining a total of 18 possible combinations. The final multicomponent matrices were obtained diluting the DMSO in water up to the final peptide concentration of 1.0 wt%. In order to trigger the hydrogel formation in homogenous manner, samples were vortexed for few seconds, immediately after the water addition. Successively, the metastable suspensions were left at room temperature until the formation of homogenous hydrogels. From the macroscopic observation of the samples over time, only seven of the prepared mixtures (samples identified from A to G, see Figure 1b) allow generating self-supporting HGs.

Table 1. Multicomponent hydrogels examined in this study and the corresponding gelation times evaluated by UV-vis kinetics.

Sample	Mixed hydrogels	Weight/weight ratio [w/w]	Molar ratio [mol/mol]	ΔW [%]
A	FmocFF/Fmoc-K1	1/1	1.5/1	4.7
B	FmocFF/FmocFF-K1	2/1	4.2/1	8.2
C	FmocFF/Fmoc-K2	1/1	1.5/1	2.9
D	FmocFF/FmocFF-K2	1/1	2.1/1	5.7
E	FmocFF/Fmoc-K3	2/1	2.9/1	5.5
F	FmocFF/FmocFF-K3	1/1	2.0/1	7.8
G	FmocFF/FmocFF-K3	1/2	1.0/1	3.1

It is important to note that, analogously to the pure FmocFF hydrogel, all the multicomponent ones appear completely formed immediately (<3 min) after vortexing the peptide suspension, thus indicating that the insertion of the cationic peptides does not slow down the formation kinetics. This evidence is in contrast with the results previously obtained for other FmocFF-based multicomponent systems,[15] in which we observed a reduction of the speed of hydrogel formation. The unaltered gelation kinetics in the systems here reported is probably due to the derivatization of the cationic peptides with the same fluorenyl group present in Fmoc-dipeptide. Moreover, it should be evidenced that, even if at different w/w ratio, all the tested peptides were able to produce at least one stable hydrogel in combination with FmocFF. This result suggests that similitudes in the peptide sequences to mix could favor the gelification process.

After hydrogel preparation, their stability was evaluated over time (up to 30 days) and compared to the stability of pure FmocFF hydrogel. All the gels were incubated in the Ringer's solution at 37 °C and the weight loss was estimated.[16] Results, collected in **Table 1** as ΔW(%), indicate very low weight loss (ranged between 2.5% and 8.2%) for all the mixed hydrogels. These values are lower than the weight loss of the pure FmocFF HG (ΔW(%) = 10%). From the inspection of ΔW(%) values, a major stability of mixed hydrogels containing Fmoc-K peptides with respect to FmocFF-K ones can be noticed.

2.2. Structural Characterization in Solution

Taking advantages from the presence of chromophoric species in the peptide components, initial molecular arrangement informa-

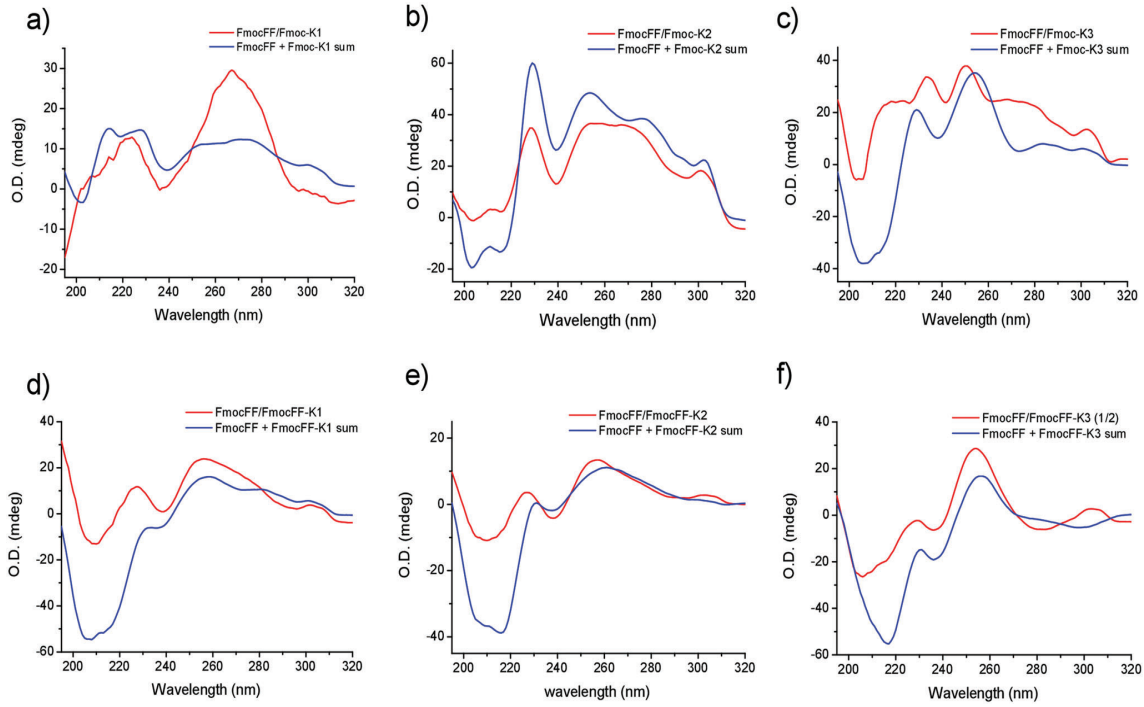

Figure 2. Comparison between CD spectra of hybrid P-HGs recorded between 320 and 195 nm and calculated spectra obtained by summing CD spectrum of each component in the same experimental conditions.

tion of the networks was deduced by fluorescence spectroscopy. Fluorescence spectra of gels, directly formed in the cuvette, were recorded exciting the sample both at $\lambda = 257$ and $\lambda = 301$ nm, which correspond to the excitation wavelengths of phenyl and Fmoc chromophores, respectively. From the inspection of spectra in Figures S2 and S3 in the Supporting Information, a similar emissive behavior of all the mixed hydrogels can be observed with the following: i) a main emission peak centered at 325–328 nm, ii) two shoulders at 350 and 361 nm, and iii) a red-shifted peak around 420 nm. The signal around 325 nm, previously observed also for these peptides in their self-assembled form, indicates that the Fmoc group is overlapped in antiparallel manner.[17] However, the simultaneous presence of the peak at 361 nm, typical of the parallel fluorenyl stacking, indicates the occurrence of both the parallel and antiparallel orientation of the aromatic groups in the hydrogel fibers.[18] The higher intensities of the first peak with respect to the second one suggest that the antiparallel overlap is preferred in the hydrogel matrix. HGs also exhibit a peak around 420 nm that could be due to the formation of excimeric species. An analogous emissive profile, with three emission peaks (at 323, 361, and 410 nm), has been observed for samples excited at 257 nm, thus indicating the occurrence of a Föster resonance energy transfer phenomenon between phenyl and fluorenyl groups, suggesting the mutual spatial proximity of chromophores.[19]

Further details on the organization of peptides in the multicomponent hydrogels were obtained by other techniques such as CD and FT-IR spectroscopies (Figure 3). These investigations are classically employed for the determination and identification of peptide secondary structure, with particular attention to β-sheets (with parallel or antiparallel β-strands) and amyloid–amyloid-like arrangements.[20]

CD spectra of all the P-HGs at 1.0 wt%, recorded between 320 and 195 nm, are reported in **Figure 2**. Although there are different experimental conditions (solvent and concentration) in which samples have been recorded, multicomponent hydrogels containing cationic peptides exhibit a dichroic signature similar to that previously observed for pure HGs.[12] From the inspection of the figure, two distinct regions can be identified, respectively, attributable to $n \rightarrow \pi^*$ transitions occurring in the β-sheet structure (210–220 nm) and to $\pi \rightarrow \pi^*$ transitions of fluorenyl absorption (between 250 and 310 nm).[21] Analogously to CD spectra of pure self-assembled peptides, in hybrid hydrogels containing FmocFF-K peptides we also observed an apparent inversion of the CD signal, with a minimum at 220 nm in place of a maximum. This apparent inversion of the signal in the spectra of FmocFF containing peptides suggests that a different orientation of the Fmoc group in the hydrogel occurs. The comparison between CD spectra of mixed hydrogels with the sum of CD ones of the single components can also provide supplementary information about the molecular organization inside the hybrid hydrogels.[22] In particular, CD profiles of self-sorted and co-assembled HGs are expected to be superimposable and not superimposable with the sum of the individual peptides, respectively. As shown in Figure 2, in our mixed P-HGs there is a sufficient overlapping between the spectra, thus suggesting a possible, but not certain, self-sorted arrangement of the two peptides.

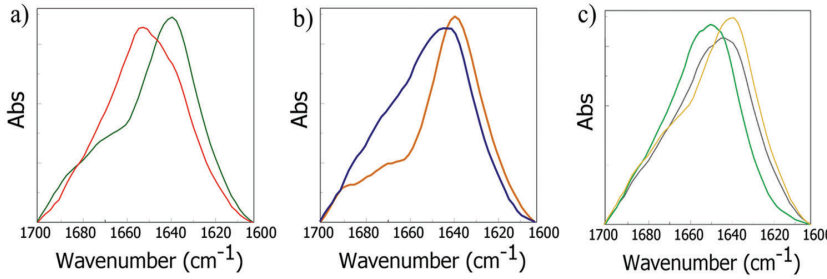

Sample	α-helix	β-sheet	β-turn	other
A	0	62	18	20
B	34	26	20	20
C	1	86	11	2
D	9	42	25	24
E	5	49	21	25
F	20	40	19	21
G	23	39	18	20

Figure 3. FT-IR amide I deconvolution profiles for a) FmocFF/Fmoc-K1 1/1(green line) and FmocFF/FmocFF-K1 2/1 (red line); b) FmocFF/Fmoc-K2 1/1 (orange line) and FmocFF/FmocFF-K2 1/1 (blue line); c) FmocFF/Fmoc-K3 2/1 (dark yellow line), FmocFF/FmocFF-K3 1/1 (gray line), and FmocFF/FmocFF-K3 (light green line). The table reports the deconvolution percentage analysis.

To further characterize P-HGs, we also studied samples at 1.0 wt% by FT-IR spectroscopy and the corresponding transmittance spectra recorded between 4000 and 400 cm^{-1} are reported in Figure S4 in the Supporting Information.

Two main signals can be identified in these IR spectra. The first signal, a broad band around 3300–3400 cm^{-1} (amide A region), is symptomatic of N–H stretching, polarized along the N–H bond, and indicates strong intermolecular amide–amide bonds interactions. The second one is in the amide I region (1700–1600 cm^{-1}), sensible to secondary conformations. After the acquisition, the deconvolution of FT-IR spectra was operated using a dedicated software. Absorbance deconvolution profiles in the amide I region and the secondary structure percentages are collected in **Figure 3**. Samples A, C, and E, identified as the prevalent β containing systems, share a common deconvolution profile, with a dominant peak at 1640 cm^{-1} associated with a 1675 cm^{-1} shoulder. This spectral imprint is generally reconducted to a β-sheet structure with an antiparallel orientation of the strands. However, this signal is wide, and could also be due to residual trifluoroacetic acid.[23] All the other samples, united by the presence in the matrix of FmocFF-K peptides, have a principal band red-shifted to 1650–1653 cm^{-1} and seem to be characterized by a mixture of secondary structures in which, however, the prevalence remains the β-arrangements.

2.3. Structural Characterization at the Solid State

Further structural information on hybrid hydrogels was obtained on xerogels (1.0 wt%) using SEM and CR assay, or on dried fibers by WAXS technique. Selected immunofluorescence images and micrographs of all the seven matrices are collected in **Figure 4**. Micrographs show that mixed HGs are composed by long fibrils, involved in a mutual physical entanglement. No substantial differences in morphology are detectable. However, it is important to note that, for Fmoc-K1, Fmoc-K2, and Fmoc-K3, fibers appear more visible and defined in mixed hydrogels with respect to the corresponding pure ones.[12] CR birefringence microscopy assay was performed in order to elucidate the nature of the fibrillary aggregates. CR is the sodium salt of benzidinediazo-bis-1-naphthylamine-4-sulfonic acid largely employed as diagnostic staining agent for amyloid and amyloid-like aggregates. CR generates dichroic and birefringent effects under cross-polarized light source with various colorations of the samples as a consequence of the staining via both hydrophobic and the electrostatic interactions.[24] Selected images of CR-stained xerogels are reported in second (bright field) and third (polarized light) rows of Figure 4. For all the multicomponent peptide-based HGs, CR exhibits birefringence suggesting that the deposited matrices have two refractive indices depending on their orientation under polarized light. Different colors are detectable, demonstrating negative birefringence (transmission of blue), positive one (transmission of yellow), or their mixture (visualized as green).[25] The positive response of all the samples to the CR assay suggests an amyloid-like organization of the matrix fibers. In order to further confirm this structural hypothesis, WAXS analyses were performed. Dried fibers of mixed hydrogels for WAXS analysis were prepared according to the stretch-frame method.[26] In this method, a droplet of the metastable gel solution was left to air-dry between the ends of a wax-coated capillary. The 2D WAXS data for Fmoc-K and FmocFF-K series and their corresponding 1D profiles are reported in **Figures 5** and **6**, respectively. The 2D data of the FmocFF/Fmoc-K1 fiber (Figure 5a) show several continuous diffraction rings, an indication of the absence of clear preferred orientation into the illuminated volume of the fiber. On the contrary, the 2D WAXS data of the other fibers containing Fmoc-K2 (Figure 5b) and Fmoc-K3 (Figure 5c) show a growing partial orientation of the

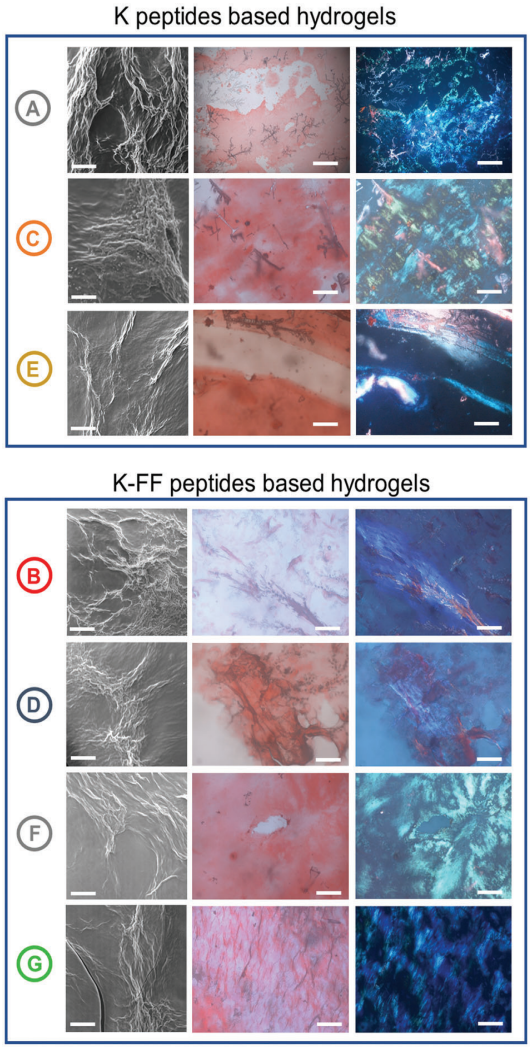

Figure 4. Characterization of xerogels: Selected SEM micrographs of hybrid hydrogels (on the left, scale bar is 10 μm) and staining of Congo Red xerogels in both bright field (at the center) and under cross-polarized light (on the right). Scale bars are 10 and 100 μm for SEM micrographs and CR images, respectively. List of samples: a) FmocFF/Fmoc-K1 1/1; b) FmocFF/FmocFF-K1 2/1; c) FmocFF/Fmoc-K2 1/1; d) FmocFF/FmocFF-K2 1/1; e) FmocFF/Fmoc-K3 2/1; f) FmocFF/FmocFF-K3 1/1; g) FmocFF/FmocFF-K3 1/2.

fiber, with the typical diffraction pattern of the cross-β amyloid structure. A similar diffraction pattern was also observed for hybrid HGs containing FmocFF-K series (see Figure 6).

The collected 2D WAXS patterns were centered and calibrated, and radially folded into 1D profiles. The 1D data were integrated along the meridional and equatorial axes to obtain the corresponding 1D profiles along the axis of the fiber and perpendicular to it, respectively. The main meridional and equatorial peaks are summarized in **Table 2**. The diffraction patterns are characterized by several common main peaks occurring at $q_1 = 0.58$ Å^{-1} ($d_1 = 10.8$ Å), $q_2 = 1.05$ Å^{-1} ($d_2 = 5.9$ Å), $q_3 = 1.32$ Å^{-1} ($d_3 = 4.8$ Å), and $q_4 = 1.53$ Å^{-1} ($d_4 = 4.1$ Å). The equatorial peak (q_1) corresponds to the main distance between two distinct β-sheets perpendicular to the fiber axis and meridional peak (q_3) corresponds to the distance between adjacent peptide backbones organized into β-strands along the fiber axis, both are typical features of amyloid-like fibers.[7d,15] These WAXS profiles and peak positions are in good agreement with those previously measured for pure FmocFF,[15] thus indicating that the structural organization of the FmocFF hydrogelator is not significantly affected by the addition of K peptides in the formulation. The absence of the typical cross-beta pattern only for sample Fmoc-K1, characterized by continuous ring, indicates a powder-like spread in the orientation of the absence of an ordered packing and orientation of the molecules along the equatorial and meridional orthogonal directions although the positions of the ring are the same for all the samples.

2.4. Rheological Characterization

All the hybrid P-HGs were characterized in relationship to their mechanical responsivity through oscillatory rheological tests carried out on preformed samples (1.0 wt% concentration). Rheological analysis, conducted using a plate geometry and a gap of 0.1 mm at 25 °C, was supported by the determination of preliminary measurement parameters, according to both a dynamic strain sweep oscillatory test (at a frequency of 1 Hz) and a frequency sweep one (at 0.1% strain) (see Figure S5, Supporting Information). Time sweep tests (see Figure S6, Supporting Information) were conducted with a frequency of 1.0 Hz and a strain stress of 0.1%. Experimental results, in terms of the G' storage (red bar) and G'' loss moduli (green bar), are collected in **Table 3** and reported as histograms in **Figure 7**a. As first evidence, the rheological test analytically confirms the viscoelastic nature of all the matrices, due to a $G' > G''$ relation and a tan $\delta > 1$ (see Table 3). From the inspection of the G' values, it can be observed that the mixed hydrogels of Fmoc-K1, Fmoc-K2, and Fmoc-K3 peptides (samples A, C, and E) have higher mechanical rigidity with respect to the corresponding self-assembled hydrogels. This is particularly true for sample E, in which the G' value increases from 2526 to 35 161 Pa. However, this is only a general consideration, because the experimental conditions used to prepare self-assembled and mixed hydrogels are quite different both in terms of solvent and concentration. On the contrary, a more objective comparison can be achieved between the mechanical properties of hydrogel couples (Fmoc-K1/FmocFF-K1, Fmoc-K2/FmocFF-K2, and Fmoc-K3/FmocFF-K3) here prepared using the same protocol. The mutual comparison of the G' values for hydrogel couples containing the same K peptide (A/B, C/D, and E/F-G) clearly indicates a trend in the mechanical strength of mixed matrices. In details, it seems that the insertion of the diphenylalanine moiety in the peptides produces a decrease of the stiffness. This behavior is more evident for the C/D couple, in which the two gels have been prepared exactly at the same volumetric ratio with FmocFF. The decrease of the G' value in samples containing the FF motif may be probably imputable to the increase, within the peptide sequence, of the aromatic portion with respect to the aliphatic one. The balance between the hydrophobic (aromatic/aliphatic) portions was previously described as a key factor for the self-assembly of K peptides in hydrogels.

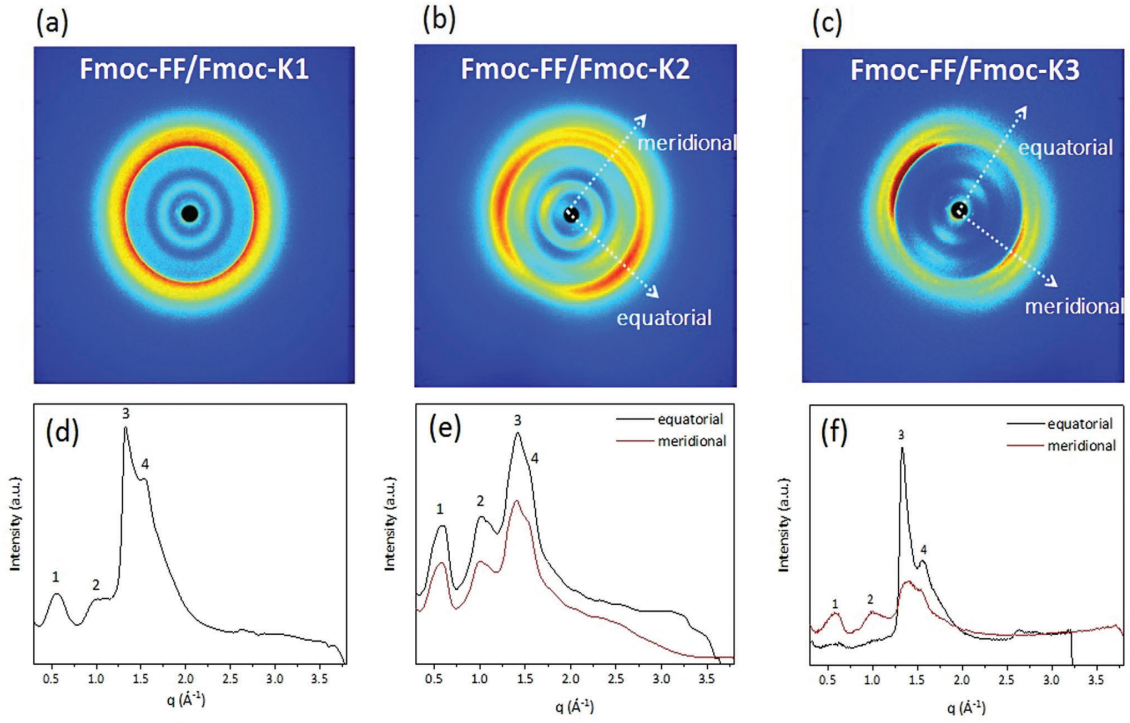

Figure 5. WAXS characterization of the mixed hydrogels FmocFF/Fmoc-Kx: 2D WAXS data (on the top row right), and 1D WAXS meridional/equatorial profiles (on the bottom row).

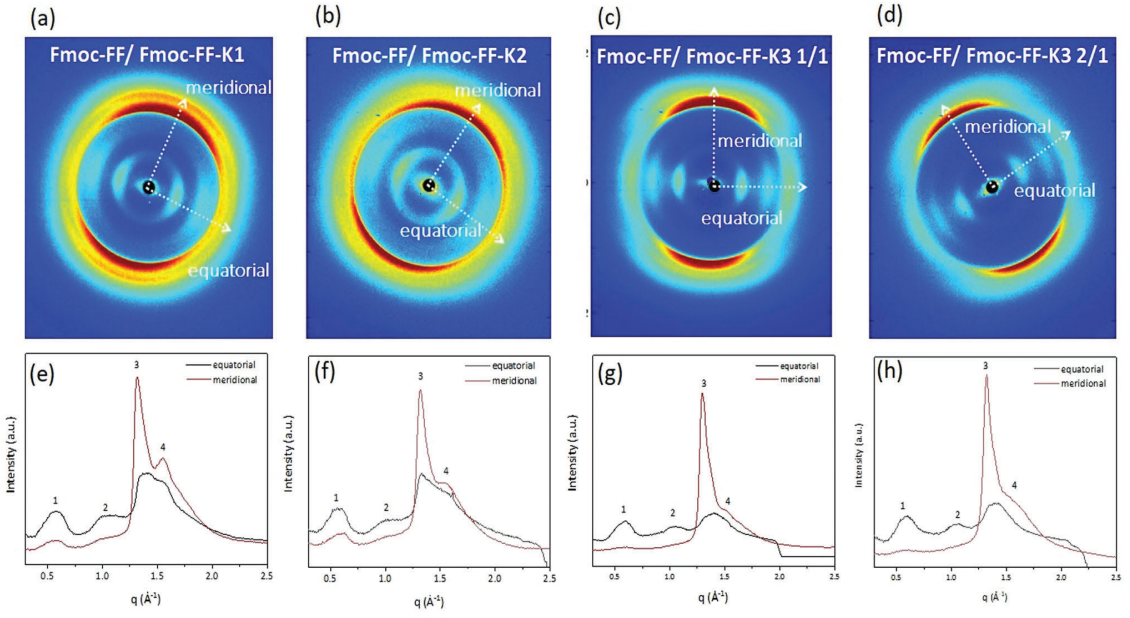

Figure 6. WAXS characterization of the mixed hydrogels Fmoc-FF/Fmoc-FF-Kx: 2D WAXS data (on the top row right), and 1D WAXS meridional/equatorial profiles (on the bottom row).

Table 2. Meridional and equatorial peak positions in q ($Å^{-1}$) and corresponding distance $d = 2\pi/q$ (Å) of the mixed hydrogels.

Systems	Equatorial reflections		Meridional reflections	
	q [$Å^{-1}$] ± 0.02	d [Å] ± 0.5	q [$Å^{-1}$] ± 0.02	d [Å] ± 0.5
FmocFF/Fmoc-K1	$q_1 = 0.58$	$d_1 = 10.8$	$q_3 = 1.32$	$d_3 = 4.8$
	$q_2 = 1.05$	$d_2 = 5.9$	$q_4 = 1.53$	$d_4 = 4.1$
FmocFF/Fmoc-K2	$q_1 = 0.58$	$d_1 = 10.8$	$q_3 = 1.32$	$d_3 = 4.8$
	$q_2 = 1.05$	$d_2 = 5.9$	$q_4 = 1.53$	$d_4 = 4.1$
FmocFF/Fmoc-K3	$q_1 = 0.58$	$d_1 = 10.8$	$q_3 = 1.32$	$d_3 = 4.8$
	$q_2 = 1.05$	$d_2 = 5.9$	$q_4 = 1.53$	$d_4 = 4.1$
FmocFF/FmocFF-K1	$q_1 = 0.58$	$d_1 = 10.8$	$q_3 = 1.32$	$d_3 = 4.8$
	$q_2 = 1.05$	$d_2 = 5.9$	$q_4 = 1.53$	$d_4 = 4.1$
FmocFF/FmocFF-K2	$q_1 = 0.58$	$d_1 = 10.8$	$q_3 = 1.32$	$d_3 = 4.8$
	$q_2 = 1.05$	$d_2 = 5.9$	$q_4 = 1.53$	$d_4 = 4.1$
FmocFF/FmocFF-K3 (1/1)	$q_1 = 0.58$	$d_1 = 10.8$	$q_3 = 1.32$	$d_3 = 4.8$
	$q_2 = 1.05$	$d_2 = 5.9$	$q_4 = 1.53$	$d_4 = 4.1$
FmocFF/FmocFF-K3 (2/1)	$q_1 = 0.58$	$d_1 = 10.8$	$q_3 = 1.32$	$d_3 = 4.8$
	$q_2 = 1.05$	$d_2 = 5.9$	$q_4 = 1.53$	$d_4 = 4.1$

Table 3. Storage modulus (G'), loss modulus (G''), and Tan δ for the studied multicomponent hydrogels.

Sample	G' [Pa]	G'' [Pa]	Tan δ
A	3226	340	9.5
B	801	76	10.5
C	2000	229	8.7
D	232	38	6.1
E	35 161	2169	16.2
F	5092	354	14.3
G	227	25	9.1

2.5. Relaxivity

A relaxometric approach has been applied for the investigation of water dynamics in the hydrogel scaffolds of all hybrid systems. The analysis of the variation of the relaxation rate (R_1) has been performed as a function of the applied magnetic field in the range of proton Larmor frequencies between 0.01 and 10 MHz (Figure 7b). This analysis allows for the identification of dynamic parameters associated with the occurrence of two levels of water motion: one, slower, associated with the water molecules constrained in the peptide scaffold, and the other, faster, relative to more free water molecules. The same approach, with different modifications, has been largely applied for the analysis of the frequency dependence of spin-lattice relaxation rates in hydrogels[27] and polymers.[28] The analysis of nuclear magnetic relaxation dispersion (NMRD) profiles reported in Figure 7c (samples A, C, E) and Figure 7d (samples B, D, F, G)

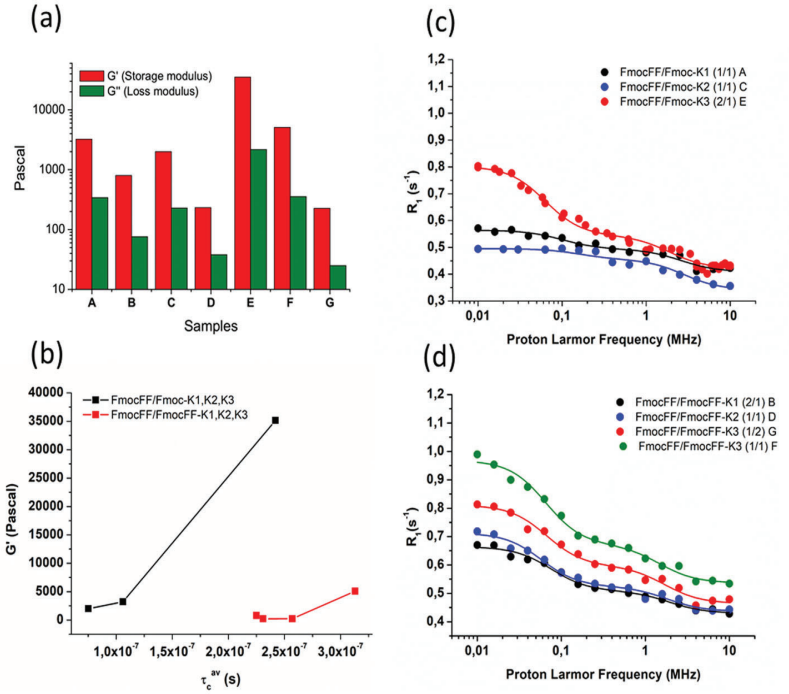

Figure 7. a) Rheological histogram analysis performed on 1.0 wt% hybrid P-HGs. Graph reports both G' (red bar) and G'' (green bar) moduli of each time sweep experiment (20 min, strain of 0.1%, frequency 1 Hz). Values are expressed in Pascal (Pa) logarithmic scale. b) Correlation between average water correlation time (τ_C^{av}) calculated from fitting of data reported in (c) and (d) and G'. c,d) ^{1}H NMRD profiles (longitudinal relaxation rate (R_1) as a function of the Proton Larmor frequency) measured on c) samples A, C, E and d) B, D, F, G at 298 K. Continuous lines represent the best fits obtained with a sum of Lorentzian functions.

Table 4. Best-fit parameters of the ^{1}H NMRD profiles of the hybrid hydrogels.

Sample	A	C	E	B	D	F	G
System	FmocFF/Fmoc-K1	FmocFF/Fmoc-K2	FmocFF/Fmoc-K3	FmocFF/FmocFF-K1	FmocFF/FmocFF-K2	FmocFF/FmocFF-K3 (1/1)	FmocFF/FmocFF-K3 (2/1)
A_0 (s^{-1})	0.41	0.34	0.42	0.42	0.43	0.54	0.46
β (s^{-1})	0.40	0.40	0.39	0.40	0.41	0.45	0.44
A_1	3.5×10^6	5.0×10^6	3.7×10^6	2.4×10^6	2.4×10^6	2.8×10^6	3.2×10^6
τ_1 (s)	6.1×10^{-8}	5.6×10^{-8}	8.4×10^{-8}	8.2×10^{-8}	8.7×10^{-8}	1.1×10^{-7}	9.3×10^{-8}
A_2	1.1×10^5	1.0×10^5	2.6×10^5	1.8×10^5	1.7×10^5	2.7×10^5	2.0×10^5
τ_2 (s)	1.6×10^{-6}	9.9×10^{-7}	2.5×10^{-6}	2.1×10^{-6}	2.7×10^{-6}	2.4×10^{-6}	2.4×10^{-6}
% slow[a)]	3.0	2.0	6.5	7.1	6.4	8.9	6.0
τ_C^{av} (s)	1.1×10^{-7}	7.5×10^{-8}	2.4×10^{-7}	2.2×10^{-7}	2.6×10^{-7}	3.1×10^{-7}	2.3×10^{-7}

[a)] The percentage of water experiencing slow motion (% slow) was obtained by comparing the weight of the Lorentzian functions (% slow = A_2/A_1+A_2) in each sample.

according to Equation (2) afforded the fitting parameters reported in **Table 4**. Moreover, the fitting parameters were also used to calculate two additional parameters (% of slow motion and average correlation time—τ_C^{av}) which can help in the interpretation of results (Table 4). From the inspection of NMRD profiles in Figure 7c,d, it can be observed that the relaxation rates values measured for our P-HGs are significantly lower (<1 s^{-1}) over all the frequency range in comparison to those previously reported for other peptide nucleic acid-based HGs.[27] These lower values can be explained by a punctual comparison of all the parameters (A_0, β, τ_1, and τ_2) extrapolated from the data fitting for our HGs with respect to the other ones. As first, it can be observed that both A_0 and β values are essentially constant for all the investigated hydrogels. Moreover, the here obtained τ_1 values (faster motion) are in the range of 5.65×10^{-8} to 1.07×10^{-7} s, thus similar to those observed in previous reports on analogous peptide-based hydrogels.[27] Instead, the values associated with the slower component of water motion (τ_2, in the range 9.9×10^{-7} to 2.74×10^{-6} s) are approximately three to six times shorter (faster motion) than those reported in refs. [27c] and [27d] ($6–7 \times 10^{-6}$ s). This acceleration in the slower component of the motion is likely to be responsible for the lower observed relaxation rates (R_1). Extrapolated data seem to highlight a different trend for the two classes of mixed hydrogels containing (B, D, F, G) or not containing (A, C, E) the diphenylalanine moiety between the Fmoc moiety and the K sequences. Indeed, in FF-K series, the obtained values of the correlation times associated with both the slow (τ_2) and fast (τ_1) motions are comparable and not dependent on the composition of the system (consequently the same applies for the % of slow motion and τ_C^{av}). On the other hand, in K series, an increasing trend of τ_1, τ_2, τ_C, and % slow is observed in the order C < A < E, which corresponds to the same trend of increasing stiffness obtained with the measure of *G'* values (Table 4 and Figure 7b). However, it is worthy to note that the values found from the fitting of NMRD profile of sample E are similar to those of hydrogels containing the diphenylalanine moiety (B, D, F, G), despite its much higher *G'* value. From this evidence, it seems that it is not always possible to extract a direct correlation between stiffness or rigidity of the hydrogel scaffold and the motional dynamics of entrapped water. Likely, other phenomena take place which should be considered for a complete understanding of water dynamics. In this context, it appears that the correlation between rigidity and water dynamics can be predictable only for hydrogels prepared using structurally similar building blocks in terms of primary amino acid sequence, hydrophobicity/hydrophilicity, and aromaticity.

2.6. Cell Viability

To test the biocompatibility of the resulting hydrogels, we evaluated the cytotoxicity of a conditioned medium collected upon incubation for 16 h with all the hydrogels on two different fibroblast cell lines, derived from mouse (pre adipocyte 3T3-L1 cell line) and from human (HaCat cell line). The selected cell lines were treated for 24, 48, or 72 h with conditioned medium of each hydrogel.[8d] As shown in **Figure 8**a, mixed hydrogels do not disturb the vitality of the HaCat cells in the least, determining only for the samples C, F, and G, a reduction of cell viability at about 20%. The cytotoxic effect in murine fibroblast seems to be increased, but in any case, it remains not significant for all the tested P-HGs (Figure 8b). Indeed, considering the hydrogel that involves the greatest lowering of cell viability (sample D), a reduction of about 35% is observed after 72 h of treatment, which is absolutely in line with biocompatibility values. These minimal changes in cell viability are not significant when compared to the untreated control (Mann–Whitney *t*-test). Finally, in order to prove the eligibility of the hydrogels as cell growing support, we performed a cell adhesion test. 3T3-L1 cells were seeded on hydrogel precasted 96-well plates. 16 h after seeding, cell adhesion and viability were estimated by acridine orange/propidium iodide staining. Compared to uncoated plastic wells, and among the tested hydrogels, sample C was able to strongly favor cell adhesion, spreading, and duplication (Figure 8c,d) confirming its nontoxicity and ability to act as extracellular matrix.

3. Conclusions

The mix of two or more peptide building blocks has been demonstrated very efficiently in the preparation of novel hybrid hydrogels with enhanced mechanical and functional properties. In

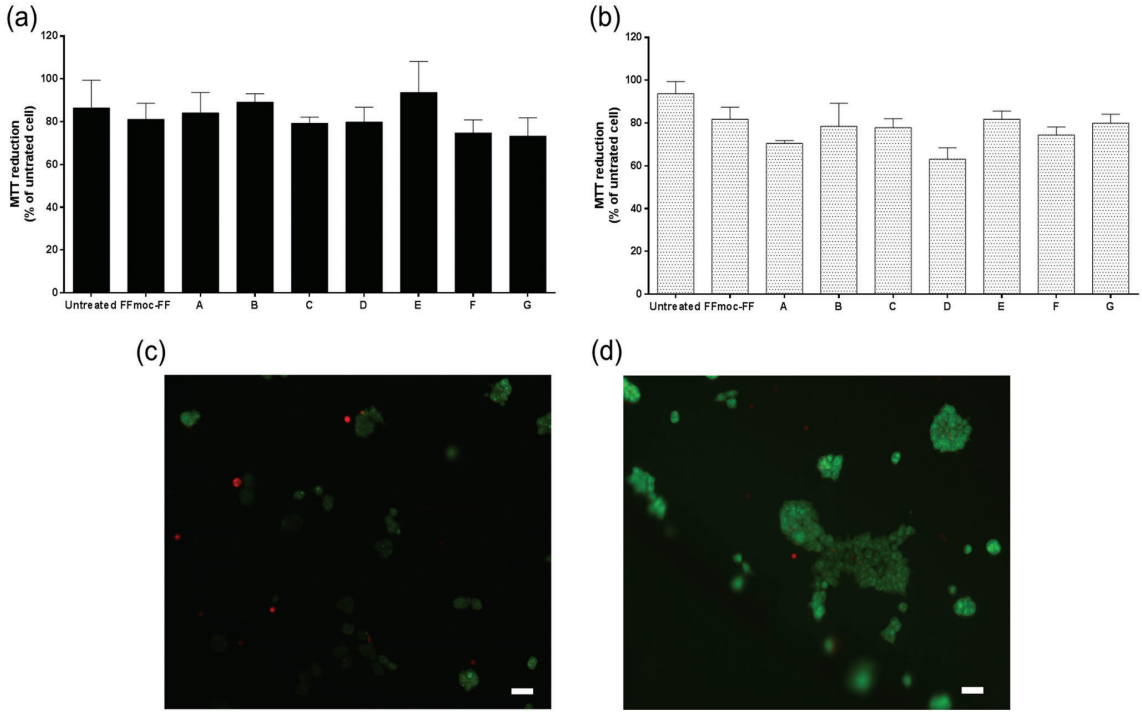

Figure 8. Cell viability analysis. MTS assay was conducted on: a) HaCat and b) 3T3-L1 cell lines. Cells were treated for 72 h with FmocFF and A–G mixed hydrogels (see table for details). Cell survival was expressed as percentage of viable cells in the presence of hydrogels, compared to control cells grown in their absence. Error represents SD of three independent experiments. All P-HGs do not perturb cell viability in a significant manner (Mann–Whitney *t*-test). For the adhesion test, 3T3-L1 cells were seeded on c) uncoated or d) on hydrogel C precasted 96-well plates. 16 h after seeding, cell adhesion and viability were estimated by acridine orange/propidium iodide stain to identify viable cell (fluorescing green) and dead cells (fluorescing red) (scale bar = 50 μm).

principle, peptide sequences can be freely chosen, without limitations related to their ability to self-assemble. This evidence was previously observed for not coded amino acids or for short peptide sequences like Fmoc-Phe(5F)-OH[13] and (FY)3;[29] and here is also confirmed for some of the presented peptides. Moreover, the combination of different hydrogelators in hybrid matrices could deeply affect the experimental conditions (preparation method, pH, solvent, and kinetics) in which the hydrogel gelificates. Indeed, differently from self-assembled K-peptides (Fmoc-K1, Fmoc-K2, and Fmoc-K3), mixed hydrogels (A, C, and E) were unable to self-aggregate in phosphate buffer solution. On the other hand, FF-K-peptides (FmocFF-K1, FmocFF-K2, and FmocFF-K3), which did not gel alone in any condition, instantaneously gave homogenous HGs, even if with low rigidity. All these considerations are obviously explained on the basis of the peptide structure with particular reference to its hydrophilicity/hydrophobicity balance and to the net charge. It is worth noting that no direct correlation can be evidenced between the rigidity of self-assembled P-HGs and multicomponent ones. Indeed, the scale of G' values, previously found for self-assembled systems, was K1 < K2 < K3, whereas in mixed systems the scale is K2 < K1 < K3, with a G' value for K3 (G' = 35 000 Pa) around tenfold higher with respect to K1 (G' = 3226 Pa) and K2 (G' = 2000 Pa). Since the three peptides differ only for two amino acids at the N-terminus, this difference in the rigidity has to be obviously correlated with the complexity of noncovalent interactions originated by peptides inside the fibrillary network. As expected, the dynamic parameters of the water molecules constrained in the peptide scaffold (slow water) are affected by the stiffness of the HG, but a direct comparison is possible only for analogous series. In vitro cell assays confirmed the high biocompatibility of P-HGs, extensively demonstrated for different systems. However, the cell adhesion tests highlight that contrarily to the expectation, the best compound is not the more rigid one, thus suggesting that many parameters are involved in the adhesion capacity of a gel.

4. Experimental Section

Materials and Methods: Protected N^{α}-Fmoc-amino acid derivatives, coupling reagents, and Rink amide MBHA (4-methylbenzhydrylamine) resin were commercially available from Calbiochem-Novabiochem (Läufelfingen, Switzerland). FmocFF was bought by Bachem (Bubendorf, Switzerland). All other chemical products, commercially accessible from Merck (Milan, Italy), Fluka (Bucks, Switzerland), or LabScan (Stillorgan, Dublin, Ireland) and unless stated otherwise, were used as delivered by the companies. Samples and peptide-based hydrogels were prepared by weight using DMSO and double distilled water. Purification of crude peptides was carried out via preparative RP-HPLC on a Phenomenex (Torrance, CA, USA) C18 column using an LC8 Shimadzu HPLC system (Shimadzu Corporation, Kyoto, Japan) equipped with an UV lambda-Max Model 481 detector. Elution solvents were H_2O/0.1% trifluoroacetic acid

(TFA) (A) and CH_3CN/0.1% TFA (B) from 30% to 80% over 25 min at a flow rate of 20 mL min^{-1}. The purity of the products was assessed by analytical reversed-phase high-performance liquid chromatography (RP-HPLC) analysis performed by using Finnigan Surveyor MSQ single quadrupole electrospray ionization (Finnigan/Thermo Electron Corporation San Jose, CA), with a C18-Phenomenex column eluting with H_2O/0.1% TFA (A) and CH_3CN/0.1% TFA (B) from 20% to 80% over 20 min at a flow rate of 200 µL min^{-1}. Identity of peptides was assessed by mass spectrometry using a LTQ XL Linear Ion Trap Mass Spectrometer, sorgent ESI.

Peptide Solid Phase Synthesis: Peptides were synthesized according to standard solid-phase peptide synthesis procedures using an Fmoc/tBu strategy as previously described.[12] Briefly, the Rink amide MBHA resin (substitution 0.73 mmol g^{-1}) was used as solid support and was swelled in dimethylformamide (DMF) for 30 min. Then, it was treated with 30%, v/v piperidine in DMF to remove the Fmoc group from the resin. After this latter deprotection step, each amino acid was coupled twice by leaving the resin reacting for 40 min with twofold molar excess of Fmoc-protected amino acid, 1-hydroxybenzotriazole, and benzotriazol-1-yl-oxytris-pyrrolidino-phosphonium, and a fourfold molar excess of diisopropylethylamine in DMF/NMP 1/1 v/v as reaction solvent. Crude peptides were cleaved from the resin by treating the resin with a TFA/triisopropylsilane/H_2O (92.5/5/2.5 v/v/v) mixture. The peptides were then precipitated with cold ether and freeze-dried for three times. The purity of crude peptides was found in the 75–90% range. Chemical structures and one code letter representation of primary sequences are reported in Figure S1 in the Supporting Information.

Preparation of Mixed Hydrogels: Total 1.0 wt% (10 mg mL^{-1}) mixed hydrogels were formulated by DMSO/H_2O solvent-switch method[14] using different balances of the aromatic dipeptide Fmoc-FF and of cationic peptides. The explored combination ratios for mixed hydrogels were 2/1, 1/1, and 1/2 w/w. More specifically, stock solutions of each peptide were prepared in DMSO (100 mg mL^{-1}). Then, these solutions were mixed, vortexed, and subsequently rehydrated with water. In the rehydration step, the mixture was additionally vortexed for 2 s in order to promote the homogeneity of the sample. The hydrogel formation was macroscopically verified by the inverted test tube.

Hydrogel Stability Studies: The determination of hydrogel degradation profile was performed by an in vitro stability assay, evaluating the percentage weight loss of the matrices. Freshly formed 1.0 wt% hydrogels (300 µL) were weighted (W_o) and then incubated at 37 °C with 1.0 mL of Ringer's solution (8.6 mg of NaCl, 0.30 mg of KCl, and 0.33 mg of $CaCl_2$).[30] After 20 days, the Ringer's solution was removed and hydrogels were weighted again (W_t). The degradation degree was expressed as percentage ratio (ΔW) between the hydrogel weight before (W_o) and after (W_t) the treatment using the following formula

$$\Delta W = \left(1 - \frac{W_t}{W_o}\right) \times 100 \quad (1)$$

Fluorescence Studies: Fluorescence spectra of mixed hydrogels were recorded using a spectrofluorophotometer Jasco (Model FP-750) in a quartz cell with 1.0 cm path length. Measurements were carried out at room temperature, by exciting the samples at both 257 and 301 nm wavelengths. The other settings were: excitation and emission bandwidths = 5 nm; recording speed = 125 nm min^{-1}; and automatic selection of the time constant.

CD Studies: Far-UV CD spectra of all the peptide-based materials were collected with a Jasco J-810 spectropolarimeter equipped with a NesLab RTE111 thermal controller unit using a 0.1 mm quartz cell at 25 °C. The spectra of samples at several concentrations were recorded from 320 to 195 nm. Other experimental settings were: scan speed = 10 nm min^{-1}, sensitivity = 50 mdeg, time constant = 16 s, bandwidth = 1 nm. Each spectrum was obtained by averaging three scans and corrected for the blank.

FT-IR Spectroscopy: FT-IR spectra of all the 1.0 wt% peptide-based hydrogels were performed on a Jasco FT/IR 4100 spectrometer (Easton, MD) in an attenuated total reflection mode and using a Ge single crystal at a resolution of 4 cm^{-1}. A total of 100 scans of each sample were recorded with a rate of 2 mm s^{-1} against a KBr background. After collection in transmission mode, amide I deconvolutions (in the 1600–1700 cm^{-1} region) were automatically returned as emission by an instrument integrated software.

Birefringence CR Assay: A dried film of each peptide was prepared by drop-casting ≈40 µL of preformed 1.0 wt% peptide hydrogel on a microscope glass slide. Peptide samples were prepared as already described and they were dried overnight at room temperature. Then, the obtained xerogels were stained for 15 s with 5 µL of a CR solution freshly prepared by adding a saturating amount of CR in a solution of 20% ethanol saturated with NaCl. The excess solution of CR on the samples was removed using filter paper, avoiding the compromise of the xerogel. The dried stained films were observed under bright-field illumination and between crossed polars by using a Nikon AZ100 microscope.

Scanning Electron Microscopy (SEM): Morphological analysis of xerogels was carried out by field-emission SEM (Phenom_XL, Alfatest). 10 µL of each peptide hydrogel was drop-casted on an aluminium stub and air-dried. A thin coat of gold and palladium was sputtered at a current of 25 mA for 75 s. The sputter-coated samples were then introduced into the specimen chamber and images were acquired at an accelerating voltage of 10 kV, through the Secondary Electron Detector (SED).

Wide-Angle X-Ray Scattering (WAXS): Fibers of FmocFF-based hybrid hydrogels for WAXS analysis were prepared using the "stretch frame" method.[30] 2D WAXS data were collected from the fibers at the X-ray MicroImaging Laboratory (XMI-L@b), equipped with an Fr-E+ SuperBright rotating anode table-top microsource (Cu Kα, $\lambda = 0.15405$ nm, 2475 W), a multilayer focusing optics (Confocal Max-Flux; CMF 15–105), and a three-pinholes camera (Rigaku SMAX-3000). An image plate (IP) Raxia detector with 100 µm pixel size and off-line reader was placed at around 10 cm from the sample to acquire the WAXS data. Once acquired, the 2D WAXS data were centered, calibrated by means of the Si NIST standard reference material (SRM 640b) and folded into 1D WAXS radial profile.[31]

Rheological Studies: Rheological measurements of freshly preformed 1.0 wt% hybrid hydrogels (460 µL) were performed with a rotational controlled-stress rheometer (Malvern Kinexus, UK) using a 1.5 cm diameter flat-plate geometry (PU20-PL61). All the analyses were conducted at 25 °C in a humidity chamber with a gap distance of 1.0 mm. Preliminary parameters optimization was performed via oscillatory frequency (0.1–100 Hz) and strain sweep (0.1–100%). Then, a 15 min time-sweep oscillatory analysis was conducted at 25 °C with a 0.1% strain and a 1.0 Hz frequency. The rheological profiles, reported in Pascal (Pa), were plotted as storage or elastic modulus (G') and shear loss or viscous modulus (G'').

Relaxometry: NMRD profiles were obtained using a Stelar SMARtracer fast-field-cycling relaxometer (Stelar S.n.c., Mede (PV), Italy) from 0.01 to 10 MHz equipped with a Stelar VTC-91 for temperature control. 1.0 wt% hybrid hydrogels (500 µL) were prepared in 10 mm NMR tubes and NMRD profiles were measured at 25 °C. For each profile, relaxation rate (R_1) was measured at 16–32 different values of applied magnetic field. Relevant acquisition parameters were: acquisition field 7.2 MHz (proton Larmor frequency); polarization field 8.5 MHz; polarization time and relaxation delay four times T_1; 16 sampled delay times; switching time 3 ms.

Each NMRD profile was fitted according to the model-free approach by using a sum of a two Lorentzians as customarily done on biomolecules in the presence of two distinct levels of motions (slow and fast).[32] Although conceptually different, the same functional form could be used to analyze water relaxation in hydrogel systems where the presence of two main water populations could be seen: one relative to water constrained in the peptide scaffold (slow motion), and a second one of more free water molecules (fast motion). Relaxation rates (R_1) as a function of the proton Larmor frequency ($\upsilon = \gamma B_0/2\pi$) were fitted by using the following equation

$$R_1 = A_0 + \beta\left[\frac{A_1\tau_1}{1+(2\pi\upsilon\tau_1)} + \frac{A_2\tau_2}{1+(2\pi\upsilon\tau_2)}\right] \quad (2)$$

where A_0 is the part of R_1 that remains in the extreme-motional narrowing regime up to the highest sampled frequency, β is the integral of the dispersion profile, τ_1 and τ_2 are the correlation times associated with fast and slow motions, respectively, and A_1 and A_2 are their relative weight coeffi-

cients. From parameters determined by fitting of experimental R_1 data to Equation (2), the average correlation time τ_C^{av}, could be calculated according to Equation (3)

$$\tau_C^{av} = \frac{A_1\tau_1 + A_2\tau_2}{A_1 + A_2} \quad (3)$$

Cell Lines: Aneuploid immortal keratinocyte cell line HaCat and mouse pre-adipocyte cell line 3T3-L1 were obtained from IRCCS-Synlab SDN Biobank (10.5334/ojb.26) and grown in Dulbecco's modified Eagle medium supplemented with 10% fetal bovine serum and 1% GlutaMAX. Cells were incubated at 37 °C and 5% CO_2 and seeded in 100 mm culture dishes.

Cell Viability Evaluation: For the adhesion test, 3T3-L1 cells were seeded in 96-well plates at a density of 0.5×10^4 cells per well. Before seeding, each well was filled with the indicated hydrogels. 16 h after seeding, cells were stained with acridine orange/propidium iodide stain to identify viable cell (fluorescing green) and dead cells (fluorescing red). In order to test the toxicity of hydrogels conditioned media, MTS (3-(4,5-dimethylthiazol-2-yl)-5-(3-carboxymethoxyphenyl)-2-(4-sulfophenyl)-2*H*-tetrazolium) assay (CellTiter 96 AQueous One Solution Cell Proliferation Assay, Promega, Italy) was used. 1×10^5 HaCat and 3T3-L1 cells per well were seeded in 96-well plates. Hydrogels formed in a hollow plastic chamber were used to obtain the conditioned media.[12] In brief, hydrogels were formed in a plastic support sealed at one end with a porous membrane, and incubated with 2 mL of completed medium for 16 h in sterile condition and in agitation at 400 rpm at room temperature. No color change of the media was detected following the incubation and the tested pH value (7.5–7.8) was suitable for culturing added to the wells. The conditioned media were used to grow the cells for 24, 48, and 72 h. Cell viability was assessed by the MTS test every 24 h using manufacturer's instructions. The samples were analyzed using the VictorNivo (Perkin Elmer, UK) at 490 nm absorbance. Cell survival was expressed as a percentage of viable cells in the presence of hydrogels, compared with the control cells grown in their absence. MTS assays were conducted in triplicate and repeated twice with similar results.

Supporting Information

Supporting Information is available from the Wiley Online Library or from the author.

Acknowledgements

E.R. and C.D. contributed equally to this work. This research was funded by PRIN–2017A2KEPL.

Open Access Funding provided by Universita degli Studi di Napoli Federico II within the CRUI-CARE Agreement.

Conflict of Interest

The authors declare no conflict of interest.

Data Availability Statement

The data that support the findings of this study are available from the corresponding author upon reasonable request.

Keywords

extracellular matrix, FmocFF, multicomponent materials, peptide hydrogel, self-assembling, tissue engineering

Received: March 29, 2022
Published online: May 18, 2022

[1] a) C. Avitabile, C. Diaferia, V. Roviello, D. Altamura, C. Giannini, L. Vitagliano, A. Accardo, A. Romanelli, *Chem. - Eur. J.* **2019**, *25*, 14850; b) R. A. Mansbach, A. L. Ferguson, *Org. Biomol. Chem.* **2017**, *15*, 5484; c) A. López-Andarias, J. López-Andarias, C. Atienza, F. J. Chichón, J. L. Carrascosa, N. Martín, *Chem. - Eur. J.* **2018**, *24*, 7755; d) B. Apter, B. Fainberg, A. Handelman, I. Lapsker, A. Accardo, C. Diaferia, G. Morelli, G. Rosenman, *Adv. Opt. Mater.* **2020**, *8*, 2000056.

[2] a) K. Basu, N. Nandi, B. Mondal, A. Dehsorkhi, I. W. Hamley, A. Banerjee, *Interface Focus* **2017**, *7*, 20160128; b) S. Bolisetty, R. Mezzenga, *Nat. Nanotechnol.* **2016**, *11*, 365; c) S. Basak, J. Nanda, A. Banerjee, *J. Mater. Chem.* **2012**, *22*, 11658; d) P. Ajitha, K. Vijayalakshmi, M. Saranya, T. Gomathi, K. Rani, P. N. Sudha, A. Sukumaran, *Int. J. Biol. Macromol.* **2017**, *104*, 1469; e) M. Peydayesh, M. K. Suter, S. Bolisetty, S. Boulos, S. Handschin, L. Nyström, R. Mezzenga, *Adv. Mater.* **2020**, *32*, 1907932.

[3] a) P. Zou, W.-T. Chen, T. Sun, Y. Gao, L.-L. Li, H. Wang, *Biomater. Sci.* **2020**, *8*, 4975; b) E. Gallo, C. Diaferia, E. Di Gregorio, G. Morelli, E. Gianolio, A. Accardo, *Pharmaceuticals* **2020**, *13*, 19; c) A. T. Preslar, G. Parigi, M. T. Mcclendon, S. S. Sefick, T. J. Moyer, C. R. Haney, E. A. Waters, K. W. Macrenaris, C. Luchinat, S. I. Stupp, T. J. Meade, *ACS Nano* **2014**, *8*, 7325; d) E. Gallo, E. Rosa, C. Diaferia, F. Rossi, D. Tesauro, A. Accardo, *RSC Adv.* **2020**, *10*, 27064.

[4] a) V. Nguyen, R. Zhu, K. Jenkins, R. Yang, *Nat. Commun.* **2016**, *7*, 13566; b) J.-H. Lee, K. Heo, K. Schulz-Schönhagen, J. H. Lee, M. S. Desai, H.-E. Jin, S.-W. Lee, *ACS Nano* **2018**, *12*, 8138; c) V. Slabov, S. Kopyl, M. P. Soares dos Santos, A. Kholkin, *Nanogenerators*, IntechOpen, London **2019**.

[5] a) P. K. Gavel, N. Kumar, H. S. Parmar, A. K. Das, *ACS Appl. Bio Mater.* **2020**, *3*, 3326; b) P. R. Turner, E. Murray, C. J. Mcadam, M. A. Mcconnell, J. D. Cabral, *ACS Appl. Mater. Interfaces* **2020**, *12*, 32328.

[6] a) A. M. Garcia, R. Lavendomme, S. Kralj, M. Kurbasic, O. Bellotto, M. C. Cringoli, S. Semeraro, A. Bandiera, R. De Zorzi, S. Marchesan, *Chem. - Eur. J.* **2020**, *26*, 1880; b) C. Diaferia, G. Morelli, A. Accardo, *J. Mater. Chem. B* **2019**, *7*, 5142; c) A. Ishida, G.o Watanabe, M. Oshikawa, I. Ajioka, T. Muraoka, *Chem. - Eur. J.* **2019**, *25*, 13523; d) E. Fuentes, K. Boháčová, A. M. Fuentes-Caparrós, R. Schweins, E. R. Draper, D. J. Adams, S. Pujals, L. Albertazzi, *Chem. - Eur. J.* **2020**, *26*, 9869; e) D. M. Ryan, B. L. Nilsson, *Polym. Chem.* **2012**, *3*, 18.

[7] a) S. H. Hiew, H. Mohanram, L. Ning, J. Guo, A. Sánchez-Ferrer, X. Shi, K. Pervushin, Y. Mu, R. Mezzenga, A. Miserez, H. Mohanram, L. Ning, J. Guo, A. Sánchez-Ferrer, X. Shi, K. Pervushin, Y. Mu, R. Mezzenga, A. Miserez, *Adv. Sci.* **2019**, *6*, 1901173; b) A. F. Dexter, N. L. Fletcher, R. G. Creasey, F. Filardo, M. W. Boehm, K. S. Jack, *RSC Adv.* **2017**, *7*, 27260; c) A. Yaguchi, H. Hiramatsu, A. Ishida, M. Oshikawa, I. Ajioka, T. Muraoka, *Chem. - Eur. J.* **2021**, *27*, 9295; d) C. Diaferia, F. Netti, M. Ghosh, T. Sibillano, C. Giannini, G. Morelli, L. Adler-Abramovich, A. Accardo, *Soft Matter* **2020**, *16*, 7006; e) S. K. Talloj, M. Mohammed, H.-C. Lin, *J. Mater. Chem. B* **2020**, *8*, 7483; f) F. Gelain, Z. Luo, S. Zhang, *Chem. Rev.* **2020**, *120*, 13434.

[8] a) M. E. Roth-Konforti, M. Comune, M. Halperin-Sternfeld, I. Grigoriants, D. Shabat, L. Adler-Abramovich, *Macromol. Rapid Commun.* **2018**, *39*, 1800588; b) C. A. Dreiss, *Curr. Opin. Colloid Interface Sci.* **2020**, *48*, 1; c) R. Dimatteo, N. J. Darling, T. Segura, *Adv. Drug Delivery Rev.* **2018**, *127*, 167. d) E. Gallo, C. Diaferia, E. Rosa, G. Smaldone, G. Morelli, A. Accardo, *Int. J. Nanomed.* **2021**, *16*, 1617; e) C. Karavasili, E. Panteris, I. S. Vizirianakis, S. Koutsopoulos, D. G. Fatouros, *Pharm. Res.* **2018**, *35*, 166.

[9] a) N. Huettner, T. R. Dargaville, A. Forget, *Trends Biotechnol.* **2018**, *36*, 372; b) L. Saunders, P. X. Ma, *Macromol. Biosci.* **2019**, *19*, 1800313; c) M. Aviv, M. Halperin-Sternfeld, I. Grigoriants, L. Buzhansky, I. Mironi-Harpaz, D. Seliktar, S. Einav, Z. Nevo, L. Adler-Abramovich, *ACS Appl. Mater. Interfaces* **2018**, *10*, 41883; d) V. M. P. Vieira, A. C. Lima, M. De Jong, D. K. Smith, *Chem. - Eur. J.* **2018**, *24*, 15112; e) M.i Zhou,

A. M. Smith, A. K. Das, N. W. Hodson, R. F. Collins, R. V. Ulijn, J. E. Gough, *Biomaterials* **2009**, *30*, 2523.
[10] a) A. Mahler, M. Reches, M. Rechter, S. Cohen, E. Gazit, *Adv. Mater.* **2006**, *18*, 1365; b) A. M. Smith, R. J. Williams, C. Tang, P. Coppo, R. F. Collins, M. L. Turner, A. Saiani, R. V. Ulijn, *Adv. Mater.* **2008**, *20*, 37.
[11] Y. Loo, A. Lakshmanan, M. Ni, L. L. Toh, S. Wang, C. A. E. Hauser, *Nano Lett.* **2015**, *15*, 6919.
[12] C. Diaferia, E. Rosa, E. Gallo, G. Smaldone, M. Stornaiuolo, G. Morelli, A. Accardo, *Biomedicine* **2021**, *9*, 678.
[13] a) M. Halperin-Sternfeld, M. Ghosh, R. Sevostianov, I. Grigoriants, L. Adler-Abramovich, *Chem. Commun.* **2017**, *53*, 9586; b) L. Xu, Q. Shen, L. Huang, X. Xu, H. He, *Front. Bioeng. Biotechnol.* **2020**, *8*, 629452; c) P. Makam, E. Gazit, *Chem. Soc. Rev.* **2018**, *47*, 3406; d) P. Chakraborty, Y. Tang, T. Guterman, Z. A. Arnon, Y. Yao, G. Wei, E. Gazit, *Angew. Chem., Int. Ed.* **2020**, *59*, 23731.
[14] R. Orbach, I. Mironi-Harpaz, L. Adler-Abramovich, E. Mossou, E. P. Mitchell, V. T. Forsyth, E. Gazit, D. Seliktar, *Langmuir* **2012**, *28*, 2015.
[15] C. Diaferia, M. Ghosh, T. Sibillano, E. Gallo, M. Stornaiuolo, C. Giannini, G. Morelli, L. Adler-Abramovich, A. Accardo, *Soft Matter* **2019**, *15*, 487.
[16] L. Chronopoulou, S. Margheritelli, Y. Toumia, G. Paradossi, F. Bordi, S. Sennato, C. Palocci, *Gels* **2015**, *1*, 179.
[17] a) Z. Yang, L. Wang, J. Wang, P. Gao, B. Xu, *J. Mater. Chem.* **2010**, *20*, 2128; b) S. M. M. Reddy, G. Shanmugam, N. Duraipandy, M. S. Kiran, A. B. Mandal, *Soft Matter* **2015**, *11*, 8126.
[18] J. Gao, H. Wang, L. Wang, J. Wang, D. Kong, Z. Yang, *J. Am. Chem. Soc.* **2009**, *131*, 11286.
[19] J. R. Lakowicz, *Principles of Fluorescence Spectroscopy*, 3rd ed., Springer, Boston, MA **2007**.
[20] S. D. Moran, M. T. Zanni, *J. Phys. Chem. Lett.* **2014**, *5*, 1984.
[21] S. M. M. Reddy, G. Shanmugam, N. Duraipandy, M. S. Kiran, A. B. Mandal, *Soft Matter* **2015**, *11*, 8126.
[22] E. R. Draper, D. J. Adams, *Chem. Soc. Rev.* **2018**, *47*, 3395.
[23] a) V. Castelletto, G. E. Newby, Z. Zhu, I. W. Hamley, L. Noirez, *Langmuir* **2010**, *26*, 9986; b) C. Diaferia, C. Avitabile, M. Leone, E. Gallo, M. Saviano, A. Accardo, A. Romanelli, *Chem. - Eur. J.* **2021**, *27*, 14307.
[24] R. Khurana, V. N. Uversky, L. Nielsen, A. L. Fink, *J. Biol. Chem.* **2001**, *276*, 22715.
[25] A. J. Howie, D. B. Brewer, D. Howell, A. P. Jones, *Lab. Invest.* **2008**, *88*, 232.
[26] M. Sunde, L. C. Serpell, M. Bartlam, P. E. Fraser, M. B. Pepys, C. C. F. Blake, *J. Mol. Biol.* **1997**, *273*, 729.
[27] a) T. Giraud, S. Bouguet-Bonnet, P. Marchal, G. Pickaert, M.-C. Averlant-Petit, L. Stefan, *Nanoscale* **2020**, *12*, 19905; b) T. Giraud, S. Bouguet-Bonnet, M.-J. Stébé, L. Richaudeau, G. Pickaert, M.-C. Averlant-Petit, L. Stefan, *Nanoscale* **2021**, *13*, 10566; c) E. Ravera, M. Fragai, G. Parigi, C. Luchinat, *ChemPhysChem* **2015**, *16*, 2803; d) U. Mikac, A. Sepe, A. Gradišek, J. Kristl, T. Apih, *Int. J. Pharm.* **2019**, *563*, 373.
[28] a) R. Kimmich, N. Fatkullin, *Advances in Polymer Science*, Vol. *170*, Springer, Berlin, Heidelberg **2004**; b) E. A. Rössler, S. Stapf, N. Fatkullin, S. Stapf, N. Fatkullin, *Curr. Opin. Colloid Interface Sci.* **2013**, *18*, 173.
[29] C. Diaferia, N. Balasco, T. Sibillano, M. Ghosh, L. Adler-Abramovich, C. Giannini, L. Vitagliano, G. Morelli, A. Accardo, *Chem. - Eur. J.* **2018**, *24*, 6804.
[30] M. Sunde, L. C. Serpell, M. Bartlam, P. E. Fraser, M. B. Pepys, C. C. F. Blake, *J. Mol. Biol.* **1997**, *273*, 729.
[31] a) D. Altamura, R. Lassandro, F. A. Vittoria, L. De Caro, D. Siliqi, M. Ladisa, C. Giannini, *J. Appl. Crystallogr.* **2012**, *45*, 869; b) T. Sibillano, L. De Caro, D. Altamura, D. Siliqi, M. Ramella, F. Boccafoschi, G. Ciasca, G. Campi, L. Tirinato, E. Di Fabrizio, C. Giannini, *Sci. Rep.* **2014**, *4*, 6985.
[32] a) B. Halle, H. Jóhannesson, K. Venu, *J. Magn. Reson.* **1998**, *135*, 1; b) I. Bertini, M. Fragai, C. Luchinat, G. Parigi, *Magn. Reson. Chem.* **2000**, *38*, 543.

pharmaceuticals

MDPI

Review

Fmoc-Diphenylalanine Hydrogels: Optimization of Preparation Methods and Structural Insights

Carlo Diaferia, Elisabetta Rosa, Giancarlo Morelli and Antonella Accardo *

Department of Pharmacy and Interuniversity Research Centre on Bioactive Peptides (CIRPeB), University of Naples "Federico II", Via Montesano 49, 80131 Naples, Italy

* Correspondence: antonella.accardo@unina.it; Tel.: +39-081-2532045

Abstract: Hydrogels (HGs) are tri-dimensional materials with a non-Newtonian flow behaviour formed by networks able to encapsulate high amounts of water or other biological fluids. They can be prepared using both synthetic or natural polymers and their mechanical and functional properties may change according to the preparation method, the solvent, the pH, and to others experimental parameters. Recently, many short and ultra-short peptides have been investigated as building blocks for the formulation of biocompatible hydrogels suitable for different biomedical applications. Due to its simplicity and capability to gel in physiological conditions, Fmoc-FF dipeptide is one of the most studied peptide hydrogelators. Although its identification dates to 15 ago, its behaviour is currently studied because of the observation that the final material obtained is deeply dependent on the preparation method. To collect information about their formulation, here are reported some different strategies adopted until now for the Fmoc-FF HG preparation, noting the changes in the structural arrangement and behaviour in terms of stiffness, matrix porosity, and stability induced by the different formulation strategy on the final material.

Keywords: Fmoc-FF; peptide hydrogels; peptide materials; hydrogel preparation; diphenylalanine

Citation: Diaferia, C.; Rosa, E.; Morelli, G.; Accardo, A. Fmoc-Diphenylalanine Hydrogels: Optimization of Preparation Methods and Structural Insights. *Pharmaceuticals* **2022**, *15*, 1048. https://doi.org/10.3390/ph15091048

Academic Editors: Giovanni N. Roviello and Rosanna Palumbo

Received: 18 July 2022
Accepted: 18 August 2022
Published: 25 August 2022

1. Introduction

Researchers have directed their gaze towards nature since the analysis of biologically relevant structures, elements, and processes can embody a motivating well for inspiration. On the evidence that numerous structures are the consequence of natural self-organization of proteinaceous materials, peptide-based building blocks and their analogues have begun to be studied [1–4]. In addition, supramolecular aggregates and misfolding protein materials were found as pathological hallmarks of major human illnesses too, including bovine spongiform encephalopathy (mad cow disease), Creutzfeldt–Jakob disease, Alzheimer's disease, Huntington's, and Parkinson's diseases [5]. Although first identified as pathological entities, a new research line has shown that amyloid proteinaceous materials contribute to support and conduct complex biological functions [6]. For all these reasons, amyloids, once exclusively affiliated as pathological and toxic structures, are now raising interest as biomimicry self-assembling class of biological elements for artificial materials production. Their potential engineering is a consequence of the study and comprehension of the supramolecular structuration [7].

Identified in the middle of the primary sequences of $A\beta_{1-40}$ and $A\beta_{1-42}$, diphenylalanine (FF) was recognized as the crucial aggregative motif in the Alzheimer's β-amyloid polypeptides [8]. This simple homopeptide revealed the capability to self-organize efficiently into well-ordered tubular architectures with a long persistence length (~100 μm) because of π-π staking and H-bonding interaction networks [9]. Due to its chemical simplicity and versatility, FF rapidly became the paradigm for the study for peptide self-assembly. Moreover, modifying its very simple chemical structure, a plethora of FF analogues was proposed during in recent years [10–18]. Cationic FF differs from FF (or zwitterionic

FF) for the amidation of the C-terminus. In the amide form, the C-terminus is unable to generate head-to-tail hydrogen-bound interactions and dipeptide preferentially self-assembles into nanowires [19]. With the rationale of generating a covalent attachment to fabricated gold electrodes for application in nano-devices, Gazit et al. designed the tripeptide Cys-FF in which the thiol group contributes to cross-linking phenomena and to the self-aggregation into nanotubes [20]. Other diphenylalanine analogues able to aggregate in micro-structures, such as flat plates, flattened micro-planks, and micro-rods, were obtained for progressive elongation of the Phe side chain with methylene groups (dihomophenylalanine (DiHpa); di-2-amino-5-phenylpentanoic acid (DiApp); di-2-amino-6-phenylhexanoic acid (DiAph)) [21]. With the aim to elucidate the supposed role of electrostatic interactions in the peptide backbone aggregation, in 2005 an FF derivative in which the N-terminal amine and the C-terminal carboxyl of the peptide are respectively acetylated and amidated (Ac-Phe-Phe-NH_2) [20] were designed and synthetized. This uncharged peptide showed the capability to efficiently self-assemble into tubular structures. Consequently, the authors analysed a small library of analogues, Ac-Phe-Phe-OH, Boc-Phe-Phe-OH, Cbz-Phe-Phe-OH, and Fmoc-Phe-Phe-OH, in which only the amino group was blocked by using conventional solid phase peptide synthesis (SPPS) protecting groups [22]. The tert-Butyloxycarbonyl (Boc)-FF monomer analogue allows to obtain peptide spheres or small peptide particles when its HFIP stock solution is diluted in ethanol [23,24]. Instead, due to the additional stacking between the Benzyloxycarbonyl (Cbz) or 9-fluorenylmethoxycarbonyl (Fmoc) aromatic moieties, the two correspondent FF protected compounds self-assembled into fibrillary structures. Fibrillary structures of Fmoc-FF-OH showed an ultrastructure and dimensions extremely similar to the amyloid fibrils. Fmoc-FF dipeptide (see Figure 1 for the chemical structure) is one of the most studied ultra-short peptides for hydrogel (HG) preparation [25,26]. The main reason for this large interest is related to the possibility to obtain stable self-supporting hydrogels at pH values compatible with physiological applications, including tissue engineering and drug delivery. Additional applicative areas cover chemical catalysis, nanoreactors development, optical engineering, wound treatments, ophthalmic preparations, energy harvesting, antifouling, and biocompatible coating applications, optoelectronics, potential immuno-responsive agents, and absorbents systems for oil/water separation [27].

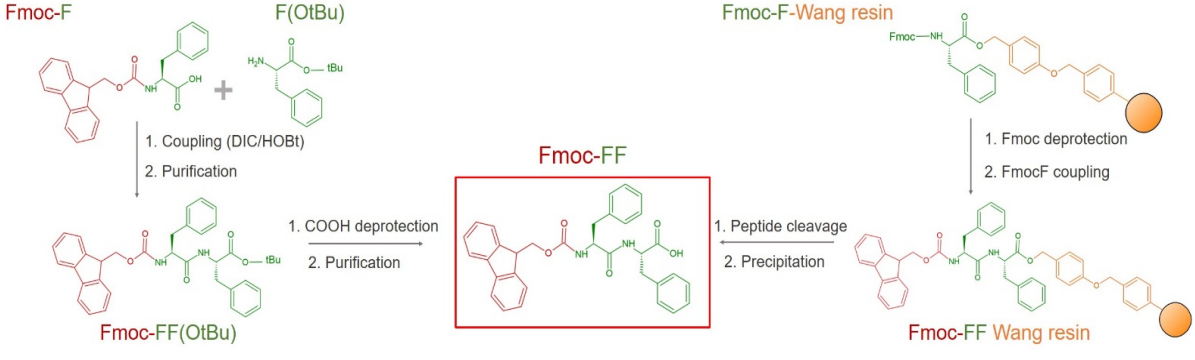

Figure 1. Scheme for the synthesis of Fmoc-FF (red rectangle) using liquid phase strategy (on the left) and solid phase peptide synthesis (SPPS) on the right. DIC: *N*,*N*′-Diisopropylcarbodiimide; HOBt: 1-Hydroxybenzotriazole.

The chemical accessibility, biodegradability, biofunctionality and the possibility to adopt specific secondary, tertiary, or quaternary architectures represent additional advantages for this simple peptide building block, alone, in combination with different chemical entities or in different morphological shapes [28,29]. Moreover, it was observed that matrix structural and functional properties can be tuned opportunely by simply modifying the gelation kinetic and other experimental parameters (such as pH, temperature, and used solvent) [30,31]. This observation pushed the research towards the development of novel

and alternative methods to achieve HG generation. On the other hand, novel peptide analogues, containing codified or non-codified amino acids, have been proposed as building blocks for the preparation of hydrogels with enhanced properties [32,33]. It is worth noting that although the identification of Fmoc-FF as a hydrogelator dates to 15 years ago, its behaviour is continuously studied. The aim of this review is to provide an overview of the different preparation methods reported until now for the fabrication of Fmoc-FF HGs. This study also notes how the used method can affect both the structural and mechanical properties of the obtained material.

2. Applicative and Biomedical Relevance of Fmoc-FF Hydrogel

In the plethora of peptide-based hydrogels, Fmoc-FF becomes a relevant system due to some specific advantages. With respect to other peptide-hydrogelators (e.g., RADA peptides, [34] MAX-1, [35], amphiphilic and no-natural containing sequences [36,37]), Fmoc-FF represents a simple and accessible chemical entity, commercially available from different companies. The structural simplicity of the molecules additionally allows its production in high purity and with contained costs, both related to a solid phase peptide synthesis (SPPS) [38] and to the synthesis in solution (Figure 1). In the SPPS, the product is obtained into a three-step synthetic route. Specifically, a preloaded Fmoc-F-Wang resin undergoes a Fmoc-F-OH coupling after a Fmoc-deprotection. The cleavage of peptide and its precipitation make available the final powder with an efficient scalability. Alternatively, the same molecule can be obtained in solution, taking advantage of the non-requested protection of the Phe side chain. In this case, a C-protected phenylalanine is coupled with a Fmoc-F-OH residue. Then, after the deprotection of the carboxylic acid, Fmoc-FF is precipitated and purified.

Another advantage of Fmoc-FF as a building block for hydrogel preparation is its fast kinetics of formation, which occurs in a few minutes. Moreover, the gel can be prepared by using both in vitro and in vivo friendly solvents (water, buffers, and cell media) [39]. Additionally, the optical transparency of the Fmoc-FF matrix is a benefit for a preliminary macroscopical evaluation in terms of homogeneity and correct formulation. Moreover, the mechanical properties and the tunability exhibited by the Fmoc-FF matrix make it compatible with extrusion, electrospinning, and filming deposition procedures [40,41]. Finally, the resulting hydrogel exhibits a good shelf stability. All these advantages make Fmoc-FF highly accessible for application in many research fields.

Early investigations carried out by Gazit and co-workers noted only the capability of the dipeptide to self-assemble into a rigid material with macroscopic characteristics of a self-supporting gel [26]. The hydrogel formation was achieved with a "solvent switch" methodology (*vide intra*), which consists into the dilution of an organic peptide stock solution (generally at 100 mg/mL) in water. In this specific case, HFIP (1,1,1,3,3,3-hexafluoro-2-propanol) was used as an organic solvent, diluted in water at a final concentration of 5 mg/mL (0.5 wt%) [26]. The pre-dissolution in HFIP is currently used as aggregative step for other aromatic peptide-based materials [42–44]. The so prepared materials were found syringable, shaped, and stable across a broad range of temperatures, over a wide pH range and in presence of aggressive chemical agents, such as guanidinium and urea. Due to the presence of hollow cavities in the supramolecular architecture, the possible use of Fmoc-FF as a reservoir was scrutinized by the encapsulation and release study of model drugs such as fluorescein (FITC) and insulin-FITC, indicating a retain of molecules of 5 kDa, and a slow release for small chemical entities [26]. The remarkable mechanical rigidity of this hydrogel compared with others physically cross-linked ones, the direct correlation between rheological properties and peptide concentration, and its capability to support Chinese Hamster Ovarian (CHO) cell adhesion led authors to suggest Fmoc-FF as a promising, tunable, and versatile scaffold for tissue engineering too. Simultaneously, the evidence reported that some Fmoc-protected dipeptides and amino acids are able to form scaffold materials [45–47], Ulijn and co-workers synthetized am Fmoc-based dipeptide library built as combination of glycine (Gly), leucine (Leu), phenylalanine (Phe), and alanine (Ala).

Using a progressive decrease in the pH (from 8 to < 4, procedure that are reported as "pH switch" method), the authors noted that all the library members were able to form fibrous-based hydrogels. Only Fmoc-FF produced low-concentration HGs after lowering the pH to a physiologically relevant value [25]. Fmoc-FF gel was also tested for its ability to support proliferation and retention of phenotype bovine chondrocytes, both in 2D and 3D experiments.

Beyond tissue engineering and drug delivery applications, Fmoc-FF nanomaterials have been investigated as innovative materials in industrial and biotechnological fields. For example, in 2010 Rosenman et al. proposed self-assembled Fmoc-FF materials as biosensors for the detection of amyloid fibrils. From the analysis of the optical properties, it was proposed a shift from a 0D-quantum dot to a 2D-quantum well with a thickness around 1 nm. This observation demonstrates the capability of this self-assembled peptide to exhibit the same quantum physical phenomenon previously observed only for semiconductor crystals [48]. Moreover, to improve the biofunctionality and the biocompatibility of bio-based materials such as silica wafers, Fmoc-FF peptide was covalently anchored on its the surface. In this case, the AFM characterization pointed out the tendency of the aromatic dipeptide to self-assemble in nanorods with a mean radius ranging from 10 to 30 nm. The structural arrangement of the peptide on the silica surface allows a modification of the functional properties of the material in terms of angle of contact. As expected, the density of nanorods on the silica surface is strictly related to the concentration of the immobilized peptide [49]. Analogously to FF-based nanomaterials, dried Fmoc-FF peptide hydrogels revealed piezoelectricity under piezoresponse force microscopy. Due to their biomimicry nature, coupled to these electric properties, Fmoc-FF gels were also proposed as advantageous tools in application in which electrical stimuli are required (e.g., axonal regeneration). The non-centrosymmetric topology of the β-sheet rich fibres were quoted as the ascribable structural reason of the electric features of the material. Indeed, an overall polarization along the fibre axis is related to dipoles, running perpendicularly to the direction of the β-strands [50]. Recently, Fmoc-FF hydrogels and some of its cationic variants (Fmoc-FFKK, Fmoc-FFFKK, and Fmoc-FFOO, in which O is the one code symbol for ornithine) have been studied for the first time as antibacterial materials [51]. Gel preparation was achieved at a final peptide concentration of 2.0 wt%. Unsurprisingly, self-assembled cationic variants exhibited high ordered antiparallel β-sheet structures and low rigidity and viscosity. Fmoc-FF hydrogels showed significant antibiofilm activity preventing the growth of bacteria and biofilm of Gram-positive (*Staphylococcus aureus* and *epidermis*) and Gram-negative (*Pseudomonas aeruginosa* and *Escherichia Coli*) bacteria that can be localized on the medical devise surface.

Recently, Adler-Abramovich and co-workers reported the prominent capability of Fmoc-FF hydrogel to specifically encage oxygen molecules and restrict its movement in absence of metal ions [52]. Molecular dynamics computations highlighted that the binding of O_2 is originated by specific interactions that take place between O_2 and the interior surface of Fmoc-FF fibrils. The ability of the gel to encage oxygen suggests its potential application as a passive mean to maintain hydrogen production by the O_2-hypersensitive enzyme [FeFe]-hydrogenase. These results leave envisage potential utilization of Fmoc-FF hydrogels in a wide range of O_2-sensitive applications.

3. Structural Organization and Proposed Model

The growing interest around Fmoc-FF as innovative material also encouraged structural studies aimed to identify the model of aggregation into fibrillary networks. In 2008, Uljin and co-workers proposed for the first time the aggregation model for Fmoc-FF [53]. The model was designed on the basis of their experimental data collected by Circular Dicrohism (CD) and Fourier Transformed Infrared spectroscopies (FT-IR). Structural characterization highlighted an anti-parallel β-sheets arrangement of the peptide building blocks and anti-parallel π-stacking of the fluorenyl groups (Figure 2A,B). In more detail, in disassembled systems such as Fmoc-Phe, Fmoc group shows two dichroic prints at 307 nm

and below 214 nm, without contribution in the far-UV region. On the contrary, in Fmoc-FF gels a negative pick centred at 218 nm is consistent with a β-sheet structure, implying that an ordered supramolecular structure is associated with the gel matrix. Gels caused a signal in the range of 304–308 nm, attributed to the $\pi \rightarrow \pi^*$ transition in the fluorenyl-moiety too. Two other CD prints (a local maximum at 192 nm and a minimum at 202 nm) are indicative for α-helix transition associate to $\pi \rightarrow \pi^*$ transition. The predominant β-arrangements were supported by FT-IR analysis too. Indeed, Fmoc-FF gels are characterized by two peaks in the amide I region (1630 and 1685 cm^{-1}), compatible with an antiparallel organization of the peptides. All these structural requirements were well-satisfied by the model proposed by the authors: this model was based on a nanocylindrical structure (with an external diameter of ~3.0 nm, Figure 2C) formed by the interlocking through lateral π-π interactions of four twisted anti-parallel β-sheets. These fibrils, forming J-aggregates, were then shown to further self-assemble laterally, forming large flat ribbons under specific pH conditions, visible in TEM microscopy (Figure 2D). The scattering pattern of the Fmoc-FF-dried gel showed a series of diffractions compatible with the structural organization of the proposed model [53]. Based on the evidence that pK_a can significantly change as a consequence of protein and peptide self-organization phenomenon, Saiani et al. studied effect of pH on the Fmoc-FF self-assembly process [54]. Their results suggested that the self-assembly of Fmoc-FF building blocks is prompted by a lowering of the pH as consequence of two apparent pK_a shifts (of ≈6.4 and 2.2 pH units, respectively) above the theoretical pK_a value (3.5) (see Figure 2E). At high pH, where the Fmoc-FF building blocks are in their ionized form, the self-assembly is mainly forbidden. Then in correspondence of the first pK_{a1}, at pH 10.2–9.5, both protonated and non-protonated molecules begin to self-assemble into paired fibrils (Figure 2F). The further pH lowering from 9.5 to 6.2 causes a decrease in the fibre surface charge that in turn brings to the formation of large rigid ribbons due to the lateral interactions of the fibres. Below pH 6.2 (between 6.2 and 5.2) the second apparent pK_a shift is observed, where a further aggregation of the ribbons occurs [54]. Recently, Yan et al. speculated on the possibility to achieve a conformational transition from a β-sheet structure to a helical one by a charge-induced strategy. To demonstrate their hypothesis, they studied the structural behaviour of Fmoc-FF hydrogel before and after the addition of $Na_2B_4O_7$-EDTA buffer (pH = 8.5) [55]. Under these basic conditions, a structural transformation was detected from antiparallel β-sheet structures to a parallel helical one, imputable to the electrostatic repulsion between the negatively charged peptide molecules. This transition was further confirmed by computational simulations studies. The interaction energy analysis also highlighted the crucial role performed from the water molecule in stabilizing the Fmoc-FF^- helix nanofibril. Successively, the same authors also demonstrated that the addition of metal ions can induce structural transformation in Fmoc-FF from an amyloid-like β-sheet into a superhelix or random coil [56]. The peptide structural organization was found dependent from the types and ratios of metal ion/dipeptide through metal.

The inner size of the hydrogel cavity was estimated by Huppert et al. by a simple and non-destructive method based on the reversible photoproteolytic cycle of the photoacid 8-hydroxypyrene-1,3,6-trisulfonate (HPTS, pyranine) [57]. HPTS, a photoacid molecule with a triple negative nature, is able to transfer H^+ ions with a time constant around 100 ps. The study was conducted on the experimental evidence that the parameter affecting the photocycles are related to water sphere radius in very small, confined volumes of media, as in hydrogel matrices. In the Fmoc-FF hydrogel the water cavity dimension between the fibril walls was found to be around 100 Å. This narrow size, inaccessible for living cells, suggests that in tissue engineering applications the scaffold peptide material is directly formed around the cells. Recently, the Point Accumulation for Imaging in Nanoscale Topography (PAINT) technique was used for the first time to 3D-image Fmoc-FF hydrogels in native conditions (no dry gel) and in absence of a direct labelling of the gel. PAINT images revealed the presence in the gel of fibres with a diameter of 50 nm and a mesh size ranged between 20 and 40 nm^2 [58].

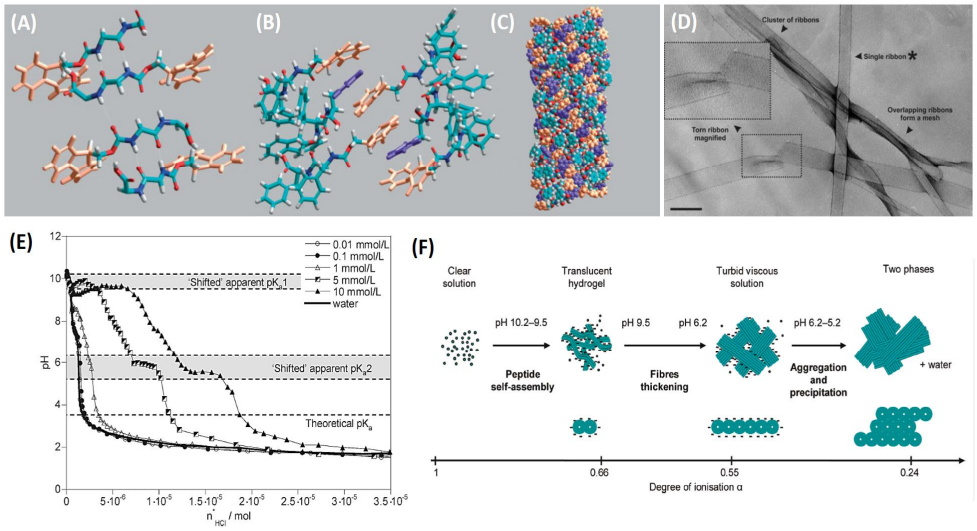

Figure 2. Structural model of Fmoc-FF peptides. (**A**) Dipeptide copies are arranged into β-sheet with an antiparallel orientation of β-strands. (**B**) π-stacked pairs due to the interlocking of fluorenyl groups from alternate β-sheets. (**C**) The final model obtained by energy minimization. In the model Fmoc and the phenyl groups are coloured in orange and in purple, respectively. (**D**) Transmission electron microscopy of Fmoc-FF xerogel (scale bar = 500 Å); the ribbon asterixed by authors was selected for other morphological analysis. (**E**) Titration curves of water and Fmoc-FF samples at different peptide concentrations (0.01, 0.1, 1, 5, and 10 mmol/L). (**F**) Mechanism proposed to explain the formation of Fmoc-FF aggregates as consequence of the pH decrease (figure adapted with permission for Refs. [53,54], Copyright 2009 American Chemical Society).

4. Preparation Methods

Fifteen years of scientific research on Fmoc-FF have been pointed out that the local organization of this peptide fragment and its structural and macroscopic architecture is deeply affected by the preparation method and by the experimental conditions used to generate the supramolecular material. After all, it is well-known and intuitively predictable that the self-assembling environmental conditions and/or the self-assembling strategy can affect both the macroscopic and the microscopic structures of the resulting hydrogel and, in turn, its functional features [59–61]. Moreover, fabrication of uniform hydrogels is often hampered by the diffusion of peptide molecules and aggregates into water medium. As a consequence of this different hierarchical organization, the physicochemical characteristic (stiffness, matrix porosity, stability, opacity, and so on) and consequently the potential applications (tissue engineering, drug delivery, biocatalysis, and biosensors) of the material change. For example, mechanical properties of the hydrogel can change up to four orders of magnitude by modification of some parameter in the formulative process, such as temperature, peptide concentration, pH of the solution, and the addition of salt/additives [62]. In this contest it is relevant to understand the key factors that can allow obtaining the material with the desired properties. To describe and distinguish between the preparation methods available until now, in this paper they were classified into three classes (Figure 3), which are named as: (i) pH-switch method, (ii) solvent-switch method and (iii) catalytic method. All of them allow gel formation as a consequence of a change/modification of the initial conditions, introducing a trigger into the peptide solution. In the first two methods, nominally pH- and solvent-switch methods, the gelation often occurs rapidly (less than a second) in the neighbourhood where the mixing of the two different solutions takes place, and in certain cases they lead to the formation of an inhomogeneous hydrogel. However, originally proposed strategies have been opportunely modified to improve the homogeneity of the gel. Analogously, catalytic methods, in which the self-aggregation process can be kinetically and thermodynamically controlled, have been proposed. It is worth noting that

the kinetic control on the self-assembly process can allow driving the aggregation towards a designed pathway and in turn, allow the formation of highly homogeneous hydrogels.

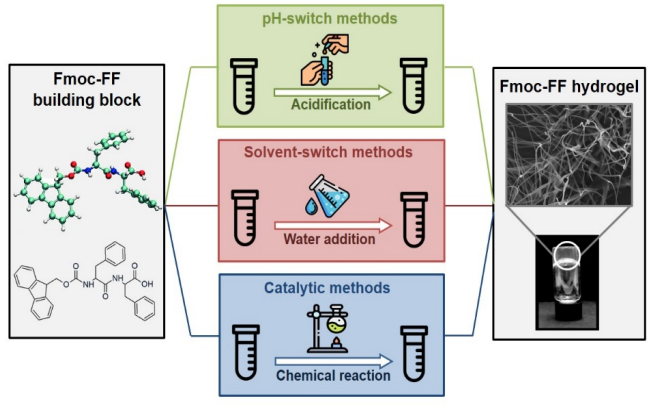

Figure 3. On the left, the molecular Fmoc-FF building block, reported both as 3D balls and sticks and as chemical formula. On the right, an inverted vial containing Fmoc-FF self-supporting gel and its TEM image. In the middle a schematic representation of three different methods (pH-switch, solvent switch, and catalytic one) commonly used for trigger gelation process.

4.1. pH-Switch Method

The pH-switch method involves the dissolution of the peptide in an aqueous solution at elevated pH (around pH 10.5) followed by a solution pH lowering via HCl addition [53]. In this preparation method, the peptide solubilisation at high pH ensures the deprotonation of the C-terminal carboxylic acid. Then the progressive acidification allows its protonation until gelation.

Due to the potential cleavage of the Fmoc protecting group under basic conditions, a careful control of the pH value and of the permanence time of the sample in NaOH is required during the peptide dissolution. It is worth noting that a negligible percentage of the fluorenyl moiety (<1%) is lost after 10 min in this basic condition. It was observed that the acidification of Fmoc-peptide solution by inorganic acids such as HCl brings to the formation of an inhomogeneous hydrogel. This result was attributed to the kinetics of mixing being slower than the initial kinetics of gelation. Indeed, at a low pH value, fibril formation and gelation are often very fast (taking place in a time lower than a second), with the consequence that it is very difficult to achieve a uniform pH in solution before the gelation process starts. Reproducible and more homogeneous hydrogels were obtained using an optimized procedure, involving a progressive addition of acid followed by a heat/cool cycle [54]. The high temperature permits to dissolve the kinetically trapped aggregates that are formed during the acidification. As described, the assembly of Fmoc-FF building blocks occurs with the appearance of two apparent pK_a: the first at pH 10.2–9.5, and the second at pH 6.2–5.2. It should be emphasised that hydrogels free from undissolved peptides exhibit a G′ modulus of 1–10 Pa, which is significantly lower than G′ (10^4 Pa) of hydrogels undergoing the heating step.

It is also important to pay the attention to each step during the gel preparation. Indeed, it was demonstrated that the method utilized to agitate the sample during and after the gelling transition can dramatically affect both the nano-scale morphology and the mechanical properties of the gel. The effect of the agitation (low shear and high shear) was evaluated on different pure and mixed hydrogels (100% Fmoc-FF, 70/30 Fmoc-FF/Fmoc-GG, and 50/50 Fmoc-FF/Fmoc-GG), all of them prepared according to the pH-dependent procedure [30]. In this study, low shear gels exhibited a higher storage modulus (≈4000 Pa) with respect to the high shear ones (≈1000 Pa). The different mechanical properties have been related to the morphology of gels obtained in the two shear modalities: high shear samples are more prone to lateral aggregation, whereas low shear ones to a regular form

of entanglement. Successively, Adams and co-workers introduced a novel strategy in which the decrease in the pH is prompted by the slow hydrolysis of the highly soluble glucono-δ-lactone (GdL) to gluconic acid (see Figure 4A) [63]. The long timescale for the hydrolysis (≈18 h) allows a slow and homogeneous pH change, which minimizes the solvent mixing effects with the consequential obtainment of homogeneous and reproducible gel. According to this procedure, only a single apparent pK_a of 8.9 was detected. The final pH of the solution can be modulated according to the amount of GdL added to the peptide. The study demonstrated that the addition of two equivalents of GdL with respect to the peptide allows reaching a final pH of 3.6–3.9, which is very similar to the pH reached by adding HCl. However, the pH begins to equilibrate after ≈350 min and is fully equilibrated only after 24 h. The combination of the GdL-mediated pH trigger method with the cryogelation at a sub-zero temperature (−12 °C) allows the formation of macroporous Fmoc-FF hydrogels [64]. In the conditions here described, the water crystallization occurs and the Fmoc-FF molecules, concentrated in the remaining non-frozen liquid phase, gelate with a structure having a pore size in the range of 10–100 µm. Even if the pore walls of cryogels are characterized by a close packing of the fibres, they exhibit low mechanical stability with respect to classical hydrogels. This low stability was attributed to the heterogeneous structure in the cryogel. To further improve the homogeneity and the reproducibility of the hydrogel, in 2013 Ding et al. described two novel pH-triggered procedures for achieving Fmoc-FF hydrogel fabrication [65]. In the first approach, termed "the colloid method", hydrogels were obtained by a colloid-to-hydrogel transition process (Figure 4B). Initially, the amphiphilic Fmoc-FF dipeptide spontaneously self-assembled in water solution in stable, rod-like micelles with a radius and a length of ≈15 and ≈180 nm, respectively. Successively, the slow formation of hydrogel (≈20 min) was triggered by adding one equivalent of a weak base such as Na_2CO_3 to the colloid solution. The addition of the base causes the progressive deprotonation of the carboxylic functions of the dipeptides present at the surface layer of the micelles. In this context, micelles serve as a trap to regulate the amount of Fmoc-FF released in the solution and hydrogels can be prepared also at pH > 9. Instead, the second approach was based on the decomposition of the $K_2S_2O_8$ in oxygen gas and protons triggered pH decrease (reaction is reported in Figure 4C). This method exhibits several advantages compared with other methods used to lower pH such as the hydrolysis of GdL. It permits to control the amount of protons released and hence the final pH of the solution. Moreover, due to the dependence of the potassium persulfate degradation from the temperature, both the gelation kinetic (from 5 min at 90 °C to 4–5 days at 25 °C) and the structural properties of the hydrogel can be programmed, as well.

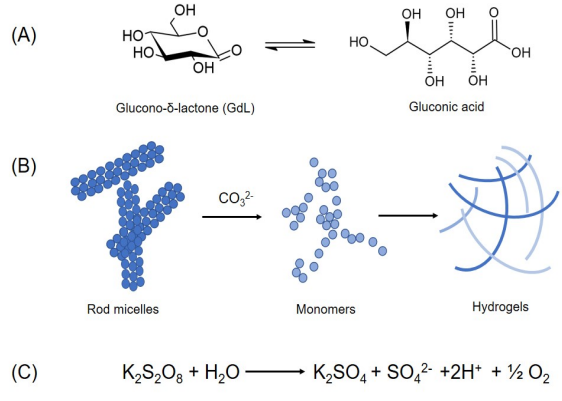

Figure 4. Preparation of Fmoc-FF hydrogel using three variants of the classic pH-switch method employing HCl: (**A**) decrease in pH induced by the slow hydrolysis (≈18 h) of the glucono-δ-lactone (GdL) to gluconic acid; (**B**) the colloid method in which the hydrogel is obtained by a progressive colloid-to-hydrogel transition triggered by adding of Na_2CO_3 to the colloid solution; (**C**) decrease in pH allowed by the decomposition of the $K_2S_2O_8$ in oxygen gas and protons.

4.2. Solvent-Switch Method

Beyond the pH-switch method, Fmoc-FF hydrogels can be also prepared with the solvent-switch method. This is based on the dissolution of the peptide in an organic solvent at high concentration. Then, gelation is trigged by adding water to the solution, so creating a three-component (peptide/solvent/water) system. Initially, Gazit and co-workers used HFIP as a solvent to dissolve Fmoc-FF [26]; later, other organic solvents able to solubilize Fmoc-FF peptides were used as an alternative to HFIP. Specifically, the first solvent used in place of the HFIP was dimethyl sulfoxide (DMSO). TEM images collected on Fmoc-FF gels prepared in DMSO/water confirm the presence of small-entangled fibres with a diameter of ≈10 nm, smaller than the wavelength of visible light. Moreover, the storage modulus value (10^4 Pa) found for these gels was similar to that one for HFIP/water preparation [66]. In 2014, Dudukovic and Zukosky established a range of concentrations under which a Fmoc-FF solution in DMSO can form hydrogels upon mixing with the water and studied the mechanical properties of the gels prepared in the different conditions [67,68]. Their results allowed to delineate a well-defined line of gel transition in a plot of water concentration as a function of ϕ (namely the particle volume fraction) and, pointed out that rigid gels can be obtained at a low Fmoc-FF volume fraction ($\phi < 1\%$) and under addition of a small amount of water to DMSO (Figure 5A). The capability of the peptide to gel also under addition of reduced quantity of water was recently demonstrated to be due to the existence of disordered oligomers and profibrils into the DMSO solution [69]. Moreover, a deep investigation on the Fmoc-FF gelation kinetics revealed that upon addition of water to DMSO solution of Fmoc-FF, initially the dipeptide self-assembles into a metastable non equilibrium state composed of spherical clusters of diameters of 2 µm, followed by a rapid rearrangement (below 5 min) into a fibrous network. The aging of the sample (up to 4 h) allows a further evolution of the gel towards a steady state in which there is the formation of a highly uniform network composed of thin fibres with a mean diameter between 5 and 10 nm. These dimensions are smaller than the wavelength of the visible light and are the reason why the gel appears transparent. The high uniformity of the fibrillary network causes an increase in the gel rigidity and provides long-term stability (years) to the gel. These studies also demonstrated the mechanical and thermal reversibility of the gels over time. Successively, the same authors speculated that the fibres in the gel can be treated as an equilibrium crystalline state, in which the gelation process is a first order phase transition resulting in the nucleation and growth of elongated anisotropic crystals. It was observed that an increase in water with respect to DMSO brought an increase in the strength of attraction between the peptide molecules that in turn can be translated into a fast nucleation rate and quasi-one-dimensional crystal growth [70]. This transition from spherulitic structures to a fibrous network was also observed by Adams and co-workers for Fmoc-FF hydrogels prepared using other polar protic or aprotic solvents (Figure 5B) such as ethanol, acetone, and HFIP in place of DMSO [71]. However, it seems that the choice of the solvent can affect the morphology of the final network and in turn rheological properties and mechanosensitivity of the final hydrogel. These differences are originated by the control exercised by the solvent on the morphology of the fibre network. For example, at a $\phi_{solvent}$ of 0.3, gels prepared in ethanol exhibit a more uniform network with respect to gels prepared in DMSO or HFIP. This high uniformity is associated with a high rigidity and a poor capability of the hydrogel to recover their mechanical strength from shear. It is worth noting that the transition from opaque to limpid state into the peptide solution is never observed for samples prepared by the pH-switch. This evidence clearly indicates that there are significant differences in the self-assembling process occurring for the two procedures.

Later, Dudukovic et al. also explored the phase behaviour of Fmoc-FF in other solvent systems (DMSO/H_2O, MeOH/H_2O, and toluene). According to the Adam's results, the authors demonstrated that gel formation can be induced also in apolar solvents and that the Fmoc-FF phase behaviour is directly correlated to the balance between the inter- and intra-molecular interactions. Indeed, it was observed that different solvents allow the formation of fibres with a different molecular order and that Fmoc-FF exhibits polymorphism in some

solvents where metastable anisotropic crystals evolve towards crystal aggregation with no preferential axis of growth. Different fibre populations can co-exist within one system and the switch between these states depends on the stability of each conformational state and on the height of barrier between the two free energy minima (Figure 5) [72]. As an alternative, hydrogels can be prepared by using buffered solutions at physiological pH. However, also the ratio of DMSO to H_2O (ϕ_{DMSO}) and the choice of the buffers used in selected systems can affect the rheological properties of the hydrogel [65].

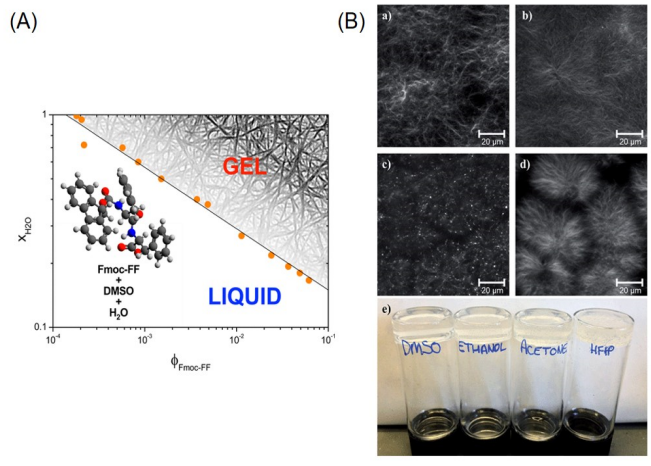

Figure 5. (**A**) Phase diagram molecular gels produced by Fmoc-FF using DMSO/H_2O solvent-switch method (figure adapted with permission from Ref. [67], Copyright 2014 American Chemical Society). (**B**) Fmoc-FF matrices stained with Nile Blue in confocal microscopy analysis (ϕsolvent = 0.3) using the solvents (**a**) DMSO (**b**) ethanol (**c**) acetone (**d**) HFIP, (**e**) macroscopical gel picture after 24 h from their preparation (at same ϕsolvent without staining) (figure reproduced from Ref. [71] with permission from the Royal Society of Chemistry).

4.3. Catalytic Methods

The catalytic process is an interesting methodology that allows directing the self-aggregation process towards structurally diverse self-assembled materials, inaccessible via classical self-assembly. This approach consists of converting precursors unable to self-assemble into building blocks able to do. Usually, this conversion can be achieved by enzymatic removal or hydrolysis of a charged or steric groups that avoids the aggregation. In this case, the nucleation site and the early stage grown mechanism are spatially confined at the site of catalytic centre. Two examples of self-assembly for Fmoc-FF and for several its analogues (FY, YL, VL and FL) were reported by the Ulijn's group [73,74]. Initially, they demonstrated the use of thermolysin, a non-specific endoprotease to catalyse in a reversible way the peptide bond formation between Fmoc-F and several dipeptides (G_2, F_2, L_2) or amino acid esters (L-OMe, F-OMe) [73]. After the bond formation, the peptide self-assembles in a spatiotemporally controlled manner, with the enzyme favouring the spatial confinement of structure grown during the early stage of the self-assembly process. On the same set of peptides, they also reported the self-assembly catalysed by subtilin, a hydrolytic enzyme from *Bacillus licheniformis*. It was observed that the enzyme concentration (ranged between 1.5 and 36 units) strongly affects the self-assembly kinetics and in turn, the supramolecular order degree, and the functional properties of the final material [74]. Chemical catalysis, achieved by starting from phenylalanine and its Fmoc-derivative and EDC/NHSS as catalysts, was described as an alternative approach with respect to the biocatalytic ones [75]. In this procedure, Fmoc-F was activated in DMSO using EDC/NHSS, then Fmoc-FF was quickly obtained by simply adding the intermediates into an aqueous solution containing phenylalanine. The continuous generation of Fmoc-FF due to the chemical reaction and its spontaneous aggregation into entangled nanofibers

allows the formation of a self-supporting and a homogeneous hydrogel. At the end of the gelling process, the catalysts were removed by washing the hydrogel with deionized water. Later, several Fmoc-FFF tripeptide, containing phenylalanine residues in *L* or *D* configuration, were synthetized by lipase-catalysed reversed hydrolysis reaction between a Fmoc-amino acid and a dipeptide [76].

5. Conclusions

Most of the peptide hydrogelators described in literature are able to gelate in only one well-defined condition, which is related to their primary sequence in terms of sterical hindrance, hydrophobicity, and polarity of amino acids. On the contrary, Fmoc-FF-based hydrogels can be prepared using different conditions of solvent, pH, temperature, ionic strength, and shear. From a predictive point of view, the versatility of Fmoc-FF was not expected on the basis of its very simple chemical nature. In this contest, many attempts have been made to understand the molecular mechanisms enabling the Fmoc-FF self-aggregation. The possibility to change preparation conditions and experimental variables allows to modulate in a controlled manner the structural properties and morphology of the resulting material. This versatility envisages a relevant number of applications in a variety of fields for this ultra-short peptide.

Author Contributions: Conceptualization of the paper, A.A.; Paper topic, organization and structure, C.D. and A.A.; Collection of literature and analysis of papers, C.D., E.R., G.M. and A.A.; Writing, A.A., C.D. and G.M.; Original draft preparation, A.A. and G.M.; Image curation and editing, C.D., E.R. and A.A.; General supervision, A.A. and G.M. All authors have read and agreed to the published version of the manuscript.

Funding: This research received no external funding.

Institutional Review Board Statement: Not applicable.

Informed Consent Statement: Not applicable.

Data Availability Statement: Not applicable.

Conflicts of Interest: Authors declare no conflict of interest.

References

1. Acar, H.; Srivastava, S.; Chung, E.J.; Schnorenberg, M.R.; Barrett, J.C.; LaBelle, J.L.; Tirrell, M. Self-assembling peptide-based building blocks in medical applications. *Adv. Drug Deliv. Rev.* **2016**, *110–111*, 65–79. [CrossRef] [PubMed]
2. Nainytė, M.; Müller, F.; Ganazzoli, G.; Chan, C.Y.; Crisp, A.; Globisch, D.; Carell, T. Amino Acid Modified RNA Bases as Building Blocks of an Early Earth RNA-Peptide World. *Chem. A Eur. J.* **2020**, *26*, 14856–14860. [CrossRef] [PubMed]
3. Diaferia, C.; Gianolio, E.; Accardo, A. Peptide-based building blocks as structural elements for supramolecular Gd-containing MRI contrast agents. *J. Pept. Sci.* **2019**, *25*, e3157. [CrossRef] [PubMed]
4. Lewandowska, U.; Corra, S.; Zajaczkowski, W.; Ochs, N.A.K.; Shoshan, M.S.; Tanabe, J.; Stappert, S.; Li, C.; Yashima, E.; Pisula, W.; et al. Positional isomers of chromophore–peptide conjugates self-assemble into different morphologies. *Chem. Eur. J.* **2018**, *24*, 12623–12629. [CrossRef]
5. Eisenberg, D.; Jucker, M. The Amyloid State of Proteins in Human Diseases. *Cell* **2012**, *148*, 1188–1203. [CrossRef]
6. Otzen, D.; Rie, R. Functional amyloids. *Cold Spring Harb. Perspect. Biol.* **2019**, *11*, a033860. [CrossRef]
7. Balasco, N.; Diaferia, C.; Morelli, G.; Vitagliano, L.; Accardo, A. Amyloid-like aggregation in diseases and biomaterials: Osmosis of structural information. *Front. Bioeng. Biotechnol.* **2021**, *9*, 641372. [CrossRef]
8. Reches, M.; Gazit, E. Casting Metal Nanowires Within Discrete Self-Assembled Peptide Nanotubes. *Science* **2003**, *300*, 625–627. [CrossRef]
9. Görbitz, C.H. Nanotube Formation by Hydrophobic Dipeptides. *Chem. A Eur. J.* **2001**, *7*, 5153–5159. [CrossRef]
10. Fuentes-Caparrós, A.M.; McAulay, K.; Rogers, S.E.; Dalgliesh, R.M.; Adams, D.J. On the Mechanical Properties of N-Functionalised Dipeptide Gels. *Molecules* **2019**, *24*, 3855. [CrossRef]
11. Amdursky, N.; Molotskii, M.; Gazit, E.; Rosenman, G. Elementary Building Blocks of Self-Assembled Peptide Nanotubes. *J. Am. Chem. Soc.* **2010**, *132*, 15632–15636. [CrossRef] [PubMed]
12. Diaferia, C.; Avitabile, C.; Leone, M.; Gallo, E.; Saviano, M.; Accardo, A.; Romanelli, A. Diphenylalanine Motif Drives Self-Assembling in Hybrid PNA-Peptide Conjugates. *Chem. A Eur. J.* **2021**, *27*, 14307–14316. [CrossRef] [PubMed]
13. Reches, M.; Gazit, E. Designed aromatic homo-dipeptides: Formation of ordered nanostructures and potential nanotechnological applications. *Phys. Biol.* **2006**, *3*, S10–S19. [CrossRef] [PubMed]

14. Yang, X.; Fei, J.; Li, Q.; Li, J. Covalently assembled dipeptide nanospheres as intrinsic photosensitizers for efficient photodynamic therapy in vitro. *Chem. Eur. J.* **2016**, *22*, 1–6. [CrossRef]
15. Kumara, V.; Vijay, K.; Shruti, K.; Khashti, K.; Joshi, B. Aggregation propensity of amyloidogenic and elastomeric dipeptides constituents. *Tetrahedron* **2016**, *72*, 5369–5376. [CrossRef]
16. Mayans, E.; Casanovas, J.; Gil, A.M.; Jimenez, A.I.; Cativiela, C.; Puiggalí, J.; Aleman, C. Diversity and hierarchy in supramolecular assemblies of triphenylalanine: From laminated helical ribbons to toroids. *Langmuir* **2017**, *33*, 4036–4048. [CrossRef]
17. Diaferia, C.; Roviello, V.; Morelli, G.; Accardo, A. Self-assembly of PEGylated diphenylalanines into photoluminescent fibrillary aggregates. *ChemPhysChem* **2019**, *20*, 2774–2782. [CrossRef]
18. Creasey, R.C.G.; Louzao, I.; Arnon, Z.A.; Marco, P.; Adler-Abramovich, L.; Roberts, C.J.; Gazit, E.; Tendler, S.J.B. Disruption of diphenylalanine assembly by a Boc-modified variant. *Soft Matter* **2016**, *12*, 9451–9457. [CrossRef]
19. Yan, X.; He, Q.; Wang, K.; Duan, L.; Cui, Y.; Li, J. Transition of Cationic Dipeptide Nanotubes into Vesicles and Oligonucleotide Delivery. *Angew. Chem. Int. Ed.* **2007**, *46*, 2431–2434. [CrossRef]
20. Reches, M.; Gazit, E. Formation of Closed-Cage Nanostructures by Self-Assembly of Aromatic Dipeptides. *Nano Lett.* **2004**, *4*, 581–585. [CrossRef]
21. Pellach, M.; Mondal, S.; Shimon, L.J.W.; Adler-Abramovich, L.; Buzhansky, L.; Gazit, E. Molecular Engineering of Self-Assembling Diphenylalanine Analogues Results in the Formation of Distinctive Microstructures. *Chem. Mater.* **2016**, *28*, 4341–4348. [CrossRef]
22. Reches, M.; Gazit, E. Self-Assembly of peptide nanotubes and amyloid-like structures by charged-termini-capped diphenylalanine peptide analogues. *Isr. J. Chem.* **2005**, *45*, 363–371. [CrossRef]
23. Adler-Abramovich, L.; Gazit, E. Controlled patterning of peptide nanotubes and nanospheres using inkjet printing technology. *J. Pep. Sci.* **2007**, *14*, 217–223. [CrossRef] [PubMed]
24. Amdursky, N.; Molotskii, M.; Gazit, E.; Rosenman, G. Self-assembled bioinspired quantum dots: Optical properties. *Appl. Phys. Lett.* **2009**, *94*, 261907. [CrossRef]
25. Jayawarna, V.; Ali, M.; Jowitt, T.; Miller, A.F.; Saiani, A.; Gough, J.E.; Ulijn, R.V. Nanostructured Hydrogels for Three-Dimensional Cell Culture Through Self-Assembly of Fluorenylmethoxycarbonyl–Dipeptides. *Adv. Mater.* **2006**, *18*, 611–614. [CrossRef]
26. Mahler, A.; Reches, M.; Rechter, M.; Cohen, S.; Gazit, E. Rigid, self-assembled hydrogel composed of a modified aromatic dipeptide. *Adv. Mater.* **2006**, *18*, 1365–1370. [CrossRef]
27. Diaferia, C.; Morelli, G.; Accardo, A. Fmoc-diphenylalanine as a suitable building block for the preparation of hybrid materials and their potential applications. *J. Mater. Chem. B* **2019**, *7*, 5142–5155. [CrossRef]
28. Ghosh, M.; Bera, S.; Schiffmann, S.; Shimon, L.J.W.; Adler-Abramovich, L. Collagen-Inspired Helical Peptide Coassembly Forms a Rigid Hydrogel with Twisted Polyproline II Architecture. *ACS Nano* **2020**, *14*, 9990–10000. [CrossRef]
29. Rosa, E.; Diaferia, C.; Gallo, E.; Morelli, G.; Accardo, A. Stable Formulations of Peptide-Based Nanogels. *Molecules* **2020**, *25*, 3455. [CrossRef]
30. Helen, W.; de Leonardis, P.; Ulijn, R.V.; Gough, J.; Tirelli, N. Mechanosensitive peptide gelation: Mode of agitation controls mechanical properties and nano-scale morphology. *Soft Matter* **2011**, *7*, 1732–1740. [CrossRef]
31. Yang, X.; Xie, Y.; Wang, Y.; Qi, W.; Huang, R.; Su, R.; He, Z. Self-Assembled Microporous Peptide-Polysaccharide Aerogels for Oil–Water Separation. *Langmuir* **2018**, *34*, 10732–10738. [CrossRef]
32. Arakawa, H.; Takeda, K.; Higashi, S.L.; Shibata, A.; Kitamura, Y.; Ikeda, M. Self-assembly and hydrogel formation ability of Fmoc-dipeptides comprising α-methyl-L-phenylalanine. *Polym. J.* **2020**, *52*, 923–930. [CrossRef]
33. Wang, Z.; Li, T.; Ding, B.; Ma, X. Archieving room temperature phosphorescence from organic small molecules on amino acid skeleton. *Chi. Chem. Lett.* **2020**, *31*, 2929–2932. [CrossRef]
34. Sankar, S.; O'Neill, K.; Bagot D'Arc, M.; Rebeca, F.; Buffier, M.; Aleksi, E.; Fan, M.; Matsuda, N.; Gil, E.S.; Spirio, L. Clinical use of the self-assembling peptide RADA16: A review of current and future trends in biomedicine. *Front. Bioeng. Biotechnol.* **2021**, *9*, 679525. [CrossRef] [PubMed]
35. Nagy-Smith, K.; Moore, E.; Schneider, J.; Tycko, R. Molecular structure of monomorphic peptide fibrils within a kinetically trapped hydrogel network. *Proc. Natl. Acad. Sci. USA* **2015**, *112*, 9816–9821. [CrossRef]
36. Yaguchi, A.; Hiramatsu, H.; Ishida, A.; Oshikawa, M.; Ajioka, I.; Muraoka, T. Hydrogel-Stiffening and Non-Cell Adhesive Properties of Amphiphilic Peptides with Central Alkylene Chains. *Chem. A Eur. J.* **2021**, *27*, 9295–9301. [CrossRef]
37. Jadhav, S.P.; Amabili, P.; Stammler, H.-G.; Sewald, N. Remarkable modulation of self-assembly in short γ-Peptides by neighboring ions and orthogonal H-bonding. *Chem. Eur. J.* **2017**, *23*, 10352–10357. [CrossRef]
38. Santagada, V.; Caliendo, G. *Peptide and Peptidomimetics*; Piccin: Padova, Italy, 2012.
39. Diaferia, C.; Ghosh, M.; Sibillano, T.; Gallo, E.; Stornaiuolo, M.; Giannini, C.; Morelli, G.; Adler-Abramovich, L.; Accardo, A. Fmoc-FF and hexapeptide-based multicomponent hydrogels as scaffold materials. *Soft Matter* **2019**, *15*, 487–496. [CrossRef] [PubMed]
40. Wang, Y.; Qi, W.; Huang, R.; Su, R.; He, Z. Jet flow directed supramolecular self-assembly at aqueous liquid–liquid interface. *RSC Adv.* **2014**, *4*, 15340–15347. [CrossRef]
41. Choe, R.; Yun, S.I. Fmoc-diphenylalanine-based hydrogels as a potential carrier for drug delivery. *e-Polymers* **2020**, *20*, 458–468. [CrossRef]

42. Diaferia, C.; Balasco, N.; Sibillano, T.; Giannini, C.; Vitagliano, L.; Morelli, G.; Accardo, A. Structural Characterization of Self-Assembled Tetra-Tryptophan Based Nanostructures: Variations on a Common Theme. *ChemPhysChem* **2018**, *19*, 1635–1642. [CrossRef] [PubMed]
43. Pachahara, S.K.; Adicherla, H.; Nagaraj, R. Self-assembly of Aβ40, Aβ42 and Aβ43 peptides in aqueous mixtures of fluorinated alcohols. *PLoS ONE* **2015**, *10*, e0136567.
44. Schiattarella, C.; Diaferia, C.; Gallo, E.; Della Ventura, B.; Morelli, G.; Vitagliano, L.; Velotta, R.; Accardo, A. Solid-state optical properties of self-assembling amyloid-like peptides with different charged states at the terminal ends. *Sci. Rep.* **2022**, *12*, 759. [CrossRef] [PubMed]
45. Zhang, Y.; Gu, H.; Yang, A.Z.; Xu, B. Supramolecular Hydrogels Respond to Ligand−Receptor Interaction. *J. Am. Chem. Soc.* **2003**, *125*, 13680–13681. [CrossRef] [PubMed]
46. Yang, Z.; Gu, H.; Zhang, Y.; Wang, L.; Xu, B. Small molecule hydrogels based on a class of anti-inflammatory agents. *Chem. Commun.* **2004**, 208–209. [CrossRef]
47. Yang, Z.; Gu, H.; Fu, D.; Gao, P.; Lam, J.K.; Xu, B. Enzymatic formation of supramolecular hydrogels. *Adv. Mater.* **2004**, *16*, 1440–1444. [CrossRef]
48. Amdursky, N.; Gazit, E.; Rosenman, G. Quantum Confinement in Self-Assembled Bioinspired Peptide Hydrogels. *Adv. Mater.* **2010**, *22*, 2311–2315. [CrossRef]
49. Liu, Y.; Ding, X.; Jing, X.; Chen, X.; Cheng, H.; Zheng, X.; Ren, Z.; Zhuo, Z. Surface self-assembly of N-fluorenyl-9-methoxycarbonyl diphenylalanine on silica wafer. *Colloids Surf. B Biointerfaces* **2011**, *87*, 192–197. [CrossRef] [PubMed]
50. Ryan, K.; Beirne, J.; Redmond, G.; Kilpatrick, J.I.; Guyonnet, J.; Buchete, N.-V.; Kholkin, A.L.; Rodriguez, B.J. Nanoscale piezoelectric properties of self-assembled Fmoc-FF peptide fibrous networks. *ACS Appl. Mat. Interfaces* **2015**, *7*, 12702–12707. [CrossRef]
51. McCloskey, A.P.; Draper, E.R.; Gilmore, B.F.; Laverty, G. Ultrashort self-assembling Fmoc-peptide gelators for anti-infective biomaterial applications. *J. Pept. Sci.* **2017**, *23*, 131–140. [CrossRef]
52. Ben-Zvi, O.; Grinberg, I.; Orr, A.A.; Noy, D.; Tamamis, P.; Yacoby, I.; Adler-Abramovich, L. Protection of Oxygen-Sensitive Enzymes by Peptide Hydrogel. *ACS Nano* **2021**, *15*, 6530–6539. [CrossRef]
53. Smith, A.M.; Williams, R.J.; Tang, C.; Coppo, P.; Collins, R.F.; Turner, M.L.; Saiani, A.; Ulijn, R.V. Fmoc-diphenylalanine self-assembles to a hydrogel via a novel architecture based on π-π interlocked β-sheets. *Adv. Mater.* **2008**, *20*, 37–41. [CrossRef]
54. Tang, C.; Smith, A.M.; Collins, R.F.; Ulijn, R.V.; Saiani, A. Fmoc-diphenylalanine self-assembly mechanism induces apparent pKa shifts. *Langmuir* **2009**, *25*, 9447–9453. [CrossRef] [PubMed]
55. Xing, R.; Yuan, C.; Li, S.; Song, J.; Li, J.; Yan, X. Charge-induced secondary structure transformation of amyloid-derived dipeptide assemblies from β-sheet to α-Helix. *Angew. Chem. Int. Ed.* **2018**, *57*, 1537–1542. [CrossRef] [PubMed]
56. Ji, W.; Yuan, C.; Zilberzwige-Tal, S.; Xing, R.; Chakraborty, P.; Tao, K.; Gilead, S.; Yan, X.; Gazit, E. Metal-Ion Modulated Structural Transformation of Amyloid-Like Dipeptide Supramolecular Self-Assembly. *ACS Nano* **2019**, *13*, 7300–7309. [CrossRef] [PubMed]
57. Amdursky, N.; Orbach, R.; Gazit, E.; Huppert, D. Probing the Inner Cavities of Hydrogels by Proton Diffusion. *J. Phys. Chem. C* **2009**, *113*, 19500–19505. [CrossRef]
58. Fuentes, E.; Boháčová, K.; Fuentes-Caparrós, A.M.; Schweins, R.; Draper, E.R.; Adams, D.J.; Silvia Pujals, S.; Albertazzi, L. PAINT-ing Fluorenylmethoxycarbonyl (Fmoc)-diphenylalanine hydrogels. *Chem. Eur. J.* **2020**, *26*, 9869–9873. [CrossRef]
59. Gulrez, S.K.H.; Al-Assaf, S.; Phillips, G.O. Hydrogels: Methods of preparation, characterisation and applications. In *Progress in Molecular and Environmental Bioengineering—From Analysis and Modeling to Technology Applications*; IntechOpen: London, UK, 2011.
60. Taylor, J.; Rahimeh, B.; Alpesh, P.; Kibret, M. Fabrication of highly porous tissue-engineering scaffolds using selective spherical porogens. *BioMed. Mater. Eng.* **2010**, *20*, 107–118.
61. Annabi, N.; Nichol, J.W.; Zhong, X.; Ji, C.; Koshy, S.; Khademhosseini, A.; Dehghani, F. Controlling the porosity and microarchitecture of hydrogels for tissue engineering. *Tiss. Eng. B* **2010**, *16*, 371–383. [CrossRef]
62. Raeburn, J.; Pont, G.; Chen, L.; Cesbron, Y.; Levy, R.; Adams, D.J. Fmoc-diphenylalanine hydrogels: Understanding the variability in reported mechanical properties. *Soft Matter* **2012**, *8*, 1168–1174. [CrossRef]
63. Adams, D.J.; Butler, M.F.; Frith, W.J.; Kirkland, M.; Mullen, L.; Sanderson, P. A new method for maintaining homogeneity during liquid–hydrogel transitions using low molecular weight hydrogelators. *Soft Matter* **2009**, *5*, 1856–1862. [CrossRef]
64. Berillo, D.; Mattiasson, B.; Yu, I.; Kirsebom, G.H. Formation of macroporous self-assembled hydrogels through cryogelation of Fmoc-Phe-Phe. *J. Coll. Interface Sci.* **2012**, *368*, 226–230. [CrossRef] [PubMed]
65. Ding, B.; Li, Y.; Qin, M.; Ding, Y.; Cao, Y.; Wang, W. Two approaches for the engineering of homogeneous small-molecule hydrogels. *Soft Matter* **2013**, *9*, 4672–4680. [CrossRef]
66. Orbach, R.; Adler-Abramovich, L.; Zigerson, S.; Mironi-Harpaz, I.; Seliktar, D.; Gazit, E. Self-Assembled Fmoc-Peptides as a Platform for the Formation of Nanostructures and Hydrogels. *Biomacromolecules* **2009**, *10*, 2646–2651. [CrossRef] [PubMed]
67. Dudukovic, N.A.; Zukoski, C.F. Mechanical Properties of Self-Assembled Fmoc-Diphenylalanine Molecular Gels. *Langmuir* **2014**, *30*, 4493–4500. [CrossRef]
68. Dudukovic, N.A.; Zukoski, C.F. Evidence for equilibrium gels of valence-limited particles. *Soft Matter* **2014**, *10*, 7849–7856. [CrossRef]

69. Levine, M.S.; Ghosh, M.; Hesser, M.; Hennessy, N.; DiGuiseppi, D.M.; Adler-Abramovich, L.; Schweitzer-Stenner, R. Formation of peptide-based oligomers in dimethylsulfoxide: Identifying the precursor of fibril formation. *Soft Matter* **2020**, *16*, 7860–7868. [CrossRef]
70. Dudukovic, N.A.; Zukoski, C.F. Gelation of Fmoc-diphenylalanine is a first order phase transition. *Soft Matter* **2015**, *11*, 7663–7673. [CrossRef]
71. Raeburn, J.; Mendoza-Cuenca, C.; Cattoz, B.N.; Little, M.A.; Terry, A.E.; Cardoso, A.Z.; Griffiths, P.C.; Adams, D.J. The effect of solvent choice on the gelation and final hydrogel properties of Fmoc–diphenylalanine. *Soft Matter* **2014**, *11*, 927–935. [CrossRef]
72. Dudukovic, N.A.; Hudson, B.C.; Paravastu, A.K.; Zukoski, C.F. Self-assembly pathways and polymorphism in peptide-based nanostructures. *Nanoscale* **2017**, *10*, 1508–1516. [CrossRef]
73. Williams, R.J.; Smith, A.M.; Collins, R.; Hodson, N.; Das, A.K.; Ulijn, R.V. Enzyme-assisted self-assembly under thermodynamic control. *Nat. Nanotech.* **2009**, *4*, 19–24. [CrossRef] [PubMed]
74. Hirst, A.R.; Roy, S.; Arora, M.; Das, A.K.; Hodson, N.; Murray, P.; Marshall, S.; Javid, N.; Sefcik, J.; Boekhoven, J.; et al. Biocatalytic induction of supramolecular order. *Nat. Chem.* **2010**, *2*, 1089–1094. [CrossRef] [PubMed]
75. Huang, R.; Wang, Y.; Qi, W.; Su, R.; He, Z. Chemical catalysis triggered self-assembly for the bottom-up fabrication of peptide nanofibers and hydrogels. *Mater. Lett.* **2014**, *128*, 216–219. [CrossRef]
76. Chronopoulou, L.; Sennato, S.; Bordi, F.; Giannella, D.; Di Nitto, A.; Barbetta, A.; Dentini, M.; Togna, A.R.; Togna, G.I.; Moschini, S.; et al. Designing unconventional Fmoc-peptide-based biomaterials: Structure and related properties. *Soft Matter* **2013**, *10*, 1944–1952. [CrossRef]

pharmaceuticals

MDPI

Article

Peptide-Based Hydrogels and Nanogels Containing Gd(III) Complexes as T_1 Relaxation Agents

Elisabetta Rosa [1], Fabio Carniato [2], Lorenzo Tei [2], Carlo Diaferia [1], Giancarlo Morelli [1], Mauro Botta [2] and Antonella Accardo [1,*]

[1] Department of Pharmacy, Research Centre on Bioactive Peptides (CIRPeB), University of Naples "Federico II", Via Montesano 49, 80131 Naples, Italy
[2] Department of Science and Technological Innovation, University of Piemonte Orientale "A. Avogadro", Viale T. Michel 11, 15121 Alessandria, Italy
* Correspondence: antonella.accardo@unina.it

Abstract: New peptide-based hydrogels incorporating Gd(III) chelates with different hydration states, molecular structures and overall negative charges ($[Gd(BOPTA)]^{2-}$), $[Gd(DTPA)]^{2-}$, and ($[Gd(AAZTA)]^{-}$) were prepared and characterized. N-terminal Fmoc- or acetyl-derivatized hexapeptides (K1, K2 and K3) containing five aliphatic amino acids (differently ordered Gly, Ala, Val, Leu and Ile) and a charged lysine at the amidated C-terminal were used for the formation of the hydrogels. Particular attention was paid to the investigation of the morphological and rheological properties of the nanoparticles, in addition to the assessment of the ability (relaxivity) of the confined complexes to accelerate the longitudinal relaxation rate of the water protons localized in the polymeric network. The relaxivity values at high magnetic fields (>0.5 T) of the paramagnetic hydrogels appear to be more than five times higher than those of isolated chelates in an aqueous solution, reaching a value of 25 $mmol^{-1}$ s^{-1} for Fmoc-K2+$[Gd(BOPTA)]^{2-}$ at 0.5 T and 310 K. Furthermore, an interesting trend of decrease of relaxivity with increasing the degree of rigidity of the hydrogel was observed. The type of interactions between the various complexes and the polymeric network also plays a key role in influencing the relaxivity values of the final materials. Nanogels were also obtained from the submicronization of the hydrogel containing $[Gd(BOPTA)]^{2-}$ chelate. Circular dichroism, dynamic light scattering and relaxometric investigations on these nanoparticles revealed the formation of nanogels endowed with higher relaxivities (r_1 = 41 mM^{-1} s^{-1} at 0.5 T MHz and 310 K) than the corresponding hydrogels.

Keywords: peptide hydrogels; nanogels; supramolecular assembly; MRI; contrast agents; diagnosis

Citation: Rosa, E.; Carniato, F.; Tei, L.; Diaferia, C.; Morelli, G.; Botta, M.; Accardo, A. Peptide-Based Hydrogels and Nanogels Containing Gd(III) Complexes as T_1 Relaxation Agents. *Pharmaceuticals* **2022**, *15*, 1572. https://doi.org/10.3390/ph15121572

Academic Editors: Angelo Maspero, Mauro Fasano and Luca Nardo

Received: 14 November 2022
Accepted: 14 December 2022
Published: 16 December 2022

1. Introduction

Soft nanostructured materials such as fibers, hydrogels (HGs) and nanogels (NGs) have been identified as promising tools for the development of biomaterials for applications in tissue engineering, targeted drug delivery, biosensors, imaging, gene delivery as well as stimuli-responsive bioactive carriers [1–9]. HGs are self-supporting three-dimensional matrices able to entrap high content of water or other biological fluids by non-covalent interactions during the swelling process [10]. Their application in drug delivery is guaranteed by their ability to provide spatial and temporal control in the release of bioactive and therapeutic compounds and by their occurrence in various structures and composition such as injectable forms, thin films, viscous gels, and nanocomposites [2,3,10]. Among these biomedical applications, examples of HGs covalently derivatized or loaded with Gd(III) complexes have been proposed for tissue engineering applications to document the in vivo degradation of implants by magnetic resonance imaging (MRI) [11–13]. For instance, Stupp and co-workers described the synthesis of HGs based on peptide amphiphiles (PAs) functionalized with Gd-DOTA-monoamide (DOTA = 1,4,7,10-tetraazacyclododecane-1,4,7,10-tetraacetic acid) complexes and followed their fate over time in tibialis anterior

muscle of mouse limbs after implantation [14]. On the other hand, NGs can be defined as nanoparticles with a size in the nano-range compatible with intravenous injection [15]. The major advantages of the nanogel-based systems in comparison to other polymeric nanoparticles characterized by a dense core is that they contain a large amount of water allowing them the capability to encapsulate diverse therapeutic and bioactive molecules, proteins, and metal complexes. One of the approaches used to obtain NGs is by HG submicronization according to top-down methodologies in the presence of stabilizing agents [16]. Following this synthetic protocol, the obtained NGs preserve the hydrated inner network (defined as core) of the HG they are derived from. Another approach describes an ionotropic gelation method that combines a positively charged polysaccharide (chitosan) and an anionic component composed of sodium hyaluronate, tripolyphosphate and anionic Gd(III) complexes to obtain a series of NGs endowed with very high relaxivity values [17]. Mono- and bis-hydrated Gd(III) complexes such as $[Gd(DOTA)(H_2O)]^-$ and $[Gd(AAZTA)(H_2O)_2]^{2-}$ (AAZTA = 6-amino-6-methylperhydro-1,4-diazepine-*N*,*N*′,*N*″,*N*‴-tetraaceticacid) were incorporated within NGs and relaxivity values up to six times higher than those of the free complexes in aqueous solution were determined [18]. Remarkably, when $[Gd(DOTP)]^{5-}$ (DOTP = 1,4,7,10-Tetraazacyclododecane-1,4,7,10-tetra(methylene phosphonic acid), a Gd(III) complex that lacks metal-bound water molecules ($q = 0$), was confined or used as a cross-linker in these type of NGs, an outstanding relaxivity value of 78.0 mM^{-1} s^{-1} was measured, at 20 MHz and 298 K, nearly 20 times greater than that found for the free complex [19].

It is worth noting that among all the proposed matrices, peptides represent a minority and no example of peptide-based NGs [4,20–22] has ever been provided for imaging applications; notwithstanding, peptides can be related to several advantages such as high biocompatibility, biodegradability and low cost [23]. Recently, we reported the synthesis, the formulation and the characterization of three peptide-based HGs for tissue engineering applications [24]. The peptide sequences (Figure 1) used to hydrogel fabrication contain five aliphatic residues (including Gly, Ala, Val, Leu and Ile) and a charged one (a Lys residue) at the amidated C-terminus. Moreover, all the peptides are protected at the N-terminus with the Fmoc (fluorenylmethyloxycarbonyl) group, which demonstrated its ability to improve the gelification properties of short and ultrashort peptides. These peptide-based HGs, named as Fmoc-K1, Fmoc-K2 and Fmoc-K3, exhibit a stiffness with storage modulus G′ values between ~500 and ~2500 Pa and very low toxicity (<5–8%) on 3T3 fibroblast and on HaCat cell lines up to 72 h. However, it is important to note that these G′ values are lower than those of some corresponding acetylated (Ac-) peptides (G′ value ~40 kPa), previously studied by Loo et al. as a scaffold for bioprinting applications [25].

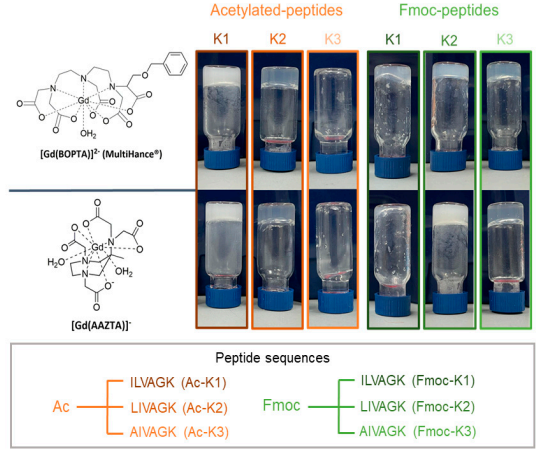

Figure 1. Schematic representation of peptide sequences according to the one code letter practice and of Gd(III) complexes ($[Gd(BOPTA)]^{2-}$) and $[Gd(AAZTA)]^-$ used for hydrogel formulations. For each combination, being peptide–Gd(III) chelates, the inverted test tube is also reported.

In this study, we demonstrated that both Ac- and Fmoc-protected peptide-based hydrogels are able to encapsulate linear ($[Gd(BOPTA)]^{2-}$ and $[Gd(DTPA)]^{2-}$) or mesocyclic ($[Gd(AAZTA)]^{-}$) CAs through ionic and/or hydrophobic interactions. Successively, a nanogel was also obtained by submicronization of the best performing Gd complex-loaded HG. All the supramolecular systems (both HGs and NG) were fully characterized from the structural point of view and their ^{1}H NMR relaxometric behavior was investigated as a function of the applied magnetic field strength.

2. Results and Discussion

2.1. Formulation and Characterization of HGs Encapsulating Gd Complexes

Empty HGs based on acetyl (Ac-) or fluorenylmethyloxycarbonyl (Fmoc-) K1, K2 and K3 peptides were recently investigated as three-dimensional matrices for cell adhesion and proliferation [24]. Due to the presence of a charged lysine residue in their sequence, these peptides are here selected as starting models for improving the electrostatic interactions and promoting the physical encapsulation of T_1-CAs such as $[Gd(AAZTA)]^{-}$ [26,27] and $[Gd(BOPTA)]^{2-}$ [28], which contain one and two negative charges, respectively. The choice of these two Gd complexes comes from the purpose of obtaining both the best encapsulation ratio and the highest relaxivity (r_1) value. This latter is a parameter that defines the efficacy of any paramagnetic complex agent to induce a change in the water protons relaxation rate (R_1) per unit concentration (mmol L^{-1}) of metal ion [29,30]. Regarding the first point, two contributes were considered: (i) the electrostatic interactions between the peptide and the two differently charged complexes and (ii) the possibility to introduce further interactions lead by the aromatic moieties of the components. Indeed, the benzene ring on the backbone of BOPTA ligand could establish π–π stacking interactions with the Fmoc group on the peptide derivatives. To study the influence of these interactions on the relaxivity, Fmoc-K2 hydrogels loaded with $[Gd(DTPA)]^{2-}$ were also prepared and studied. On the other hand, $[Gd(AAZTA)]^{-}$ was chosen because of the high relaxivity value (r_1=6.6 mM^{-1} s^{-1} at 32 MHz and 298 K) due to the presence of two inner sphere water molecules coordinated to the metal ion. Recent studies evidenced that the formulation of empty HGs of these cationic peptides is easily obtained by adding 50 μL of 0.1 mol L^{-1} phosphate buffer to an aqueous suspension (300 μL of the peptide solution) of each peptide at a concentration of 2 wt% [24]. In this procedure, the hydrogel formation is triggered by the phosphate buffer, which has probably a role in decreasing the electrostatic repulsions between the positive charges of lysine residues. The rheological characterization of these two classes of peptides evidenced a different mechanical rigidity, with a higher stiffness for some of the Ac-derivatives with respect to Fmoc-ones. It is easy to infer that the stiffness of each formulation can significantly affect the application of the final biomaterial.

For $[Gd(BOPTA)]^{2-}$- and $[Gd(DTPA]^{2-}$-loaded HGs, due to the presence of residual negative charges on the metal complex, we observed the spontaneous formation of the gel by simply adding 50 μL of the 30 mmol L^{-1} complex solution to the 2 wt% peptide one. On the other hand, the $[Gd(AAZTA)]^{-}$-loaded HGs formulations (2 wt%) were obtained by dissolving the peptide powder in a 5 mmol L^{-1} complex solution, followed by the addition of 50 μL of phosphate buffer. This last step was necessary since the single residual negative charge of $[Gd(AAZTA)]^{-}$ was not enough to prompt the gelation process.

The capability of each peptide to gel also in the presence of the Gd(III) complex was evaluated by the inverted test tube (Figures 1 and S4C). As observed in the pictures, not all the peptides keep their propensity to gel: Ac-K3 does not form gels with both complexes and Fmoc-K1 is not able to gel in the presence of $[Gd(AAZTA)]^{-}$ and seems to form very soft, not completely supporting gels with $[Gd(BOPTA)]^{2-}$. This latter evidence is not surprising since Fmoc-K1 was previously identified as the softer hydrogel of the series with a storage module (G′) of 557 Pa [24]. However, the encapsulation of $[Gd(BOPTA)]^{2-}$ in Fmoc-K1 is not completely forbidden thanks to the interactions between the aromatic ring of the chelating agent and the Fmoc group. Instead, the inability of Ac-K3 to gel could be probably explained based on its different peptide sequence, in which the presence of

an alanine residue in place of a leucine or an isoleucine, together with the absence of the fluorenyl group, hinders a good packaging. The stability of filled HGs was also evaluated over time (up to 30 days) by incubating them in the Ringer's solution at 37 °C and by evaluating their weight loss. Results, reported in Table 1 as ΔW(%), indicate a low weight loss for all the hydrogels (<7.79%), thus pointing to a high stability.

Table 1. Degradation degree, expressed as percentage ratio (ΔW), storage modulus (G′), loss modulus (G″) and Tanδ for the different paramagnetic formulations. Rheological parameters of empty hydrogels are also reported for comparison.

	Sample	ΔW (%)	G′ (Pa)	G″ (Pa)	Tan (δ)
Fmoc-K1	Fmoc-K1	—	557	40	13.9
	Fmoc-K1 + $[Gd(BOPTA)]^{2-}$	3.74	11	2	5.5
	Fmoc-K1 + $[Gd(AAZTA)]^{-}$		-	-	-
Fmoc-K2	Fmoc-K2	—	925	89	10.4
	Fmoc-K2 + $[Gd(BOPTA)]^{2-}$	2.65	57	6	9.5
	Fmoc-K2 + $[Gd(AAZTA)]^{-}$	4.91	500	102	4.9
	Fmoc-K2 + $[Gd(DTPA)]^{2-}$	—	36	3	12
Fmoc-K3	Fmoc-K3	—	2526	273	9.2
	Fmoc-K3 + $[Gd(BOPTA)]^{2-}$	1.08	425	51	8.3
	Fmoc-K3 + $[Gd(AAZTA)]^{-}$	0.01	4210	508	8.3
Ac-K1	Ac-K1	—	306	40	7.6
	Ac-K1 + $[Gd(BOPTA)]^{2-}$	0.20	18,280	3826	4.8
	Ac-K1 + $[Gd(AAZTA)]^{-}$	0.67	42,583	5182	8.2
Ac-K2	Ac-K2	—	2677	192	13.9
	Ac-K2 + $[Gd(BOPTA)]^{2-}$	7.79	520	102	5.1
	Ac-K2 + $[Gd(AAZTA)]^{-}$	2.81	11,018	2304	4.8

2.2. Structural Characterization of Hydrogels: FTIR, SEM and Rheology

Further structural characterization of paramagnetic hydrogels was assessed by Fourier transmission infrared (FTIR) and scanning electron microscopy (SEM) techniques. Selected FTIR spectra of Gd complexes loaded into hydrogels and of the corresponding empty ones are reported in Figure S5. From the inspection of the spectra, a common transmittance profile can be observed for all the examined samples. In detail, IR profiles are dominated by two main signals, typically observed in the case of aggregates rich in β-sheet structures. The first very broad signal is detectable in the amide A region (~3500–3300 cm^{-1}) and the second one in the amide I region (1700 to 1600 cm^{-1}). More precisely, the band around 3395 cm^{-1} is originated by the NH stretching vibrations polarized along the N-H bond and by the O-H stretching occurring between the hydrogel matrix and the surrounding water. The high intensity of this band is indicative of the extended network of inter- and intramolecular hydrogen bonds existing in the supramolecular structure. On the other hand, the band around 1650 cm^{-1} is due to the C=O stretching vibration and used to confirm the presence of β-sheet structures. Micrographs of selected samples (Fmoc-K1, Fmoc-K2 and Fmoc-K3 encapsulating $[Gd(BOPTA)]^{2-}$) are reported in Figure 2A–C. SEM images of the xerogels show fibrillary interconnected networks, typically observed for peptide-based hydrogels. By comparison with the corresponding empty hydrogels, it can be concluded that the insertion of the metal complex does not affect the overall morphology. Similar results were obtained also for Fmoc-peptide-based hydrogels encapsulating $[Gd(AAZTA)]^{-}$ and $[Gd(DTPA]^{2-}$ (see Figure S6) and for Ac-peptide HGs encapsulating the same complexes. A rheological analysis was carried out to assess the effect of Gd(III) complexes physical

entrapment on the mechanical properties of the final matrix. A rotational controlled stress rheometer was used, and the experiments were carried out in the linear viscoelastic region after a preliminary parameter evaluation.

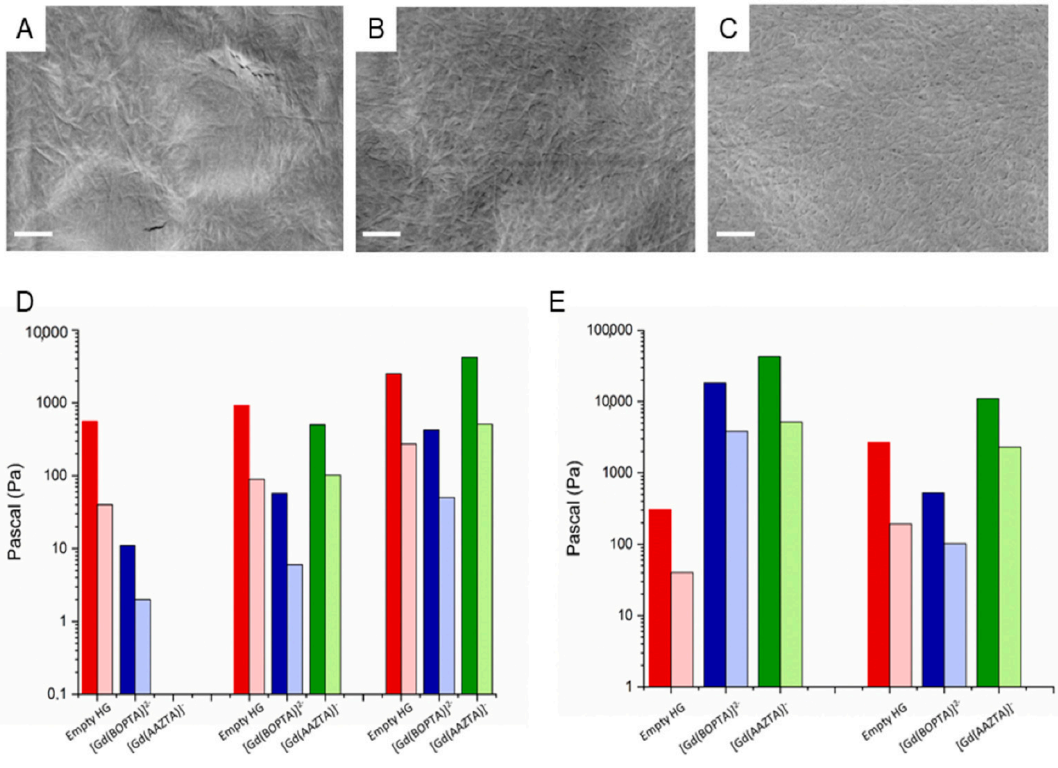

Figure 2. Structural characterization of hydrogels filled with Gd complexes. SEM micro-photos of Fmoc-K1 (**A**), Fmoc-K2 (**B**), and Fmoc-K3 (**C**) loaded with $[Gd(BOPTA)]^{2-}$ (scale bar is 500 nm). Rheological histogram analysis performed on hydrogels loaded with Gd complexes. (**D**) Fmoc-peptides; (**E**) Ac-peptides. Graph report both G′ (dark bar) and G″ (light bar) moduli of each time sweep experiment (20 min, strain of 0.1%, frequency 1 Hz). Values are expressed as a Pascal (Pa) logarithmic scale. Time sweep measurements are not in triplicate.

Rheological results, collected in Figures 2D,E and S4D, are reported in terms of G′ (storage modulus) and G″ (loss modulus). All the acquired time sweep oscillatory profiles (1.0 Hz and 0.1% strain, 20 min) are in Figures S7 and S8 and viscoelastic parameters (G′, G″ and tangent of the phase angle, tanδ) are grouped in Table 1. All the samples keep the gel state, possessing values of tanδ > 1 and G′ > G″, consistent with materials that behave similarly to an elastic solid. The $[Gd(BOPTA)]^{2-}$ entrapment in Fmoc-K series generates a sensible decrease of the G′ modulus, particularly relevant for Fmoc-K1 (around 50-fold decrease), which is the softer peptide of the series. This trend is also visible in the tanδ decrease for each couple of empty and $[Gd(BOPTA)]^{2-}$ filled Fmoc-K-based hydrogels. This general behaviour could be probably explained considering the chemical structure of the Gd(III) chelate. The presence of an aromatic moiety in the complex and its overall steric hindrance is probably able to alter the aggregative interaction pathway of Fmoc-hexapeptides, reducing the Fmoc–Fmoc interactions responsible for the self-assembling phenomena. This explanation is also supported by the inverse trend observed in Ac-K peptides, for which the G′ values increase with the encapsulation of $[Gd(BOPTA)]^{2-}$ (increase of around 60-fold for Ac-K1).

The $[Gd(AAZTA)]^{-}$ entrapment within the hydrogel matrices induces an increase of the mechanical rigidity in Fmoc-K3 (G′ value from 2526 Pa to 4210 Pa for empty and filled, respectively), a decrease of G′ (~2-fold) in Fmoc-K2 (500 Pa respect to 925 Pa previously

measured for the empty HG) and it prevents the formation of hydrogels in Fmoc-K1. As observed for $[Gd(BOPTA)]^{2-}$, $[Gd(AAZTA)]^{-}$ also causes an increase of the G′ values in the Ac-K series, which is especially evident for Ac-K1, with an increase of G′ of 140-fold. Likely, this exceptional increase can be explained by taking into account the three-dimensional distribution of the complexes in the supramolecular space.

2.3. Hydrogel Relaxivity Studies

The relaxometric properties of Fmoc-K2 hydrogels were further investigated by measuring the relaxivity values as a function of the applied magnetic field strength in the 0.01–120 MHz range, at three different temperatures (283, 298 and 310 K) and these were compared with those of the free chelates in aqueous solution at 298 K and neutral pH. In principle, the values of r_1 receive contributions from three different mechanisms: the inner sphere mechanism (r_1^{IS}) generated by the direct dipolar interaction of the coordinated water molecules with the metal ion; the second sphere mechanism (r_1^{SS}), promoted by the interaction of the water molecules hydrogen-bonded to the polar groups of the ligand with the paramagnetic site; the outer sphere contribution (r_1^{OS}) defined by the weak interactions of rapidly diffusing bulk water molecules next to the complex. Typically, the first mechanism dominates the observed relaxivity and mainly depends on the hydration state of the chelate (q), as well as the residence lifetime (τ_M) of the metal-coordinated water molecule(s), the rotational correlation time of the probe (τ_R) and the electronic relaxation times [31]. The ^{1}H NMRD profile of Fmoc-K2+$[Gd(BOPTA)]^{2-}$ showed a field-dependence relaxivity typical of probes containing Gd(III) chelates with restricted mobility, with a marked hump centered around 20 MHz [18]. The strong π–π interactions of the aromatic group of the complex with the Fmoc functionality of the peptide-based hydrogel are responsible of both the shape of the profile and the relatively high r_1 values observed. At 20 MHz and 298 K, the relaxivity of the hydrogel is ca. five times higher than that of mono-hydrated $[Gd(BOPTA)]^{2-}$ free complex (Figures 3A and 4). Surprisingly, the relaxivity of the hydrogel increases with the temperature, a behavior opposite to that typically observed of negatively charged Gd(III) chelates [32]. This suggests the occurrence of a slow water exchange process, probably due to a reduced diffusion of water inside the gelled matrix (Figure 3A). In order to confirm the importance of the interactions between aromatic moieties in Fmoc-K2+$[Gd(BOPTA)]^{2-}$ hydrogels, the corresponding sample containing $[Gd(DTPA)]^{2-}$ was also analyzed. The Fmoc-K2+$[Gd(DPTA)]^{2-}$ hydrogel shows a different ^{1}H NMRD profile with a less pronounced peak at high magnetic fields and lower relaxivity values (Figures 3B and 4), likely due to a weaker interaction of the complex with the peptide matrix. Nevertheless, the relaxivity at 20 MHz and 298 K is ca. three times higher than that of free $[Gd(DTPA)]^{2-}$ in aqueous solution. Furthermore, although r_1 does not increase with increasing temperature, as observed for Fmoc-K2+$[Gd(BOPTA)]^{2-}$, the water exchange regime is still slow and limited by the diffusion processes.

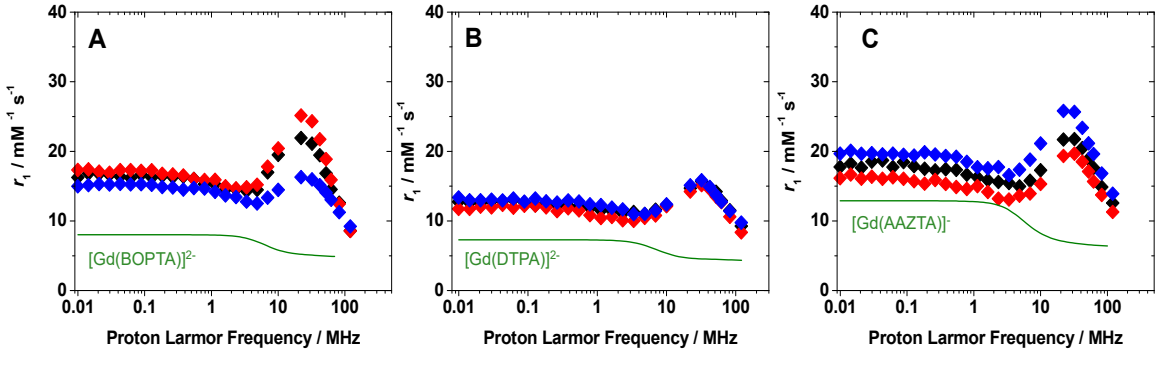

Figure 3. ^{1}H NMRD profiles of Fmoc-K2+$[Gd(BOPTA)]^{2-}$ (**A**), Fmoc-K2+$[Gd(DTPA)]^{2-}$ (**B**) and Fmoc-K2+$[Gd(AAZTA)]^{-}$ (**C**) at 283 (blue), 298 (black) and 310 K (red). The profiles of the corresponding chelates in aqueous solution are also reported as solid lines.

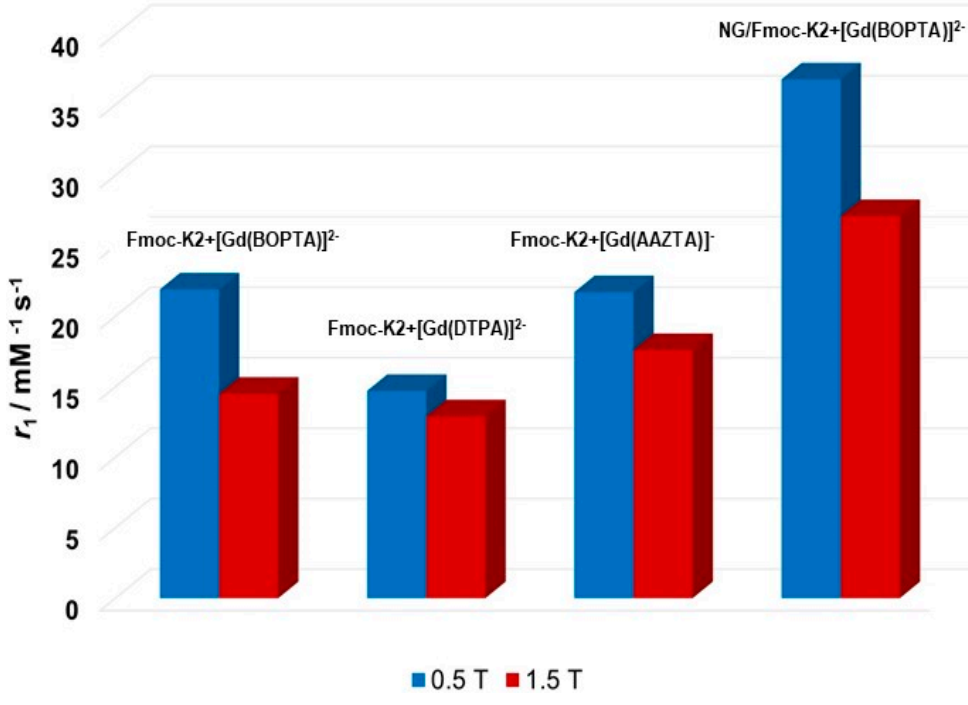

Figure 4. Comparison of the r_1 values calculated at 0.5 and 1.5 T (298 K) for Fmoc-K2+[Gd(BOPTA)]$^{2-}$, Fmoc-K2+[Gd(DTPA)]$^{2-}$, Fmoc-K2+[Gd(AAZTA)]$^{-}$ and NG/Fmoc-K2+[Gd(BOPTA)]$^{2-}$. Relaxometric measurements are not in triplicate.

Finally, ^{1}H NMRD profiles of the same peptide hydrogel entrapping the bis-hydrated [Gd(AAZTA)]$^{-}$ complex were measured. The increment of the r_1 values at 20 MHz with respect to the pure complex is comparable to that observed for Fmoc-K2+[Gd(BOPTA)]$^{2-}$, because of the presence of two inner sphere water molecules coordinated to Gd^{3+}. Moreover, as r_1 decreases with increasing temperature, we can conclude that the water exchange process is fast enough not to limit relaxivity (Figure 3C).

Some hypotheses could explain the different water dynamics in the various hydrogels: (i) localization of the complexes to sites of the hydrogel characterized by different water accessibilities; (ii) different organization of the water network in the three hydrogels; (iii) alteration of the rigidity of the matrix in the presence of different chelates, as indicated by the G′ values shown in Table 1. One or more of these conditions can occur simultaneously and result from the high complexity of these systems. Under these conditions, it has no physical meaning to try to apply well-known models, which describe the paramagnetic relaxation and allow assessing the molecular parameters responsible for the relaxivity values. Moreover, the modification of the peptide structure, responsible for the gelation, can dramatically change the relaxometric properties of the final hydrogel. In fact, a marked decrease of r_1 takes place moving from Fmoc-K2 to the more rigid Fmoc-K3 hydrogels (Figures 5 and S9). A similar behavior was observed also for the peptide functionalized with acetyl groups (Ac-K1 and Ac-K2), where only a weak interaction occurs between the [Gd(BOPTA)]$^{2-}$ complexes and the polymeric matrix (Figures 5 and S10). Indeed, in Ac-K1 and Ac-K2 peptidic variants the aromatic fluorenyl group is replaced by the acetyl group, which cannot provide π–π stacking interactions with the aromatic ring of the BOPTA chelating agent. The comparison between the encapsulation of DTPA and BOPTA Gd complexes into the hydrogel has clearly highlighted the relevance of such interactions in enhancing the r_1 value. The decrease of r_1 with an increasing storage modulus of HGs encapsulating [Gd(BOPTA)]$^{2-}$ is clearly highlighted in Figure 5.

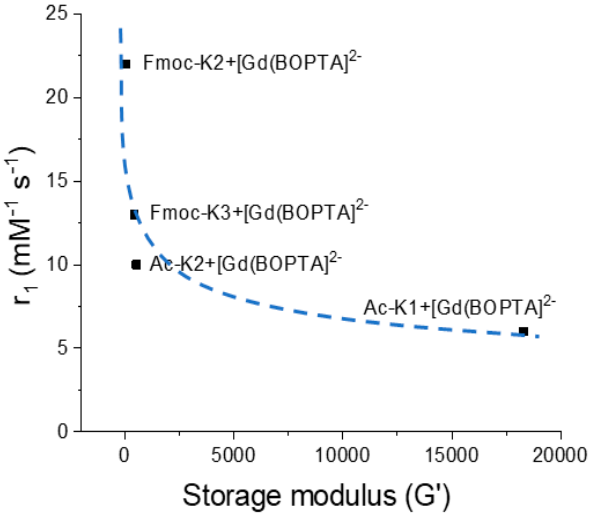

Figure 5. Dependence of r_1 values (20 MHz and 298 K) on the storage modulus (G′) of hydrogels based on $[Gd(BOPTA)]^{2-}$.

2.4. Nanogel Formulation and Structural and Relaxivity Characterization

In view of the interesting relaxometric properties of the Fmoc-K2+$[Gd(BOPTA)]^{2-}$ hydrogel, this sample was treated with a submicronization process and converted into the corresponding nanogel (NG/Fmoc-K2+$[Gd(BOPTA)]^{2-}$) using the top-down approach. Submicronization of the hydrogel was carried out in presence of two commercial surfactants TWEEN® 85 (Polyoxyethylenesorbitan Trioleate) and SPAN® 85 (Sorbitane trioleate), which have the role to stabilize the supramolecular formulation. The 89/11 (*w*/*w*) ratio between TWEEN®85 and SPAN®85 was chosen to obtain an HLB value of 10, which previously emerged as the optimal one for similar peptide-based NG formulations [22]. At the end of the preparation the resulting NGs were purified from free Gd complex by gel filtration and the encapsulated fraction of the complex was estimated by inductively coupled plasma-mass spectrometry (ICP-MS). The size and the stability of the NG formulation were assessed over time using the dynamic light scattering (DLS) technique, by measuring the mean diameter up to seven days. he mean diameter and the polydispersity index reported in Figure 6A (~190 nm and 0.272, respectively) are compatible with the possibility of a systemic administration. In order to obtain structural information on the resulting nanogel, circular dichroism (CD) studies were performed. The shape of the CD profile upholds that the structuration of the HG is preserved also in its nano-derivative (Figure 6B) [24]. The positive band, with a maximum around 212 nm, is attributable to n→π* transitions occurring in the β-sheet organization, while the one around 250 nm is associated with the π–π* transition of fluorenyl moiety. Moreover, the nanogel presents a unique negative band at ~230 nm, which has been demonstrated to be relative to the presence of strongly twisted β-sheets in which both the inter-β-sheet distance and the solvent exposure increase [33]. This higher accessibility to water is well justified by the concept of nanogels itself, characterized by the retention of the fibrillary network of HGs and by the increase of the surface area.

The relaxometric properties of an aqueous suspension of nanogel containing 0.4 mmol L^{-1} of $[Gd(BOPTA)]^{2-}$ were investigated. The shape of the ^1H NMRD profile and the temperature dependence of the r_1 values are comparable to those observed for the corresponding hydrogel (Figure 6C). A strong limitation of the mobility of the complex in interaction with the aromatic functionalities of the peptide matrix is still evident after the submicronization process of the hydrogel and the water exchange process follows a slow regime. Furthermore, it is important to note that the maximum relaxivity at 20 MHz and 298 K is 36.8 mM^{-1} s^{-1}, a value higher than that measured for the corresponding hydrogel,

probably because of a different degree of rotational freedom of the complexes within the polymeric matrix.

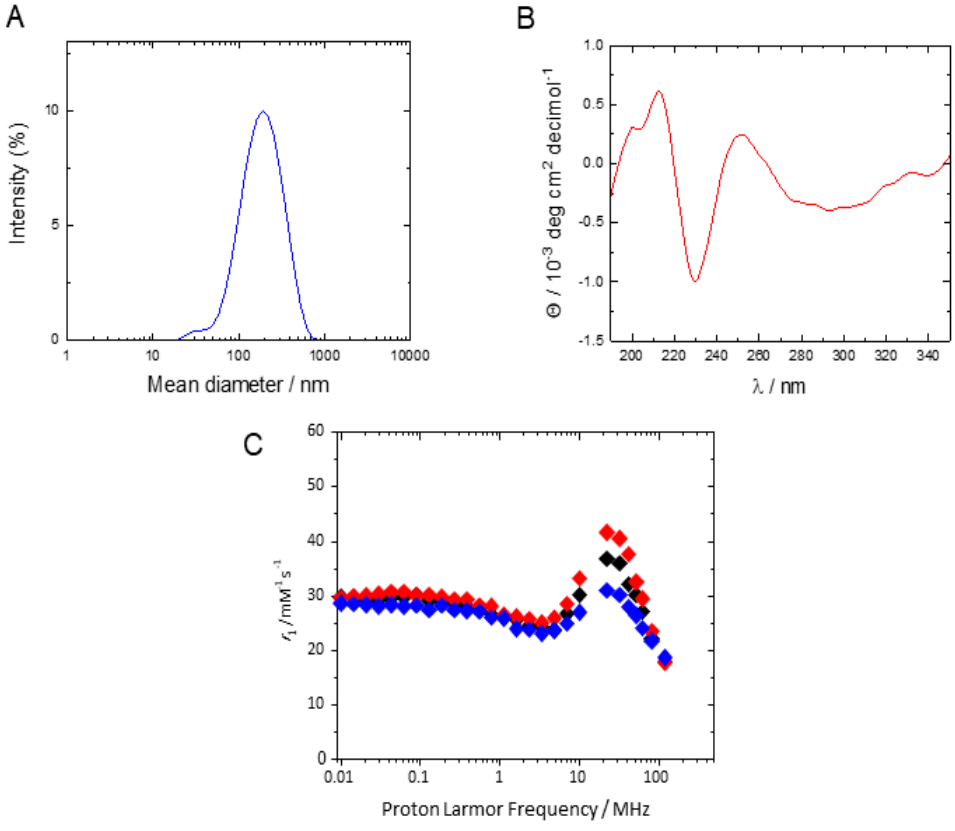

Figure 6. Structural and relaxometric characterization of Fmoc-K2 NG loaded with $[Gd(BOPTA)]^{2-}$. (**A**) CD profile of the NG solution recorded in the range between 350 and 190 nm; (**B**) Dynamic light scattering profile and the paramagnetic NG; (**C**) ^{1}H NMRD profile of the nanogel at 283 (blue), 298 (black) and 310 K (red).

3. Materials and Methods

Protected N^{α}-Fmoc-amino acid derivatives, coupling reagents and Rink amide MBHA (4-methylbenzhydrylamine) resin are commercially available from Calbiochem-Novabiochem (Laufelfingen, Switzerland). All other chemicals are commercially available from Merck (Milan, Italy), Fluka (Bucks, Switzerland), or LabScan (Stillorgan, Dublin, Ireland) and unless stated otherwise, they were used as delivered. $[Gd(BOPTA)]^{2-}$ (Gadobenate dimeglumine, MultiHance) was kindly provided by Bracco Imaging S.p.A. $[Gd(AAZTA)]^{-}$ was synthesized as reported previously [26]. Peptide solutions were prepared by weight using double distilled water.

To promote the complexation in $[Gd(DTPA)]^{2-}$, Diethylenetriaminepentaacetic acid (DTPA) (20 mg, 0.05 mmol) was dissolved in 2 mL of pure water in the presence of a molar excess of $GdCl_3 \cdot 6H_2O$. The pH of the solution was corrected to 6 with NaOH 0.1 M and the reaction was maintained under stirring at room temperature for 1h. Then, the pH was increased to 9.5 to promote the precipitation of unreacted Gd^{3+} that was filtered out, and the pH of the solution was corrected to 7 with diluted HCl (0.1 M).

3.1. Peptide Solid Phase Synthesis

All the peptide derivatives were synthesized using standard solid-phase peptide synthesis (SPPS) protocols according to Fmoc/tBu strategy as previously described [24]. Briefly, the solid support (Rink amide MBHA resin, substitution grade 0.73 mmol/g)

was swelled in dimethylformamide (DMF) under stirring for 30 min. Successively, the Fmoc protecting group was removed from the resin using a piperidine/DMF mixture (30/70, *v*/*v*). After the deprotection step, amino acids were sequentially coupled on the support by adding to the reactor a 2-fold molar excess of Fmoc-protected amino acid, 1-hydroxybenzotriazole (HOBt) and benzotriazol-1-yl-oxytris-pyrrolidino-phosphonium (PyBOP), as well as a 4-fold molar excess of diisopropylethylamine (DIPEA) in DMF/NMP 1/1 (*v*/*v*). Each coupling was repeated twice for 40 min under stirring at room temperature. The Fmoc-derived peptides (Fmoc-ILVAGK (Fmoc-K1), Fmoc-LIVAGK (Fmoc-K2) and Fmoc-AIVAGK (Fmoc-K3)) were directly cleaved from the resin using a TFA (trifluoroacetic acid)/TIS (triisopropylsilane)/H_2O (92.5/5/2.5 *v*/*v*/*v*) mixture for 2 h. Instead, Ac-K1, Ac-K2 and Ac-K3 peptides were obtained by removing the Fmoc group from the last amino acid and acetylating twice the N-terminus with a solution of pyridine/acetic anhydride (4/4.7 *v*/*v*) in DMF (each treatment for 10 min). After the acetylation step, these peptides were cleaved from the resin according to the above-described procedure. All the peptides were then precipitated with cold ether and freeze-dried for three times.

Purification was achieved using preparative RP-HPLC with a LC8 Shimadzu HPLC system (Shimadzu Corporation, Kyoto, Japan) equipped with a UV lambda-Max Model 481 detector, using a Phenomenex (Torrance, CA, USA) C_{18} column. H_2O/0.1% TFA (A) and CH_3CN/0.1% TFA (B) were used as elution solvents with the concentration of (B) increasing from 30 to 80% over 30 min at a flow rate of 20 mL/min. The purity of Ac-K1, Ac-K2 and Ac-K3 products was confirmed by analytical RP-HPLC-MS analysis (Figures S1–S3) performed by using a Finnigan Surveyor MSQ single quadrupole electrospray ionization detector (Finnigan/Thermo Electron Corporation, San Jose, CA, USA), with a C_{18}-Phenomenex column eluting with (A) and (B) at a flow rate of 1 mL/min. The analytical method is characterized by a gradient from 5 to 70% of (B) occurring over 10 min. The identity of peptides was assessed by MS spectrometry conducted by the use of a LTQ XL Linear Ion Trap Mass Spectrometer, ESI source (Figures S1–S3).

Ac-K1: t_R = 11.62 min, MS (ESI+): m/z 640.82 calcd. for $C_{30}H_{56}N_8O_7$: $[M+H^+]$ = 641.4 u.m.a.

Ac-K2 t_R = 11.51 min, MS (ESI+): m/z 640.82 calcd. for $C_{30}H_{56}N_8O_7$: $[M+H^+]$ = 641.5 u.m.a.

Ac-K3: t_R = 10.13 min, MS (ESI+): m/z 598.74 calcd. for $C_{27}H_{50}N_8O_7$: $[M+H^+]$ = 599.4 u.m.a.

3.2. Preparation of Peptide Hydrogels Loaded with Gd-Complexes

Peptide-based HGs loaded with different Gd complexes were prepared at the final Gd(III) concentration of 4.28 mmol L^{-1}. To this effect, for $[Gd(BOPTA)]^{2-}$ and $[Gd(DTPA)]^{2-}$-loaded HGs, peptide solutions were prepared at a concentration of 2 wt% by dissolving 6 mg of each lyophilized peptide into 300 µL of bidistilled water; then, 50 µL of an aqueous solution of the Gd complex (at a concentration of 30 mmol L^{-1}) was added to the suspension. The resulting solution was sonicated for 5 min and left to gelatinate at room temperature. Since $[Gd(AAZTA)]^-$ presents only one negative charge on its structure, one less than the other two linear complexes previously mentioned, $[Gd(AAZTA)]^-$-loaded HGs were formulated by a different procedure. In more detail, 6 mg of the lyophilized peptide powder were first dissolved into 300 µL of an aqueous solution of $[Gd(AAZTA)]^-$ at a concentration of 5.0 mmol L^{-1}, and then, to better balance electrostatic forces of the HG inner structure, 50 µL of 0.1 mol L^{-1} phosphate-buffered solution were added. This procedure allowed the gel formation.

3.3. Hydrogel Stability Studies

The determination of the HG degradation profile was performed by an in vitro stability assay, evaluating the percentage weight loss of the matrices. Freshly formed HGs (300 µL) were weighted (W_o) and then incubated at 37 °C with 1.0 mL of Ringer's solution (8.6 mg of NaCl, 0.30 mg of KCl and 0.33 mg of $CaCl_2$) [34]. After 20 days, the Ringer's solution was

removed and HGs were weighted again (W_t). The degradation degree was expressed as the percentage ratio (ΔW) between the HG weight before (W_o) and after (W_t) the treatment using the following formula (1):

$$\Delta W = \left(1 - \frac{Wt}{Wo}\right) * 100 \quad (1)$$

3.4. Scanning Electron Microscopy (SEM)

Morphological analysis of derivative xerogels was carried out by a field emission scanning electron microscope (PhenomXL, Alfatest). A total of 10 µL of peptide HG was drop-casted on an aluminum stub and air-dried. A thin coat of gold and palladium was sputtered at a current of 25 mA for 75 s. The sputter-coated samples were then introduced into the specimen chamber and the images were acquired at an accelerating voltage of 10 kV, spot 3, through the Secondary Electron Detector (SED).

3.5. Fourier Transform Infrared Spectroscopy (FT-IR)

Fourier transform infrared spectra of Gd complex-loaded hydrogels prepared as described above were performed on a Jasco FT/IR 4100 spectrometer (Easton, MD) in an attenuated total reflection (ATR) mode and using a Ge single crystal at a resolution of 4 cm-1as previously reported [24].

3.6. Rheological Studies

Rheological properties of HGs loaded with each Gd-complex were evaluated using a rotational controlled stress rheometer (Malvern Kinexus) using a 15 mm flat-plate geometry (PU20:PL61). Freshly prepared hydrogel samples (400 µL) at the concentration of 2.0 wt% were tested. Each experiment was performed at 25 °C using a humidity chamber and a gap of 1 mm. Preliminary dynamic rheological tests were carried out in order to identify the regime of linear viscoelasticity. The viscous elastic region was determined by the oscillatory frequency (0.1–100 Hz) and the strain sweep (0.01–100%). A time-sweep oscillatory evaluation test (using a constant 0.1% strain and 1 Hz frequency) was then performed for 20 min. Results are reported in Pascal (Pa) as shear storage or elastic modulus (G') and shear loss or viscous modulus (G'').

3.7. Nanogel Formulation

$[Gd(BOPTA)]^{2-}$-loaded nanogel was obtained as previously described according to the top-down method [22]. Briefly, 350 µL of $[Gd(BOPTA)]^{2-}$-loaded Fmoc-K2 gel disk (1.7% wt), prepared into a silicone mold, was added to 1.650 mL of a water suspension of two surfactants, TWEEN® 85 (Polyoxyethylenesorbitan Trioleate) and SPAN® 85 (Sorbitane trioleate) at a w/w ratio of 89/11 ($2.34 \cdot 10^{-5}$ total mol of surfactants). The two surfactants were thus combined to form an HLB (hydrophilic lipophilic balance) value of 10. Successively, the sample was first homogenized at 35,000 min^{-1} for 5 min, and then subjected to tip-sonication for 5 min at 9 W. Purification of the NG from free Gd complexes was achieved by gel filtration on a pre-packed Sephadex G-50 column and the amount of encapsulated complex was quantified by inductively coupled plasma-mass spectrometry (ICP-MS).

3.8. Dynamic Light Scattering (DLS) Measurements

Mean diameters and diffusion coefficients (D) of CA-filled NGs were estimated by DLS using a Zetasizer Nano ZS (Malvern Instruments, Westborough, MA, USA). Analogously, nanogel stability over time was checked measuring the mean diameter into different time points up to seven days. Instrumental settings for the measurements are a backscatter detector at 173° in automatic modality mode, at room temperature and using a disposable sizing cuvette as a cell. DLS measurements in triplicate were carried out on aqueous samples after centrifugation at room temperature at 13,000 rpm for 5 min.

3.9. Circular Dichroism (CD) Studies

Far-UV CD spectra of $[Gd(BOPTA)]^{2-}$ loaded Fmoc-K2 nanogel were collected with a Jasco J-810 spectropolarimeter equipped with a NesLab RTE111 thermal controller unit using a 0.5 mm quartz cell at 25 °C. Other experimental settings were the following: scan speed = 50 nm/min, sensitivity = 50 mdeg, time constant = 16 s, bandwidth = 1 nm, response = 2 s and data pitch = 1 nm. The spectrum was recorded in triplicate from 350 to 190 nm, subtracted from the blank and adjusted for the concentration.

3.10. Relaxometric Characterization

$1/T_1$ ^{1}H nuclear magnetic relaxation dispersion (NMRD) profiles were collected with a fast-field cycling (FFC) Stelar SmarTracer Relaxometer over a continuum of magnetic field strengths from 0.00024 to 0.25 T. The relaxometer operates under computer control with an absolute uncertainty in $1/T_1$ of ±1%. Additional data in the 0.5–3.0 T were obtained with a High Field Relaxometer (Stelar) equipped with the HTS-110 3T Metrology cryogen-free superconducting magnet. The data were obtained by using the standard inversion recovery sequence (20 experiments, 2 scans) with a 90° pulse width of 3.5 μs, and the reproducibility of the data was within ±0.5%. The NMRD profiles were collected at 283, 298 and 310 K.

4. Conclusions

Hydrogels based on cationic peptide sequences (derivatized at their N-terminus with the acetyl or the fluorenyl group) demonstrated the capability of stably encapsulate linear or mesocyclic Gd complexes such as $[Gd(BOPTA)]^{2-}$, $[Gd(DTPA)]^{2-}$, $[Gd(AAZTA)]^{-}$, having one or two residual negative charges. When formed, the physical encapsulation of the complex does not significantly alter the hydrogel morphology, in which the fibrillary network is kept. On the other hand, rheological characterization highlighted how the encapsulation of a cargo within the gel can allow an increase or a decrease of the matrix rigidity as a consequence of the non-covalent interactions (π–π stacking, hydrogen bonding and electrostatic interactions). As expected, the CAs loaded into the macroscopic hydrogel exhibit a relaxivity value higher than the corresponding free Gd complex (up to five-fold). Beyond the typical relaxometric parameters (τ_R, τ_M and q), which affect the relaxivity, the r_1 value seems to be influenced by other key factors such as the mechanical properties of the hydrogel, the interactions between the complex and the peptide matrix and the water accessibility to the complex within the hydrogel. As a whole, the cited parameters must be deeply investigated and optimized to improve the relaxivity performance of the resulting CA. The relaxometric study performed on the injectable nanoparticles, obtained from the hydrogel submicronization, evidenced a reduced mobility of the complex into the peptide matrix and a slow regime of the water exchange process. The higher relaxivity at 20 MHz and 298 K (r_1 = 36.8 mM^{-1} s^{-1}) measured for the nanogel with respect to the corresponding hydrogel can be probably attributed to the different degree of rotational freedom of the complexes within the polymeric matrix.

Supplementary Materials: The following supporting information can be downloaded at: https://www.mdpi.com/article/10.3390/ph15121572/s1, Figures S1–S3: Chemical structures, RP-HPLC chromatograms and ESI mass spectra of peptides. Figure S4: Characterization of $[Gd(DTPA)]^{2-}$ loaded Fmoc-K2 hydrogel. Figure S5: FTIR spectra of hydrogels. Figure S6: SEM micro-photos of Fmoc-K2 and Fmoc-K3 (B) loaded with $[Gd(AAZTA)]^{-}$. Figures S7 and S8: Rheological profiles of time sweep measurements. Figures S9 and S10: ^{1}H NMRD profiles of Fmoc-K3, Ac-K1 and Ac-K2 hydrogels loaded with Gd-complexes.

Author Contributions: The manuscript was written through contributions of all authors. M.B., F.C. and L.T. synthesized the paramagnetic complexes, collected all the relaxometric data and analyzed the results. E.R., C.D., A.A. and G.M. synthetized peptides derivatives, formulated hydrogels and nanogels loaded with Gd-complexes and characterized them. All authors have read and agreed to the published version of the manuscript.

Funding: This research was founded by the Ministero dell'Università e della Ricerca (PRIN 2017A2KEPL project "Rationally designed nanogels embedding paramagnetic ions as MRI probes").

Data Availability Statement: Data is contained within the article and Supplementary Materials.

Acknowledgments: The authors acknowledge the financial support of the Ministero dell'Università e della Ricerca (PRIN 2017A2KEPL project "Rationally designed nanogels embedding paramagnetic ions as MRI probes"). The authors thank Marco Ricci (UPO) for his support to the relaxometric analysis.

Conflicts of Interest: The authors declare no conflict of interest.

References

1. Roth-Konforti, M.E.; Comune, M.; Halperin-Sternfeld, M.; Grigoriants, I.; Shabat, D.; Adler-Abramovich, L. UV Light-Responsive Peptide-Based Supramolecular Hydrogel for Controlled Drug Delivery. *Macromol. Rapid Commun.* **2018**, *39*, e1800588. [CrossRef] [PubMed]
2. Dreiss, C.A. Hydrogel design strategies for drug delivery. *Curr. Opin. Colloid Interface Sci.* **2020**, *48*, 1–17. [CrossRef]
3. Dimatteo, R.; Darling, N.J.; Segura, T. In situ forming injectable hydrogels for drug delivery and wound repair. *Adv. Drug Deliv. Rev.* **2018**, *127*, 167–184. [CrossRef]
4. Gallo, E.; Diaferia, C.; Rosa, E.; Smaldone, G.; Morelli, G.; Accardo, A. Peptide-Based Hydrogels and Nanogels for Delivery of Doxorubicin. *Int. J. Nanomed.* **2021**, *16*, 1617–1630. [CrossRef] [PubMed]
5. Karavasili, C.; Panteris, E.; Vizirianakis, I.S.; Koutsopoulos, S.; Fatouros, D.G. Chemotherapeutic Delivery from a Self-Assembling Peptide Nanofiber Hydrogel for the Management of Glioblastoma. *Pharm. Res.* **2018**, *35*, 166. [CrossRef] [PubMed]
6. Huettner, N.; Dargaville, T.R.; Forget, A. Discovering Cell-Adhesion Peptides in Tissue Engineering: Beyond RGD. *Trends Biotechnol.* **2018**, *36*, 372–383. [CrossRef] [PubMed]
7. Saunders, L.; Ma, P.X. Self-Healing Supramolecular Hydrogels for Tissue Engineering Applications. *Macromol. Biosci.* **2019**, *19*, e1800313. [CrossRef]
8. Aviv, M.; Halperin-Sternfeld, M.; Grigoriants, I.; Buzhansky, L.; Mironi-Harpaz, I.; Seliktar, D.; Einav, S.; Nevo, Z.; Adler-Abramovich, L. Improving the Mechanical Rigidity of Hyaluronic Acid by Integration of a Supramolecular Peptide Matrix. *ACS Appl. Mater. Interfaces* **2018**, *10*, 41883–41891. [CrossRef]
9. Vieira, V.M.P.; Lima, A.C.; De Jong, M.; Smith, D.K. Commercially Relevant Orthogonal Multi-Component Supramolecular Hydrogels for Programmed Cell Growth. *Chem. Eur. J.* **2018**, *24*, 15112–15118. [CrossRef]
10. Chamkouri, H.; Chamkouri, M. A Review of Hydrogels, Their Properties and Applications in Medicine. *Am. J. Biomed. Sci. Res.* **2021**, *11*, 485–493. [CrossRef]
11. Berdichevski, A.; Yameen, H.S.; Dafni, H.; Neeman, M.; Seliktara, D. Using bimodal MRI/fluorescence imaging to identify host angiogenic response to implants. *Proc. Natl. Acad. Sci. USA* **2015**, *112*, 5147–5152. [CrossRef]
12. Fragai, M.; Ravera, E.; Tedoldi, F.; Luchinat, C.; Parigi, G. Relaxivity of Gd-Based MRI Contrast Agents in Crosslinked Hyaluronic Acid as a Model for Tissues. *ChemPhysChem* **2019**, *20*, 2204–2209. [CrossRef] [PubMed]
13. Diaferia, C.; Gianolio, E.; Accardo, A. Peptide-based building blocks as structural elements for supramolecular Gd-containing MRI contrast agents. *J. Pept. Sci.* **2019**, *25*, e3157. [CrossRef] [PubMed]
14. Preslar, A.T.; Parigi, G.; McClendon, M.T.; Sefick, S.S.; Moyer, T.Y.; Haney, C.R.; Waters, E.A.; MacRenaris, K.W.; Luchinat, C.; Stupp, S.I.; et al. Gd(III)-Labeled Peptide Nanofibers for Reporting on Biomaterial Localization in Vivo. *ACS Nano* **2014**, *8*, 7325–7332. [CrossRef] [PubMed]
15. Yin, Y.; Hu, B.; Yuan, X.; Cai, L.; Gao, H.; Yang, Q. Nanogel: A Versatile Nano-Delivery System for Biomedical Applications. *Pharmaceutics* **2020**, *12*, 290. [CrossRef] [PubMed]
16. Glangchai, L.C.; Caldorera-Moore, M.; Shi, L.; Roy, K. Nanoimprint lithography based fabrication of shape-specific, enzymatically-triggered smart nanoparticles. *J. Control. Release* **2008**, *125*, 263–272. [CrossRef]
17. Gheran, C.V.; Rigaux, G.; Callewaert, M.; Berquand, A.; Molinari, M.; Chuburu, F.; Voicu, S.N.; Dinischiotu, A. Biocompatibility of Gd-loaded chitosan-hyaluronic acid nanogels as contrast agents for magnetic resonance cancer imaging. *Nanomaterials* **2018**, *8*, 201. [CrossRef]
18. Carniato, F.; Tei, L.; Botta, M.; Ravera, E.; Fragai, M.; Parigi, G.; Luchinat, C. ^{1}H NMR Relaxometric Study of Chitosan-Based Nanogels Containing Mono- and Bis-Hydrated Gd(III) Chelates: Clues for MRI Probes of Improved Sensitivity. *ACS Appl. Bio Mat.* **2020**, *3*, 9065–9072. [CrossRef]
19. Carniato, F.; Ricci, M.; Tei, L.; Garello, F.; Terreno, E.; Ravera, E.; Parigi, G.; Luchinat, C.; Botta, M. High Relaxivity with No Coordinated Waters: A Seemingly Paradoxical Behavior of $[Gd(DOTP)]^{5-}$ Embedded in Nanogels. *Inorg. Chem.* **2022**, *61*, 5380–5387. [CrossRef]
20. Ischakov, R.; Adler-Abramovich, L.; Buzhansky, L.; Shekhter, T.; Gazit, E. Peptide-based hydrogel nanoparticles as effective drug delivery agents. *Bioorg. Med. Chem.* **2013**, *21*, 3517–3522. [CrossRef]
21. Panda, J.J.; Kaul, A.; Kumar, S.; Alam, S.; Mishra, A.K.; Kundu, G.C.; Chauhan, V.S. Modified dipeptide-based nanoparticles: Vehicles for targeted tumor drug delivery. *Nanomedicine* **2013**, *8*, 1927–1942. [CrossRef] [PubMed]

22. Rosa, E.; Diaferia, C.; Gallo, E.; Morelli, G.; Accardo, A. Stable Formulations of Peptide-Based Nanogels. *Molecules* **2020**, *25*, 3455. [CrossRef] [PubMed]
23. Tesauro, D.; Accardo, A.; Diaferia, C.; Milano, V.; Guillon, J.; Ronga, L.; Rossi, F. Peptide-Based Drug-Delivery Systems in Biotechnological Applications: Recent Advances and Perspectives. *Molecules* **2019**, *24*, 351. [CrossRef] [PubMed]
24. Diaferia, C.; Rosa, E.; Gallo, E.; Smaldone, G.; Stornaiuolo, M.; Morelli, G.; Accardo, A. Supporting Hydrogels Based on Fmoc-Derivatized Cationic Hexapeptides for Potential Biomedical Applications. *Biomedicines* **2021**, *9*, 678. [CrossRef]
25. Loo, Y.; Lakshmanan, A.; Ni, M.; Toh, L.L.; Wang, S.; Hauser, C.A.E. Peptide Bioink: Self-Assembling Nanofibrous Scaffolds for Three-Dimensional Organotypic Cultures. *Nano Lett.* **2015**, *15*, 6919–6925. [CrossRef]
26. Lalli, D.; Carniato, F.; Tei, L.; Platas-Iglesias, C.; Botta, M. Surprising Complexity of the $[Gd(AAZTA)(H_2O)_2]^-$ Chelate Revealed by NMR in the Frequency and Time Domains. *Inorg. Chem.* **2021**, *61*, 496–506. [CrossRef]
27. Aime, S.; Calabi, L.; Cavallotti, C.; Gianolio, E.; Giovenzana, G.B.; Losi, P.; Maiocchi, A.; Palmisano, G.; Sisti, M. $[Gd\text{-}AAZTA]^-$: A New Structural Entry for an Improved Generation of MRI Contrast Agents. *Inorg. Chem.* **2004**, *43*, 7588–7590. [CrossRef]
28. Uggeri, F.; Aime, S.; Anelli, P.L.; Botta, M.; Brocchetta, M.; de Haen, C.; Ermondi, G.; Grandi, M.; Paoli, P. Novel Contrast Agents for Magnetic Resonance Imaging. Synthesis and Characterization of the Ligand BOPTA and its Ln(III) Complexes (Ln = Gd, La, Lu). X-ray Structure of Disodium (TPS-9-145337286-C-S)-[4-Carboxy-5,8,ll-tris(carboxymethyI)-l-phenyl-2-oxa5,8,ll-triazatridecan-13-oato(5-)]gadolinate(2-) in a Mixture with its Enantiomer. *Inorg. Chem.* **1995**, *34*, 633–642.
29. Xiao, Y.D.; Paudel, R.; Liu, J.; Ma, C.; Zhang, Z.S.; Zhou, S.K. MRI contrast agents: Classification and application (Review). *Int. J. Mol. Med.* **2016**, *38*, 1319–1326. [CrossRef]
30. Aime, S.; Botta, M.; Terreno, E. Gd(III)-based contrast agents for MRI. *Adv. Inorg. Chem.* **2005**, *57*, 173–237.
31. Helm, L.; Morrow, J.R.; Bond, C.J.; Carniato, F.; Botta, M.; Braun, M.; Baranyai, Z.; Pujales-Paradela, R.; Regueiro-Figueroa, M.; Esteban-Gómez, D.; et al. *Contrast Agents for MRI: Experimental Methods*; Royal Society of Chemistry: London, UK, 2018; pp. 121–242.
32. Caravan, P.; Ellison, J.J.; McMurry, T.J.; Lauffer, R.B. Gadolinium(III) Chelates as MRI Contrast Agents: Structure, Dynamics, and Applications. *Chem. Rev.* **1999**, *99*, 2293–2352. [CrossRef] [PubMed]
33. Iyer, A.; Roeters, S.J.; Kogan, V.; Woutersen, S.; Claessens, M.M.A.E.; Subramaniam, V. C-Terminal Truncated α-Synuclein Fibrils Contain Strongly Twisted β-Sheets. *J. Am. Chem. Soc.* **2017**, *139*, 15392–15400. [CrossRef] [PubMed]
34. Chronopoulou, L.; Margheritelli, S.; Toumia, Y.; Paradossi, G.; Bordi, F.; Sennato, S.; Palocci, C. Biosynthesis and Characterization of Cross-Linked Fmoc Peptide-Based Hydrogels for Drug Delivery Applications. *Gels* **2015**, *1*, 179–193. [CrossRef] [PubMed]

gels

MDPI

Article

Incorporation of PEG Diacrylates (PEGDA) Generates Hybrid Fmoc-FF Hydrogel Matrices

Elisabetta Rosa [1,†], Enrico Gallo [2,†], Teresa Sibillano [3], Cinzia Giannini [3], Serena Rizzuti [4], Eliana Gianolio [4], Pasqualina Liana Scognamiglio [5], Giancarlo Morelli [1], Antonella Accardo [1] and Carlo Diaferia [1,*]

[1] Department of Pharmacy, Research Centre on Bioactive Peptides (CIRPeB), University of Naples "Federico II", Via Montesano 49, 80131 Naples, Italy
[2] IRCCS Synlab SDN, Via E. Gianturco 113, 80143 Naples, Italy
[3] Institute of Crystallography (IC), CNR, Via Amendola 122, 70126 Bari, Italy
[4] Department of Molecular Biotechnologies and Health Science, University of Turin, Via Nizza 52, 10125 Turin, Italy
[5] Department of Sciences, University of Basilicata, Via dell'Ateneo Lucano 10, 85100 Potenza, Italy
* Correspondence: carlo.diaferia@unina.it; Tel.: +39-0812-534-526
† These authors contribute equally to this work.

Abstract: Generated by a hierarchical and multiscale self-assembling phenomenon, peptide-based hydrogels (HGs) are soft materials useful for a variety of applications. Short and ultra-short peptides are intriguing building blocks for hydrogel fabrication. These matrices can also be obtained by mixing low-molecular-weight peptides with other chemical entities (e.g., polymers, other peptides). The combination of two or more constituents opens the door to the development of hybrid systems with tunable mechanical properties and unexpected biofunctionalities or morphologies. For this scope, the formulation, the multiscale analysis, and the supramolecular characterization of novel hybrid peptide-polymer hydrogels are herein described. The proposed matrices contain the Fmoc-FF (N^{α}-fluorenylmethyloxycarbonyl diphenylalanine) hydrogelator at a concentration of 0.5 wt% (5.0 mg/mL) and a diacrylate α-/ω-substituted polyethylene-glycol derivative (PEGDA). Two PEGDA derivatives, PEGDA 1 and PEGDA2 (mean molecular weights of 575 and 250 Da, respectively), are mixed with Fmoc-FF at different ratios (Fmoc-FF/PEGDA at 1/1, 1/2, 1/5, 1/10 mol/mol). All the multicomponent hybrid peptide-polymer hydrogels are scrutinized with a large panel of analytical techniques (including proton relaxometry, FTIR, WAXS, rheometry, and scanning electronic microscopy). The matrices were found to be able to generate mechanical responses in the 2–8 kPa range, producing a panel of tunable materials with the same chemical composition. The release of a model drug (Naphthol Yellow S) is reported too. The tunable features, the different topologies, and the versatility of the proposed materials open the door to the development of tools for different applicative areas, including diagnostics, liquid biopsies and responsive materials. The incorporation of a diacrylate function also suggests the possible development of interpenetrating networks upon cross-linking reactions. All the collected data allow a mutual comparison between the different matrices, thus confirming the significance of the hybrid peptide/polymer-based methodology as a strategy for the design of innovative materials.

Keywords: Fmoc-FF; PEGDA; peptide hydrogels; supramolecular assembly; peptide materials; multicomponent hydrogels; biohybrid materials

Citation: Rosa, E.; Gallo, E.; Sibillano, T.; Giannini, C.; Rizzuti, S.; Gianolio, E.; Scognamiglio, P.L.; Morelli, G.; Accardo, A.; Diaferia, C. Incorporation of PEG Diacrylates (PEGDA) Generates Hybrid Fmoc-FF Hydrogel Matrices. *Gels* **2022**, *8*, 831. https://doi.org/10.3390/gels8120831

Academic Editor: Jun Huang

Received: 14 November 2022
Accepted: 13 December 2022
Published: 16 December 2022

1. Introduction

Hydrogels (HGs) are hydrophilic materials structurally characterized by a three-dimensional (3D) network originated by the macroscopic organization of polymer chains or of supramolecular elements [1–3]. The ability of these matrices to retain a large amount of aqueous fluid (~95/99%) confers on them a non-Newtonian flow behavior associated with a self-supporting tendency. The physicochemical properties of hydrogels (e.g., durability,

reproducibility, and bio-restorability) and their resemblance to the human body tissue microenvironment were found to be determinant features for their application in both the biotechnological and industrial fields, including drug delivery [4], optoelectronics [5], water purification [6], and tissue engineering [7].

Peptide-based low-molecular-weight gelators (LMWGs) are a typical class of molecular entities that can be used for the generation of self-supporting three-dimensional gel networks [8–10]. The interest in this class of LMWGs is related to the advantages they offer with respect to natural or synthetic polymers. For instance, peptides can easily be synthetized and modified; moreover, they exhibit good biocompatibility profiles and moderately inexpensive manufacturing procedures. Additionally, in comparison to covalently-based polymeric hydrogels, the peptide gelation phenomenon is a multiscale process, which allows one to avoid crosslinking agents. Specifically, peptide-based LMWGs are designed as self-assembling sequences able to produce fibrillary aggregates [11–13]. These latter, above a critical gelation concentration (CGC), undergo a mutual physical cross-link. The final non-covalent entanglement leads to further association in a space-spanning network, giving rise to the macroscopic self-supporting gels.

Fmoc-FF (N^{α}-fluorenylmethoxycarbonyl-diphenylalanine, Figure 1A) represents a typical case of peptide-based LMWGs [14–19]. HGs of Fmoc-FF can be obtained under physiological conditions (pH, temperature, and ionic strength) without the use of cross-linking agents by using different methodologies [20]. Since its identification in 2006 [14,15] as a suitable building block for the preparation of hydrogels, Fmoc-FF has been deeply studied for many biomedical applications [21–24]. The addition of other components (like natural or synthetic polymers [25], peptides [26,27], polysaccharides [28], or dyes [29]) to Fmoc-FF has been found to improve and tune the physiochemical features of the final material.

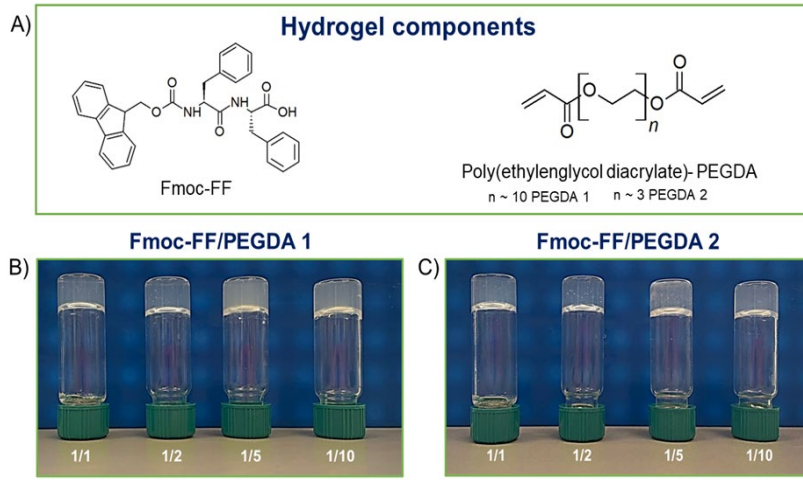

Figure 1. (**A**) Chemical structures of hydrogel components. Inverted tube test for mixed hydrogel formulations (0.5 wt% in Fmoc-FF) with PEGDA1 (**B**) and PEGDA2 (**C**).

At the state of the art, co-assembly of two different chemical entities can sponsor the formation of novel functional materials with improved mechanical or biocompatibility profiles [30–32]. By way of examples, Fmoc-FF/pentafluorinate Fmoc-F [33] and Fmoc-FF/Phe-Tyr-containing peptides [34] systems have been recently formulated and proposed as innovative all-peptidic scaffolds for both tissue regeneration and drug delivery applications. The incorporation of different kinds of polymers was also estimated by studying hybrid Fmoc-FF-based matrices containing chitosan, polyethylene-glycol (PEG) [35], or polyaniline (PAni) [36]. Specifically, PEG and its α- and/or ω-substituted derivatives are particularly interesting due to their biocompatibility and pharmaceutical and biomedical advantages, including the increase in solubility and the in vivo protection of bioactive macromolecules, antibodies, and oligonucleotides [37–40].

After FDA approval, PEGylation has indeed become the method of choice for the delivery of biopharmaceuticals. For this, here is described the formulation and the supramolecular architecture of multicomponent hydrogels containing some derivatives of polyethylene glycol, the PEG diacrylates (PEGDA, Figure 1A), into the gelled Fmoc-FF matrix to expand the class of hydrogels as biotechnological tools. The advantage of using PEGDA derivatives is the presence in their formula of a diacrylate moiety that, according to opportune synthetic protocols, can undergo a controlled polymerization reaction.

For this study, two PEGDAs with different mean molecular weights (PEGDA 575 and PEGDA 250, named PEGDA1 and PEGDA2, respectively) were selected. Additionally, different molar ratios between Fmoc-FF and PEGDA derivatives (1/1, 1/2, 1/5, and 1/10 mol/mol) were studied with the aim of analyzing the effect of both molecular weight and relative polymer abundance on the organization and on the properties of the final hybrid matrix. The gelation process was prompted using the DMSO/H_2O solvent switch methodology, incorporating PEGDA in the hydrogels during the organic solvent rehydration step. The water behavior in all the matrices was scrutinized, reporting the swelling ratio, the Langmuir frequency, the dehydration curves, and the relaxometric properties. Secondary structuration analysis was conducted recurring to fluorescence, circular dichroism (CD), FTIR spectroscopies, and wide-angle X-ray scattering (WAXS). Moreover, the mechanical properties of hybrid matrices were studied in rheological experiments, and their capability to encapsulate and release a drug was also preliminary evaluated using a fluorescent dye (Naphthol Yellow S) as a model.

2. Results and Discussion

2.1. Fmoc-FF/PEGDA Matrices Formulation

The Fmoc-N^{α}-protected variant of diphenylalanine (FF), Fmoc-FF, represents one of the most studied ultra-short peptide sequences able to efficiently self-organize into β-sheet nanostructured fibrous hydrogels in physiological conditions [14,15]. Due to their easy preparation and long shelf-stability, Fmoc-FF matrices have been proposed as tools for the development of hybrid systems too, thus allowing enlargement of the available biomaterials for nanotechnology applications.

Fmoc-FF HGs can be produced using different approaches: solvent switch, pH switch, and the enzymatic method [20]. Due to the hydrophilic nature of the PEGDA components, the formulation of hybrid Fmoc-FF/PEGDA HGs at 0.5 wt% (5.0 mg/mL) was achieved using the solvent switch procedure. The Fmoc-FF concentration chosen for the present study was 0.5 wt% because it is above the critical gelation concentration (CGC) and is one of the most studied concentrations in literature [14,15,34]. According to the solvent-switch method, Fmoc-FF was primarily dissolved in DMSO as the organic phase at a concentration of 100 mg/mL. The resulting solution was then diluted in water (an antisolvent) to the desired final gel concentration. The rehydration triggers gel formation, and a vertexing step promotes efficient mixing of the solvent/antisolvent phases, ensuring sample homogeneity. For mixed Fmoc-FF/PEGDA HGs, the solvent switch procedure was modified to use PEGDA solution instead of water to trigger the hydrogel formation during the DMSO hydration phase. This methodology allows the Fmoc-FF matrix enrichment of polymer with different molar ratios with respect to the peptide component ($9.53 \cdot 10^{-6}$ mol) by preparing different PEGDA solutions. The Fmoc-FF/PEGDA ratios selected for the study are 1/1, 1/2, 1/5, and 1/10 mol/mol. In all the tested ratios, we can produce self-supporting materials, as testified by the inverted tube test in Figure 1B,C.

The maximum hydrogel ratio formation for PEGDA 1 was found for a 1/50 ratio (see Figure S1). On the contrary, no hydrogel formation was observed for PEGDA2 above a ratio of 1/10, indicating the impossibility of forming stable and reproducible PEGDA2 solutions. Fmoc-FF represents a key structural element for the formation of the proposed mixed matrices. Indeed, at the tested concentrations, both PEGDA derivatives are not able to gel alone. Fmoc-FF dipeptide, driving the initial aggregation process, probably allows the formation of PEGDA hydrogels at a concentration value lower than their CGC. As

previously reported for pure or multicomponent HGs based on Fmoc-FF, the formation of the self-supporting matrix is associated with an opaque-to-limpid macroscopic transition. This change in optical transparency is attributed to the progressive fibril growth from spherulitic architectures acting as nucleation points [41]. The same macroscopic behavior was observed for all the tested Fmoc-FF/PEGDA samples. Moreover, no significant variations were detected in the gelation kinetics of multicomponent hydrogels of both PEGDA derivatives (at 1/1, 1/2 and 1/5 ratio) with respect to pure Fmoc-FF (~3 min). A slight increase in the gelation time (~1 min plus) is only detected for 1/10 PEGDAs ratio. As clearly shown in Figure 1, samples differ in turbidity. Whilst relatively translucent matrices are formed for 1/1 and 1/2 ratios, both PEGDA-containing HGs at 1/5 and 1/10 ratios are opaque. The macroscopic evidence of turbidity is quantified by UV-Vis measurements, looking at the absorbance values at 600 nm. At this wavelength, the light absorption from peptide chromophores is absent, and absorbance values can be ascribed to matrix turbidity, arising from scattering phenomena [42]. The absorbance values for Fmoc-FF/PEGDA 1 increase from 0.183 to 0.270 a.u. by passing from the ratio of 1/1 to 1/10 one. A similar behavior was also observed for PEGDA 2 containing HGs, but with a slightly lower increase in turbidity (from 0.166 to 0.224 a.u. from 1/1 and 1/10 ratios). The aging of HGs was evaluated over 6 months, keeping the material inverted. All the samples showed very good shelf stability without any macroscopic change in terms of homogeneity, visual appearance, and self-supporting behavior. Only a modest syneresis event (weight lost ~5%) was found for 1/10 ratio samples.

2.2. Water Behavior in Multicomponent HGs

Water represents the main component in gelled matrices, and it can be classified as strongly bound, weekly bound, and free (non-bound) water [43]. The analysis of the water behavior can provide valuable information about the supramolecular organization, permeation properties, pore architecture, and solute diffusion. The water behavior in the proposed multicomponent matrices was characterized using several macroscopic assays (swelling ratio, stability test longitudinal relaxation rate (R1 = 1/T1) as a function of the applied magnetic field.

The swelling ratio q at room temperature of each mixed HG was established as the percentage difference between the weight before and after overnight gel incubation in water. Values of q, reported in the Table 1, increase with the amount of PEGDA in the hybrid materials and with respect to pure Fmoc-FF (q = 29.7%). Moreover, q values for PEGDA1 were found to be higher than those of the corresponding PEGDA 2 containing matrices. This difference can probably be attributed to the more hydrophilic nature of PEGDA1 polymer respect to PEGDA2. Indeed, the higher number of ethoxy repetitions in PEGDA1 (around 3-fold higher) with respect to PEGDA2 could cause an increase in the number of H-bonding acceptor groups, thus expanding the interactions with water and consequently the swelling properties.

Table 1. Results of swelling and stability tests. The swelling ratio (q) and the weight loss ratio (ΔW) was calculated as a percentage according to Equations (1) and (2), respectively.

	Swelling Ratio (q)				**Weight Loss Ratio (ΔW)**			
Sample	1/1	1/2	1/5	1/10	1/1	1/2	1/5	1/10
Fmoc-FF/PEGDA 1	31.5	32.9	35.4	39.7	5.53	1.23	1.31	1.15
Fmoc-FF/PEGDA 2	30.1	31.2	33.1	36.1	4.47	3.01	2.85	2.09

Analogously, the stability ratios (ΔW) were found depending on the PEGDA incorporation amount (see Table 1). The matrices' stability was tested using a Ringer's solution, which mimics the physiological ionic strength. As clearly shown by ΔW values, all the Fmoc-FF/PEGDA hydrogels are more stable than the pure Fmoc-FF matrix, which has a ΔW = 27.4% in the same experimental conditions.

The stability of hybrid hydrogels seems to improve with the increasing percentage of polymer in the gel, thus indicating that the presence of PEG diacrylate in the formulation preserves the materials from degradation. This major stability could also be attributed to the higher rigidity of mixed hydrogels with respect to the pure Fmoc-FF one (vide intra, rheological section). PEGDA incorporation additionally confers on matrices a functional property of water retention, which is evaluated by studying the dehydration phenomenon of both PEGDA at 1/1 and 1/10 mol/mol. As clearly visible in Figure S2, PEGDA-containing HGs were found to be able to hold back elevated percentages (>92%) of entrapped water with respect to pure Fmoc-FF matrices (<9%). This feature was found to be substantially independent from both PEGDA molecular weight and amount. The unexpected behavior related to water retention can be imputed to the hydrophilic nature of PEGDA, which is able to avoid the evaporation of water by keeping it strongly anchored via non-covalent interactions.

Finally, water dynamics in the hydrogel matrix have been investigated using a relaxometric approach. The analysis and quantification of the dynamic parameters related to water motion have often been investigated through the measurement of the applied magnetic field dependence of the relaxation rate (nuclear magnetic resonance dispersion (NMRD) profiles) of different water-containing materials [44–49]. Fitting of the experimental data in the proton frequency range between 0.01 MHz and 10 MHz allows one to distinguish between slower and faster motions, respectively, associated with water molecules constrained in the hydrogel scaffold or more freely diffusing water.

In Figure 2A,B, the NMRD profiles acquired for Fmoc-FF/PEGDA HGs are reported. In the case of PEGDA1 containing HGs, two additional samples with higher polymer contents (1/20 and 1/30) were investigated. The data were fitted as previously reported, and the parameters extracted from fitting are collected in Table 2. In general, the here obtained τ1 (faster motion) and τ2 (slower motion) correlation times are rather similar to those previously observed for analogous Fmoc-FF-containing hybrid HGs [27]. Likewise, the percentage of slow motion (% slow) and the average correlation time ($\tau_C{}^{av}$), which can be calculated as previously achieved [27], are close to the previous values. For both PEGDA1 and PEGDA2, the values of % slow and $\tau_C{}^{av}$ (Table 2 and Figure 2C) increase with the amount of PEGDA in the hybrid materials but, quite surprisingly, are considerably lower with respect to pure Fmoc-FF. Moreover, the parameters associated with water mobility were found to be independent from PEGDA molecular weight.

Table 2. Parameters obtained through fitting of the ^{1}H-NMRD profiles.

Sample	A_0 (s^{-1})	β (s^{-1})	A_1	τ_1 (s)	A_2	τ_2 (s)	% slow	$\tau_C{}^{av}$ (s)
Fmoc-FF	0.41	0.30	3.2×10^6	1.3×10^{-7}	2.6×10^5	3.1×10^{-6}	7.6	3.5×10^{-7}
Fmoc-FF/PEGDA1 *1/1*	0.38	0.35	2.3×10^6	7.8×10^{-8}	6.5×10^4	4.3×10^{-6}	2.8	1.9×10^{-7}
Fmoc-FF/PEGDA1 *1/5*	0.39	0.41	2.3×10^6	5.2×10^{-8}	7.5×10^4	2.4×10^{-6}	3.2	1.3×10^{-7}
Fmoc-FF/PEGDA1 *1/10*	0.51	0.35	1.9×10^6	9.3×10^{-8}	5.5×10^6	3.0×10^{-6}	2.8	1.7×10^{-7}
Fmoc-FF/PEGDA1 *1/20*	0.59	0.22	3.4×10^6	1.8×10^{-7}	1.6×10^5	3.2×10^{-6}	4.5	3.2×10^{-7}
Fmoc-FF/PEGDA1 *1/30*	0.58	0.33	1.7×10^6	1.6×10^{-7}	1.0×10^5	3.6×10^{-6}	5.6	3.5×10^{-7}
Fmoc-FF/PEGDA2 *1/1*	0.37	0.49	1.6×10^6	4.5×10^{-8}	4.7×10^4	1.6×10^{-6}	2.8	9.0×10^{-8}
Fmoc-FF/PEGDA2 *1/5*	0.36	0.80	1.1×10^6	4.5×10^{-8}	4.3×10^4	1.6×10^{-6}	3.8	1.0×10^{-7}
Fmoc-FF/PEGDA2 *1/10*	0.38	0.40	1.1×10^6	2.0×10^{-7}	4.2×10^4	3.9×10^{-6}	3.7	3.3×10^{-7}

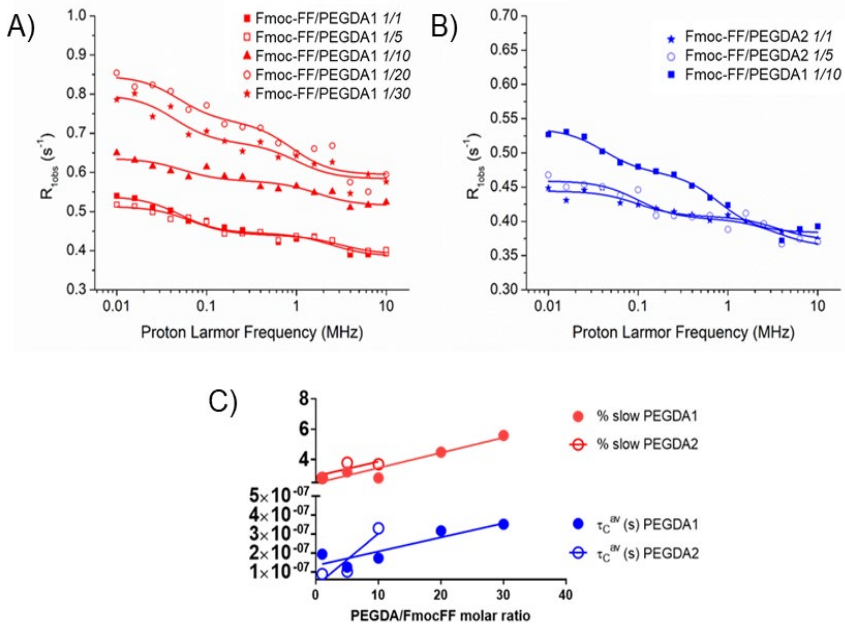

Figure 2. ^{1}H NMRD profiles measured on HGs with PEGDA1 (**A**) and PEGDA2 (**B**) at 298 K. Continuous lines represent the best fits obtained with a sum of Lorentzian functions. (**C**) Variation of the average water correlation time (τ_c^{av}) and the percentage of slowing moving water (% slow) as a function of PEGDA molar content.

2.3. Secondary Structure Characterization

It is well known from the literature that the Fmoc-FF peptide self-assembles into hydrogels with a β-sheet amyloid-like organization of the peptide moiety [14,15]. This structural motif is commonly investigated in peptide nanostructures using a combination of spectroscopic techniques (e.g., circular dichroism (CD) and Fourier transform infrared spectroscopy (FTIR)) and qualitative staining assays with Thioflavin T (ThT) and Congo Red (CR). The effect of PEGDA incorporation in the structural arrangement of the Fmoc-FF network was evaluated by comparing pure and hybrid peptide hydrogels.

CD spectra (Figure 3A) were acquired for Fmoc-FF/PEGDA hydrogels at 1/1 and 1/10 ratios between 350 and 190 nm and reported as optical density (mdeg/O.D.). The CD signature, deriving from the supramolecular packing of monomers, is related to the configurational alignment of the formed fibers, leading to higher order architectures. Independently from PEGDA molecular weight or their relative amounts, all the spectra show a similar signature, thus suggesting no significant differences in the gel organization and topography. Fmoc-FF/PEGDA systems present some differences in the dichroic signature with respect to the pure Fmoc-FF hydrogel alone [34], which exhibits a minimum at 220 nm and a broad maximum around 259 nm.

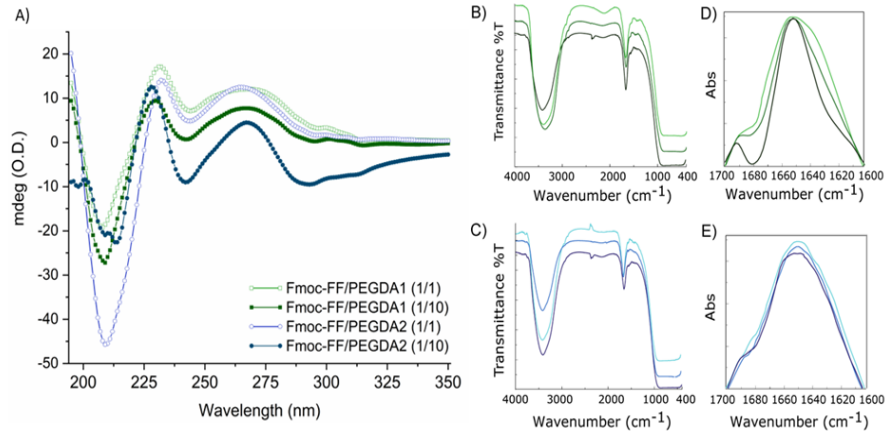

Figure 3. (**A**) CD spectra (in the 190 and 350 nm range) of Fmoc-FF/PEGDA1 (1/1 and 1/10) and Fmoc-FF/PEGDA2 (1/1 and 1/10). FTIR characterization. (**B**) FTIR spectra of Fmoc-FF/PEGDA1 matrices (1/1, light green; 1/5, green grass; and 1/10, dark green). (**C**) FTIR spectra of Fmoc-FF/PEGDA2 matrices (1/1, light blue; 1/5, blue; and 1/10, dark blue). Amide I deconvolution profiles of PEGDA1 (**D**) and PEGDA2 matrices (**E**).

Indeed, the spectra of all the PEGDA-doped hydrogels showed four main dichroic signals: two negative peaks (around 209 and 240 nm) and two positive ones (at 231 and at 267 nm). These differences can be attributed to the presence of the PEG moiety since they were observed for other hybrid hydrogels containing Fmoc-FF in combination with PEG-peptide derivatives [34]. The signal located at 231 nm is generally indicative of β-sheet structuration of the peptide building block in supramolecular architectures [50–52]. This signal undergoes an hypsochromic effect (228 nm) in 1/10 matrices, imputable to the decreasing of the materials' ability to absorb light because of the increased turbidity. Instead, the positive and broad band at 267 nm, detectable for all the mixed PEGDA hydrogels, can be attributed to the fluorenyl group on the peptide. The significant bathochromic effect at the typical wavelength (259 nm) can be explained considering the difference in the dielectric constant induced by the incorporation of PEGDA into the hybrid peptide-polymer matrices. The comparison with the CD profile of nude Fmoc-FF suggests a substantial maintenance of gel matrix topology without alteration of the β-sheet organization, with an antiparallel left-twisted structuration [53].

An additional investigation about the secondary structuration in the final material was carried out by FTIR spectroscopy. The IR spectra of peptides and proteins are described as containing nine different amide bands (I to VII, A and B). These IR signals are generated from both the vibrational contributions of the backbone and of amino acid side chains [54]. The IR spectra for all the matrices at 0.5 wt% in water are collected in Figure 3B,C. All the spectra share a common tendency, dominated by only two different bands: (i) an intense signal in the amide A region (~3300 cm^{-1}), occurring as a consequence of water exposure of the aggregate with asymmetric and symmetric O-H and N-H stretching and indicative of intermolecular amide-amide bond interactions; (ii) a band in the amide I region (centered at 1636 cm^{-1}) related to the presence of β-rich assemblies. This spectral region (ranging between 1700 and 1600 cm^{-1} associated with the C=O stretching motus) is of relevance for the secondary structuration analysis [55]. According to this consideration, an absorbance deconvolution was acquired (Figure 3D,E). For all the samples, the spectral deconvolution is dominated by a main peak around 1650 cm^{-1}, conducive to C=O stretching and suggesting the presence of β-sheets secondary structures. Moreover, the additional band at ~1690 cm^{-1} is typically observed for the antiparallel orientation of the β-strands in assemblies [56–58].

The common IR signature for all the matrices suggests that the fundamental β-secondary structure organization is not significantly altered by both the PEGDA length and the percentage of polymer incorporation, as supported by CD measurements. The

formation of β-sheets rich matrices was further confirmed on xerogels by the thioflavin T (ThT) assay. Thioflavin T (ThT, alternatively named methylene yellow or Basic Yellow 1) is a benzothiazole fluorescent dye regularly used for the quantification of amyloid and amyloid-like fibrils. Binding amyloid-like structures, ThT changes its fluorescent behavior, with a strong fluorescence signal located approximately at 482 nm (λ_{exc} = 450 nm) [59,60]. The fluorescence activation of ThT is imputable to the rotational immobilization of the central C–C bond connecting the benzothiazole and aniline rings. As visible in Figure 4, the ThT dye can stain the PEGDA-containing HGs, giving rise to a fluorescent emission in the GFP spectral window. This evidence highlights the presence of an amyloid-like structure as a supramolecular element of the hydrogels.

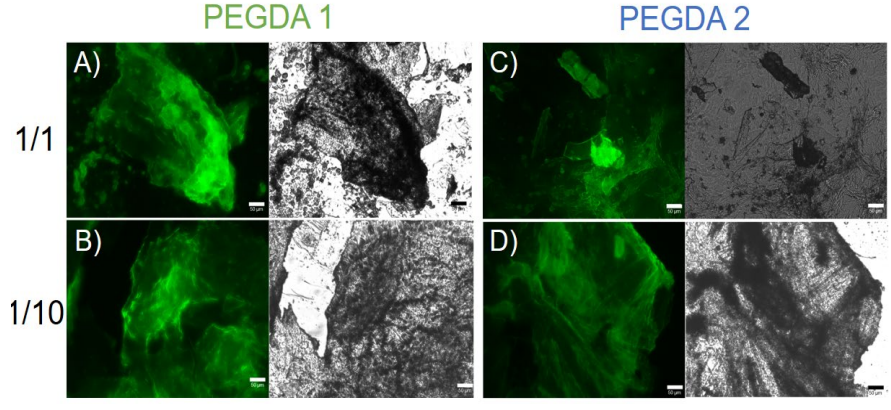

Figure 4. For each panel, fluorescence images (left) and optical images (right) of mixed xerogels (**A**) Fmoc-FF/PEGDA1 1/1, (**B**) Fmoc-FF/PEGDA1 1/10, (**C**) Fmoc-FF/PEGDA2 1/1 and (**D**) Fmoc-FF/PEGDA2 1/10 stained with 50 μmol/L ThT solution. Samples are imaged in the spectral regions of the GFP (Green Fluorescent Protein, λ_{exc} = 488 nm, λ_{em} = 507 nm) and in the bright field. Scale bar = 50 μm.

The presence of an amyloid-like structure was further confirmed using the Congo Red (sodium salt of benzidinediazo-bis-1-naphthylamine-4-sulfonic acid) assay, both on samples in solution and in the solid state (Figure 5).

The UV-Vis spectra of mixed hydrogels prepared in a CR solution at the final dye concentration of 10 μM are reported in Figure 5A,B. The spectrum of the dye alone in water is also reported for comparison. From the inspection of the figure, a red shift of the absorbance peak can be observed from 480 to 540 nm. This bathochromic shift of the maximum is typically associated with the detection of β-sheet secondary structures in the sample. Analogously, amyloid-like structures are also confirmed by optical microscopy images, under bright field and cross-polarized light, of mixed xerogels stained with CR (Figure 5C). Images showed that, independently from the composition and the PEGDA molecular weight, all the xerogels exhibit birefringence.

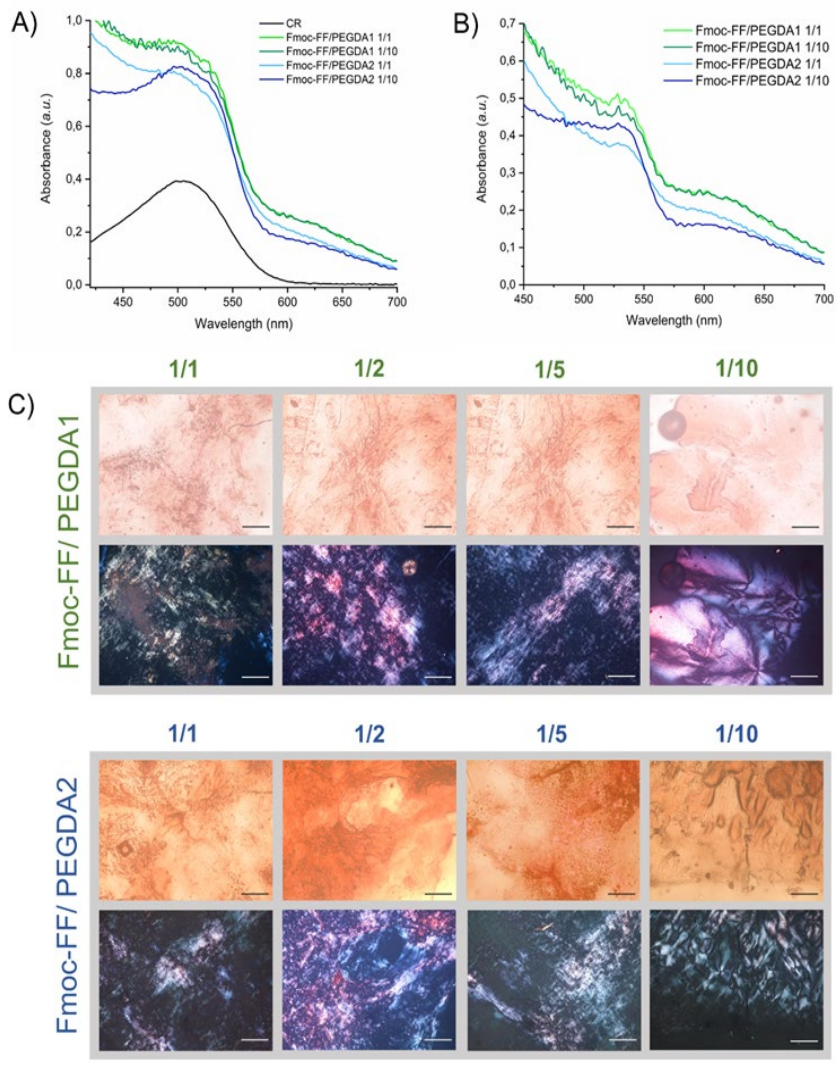

Figure 5. CR assay in solution and in the solid state. UV-Vis spectra of CR alone and co-incubated with Fmoc-FF/PEGDA1 (**A**) or with Fmoc-FF/PEGDA2 (**B**) at the different molar ratios. (**C**) Staining of Congo Red xerogels in both bright field (first row) and under cross-polarized light (second row). Scale bar =100 μm.

2.4. Solid State Characterization

To collect information about the morphology of mixed xerogels, scanning electron microscopy (SEM) images were acquired. A set of representative microphotos for samples containing increasing amounts of diacrylate are shown in Figure 6. A substantial difference in the surface topography of systems can be detected with respect to the sponge-like structure (generally reported for PEGDA-based matrices) [61,62] and the entangled fiber network (noticed for HGs of Fmoc-FF) [14,15,34]. This primary evidence is indicative of a modification of the aggregation properties of both chemical building blocks, reinforcing the evidence that co-aggregation enlarges the plethora of supramolecular behaviors of molecules. More specifically, the PEGDA1 and PEGDA2 matrices mutually differ.

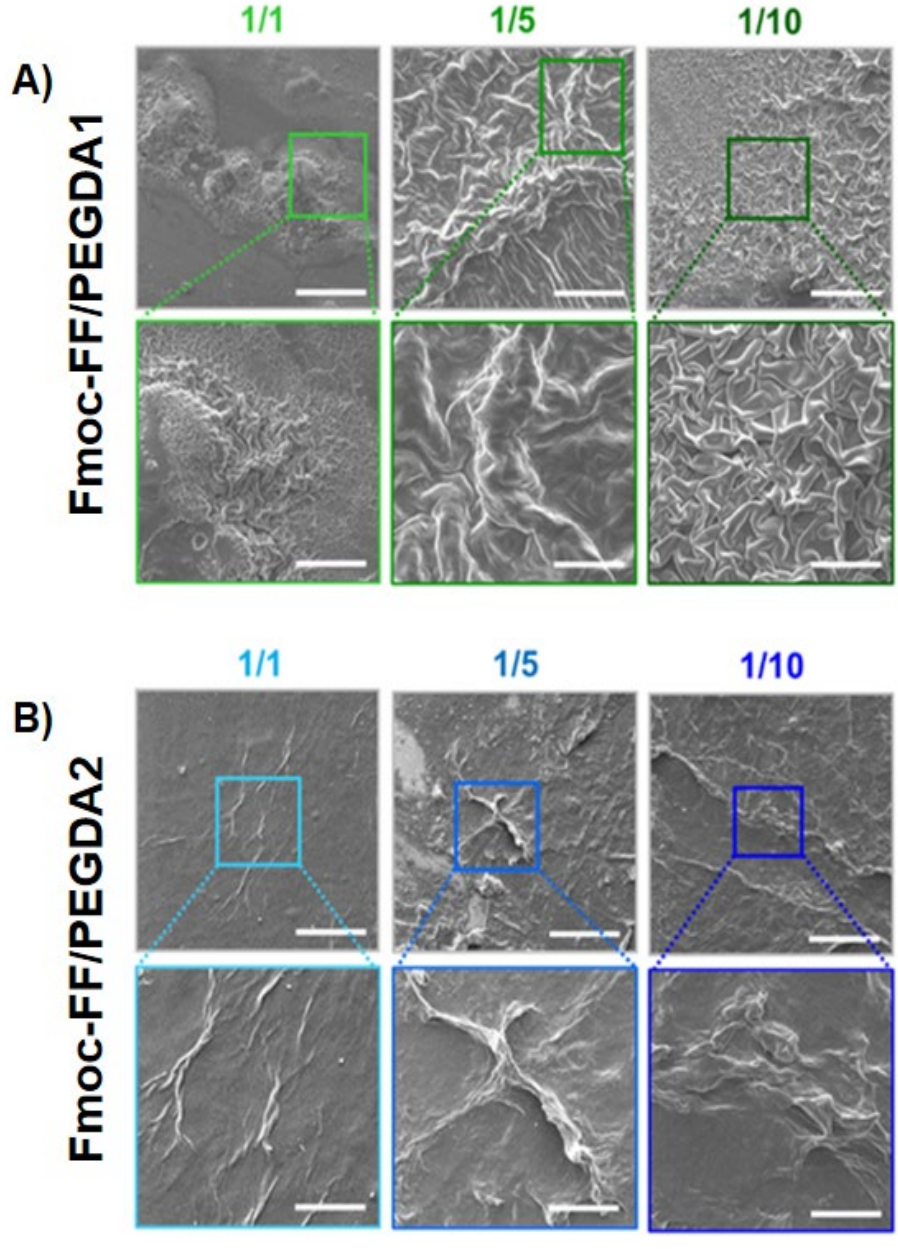

Figure 6. Selected microphotos of mixed xerogels of PEGDA1 (**A**) and PEGDA2 (**B**) series. Scale bar = 100 μm and 30 μm.

For PEGDA1 xerogels, a quasi-fractal drapery surface is detected. The geometric distribution, the fineness, and the grade of detail increase with the amount of PEGDA polymer, letting us postulate that the change in surface morphology is attributed to its intermolecular interaction. On the contrary, PEGDA2 hydrogels show fiber-like architectures, which manifest more in matrices with higher polymer ratios.

The evident discrepancies between PEGDA1 and the two samples indicate a rule of polymer molecular weight in the topological arrangements of the matrices, probably imputable to a different network of H-bonds. This specific physicochemical parameter also changed the peptide-polymer interaction networking, in turn producing very different superficial morphologies in hybrid matrices.

Further structural characterization of the peptide's supramolecular architecture was achieved by a wide-angle X-ray scattering (WAXS) study. Measurements were collected on the macroscopic fibers of samples prepared according to the stretch-frame method [63].

In all the cases, the WAXS data present the typical fiber diffraction pattern with two crossed main axes: the meridional along the fiber direction and the equatorial perpendicular to it (depicted by white arrows in 2D WAXS patterns). The 1D profiles, reported in Figures 7 and 8E–H, have been obtained from the integration along both meridional and equatorial axes of 2D data, and the principal peaks along the axis are schematically summarized in Table S1.

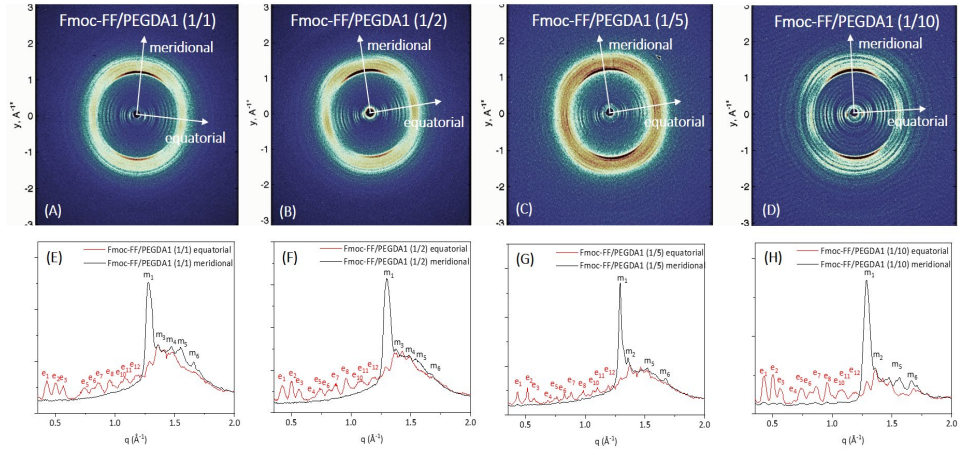

Figure 7. WAXS characterization of the mixed hydrogels Fmoc-FF/PEGDA1 at different concentrations: 2D WAXS data (on the top row right) and 1D WAXS meridional (black line)/equatorial (red line) profiles (on the bottom row).

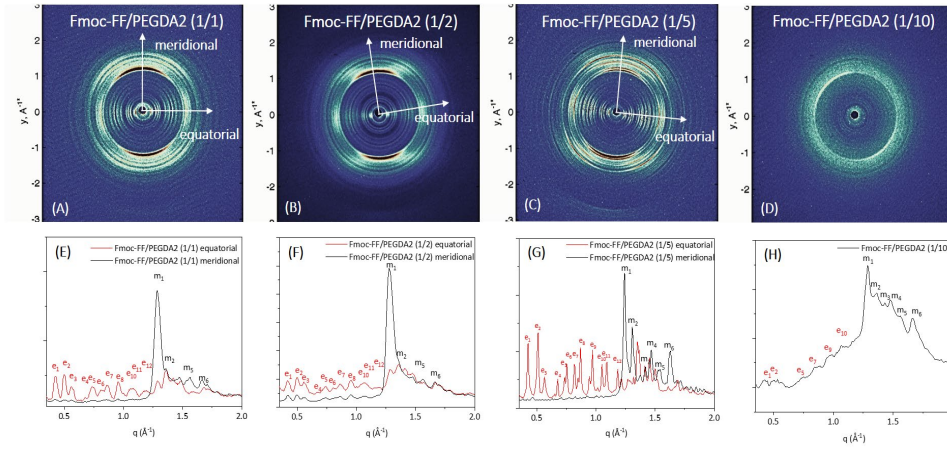

Figure 8. WAXS characterization of the mixed hydrogels Fmoc-FF/PEGDA2 at different concentrations: 2D WAXS data (on the top row right) and 1D WAXS meridional (black line)/equatorial (red line) (on the bottom row).

In all the cases, the WAXS data present the typical fiber diffraction pattern with two crossed main axes: the meridional along the fiber direction and the equatorial perpendicular to it (depicted by white arrows in 2D WAXS patterns). As reported in Figures 7 and 8E–H, 1D profiles have been obtained from the integration along both meridional and equatorial axes of 2D data, and the principal peaks along the axis are schematically summarized in Table S1.

According to data previously collected on the Fmoc-FF hydrogel, hybrid gels containing PEGDA1 or PEGDA2 polymers exhibit the well-known diffraction pattern of cross-β amyloid-like structures, and the two axes (meridional and equatorial) correspond to the axis along the fiber and perpendicular to it, respectively [64]. The main diffraction peak at q = 1.29 $Å^{-1}$ (d = 4.9 Å) gives information on the distance existing between adjacent peptide backbones organized into β-strands along the fiber axis. On the other hand, the peak at q ~ 0.5 $Å^{-1}$ (d = 12.5 Å) can be associated with the distance between two distinct β-sheets. The only exception is the absence of cross-β amyloid-like structures for the sample Fmoc-FF/PEGDA2 (1/10) due to the difficulty of realizing the solid fiber with the described method. The WAXS profiles of mixed hydrogels are very similar to those previously measured for pure Fmoc-FF, whose 2D and 1D WAXS results are reported in Figure S3.

The relevant difference we detect in mixed Fmoc-FF/PEGDA1 and Fmoc-FF/PEGDA2 hydrogels (at different ratios) with respect to pure Fmoc-FF is the presence of several additional equatorial and meridional reflections (see Figures S4 and S5 and Table S1 for positions and corresponding distances). This finding suggests a significant increase in the hierarchical order along the fiber induced by PEGDA1 and PEGDA2 (especially at the higher concentrations of the polymeric component).

2.5. Rheological Characterization

The mechanical response of matrices was evaluated via rheological analysis, describing the viscoelastic behavior of each Fmoc-FF/PEGDA hydrogel (at 0.5 wt%) in terms of G′ (storage modulus) and G″ (loss modulus). The analysis was conducted by performing time-sweep oscillatory measurements (for 15 min, with 1.0 Hz frequency and 0.1% strain), supported by a preliminary identification of the optimal measurement conditions. Specifically, dynamic oscillation strain sweep (at a frequency of 1.0 Hz) and dynamic frequency sweep (at 0.1% strain) were acquired for Fmoc-FF/PEGDA at the two ratios of 1/1 and 1/10 (Figures S6 and S7).

Collectively, the linear viscoelastic region (LVE region) was found in the 0.02–3.0% stain range. The G′ and G″ time sweep values, collected in the histograms of Figure 9 and Table 3, analytically demonstrate the gel state of all the tested matrices due to the values of G′ higher than G″ and tan δ > 1 (G′/G″> 1). All these values are higher than the ones for pure Fmoc-FF at the same concentration (G′~950 Pa), indicating that the multicomponent systems are characterized by enhanced mechanical properties.

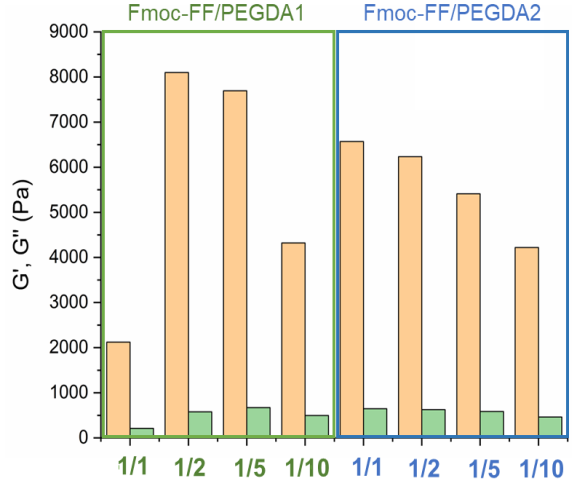

Figure 9. Rheological bar plots of 0.5 wt% mixed HGs. Plot reports both G′ (orange bar) and G″ (green bar) moduli of each time sweep experiment (20 min, strain of 0.1%, frequency 1 Hz). Values are expressed on the Pascal (Pa) logarithmic scale.

Table 3. Hydrogel rheological analysis. Reported data are storage modulus (G′), loss modulus (G″) and tan δ (G′/G″).

Sample	G′ (Pa)	G″ (Pa)	tan δ
Fmoc-FF/PEGDA1 *1/1*	2123	210	10.1
Fmoc-FF/PEGDA1 *1/2*	8099	577	14.0
Fmoc-FF/PEGDA1 *1/5*	7695	672	11.5
Fmoc-FF/PEGDA1 *1/10*	4323	497	8.70
Fmoc-FF/PEGDA2 *1/1*	6569	646	10.2
Fmoc-FF/PEGDA2 *1/2*	6233	625	9.97
Fmoc-FF/PEGDA2 *1/5*	5411	586	9.23
Fmoc-FF/PEGDA2 *1/10*	4220	462	9.13

This evidence has already been reported for other hybrid peptide/polymer or peptide/peptide matrices, suggesting the co-assembly and co-aggregation strategies as suitable methodologies to modify the mechanical performance of matrices [33,34].

In detail, it can be noted that PEGDA1-containing matrices result in greater rigidity than PEGDA2 ones at the same polymer ratio. This evidence is also pointed out by observing comparable strain break points (5 and 6% for PEGDA1 and PEGDA2, respectively) for systems at 1/10 ratios. In contrast, significant differences were found for the strain break points of PEGDA 1 and PEGDA2 at 1/1 ratios (61 and 12%, respectively).

All these data suggest a positive impact of the higher number of non-covalent interactions (H-bound) related to the number of PEG repetitions. According to thermodynamic principles, it is also suggested that there is a linear correlation between the modulus of rigidity and both the molecular weight and concentration of the polymer for pure PEG hydrogels. In the analysis of the Fmoc-FF/PEGDA series, a different trend can be detected for the two polymers. In the PEGDA1 series, G′ value is four times higher when passing from 1/1 to 1/2 ratios (2123 Pa to 8099 Pa). However, a further increase in the polymer does not cause an additional increase of the gel rigidity (7695 Pa for a 1/5 ratio). Finally, it can be observed a decrease in G′ for the gel at a 1/10 ratio (4323 Pa). This trend is also visible by comparing the tan δ values. On the contrary, a gradual and constant reduction of the G′ value is associated with the PEGDA2 series. Analogously, this decrease is also detectable in tan δ ratios. The general rheological behavior of Fmoc-FF/PEGDA hydrogels is not the expected one. Indeed, it was previously observed that an increase in the PEG concentration can allow an improvement in the mechanical modification of supramolecular entanglement. This evidence is indicative of a multifactorial correlation between the final G′ and the total intermolecular network interactions and physical parameters (including water mobility, the total hydrophilicity of the system, a progressive increase in the hydrophilicity for a higher PEGDA ratio, and predictable matrix rigidity).

The modulable mechanical responses of these matrices suggest good applicative versatility. The viscoelastic nature of the HGs recalls their potential employment as scaffold elements for tissue engineering or as tridimensional supporting materials for cell attachments. According to the G′ values, the proposed hydrogels are also candidates as reservoirs for the delivery of active pharmaceutical ingredients (APIs). The G′ values suggest suitable physical entrapment of host molecules and tunability in shape, thickness, and resistance. All these features are compatible with implant development. To further scrutinize this latter purpose, the capability of the resulting matrices to encapsulate and retain a drug was tested.

2.6. Release of Naphthol Yellow S

HGs are often proposed as matrices able to serve as drug reservoirs. Prolonged and modified release of active pharmaceutical ingredients, including small drugs or diagnostics, can be modulated via encapsulation in hydrogel matrices. According to this evidence, we attempted to load the hydrogels with Naphthol Yellow S (NYS), which is a water-soluble disodium salt of 5,7-dinitro-8-hydroxynaphthalene-2-sulfonic acid used as a histological dye and here employed as a drug model (Figure 10A). The hydrophilic nature of NYS

allows for its incorporation it into the hydrogel during the rehydration step of the Fmoc-FF stock solution prepared in DMSO. The macroscopic observation of gels clearly indicates that the loading of the dye into the matrices does not affect the gelation process at the tested concentration (6.02 mmol·L^{-1}). The amount of NYS encapsulated in the gel was considered to be 100% of the loaded dye. Release profiles of NYS from PEGDA-based HGs over time (up to 144 h) are reported in Figure 10 in terms of NYS released percentage.

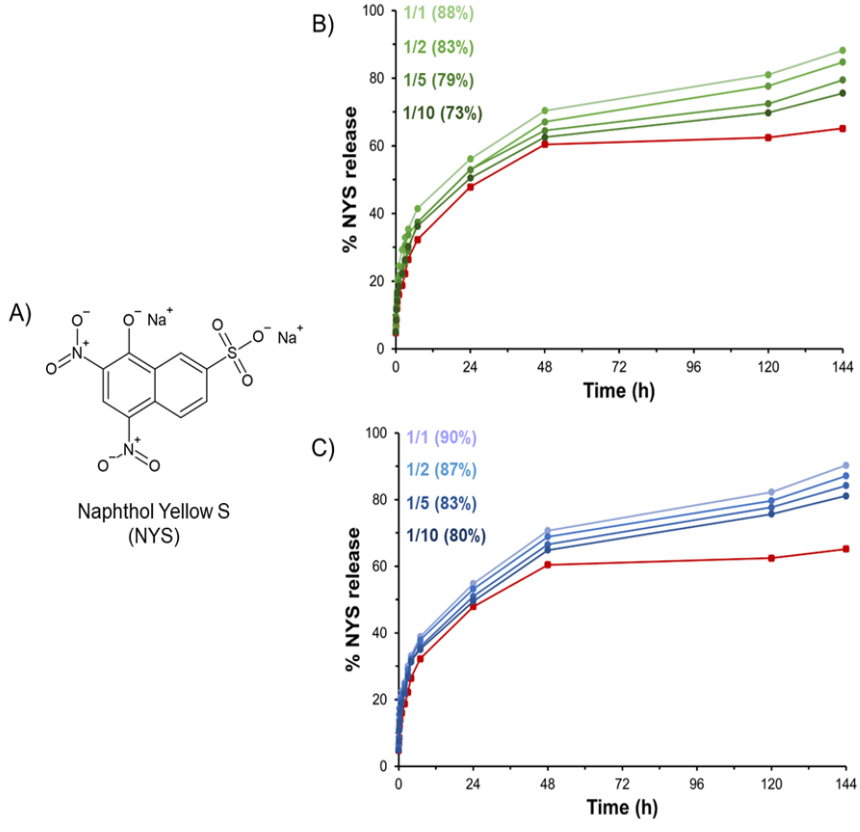

Figure 10. (**A**) Chemical structure of Naphthol Yellow S (NYS). Release profiles of NYS for Fmoc-FF/PEGDA1 (**B**) and for Fmoc-FF/PEGDA2 (**C**) hydrogels at different molar ratios. The NYS release from pure Fmoc-FF hydrogel is also reported for comparison (red line).

From the inspection of Figure 10, it appears that all the mixed hydrogels exhibit a slower release with respect to pure Fmoc-FF HG (red line). This result can be explained as function of the higher swelling ratio q of hybrid hydrogels with respect to Fmoc-FF ones (see Table 1). Indeed, it is reasonable to expect the existence of a relationship between the passive water permeation of the hydrogel and the swelling ratio q, which is indicative of the mobile water in a completely swollen state. Moreover, the released percentage decreases from 88 to 73% and from 90 to 80% for PEGDA1 and PEGDA2, respectively, within the series by moving from a 1/1 to a 1/10 molar ratio. This trend suggests that the increase of PEGDA in the mix allows for higher retention of the NYS into the aqueous hydrogel matrix.

This result is not surprising considering the ability of PEGDA to establish non-covalent interactions such as hydrogen bonds with the NYS. According to this consideration, it is reasonable to expect that the percentage of the drug release decreases with the increase in the PEGDA amount and the PEGDA molecular weight.

3. Conclusions

Short and ultrashort peptides have been identified as manageable, tunable, and versatile building blocks for the fabrication of supramolecular systems. The features of peptides

allow the combination, in the same system, of two or more molecular constituents, which can also differ in chemical characteristics. In the case of the study herein reported, for the first time, the development of mixed peptide-polymer matrices using Fmoc-FF and two different polydisperse diacrylate-capped PEGs (PEGDA, specifically PEGDA 575, PEGDA1, and PEGDA 250, PEGDA2) was evaluated. A solvent switch methodology was used for the hydrogel formulation, and different molar ratios of peptide/polymer (1/1, 1/2, 1/5, and 1/10 mol/mol) were evaluated. Both the polymer molecular weight and abundance were found to be able to modify the features of the hybrid materials in terms of water content, surface topology, stability, and model drug release (Napthol Yellow S) profiles. The supramolecular organization of the hydrogels is dictated by Fmoc-FF self-assembling, as supported by CD, FTIR, and WAXS analysis. Additionally, by simply modifying the quantity of the inserted polymer, a range of mechanically multivalent materials can be formulated, and each of them is easily adaptable to the desired application scope. The rheological analysis pointed out the versatility of the proposed matrices that, even if formed from the same chemical constituents, present different mechanical response. This evidence suggests the potential use of these materials in different application areas. Collectively, the data reported make possible a mutual comparison between the hybrid systems and the pure components, thus confirming the peptide-based approach as an easy, modulable, and accessible strategy for the design of novel nanostructured materials. The capability of these hydrogels to encapsulate NYS, as a very preliminary model drug, demonstrates the proof of concept that they can potentially serve as drug reservoirs for drug delivery applications. However, other important issues such as the hydrogel biocompatibility (at their different molar ratios) and the choice of the drug (in terms of net charge, lipophilicity, and molecular weight) have to be investigated before an in vivo application. Finally, the presence of diacrylate functionalities in the supramolecular Fmoc-FF hydrogel network could be employed to promote a photo-activated cross-linking reaction, thus providing the generation of interpenetrating networks (IPNs) with a higher organization level in the system.

4. Materials and Methods

Material and Methods: Fmoc-FF (in a lyophilized powder state) was purchased from Bachem (Bubendorf, Switzerland). Poly(ethylene glycol) diacrylate (PEGDA) with an average MW of 250 and 575 u.m.a. is commercially available from Merck (Bari, Italy). All the other chemicals are available from Fluka (Bucks, Switzerland), Carlo Erba (Emmendingen, Germany), or LabScan (Stillorgan, Ireland). They were used as received unless otherwise stated. UV-Vis measurements were carried out using a Thermo Fisher Scientific Inc. (Wilmington, Delaware, USA) Nanodrop 2000c, equipped with a 1.0 cm quartz cuvette (Hellma).

Formulation of multicomponent hydrogels: Hydrogels were prepared using the DMSO/H_2O solvent switch methodology. Fmoc-FF was initially dissolved in DMSO at 100 mg/mL. HGs (a volume of 400 µL at a 0.5 wt% concentration) were obtained via hydration of 20 µL of the Fmoc-FF stock with 380 µL of PEGDA solutions. The metastable and opaque mixtures were vortexed (2 s) and aged at room temperature until the formation of a clear, self-supporting hydrogel. The efficiency of gel formation was macroscopically evaluated using the inverted tube test. The different Fmoc-FF/PEGDA molar ratios were obtained using several PEGDA solutions prepared in double distilled water (5.0 mL) by adding different amounts of pure polymers to water. ρ = 1.11 g/mL and ρ = 1.12 g/mL for PEGDA 250 (PEGDA2) and PEGDA 575 (PEGDA1), respectively.

Swelling ratio (q) determination: Hydrogel swelling ratios (*q*) were determined by adding a volume of 1.2 mL of doubly distilled water to each preformed matrix sample (0.50 wt%, V = 400 µL). The samples were then incubated overnight at room temperature. After this period of incubation, the water on top of the matrix was removed and the sample was weighted to collect the *Ws* value, which represents the weight of the swollen hydrogel.

Then, the sample was freeze-dried and weighed again (*Wd*). The determined values were used in Equation (1) to calculate the gelling ratio, *q*.

$$q = \left(\frac{Ws - Wd}{Ws}\right) \cdot 100 \quad (1)$$

Ringer's solution stability test: The degradation of the hydrogels was estimated according to the Ringer's solution stability test, which consists in the estimation of the change in the hydrogel weight when 400 µL of gel (0.50 wt%) is incubated in an oven at 37 °C for 40 days with 1.2 mL of Ringer's solution. This solution contains 12.9 mg of NaCl, 0.45 mg of KCl, and 0.48 mg of $CaCl_2$. The experiment was performed in triplicate. The weight loss ratio (ΔW) was calculated as a percentage according to Equation (2):

$$\Delta W = \left(1 - \frac{Wt}{Wo}\right) \cdot 100 \quad (2)$$

In which *Wo* and *Wt* are the weights of the hydrogel before and after the addition of the Ringer's solution, respectively.

Dehydration curve: Dehydration profiles were acquired on 100 µL of each of the gel samples (0.5 wt%), located in a silicon mask on a glass slide. Each sample was initially weighed. Then, weight points were collected at: 0 min, 5 min, 10 min, 20 min, 30 min, 1 h, 2 h, 3 h, 4 h, 5 h, 6 h, 7 h, and 24 h. Dehydration was evaluated in terms of weight variation. The curve was reported as a residual weight percentage.

Relaxometry: NMRD (nuclear magnetic relaxation dispersion) profiles were measured on a SMARtracer fast-field-cycling relaxometer (Stelar S.n.c., Mede (PV), Italy) equipped with a Stelar VTC-91 for temperature control, from 0.01 to 10 MHz at 25 °C. Relaxation rates were measured at 16 different values of the applied magnetic field with an acquisition field of 7.2 MHz, a polarization field of 8.5 MHz, polarization time, and relaxation delay 4 times T1, 16 sampled delay times, and a switching time of 3 ms. Each NMRD profile was fitted according to the same model-free approach used in our previous investigation [27], similarly to that performed on other biomolecules in the presence of two distinct levels of motion (slow and fast) [65,66].

Circular Dichroism (CD): Far-UV CD profiles were collected in the 350–190 nm wavelength range on a Jasco J-810 spectropolarimeter (equipped with a NesLab RTE111 thermal controller unit) and performed at 25 °C in a 0.1 mm quartz cell. A total of 150 µL of metastable mixtures (immediately after their generation) were kept undergoing gelation in cells. Other experimental settings used for the measurements are the following: sensitivity = 5 mdeg, scan speed = 20 nm·min^{-1} time constant = 16 s, bandwidth = 1 nm. Each spectrum was obtained by averaging three different scans. All the spectra are reported in optical density (mdeg/O.D.).

Fourier-transform infrared spectroscopy (FTIR): FTIR analysis was conducted on 400 µL of each gel (0.5 wt%) on a Jasco FT/IR 4100 spectrometer (Easton, MD) in the 400–4000 cm^{-1} acquisition range. The deconvolution of the amide I region was performed with built-in software. The spectra were collected in transmission mode and then converted into emission. Each sample was recorded with a total of 120 scans at a rate of 4 mm·s^{-1} against a KBr background.

Xerogel Thioflavin T (ThT) assay: the ThT assay was conducted on Fmoc-FF/PEGDA hydrogels in their xerogel forms. Macroscopic HGs were spread on a clean coverslip glass and dried overnight. The obtained samples were stained for 30 sec with 50 µL of a water solution of ThT (50 µmol·L^{-1}). After removing the dye excess with filter paper, samples were dried overnight. Stained xerogels were imaged using a fluorescence Leica DFC320 video-camera (Leica, Milan, Italy) connected to a Leica DMRB microscope equipped with a 20 X objective and a Green Fluorescent Protein (GPF) filter. The software Image J (National Institutes of Health, Bethesda, MD) was used for analysis.

Congo Red assay: Congo Red (CR) assay was performed on samples both in solution and in the solid state. In solution, absorbance measurements of CR solution alone or mixed with hydrogels were recorded on a Nanodrop 2000c spectrophotometer equipped with a 1.0 cm quartz cuvette (Hellma). A stock solution of CR (3.5 mg in 500 μL) was freshly prepared in water and filtered through a 0.2 μm syringe. A total of 5 μL of this solution, 12-fold diluted, was added into 380 μL of each PEGDA solution used for hydration of the Fmoc-FF stock solution. The final CR concentration is 10 $\mu mol \cdot L^{-1}$. UV-Vis spectra of the samples were recorded between 400 and 700 nm at room temperature, and background was subtracted using a Congo Red spectrum in water as a reference solution. Xerogels, prepared on glass slides for deposition and air-drying of preformed hydrogels (~40 μL), were stained for a few seconds with a droplet (~5 μL) of a fresh CR solution, prepared as previously described [27]. Films were then observed under bright-field illumination and between crossed polars by using a Nikon AZ100 microscope.

Scanning Electron Microscopy (SEM): Fmoc-FF/PEGDA hydrogels were positioned on aluminum cover slips and left to air-dry at ambient conditions overnight. Then, the obtained xerogels were coated with Au film and imaged using a SEM (JEOL, Tokyo, Japan) operating at 20 kV.

Wide-Angle and Small-Angle X-Ray scattering: WAXS patterns were recorded from solid fibers prepared by the stretch frame method. An aliquot of ~20 μL of metastable, freshly prepared DMSO/H2O solutions (0.5 wt% final gel concentration) was placed between the ends of a wax-coated capillary (spaced 1.5 mm apart). The droplet was air-dried overnight, obtaining solid fibers [32]; 2D WAXS data were collected, as previously described, from the fibers at the X-ray MicroImaging Laboratory (XMI-L@b), equipped with an Fr-E + SuperBright rotating anode table-top microsource (Cu Kα, λ = 0.15405 nm, 2475 W), a multilayer focusing optics (Confocal Max-Flux; CMF 15-105), and a three-pinhole camera (Rigaku SMAX-3000) [67,68].

Rheological characterization: Rheological measurements were performed at 25 °C using a rotationally controlled stress rheometer (Malvern Kinexus) equipped with a 15.0 mm flat-plate geometry (PU20:PL61). A freshly prepared hydrogel sample (360 μL) at a concentration of 0.5 wt% was used for each experiment and located in a humidity chamber. A gap of 1.0 mm was used during measurements. Preliminary strain (0.01–100%) and oscillatory frequency (0.01–100 Hz) sweeps were conducted to identify the regime of linear viscoelasticity. Time-sweep oscillatory tests (in a 0.1% strain and 1.0 Hz frequency regime) were performed for 20 min. Final analyses are reported as G'(storage elastic modulus)/G" (shear loss or viscous modulus) ratio in Pascal [Pa].

Naphthol yellow S encapsulation and release: Naphthol yellow S (NYS) was encapsulated (at a final concentration of 6.02 mmol/L) in 400 μL of hybrid HGs, modifying the previously reported methodology. A solution of NYS, prepared in water, was analytically quantified via UV-Vis, using the molar extinction coefficient ε_{430} = 9922 $L \cdot cm^{-1} \cdot mol^{-1}$. ([NYS] = 0.012 $mol \cdot L^{-1}$). Then, 200 μL was added to properly prepare more concentrated solutions of PEGDA. These bicomponent solutions were used to rehydrate the Fmoc-FF DMSO stock in conical tubes (1.5 mL). On the top of the HGs, 800 μL of water was located. At well-defined time points, 400 μL of the top solution was replaced with an equal aliquot of water. The quantification of the NYS released from the hydrogels was assessed on the collected supernatants by UV-Vis spectroscopy (Abs at 430 nm). The amount of released dye was plotted as a percentage of the ratio between the amount released over time and the total loaded one. All the experiments were performed in triplicate.

Supplementary Materials: The following supporting information can be downloaded at: https://www.mdpi.com/article/10.3390/gels8120831/s1, Figure S1: Self-supporting hydrogel of Fmoc-FF/PEGDA1 1/50 mol/mol ratio; Figure S2: Water retention curve of mixed Fmoc-FF/PEGDA hydrogels. Figure S3: WAXS characterization of the mixed hydrogels Fmoc-FF: 2D WAXS data (on the left) and 1D WAXS meridional/equatorial profiles (on the right). Figure S4: Superimposition of 1D WAXS equatorial (A, B, C, D) and meridional (E, F, G, H) profiles for Fmoc-FF HG and PEGDA1 based HGs at the studied molar ratio. Figure S5: Superimposition of 1D WAXS equatorial (A, B,

C, D) and meridional (E, F, G, H) profiles for Fmoc-FF HG and PEGDA2-based HGs at the studied molar ratio. Figure S6: Oscillation time sweeps tests for PEGDA1 1/1 (A) and PEGDA1 1/10 (C); frequency time sweeps tests for PEGDA1 1/1 (B) and PEGDA1 1/10 (D). Figure S7: Oscillation time sweeps tests for PEGDA2 1/1 (A) and PEGDA2 1/10 (C); frequency time sweeps tests for PEGDA2 1/1 (B) and PEGDA2 1/10 (D). Table S1: Meridional and equatorial peak positions in q ($Å^{-1}$) and corresponding distance d = 2π/q (Å) of the mixed hydrogels; in red, the common peak with the Fmoc-FF reference fiber.

Author Contributions: Conceptualization, C.D., A.A. and G.M.; methodology, all authors; software, E.R., C.D. and E.G. (Eliana Gianolio); validation, E.R., E.G. (Enrico Gallo), T.S., S.R., P.L.S. and C.D.; formal analysis, C.D., C.G., A.A., G.M. and E.G. (Eliana Gianolio); investigation, all authors; resources, A.A., G.M., C.G. and E.G. (Eliana Gianolio); data curation, all authors; writing—original draft preparation, all authors; writing—review and editing, all authors; visualization, E.R., E.G. (Enrico Gallo), S.R., T.S., P.L.S. and C.D.; supervision, C.G., E.G. (Eliana Gianolio), A.A. and C.D.; funding acquisition, A.A., G.M., E.G. (Eliana Gianolio) and C.G. All authors have read and agreed to the published version of the manuscript.

Funding: This research received no external funding.

Institutional Review Board Statement: Not applicable.

Informed Consent Statement: Not applicable.

Data Availability Statement: Not applicable.

Conflicts of Interest: The authors declare no conflict of interest.

References

1. Yao, S.; Brahmi, R.; Portier, F.; Putaux, J.-L.; Chen, J.; Halila, S. Hierarchical self-assembly of amphiphilic β-C-glycosylbarbiturates into multiresponsive alginate-like supramolecular hydrogel fibers and vesicle hydrogel. *Chem. Eur. J.* **2021**, *27*, 16716–16721. [CrossRef] [PubMed]
2. Das, D.; Ghosh, P.; Dhara, S.; Panda, A.B.; Pal, S. Stimulus-responsive, biodegradable, biocompatible, covalently cross-linked hydrogel based on dextrin and poly(N-isopropylacrylamide) for in vitro/in vivo controlled drug release. *ACS Appl. Mater. Interf.* **2015**, *7*, 4791–4803. [CrossRef] [PubMed]
3. Cho, I.S.; Ooya, T. Cell-encapsulating hydrogel puzzle: Polyrotaxane-based self-healing hydrogels. *Chem. Eur. J.* **2020**, *26*, 913–920. [CrossRef]
4. Gallo, E.; Diaferia, C.; Rosa, E.; Smaldone, G.; Morelli, G.; Accardo, A. Peptide-based hydrogels and nanogels for delivery of doxorubicin. *Int. J. Nanomed.* **2021**, *16*, 1617–1630. [CrossRef] [PubMed]
5. Gogurla, N.; Roy, B.; Min, K.; Park, J.-Y.; Kim, S. A Skin-inspired, interactive, and flexible optoelectronic device with hydrated melanin nanoparticles in a protein hydrogel–elastomer hybrid. *Adv. Mater. Technol.* **2020**, *5*, 1900936. [CrossRef]
6. Giuri, D.; D'Agostino, S.; Ravino, P.; Faccio, D.; Falini, G.; Tommasini, C. Water remediation from pollutant agents by the use of an environmentally friendly supramolecular hydrogel. *ChemNanoMat* **2022**, *8*, e202200093. [CrossRef]
7. Diaferia, C.; Netti, F.; Ghosh, M.; Sibillano, T.; Giannini, C.; Morelli, G.; Adler-Abramovich, L.; Accardo, A. Bi-functional peptide-based 3D hydrogel-scaffolds. *Soft Matter* **2020**, *16*, 7006–7017. [CrossRef]
8. Draper, E.R.; Adams, D.J. Low-molecular-weight gels: The state of the art. *Chem* **2017**, *3*, 390–410. [CrossRef]
9. Aykent, G.; Zeytun, C.; Marion, A.; Özçubukçu, S. Simple tyrosine derivatives act as low molecular weight organogelators. *Sci. Rep.* **2019**, *9*, 4893. [CrossRef]
10. Giuri, D.; Zanna, N.; Tommasini, C. Low molecular weight gelators based on functionalized l-dopa promote organogels formation. *Gels* **2019**, *5*, 27. [CrossRef]
11. Prince, E.; Kumacheva, E. Design and applications of man-made biomimetic fibrillar hydrogels. *Nat. Rev.* **2019**, *4*, 99–115. [CrossRef]
12. Diaferia, C.; Rosa, E.; Balasco, N.; Sibillano, T.; Morelli, G.; Giannini, C.; Vitagliano, L.; Accardo, A. The introduction of a cysteine residue modulates the mechanical properties of aromatic-based solid aggregates and self-supporting hydrogels. *Chem. Eur. J.* **2021**, *27*, 14886–14898. [CrossRef] [PubMed]
13. Wychowaniec, K.; Smith, A.M.; Ligorio, C.; Mykhaylyk, O.O.; Miller, A.F.; Saiani, A. Role of sheet-edge interactions in β-sheet self-assembling peptide hydrogels. *Biomacromolecules* **2020**, *21*, 2285–2297. [CrossRef] [PubMed]
14. Jayawarna, V.; Ali, M.; Jowitt, T.; Miller, A.F.; Saiani, A.; Gough, J.E.; Ulijn, R.V. Nanostructured hydrogels for three-dimensional cell culturethrough self-assembly of fluorenylmethoxycarbonyl–dipeptides. *Adv. Mater.* **2006**, *18*, 611–614. [CrossRef]
15. Mahler, A.; Reches, M.; Rechter, M.; Cohen, S.; Gazit, E. Rigid, Self-assembled hydrogel composed of a modified aromatic dipeptide. *Adv. Mater.* **2006**, *18*, 1365–1370. [CrossRef]

16. Fuentes, E.; Boháčová, K.; Fuentes-Caparrós, A.M.; Schweins, R.; Draper, E.R.; Adams, D.J.; Pujals, S.; Albertazzi, L. PAINT-ing fluorenylmethoxycarbonyl (Fmoc)-diphenylalanine hydrogels. *Chem. Eur. J.* **2020**, *26*, 9869–9873. [CrossRef]
17. Fuentes-Caparrós, A.M.; Canales-Galarza, Z.; Barrow, M.; Dietrich, B.; Läuger, J.; Nemeth, M.; Draper, E.R.; Adams, J.D. Mechanical characterization of multilayered hydrogels: A rheological study for 3D-printed systems. *Biomacromolecules* **2021**, *22*, 1625–1638. [CrossRef]
18. Dudukovic, N.; Hudson, B.C.; Paravastu, A.K.; Zukoski, C.F. Self-assembly pathways and polymorphism in peptide-based nanostructures. *Nanoscale* **2018**, *10*, 15081516. [CrossRef]
19. Levine, M.S.; Ghosh, M.; Hesser, M.; Hennessy, N.; Di Guiseppi, D.M.; Adler-Abramovich, L.; Schweitzer-Stenner, R. Formation of peptide-based oligomers in dimethylsulfoxide: Identifying the precursor of fibril formation. *Soft Matter* **2020**, *16*, 7860–7878. [CrossRef]
20. Diaferia, C.; Rosa, E.; Morelli, G.; Accardo, A. Fmoc-diphenylalanine hydrogels: Optimization of preparation methods and structural insights. *Pharmaceuticals* **2022**, *15*, 1048. [CrossRef]
21. Najafi, H.; Abolmaali, S.; Heidari, R.; Valizadeh, H.; Tamaddon, A.M.; Azarpira, N. Integrin receptor-binding nanofibrous peptide hydrogel for combined mesenchymal stem cell therapy and nitric oxide delivery in renal ischemia/reperfusion injury. *Stem. Cell Res. Ther.* **2022**, *13*, 344. [CrossRef] [PubMed]
22. Chen, J.; Zhang, S.; Chen, X.; Wang, L.; Yang, W. A Self-Assembled Fmoc-diphenylalanine hydrogel-encapsulated Pt nanozyme as oxidase- and peroxidase-like breaking pH limitation for potential antimicrobial application. *Chem. Eur. J.* **2022**, *28*, e202104247. [CrossRef] [PubMed]
23. Diaferia, C.; Morelli, G.; Accardo, A. Fmoc-diphenylalanine as a suitable building block for the preparation of hybrid materials and their potential applications. *J. Mater. Chem. B* **2019**, *7*, 5142–5155. [CrossRef] [PubMed]
24. Nikolaou, V.; Charalambidis, G.; Coutsolelos, A. Photocatalytic hydrogen production of porphyrin nanostructures: Spheres vs. fibrils, a case study. *Chem. Commun.* **2021**, *57*, 4055–4058. [CrossRef] [PubMed]
25. Netti, F.; Aviv, M.; Dan, Y.; Rudnick-Glick, S.; Halperin-Sternfeld, M.; Adler-Abramovich, L. Stabilizing gelatin-based bioinks under physiological conditions by incorporation of ethylene-glycol-conjugated Fmoc-FF peptides. *Nanoscale* **2022**, *14*, 8525–8533. [CrossRef]
26. MacPherson, D.; Bram, Y.; Park, J.; Schwartz, R.E. Peptide-based scaffolds for the culture and maintenance of primary human hepatocytes. *Sci. Rep.* **2021**, *11*, 6772. [CrossRef] [PubMed]
27. Rosa, E.; Diaferia, C.; Gianolio, E.; Sibillano, T.; Gallo, E.; Smaldone, G.; Stornaiuolo, M.; Giannini, C.; Morelli, G.; Accardo, A. Multicomponent hydrogel matrices of Fmoc-FF and cationic peptides for application in tissue engineering. *Macromol. Biosci.* **2022**, *22*, 2200128. [CrossRef] [PubMed]
28. Shim, J.; Kang, J.; Yun, S.I. Chitosan-dipeptide hydrogels as potential anticancer drug delivery systems. *Int. J. Biol. Macromol.* **2021**, *187*, 399–408. [CrossRef]
29. Son, G.; Kim, J.; Park, B.C. Interference of solvatochromic twist in amyloid nanostructure for light-driven biocatalysis. *ACS Appl. Energy Mater.* **2020**, *3*, 1215–1221. [CrossRef]
30. Inostroza-Brito, K.E.; Collin, E.; Siton-Mendelson, O.; Smith, K.H.; Monge-Marcet, A.; Ferreira, D.S.; Rodríguez, R.P.; Alonso, M.; Rodríguez-Cabello, J.C.; Reis, R.L.; et al. Co-assembly, spatiotemporal control and morphogenesis of a hybrid protein–peptide system. *Nat. Chem.* **2015**, *7*, 897–904. [CrossRef]
31. Okesola, B.O.; Lau, H.K.; Berkus, H.; Boccorh, D.K.; Wu, Y.; Wark, A.W.; Kiick, K.L.; Mata, A. Covalent co-assembly between resilin-like polypeptide and peptide amphiphile into hydrogels with controlled nanostructure and improved mechanical properties. *Biomater. Sci.* **2020**, *8*, 846–857. [CrossRef] [PubMed]
32. Wakabayashi, R.; Imatani, R.; Katsuya, M.; Higuchi, Y.; Noguchi, H.; Kamiya, N.; Goto, M. Hydrophobic immiscibility controls self-sorting or co-assembly of peptide amphiphiles. *Chem. Commun.* **2022**, *58*, 585–588. [CrossRef] [PubMed]
33. Halperin-Sternfeld, M.; Ghosh, M.; Sevostianov, R.; Grigoriants, I.; Adler-Abramovich, L. Molecular co-assembly as a strategy for synergistic improvement of the mechanical properties of hydrogels. *Chem. Commun.* **2017**, *53*, 9586–9589. [CrossRef] [PubMed]
34. Diaferia, C.; Ghosh, M.; Sibillano, T.; Gallo, E.; Stornaiuolo, M.; Giannini, C.; Morelli, G.; Adler-Abramovich, L.; Accardo, A. Fmoc-FF and hexapeptide-based multicomponent hydrogels as scaffold materials. *Soft Matter* **2019**, *15*, 487–496. [CrossRef] [PubMed]
35. Hassan, M.; Martin, A.D.; Thordarson, P. Macromolecular crowding and hydrophobic effects on Fmoc-diphenylalanine hydrogel formation in PEG: Water mixtures. *J. Mater. Chem. B* **2015**, *3*, 9269–9276. [CrossRef]
36. Chakraborty, P.; Guterman, T.; Adadi, N.; Yadid, M.; Brosh, T.; Adler-Abramovich, L.; Dvir, T.; Gazit, E. A self-healing, all-organic, conducting, composite peptide hydrogel as pressure sensor and electrogenic cell soft substrate. *ACS Nano* **2019**, *13*, 163–175. [CrossRef]
37. Knop, K.; Hoogenboom, R.; Fischer, D.; Schubert, U.S. Poly(ethylene glycol) in drug delivery: Pros and cons as well as potential alternatives. *Angew. Chem. Int. Ed.* **2010**, *49*, 6288–6308. [CrossRef]
38. Diaferia, C.; Sibillano, T.; Balasco, N.; Giannini, C.; Roviello, V.; Vitagliano, L.; Morelli, G.; Accardo, A. Hierarchical Analysis of Self-Assembled PEGylated hexaphenylalanine photoluminescent nanostructures. *Chem. Eur. J.* **2016**, *22*, 16586–16597. [CrossRef]
39. Trucillo, P.; Reverchon, E. Production of PEG-coated liposomes using a continuous supercritical assisted process. *J. Supercri. Flu.* **2021**, *167*, 105048. [CrossRef]

40. Accardo, A.; Morisco, A.; Gianolio, E.; Tesauro, D.; Mangiapia, G.; Radulescu, A.; Brandt, A.; Morelli, G. Nanoparticles containing octreotide peptides and gadolinium complexes for MRI applications. *J. Pept. Sci.* **2011**, *17*, 154–162. [CrossRef]
41. Raeburn, J.; Mendoza-Cuenca, C.; Cattoz, B.N.; Little, M.A.; Terry, A.E.; Cardoso, A.Z.; Griffiths, P.C.; Adams, D.J. The effect of solvent choice on the gelation and final hydrogel properties of Fmoc–diphenylalanine. *Soft Matter* **2015**, *11*, 927–935. [CrossRef] [PubMed]
42. Fuentes-Caparros, A.M.; McAulay, K.; Rogers, S.E.; Dalgliesh, M.R.; Adams, D.J. On the mechanical properties of N-functionalised dipeptide gels. *Molecules* **2019**, *24*, 3855. [CrossRef] [PubMed]
43. Gun'ko, V.M.; Savina, I.N.; Mikhalovsky, S.V. Properties of water bound in hydrogels. *Gels* **2017**, *3*, 37. [CrossRef] [PubMed]
44. Giraud, T.; Bouguet-Bonnet, S.; Stébé, M.J.; Richaudeau, L.; Pickaert, G.; Averlant-Petit, M.C.; Stefan, L. Co-assembly and multicomponent hydrogel formation upon mixing nucleobase-containing peptides. *Nanoscale* **2021**, *13*, 10566. [CrossRef] [PubMed]
45. Mikac, U.; Sepe, A.; Gradišek, A.; Kristl, J.; Apih, T. Dynamics of water and xanthan chains in hydrogels studied by NMR relaxometry and their influence on drug release. *Int. J. Pharm.* **2019**, *563*, 373–383. [CrossRef]
46. Kimmich, R.; Fatkullin, N. Polymer chain dynamics and NMR. *Adv. Pol. Sci.* **2004**, *170*, 1–113.
47. Rössler, E.A.; Stapf, S.; Fatkullin, N. Potential and limits of a colloid approach to protein solutions. *Curr. Op. Coll. Interf. Sci.* **2013**, *18*, 173–182. [CrossRef]
48. Giraud, T.; Bouguet-Bonnet, S.; Marchal, P.; Pickaert, G.; Averlant-Petit, M.C.; Stefan, L. Improving and fine-tuning the properties of peptide-based hydrogels via incorporation of peptide nucleic acids. *Nanoscale* **2020**, *12*, 19905. [CrossRef]
49. Ravera, E.; Fragai, M.; Parigi, G.; Luchinat, C. Differences in Dynamics between crosslinked and non-crosslinked hyaluronates measured by using Fast Field-Cycling Relaxometry. *ChemPhysChem* **2015**, *16*, 2803–2809. [CrossRef]
50. Castelletto, V.; Hamley, I.W. Self-assembly of a model amphiphilic phenylalanine peptide/polyethylene glycol block copolymer in aqueous solution. *Biophys. Chem.* **2009**, *141*, 169–174.
51. Joshi, V.; Shivach, T.; Yadav, N.; Rathore, A.S. Circular dichroism spectroscopy as a tool for monitoring aggregation in monoclonal antibody therapeutics. *Anal. Chem.* **2014**, *86*, 11606–11613. [CrossRef] [PubMed]
52. Diaferia, C.; Sibillano, T.; Altamura, D.; Roviello, V.; Vitagliano, L.; Giannini, C.; Morelli, G.; Accardo, A. Structural characterization of PEGylated hexaphenylalanine. *Chem. Eur. J.* **2017**, *23*, 14039–14048. [CrossRef] [PubMed]
53. Micsonai, A.; Wien, F.; Kernya, L.; Lee, Y.-H.; Goto, Y.; Réfrégiers, M.; Kardos, J. Accurate secondary structure prediction and fold recognition for circular dichroism spectroscopy. *Proc. Natl. Acad. Sci. USA* **2015**, *112*, E3095–E3103. [CrossRef] [PubMed]
54. Bakshi, K.; Liyanage, M.R.; Volkin, D.B.; Middaugh, C.R. Fourier transform infrared spectroscopy of peptides. *Meth. Mol. Biol.* **2014**, *1088*, 255–269.
55. Yang, H.; Yang, S.; Kong, J.; Dong, A.; Yu, S. Obtaining information about protein secondary structures in aqueous solution using Fourier transform IR spectroscopy. *Nat. Prot.* **2015**, *10*, 382–396. [CrossRef] [PubMed]
56. Lomont, J.P.; Ostrander, J.S.; Ho, J.-J.; Petti, M.K.; Zanni, M.T. Not all β-Sheets are the same: Amyloid infrared spectra, transition dipole strengths, and couplings investigated by 2D IR spectroscopy. *J. Phys. Chem. B.* **2017**, *121*, 8935–8945. [CrossRef]
57. Adochitei, A.; Drochioiu, G. Rapid characterization of peptide secondary structure by FT-IR spectroscopy. *Rev. Roum. Chim.* **2011**, *56*, 783–791.
58. Diaferia, C.; Balasco, N.; Sibillano, T.; Giannini, C.; Vitagliano, L.; Morelli, G.; Accardo, A. Structural characterization of self-assembled tetra-tryptophan based nanostructures: Variations on a common theme. *ChemPhysChem* **2018**, *19*, 1635–1642. [CrossRef]
59. Hudson, S.A.; Ecroyd, H.; Kee, T.W.; Carver, J.A. The thioflavin T fluorescence assay for amyloid fibril detection can be biased by the presence of exogenous compounds. *FESEB J.* **2009**, *276*, 5960–5972. [CrossRef]
60. Apter, B.; Lapshina, N.; Barhom, H.; Fainberg, B.; Handelman, A.; Accardo, A.; Diaferia, C.; Ginzburg, P.; Morelli, G.; Rosenman, G. Fluorescence phenomena in amyloid and amyloidogenic bionanostructures. *Crystal* **2020**, *10*, 668. [CrossRef]
61. Orsi, S.; Guarnieri, D.; Netti, P.A. Design of novel 3D gene activated PEG scaffolds with ordered pore structure. *J. Mat. Sci. Mater. Med.* **2010**, *21*, 1013–1020. [CrossRef] [PubMed]
62. Madaghiele, M.; Salvatore, L.; Demitri, C.; Sannino, A. Fast synthesis of poly(ethylene glycol) diacrylate cryogels via UV irradiation. *Mater. Lett.* **2018**, *218*, 305–308. [CrossRef]
63. Sunde, M.; Serpell, L.C.; Bartlam, M.; Fraser, P.E.; Pepys, M.B.; Blake, C.C.F. Common core structure of amyloid fibrils by synchrotron X-ray diffraction. *J. Mol. Biol.* **1997**, *273*, 729. [CrossRef] [PubMed]
64. Serpell, L.C. Alzheimer's amyloid fibrils: Structure and assembly. *Biochim. Biophys. Acta* **2000**, *1502*, 16–30. [CrossRef]
65. Halle, B.; Jóhannesson, H.; Venu, K. Model-free analysis of stretched relaxation dispersions. *J. Magn. Reson.* **1998**, *135*, 1–13. [CrossRef]
66. Bertini, I.; Fragai, M.; Luchinat, C.; Parigi, G. ^{1}H NMRD profiles of diamagnetic proteins: A model-free analysis. *Magn. Reson. Chem.* **2000**, *38*, 543–550. [CrossRef]
67. Altamura, D.; Lassandro, R.; Vittoria, F.A.; De Caro, L.; Siliqi, D.; Ladisa, M.; Giannini, C. X-ray microimaging laboratory (XMI-LAB). *J. Appl. Crystallogr.* **2012**, *45*, 869–873. [CrossRef]
68. Sibillano, T.; De Caro, L.; Altamura, D.; Siliqi, D.; Ramella, M.; Boccafoschi, F.; Ciasca, G.; Campi, G.; Tirinato, L.; Di Fabrizio, E.; et al. An optimized table-top small-angle X-ray scattering set-up for the nanoscale structural analysis of soft matter. *Sci. Rep.* **2014**, *4*, 6985. [CrossRef]